AFAL-TR-79-1012

12

IR SIGNATURE STUDY

Alexander S. Zachor, James A. Holzer, Frederick G. Smith

Honeywell Electro-Optics Center
2 Forbes Road
Lexington, MA 02173

FEBRUARY 1979

Final Technical Report for Period 15 August 1977 - 30 November 1978

Approved for public release; distribution unlimited

Prepared for

AIR FORCE AVIONICS LABORATORY
AIR FORCE WRIGHT AERONAUTICAL LABORATORIES
AIR FORCE SYSTEMS COMMAND
WRIGHT-PATTERSON AIR FORCE BASE, OHIO

NOTICE

This report has been reviewed by the Information Office (OI) and is releasable to the National Technical Information Service (NTIS). At NTIS, it will be available to the general public, including foreign nations.

This technical report has been reviewed and is approved for publication.

Richard B. Sanderson
RICHARD B. SANDERSON
Project Engineer

William F. Bahret
WILLIAM F. BAHRET
Chief, Passive ECM Branch
Electronic Warfare Division

AIR FORCE/56780/24 July 1979 — 100

SECURITY CLASSIFICATION OF THIS PAGE (When Data Entered)

REPORT DOCUMENTATION PAGE		**READ INSTRUCTIONS BEFORE COMPLETING FORM**
1. REPORT NUMBER (19) (18) AFAL-TR-79-1012	2. GOVT ACCESSION NO.	3. RECIPIENT'S CATALOG NUMBER rept.
4. TITLE (and Subtitle) (6) IR SIGNATURE STUDY	(9)	5. TYPE OF REPORT & PERIOD COVERED FINAL 15 AUG 1977 to 30 NOV 1978
		6. PERFORMING ORG. REPORT NUMBER (14) 7812-8
7. AUTHOR(s) (10) Alexander S. Zachor, James A. Holzer, Frederick G. Smith (Science Applications Inc.)	(15)	8. CONTRACT OR GRANT NUMBER(s) F33615-77-C-1124
9. PERFORMING ORGANIZATION NAME AND ADDRESS HONEYWELL Electro-Optics Center 2 Forbes Road Lexington, MA 02173	(16)	10. PROGRAM ELEMENT, PROJECT, TASK AREA & WORK UNIT NUMBERS (17) 7633-11-39
11. CONTROLLING OFFICE NAME AND ADDRESS AFAL/WRP Wright-Patterson AFB, OHIO 45433 Contract Monitor: Richard B. Sanderson (WRP-1)	(11)	12. REPORT DATE February 1979
		13. NUMBER OF PAGES 282
14. MONITORING AGENCY NAME & ADDRESS (if different from Controlling Office) (12) 282p.		15. SECURITY CLASS. (of this report) UNCLASSIFIED
		15a. DECLASSIFICATION/DOWNGRADING SCHEDULE

16. DISTRIBUTION STATEMENT (of this Report)

Approved for public release; distribution unlimited.

17. DISTRIBUTION STATEMENT (of the abstract entered in Block 20, if different from Report)

18. SUPPLEMENTARY NOTES

19. KEY WORDS (Continue on reverse side if necessary and identify by block number)

Background models
Infrared background signatures
Spectral signatures
False Threats
Blue Spike emission

20. ABSTRACT (Continue on reverse side if necessary and identify by block number)

Infrared signature models covering the 3.5 to 5-micrometer spectral region have been developed for events likely to produce false alarms in airborne IR warning receivers defending against SAM and AAM threats. The models can be used to predict the spectral radiation of clouds, ocean sunglitter, uniform specular sunglints, hot gas effluents representing industrial emissions and threat plumes, and the apparent spectral

next page

DD FORM 1 JAN 73 1473 EDITION OF 1 NOV 65 IS OBSOLETE

SECURITY CLASSIFICATION OF THIS PAGE (When Data Entered)

313 776

intensities of hot graybody sources. The spectral resolution is limited by the radiative transfer codes utilized (LOWTRAN 4 and ATLES) except in the blue spike region (2380-2400 reciprocal centimeters), for which a new pseudo line-by-line procedure was developed yielding fully-resolved spectra. All of the models have been successfully validated against measurements and/or results of more elaborate theoretical calculation. Included in this report are new AFGL and EPA spectral data on clouds, sunglints and industrial emissions.

PREFACE

Useful discussions, data and computer codes were supplied during this effort by Eric Shettle and Brian Sandford of the Air Force Geophysics Laboratory, Warren Wiscombe of the National Center for Atmospheric Research, Horace Ory of R&D Associates, William Herget of the Environmental Protection Agency, Frederick Simmons and Stephen Young of the Aerospace Corporation, and William Keslar and G. Behrens of U.S. Steel Corporation. Fred Smith and Paul Eitner of Science Applications, Ann Arbor, MI, performed the work reported in Sections 6 through 8 under subcontract for Honeywell; they also assisted in developing a code for the blue spike model described in Section 5. Richard Sanderson of the Air Force Avionics Laboratory was project monitor for the study.

TABLE OF CONTENTS

TABLE OF CONTENTS (Continued)

APPENDIX PAGE

LIST OF ILLUSTRATIONS

LIST OF ILLUSTRATIONS (Continued)

LIST OF ILLUSTRATIONS (Continued)

LIST OF ILLUSTRATIONS (Continued)

LIST OF ILLUSTRATIONS (Continued)

LIST OF TABLES

SECTION I
INTRODUCTION

Detection of valid threats and attainment of very low sensor false alarm rate remain essential objectives for infrared threat warning receivers. Conventional single-color systems using spatial and temporal discriminants have failed to demonstrate adequate protection commensurate with insensitivity to false threats. It is now generally recognized that superior warning receiver performance may be attainable through spectral discrimination. However, there has not existed an adequate data base or analytical standard of evaluation for measuring the performance improvement to be realized through multispectral discrimination. These deficiencies are addressed in two study contracts awarded by the Air Force Avionics Laboratory: the IR Signature Studies documented in this report and the IR Receiver Analysis in progress at Nichols Research.

The long-term objective of these two studies and the planned IR Signature Studies II procurement is to develop for the Air Force a performance assessment model applicable to warning receivers employing a wide range of spectral discrimination techniques. This capability will allow the effectiveness of any existing or proposed technique to be estimated from computer analysis rather than costly hardware development and testing.

The purpose of the IR Signature Studies has been to identify events which constitute potential false threats in the 3.5 to 5-micrometer spectral region, and to select, develop and validate models to represent their spectral signatures at resolutions sufficient to evaluate both spectral line correlation and broad band discrimination techniques. The false threats of interest are those which could be encountered by airborne sensors operating in the 5 kft to 30 kft altitude range and defending against AAM and SAM threats. It was a requirement of the study that the models be capable of predicting the signatures at essentially infinite spectral resolution in the blue spike region of the real threats, since potential discrimination techniques could utilize the regular line structure of the blue spike threat emission. Elsewhere in the 3.5 to 5-micrometer spectral region, lower resolution band-model techniques were deemed adequate, with the possible exception of regions in which regularly-spaced HCl or CO emission lines offer additional discrimination potential. The contract called for similar modeling of AAM and SAM spectral signatures based on simple generic models that assume homogeneous isothermal plumes. The study emphasizes false threat spectral signatures as compared to threat signatures.

The model validation task involved the collection of measured spectral signatures, and a requirement of the study was to identify to the Air Force Geophysics Laboratory specific scenes/locations which should be measured as part of the AFGL Background Measurement Program (Sandford et al[1]). Generally the type of data asked for, and supplied by AFGL, was not available in the literature or from other sources. The AFGL spectra, representing mostly clouds, sunglints from lakes and ponds, and industrial site emissions, were extremely useful in the model validations. Many of these are reproduced in this report, since AFGL does not plan to publish them.

Section 2 summarizes the study results and conclusions. The remaining sections and Appendixes define the signature models selected and developed in the study, and the validations of the models.

SECTION II

SUMMARY AND CONCLUSIONS

This report describes a set of models that accurately characterize the spectrally resolved infrared signatures of AAM and SAM threat models, and of background events likely to cause false alarms in airborne IR threat warning receivers. The general prescriptions, equations, identifications of utilized (available) codes, and literature references constitute a fairly complete definition of the models and the procedures required in their implementation.

The potential false threats identified in the study are:

- Clouds (solar scattering by),
- Ocean sunglitter,
- Protected small lakes and pools, swamps, discharge basins, artifacts (specular solar reflections by),
- Industrial sites:
    - Flares,
    - Stack plumes,
    - Refinery emissions,
    - Hot solid objects,
- Fires:
    - Incendiary fires,
    - Refuse fires (battlefield, industrial, agricultural),
    - Brush and forest fires,
- Munitions:
    - Muzzle flash,
    - Shell bursts,
    - Flares,
    - Munition-induced explosions,
- Battlefield smokes,
- Vehicular emissions.

The model that predicts cloud spectral signatures is the result of an extensive mathematical analysis that produced new approximate solutions of the radiative transfer equation. The model is fairly general, and its predictions are in excellent agreement with AFGL measurements.

The ocean sunglitter model represents a generalization of the well-known Cox-Munk model to include spectral variations calculated from the Fresnel spectral reflection coefficients for a clean water surface. A simplified version of the model gives the spectral signatures of specular sunglints from smooth water surfaces. Both versions were successfully validated against AFGL measurements.

A new model and computer code (BLUESPIKE) were developed to calculate the fully-resolved spectrum of the blue spike region of threats and false threats. Line-by-line and band-model techniques were combined in the model to achieve a computational efficiency much higher than is typical in conventional line-by-line calculations. Very little accuracy was sacrificed, as demonstrated by comparisons to line-by-line calculations and high resolution measurements.

A substantial part of the study effort consisted of acquiring, modifying, and testing radiative transmission/emission computer codes needed in the cloud and water reflection models, and needed in generating signatures of gaseous threats/false threats outside the blue spike region. We developed a modified version of LOWTRAN 4 that is applicable to the folded-path geometries involved in solar reflections from clouds and water surfaces. We extended the capabilities of the ATLES band-model code, validated the code against measurements, and increased its efficiency.

With respect to gaseous emission sources, we have concluded that the procedures used in this study are adequate for modeling events likely to cause false alarms in warning receivers. These validated procedures are:

a) Use of ATLES for moderate resolution hot gas emission

b) Use of BLUESPIKE for high resolution gaseous emission in the blue spike region, and

c) Use of LOWTRAN 4 for low resolution graybody emission sources.

While generally adequate for most warning receiver evaluations, the ATLES and LOWTRAN codes are of course limited in resolution and thus not useful for modeling discrimination schemes requiring high spectral resolution.

In the course of the study a number of possible discrimination techniques were identified. In general, these techniques rely on inference of physical source characteristics from the observed spectra. The potentially useful inferences and methods demonstrated include:

1) Temperatures of graybody sources (from 3.5 to 4.2 continua emission)
2) Identification of CO_2 gaseous emission (from the blue spike)
3) Thickness determination for CO_2 plume (from red wing emission)
4) Identification of various gaseous species in the plume including SO_2, HCl and CO (from spectral emission lines).

In the order given, each inference requires higher resolution instrumentation, varying from 40 cm^{-1} for a temperature determination to 1 cm^{-1} for determination of CO or HCl in the source.

A detailed analysis of discrimination techniques has not been performed here; however, it does appear that the above methods will be useful for discrimination of aircraft or missiles from false threats.

We could not find models (or adequate data for the development of models) for predicting the spectral signatures of fires, munitions-related events or battlefield smokes. The data collected on these sources is given in Sections 7 and 8.

SECTION III
CLOUD RADIANCE MODEL

The cloud radiance model developed in this study predicts the infrared spectral radiance field above thick sunlit clouds. It can probably be proved that the maximum reflected radiance above a cloud exceeds or equals the maximum diffusely transmitted radiance, and it is a fact that the reflected radiance increases with the thickness of the cloud. In this sense the model predicts the brightest IR spectral signatures to be expected from clouds. The model could be generalized to deal with arbitrarily thin clouds and the transmitted radiance field by working out additional solutions according to the methods defined in Section 3.2.

The model has three parts. The first is an approximate solution of the integro-differential radiative transfer equation describing the reflected radiance field in terms of the incident flux and the aerosol scattering parameters of the cloud. The solution was obtained by applying the double-delta approximation of Turner[2] to a nonconservative scattering medium; Turner treated the conservative case only. The solution can be used to predict atmospheric backscatter (for a homogeneous atmosphere) as well as cloud scattering. This part of the model is described in Sections 3.1 through 3.3.

The second part of the model is an extensive data set describing the basic scattering and extinction properties of different size distributions of water droplets and ice crystals. The data consists of:

$K_0(\nu)$,	the extinction cross section per particle
$\omega_0(\nu)$,	the single scattering albedo (scattering coefficient ÷ sum of absorption and scattering coefficients)
$g(\nu)$,	the scattering phase function asymmetry parameter.

The Mie series computations required to obtain these parameters was performed by Eric Shettle of AFGL using the log-normal size distribution:

$$\frac{dN(r)}{dr} = n(r) = \frac{1}{\sqrt{2\pi}\,\sigma} \exp\left[- \frac{(\log r - \log r_m)^2}{2\sigma^2} \right]$$

where $\sigma = 0.3$, and r_m is the mean radius of the particles (the computations assume spherical water droplets and spherical ice "crystals"). The water and ice indices of refraction were taken from Hale and Querry[3]. Dr. Shettle provided 10 sets of $K_0(\nu)$, $\omega_0(\nu)$ and $g(\nu)$ corresponding to 5 different sizes of water droplets and ice crystals. In each set, which covers the spectral region 2.6 to 5-micrometer, the wavenumber spacing is sufficient to define completely the spectral variations in the three quantities. The data are given in Appendix A. The scattering phase function was not computed since this would have involved a considerable expenditure of computer time for the number of wavelengths involved. This means that a phase function with g as an adjustable parameter must be assumed (see Section 3.3).

The third part of the model is a modified version of the LOWTRAN 4 computer code.[4] This part of the model accounts for atmospheric absorption of the incident and reflected radiation, for atmospheric absorption of thermal radiation emitted by the cloud, and for atmospheric emission.

Figure 1 shows the transmission/emission geometry used in the modified LOWTRAN code. Point A is the location where the cloud spectral radiance is to be determined. The code computes the spectral transmittances of paths SCA and CA, and the spectral radiance of path CA. It also computes the blackbody spectral emission of the cloud, multiplies it by the transmittance of path CA, and adds the result to the spectral radiance of path CA to obtain the thermal contribution to the predicted spectral signature.

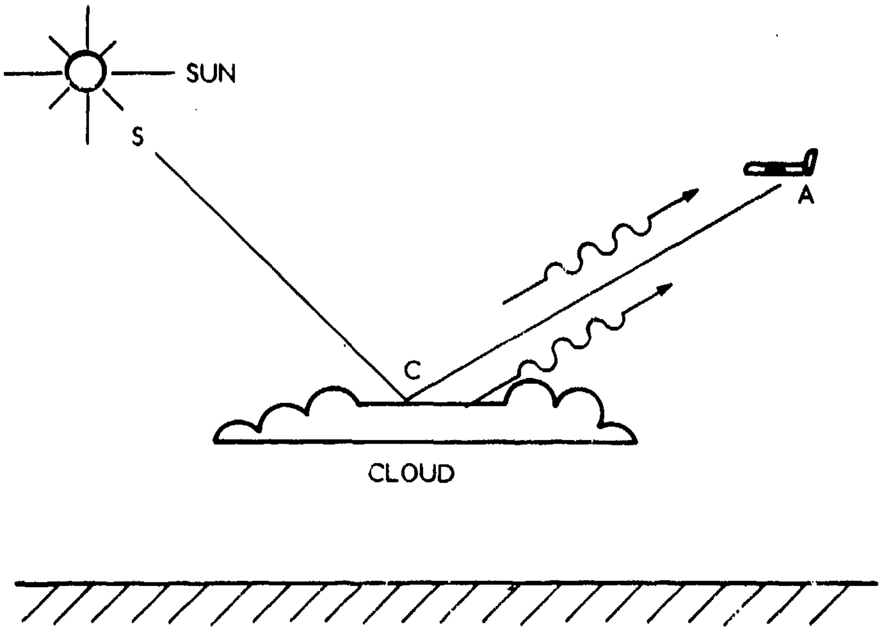

Figure 1. Geometry Used in Modified LOWTRAN 4 Code

The solar spectrum reflected by the cloud in a given direction is performed according to the calculations described in Section 3.2. This spectrum is multiplied by the spectral transmittance of path SCA, and added to the thermal spectrum computed by the modified LOWTRAN code. Note that the model does not include effects of scattering by the atmosphere outside the cloud (except for extinction), reflection of atmospheric thermal radiation by the cloud, scattering of cloud thermal emission within the cloud, or molecular absorption inside the cloud. These processes are assumed to have relatively small effects in the cloud spectral radiance over the 3 to 5-micrometer region.

3.1 DEFINITIONS AND FORMAL SOLUTION

Figure 2 defines the geometry used to characterize the radiance field and the scattering layer (atmosphere and/or cloud). The scattering layer is assumed to be plane-parallel and homogeneous. By homogeneous we mean that the aerosol scattering properties, namely the single scattering albedo and phase function, are independent of height z or optical thickness τ. Optical thickness is one of the independent variables used to define the radiance field; hence, the variation $\tau(z)$ and the vertical distribution of the density of scatterers is arbitrary.

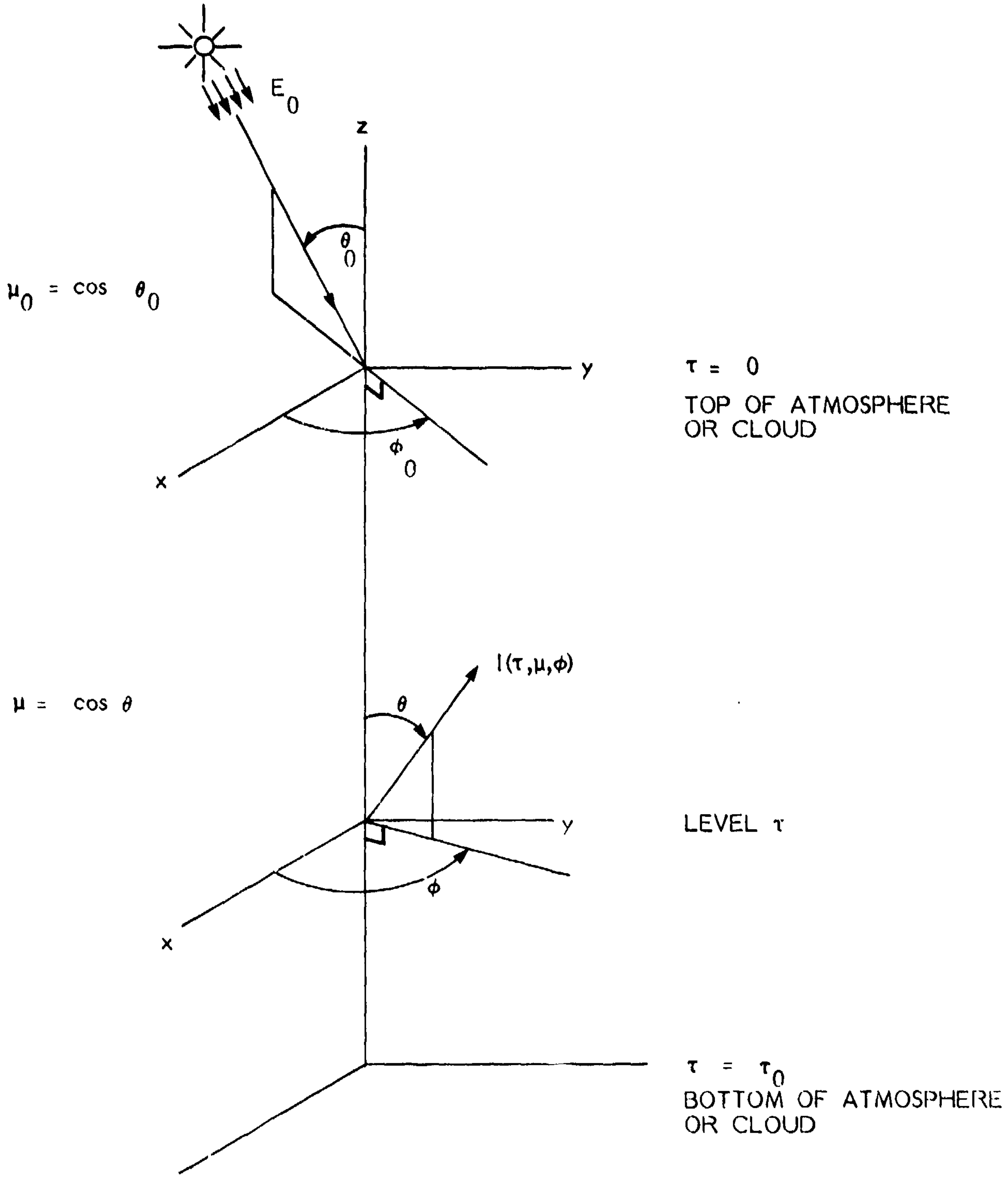

Figure 2. Geometry Defining the Scattering Layer and Diffuse Radiance $I(\tau,\mu,\phi)$

Solar radiation is incident at $\tau = 0$, and the total optical thickness of the atmosphere and/or cloud is τ_0. The coordinates of the sun will be denoted by μ_0 and ϕ_0, where μ_0 is the cosine of the solar zenith angle and ϕ_0 is the solar azimuth direction. The field coordinates of direct solar or diffuse (scattered) radiation are (τ, μ, ϕ) with the convention that positive $\mu = \cos\theta$ corresponds to "upwelling" radiation and negative μ to "downwelling" radiation. Thus, the sun's rays or a diffuse stream parallel to the sun's rays has the direction $-\mu_0, \phi_0$, and a stream towards the sun has the direction $\mu_0, \phi_0 + \pi$. We will refer to these two directions in calculating the diffuse radiance $I(\tau,\mu,\phi)$, but the final result will represent only the upwelling component; i.e., μ will be restricted to positive values.

As mentioned earlier, emission by the atmosphere/cloud is handled separately, with the assumption that there is no scattering of the emitted radiation.

The radiative transfer equation for the <u>diffuse</u> radiance $I(\tau,\mu,\phi)$ in a plane-parallel, one-dimensional, homogeneous, nonemitting atmosphere is:

$$\mu \frac{dI}{d\tau}(\tau,\mu,\phi) = I(\tau,\mu,\phi) - \frac{\omega_0}{4\pi}\int_0^{2\pi}\int_{-1}^{1} p(\mu,\phi,\mu',\phi')\, I(\tau,\mu',\phi')\,d\mu'\,d\phi'$$

$$- \frac{\omega_0}{4\pi} E_s(\tau)\, p(\mu,\phi,-\mu_0,\phi_0) \qquad (1)$$

where ω_0 is the albedo for single scattering (ratio of scattering coefficient to sum of absorption and scattering coefficients),

$$\omega_0 = \frac{\beta(z)}{\alpha(z) + \beta(z)} \equiv \frac{\beta(z)}{k(z)} = \text{constant}, \qquad (2)$$

and τ is the optical thickness of the atmosphere above level z:

$$\tau(z) = \int_{z}^{\infty} k(z')dz'. \tag{3}$$

The constant function $p(\mu_s)$ is the single-scattering phase function for scattering angle $\mu_s = \cos\theta_s$, which is defined by the directions of the incident (μ',ϕ') and scattered (μ,ϕ) rays; it is normalized according to:

$$\int_{4\pi} p(\cos\theta)\,\frac{d\omega(\theta)}{4\pi} = 1. \tag{4}$$

The second term of Eq. (1) represents the scattering of direct solar flux (irradiance) $E_s(\tau) = E_0 \exp(-\tau/\mu_0)$ which has penetrated to level τ; E_0 denotes the extraterrestrial solar irradiance on a plane normal to the sun's rays.

By multiplying Eq. (1) by the integrating factor $\exp(-\tau/\mu)$, dividing by μ and integrating from τ_0 to τ, we get, for the <u>upwelling radiance</u>

$$\begin{aligned} I(\tau,\mu,\phi) &= I(\tau_0,\mu,\phi)\exp\left[(\tau_0-\tau)/\mu\right] \\ &+ \frac{\omega_0}{4\pi}\int_0^{2\pi}\int_{-1}^{1} p(\mu,\phi,\mu',\phi')\int_{\tau}^{\tau_0} e^{-(\tau'-\tau)/\mu} I(\tau',\mu',\phi')d\tau'd\mu'd\phi' \\ &+ \frac{\omega_0\mu_0\,E_0\,p(\mu,\phi,-\mu_0,\phi_0)}{4\pi(\mu+\mu_0)}\left[e^{-\tau/\mu_0} - e^{-\tau_0/\mu_0}\,e^{-(\tau_0-\tau)/\mu}\right] \end{aligned} \tag{5}$$

By integrating Eq. (1) from 0 to τ we could also obtain an expression for the downwelling radiance, but as stated, we will obtain a final solution for the upwelling case only. We emphasize that $I(\tau,\mu,\ )$ in Eq. (1) and in the integral term in Eq. (5) represents the radiance in <u>any</u> direction.

Our objective is to reduce Eq. (5) to an approximate closed-form solution using a technique described by Turner[2]. This will be accomplished by introducing approximations in Eq. (1) which reduce it to a pair of first-order differential equations, whose solution yield a first approximation to $I(\tau,\mu,\phi)$. This result will then be substituted into Equation 3.5 to obtain a second approximation to $I(\tau,\mu,\phi)$. The first approximation is basically a two-stream model that involves the diffuse fluxes (irradiances) in the positive and negative z directions, which are defined by

$$E_+(\tau) = \int_0^{2\pi} \int_0^1 \mu \; I(\tau,\mu,\phi) d\mu d\phi, \qquad (6)$$

and $$E_-(\tau) = -\int_0^{2\pi} \int_{-1}^0 \mu \; I(\tau,\mu,\phi) d\mu d\phi,$$

respectively. The corresponding upward and downward <u>average</u> diffuse radiances are

$$\langle I(\tau)\rangle_\pm = \frac{1}{2\pi} \int_0^{2\pi} \int_0^{\pm 1} I(\tau,\mu,\phi) d\mu d\phi \qquad (7)$$

3.2 APPLICATION OF THE DOUBLE-DELTA APPROXIMATION

We will outline the steps in deriving the radiance field in the double-delta approximation and will write out only a few of the intermediate results. We will present the final result in a simplified form applicable to optically thick clouds.

The method derives its name from the form used to represent the phase function in the first approximation. We assume initially that the phase function consists of forward and backward delta functions; i.e.,

$$p(\mu,\phi,\mu',\phi') = 4\pi\eta\delta(\mu-\mu')\delta(\phi-\phi')$$

$$+ 4\pi(1-\eta)\delta(\mu+\mu')\delta(\phi-\phi'+\pi), \tag{8}$$

where η is the fraction of radiation scattered into a forward hemisphere. Consistent with this representation of the phase function, we initially approximate the diffuse radiance field by delta-functions directed towards and away from the sun:

$$I(\tau,\mu,\phi) = \frac{1}{\mu_0}\left[E_+(\tau)\delta(\mu-\mu_0)\delta(\phi-\phi_0+\pi)\right.$$

$$\left.+ E_-(\tau)\delta(\mu+\mu_0)\delta(\phi-\phi_0)\right], \tag{9}$$

where $E_{\pm}(\tau)$ is defined by Eq. (6). Substituting Eq. (8) into Eq. (1) we obtain

$$\mu\frac{dI}{d\tau} = (1-\omega_0\eta)I(\tau,\mu,\phi) - \omega_0(1-\eta)I(\tau,-\mu,\phi+\pi)$$

$$-\omega_0 E_s(\tau)\left[\eta\delta(\mu+\mu_0)\delta(\phi-\phi_0) + (1-\eta)\delta(\mu-\mu_0)\delta(\phi-\phi_0+\pi)\right]. \tag{10}$$

Substitution of (9) into (10) yields the coupled linear differential equations

$$\frac{dE_+}{d\tau} = \frac{(1-\omega_0\eta)}{\mu_0}E_+(\tau) - \frac{\omega_0(1-\eta)}{\mu_0}E_-(\tau) - \omega_0(1-\eta)E_s(\tau)$$

$$\frac{dE_-}{d\tau} = \frac{\omega_0(1-\eta)}{\mu_0}E_+(\tau) - \frac{(1-\omega_0\eta)}{\mu_0}E_-(\tau) + \omega_0\eta E_s(\tau). \tag{11}$$

If the albedo of the surface at $\tau = \tau_0$ is zero, or if the atmosphere/cloud has sufficiently large optical thickness, one of the boundary conditions on Eq. (11) is

$$E_+(\tau_0) = 0 \tag{12}$$

The other boundary condition, which always applies, is

$$E_-(0) = 0; \tag{13}$$

i.e., the downward diffuse irradiance is zero at the upper boundary ($\tau = 0$). The solutions of Eq. (11) for these boundary conditions will be denoted $E_+'(\tau)$ and $E_-'(\tau)$. After obtaining these solutions, we can relax the condition that the surface albedo equal zero. That is, we can obtain a second solution, denoted $E_+''(\tau)$ and $E_-''(\tau)$, which assumes no solar input, and, via appropriate boundary conditions, represents the reradiation of (reflection by) the lower boundary. The two solutions can be superimposed to obtain the total irradiance, and then the total radiance.

With the boundary conditions (12) and (13), the solution of (11) is

$$\begin{aligned} E_+'(\tau) &= \frac{\mu_0 E_0 \omega_0 (1-\eta) \sinh\left[\lambda(\tau_0-\tau)\right]}{(1-\omega_0\eta)\sinh \lambda\tau_0 + \mu_0\lambda \cosh \lambda\tau_0} \\ E_-'(\tau) &= \mu_0 E_0 \left[\frac{(1-\omega_0\eta)\sinh\left[\lambda(\tau_0-\tau)\right] + \mu_0\lambda\cosh\left[\lambda(\tau_0-\tau)\right]}{(1-\omega_0\eta)\sinh\lambda\tau_0 + \mu_0\lambda\cosh\lambda\tau_0} - e^{-\tau/\mu_0} \right] \end{aligned} \tag{14}$$

where

$$\lambda = (1/\mu_0)\left[(1-\omega_0\eta)^2 - \omega_0^{\,2}\,(1-\eta)^2\right]^{1/2} \tag{15}$$

Note that $\lambda = 0$ for $\omega_0 = 1$; for this case Eq. (14) must be evaluated in the limit as $\lambda \to 0$. If (12) and (13) are the appropriate boundary conditions, then the upwelling radiance in the second approximation is obtained by substituting (14) into (9) and then (9) into (5). This solution is given in Section 3.3

When the underlying surface is diffuse and has non-zero albedo ρ, the solution for the upwelling radiance can be obtained as follows: we assume no solar input and an isotropic source at the bottom of the atmosphere, representing the diffusely reflected radiation. It is reasonable under these conditions to assume that the radiance field is nearly isotropic, i.e., that

$$I(\tau,\mu,\phi) \simeq \langle I(\tau)\rangle_{\pm} \simeq 2E_{\pm}(\tau)/2\pi, \tag{16}$$

where the second relationship follows from the definitions 3.6 and 3.7. Note that, in general,

$$\langle \mu I(\tau)\rangle_{\pm} = E_{\pm}(\tau)/2\pi \tag{17}$$

according to these definitions. Thus, by averaging Eq. (10) first over the upward hemisphere and then over the downward hemisphere, and setting $E_S = 0$, we obtain the pair of equations

$$\begin{aligned} \frac{dE_+}{d\tau} &= 2(1-\omega_0\eta)E_+(\tau) - 2\omega_0(1-\eta)E_-(\tau) \\ \frac{dE_-}{d\tau} &= 2\omega_0(1-\eta)E_+(\tau) - 2(1-\omega_0\eta)E_-(\tau). \end{aligned} \tag{18}$$

The boundary conditions are

$$\begin{aligned} E_+(\tau_0) &= \rho\left[E'_-(\tau_0) + \mu_0 E_S(\tau_0)\right] = \rho\left[E'_-(\tau_0) + \mu_0 E_0 e^{-\tau_0/\mu_0}\right] \\ E_-(0) &= 0 \end{aligned} \tag{19}$$

where $E'_-(\tau)$ is the previously obtained solution for $\rho = 0$ (second of Eq. (14)).

Let $E'_{\pm}(\tau)$ denote the solutions of Eq. (18) with the boundary conditions (19). Then the average value of the nearly-isotropic radiance field, according to (16), is

$$\frac{1}{2}\left[\langle I(\tau)\rangle_{+} + \langle I(\tau)\rangle_{-}\right] = \left[E''_{+}(\tau) + E''_{-}(\tau)\right]/2\pi \qquad (20)$$

Eq. (9), with $E'_{+}(\tau)$ in place of $E_{+}(\tau)$, gives the solar-generated anisotropic field, in the first approximation. The sum of this field and the one arising from surface reflection is

$$\begin{aligned} I(\tau,\mu,\phi) = \frac{1}{\mu_0} & \Big[E'_{+}(\tau)\delta(\mu-\mu_0)\delta(\phi-\phi_0+\pi) \\ & + E'_{-}(\tau)\delta(\mu+\mu_0)\delta(\phi-\phi_0)\Big] \\ & + \left[E''_{+}(\tau) + E''_{-}(\tau)\right]/2\pi. \end{aligned} \qquad (21)$$

This result would be substituted into Eq. (5) to obtain the second approximation to the upwelling radiance. Because of the forms of (21) and the solutions E' and E", the integrations can be performed to yield a closed-form result, without specification of the scattering phase function. Thus, any appropriate phase function may be used in place of the double-delta function given by Eq. (8).

3.3 SOLUTION APPLICABLE TO OPTICALLY THICK CLOUDS

Very little diffused sunlight emerges from the undersides of thick water or ice clouds in the 3 to 5-micrometer spectral region, where the single-scattering albedo is always appreciably less than unity. Hence, it is reasonable, for the purposes of this study, to assume that the surface albedo is zero, and to utilize the simpler solution that results from this assumption.

For $\rho = 0$, the second approximation to the upwelling radiance $I(\tau,\mu,\ )$ is obtained by substituting (14) into (9) and then (9) into (5). Note that the first term of (5) is zero when $\rho = 0$. Evaluation of the integrals in (5) yields the desired result:

$$
\begin{aligned}
I(\tau,\mu,\phi) &= \frac{\omega_0 E_0/4\pi}{(1-\omega_0\eta)\sinh\lambda\tau_0 + \mu_0\lambda\cosh\lambda\tau_0} \\
&\bullet \left\{ \frac{P_1\omega_0(1-\eta)}{1-\mu^2\lambda^2}\left[\mu\lambda\left(e^{-(\tau_0-\tau)/\mu} - \cosh\lambda(\tau_0-\tau)\right) + \sinh\lambda(\tau_0-\tau)\right]\right. \\
&\quad + \frac{P_2\lambda}{1-\mu^2\lambda^2}\left[\left(\frac{1-\omega_0\eta}{\lambda} - \mu_0\mu\lambda\right)\sinh\lambda(\tau_0-\tau)\right. \qquad (22) \\
&\quad \left.\left. + \left(\mu_0-\mu(1-\omega_0\eta)\right)\left(\cosh\lambda(\tau_0-\tau)-e^{-(\tau_0-\tau)/\mu}\right)\right]\right\},
\end{aligned}
$$

where

η = fraction of radiance scattered by the aerosols into a forward hemisphere

ω_0 = single-scattering albedo

τ_0 = total optical thickness of atmosphere/cloud

E_0 = extraterrestrial solar irradiance (or spectral irradiance) on plane normal to the sun's rays

λ = $(1/\mu_0)\left[(1-\omega_0\eta)^2 - \omega_0^2(1-\eta)^2\right]^{1/2}$

P_1 = $p\left[\mu\mu_0 - \sqrt{(1-\mu^2)(1-\mu_0^2)}\cos(\phi-\phi_0)\right]$

P_2 = $p\left[-\mu\mu_0 + \sqrt{(1-\mu^2)(1-\mu_0^2)}\cos(\phi-\phi_0)\right]$

$p(\mu_s)$ = single-scattering phase function

μ_0 = cosine of solar zenith angle

ϕ_0 = azimuth of sun

μ = cosine of zenith angle of upwelling radiance $(0 < \mu \leq 1)$

ϕ = azimuth of upwelling radiance

τ = optical thickness (level) at which upwelling radiance is observed.

Note that the units of $I(\tau,\mu,\phi)$ are those of E_0 times sr^{-1}. The arguments of the phase functions P_1 and P_2 are simply the cosines of the angles (scattering angles) between (μ,ϕ) and $(\mu_0, \pi + \phi_0)$ and between (μ,ϕ) and $(-\mu_0,\phi_0)$, respectively. For $\omega_0 = 1$, Eq.(22) must be evaluated in limit $\lambda \to 0$.

The scattering phase function that we elected to use with Eq. (22) is the Henyey-Greenstein function

$$p(\mu_s) = p_{H-G}(\mu_s) = (1-g^2)(1+g^2-2g\mu_s)^{-3/2}, \tag{23}$$

where g is an anisotropy parameter defined as the average value of μ_s, the cosine of the scattering angle:

$$g = \int_0^{2\pi} \int_{-1}^{1} \mu_s \, p_{H-G}(\mu_s) \frac{d\mu_s d\phi}{4\pi} \; . \tag{24}$$

The anisotropy parameter η in Eq. (22) is related to g by

$$\eta = \frac{1+g}{2g} \left[1 - \frac{1-g}{(1+g^2)^{1/2}} \right] . \tag{25}$$

All of the cloud spectral radiance calculations presented in the following two sections were obtained using Eqs. (22), (23) and (25). The calculated spectra always represent radiance fields above the clouds: hence $\tau = 0$. Note that the geometry of the scattering calculation (before we apply corrections for atmospheric molecular absorption/emission) is defined completely by the three parameters μ_0, μ and $\Delta\phi \equiv \phi-\phi_0$.

As mentioned earlier, the aerosol scattering parameters used for calculations consist of the AFGL-supplied spectral data $\omega_0(\nu)$, $g(\nu)$ and $K_0(\nu)$ (the extinction coefficient per particle). The data sets corresponding to different size distributions of water droplets and ice spheres are given in Appendix A. In performing the cloud spectral reflection calculations we first select the cloud type (water or ice), the cloud optical thickness at 2.6 micrometers, and the mean radius of the cloud particles. Then, using the appropriate data set, we convert $g(\nu)$ to $\eta(\nu)$ via Eq. (25), and convert $K_0(\nu)$ to $\tau_0(\nu)$ using

$$\tau_0(\nu) = \left[K_0(\nu)/K_0(2.6\ \mu\mathrm{m})\right] \tau_0(2.6\ \mu\mathrm{m}). \tag{26}$$

For the calculations we chose $\tau_0(2.6\ \mu\mathrm{m}) = 10$, which insures that the cloud will optically thick over the entire 2.6 to 5-micrometer region for any selected cloud type or mean radius. Thus, it was not necessary to perform the scaling defined by Eq. (26), but this operation was included in the computer code so that it would have a greater range of application (i.e., to arbitrary cloud optical thickness and $\rho = 0$).

3.4 EXAMPLE CALCULATIONS

Figures 3 through 7 show some of the spatial radiance variations predicted by the model. The calculations do not include atmospheric absorption or emission, or cloud emission. Figure 3 shows the variation of $I(0,\mu,\phi)$ with $\theta = \cos^{-1}\mu$ at wavelength 3.9 micrometers, for $\theta_0 = \cos^{-1}\mu_0 = 60$ degrees and $\phi-\phi_0 = 0$ or 180 degrees. The cloud consists of water droplets with $r_m = 4$ micrometers. Note that the radiance increases with τ_0, but for $\tau_0 \geq 4$ the cloud is optically thick and there is essentially no further increase. Note also that the radiance is a maximum in the backscatter direction for optically thick clouds, but for thin clouds the largest radiance occurs at $\theta = 90^\circ$, $\phi-\phi_0 = 0$. Figure 4 is the same as Figure 3 except $r_m = 16$ micrometers. Figure 5 shows that the reflected radiance can have a strong wavelength dependence through ω_0 and g. Figures 6 and 7 show the azimuth variation of the radiance for three different solar zenith angles; Figure 6 represents a water cloud with $r_m = 16$ micrometers at the wavelength 3.9 micrometers; Figure 7 represents an ice cloud with $r_m = 32$ micrometers at the wavelength 4.0 micrometers.

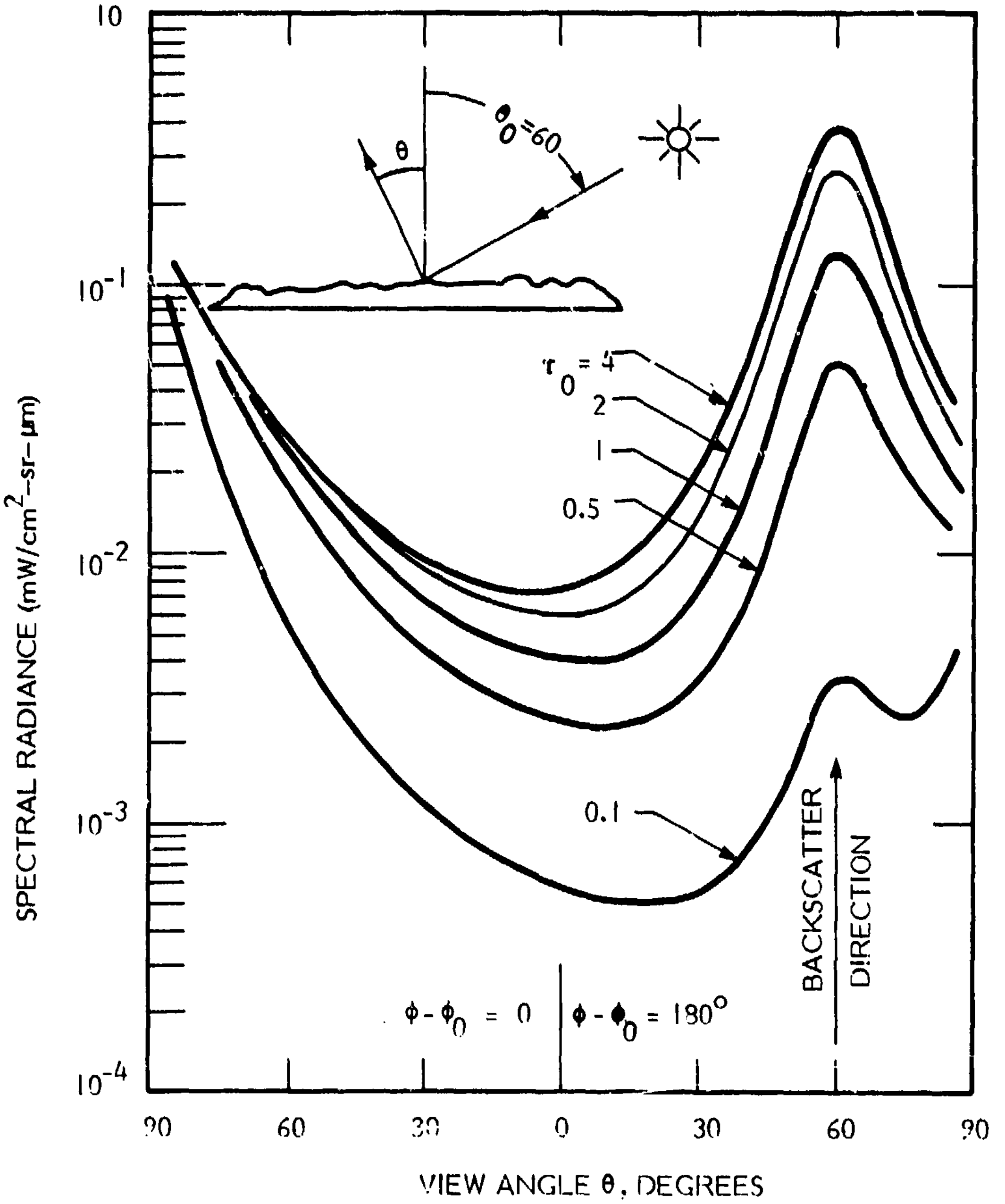

Figure 3. Radiance Variation with Zenith View Angle; λ = 3.9 μm, WATER CLOUD, r_m = 4 μm

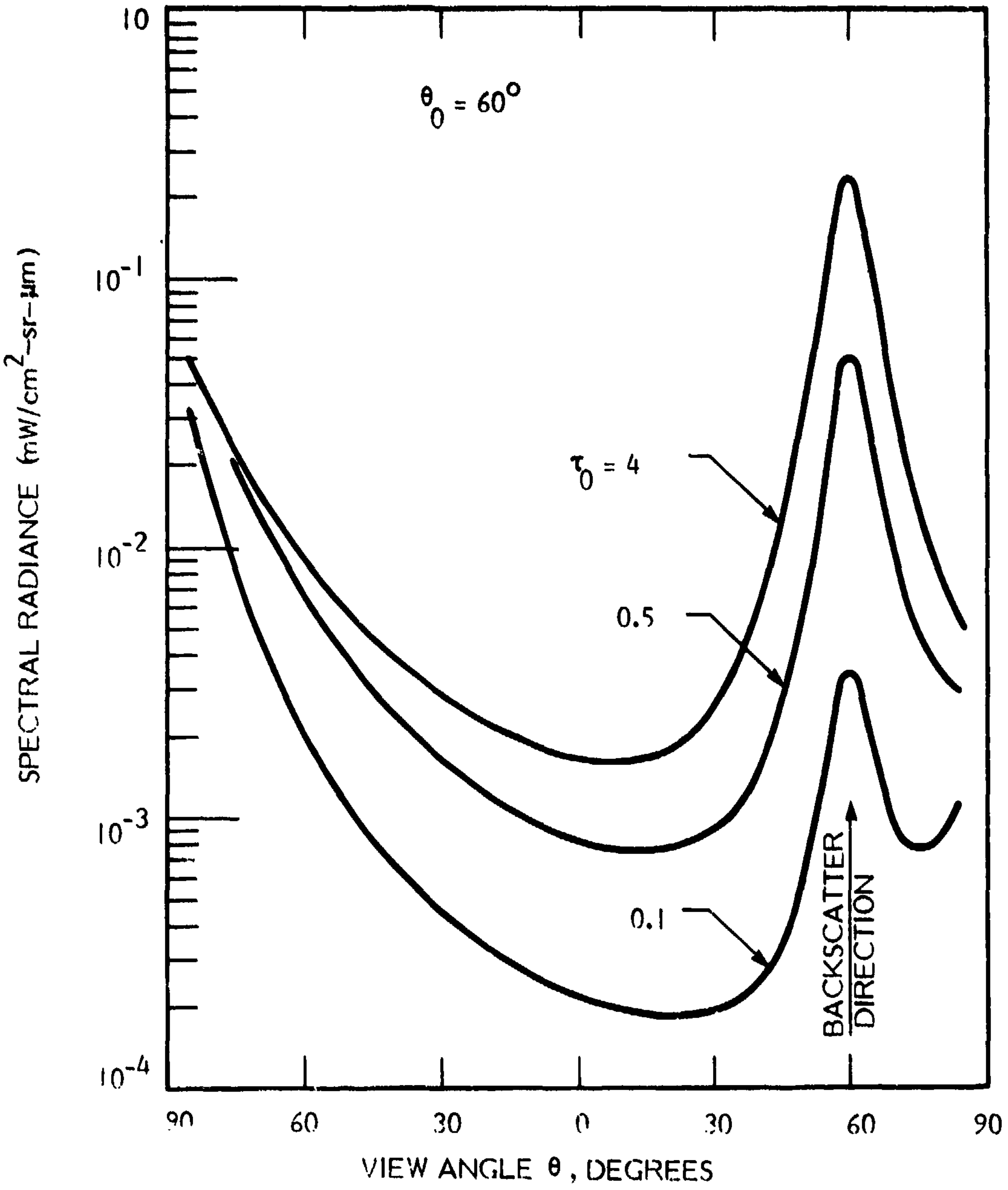

Figure 4. Effect of Cloud Droplet Mean Radius; $\lambda = 3.9\,\mu m$, WATER CLOUD, $r_m = 16\,\mu m$

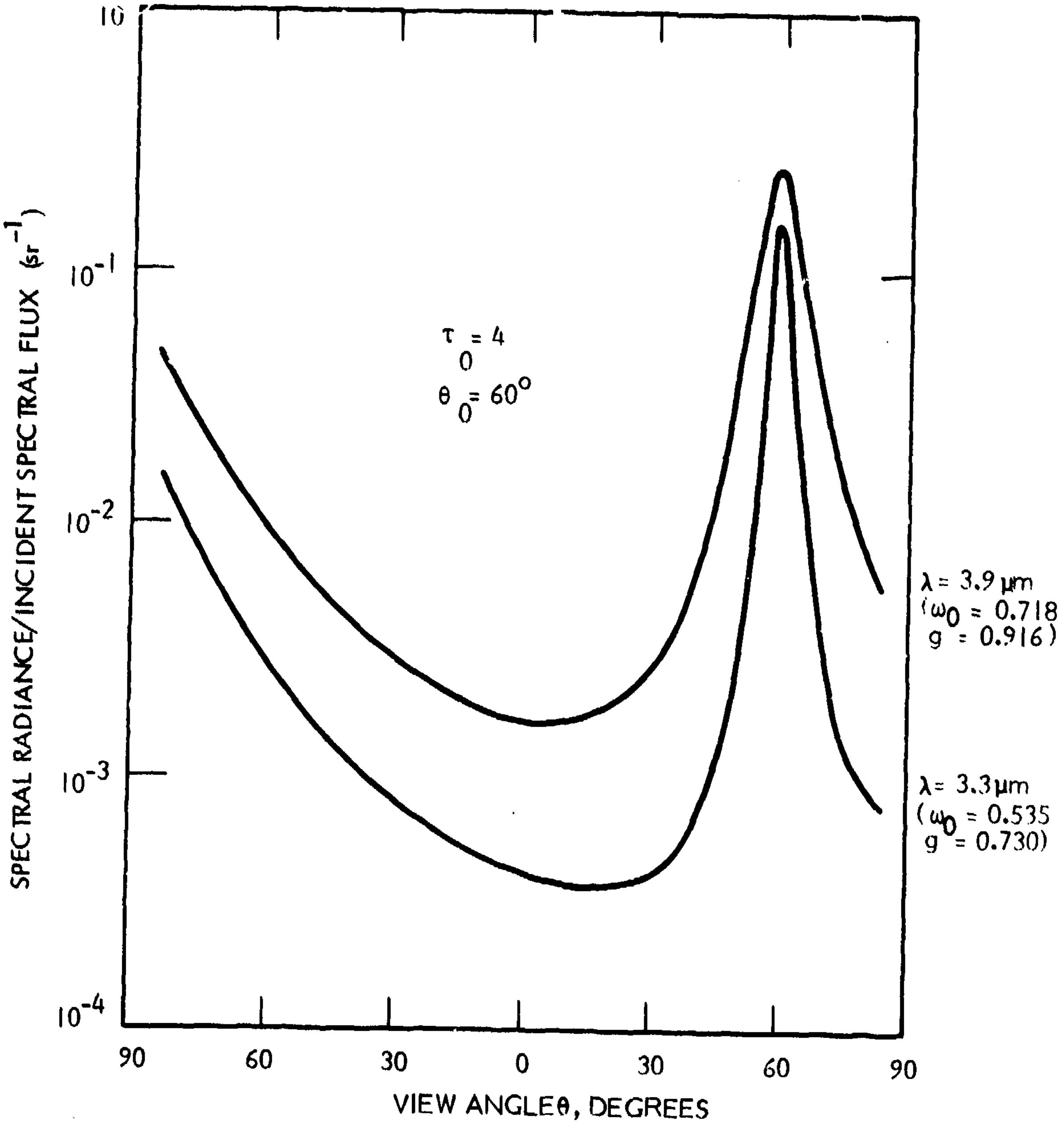

Figure 5. Effects of $\omega_0(\lambda)$, $g(\lambda)$; WATER CLOUD, $r_m = 16\,\mu m$

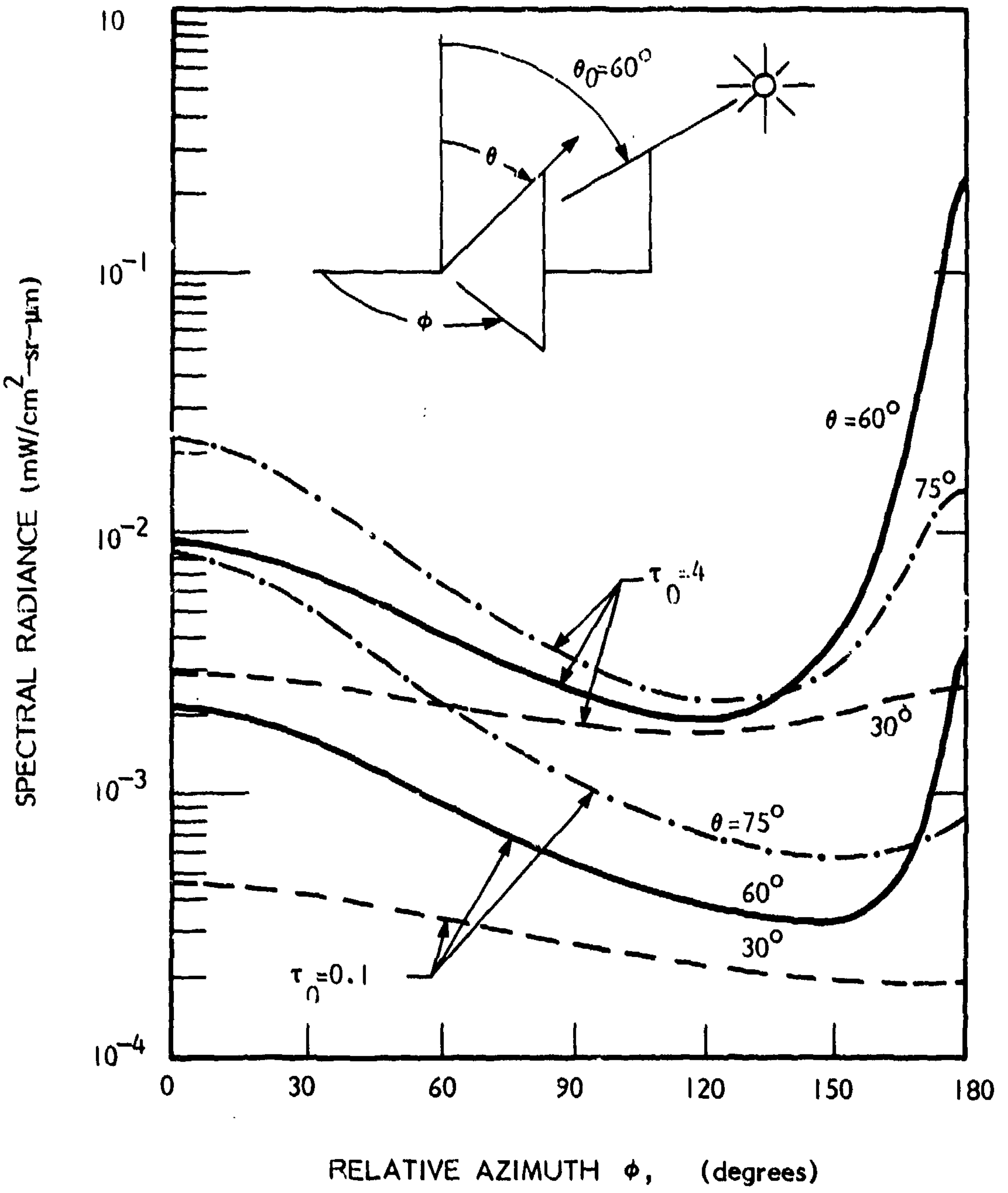

Figure 6. Radiance Variation with Azimuth; λ= 3.9 µm, WATER CLOUD. r_m = 16 µm

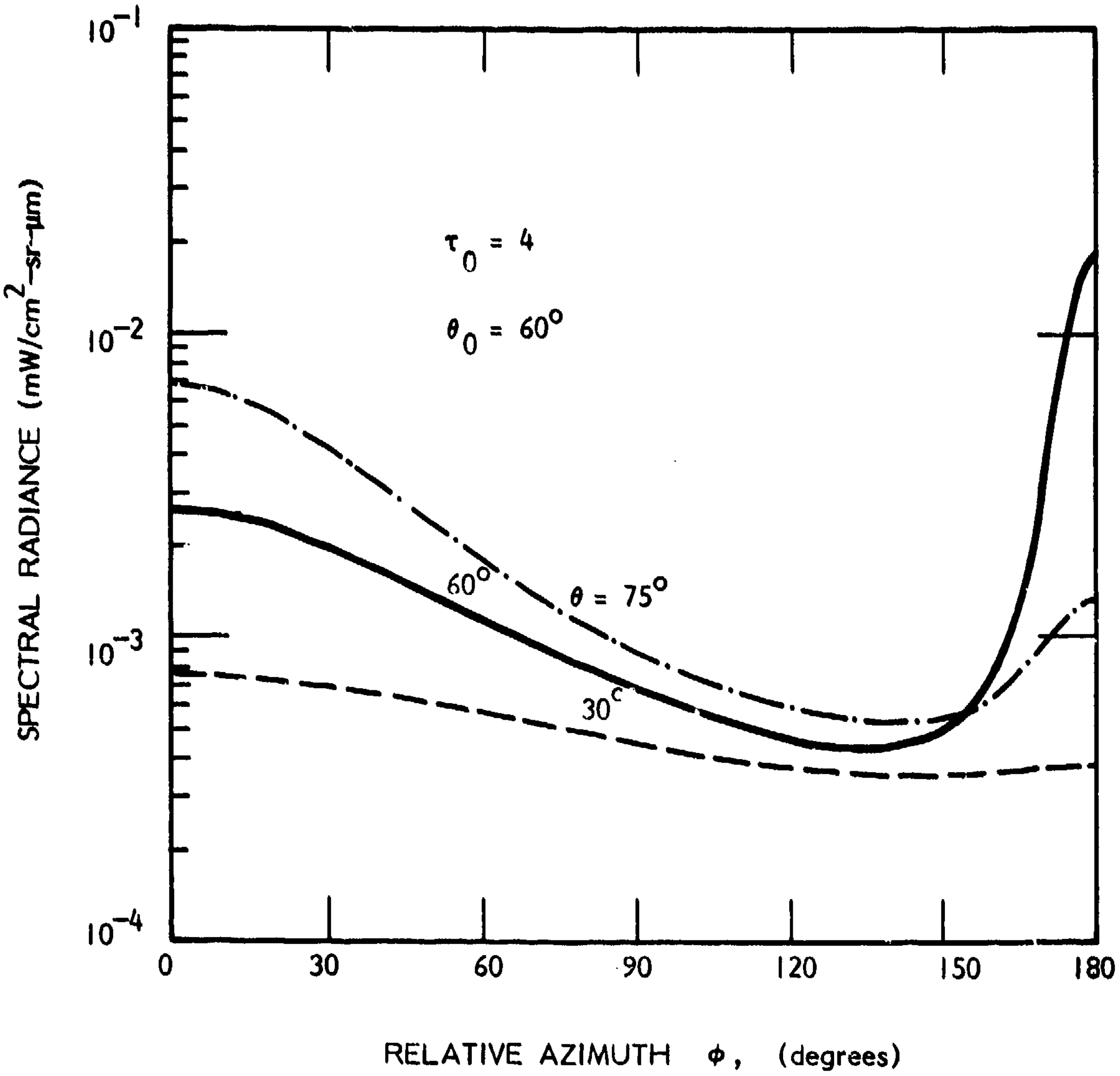

Figure 7. Azimuth Variation for Ice Cloud; $\lambda = 4.0\,\mu m$, $r_m = 32\,\mu m$

3.5 VALIDATION OF THE CLOUD RADIANCE MODEL

Seventeen cloud radiance spectra were selected from data tapes provided by AFGL, for the purpose of validating the cloud radiance model. These data, from the Background Measurement Program,[1] were obtained by AFGL in support of the IR Signature Studies program, and to our knowledge have not been reported elsewhere. AFGL provided all of the data defining the solar illumination and measurement geometries, as well as radiosonde data closely matching the time and location of measurements. The clouds were thick in all but one of the measurements; for all of these cases the only model parameters that were unspecified are the mean radius of the cloud water droplets or ice crystals and the cloud temperature. Cloud temperatures were assumed equal to the radiosonde temperature at the cloud top altitude.

Table 1 gives the geometrical data and cloud descriptions provided by AFGL with the radiance spectra. Note that in Mission 727 the aircraft observed "transmitted" radiance, i.e., it viewed the brightest section of the edge of a cirrus cloud from an altitude below the cloud. While the cloud radiance model is not intended to describe the transmitted radiance field, it is possible to define a reflection geometry that represents the same net scattering angle as the AFGL measurement geometry (other arguments can be given to support the definition of an equivalent reflection geometry for this particular case; see Section 3.5.2). Table 1 also gives the assumed mean radius of the cloud particles.

Each of the three different missions represented in Table 1 corresponds to a particular time and location, and is associated with a radiosonde data set (pressure, temperature and dew point versus altitude). Some of supplied radiosondes had no dew point data for the higher levels. In these cases we augmented the radiosonde dew points using average mid-latitude values given in the Air Force Handbook of Geophysics.[5] Appendix B gives the complete profiles used in the calculations, i.e., the atmospheric data used as inputs to the modified LOWTRAN 4 code. (Appendix B also contains augmented profiles for the AFGL missions that provided data relevant to the other models developed in this study).

TABLE 1

DATA FOR AFGL MEASUREMENTS OF CLOUD SPECTRAL RADIANCE

Mission/Run/ Tape/Record	Cloud Description	Cloud Top Alt. (kft)	Aircraft Altitude (kft)	Solar Elev. (deg)	LOS* Depr. (deg)	Solar Az. (deg)	Rel. Az.** $\|\phi-\phi_0\|$ (deg)	Assumed Type/ Radius (μm)	See Figures
726/7/FB43/175 /176 /177 /178	Low thick stratus deck over ocean	3.0	6.0	8.88	5.0	261.51	94.5 175.5 95.5 5.51	Water/16	8, 9
727/9/FB43/387	Cirrus cloud edge seen from below	27.5?	19.7	14.25	-14.25	254.52	~5.0	ICE/32	10, 11
817/1/FB48/364 /365 /366 /367	Uniform strato-cirrus, thick, usually opaque	32	33	8.0	2.5	295	90 0 270 180	ICE/32	12, 13
817/2/FB48/370 /371 /368 /369	Same as 817/1	32	33	5.3	2.5	300	90 0 300 180	ICE/32	14, 15
817/3/FB48/372 /373 /374 /375	Same as 817/1	32	33	2.6	2.5	300	90 0 270 180	ICE/32	15, 16

* Depression angle of line-of-sight below local horizontal

** Difference between solar azimuth and line-of-sight azimuth

3.5.1 Mission 726/7

Figure 8 shows four AFGL spectra of a low stratus cloud deck observed over the ocean near San Louis Obispo, California, on 28 September 1977, and the corresponding calculated spectra (the lower-resolution curves). The logarithmic ordinate scale applies to record 178 of Mission 726/7; the other three spectra, records 176, 175 and 177, have been displaced downward by factors of 2, 4 and 8, respectively. The brightest spectrum is record 178, corresponding to a relative solar azimuth direction of 5.51 degrees, while the second brightest is record 176, corresponding to a solar azimuth of 175.5 degrees; i.e., "forward" scattering results in higher radiances then "backscattering" for these particular solar elevation and line-of-sight depression angles. The N_2O band at 2563 cm^{-1} and the HDO bands near 2720 cm^{-1} are prominent features in these and many other of the AFGL cloud spectra. The 4.3-micrometer CO_2 band is not a strong feature in these spectra because thermal emission dominates reflected solar radiation in this spectral region, and because there is a nearly isothermal layer immediately below the aircraft (see Appendix B).

The calculated cloud radiance spectra are shown separately (and on a common ordinate scale) in Figure 9. Results are shown for mean water droplet radii of 8 and 16 micrometers. The calculated spectra in Figure 8 correspond to a mean radius of 16 micrometers. It is evident that the larger radius gives better agreement with the AFGL data.

The AFGL spectral radiances below 2100 cm^{-1} in Figure 8 are probably too large as a result of known calibration inaccuracies.[6] The calculated radiances between 2400 cm^{-1} and 2500 cm^{-1} are too large, probably because of a deficiency in the LOWTRAN model, which seems always to predict too high a transmittance in this portion of the wing of the 4.3-micrometer CO_2 band. We have found that the LOWTRAN code also tends consistently to overestimate the transmittance in the most transparent region of the 3.2-micrometer H_2O band, near 3150 cm^{-1}. Differences between the measured and calculated spectra near 2560 cm^{-1} clearly indicate that the atmosphere contains significantly more N_2O than is assumed in the LOWTRAN code.

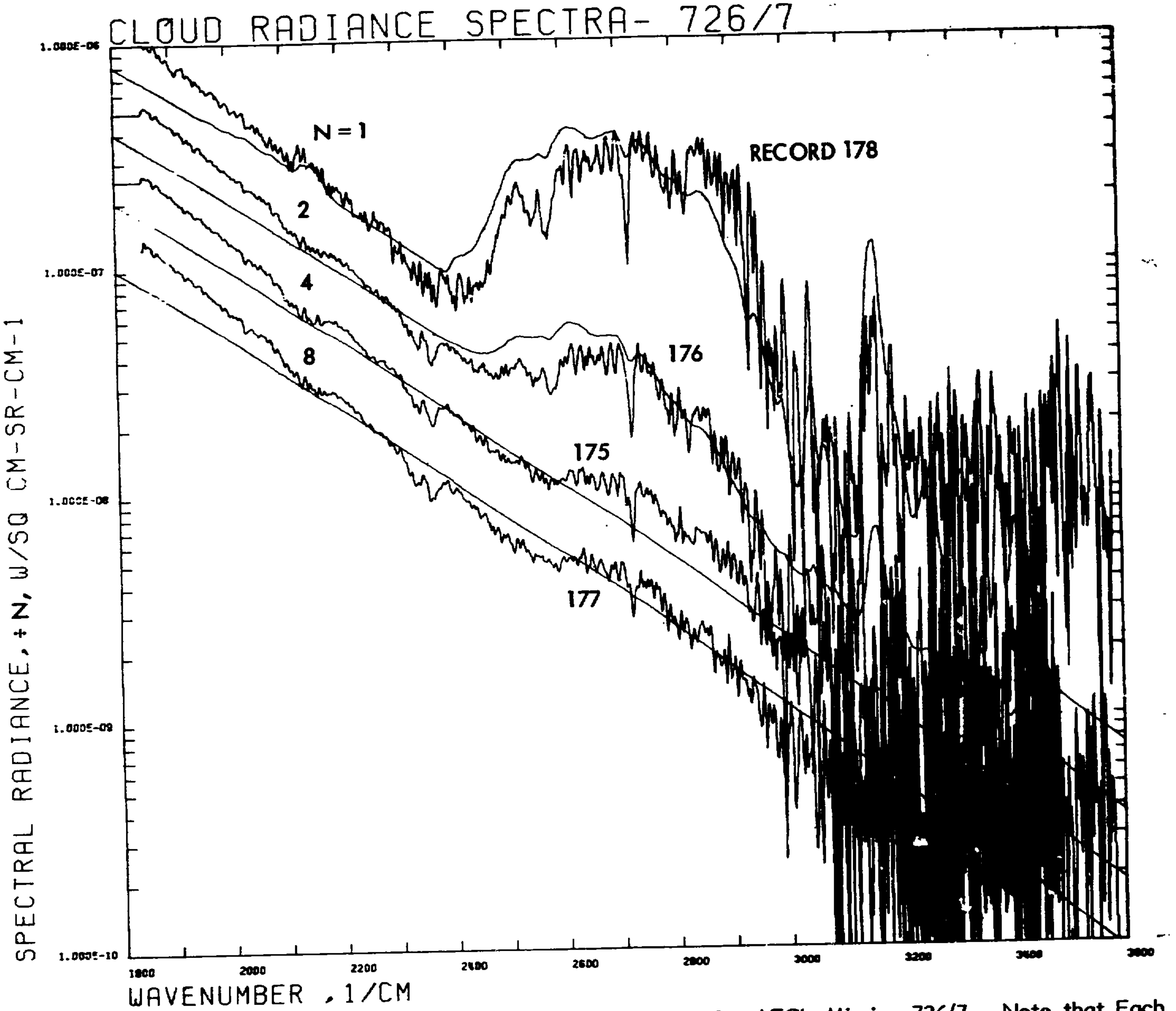

Figure 8. Measured and Calculated Cloud Radiance Spectra for AFGL Mission 726/7. Note that Each Spectrum has been Divided by a Different Factor N. Measurement Conditions are given in Table 3-1.

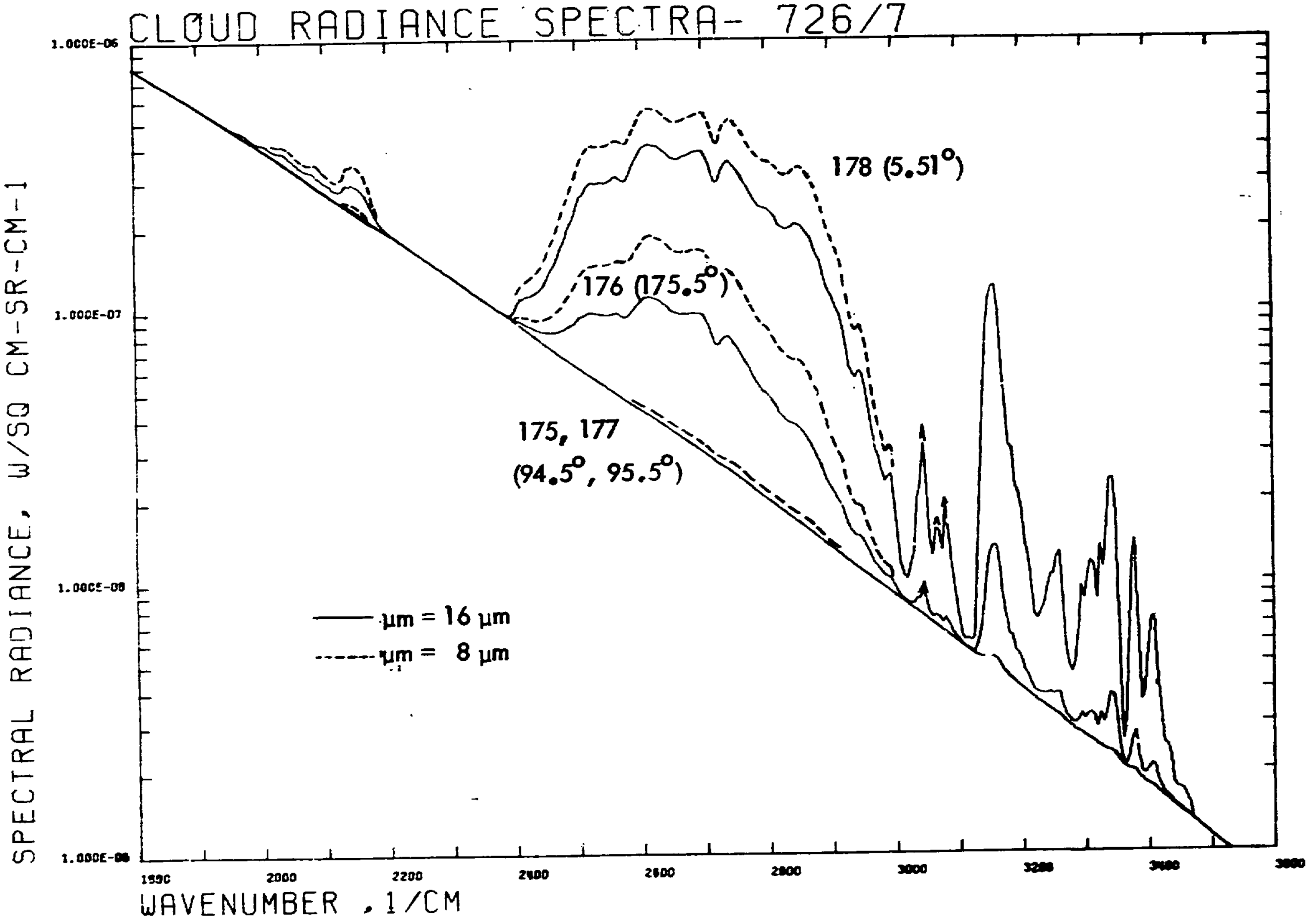

Figure 9. Calculated Cloud Radiance Spectra for AFGL Mission 726/7, for Assumed Cloud Droplet Mean Radii of 8 µm and 16 µm

Considering that the differences noted above are all explainable, at least qualitatively, and are attributable mostly to the atmospheric transmission part of the calculation, it appears that scattering model developed in Section 3.3 gives essentially correct results for the conditions represented by mission 726/7.

3.5.2 Mission 727/9

As mentioned, the AFGL aircraft observed "transmitted" radiance, while the model describes only "reflected" radiance. The underside of the cirrus cloud was observed at the same elevation as the sun (14.25 deg) but at an azimuth approximately 5 degrees different from the solar azimuth. Thus, the net scattering angle undergone by the observed radiation is roughly 5 degrees. It was reported that the AFGL interferometer observed the brightest part of the underside of the cloud (the so-called "silver lining").

Figure 10 shows the actual measurement geometry (1) and the scattering geometry assumed in calculating the cloud spectral radiance (2). That is, in the scattering calculation (which determines the ratio of reflected to incident spectral radiance at the top of the cloud) we assumed the solar elevation and line-of-sight depression angles were both 2.5 degrees, which corresponds to a net scattering angle of 5 degrees. However, in the atmospheric transmittance and radiance calculations the actual measurement geometry was used. Because the net scattering angles are approximately equal for the two geometries, one might expect the calculated spectral radiance to equal the measured spectral radiance, provided the average optical thickness traversed by received photons is the same for both geometries.

The lower part of Figure 10 indicates the general trends to be expected in the transmitted and reflected radiances as a function of distance from the cloud edge (increasing optical thickness). Normally, the transmitted diffuse radiation will first increase due to the increased number of scatterers, but will eventually decrease to zero (for $\omega_0 < 1$) due to absorption by the cloud crystals. AFGL measured the transmitted spectral radiance at the location that corresponded to maximum visual brightness. The reflected radiance is predicted by our model to

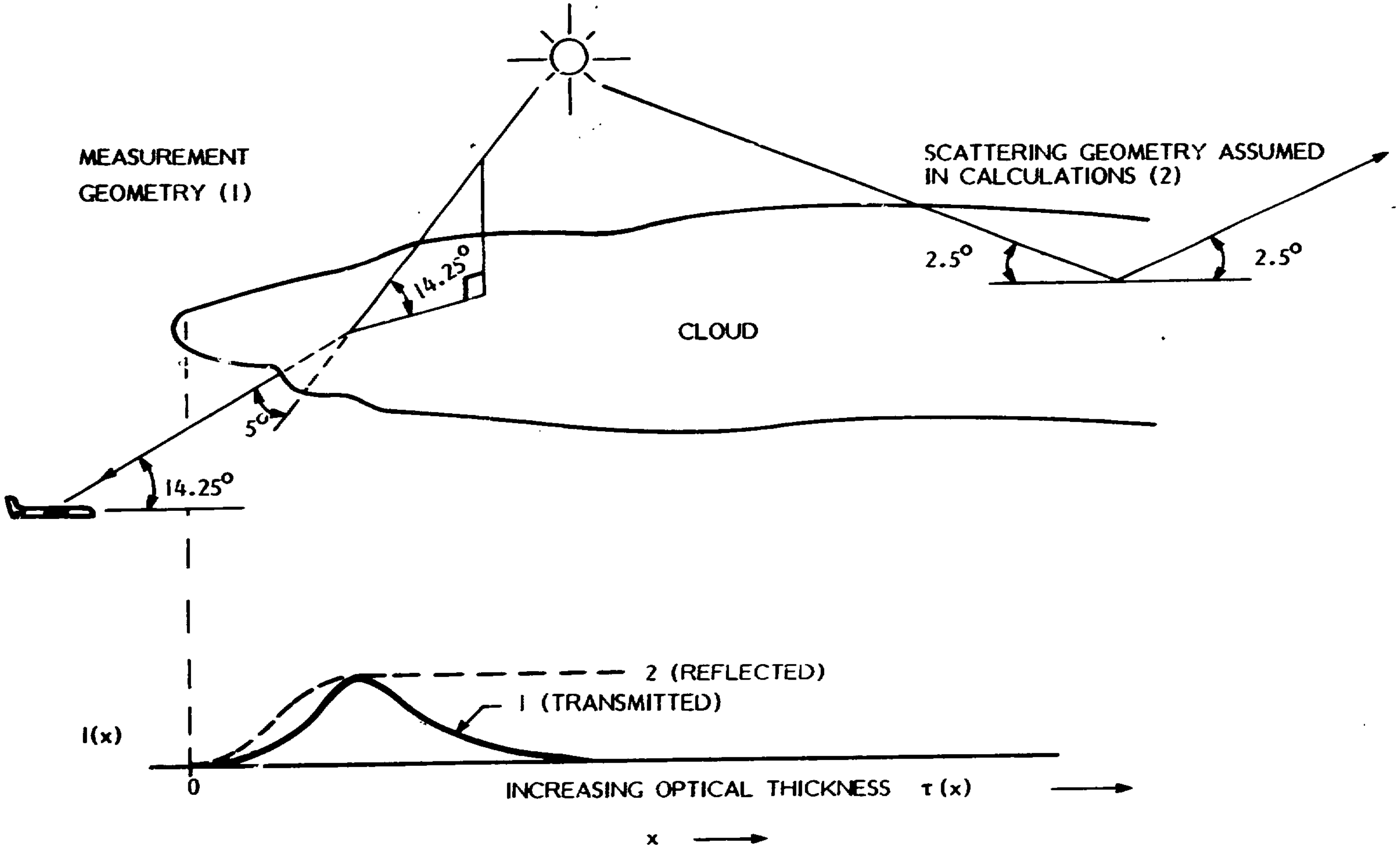

Figure 10. Scattering Geometry for AFGL Mission 727/9 versus Scattering Geometry Used in Calculations

increase monotonically with optical thickness, and to approach an asymptote (which is effectively reached at $\tau \simeq 4$). It is not unreasonable to expect that the average optical thickness traversed by the reflected radiation, when it has reached its asymtote, is the same as the optical thickness traversed by the transmitted radiation when it is a maximum, if the net scattering angles are the same in both cases. This assumption implies that the maximum transmitted and asymptotic reflected radiances are equal. This, in any case, was the basis for choosing an "equivalent" reflection geometry for the scattering calculation. We assumed an optically thick cloud ($\tau_0 = 10$) and a mean ice particle radius equal to 32 micrometers, which is a reasonable value for cirrus clouds.

Figure 11 shows the measured and calculated spectral radiances. The agreement is excellent, but it may be fortuitous, since we cannot prove the equivalence of the transmission and reflection geometries, and because the mean radius was selected arbitrarily.

3.5.3 Mission 817, Runs 1, 2 and 3

In mission 817 the spectral radiance of a thick, uniform stratocirrus cloud deck was measured between late afternoon and evening, corresponding to solar elevations ranging from 8 degrees to −1.5 degrees. The selected spectra, runs 1, 2 and 3 represent the range of elevations 8 to 2.6 degrees, and four different azimuth directions for each elevation angle.

Figure 12 shows the measured and calculated radiance spectra for Run 1. The brightest AFGL spectrum is record 365, corresponding to zero relative azimuth; the second brightest is record 367 ($\Delta\phi = 180$ degrees). The other two AFGL spectra, for relative azimuths of 90 and 270 degrees, are nearly equal, as one would expect.

Agreement between the calculated and measured spectra is generally poor. Disagreement in the 1800 to 2200 cm^{-1} region for the $\Delta\phi = 90$ and 270 degree cases suggests the cloud was warmer than assumed. Disagreement in the 2400 to 3400 cm^{-1} region for the $\Delta\phi = 0$ and $\Delta\phi = 180$ cases and the general trends predicted by the model suggest that the cloud crystals may be significantly larger

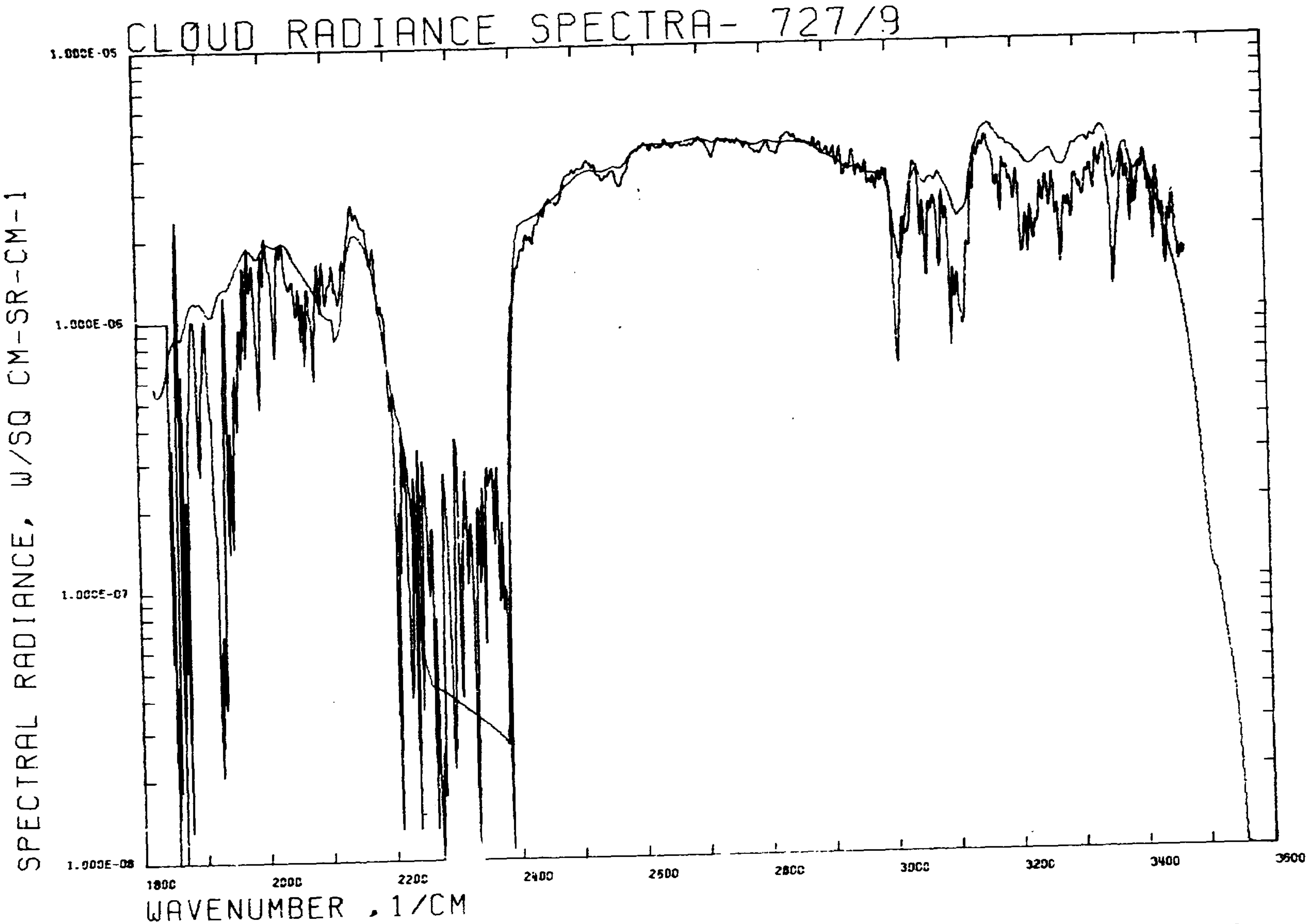

Figure 11. Measured and calculated spectra for AFGL Mission 727/9. The calculated spectrum uses a reflection geometry that is assumed equivalent to the actual measurement geometry.

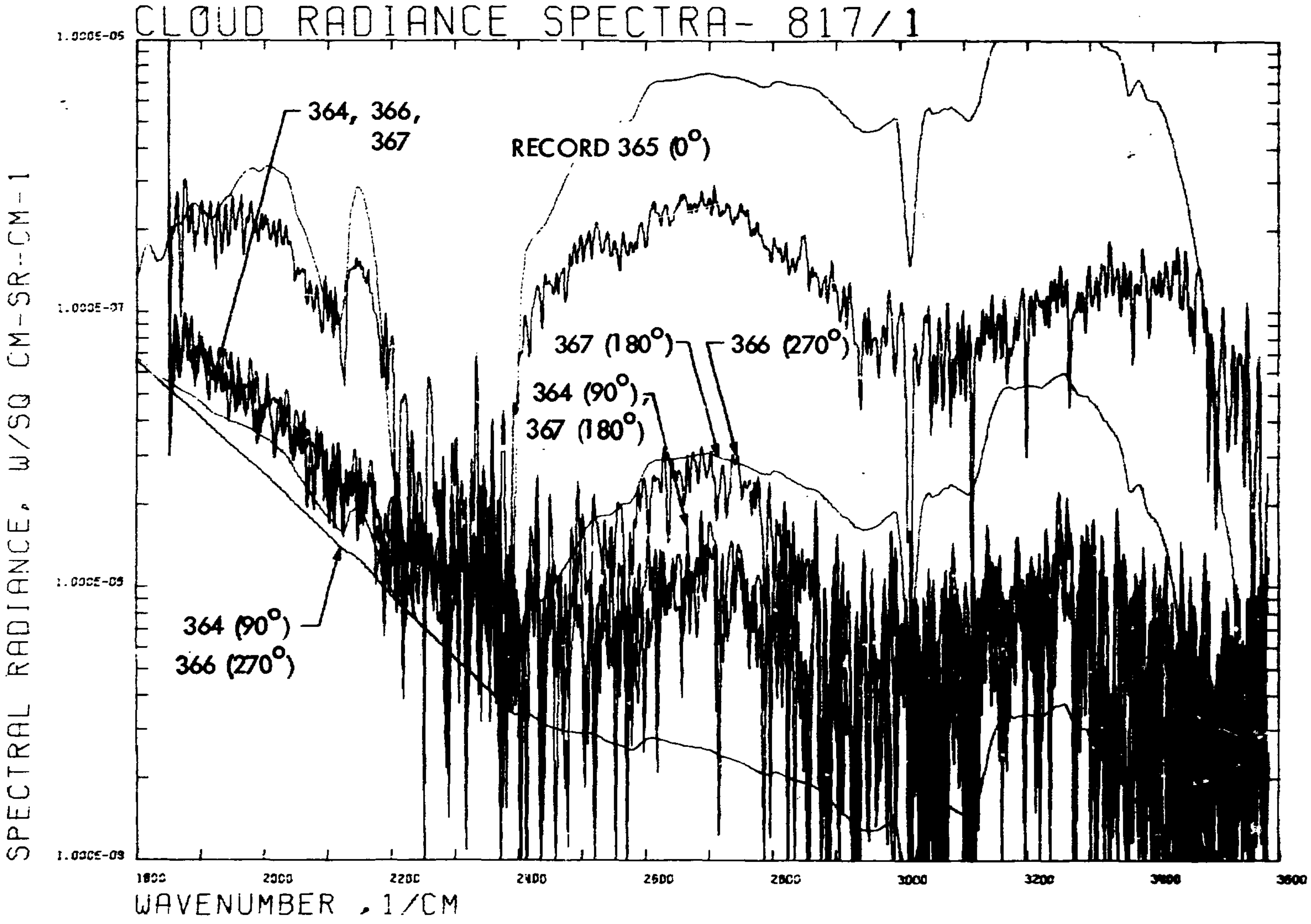

Figure 12. Measured and Calculated Spectra for AFGL Mission 817/1

than the assumed value, 32 micrometers. Also, there may have been some structure in the cloud top which cannot be accounted for in the model: note that at 2700 cm^{-1} the measured radiance is the same for $\Delta\phi = 90$ degrees and 180 degrees, and is less than that measured for $\Delta\phi = 270$ degrees. Generally, the agreement was worse when smaller optical thicknesses and/or particle sizes were used. We could not perform calculations for larger cloud particle sizes because the largest radius represented in the scattering parameter data set is 32 micrometers. Figure 13 reproduces the calculated spectra shown in Figure 12.

Figures 14 and 15 show the measured and computed spectra for mission 817, run 2. Note that there are four distinct spectra for this case because the relative azimuths are 0, 90, 180 and 300 (rather than 270) degrees. Figures 16 and 17 show the results for mission 817, run 3. As for run 1, the agreement between measured and calculated spectra is poor, and suggests that the assumed cloud temperature and particle size are both too small. For run 3, however, the brightest calculated spectrum reproduces the spectral variation of the corresponding measured radiance quite well.

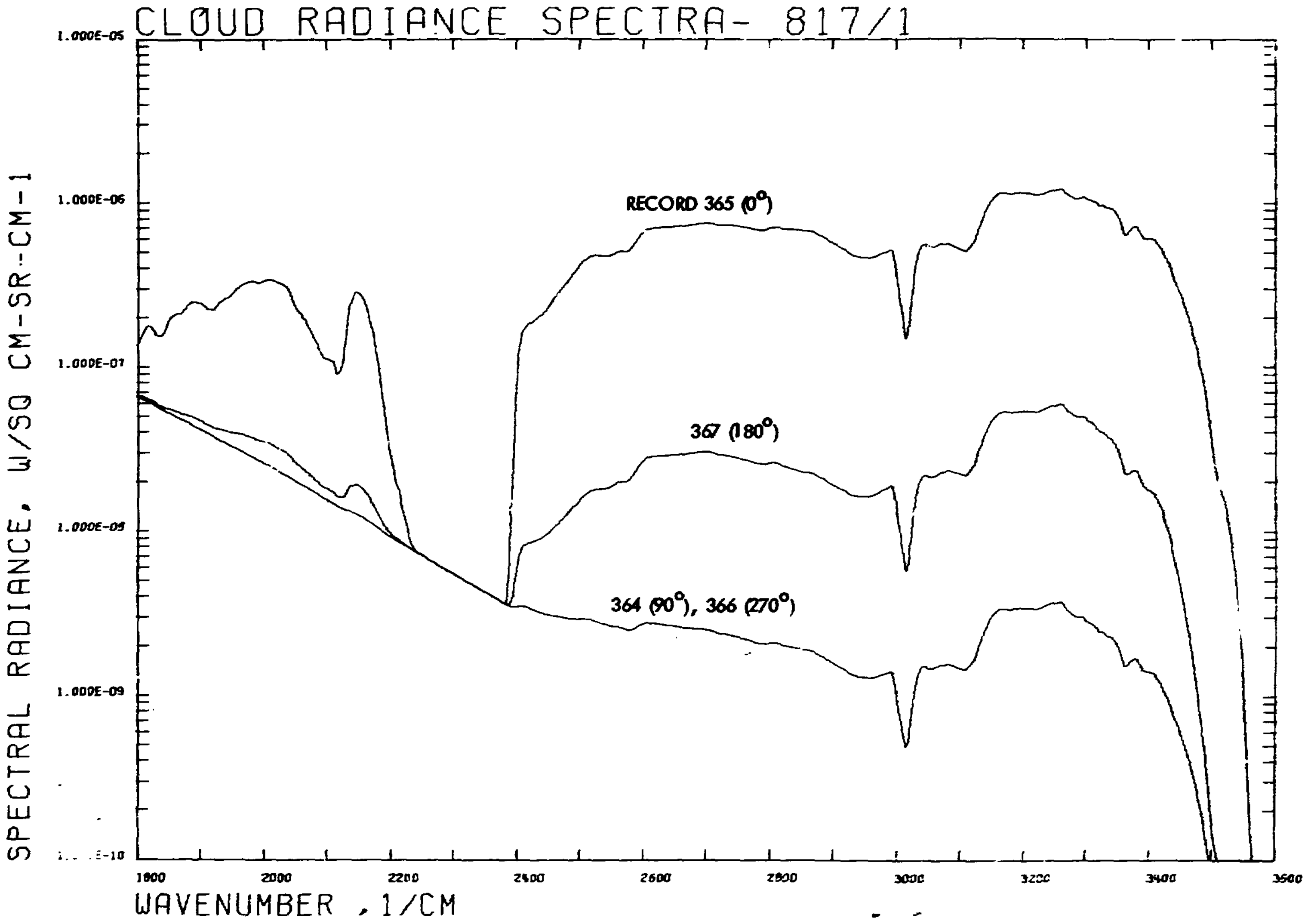

Figure 13. Calculated Radiance Spectra for AFGL Mission 817/1

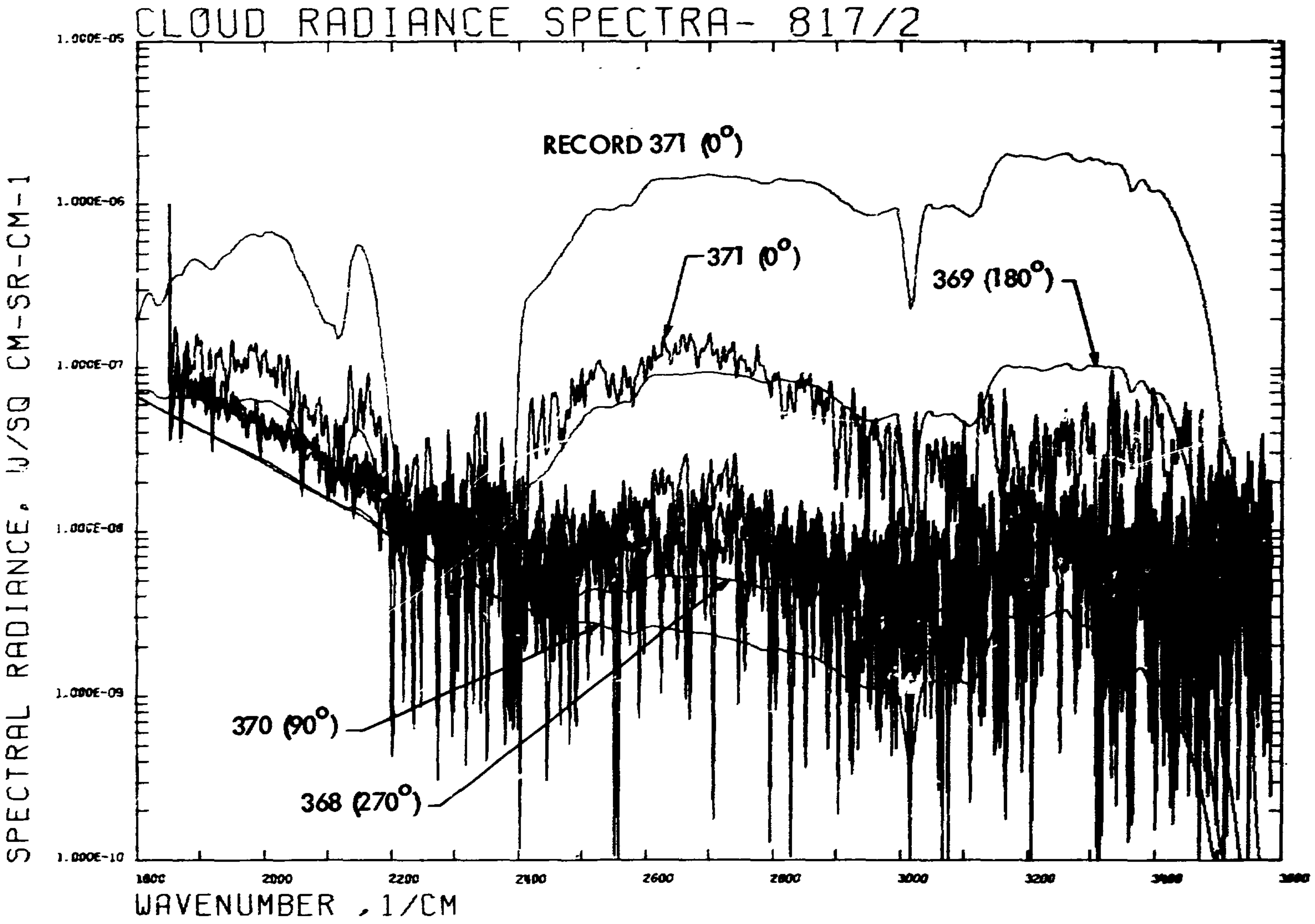

Figure 14. Measured and Calculated Radiance Spectra for AFGL Mission 817/2

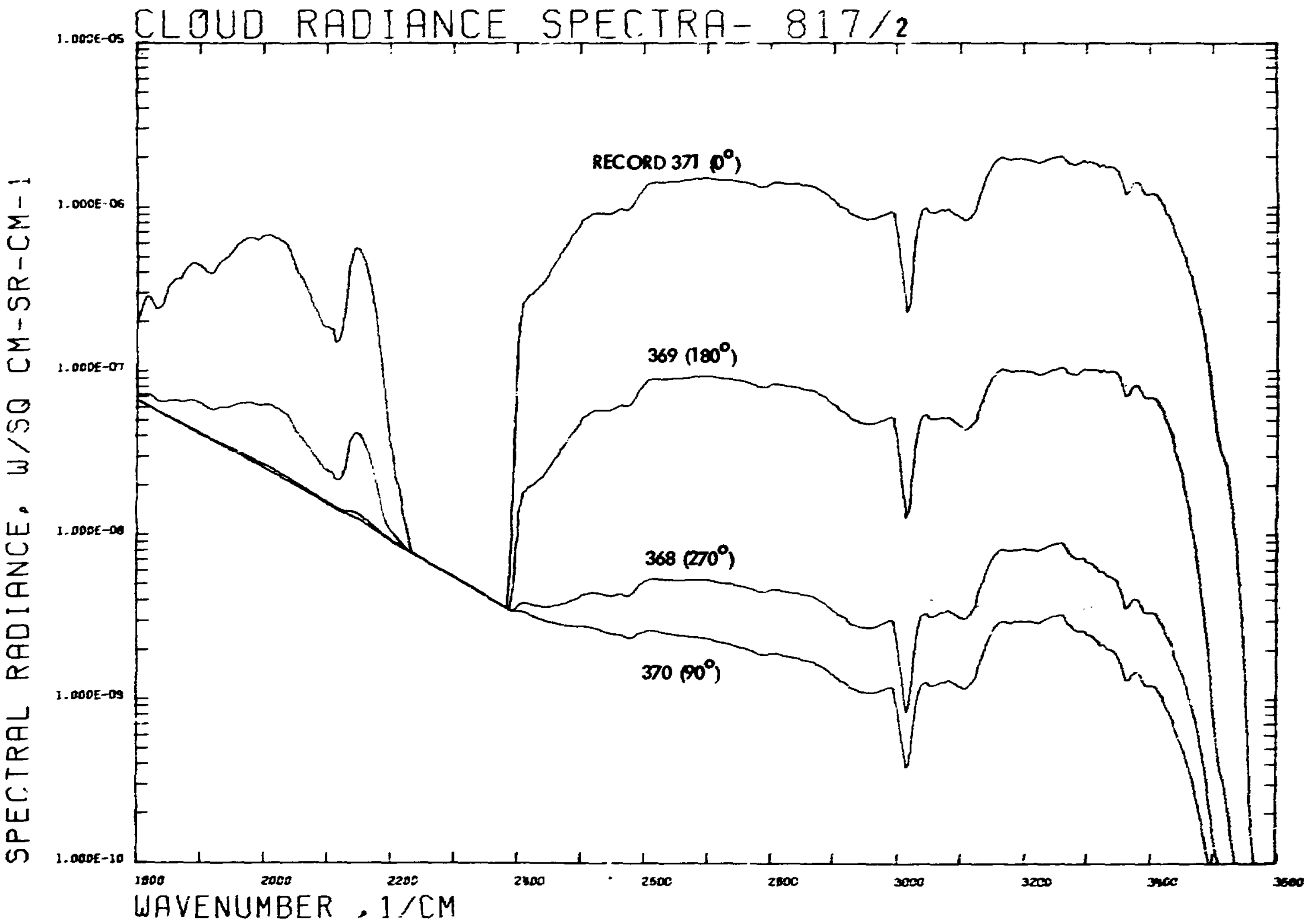

Figure 15. Calculated Radiance Spectra for AFGL Mission 817/2

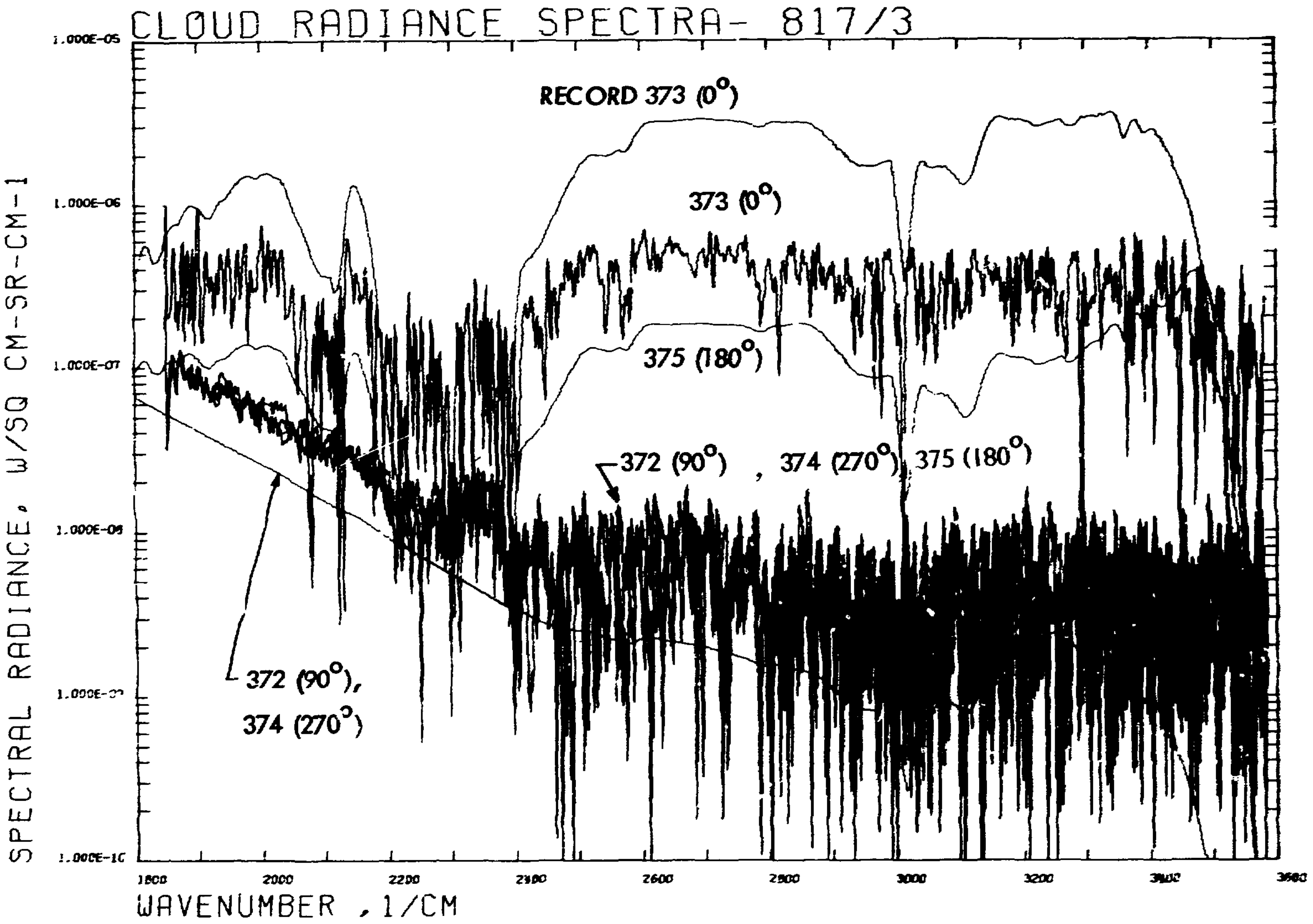

Figure 16. Measured and Calculated Radiance Spectra for AFGL Mission 817/3

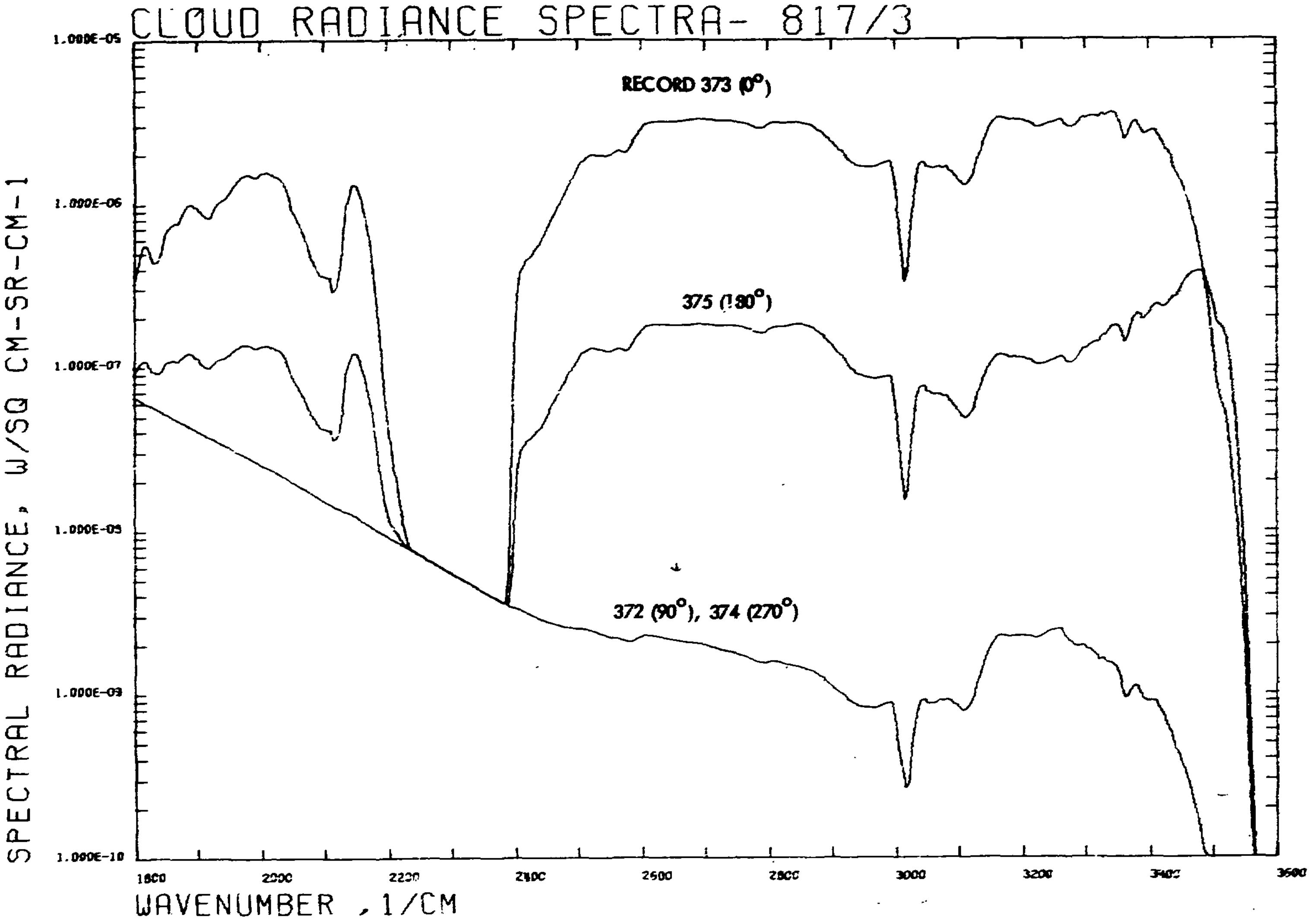

Figure 17. Calculated Radiance Spectra for AFGL Mission 817/3

SECTION IV

MODELS FOR SUNGLITTER AND SPECULAR REFLECTION BY WATER

4.1 SUNGLITTER MODEL

The reflection of sunlight from a rough water surface is visually observed to consist of a broad intense glitter pattern. This pattern is brightest when looking along the azimuth toward the sun and diminishes symmetrically on either side of this direction. At any given instant in time the glitter pattern is seen to consist of many highlights. These highlights are single small reflecting elements or facets of the surface which are momentarily oriented to specularly reflect the image of the sun in the direction of the observer. The number of specularly reflecting highlights in a fixed IFOV is a random function of the surface wind direction and velocity. Consequently, the apparent brightness within the IFOV results from spatial averaging over many unresolved highlights in the scene.

The problem of calculating the average sunglitter radiance has attracted the attention of many investigators who were motivated by the need for an analytical model to aid in assessing the performance of shipboard infrared and radar search and track systems operating against a sunglint ocean background. The radar system analysts have traditionally treated sunglitter as a physical optics problem involving a vector form of the Kirchoff integral. On the other hand, the infrared systems community have preferred the geometric optics approach which consists of spatially averaging the contributions from many randomly oriented, unresolved highlights about the point of interest.

The validity of both the geometric optics and the physical optics solutions is the subject of current research. The geometric optics approach of Cox and Munk[7] is employed in this study because of its simple and physically intuitive interpretation of the sunglitter phenomenon.

The basic expression for the average reflected spectral radiance for surface wind speed W, local angle of incidence ω, and reflection geometry angles $\alpha, \beta, \nu, \varphi$ is:

$$\langle N_{sun}(\lambda)\rangle = \left[\rho(\omega,\lambda)\ H_0(\lambda)\ T(\lambda)\right] S(\omega)g(\alpha,\beta;\ \nu,\varphi)P(Z_u,Z_v,W)/\pi \qquad (27)$$

The angular behavior of the sunglitter is given by the products of the surface slope shadowing factor (S), a geometric factor (g), and a probability factor (P) which expresses the probability of occurrence of wave slopes having components Z_u and Z_v. The spectral distribution of the radiance is determined by the product of the atmospheric spectral transmission (T) along the sun-surface-observer path, the solar spectral irradiance (H_0) at the top of the atmosphere, and the spectral reflectivity (ρ) of the ocean surface.

It is assumed that warning sensors are insensitive to the polarization properties of the surface, so that $\rho(\lambda)$ is the unpolarized surface reflectivity:

$$2\,\rho\,(\omega,\lambda) = \rho_v\ (\omega,\lambda) + \rho_h\ (\omega,\lambda) \qquad (28)$$

where ρ_v and ρ_h are the Fresnel spectral reflection coefficients for vertical and horizontal polarization, respectively.

Each of the factors in Eq. (27) is a complicated function of source-receiver geometry, wind speed and direction, surface reflectivity, and wavelength. Explicit expressions for each of these factors — ρ,S,g, and P — are given in Appendix C. These expressions are sufficiently complicated to require a computer code to calculate $\langle N_{sun}(\lambda)\rangle$.

A search of the available literature revealed that the only available validations of the Cox-Munk model involved broad-band IR measurements of the angular variation of $\langle N_{sun}\rangle$ with wind speed and source-receiver geometry. Furthermore, all of the previous validations included other components of the sea background, such as reflected skylight, upwelling ocean radiance, and thermal sea surface emission.

The strong liquid water absorption in the infrared allows us to safely ignore the upwelling ocean radiation caused by volume scattering of the incident solar radiation from beneath the ocean surface.

Thermal emission is a significant component of the ocean background radiance and can be evaluated using the Cox-Munk technique. Krishnan and Peppers[8] have found that average thermal emission for strong ocean absorption is given by:

$$\langle N(\lambda)\rangle_{th} = \left[1 - f(\beta, W_u, W_v)\right] N_0(\lambda, T) \qquad (29)$$

where $N_0(\lambda,T)$ is the blackbody radiance for sea temperature T, and $f(\beta, W_u, W_v)$ represents an average surface reflectance:

$$f(\beta, W_u, W_v) = \cos\beta\ \rho(\beta) \left\{1 + \frac{1}{2\rho(\beta)}\rho''(\beta) - 2\rho'(\beta)\tan(\rho)\right\}$$

$$\left[\sigma_u^2 \cos^2\alpha + \sigma_v^2 \sin^2\alpha\right]$$

$$+ \frac{1}{2\rho(\beta)}\left[\rho'(\beta)\ \mathrm{ctn}\ (\beta)\right]\bullet\left[\sigma_u^2 \sin^2\alpha + \sigma_v^2 \cos^2\alpha\right] \qquad (30)$$

The quantities ρ' and ρ'' are the first and second derivations of the reflection coefficient with respect to surface slopes, α and ρ are the elevation and azimuth of the observed radiance, and σ_u, σ_v are the rms variation in surface slopes in directions u and v. These quantities are all defined in greater detail in Appendix C.

The other significant component of the ocean background spectral radiance is reflected skylight. Reflected skylight can be calculated from the expression used for sunglitter (Eq. 27) if one replaces the solar irradiance term $H_0(\lambda)\ T(\lambda)$ by the irradiance at the sea surface due to a small segment of the sky and then integrates the resulting expression over the sky dome. Krishnan and Peppers[8] assumed the sky spectral radiance $N_s(\lambda)$ was uniform over the entire sky dome and derived an expression for the average reflected skylight spectral radiance in terms of $N_s(\lambda)$ and the average ocean reflectance $f(\beta, W_u, W_v)$:

$$\langle N(\lambda)\rangle_{sky} = N_s(\lambda)\ f(\beta, W_u, W_v) \tag{31}$$

Thermal emission and reflected skylight backgrounds are always present in sunglitter measurements, adding an additional complication to the task of verifying a sunglitter model.

Fortunately the AFGL measurements[1] of 5 December, 1974 are available in a form which can be used to obtain only the sea glitter component. This data was obtained from an altitude of 15,000 feet over the Atlantic Ocean off the coast of New Hampshire (pertinent mission parameters are given in Table 2. Two sets of measurements were made while the aircraft was banked at an angle of 45 degrees to the horizon. The first measurement (Figure 18) was made looking directly into the glitter patch. The second measurement (Figure 19) was made at an azimuth of 30 degrees away from the visible sunglint path. A computer calculation for the second case indicated that the sunglint should be reduced by a factor of 1000 when compared to the first measurement. Consequently, the second spectrum contains only background and atmospheric emissions which may be removed from the first spectrum.

TABLE 2

MISSION PARAMETERS FOR AFGL FLIGHT TR3, RUN 1

Date:	5 December 1974	Universal Time:	1639
Latitude (deg):	43.26	Longitude (deg):	70.08
Wind Direction (deg):	320-Concord, N.H. 260-Pease AFB	Wind Speed (knots):	5.0
Visibility (nmi):	30.0	Radiosonde Data:	1200 UT Portland, Maine

Figure 20 shows the difference between Figures 19 and 18. A very large sunglint component appears in the data between 3000 and 6000 cm^{-1}. The deep atmospheric absorption bands from 5100 to 5650 cm^{-1} and from 3000 to 4000 cm^{-1} are caused by the 1.9 and 2.7-micrometer water vapor absorption bands. Two narrow CO_2

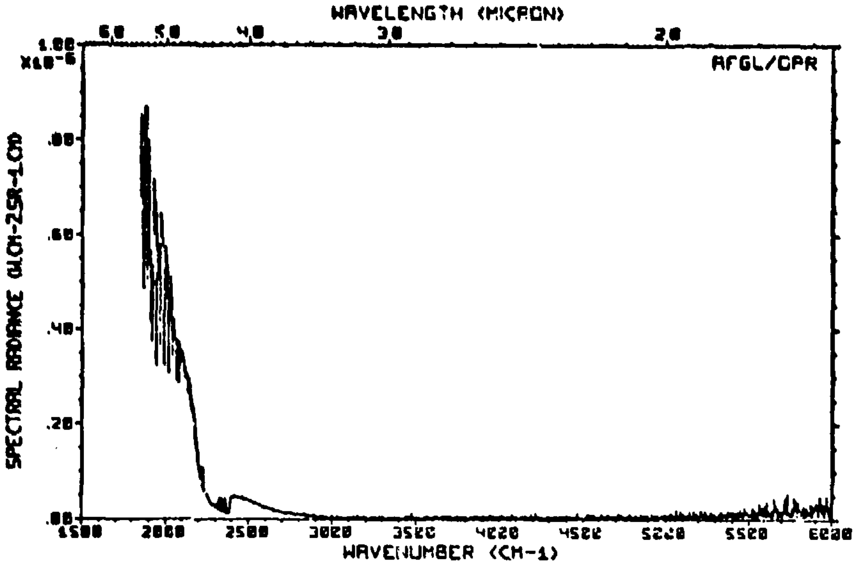

Figure 18. Spectral Radiance of the Atlantic Ocean near noon facing away from the sun at 15,000 feet

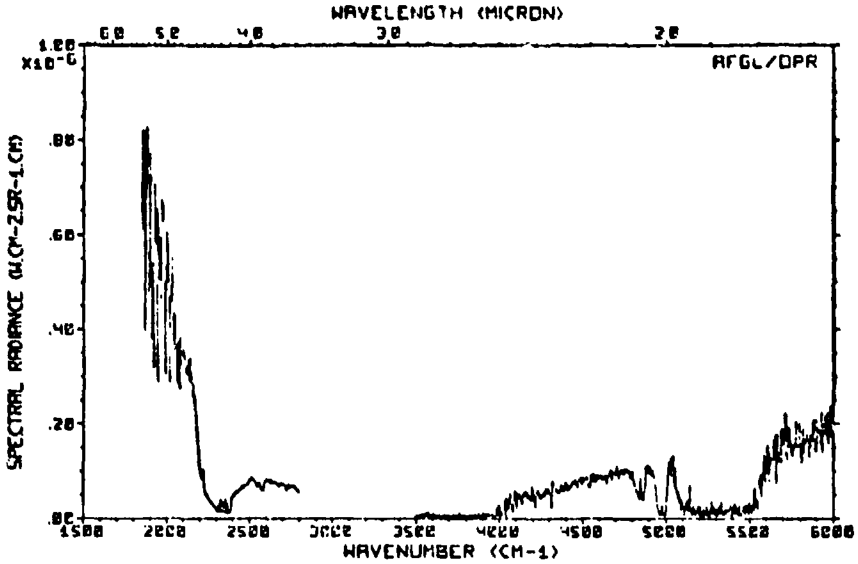

Figure 19. Spectral Radiance of the Atlantic Ocean near noon facing towards the sunglint from 15,000 feet

absorption bands are also present between 4800 and 5000 cm^{-1}. AFGL suspects the validity of their data in the blank area from 2800 to 3500 cm^{-1} in Figure 19.

The sunglint spectrum, unlike other natural backgrounds is decidedly non-Planckian because of the abrupt change in the ocean surface reflectivity at 2.94 micrometer This feature is evident in the curve labeled CM in Figure 20. The CM curve is the computed result using the Cox-Munk expression for sunglint with 100% atmospheric transmission for the geometry and wind conditions given in Table 2. This curve also ignores shadowing (S) which only becomes significant at grazing angles.

The values displayed as crosses in Figure 20 represent the reflected spectral radiance when atmospheric attenuation is included. The atmospheric spectral transmittance of the sun-surface-aircraft path was computed using the modified LOWTRAN 4 code described in Section III.

In general the model predictions agree well with the AFGL measurements. The differences between the AFGL data and the transmittance-corrected theoretical spectrum are probably due to an inaccurate estimate of the aerosol optical thickness along the transmission path.

4.2 SPECULAR REFLECTION MODEL

The spectral radiance reflected specularly by a smooth water surface is simply

$$N(\omega,\lambda) = \rho(\omega,\lambda)T(\lambda)N_0(\lambda), \qquad (32)$$

where $\rho(\omega,\lambda)$ is the surface reflectivity for incidence angle ω, $N_0(\lambda)$ is the extraterrestrial spectral radiance of the sun, and $T(\lambda)$ is the spectral transmittance of the path from the sun to the water surface and then to the receiver. The reflectivity is given by Eq. (28) (see Appendix C also).

AFGL spectra of specular reflections were compared to the predictions of Eq. (32). In calculating (ω,λ) we used the water indices of refraction tabulated

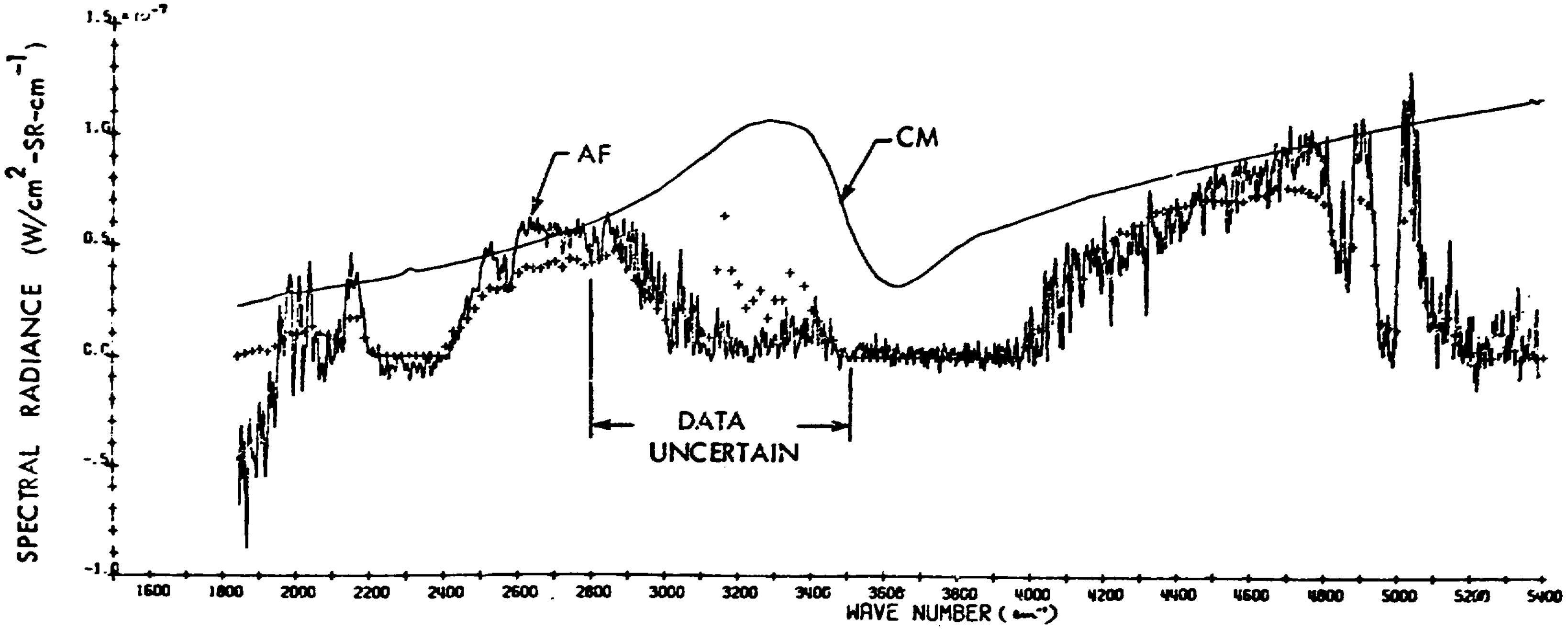

CM - COX, MUNK MODEL (100% TRANSMITTANCE)
AF - AFGL DIFFERENTIAL RADIANCE
\+ - COX, MUNK (LOWTRAN 4 TRANSMITTANCE)

Figure 20. The differential spectral radiance between Figures 19 and 18 (curve AF). AFGL suspects the accuracy of their observations over the 2800 to 3500 cm^{-1} region. The Cox Munk theoretical prediction with S = T = 1 is labeled CM. A + sign denotes the Cox Munk predictions with S = 1 and T(λ) determined by the modified LOWTRAN 4 atmospheric transmission code.

by Hale and Querry[3]. These data apply to pure water, but the solutes typical in ocean water will not appreciably change the refractive indices. However, the presence of films such as oil slicks or other pollutants can have a large effect on $\sigma(\omega,\lambda)$. One of the objectives in analyzing the AFGL spectra was to determine whether they differ significantly from predictions based on the assumption of pure water. The $N_0(\lambda)$ values used were based on the solar irradiance spectrum of Thekaekara[9] and the value $1.9\pi \times 10^{-5}$ sr for the average solid angle subtended by the sun.

Validation of the specular sunglint model for smooth water surfaces is complicated by other backgrounds in the receiver field of view. Thermal emission and reflected skylight are always present in measurements. Fortunately, the AFGL flight data consists of 2 sets of spectra. One set contains glint plus background and the other set consists of background only. The difference between the two sets of data allows one to isolate the glint data for model verification.

Five spectra of specular sunglints and associated backgrounds were selected from AFGL missions 729 and 803. These are identified in Table 3. The atmospheric profiles used in the modified LOWTRAN 4 calculations were based on AFGL-supplied radiosondes, and are given in Appendix B. The differential radiance spectra (glint-plus-background minus background only) were calculated and are displayed as curves labeled "AFGL" in Figures 21 through 25. Included in each of these spectra is a multiplication factor of 16 which converts "apparent" spectral radiance to true spectral radiance within the solar image; i.e., the instrument IFOV diameter was two degrees and the sun's image subtends approximately 0.5 degrees.

Figures 21 through 25 also show the predicted spectral radiances with and without atmospheric attenuation included (the cross symbols and the low resolution solid curves, respectively). Each pair of predicted spectra have been multiplied by a scaling factor σ that forces agreement between the predicted values (those with atmospheric attenuation included) and the measured line radiance values in the window regions 2400–3000 cm^{-1} and 4000–4800 cm^{-1}. These scale factors, given in Table 4, may be regarded as the fraction of the solar disc observed; i.e., in some cases a broken image may have been observed due to surface

TABLE 3
MISSION IDENTIFIERS FOR AFGL SPECULAR GLINT SPECTRA

REFLECTION SOURCE	AFGL MISSION/RUN	AIRCRAFT ALTITUDE (kft)	SOLAR ELEVATION (degs)	COMMENTS
Thermalito Pond	729 / 6	15	25.93	power plant holding basin
Swamp in Sacramento Valley	729 /15	15	7.34	no background data
Mono Lake	803 / 4	19	23.63	high sun angle
Mono Lake	803 / 9	19	18.58	low sun angle
Walker Lake	803 /15	19	5.85	low sun masked by mountains

TABLE 4
SCALE FACTORS FOR EACH MISSION

MISSION/RUN	σ(2400–3000 cm^{-1})	σ (4000–4800 cm^{-1})	σ(USED IN FIGURES)
729 / 6	0.0062	0.0050	0.0055
729 /15	0.0526	0.0327	0.0403
803 / 4	0.0321	0.0128	0.0183
803 / 9	1.0560	0.8260	0.9290
803 /15	0.4350	0.5460	0.4840

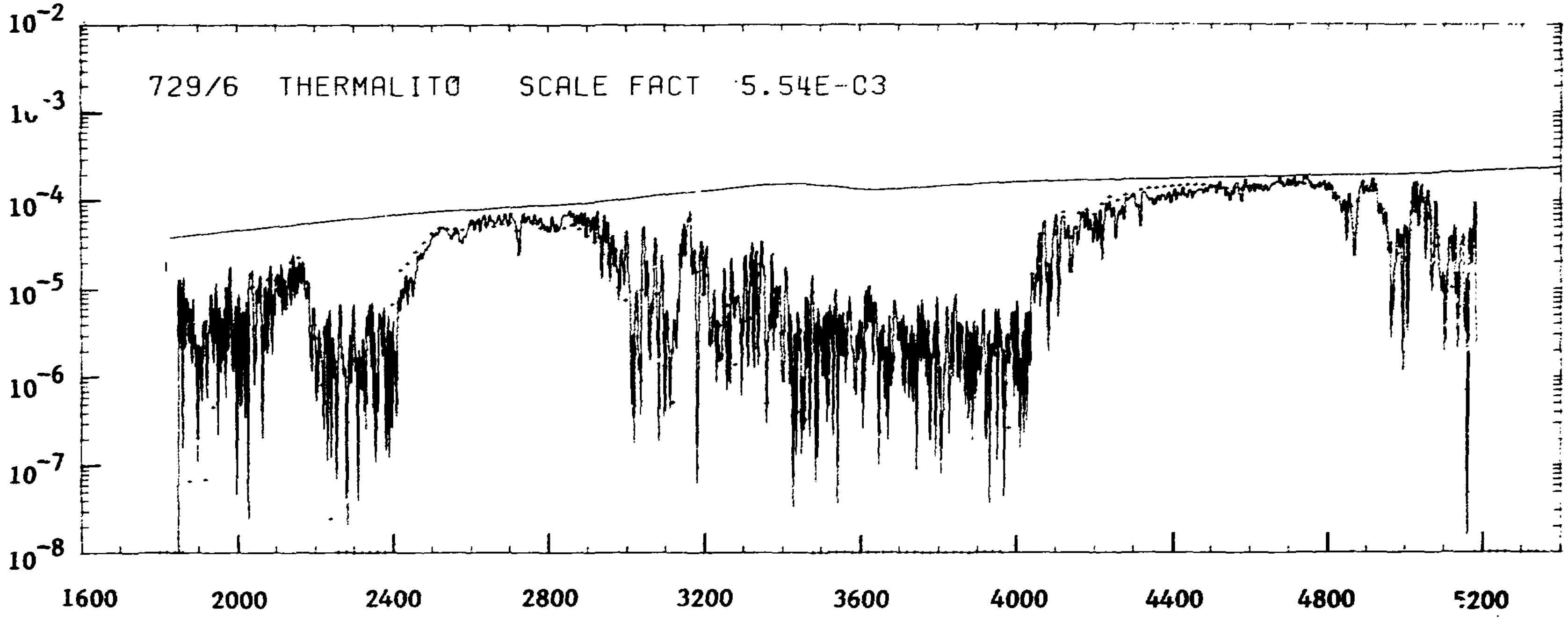

Figure 21. Measured and calculated spectra of specular sunglint for AFGL mission 729/6

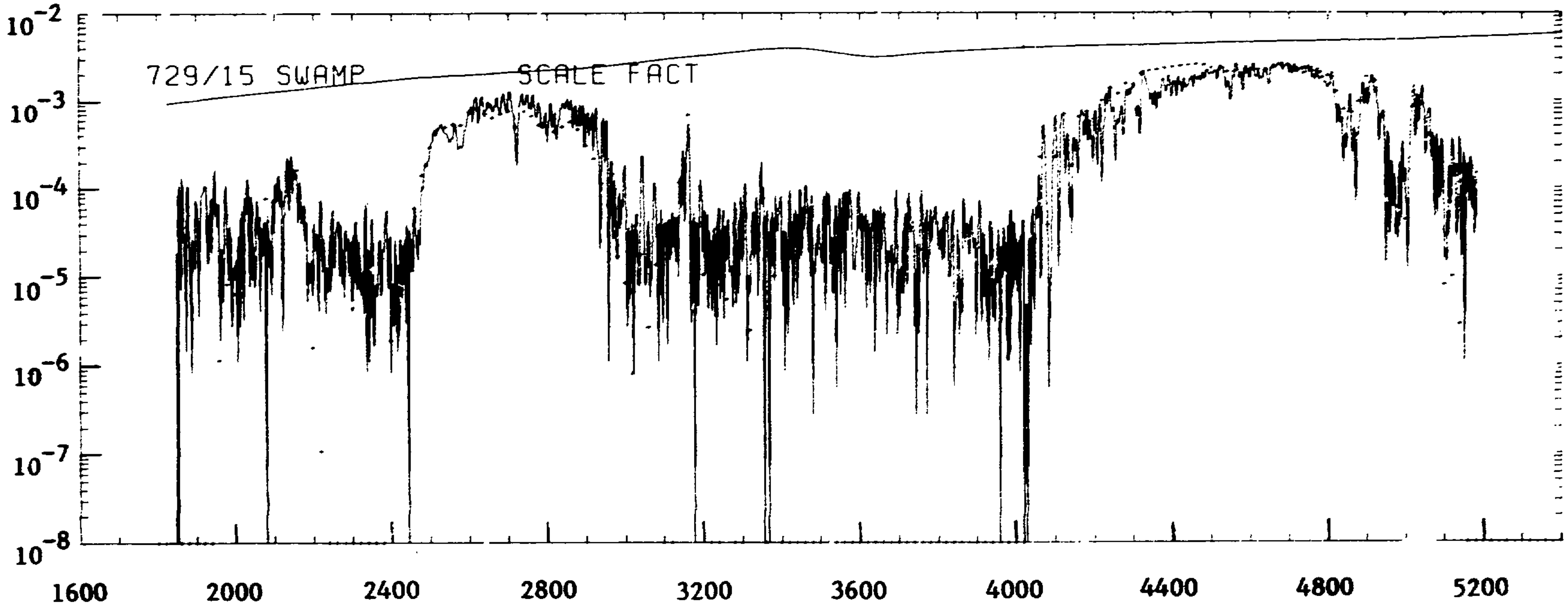

Figure 22. Measured and calculated spectra of specular sunglint for **AFGL** mission 729/15

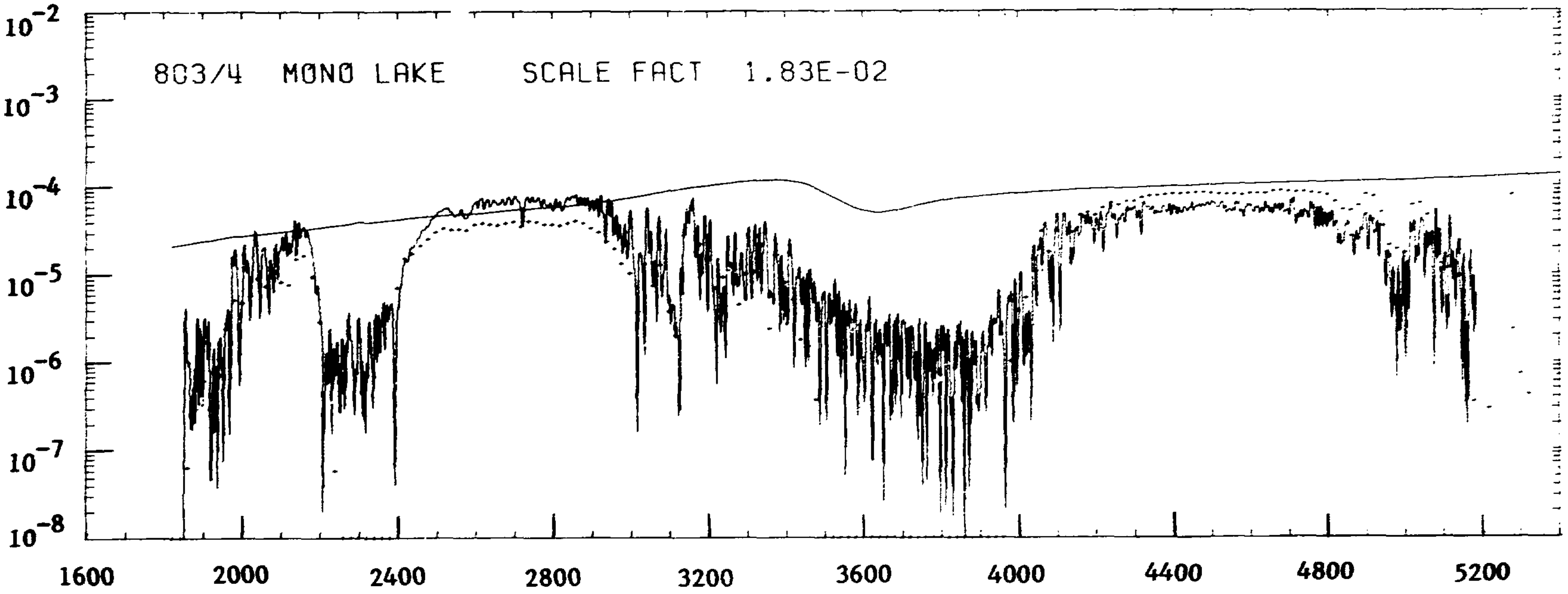

Figure 23. Measured and calculated spectra of specular sunglint for AFGL mission 803/4

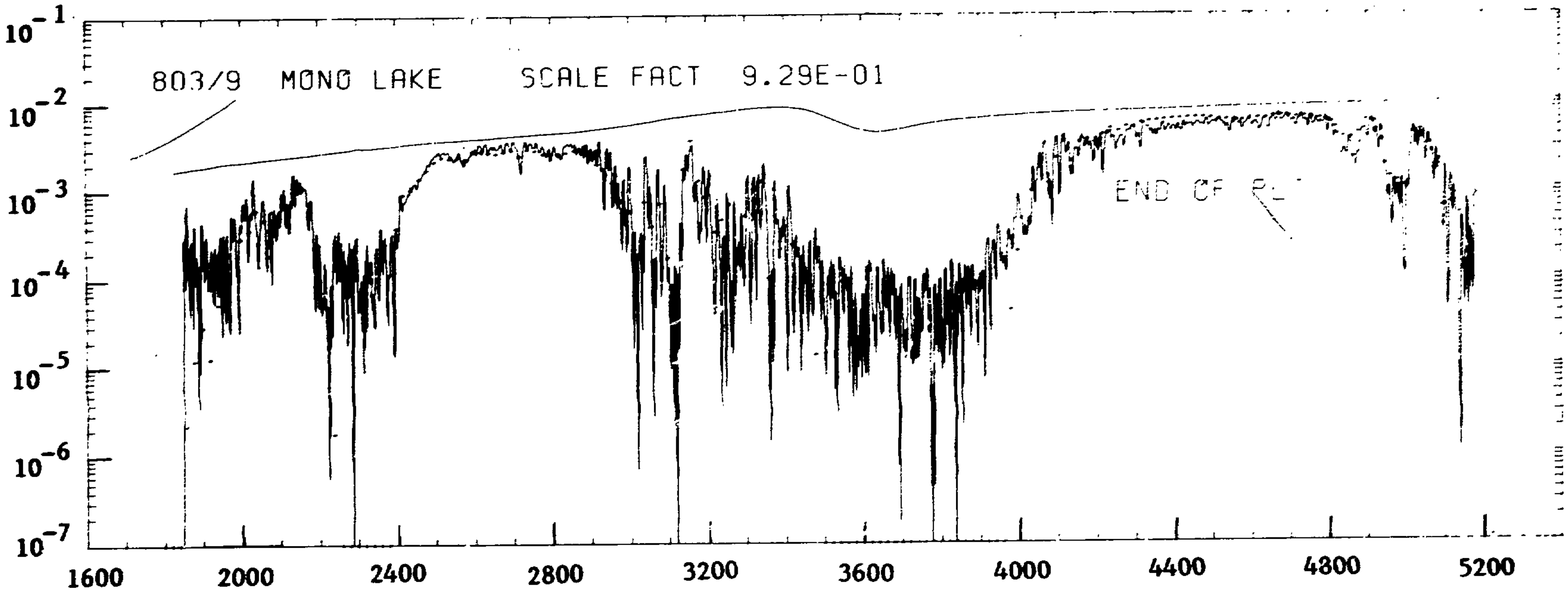

Figure 24. Measured and calculated spectra of specular sunglint for AFGL mission 803/9

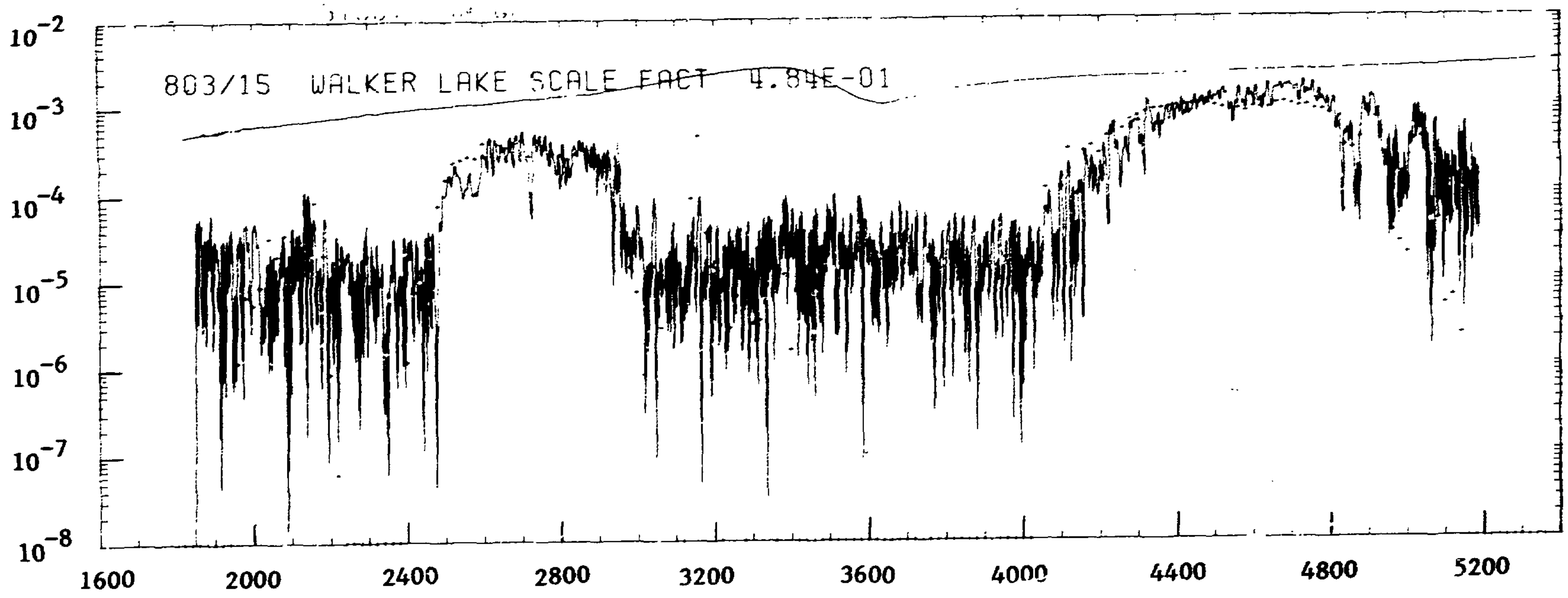

Figure 25. Measured and calculated spectra of specular sunglint for AFGL mission 803/15

roughness (wind), and in at least one case (803/15) the image was not whole because mountains blocked some of the low-angle incident sunlight. Scale factors were determined separately for each of the two window regions (see Table 4); a weighted average was used for the plots shown in Figures 21 through 25.

There appears to be excellent spectral agreement between theory and observation in all of the plots. The slight spectral discrepancies are probably caused by the inability of LOWTRAN 4 to accurately model the atmospheric transmission over the long slant ranges corresponding to the low sun angles. (There is at least 2.27 air masses between the sun and the water surface for the highest solar elevation – 26 degrees and at least 8.90 air masses for the lowest solar elevation – 6 degrees. The only suggestion of a spectral reflectivity variation different from that of pure water is in the mission 803/4 case for Mono Lake. However the predicted spectrum for the same lake observed at lower sun elevation (803/9) shows excellent spectral agreement with the AFGL data, and has a scale factor of 0.93.

The only disturbing aspect of the results is the case-to-case variation in the predicted radiance levels. The best theoretical agreement with data occurs for the Mono Lake spectrogram at a low sun angle where $\sigma = 0.93$. Yet the same scene recorded at a higher solar elevation has $\sigma = 0.02$. In other words, a nearly a fifty-fold reduction in scaling factor is needed to explain the AFGL data for the same scene observed at slightly different sun angles.

SECTION V

BLUE SPIKE SPECTRAL EMISSION/ABSORPTION MODEL

An efficient model and computer code were developed to calculate the fully resolved spectrum of the blue spike of the 4.3-micrometer CO_2 band, a well-understood phenomenon resulting from the emission of hot CO_2 transmitted through a cooler layer (atmospheric path) also containing CO_2. The model avoids using the lengthy line-by-line procedure by representing the hot-and cold-gas spectral absorption coefficients as two different Elsasser bands with spectrally varying line intensity S and spacing d. Theoretical formulas for the intensities, halfwidths and spacings of the rotational lines of the 00^01-00^00 transition are used with empirical modifications that force agreement with measured spectra and computed line-by-line spectra. The model places the Elsasser spectral absorption maxima at the exact theoretical line positions, which preserves the observed spectrum features and, in particular, the correlation of emission and absorption lines. The model sacrifices very little accuracy and is potentially 30 to 60 times faster than a conventional line-by-line calculation of the blue spike spectrum.

Figure 26 shows a measured absorptance spectrum of the 4.3-micrometer blue spike produced by a flame at 2330 K. A notable characteristic of the spectrum is its resemblance to the periodic Elsasser[10] absorption coefficient

$$k(\nu) = \frac{S}{d} \frac{\sinh \beta}{\cosh \beta - \cos (2\pi\nu/d)} \; ; \; \beta = 2\pi\gamma/d, \qquad (33)$$

which represents exactly an infinite periodic succession of equal Lorentz lines of intensity S, halfwidth γ and spacing d. In this equation ν represents the frequency measured from the center of any line. Of course, the intensities and spacings are not constant in the actual (measured) spectrum, but one might assume that its absorption coefficient can be approximated by Eq. (33) if S and d are allowed to be slowly varying functions of frequency ν.

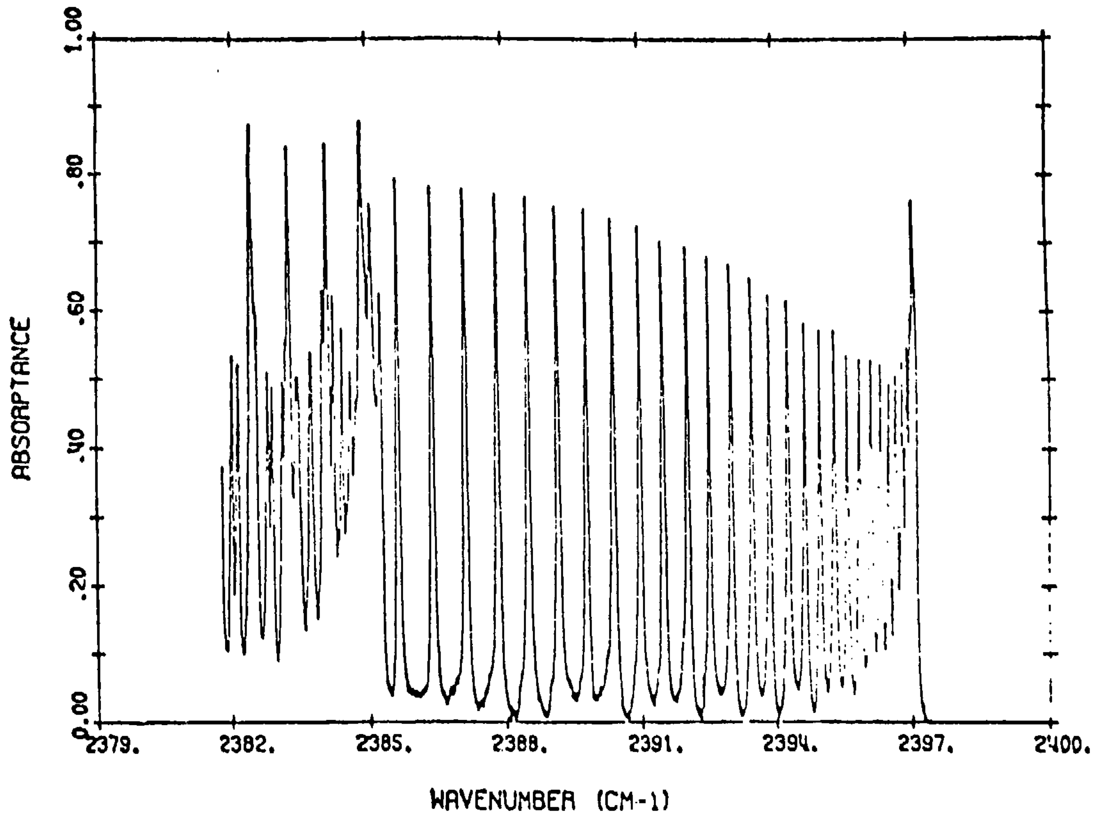

Figure 26. Experimentally Observed Absorptance Spectrum of the CO_2 "BLUESPIKE" in an Isothermal Flame at 2330 K. Path length = 3.3 cm, $p_{CO_2} = 0.383$ atm, $p_{N_2} = 0.616$ atm

In fact, the Elsasser model cannot represent the actual spectrum, even when variable S and d are used, because the model assumes Lorentz lines whereas measurements show that the true CO_2 line shape is "sub-Lorentzian," i.e., is described by the well-known Benedict line shape[11] or those propounded by Burch[12] or Yamamoto.[13] However, it is still possible to use a modified form of the Elsasser model to mimic the essential features of a measured spectrum, namely the heights of the absorption maxima and the levels of the minima between absorption lines. The only differences then remaining are the values of absorption coefficient between maxima and minima, which for the purposes of this study can surely be considered a second-order effect.

The heights of the maxima and minima in the Elsasser absorption coefficient are obtained by setting the denominator term $\cos(2\pi\nu/d)$ equal to ± 1. We find that:

$$\begin{aligned} k_{max} &= \frac{S}{d} \; \frac{1}{\tanh(\beta/2)}, \\ k_{min} &= \frac{S}{d} \; \tanh(\beta/2). \end{aligned} \tag{34}$$

Hence, the product of maximum and minimum absorption coefficients is:

$$k_{max}k_{min} = (S/d)^2, \tag{35}$$

which is equivalent to the equation

$$\log(S/d) = \frac{1}{2}\left[(\log k_{max} + \log k_{min}).\right] \tag{36}$$

This shows that the median ordinate of the upper and lower envelopes of the absorption coefficient plotted on a logarithmic scale is equal to log(S/d). We can also show that:

$$\beta = 2\tanh^{-1}\left[10^{1/2\,(\log_{10}k_{min} - \log_{10}k_{max})}\right] \tag{37}$$

In other words, the average of the logarithmic absorption coefficient and the total logarithmic excursion uniquely determine S/d and β, the two parameters of the Elsasser model. It is easy to see how $S(\nu)$ and $\gamma(\nu)$ [which determines $\beta(\nu) = 2\pi\gamma(\nu)/d(\nu)$] can be empirically adjusted so that the Elsasser model fits the maxima and minima of a measured blue spike spectrum, and also retains the actual line positions and line spacing $d(\nu)$.

Our calculations represent the $00^{o}1$–$00^{o}0$ transition, which is the only one of importance in the blue spike region. The rotational lines included have J values from 50 to 122 (corresponding to the bandhead), and from 122 to 172 in the return line spectrum. Beyond the bandhead we represent the line component of the spectrum as one side of a Benedict spectral line centered at the bandhead and matching the absorption coefficient at the center of the $J = 122$ line. However, in the region near and beyond the bandhead, in the case of the cool gas (atmospheric) absorption coefficient, we add a continuum contribution represented by the sum of the wings of two Benedict lines placed near the "centers of gravity" of the P and R branches of the $00^{o}1$–$00^{o}0$ band; this follows a procedure defined by Carpenter[14] to represent the band continuum. This continuum correction is unnecessary for the hot gas absorption coefficient at gas temperatures above 500 K.

After computing the hot-gas and cool-gas spectral absorption coefficients in this manner, the code computes the spectral radiant emission of a hot-gas slab or cylinder of specified properties, and the spectral transmittance of a specified cool-gas (atmospheric) path. Finally, it multiplies these two spectra together on a point-by-point basis to obtain the received blue-spike spectral radiance.

5.1 DETAILS OF THE MODEL

We will first define the basic equations of the model, then the empirical adjustments. The $00^{o}1$–$00^{o}0$ line positions are obtained using the molecular constants in the AFGL Line Parameters Compilation.[15] The line corresponding to ordinal number $m = J + 1$ is centered at wavenumber

$$\nu_m(\mathrm{cm}^{-1}) = 2349.146 + m\Big\{0.777358 - m\big[0.003078 + m(5.312 \times 10^{-7} - 6 \times 10^{-10}\, m)\big]\Big\}, \qquad (38)$$

$$m = 51(2)173$$

Note that m assumes only odd values, corresponding to even J.

The approximate line spacing d is obtained by differentiating Eq. (38) with respect to m and then multiplying by 2:

$$d_m(\mathrm{cm}^{-1}) = 2\Big\{0.777358 - m\big[0.006156 + m(1.5936 \times 10^{-6} - 2.4 \times 10^{-9}\, m)\big]\Big\}, \qquad (39)$$

$$m \leq 121$$

This equation is not sufficiently accurate at the band head (m = 123); Eq. (38) is used to obtain the distance between the lines m = 121 and m = 123.

The R-branch return lines corresponding to m > 123 are assumed to fall precisely on the outgoing lines; i.e., the lines m = 125, 127, ... are assumed to fall on top of the lines m = 121, 119, ..., respectively, so that the corresponding line intensities can be added. This is actually a very good approximation for the first few return lines, and beyond these the line intensities have decreased to such a low level that their contributions are insignificant.

For the individual line intensities we used the well-known approximate formula

$$S_m = S_o(300\ \mathrm{K})\ \frac{Q(300\ \mathrm{K})}{Q(T)}\ \frac{2 \times 1.439}{T}\ B''_v\ m\ \exp(-1.439m(m-1)\ \frac{B''_v}{T}) \qquad (40)$$

together with the values (McClatchey[15] and Gray[16])

$$S_o(300\ \text{K}) = 2448.0\ \text{cm}^{-2}$$

$$B''_v = 0.39022$$

The temperature dependence of the vibrational partition function Q(T) is based on values given in Table 5, which were obtained from Figure 5 of Carpenter.[14] The code uses table lookup and interpolation to obtain Q for a given temperature.

TABLE 5
APPROXIMATE VIBRATIONAL PARTITION FUNCTION FOR CO_2 UP TO 1500 K

T (K)	Q(T)
100	1.00
200	1.02
300	1.15
400	1.27
500	1.45
600	1.75
700	1.9
800	2.2
900	2.6
1000	3.0
1200	4.3
1500	6.7

The Lorentz line halfwidths γ are calculated from:

$$\gamma(\text{cm}^{-1}) = 0.07(p + 0.3\ p_{CO_2})\sqrt{\frac{300}{T}} \tag{41}$$

where p is the gas total pressure in atmospheres, T is its absolute temperature, and p_{CO_2} is the partial pressure of carbon dioxide.

The absorption coefficient in the vicinity of the m^{th} line is assumed to vary as:

$$k_m(\nu) = \left(\frac{S_m}{d_m}\right)' \frac{\sinh \beta'_m}{\cosh \beta'_m - \cos\left[2\pi(\nu-\nu_m)/d'_m\right]} \tag{42}$$

$$\beta'_m = (2\pi\gamma/d_m)'$$

where the primed quantities denote linear interpolates of S/d, β and d between the m^{th} line and its nearest neighbors. The absorption coefficient is calculated by the code at 20 equal-spaced points over the interval d_m centered at $\nu = \nu_m$. Near the bandhead S_m is taken as the sum of the intensities of the outgoing and return spectrum lines. Beyond the bandhead the absorption coefficient is expressed as:

$$k(\nu) = \frac{S_{123}\,\gamma^2}{d_{123}\,\tanh(\beta_{123}/2)}\;\frac{e^{-0.135\,(\nu-\nu_{123})^{0.7}}}{(\nu-\nu_{123})^2+\gamma^2} \qquad (43)$$

which represents a Benedict line whose line center absorption coefficient matches that of Eq. (42) at $\nu = \nu_{123}$ = the bandhead.

The continuum (wing effect) for the cool gas path is defined by the absorption coefficient (Carpenter[14]):

$$\frac{S_p\gamma}{\pi}\left[\frac{1}{(\nu-\nu_R)^2}+\frac{1}{(\nu-\nu_p)^2}\right]e^{-0.135\,(\nu-\nu_o)^{0.7}} \qquad (44)$$

where $\nu_o = 2349.146\ \mathrm{cm}^{-1}$ = the 00^01-00^00 band center, and S_p, ν_R and ν_P are intensities and wavenumbers that depend on temperature. For T = 288 K,

$$\begin{aligned} S_p &= 6.61 \times 10^5\ \mathrm{cm/gm} \\ &= 1.30 \times 10^3\ \mathrm{cm}^{-2}, \\ \nu_R &= 2362.5\ \mathrm{cm}^{-1}, \\ \nu_p &= 2331.5\ \mathrm{cm}^{-1}, \end{aligned} \qquad (45)$$

(see Figure 11 of Carpenter[14]). The absorption coefficient given by Eq. (44) is added to the net "line absorption coefficient" given by the previous equations.

The absorption coefficients k, as defined, have the units (cm STP of $CO_2)^{-1}$. They may be multiplied by 273 p/T times the CO_2 mole fraction (cm STP/km) to obtain a corresponding coefficient K in units of km^{-1} (per km of <u>physical</u> path length), if p is the path total pressure in atmospheres and T is its absolute temperature.

After the spectral transmittances of the hot-gas slab and cool-gas path ($t_{\nu E}$ and $t_{\nu A}$) are calculated, the observed spectral radiance is computed from:

$$N_\nu = B_\nu(T_B)t_{\nu E}t_{\nu A} + t_{\nu A}(1-t_{\nu E})B_\nu(T_E) + (1-t_{\nu A})B_\nu(T_A), \tag{46}$$

where $t_{\nu E} = \exp(-K_E L_E)$ and $K_E L_E$ is the product of absorption coefficient and path length (optical thickness) for the exhaust; similarly, $t_{\nu A} = \exp(-K_A L_A)$. $B_\nu(T)$ denotes Planck's function, and T_E, T_A, T_B denote the temperatures of the hot gas, the cooler path, and a background assumed to be behind the hot slab and to have unit emissivity. Note that the cool path emission is included in the computed radiance.

Eq. (46) gives the observed spectral radiance of a hot slab source that fills the IFOV. A more realistic geometry for a gaseous threat or false threat source is a cylinder of arbitrary radius and length. Then, of course, the appropriate quantity to calculate is the spectral intensity (watts/sr–cm^{-1}) received at some distant point.

Consider a cylinder of radius R and length ℓ which has been sliced into a series of slabs of thickness dz (Figure 27). The spectral radiance emitted in the x–direction by a typical slab is

$$\left[1 - \exp(-2xK_E)\right] B_\nu(T_E), \tag{47}$$

and the total emergent intensity of the entire cylinder is

$$I = 2\ell B_\nu(T_E)\int_0^R \left[1 - e^{-2x(z)K_E}\right] dz$$

$$= 2\ell RB_\nu(T_E)\left[1 - \int_0^1 \frac{t}{(1-t^2)^{1/2}} e^{-2RK_Et}\, dt\right] \qquad (48)$$

where the second form is obtained by substituting $z = (R^2-x^2)^{1/2}$ and $t = x/R$ in the first form. The integral in (48) can be solved (cf. Gradshteyn and Ryzhik[17], page 316) in terms of known functions to obtain

$$I = R\ell B_\nu(T_E)\left[I_1(2RK_E) - L_1(2RK_E)\right]. \qquad (49)$$

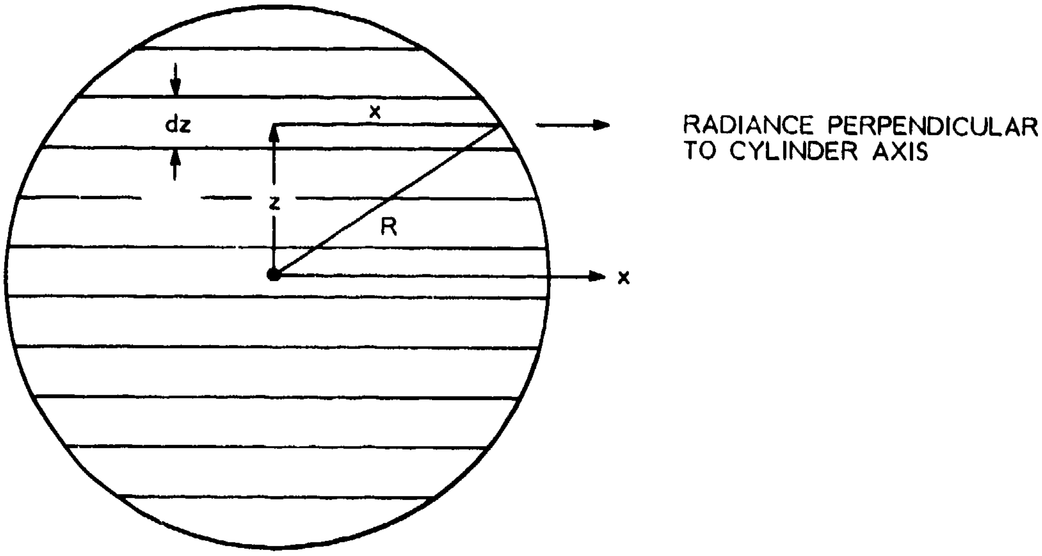

Figure 27. Geometry for Calculating the Radiant Intensity of a Hot Cylinder of Gas

The Struve function $I_1(x) - L_1(x)$ is tabulated in Abramowitz and Stegun[18]. The spectral intensity observed perpendicular to the cylinder axis at distance L_A is equal to the product of (5.17) and the cool-path spectral transmittance $t_{\nu A} = \exp(-K_A L_A)$.

5.2 EMPIRICAL ADJUSTMENTS

The model described above was written as a computer code that includes the option of selecting either the slab or cylinder geometry for the hot source. Note that the effects of atmospheric and background emission are included in the apparent slab radiance calculation but not in the apparent cylinder intensity calculation. Spectra obtained by the code were compared to measurements and independent line-by-line calculations to determine the kinds of empirical adjustments that would improve the model predictions. The line-by-line spectra used in the comparisons were supplied by Horace Ory of R and D Associates[19]; these previously unpublished spectra represent the cylindrical source geometry. The comparisons resulted in the following modifications to the equations of Section 5.1.

5.2.1 Variation of Line Width with Temperature and Rotational Quantum Number

The Lorentz halfwidth at STP (the factor 0.07 in Eq. (41) was made a linear function of ordinal number $m = J+1$ by fitting a straight line to theoretical results of Yamamoto et al.[20] We also included a halfwidth-temperature relationship derived by Ory from Yamamoto's results (which he used in the line-by-line calculations). The result of these corrections is to change Equation 5.9 to

$$\gamma(\mathrm{cm}^{-1}) = (0.077 - 2.7 \times 10^{-4}\, m)\ (p + 0.3\, p_{CO_2})\ (300/T)^n$$

$$\begin{aligned} n &= 0.75 - 0.004(m-1) \text{ for } m < 101 \\ &= 0.35 \quad \text{for } m \geq 101 \end{aligned} \tag{50}$$

This halfwidth appears in Eqs. (42) through (44).

5.2.2 Depth of Absorption Minima

The absorption coefficient minima between line pairs will be too high without some kind of correction, because the Elsasser band represents Lorentz lines. It was found that the trough depth could be matched approximately to the line-by-line (Ory's) spectra by multiplying the β_m in Eq. (42) by the factor

$$\mathrm{EMPIR} = \left[0.726 + 0.00417(m-51)\right]^{1/2} \qquad (51)$$

A compensating correction is applied to the line intensities S_m Eq. (40) so that the absorption coefficient at the line centers will not change; i.e., S_m is multiplied by

$$\tanh(\beta_m/2)/\tanh\left[\beta_m/(2\cdot \mathrm{EMPIR})\right] \qquad (52)$$

where β_m is the new (empirically corrected) value of β (see Eq. (34).

5.2.3 End Correction to Elsasser Band

This correction is equivalent to replacing an infinite array of lines (the Elsasser band) by a semi-infinite array of lines that ends at the band head. It consists of first computing the quantity

$$\frac{1}{2}\,\frac{S_m}{d_m}\left[\frac{\sinh \beta_m}{\cosh \beta_m - 1} - \frac{2}{\beta_m}\right] - 2\beta_m\,\frac{S_m}{d_m}\sum_{j=1}^{\frac{123-m}{2}} \frac{1}{(2\pi j)^2+\beta_m^{\,2}}\,,$$

$$m = 85(2)\ 123, \qquad (53)$$

and evaluating the linear interpolate of (53) at the same frequencies used in evaluating Eq. (42). These values are then subtracted from the absorption coefficients determined from Eq. (42). Note that the correction affects only the spectral region spanned by the 20 lines nearest the bandhead; it is performed after the corrections on β_m and S_m.

5.2.4 Modification of Line Intensities and Cool-Gas Continuum

The intensities of the three lines nearest the bandhead (m = 119, 121 and 123) are multiplied by 0.94, 0.70 and 0.30, respectively. The cool-path continuum coefficient given by Eq. (44) is increased uniformly by the factor 1.74. During validations of the model the continuum correction factor was revised a second time (see Section 5.3). Note that this factor and the overall shape of the continuum correction are strongly determined by the extreme wings of strong CO_2 lines; the far-wing line shape and its temperature dependence are still uncertain (see Burch and Gryvnak[21]).

5.3 VALIDATION OF THE BLUE SPIKE MODEL

Table 6 lists some of the cases for which predicted spectral intensity or absorptance spectra were compared to Ory's line-by-line calculations and measured spectra. The effective broadening pressures given in the table are defined as the sum of the total pressure and 0.3 times the CO_2 partial pressure (cf. Eqs. (41) and (50)).

The results of the validations are presented as a series of figures which each have a part (a) and part (b). Part (a) always shows a spectral quantity computed using the blue spike model, while part (b) shows the same quantity determined from measurements or Ory's line-by-line calculations.[19] Table 6 identifies the figure applicable to each case.

Figures 28 through 37 show excellent agreement between the model predictions and the independently computed/measured spectra. The measured spectrum of Figure 34b contains emission lines of the isotope $C^{13}O_2^{16}$, which has a bandhead near 2385 cm^{-1}. These lines are not included in the blue spike model because the atmospheric paths corresponding to typical AAM and SAM detection geometries will usually be opaque at wavenumbers less than 2385 cm^{-1}. Figure 5-10 shows that our model predicts substantially lower radiance than SAI's line-by-line code when an optically thick slab is observed at long ranges (10 km in this case). This is due entirely to the atmospheric continuum (wing effect) used in our model,

TABLE 6
GAS PARAMETERS FOR VALIDATION CALCULATION

		"EXHAUST"						AMBIENT				
Figure	Data Source (b Figs)	Configuration*	Temperature (°K)	CO_2 Mole Fraction	Effective Pressure (atm)	Δx or R* (ft)	L* (ft)	Temperature (°K)	CO_2 Mole Fraction	Total Pressure (atm)	Range (ft)	Comments
28	Ory	2	500	0.01	1.0	2.5	10	288	3.2×10^{-4}	1.0	5000	
29	Ory	same as 5-3										
30	Ory	2	800	0.01	1.0	2.5	10	288	3.2×10^{-4}	1.0	1000	
31a		same as 30										
31b	Block	2	unknown									
32	Ory	2	1000	0.01	1.0	2.5	10	288	3.2×10^{-4}	1.0	5000	
33	Ory	same as 5-7										
34	ERIM	1	2330	0.383	1.115	0.108					0	Absorptance spectrum
35	SAI†	1	1450	0.08	0.481	15.75		250	3.3×10^{-4}	0.481	32810	
36		same as 35										Revised Atm. Continuum
37		same as 32										Revised Atm. Continuum

* Configuration 1 is slab of thickness Δx; configuration 2 is cylinder of radius R and length L

† Line-by-line computation by Science Applications, Inc.

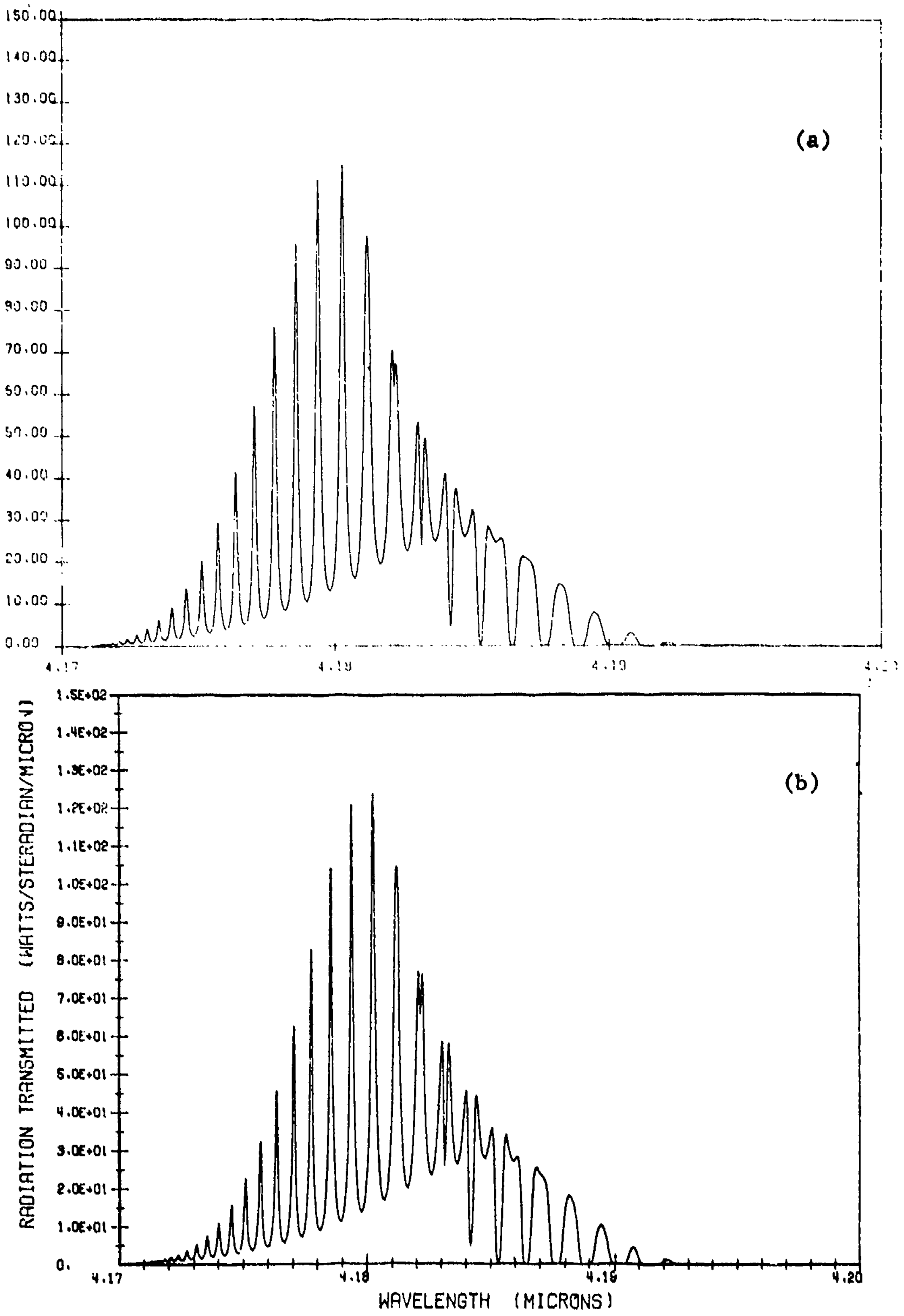

Figure 28. Validation of Blue Spike Model for 500 K Source

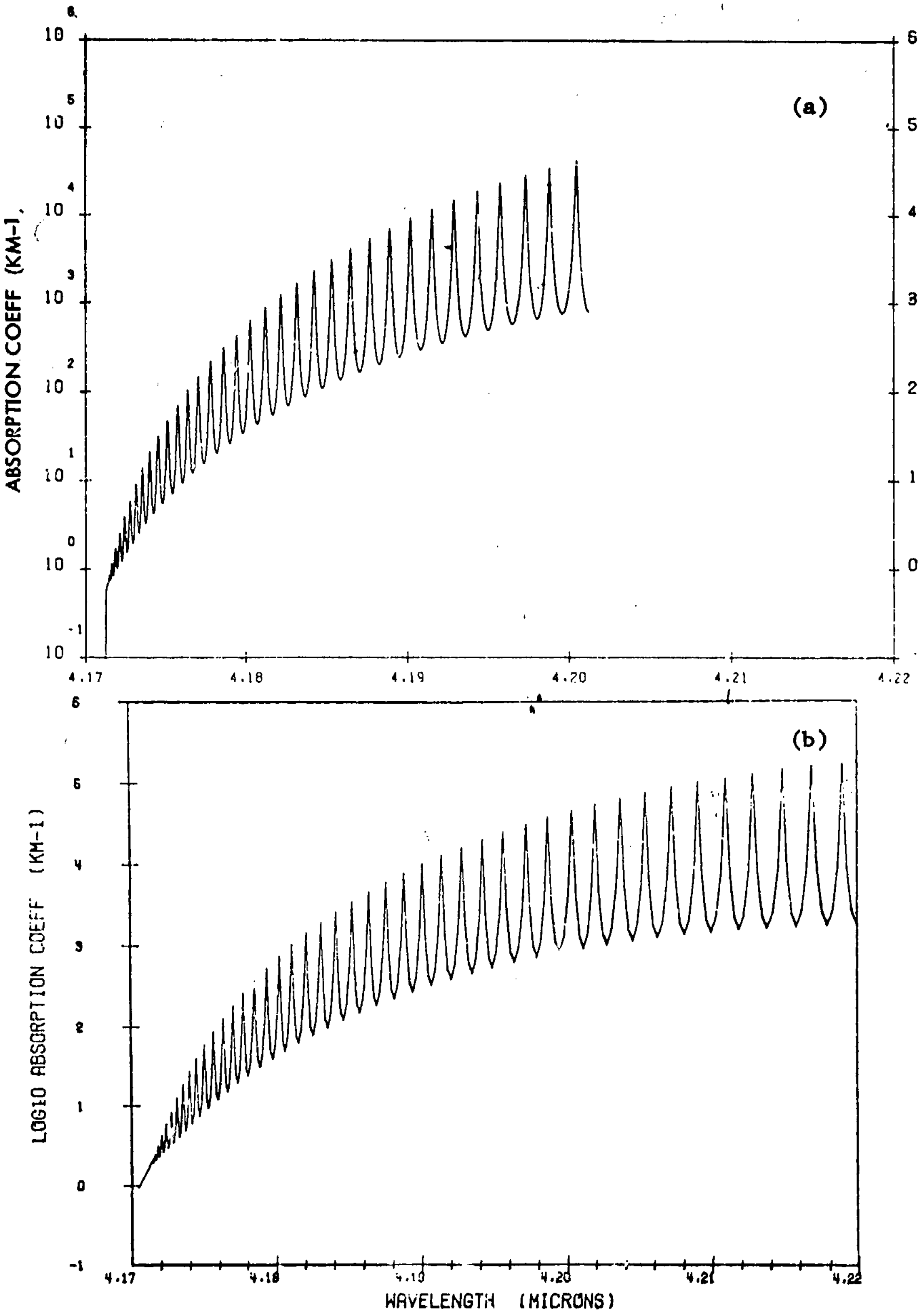

Figure 29. Validation of Blue Spike Model for "Exhaust" Spectral Absorptance (Same Conditions as Figure 28)

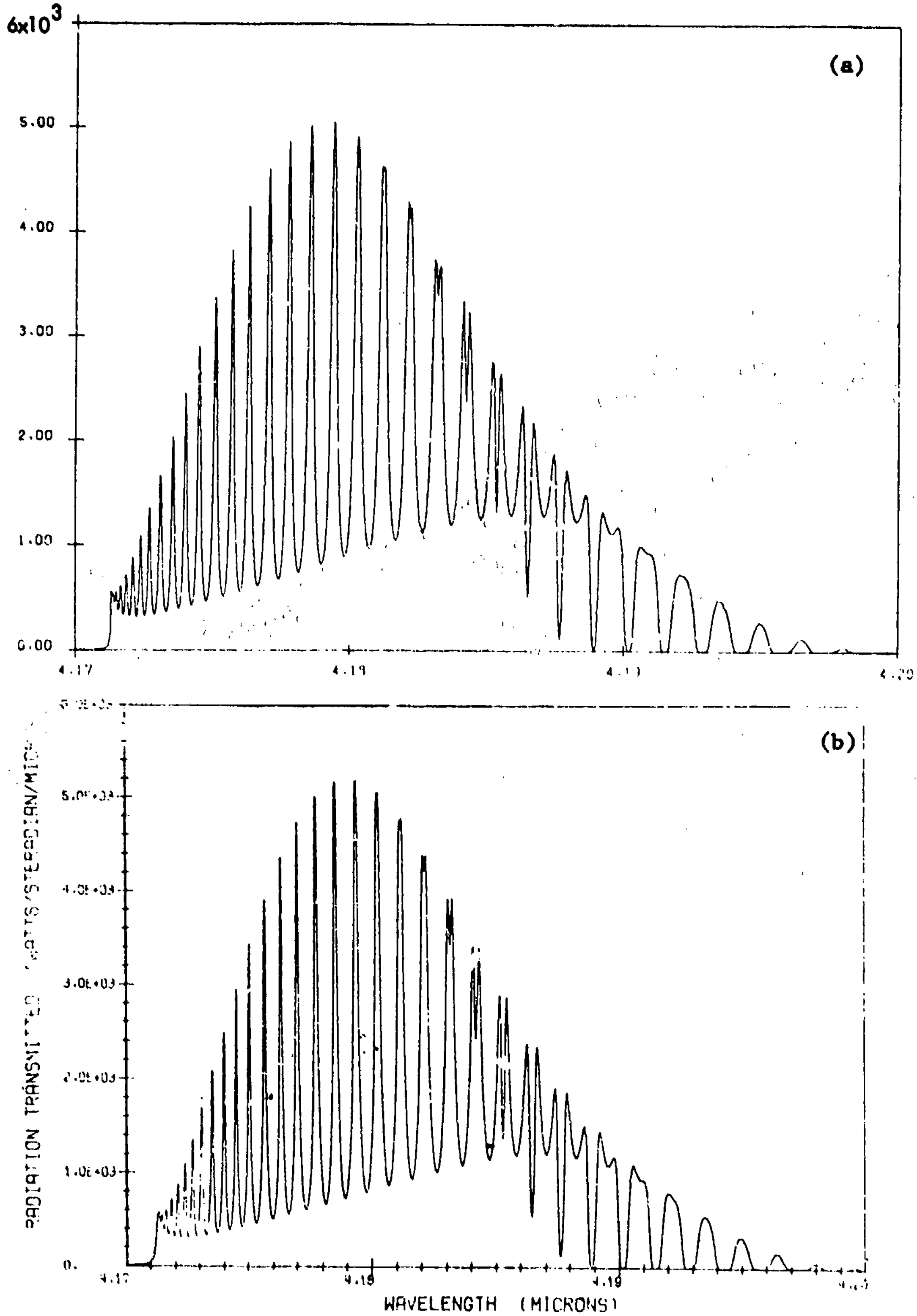

Figure 30. Validation of Blue Spike Model for 800 K Source

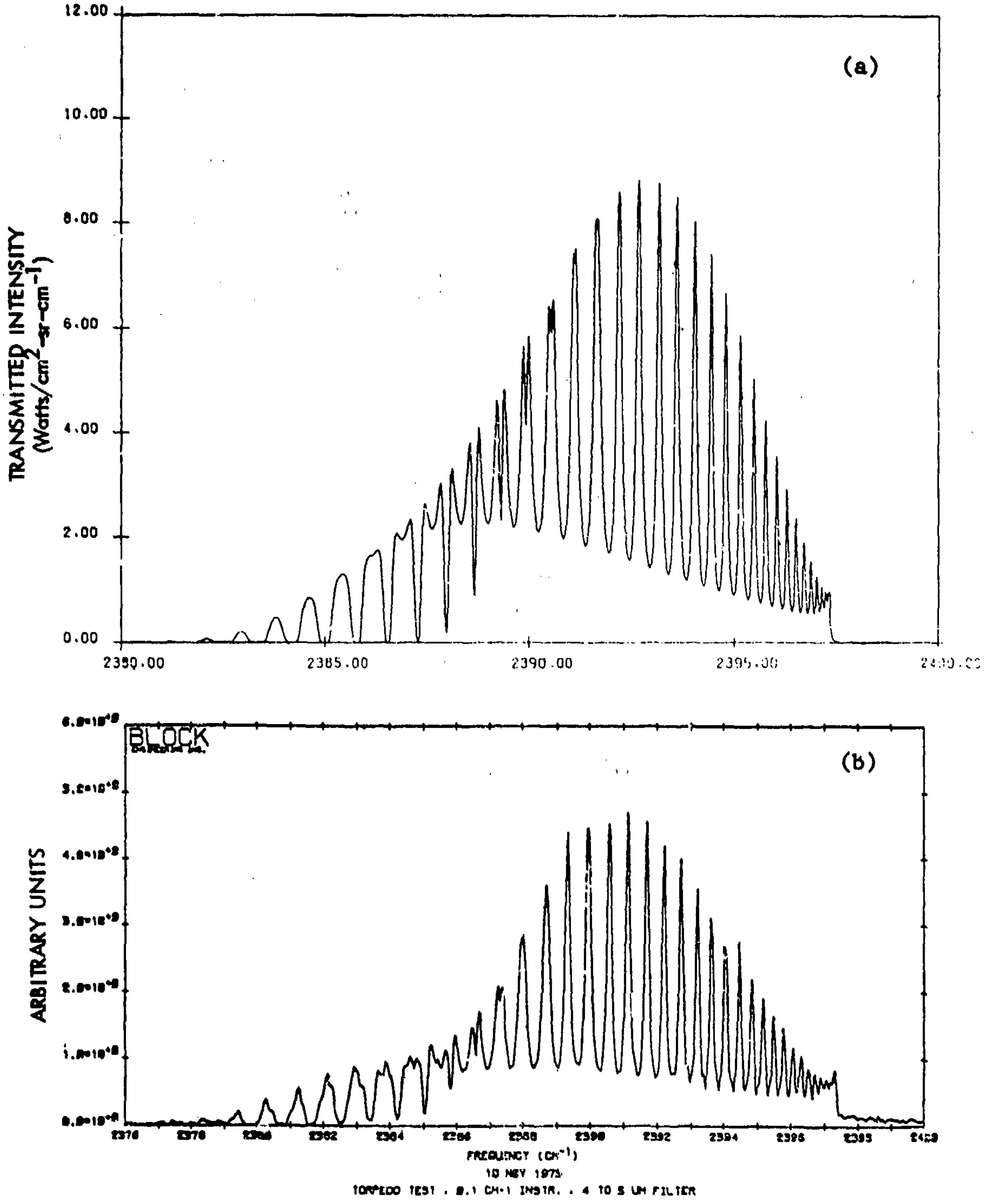

Figure 31. Comparison of Blue Spike Model Prediction for 800 K Source to Measured Spectrum for Unknown Conditions

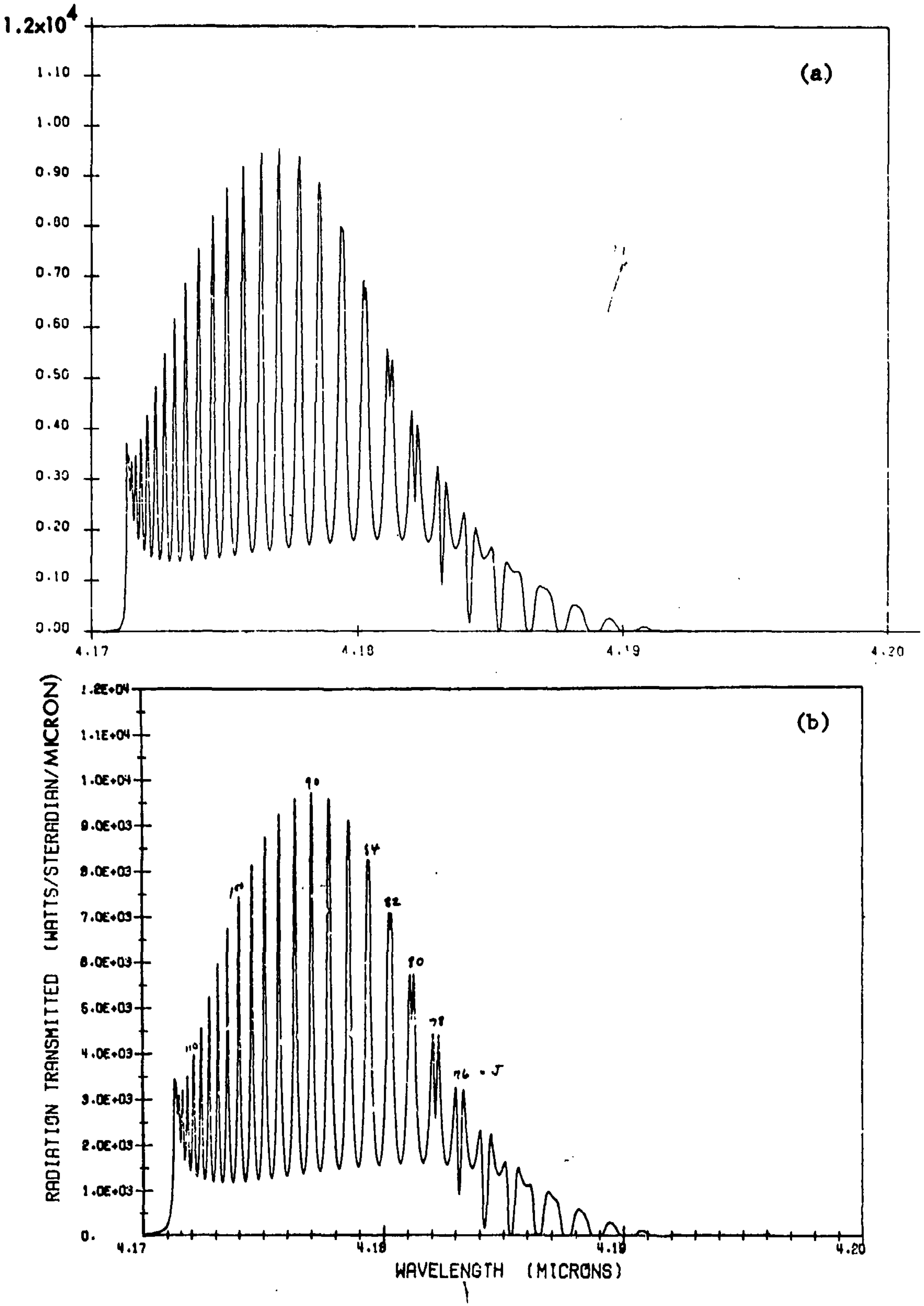

Figure 32. Validation of Blue Spike Model for 1000 K Source

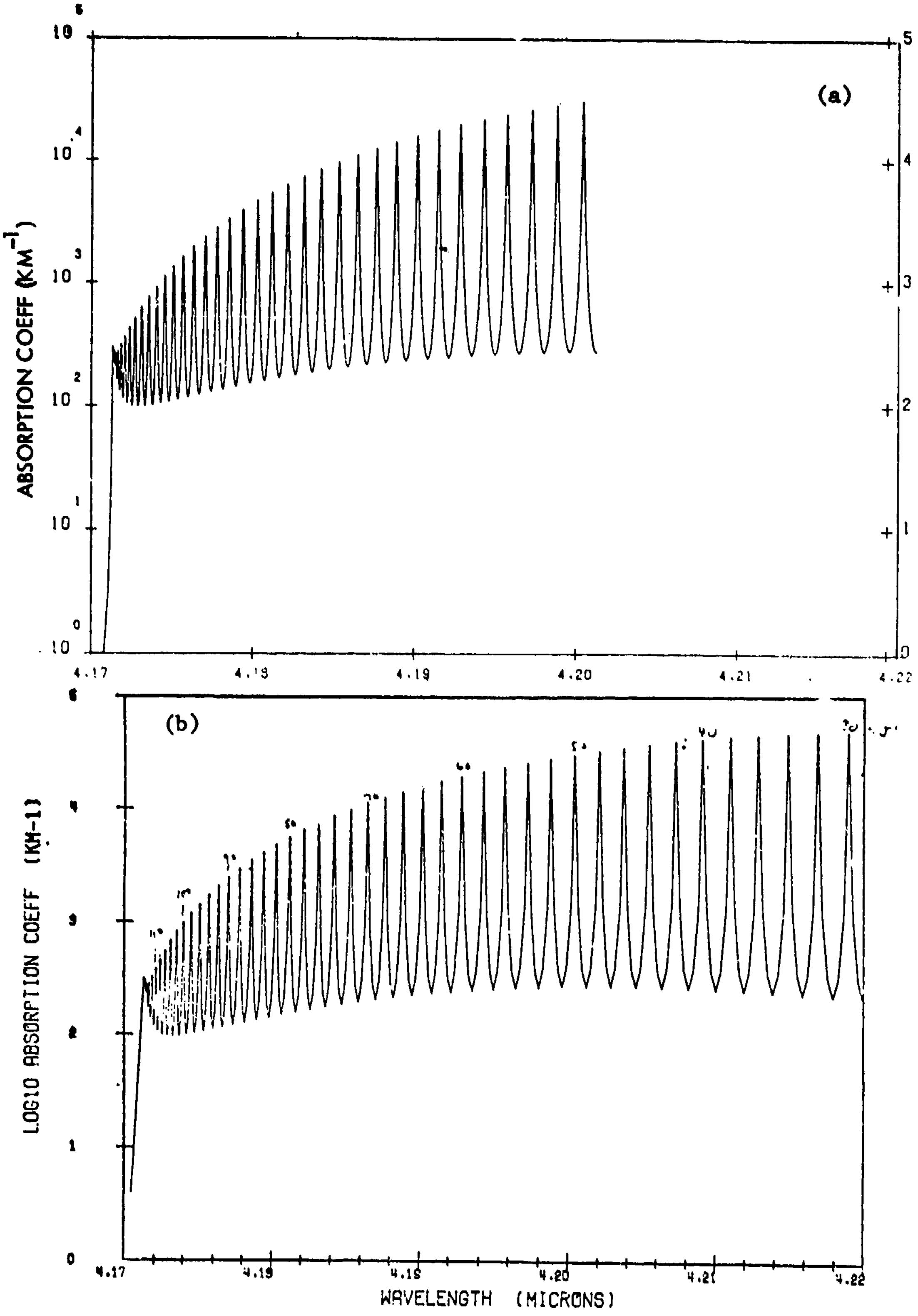

Figure 33. Validation of Blue Spike Model for "Exhaust" Spectral Absorptance (Same as Figure 32)

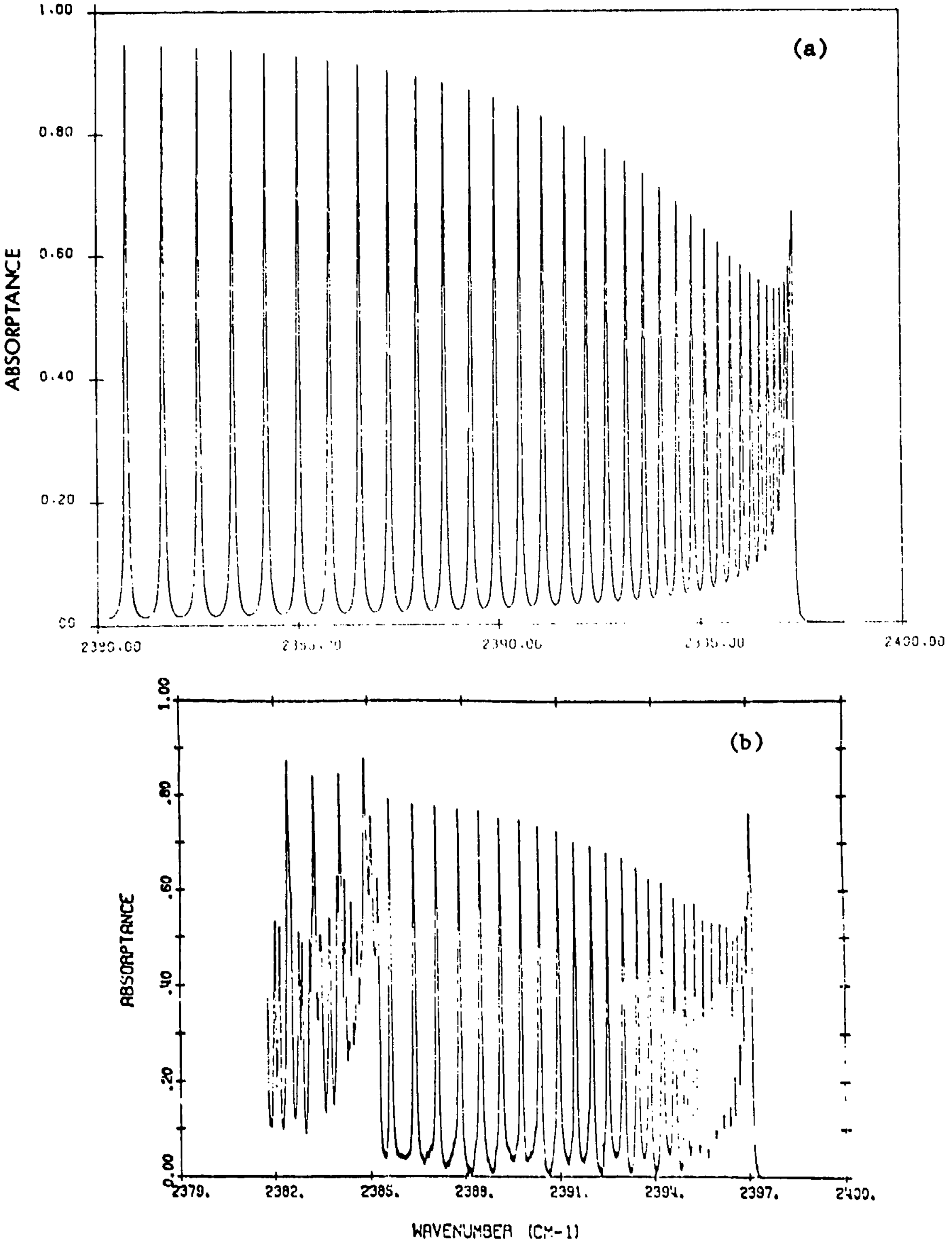

Figure 34. Validation of Blue Spike Model for Spectral Absorptance for 2330 K Source

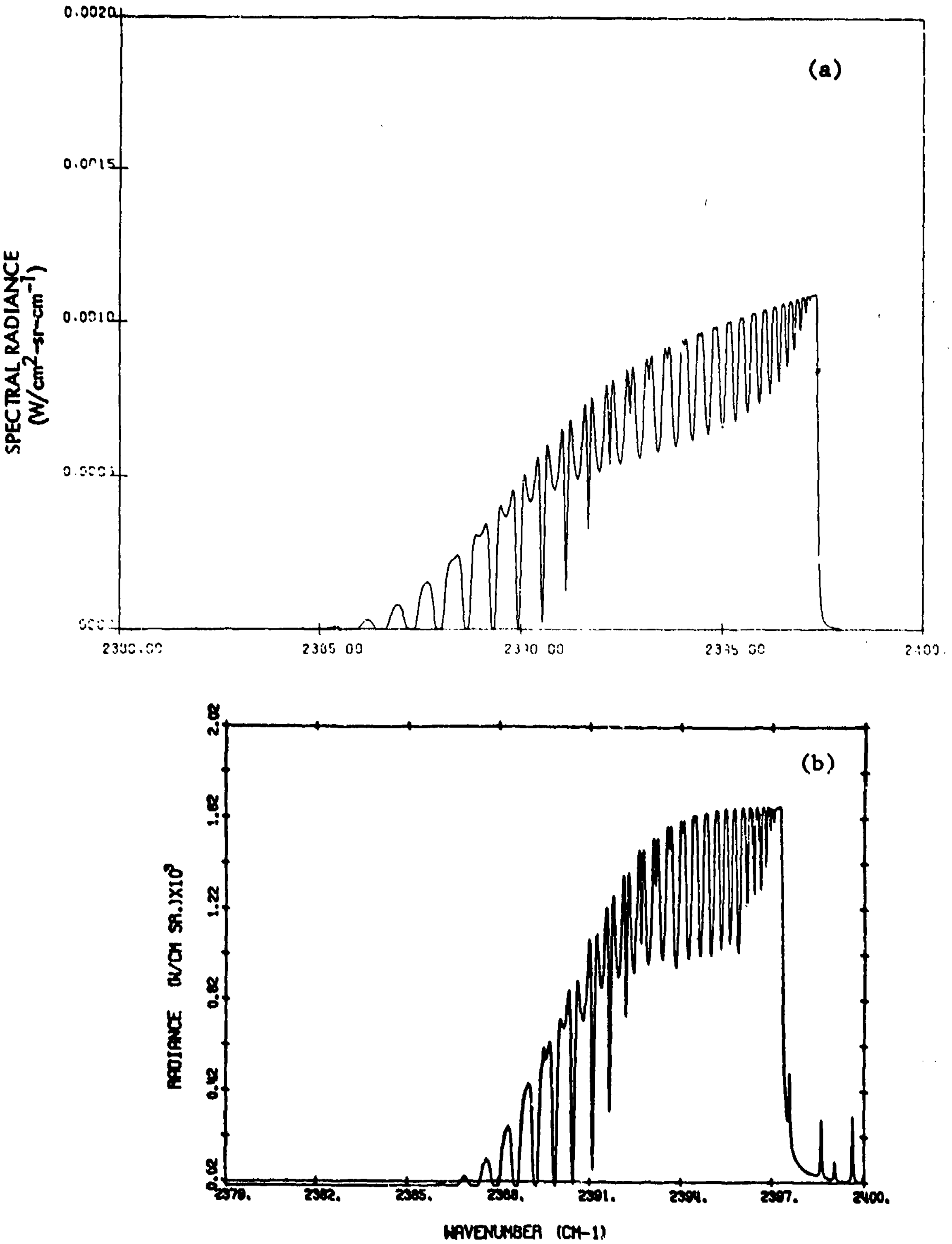

Figure 35. Validation of Blue Spike Model for 1450 K Source

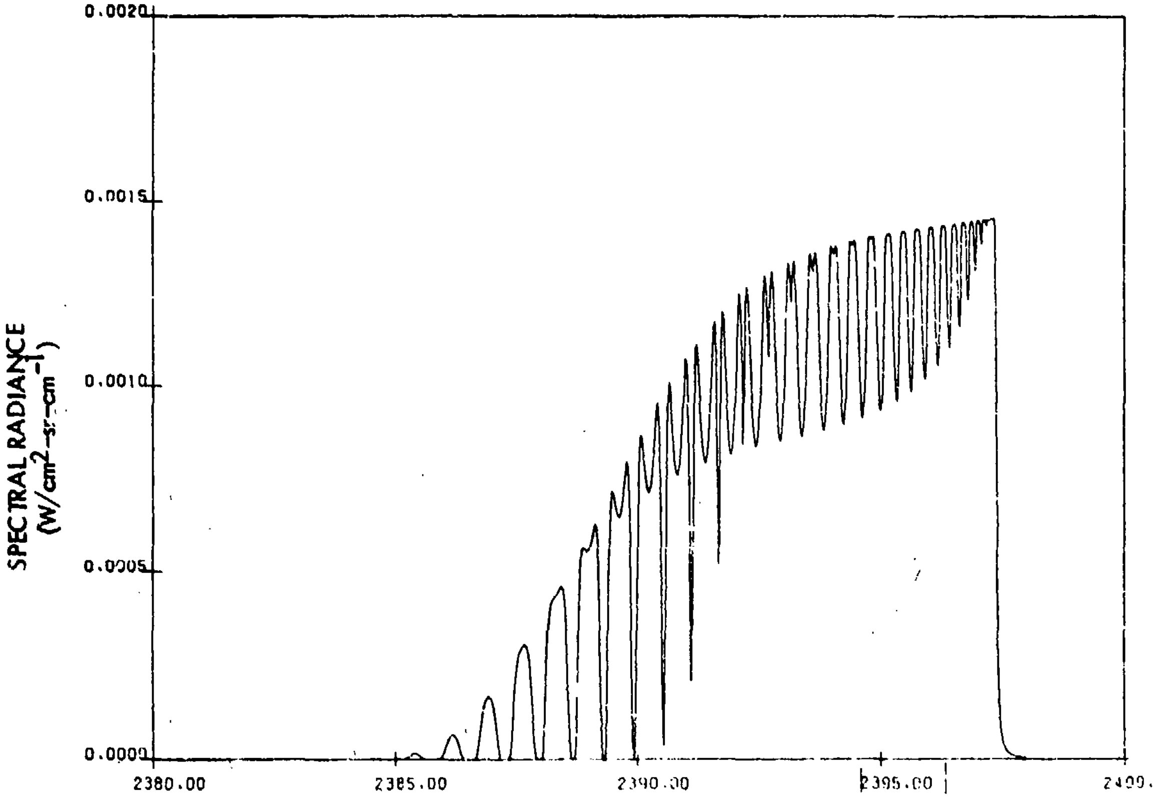

Figure 36. Same as Figure 35a, Except Based on a Revised Correction Factor for the Atmospheric Continuum

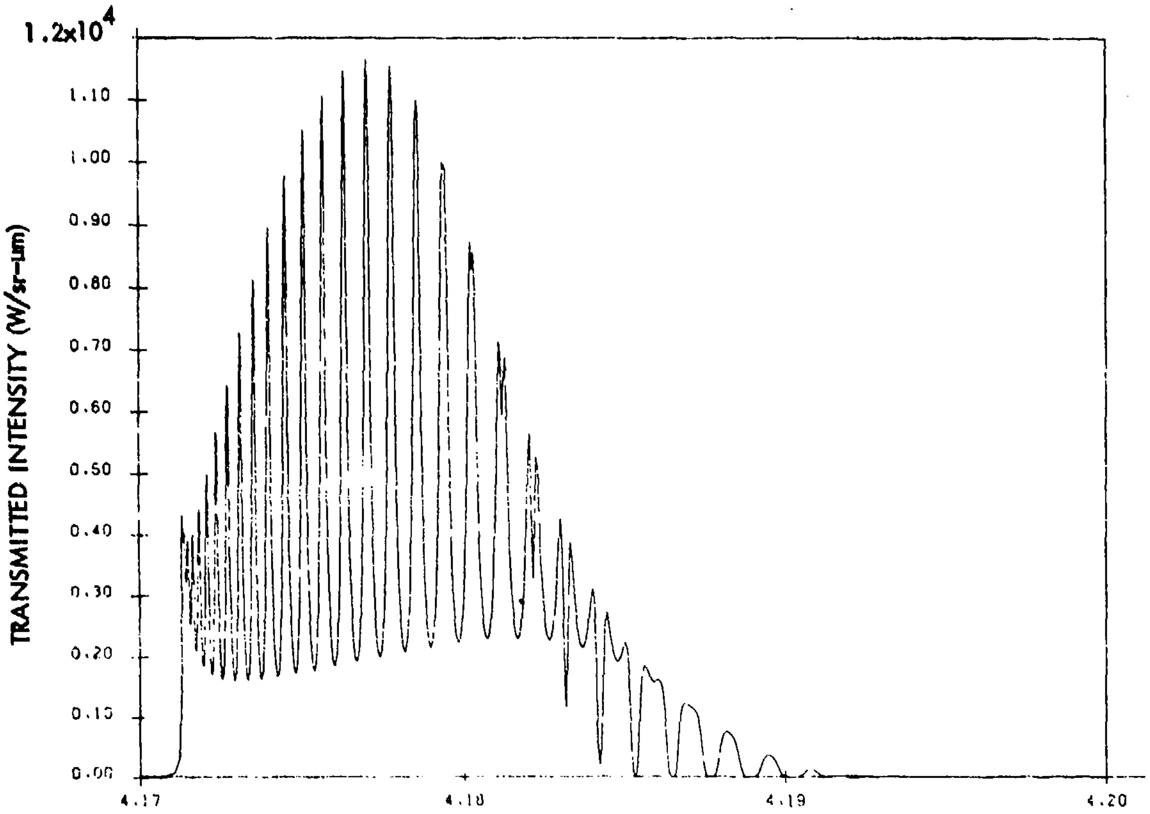

Figure 37. Same as Figure 32a, Except Based on a Revised Correction Factor for the Atmospheric Continuum

for if we reduce the continuum coefficient by a factor of 3 (after the empirical 1.74 increase referred to in Section 5.2.4) we obtain the spectrum shown in Figure 36, which is in much better agreement with Figure 35b. Figure 37 shows how the predicted spectrum of Figure 32a would be affected by the same factor-of-3 change in the atmospheric continuum.

The blue spike model was also validated against ERIM measurements of the spectral absorptance of hot, undiluted CO_2 at a pressure of 20 Torr, and at temperatures of 500 K, 700 K and 900 K. These results, reported in the 11th R&D Status Report of the study, show excellent agreement between the calculations and measurements.

5.4 UTILITY OF THE MODEL

The computer code written to perform the blue spike spectral calculations has the capability to represent both emission and absorption paths by up to 20 segments of different pressure, temperature and CO_2 fraction. It can also degrade spectral resolution according to a triangular slit function of specified width. The blue spike model/code should be useful for:

1. Calculating the blue spike spectral signatures of generic threat models
2. Calculating the same for hot-gas type false threats (e.g., industrial emissions)
3. Calculating the spectral signatures of continuum-like false threats in the region of the blue spike (i.e., use the model to calculate the fully resolved atmospheric spectral transmittance)
4. Analyzing lower resolution false threat spectral signature data.

SECTION VI

INDUSTRIAL SITE BACKGROUND MODELS

Procedures have been developed for representing industrial site processes that result in intense infrared spectral signatures in the 3.5 to 5.0-micrometer region. In the majority of this work we have relied on high resolution Fourier Transform Spectrometer (FTS) measurements obtained by the Air Force Geophysics Laboratory (AFGL)[1] and by the Environmental Protection Agency (EPA). While both of these laboratories provided excellent calibrated spectra of industrial processes, comparable data on physical parameters (e.g., exact sizes, temperatures, compositions) has generally not been available. Thus in most cases it has been necessary to rely on estimates or perform parametric calculations to obtain physical parameters in modeling the spectra. However, no unreasonable assumptions were required, and we feel that the procedures developed and site parameters inferred in this program have been adequately validated for use in analyzing the discrimination capabilities of IR threat warning receivers.

6.1 RADIATIVE MODELING OF HOT GAS FALSE THREAT SOURCES

Our primary data base for analyzing and validating hot gas emission sources has been the high resolution FTS spectra supplied by William Herget of EPA[22]. These measurements consist of high resolution (0.25 – 1.0 cm^{-1}), narrow field-of-view (0.5 degree), short range (0.5 – 1.0 km) spectra of various hot gas emission sources. Included in the measurements are gas burnoff flares, boiler stack plumes, refinery tower emission plumes, aircraft plumes and other similar sources. Since the EPA interferometer was ground based, and the instrument field of view is comparable to the plume sizes of these sources, the measurements represent the source signatures with little or no background interference. We have used this data as the primary resource in validating the hot gas emission models.

The computer codes used in the analysis of the hot gas emission spectra are ATLES and BLUESPIKE. The ATLES code is a moderate resolution band model code developed by Stephen Young of Aerospace Corporation[23]. This is probably the most sophisticated band model code (and associated parameter set) currently available. In the course of the present study a number of minor modifications and improvements were made to the ATLES code.

Four modifications have been made to ATLES which substantially increase its capability and computational efficiency:

1. The program flow has been altered such that PTC (pressure, temperatures and composition) variation along an emission path need only be calculated once rather than recalculated at each spectral position, as is done in the original code.

2. Pointers to desired band model parameters are calculated by subroutine SPCLOP at the beginning of each run rather than recalculated on each call to BPARAM.

3. Up to five species may be used in the absorption and/or emission path segments.

4. Transmittance and transmittance derivatives can optionally be calculated for water and/or nitrogen continuum for the absorption path only. Coupled path calculations assume that the continuum transmittance derivatives go to zero upon entering the emission path.

The BLUESPIKE code is described in Section V. This model predicts line-by-line CO_2 emission and atmospheric absorption in the blue spike region between 2375 and 2400 cm^{-1}.

6.2 STACK PLUMES

The most commonly encountered hot gas emission source will be various types of stack plumes. Some examples of these are the EPA spectra shown in Figures 38, 39, 40 and 41. The first two spectra present the emission of refinery stacks. In these spectra nearly all of the spectral structure is the result of CO_2 emission. The only exceptions seen are isolated H_2O emission lines beyond 2000 cm^{-1} and, in the case of the sulfur recovery unit exhaust, the SO_2 emission centered at 2500 cm^{-1} (Figure 39). Both of these spectra represent relatively small plumes estimated to be less than one-half meter in diameter.

Spectra 40 and 41 are typical of boiler exhaust plumes. Figure 40 is the exhaust from a power plant boiler at Duke University. The familiar blue spike and red spike plume structures are readily apparent. Also visible is the CO fundamental band centered at 2140 cm^{-1} and a CO_2 band with its Q-branch at 2175 cm^{-1}. This red wing CO_2 band is prominent in large optical depth CO_2 plumes and appears to be a good discriminant between boiler plumes and aircraft or missile plumes.

The CO boiler plume spectra in Figures 41 and 42 result when CO (which is a byproduct of another refinery process) is burned to heat a boiler. Clearly, this spectra is similar to the other three even though it results from purely CO_2 emission. Superimposed on Figure 42 is an ATLES computation of the predicted spectra. Except for the obvious difference in resolution, the ATLES spectra is generally a good representation of the measured result. There is a discrepancy in the weaker CO_2 bands between 2040 and 2140 cm^{-1}, the reason for this discrepancy is unclear. Two possibilities are that it either results from inaccurate assumptions of the plume optical thickness or from inaccurate band model parameters in this region.

To get a more general representation of the variation which is to be expected with stack plumes we have made parametric calculations of the peak radiances predicted for the blue spike (near 2390 cm^{-1}), the red spike (near 2210 cm^{-1}) and the red wing (near 2050 cm^{-1}). These results are shown in

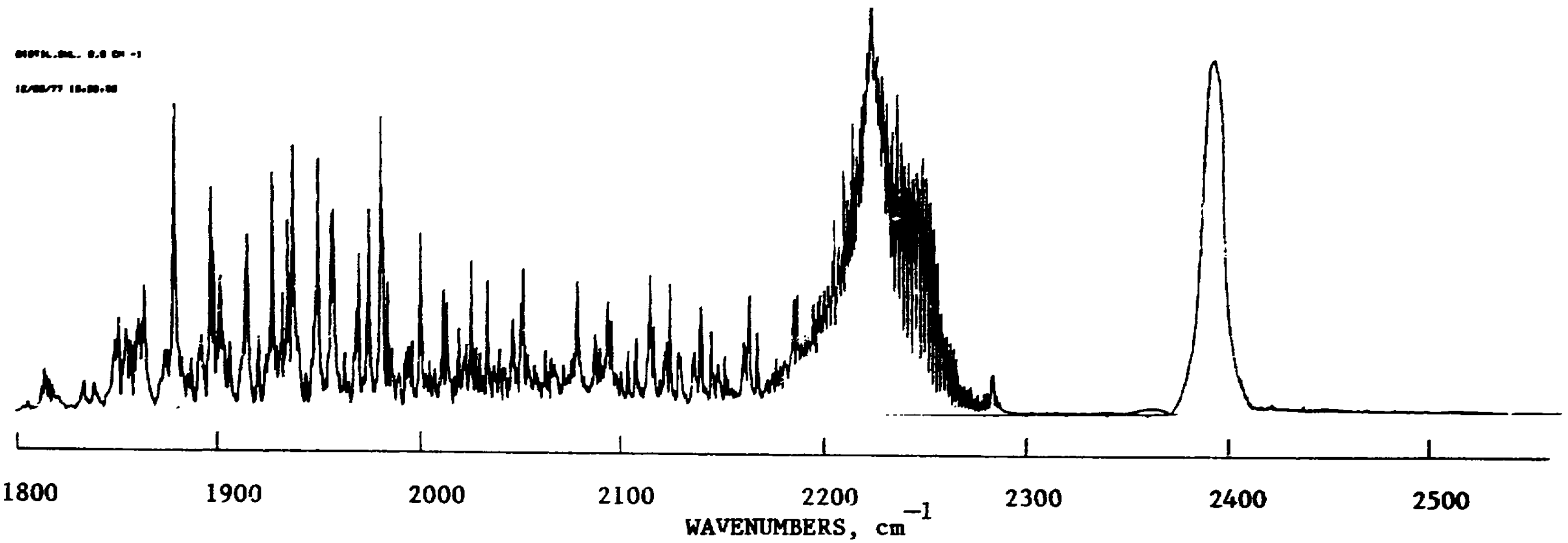

Figure 38. Measured Emission Spectrum of Refinery Distillation Tower Exhaust

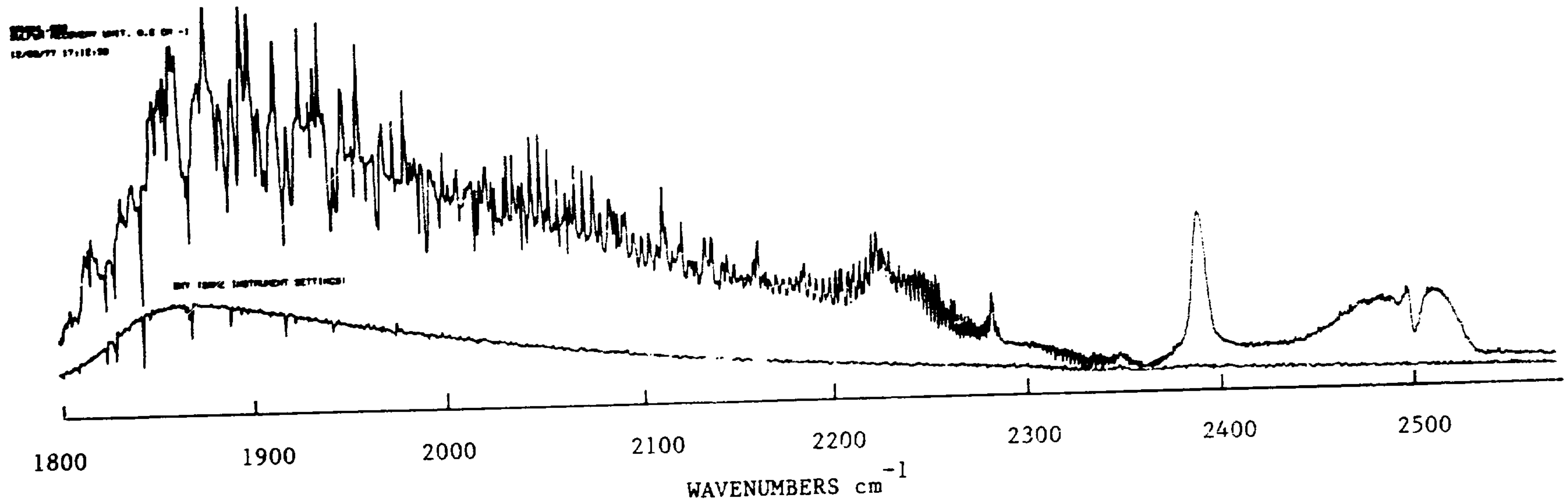

Figure 39. Measured Emission Spectra of Refinery Sulfur Recovery Unit Exhaust and Sky Background

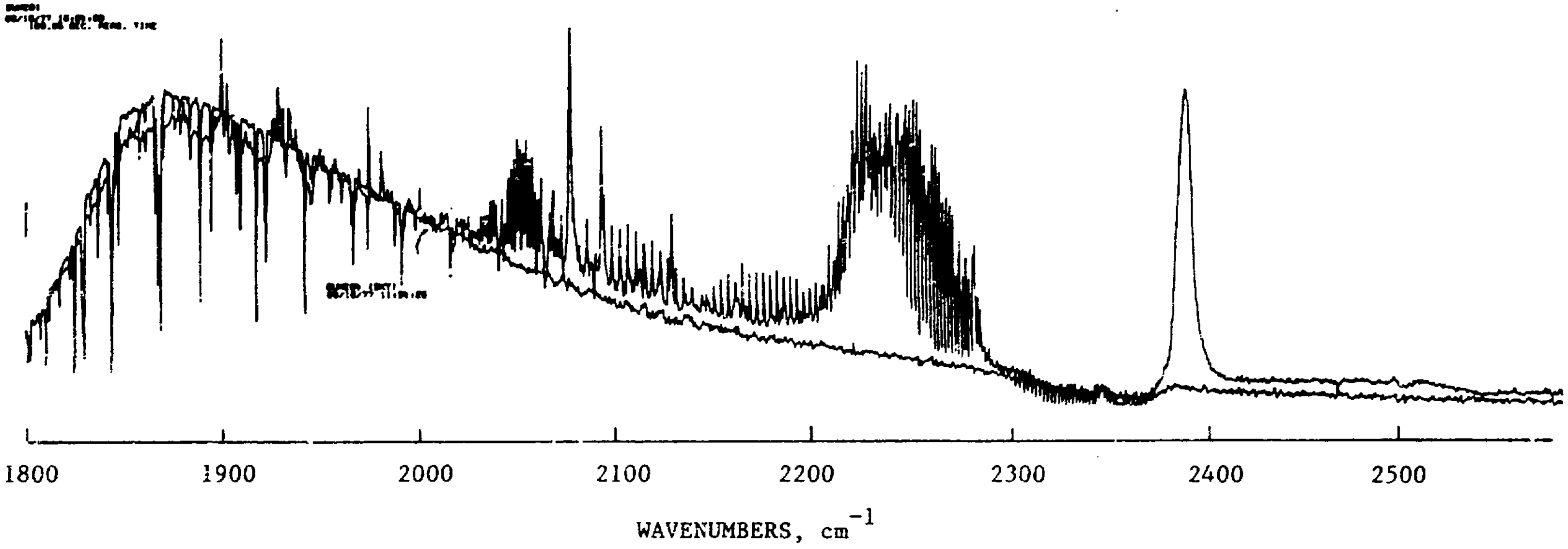

Figure 40. Measured Emission Spectra of the Power Plant Stack Exhaust at Duke University and the Sky Background

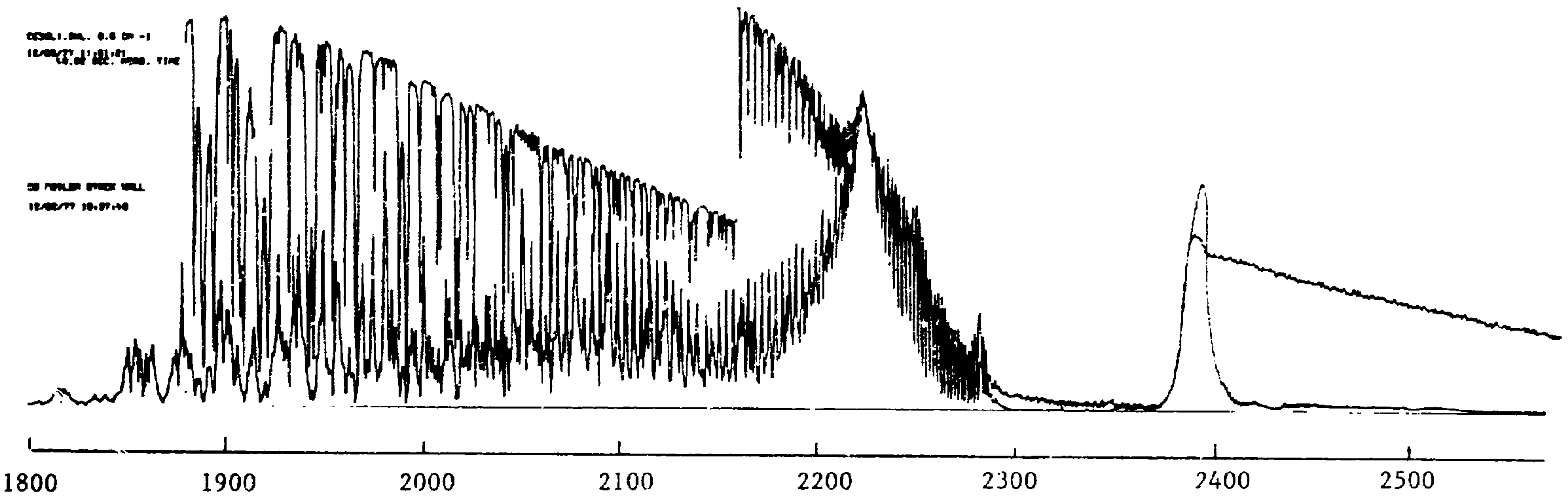

Figure 41. Measured Emission Spectra of the Exhaust Plume of a CO Fueled Boiler Stack (Lower Curve) and the External Stack Wall (Upper Curve)

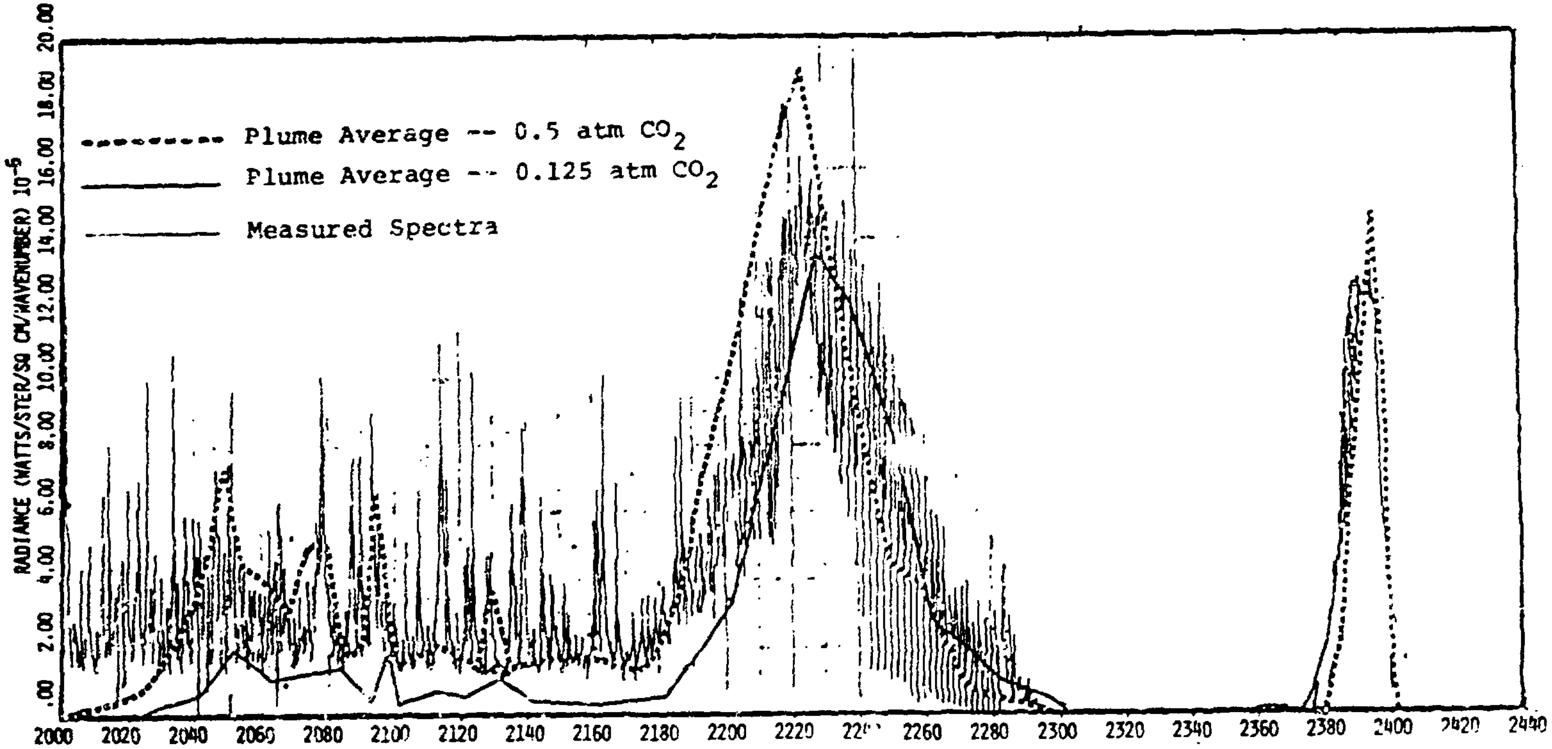

Figure 42. Comparison of Measured and Computed Plume Radiance for a CO Fueled Boiler Plume Emission

Figures 43, 44 and 45. As is seen from those figures, the radiance values of all three bands increase similarly with temperature. This prediction is in agreement with the behavior exhibited by all other spectra examined in this study. Similarly, for the temperatures considered here, the blue spike and red spike peaks are relatively independent of CO_2 optical thickness. Thus the relative peak intensities in the red spike and blue spike cannot be used to infer either plume temperature or plume optical thickness. If, however we examine Figure 45 it is seen that the red wing peak radiance is approximately linearly related to the plume CO_2 optical depth for all three temperatures considered.

Since aircraft or missile plumes are typically much thinner optically than power plant stack plumes, the ratio of the red wing to red spike radiation may be a viable discriminant between threats and stack plumes. An indication of the validity of this type of discrimination can be seen by examining the measured aircraft plume shown in Figure 46. Compare the noticeable lack of a red wing signature in that figure with the prominent red wing in Figures 39 , 40 and 41.

6.3 FLARES

Flares (open gas-fueled flames) are widely used in the chemical and steel industries to dispose of flammable, unwanted gaseous waste products. They are also used in many locations to burn off unusable natural gas from oil fields. EPA has provided us with two examples showing the spectral structure of flares; these are presented in Figures 47 and 48. The flare represented in Figure 47 is used to burn off waste gases at a refinery, and that represented in Figure 48 is used to burn off vinyl chloride related wastes at a chemical plant. The similarities between these two spectra is obvious, particularly with respect to the shape and relative magnitudes of the red spike and blue-spike. Generally, the width of the redspike and the pinpoint extending from the blue spike are very characteristic of these very high temperature sources.

The spectra shown in Figure 48 also contains other molecular emission besides the expected H_2O and CO_2. The overtone band of CO is clearly visible as uniformly spaced emission lines between 2040 and 2120 cm^{-1}. Also visible is HCL

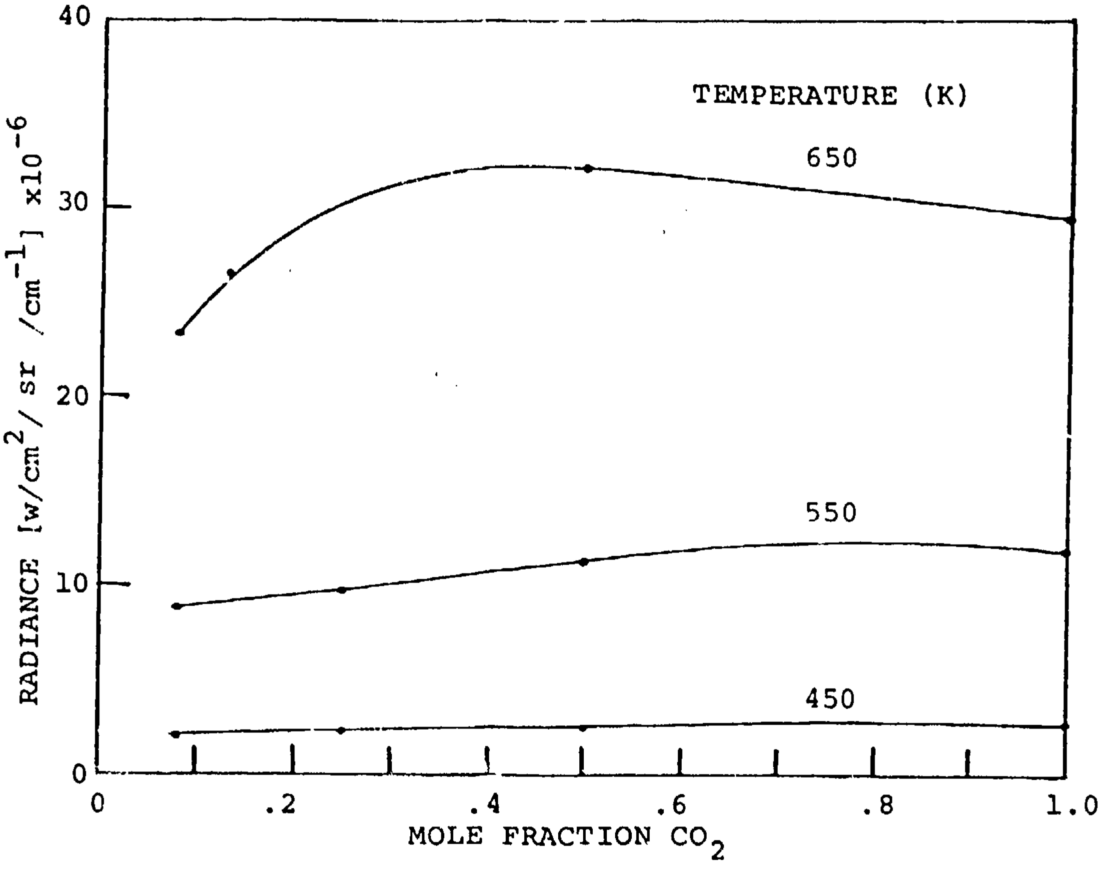

Figure 43. Computed Radiance of the Blue Spike Peak for an Assumed Stack Plume Viewed through a One Kilometer Atmospheric Path

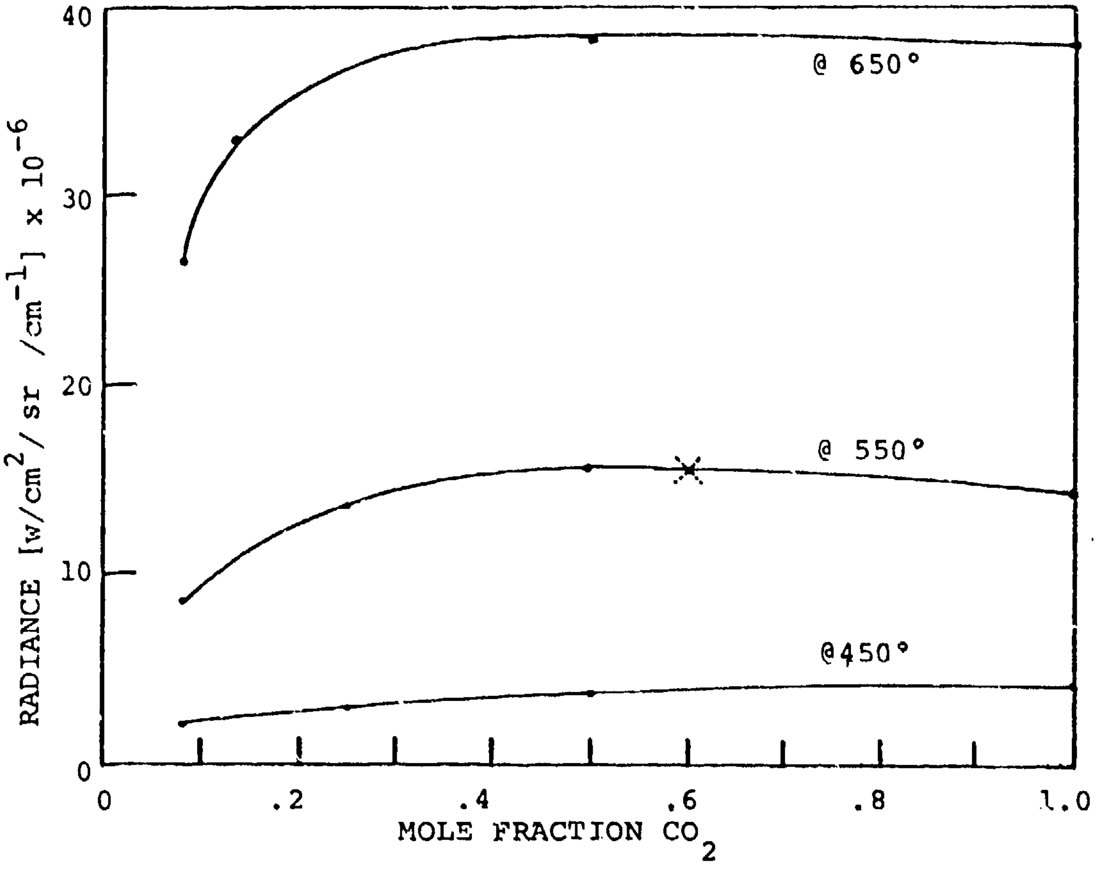

Figure 44. Computed Radiance of the Red Spike Peak for an Assumed Stack Plume Viewed Through a One Kilometer Atmospheric Path

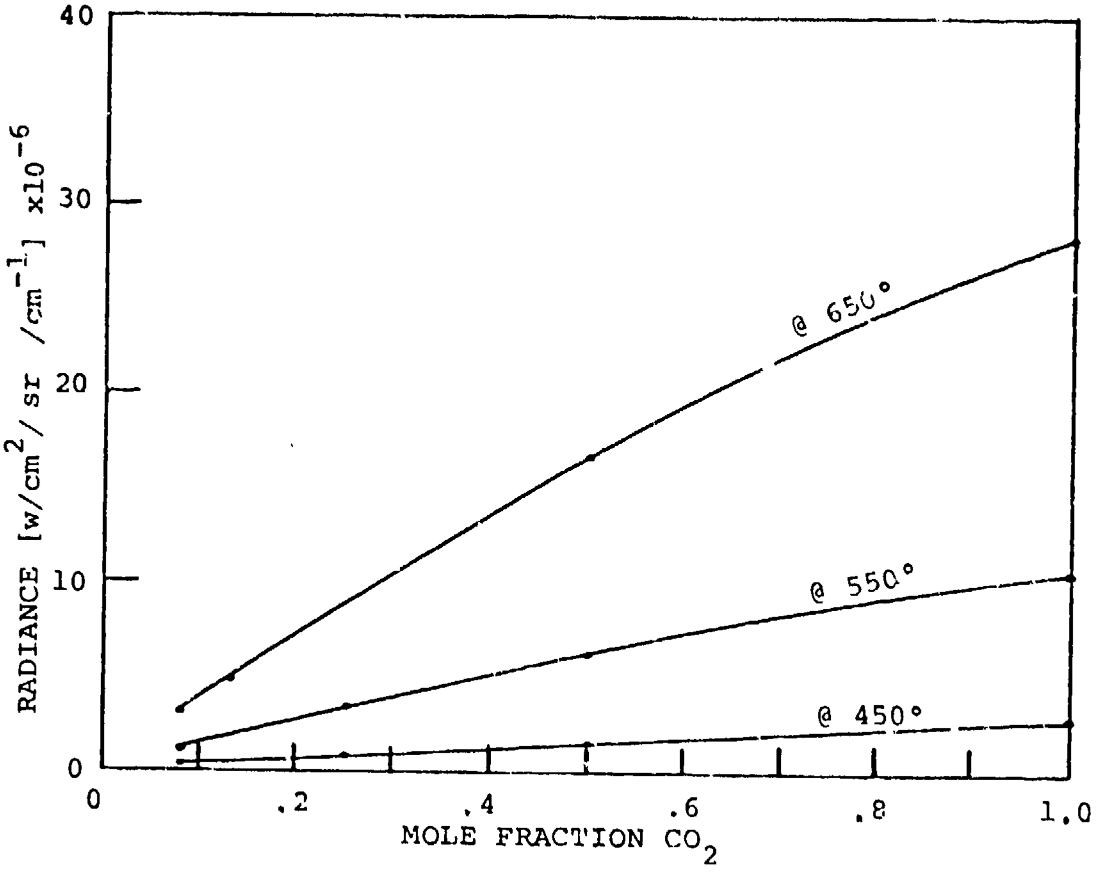

Figure 45. Computed Radiance of the Red Wind Peak for an Assumed Stack Plume Viewed through a One Kilometer Atmospheric Path

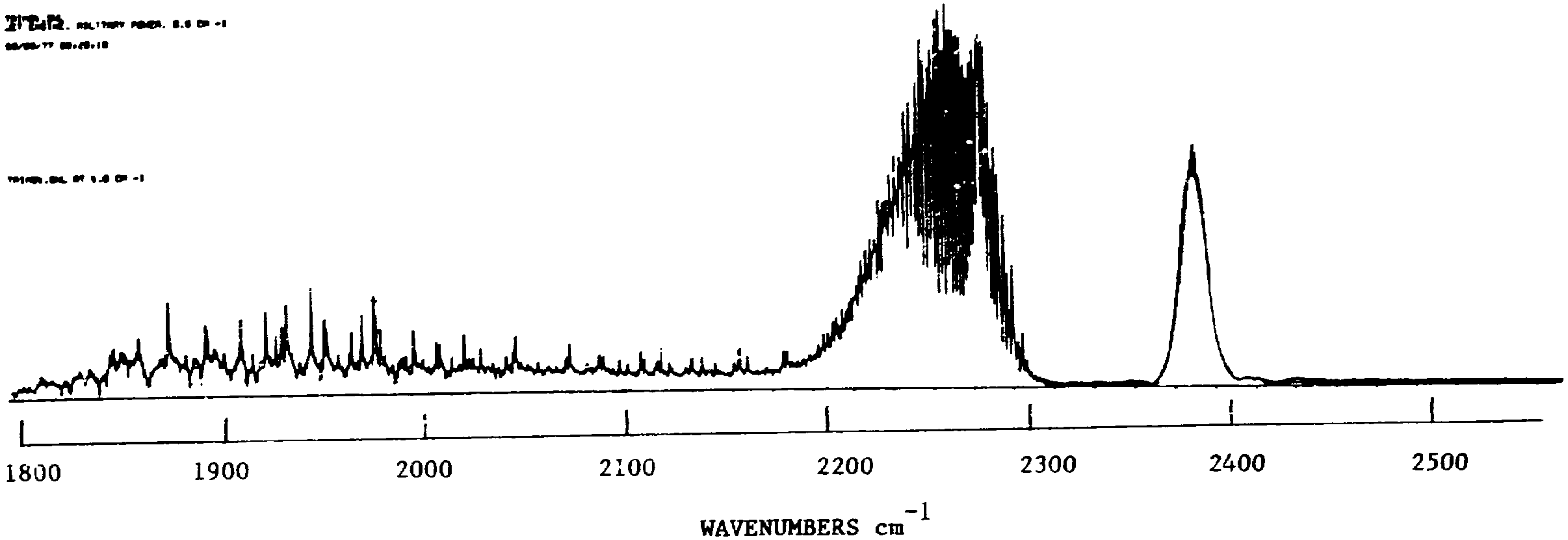

Figure 46. Measured Emission Spectra of a Tied Down Small Jet Aircraft Operating at Military Power

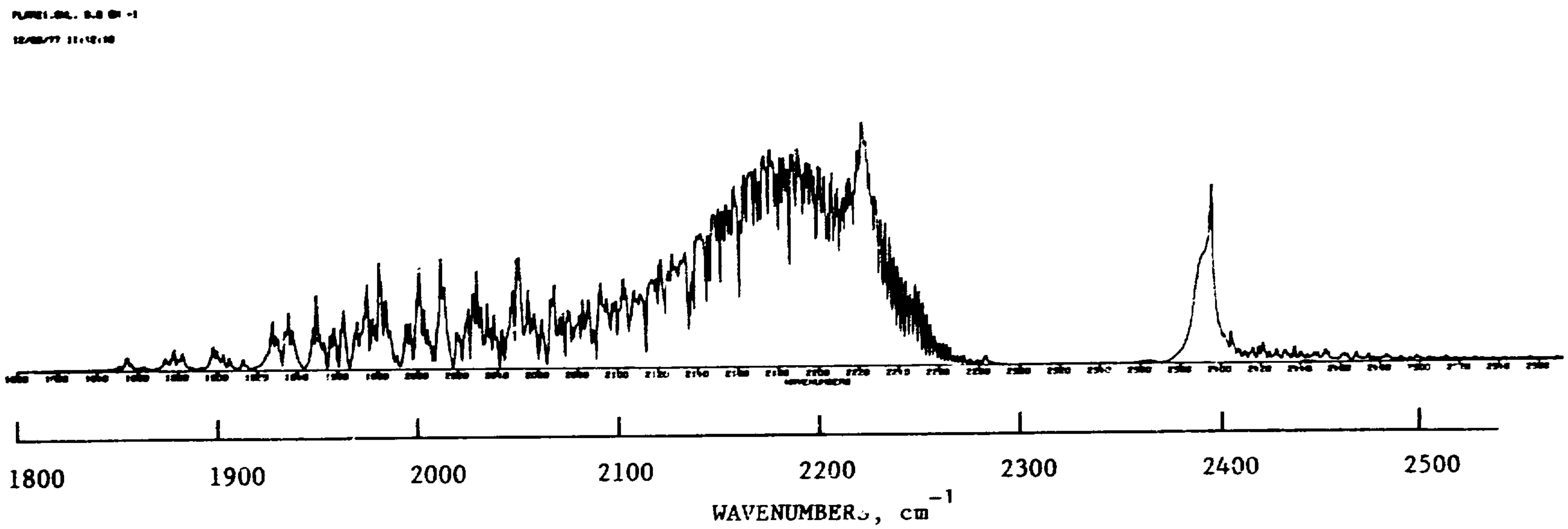

Figure 47. Measured Emission Spectrum of a Refinery Gas Burn off Flare

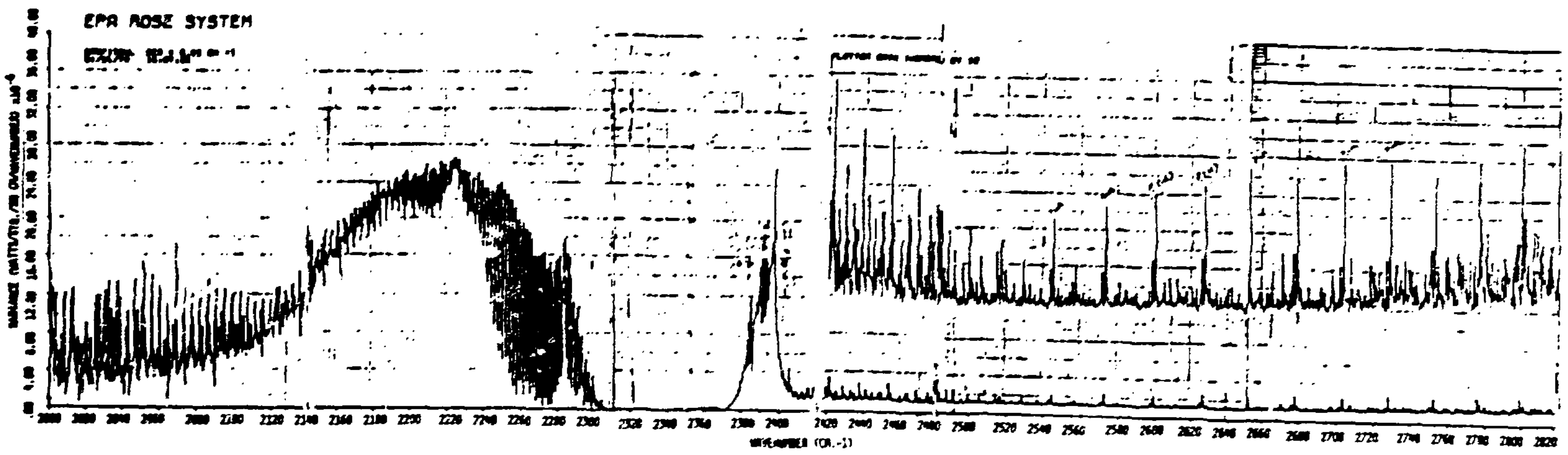

a) Measured

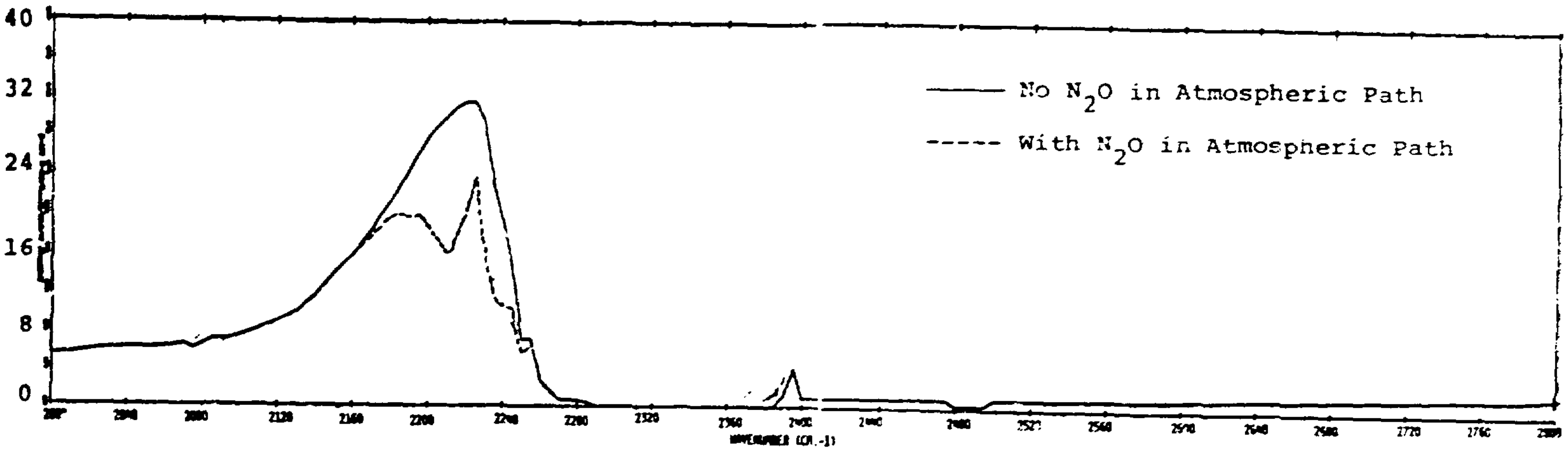

b) Calculated

Figure 48. Flare Radiance Measured by EPA and Calculated Using the ATLES Computer Code.

emission lines with regular spacing of approximately 20 cm^{-1} between 2500 and 2900 cm^{-1}. This molecule results from the combustion of the chlorine compounds by the flare.

The peak intensities of the HCL lines were used to deduce a rotational temperature of 2400 K for the flame. Using this temperature and the emission and absorption path quantities given in Table 7, calculations were made of the predicted emission spectra using ATLES. As shown in Figure 48 the absorption from atmospheric N_2O must be included to obtain shape agreement between the prediction and the measurement. In general, the agreement between the measurement and the prediction is good. Of course, the prediction does not show the line structure of either the CO or the HCl bands. The sharp depression at 2500 cm^{-1} results from a gap in the H_2O band model parameters caused by the merging of two not-quite-overlapping band model parameter sets.

It is also apparent from the comparison that band model parameters currently available for ATLES are inadequate for modeling the bluespike at high temperature. The prediction of the BLUESPIKE computer code when applied to this measurement is shown in Figure 49. While this result is significantly better than given by ATLES it is still somewhat inadequate. In fact, for most situations the BLUESPIKE predictions will be better than indicated by Figure 49, since with longer atmospheric paths the lines below 2390 cm^{-1} will be strongly attenuated by CO_2 absorption.

Figure 50a, b, c and d show the contributions of the various active species in the flare as computed by ATLES. These calculations do not contain N_2O in the atmospheric path. One fact to notice is the comparison between the measured high resolution spectra (Figure 48a) and the computed ATLES spectra. In particular, note the strikingly simple manner with which the constituent molecules can be identified from the measured spectra as compared with the computed low resolution spectra where everything merges together into a continuum.

TABLE 7

PHYSICAL CONDITIONS USED FOR CHEMICAL BURNOFF FLARE MODEL

EMISSION PATH		
Thickness:		50 cm
Temperature:		2400 K
Total Pressure:	1.0 atm	
Partial Pressures of Active Species		
H_2O:		0.015 atm
CO_2:		0.010 atm
CO:		0.002 atm
HCL:		0.001 atm
ABSORPTION PATH		
Length:		1 km
Temperature:		272.2 K
Total Pressure:	1.0 atm	
Partial Pressure of Active Species		
H_2O:		4.344 E-03 atm
CO_2:		0.00033 atm
CO:		7.5 E-08 atm
N_2O:		2.8 E-07 or 0 atm

Water and Nitrogen Continuum is included.

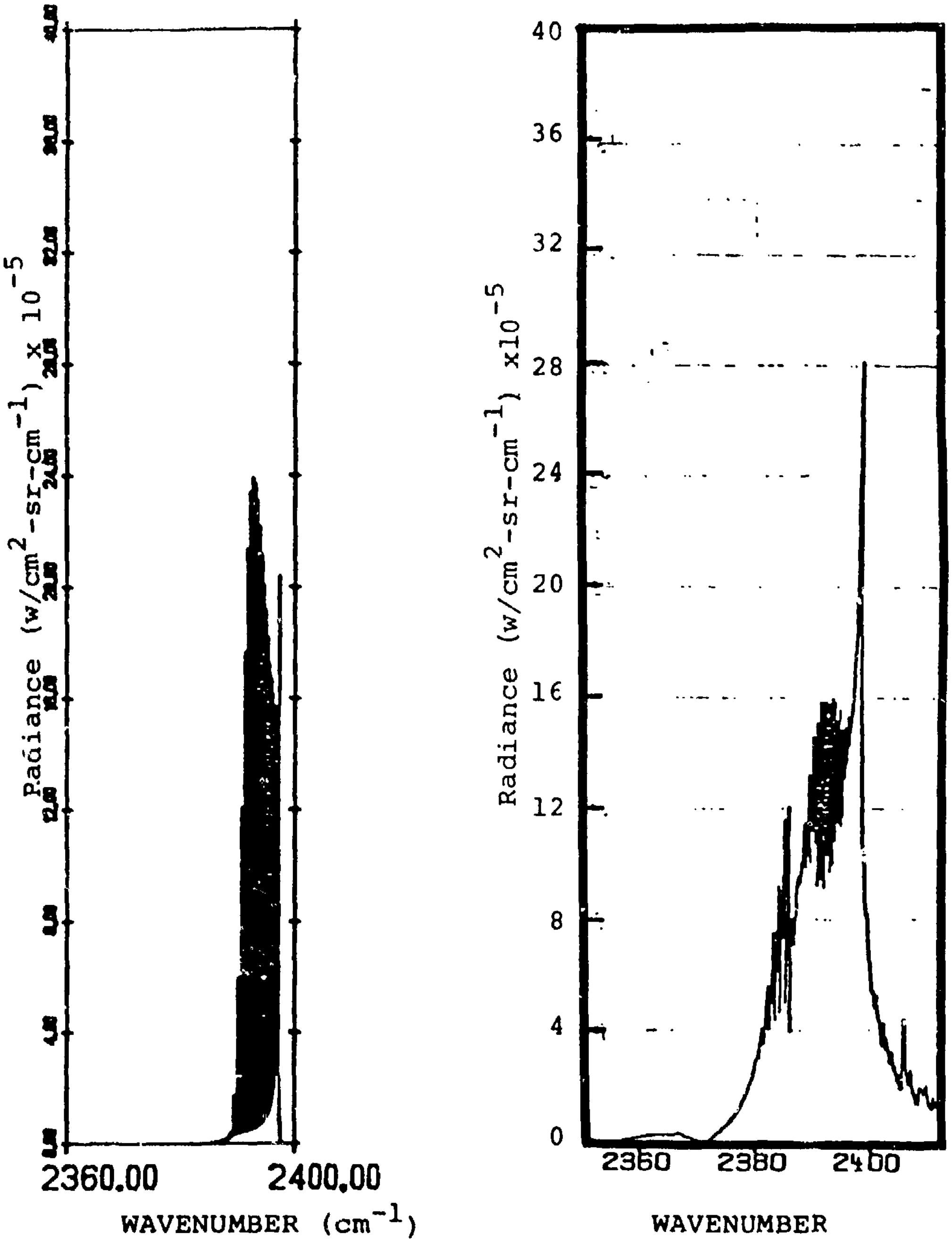

a) Calculated

b) Measured

Figure 49. Blue Spike Radiance Calculated by the BLUESPIKE Computer Code Compared With Flare Measurements

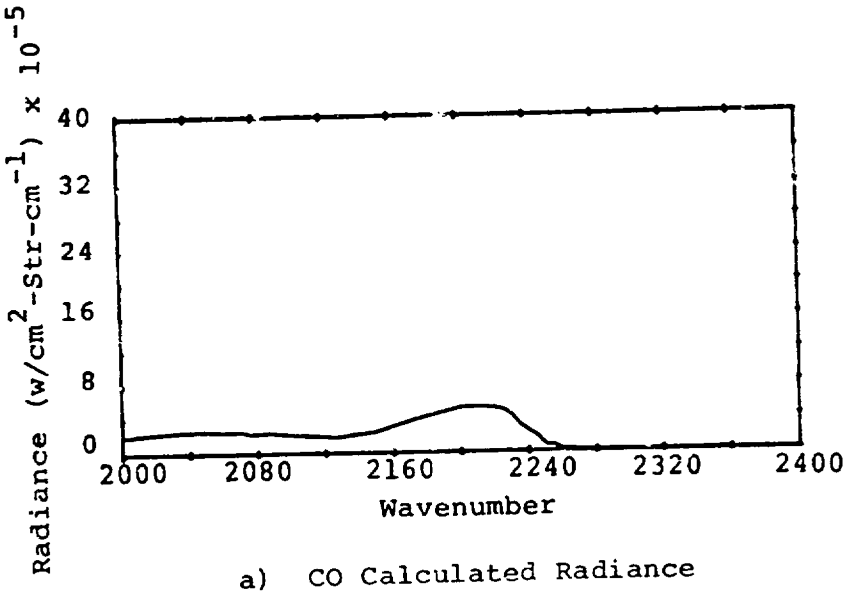

a) CO Calculated Radiance

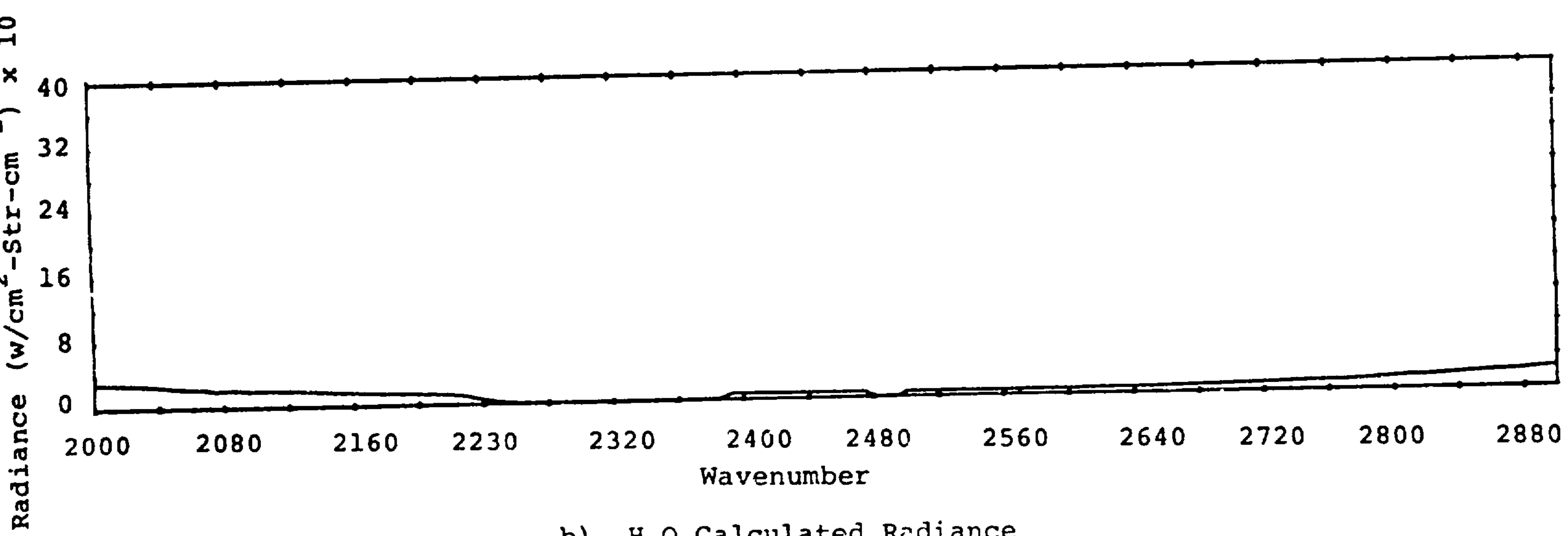

b) H_2O Calculated Radiance

Figure 50. Radiances Calculated for Various Molecular Constituents of the Flare

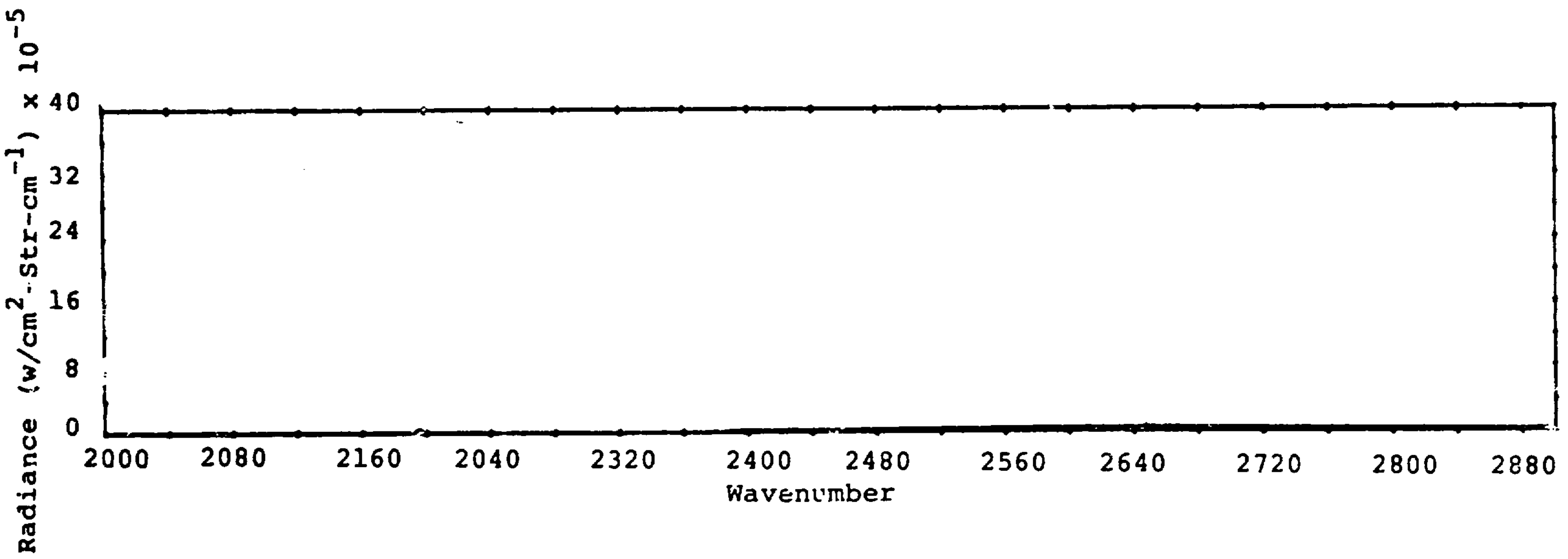

c) HCl Calculated Radiance

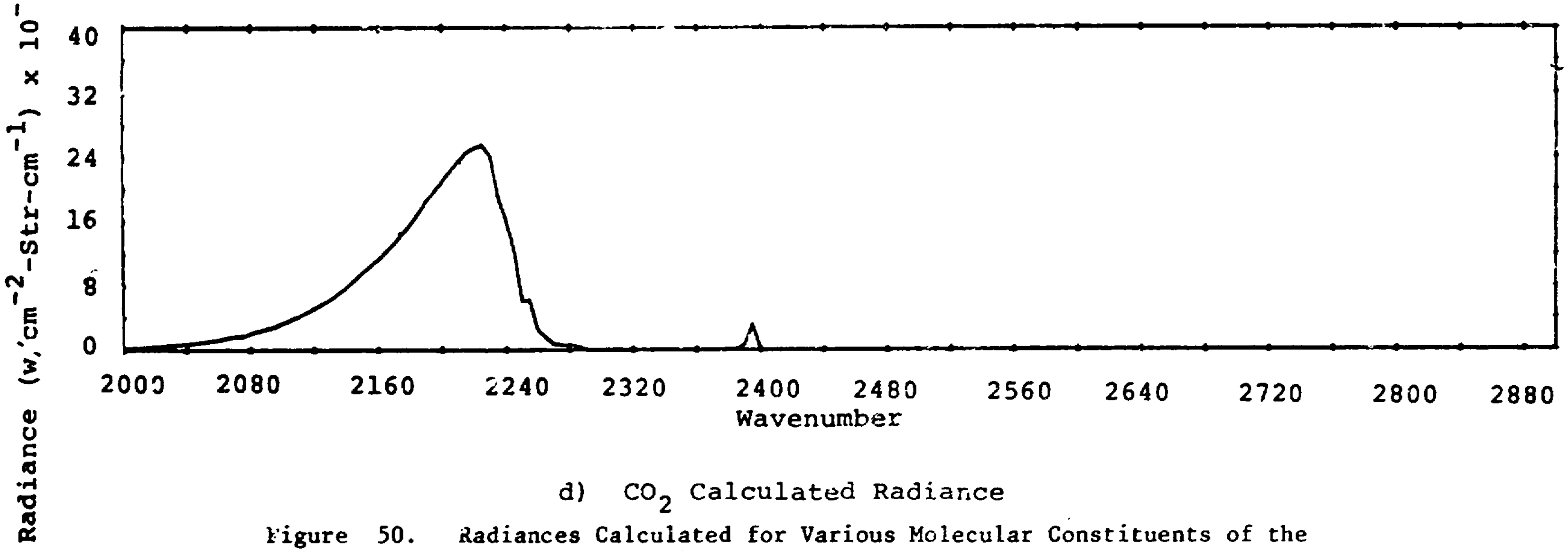

d) CO_2 Calculated Radiance

Figure 50. Radiances Calculated for Various Molecular Constituents of the Flare (Continued).

6.4 HEATED GRAYBODY RADIATIVE SOURCES

The measurements available for graybody sources were obtained by AFGL over industrial areas of the Southeast and Midwest in June 1978. The measurements were taken from the AFGL KC-135 aircraft primarily with the number 103 FTS system, which has a one-degree field-of-view. The measurements were made while the aircraft circled the target at a range of approximately 3500 meters. Thus, the field-of-view projects a 60-meter diameter spot on the ground. Since this is significantly larger than the diameters of most sources, the resulting spectra contain contributions from the backgrounds as well as localized hot sources. Auxiliary data was available for some of the measurements in the form of thermal imagery, movies and still photographs. However, this data was of limited utility in analysis of the spectral data. The radiometric imagery was used to locate the sources and approximate areas of the hot spots, and the photography was useful for the same purpose. However, because of blooming in the thermal images and the difficulty in identifying hot spots from the photography, the source areas could only be estimated. The radiometric imagery was uncalibrated and therefore was not useful for estimating source radiance or intensity values.

The complete set of industrial site spectra obtained from AFGL are given in Appendix D. (AFGL obtained these spectra in support of the IR Signature Study, and does not plan to publish them as an AFGL report.) The corresponding radiosonde data are included in Appendix B. The spectra cover the wavelength range measured by AFGL; however the present study only examined the 3.5 to 5.0-micrometer region. Although significant solar scattering was observed at the shorter wavelengths, no solar contributions were observed in the 3.5 to 5.0-micrometer region. Therefore the present analysis ignored solar scattering.

Figures 51, 52 and 53 are typical examples of the measured spectra of various graybody sources. The most conspicuous structure is the dip in the radiance due to the CO_2 absorption band between 2220 and 2380 cm^{-1}. Another prominent feature observable in all of the graybody spectra is the small emission peak near 2220 cm^{-1} resulting from the higher transmittance between the P and R branches of the N_2O atmospheric absorption band. The appearance of this feature makes many of the graybody spectra look similar to the red spike structure seen in molecular spectra in this wavelength region.

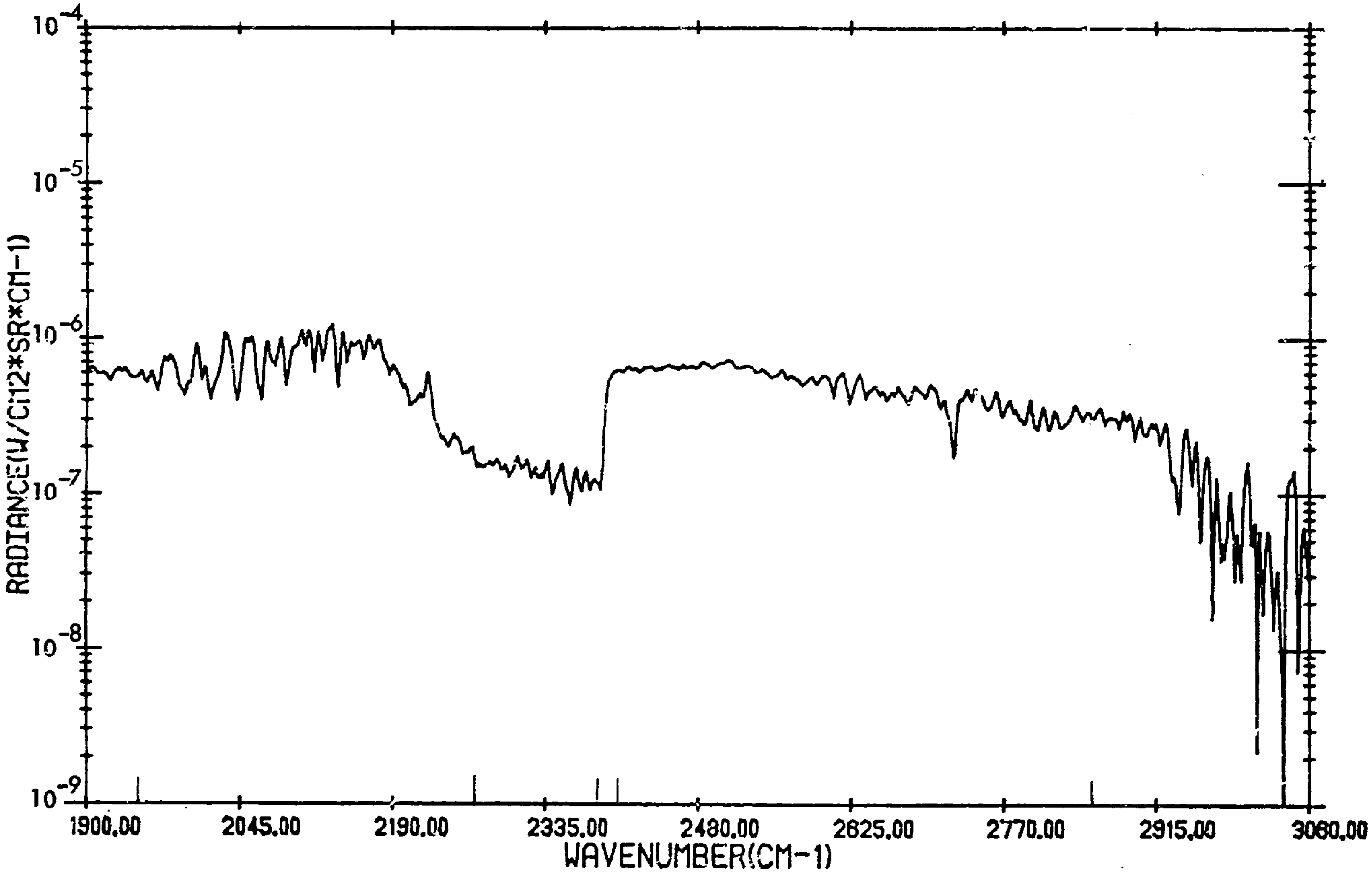

Figure 51. Measured Average Apparent Radiance Observed When Viewing Hot Gray Building at Steel Mill in Fairfield, AL (Effective Temperature - 500 K, Effective Hot Area - 5% of FOV)

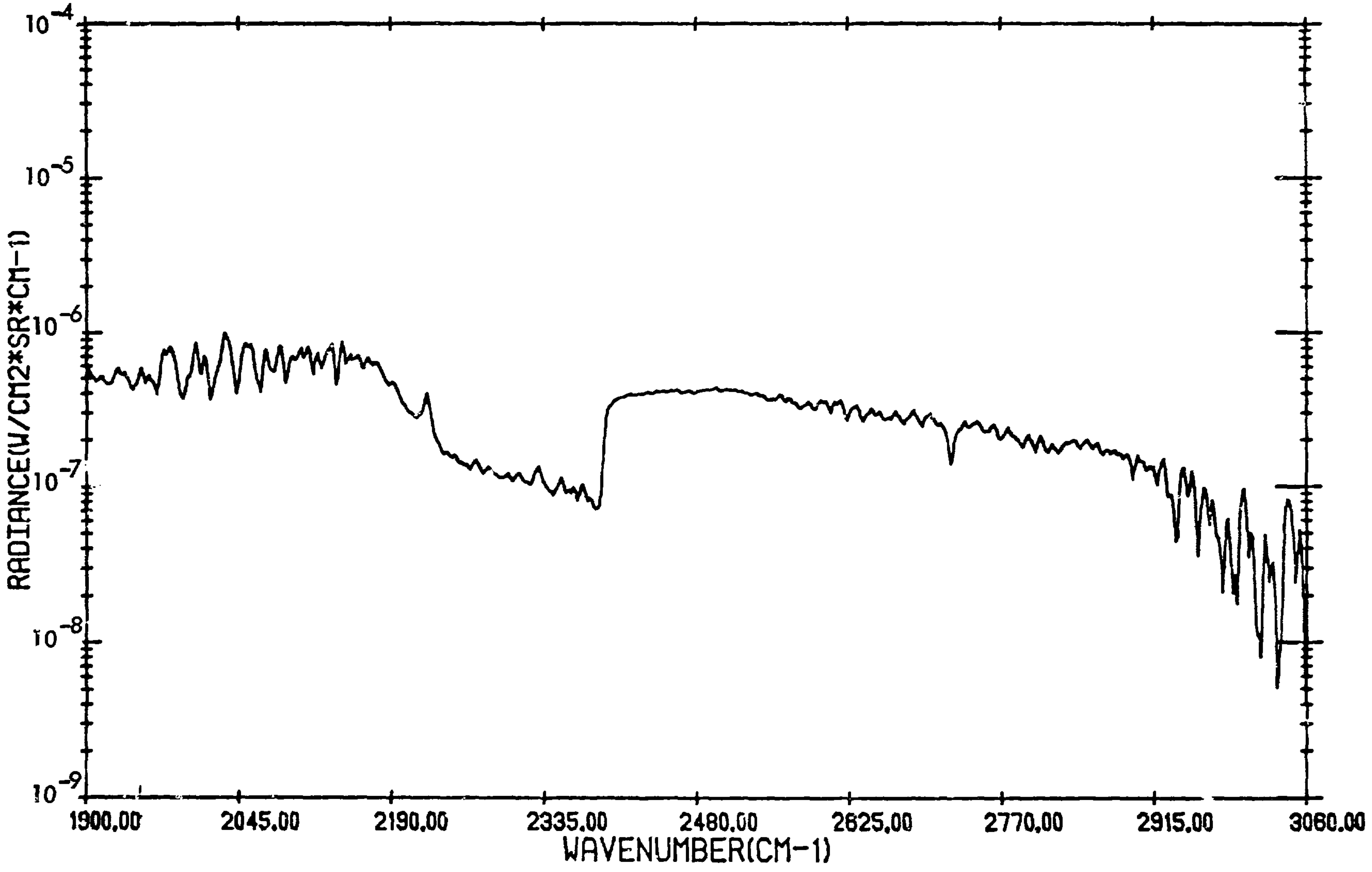

Figure 52. Measured Average Apparent Radiance Observed When Viewing Coke Ovens At Steel Plant in Wyandotte, MI (Effective Temperature - 600 K, Effective Hot Area - 1% of FOV)

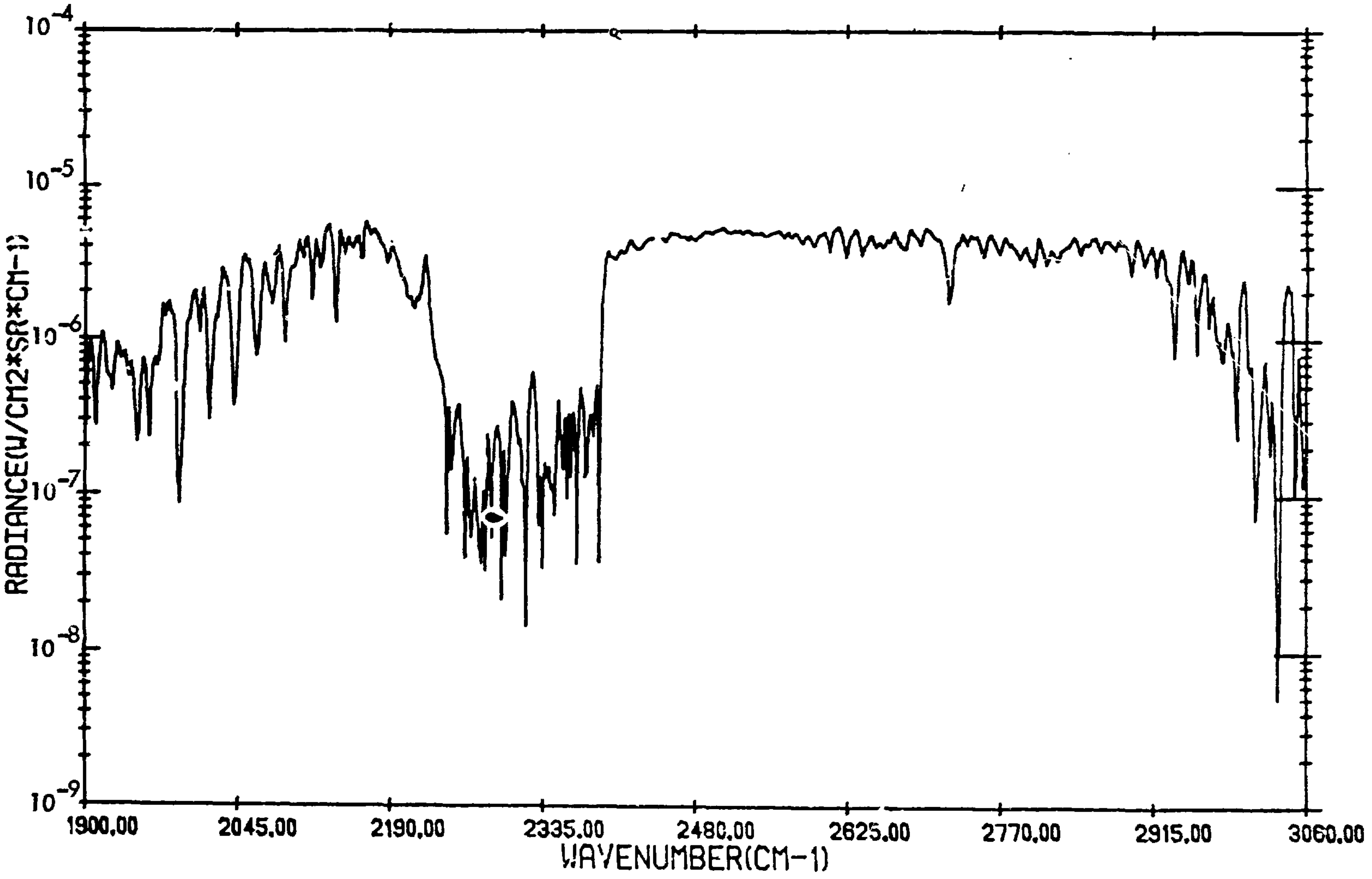

Figure 53. Measured Average Apparent Radiance Observed When Viewing "Orange Hot Metal" and Nearby Buildings at Steel Mill in Fairfield, AL (Effective Temperature - 1300 K, Effective Hot Area - 0.5% of FOV)

We carefully analyzed a number of the AFGL spectra in two respects: we estimated the temperatures and emissivity-areas of the sources, and we also obtained the apparent intensity of the sources.

6.4.1 Temperatures and Emissivity-Areas of Graybody Sources

LOWTRAN 4[4] was used in the emission mode to analyze the measured graybody spectra. The following procedure was used: first, the measured data was plotted on semi-log ordinate scales. Measured spectra which showed molecular emission were put aside for later analysis. Next, a number of LOWTRAN radiance calculations were made assuming source temperatures between 400 and 1000 K and unit emissivity. These calculations were also plotted in semi-log form. An example computation with a source temperature of 600 K is shown in Figure 54. With the calculations in this form a vertical offset in the graphs is approximately equivalent to changing the emissivity-area of the source. (This would be rigorously true except for the contributions of path radiance which are negligible in the infrared window regions.) Finally, by overlaying the LOWTRAN calculations on the measured spectra, the approximate temperature and emissivity-area of the graybody source was obtained. In this process the temperature was determined by selecting the LOWTRAN spectra which best fit the shape of the measured spectra in the 3.5 to 4.1-micrometer window region regardless of the level of the curve. The temperature of the best-fit LOWTRAN spectrum was then taken as the approximate temperature of the source. We estimate the accuracy of this procedure is approximately ±100 K. The offset of the best-fit LOWTRAN calculation when overlayed on the measured spectra gives the source emissivity-area as a ratio of the total area within the field-of-view of the instrument. A similar procedure has also been defined based on the computer algorithm described in Appendix E. The emissivity-areas inferred by either procedure are critically dependent on the inferred temperatures of the sources; however, if the emissivity-area and temperature pairs are used together, results consistent with the measurement will be obtained.

The temperatures and emissivity-areas obtained are given in Table 8. Not all of the spectra were analyzed in this manner, but the values given in the table encompass the range of sources measured. Of course the measurements

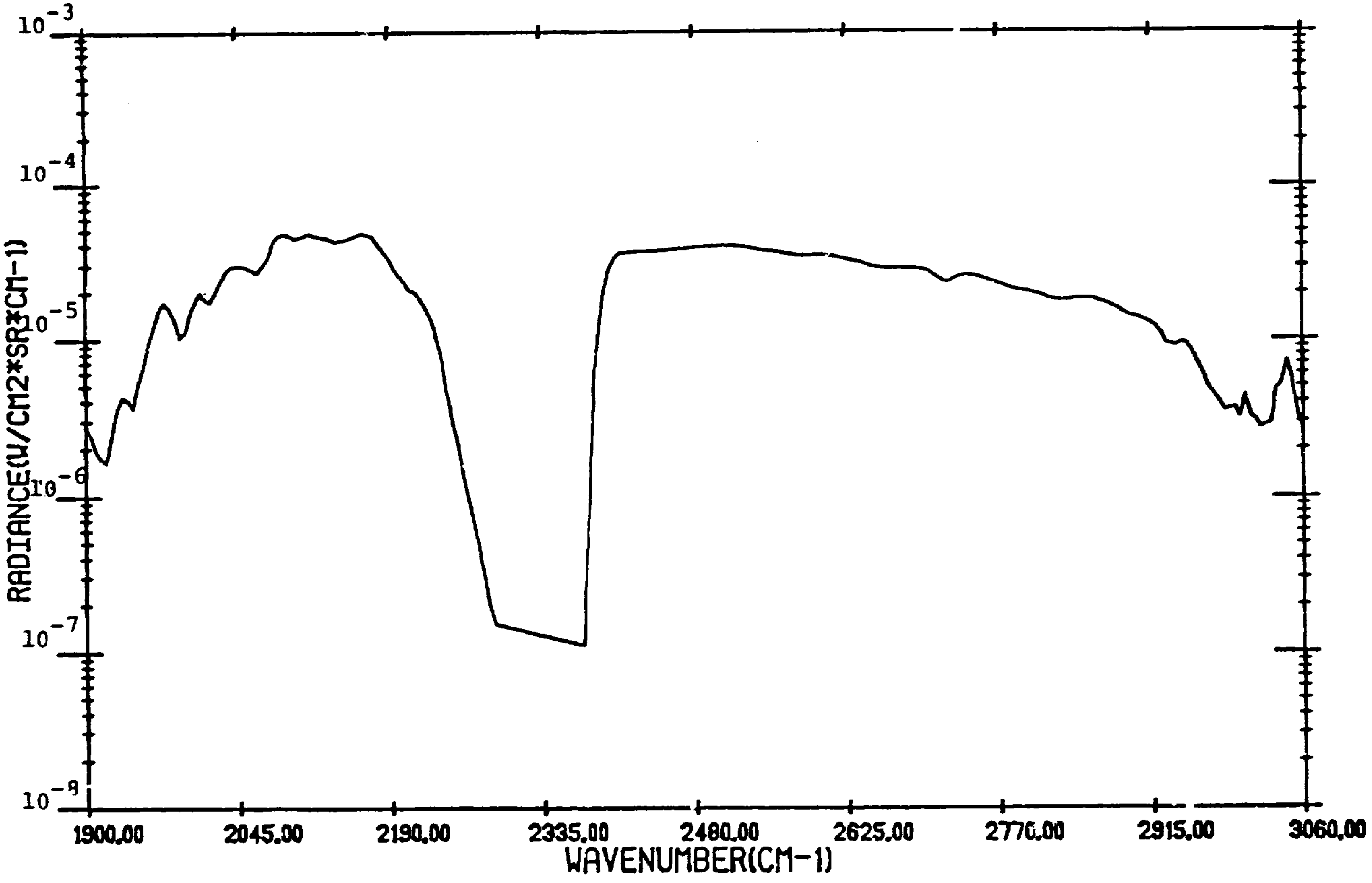

Figure 54. LOWTRAN 4 Calculation of the Apparent Radiance of a Blackbody Source as Observed from an Aircraft (Temperature - 600 K, Hot Area - 100% of FOV)

represent complex scenes and thus the temperatures must be considered effective temperatures, which will be near the peak temperature observed within the scene. In general, similar physical sources are inferred to have similar temperatures. Any scene which was identified as having molten or "orange" metal visible was anlayzed to have a temperature of 800 K or slightly higher. Hot coke ovens and other hot buildings have temperatures ranging from 500 to 600 K. The emissivity-areas are typically 20–200 square meters; these are small compared to the instrument field-of-view or the physical sizes of the buildings. These values are also in agreement with areas obtained from the infrared imagery for cases where imagery was available. The small effective sizes indicate the difficulties in obtaining the emitting areas from visible photography, which does not distinguish the hot areas from the remainder of the structure.

6.4.2 Graybody Source Intensities

The apparent radiant intensities of sources were also obtained directly from the measured spectra. These results were obtained for the mid-IR window (3.5 – 4.15 micrometer), the blue spike (4.15 – 4.20 micrometer) and the red spike and wing (4.4 – 5.0 micrometer) spectral regions; these results are shown in Table 9. These values were obtained by integrating the measured spectra over the wavelength bands of interest and subtracting similarly integrated background intensities. Since these values were obtained directly from the measured spectra they are independent of the temperature and emissivity-area results and the uncertainties therein. Because the ranges and background radiances are somewhat uncertain, these values have associated uncertainties of perhaps ±25 percent, but they do show the typical intensities expected for these types of sources.

The intensity ratios given in Tables 8 and 9 were computed in the hope that a unique indication of a graybody source could be obtained from these ratios. Unfortunately, it was found that the ratios varied considerably from source to source; probably because of the sensitivity of the blackbody function to temperature within the region examined.

TABLE 8

CHARACTERISTICS OF SELECTED GRAYBODY EMISSION SOURCES

Source Description (Time of Measurement)	T (K)	Hot Area (%FOV)	Hot Area (m^2)	Range (km)	Integrated Intensity (KW/str)			Intensity Ratios	
					Window 3.5-4.17	Blue Spike 4.17-4.20	Red Spike 4.4-5.0	Blue Spike / Window	Red Spike / Window
Gray Building Fairfield, AL (13:03 : 26.9)	500* (562)†	5.0 (3.7)	112.4 (83.2)	3.065	4.082	0.106	2.052	0.026	0.503
Coke Oven Gary, IN (14:01 : 55.5)	600 (496)	1.7 (6.4)	60.9 (229.4)	3.872	6.864	0.183	4.847	0.041	0.706
Coke Oven Wyandotte, MI (15:07 : 42.7)	600 (481)	1.0 (4.9)	18.1 88.9)	2.754	1.721	0.0317	1.005	0.018	0.584
Blast Furnace Wyandotte, MI (15:02 : 25.0)	600 (574)	0.37 (0.40)	8.9 (9.6)	3.175	17.64	0.439	10.58	0.025	0.600
Hot Ore Gary, IN (13:44 : 12.6)	800 (819)	0.7 (0.69)	20.6 (20.3)	3.505	14.25	0.172	5.671	0.012	0.398
Stacks & Hot Railroad Cars Wyandotte, MI (15:27 : 34.3)	800 (704)	1.1 (2.5)	31.3 (71.2)	3.450	21.65	0.457	9.25	0.021	0.427
Railroad Cars w. Hot Metal Wyandotte, MI (15:28 : 05.4)	800 (746)	1.4 (2.4)	33.8 (57.9)	3.175	24.55	0.481	9.39	0.020	0.382
Orange Hot Metal Fairfield, AL (13:07 : 05.9)	>600 (1367)	2.5 (0.45)	40.2 (7.2)	2.553	31.73	0.540	9.22	0.017	0.291
Hot Slag Gary, IN (13:48 : 45.1)	>800 (845)	3.0 (2.3)	88.2 (67.6)	3.505	58.53	1.057	21.05	0.018	0.360

*Temperatures and Areas extracted from graphical analysis described in text.

†Temperature and Areas extracted using computer analysis described in Appendix B

TABLE 9

CHARACTERISTIC OF SELECTED GRAYBODY SOURCES DETERMINED FROM MEASURED SPECTRA

Source Description (Time of Measurement)	$T_{Graybody}$	Hot Area		T_{gas}	Gaseous Area		Range	Integrated Intensity Kw/str			Intensity Ratios	
								Window	Blue Spike	Red Spike	Blue Spike	Red Spike
	K	%FOV	m^2	K	%FOV	m^2	km	3.5-4.17	4.17-4.20	4.4-5.0	Window	Window
Stack Flare (Gas Burnoff) Gary, IN (14:06 : 33.8)	> 800	1.4	72.8	2400	6.7	444	4.663	67.21	3.41	65.296	0.051	0.972
Flame from Stack Ashland, KY (1[illegible]:33 : 26.5)	> 800 (1519)	0.28 (0.03)	7.2 (0.8	2400	0.75	4.4	3.269	3.95	0.129	2.06	0.033	0.522

6.4.3 Combined Graybody and Gaseous Emission Sources

A number of the AFGL measurements include both graybody emission and gaseous emission sources within the field-of-view. Examples of this type of source are shown in Figures 55, 56 and 57. The measured stack flare emission spectrum shown in Figure 55 was one of the strongest sources of gaseous emission as well as the brightest radiator of all sources measured. As can be seen from Figure 55, the "red spike" region is very similar in structure to some of the hotter graybody sources. (Compare with Figure 53.) This is because the primary structure in the red spike region for high temperature or graybody sources results from the absorption structure in the atmosphere. Some of the molecular line complexes in the region show a "W" shape which may be characteristic of a gaseous emission source. This type of structure is not evident in the graybody measurements.

The blue spike is clearly visible in all of the molecular emission spectra at 2395 cm^{-1}. This feature was clearly distinguishable in every spectrum where molecular emission was expected and thus appears to be an unambiguous indication of molecular emission.

These composite spectra were also analyzed in a manner similar to that described for the graybody spectra. The graybody component was extracted by concentrating on the 3.5 to 4.15-micrometer window region where little or no molecular emitting areas were inferred from the expected temperatures of the sources and the peak radiances of the red spike and blue spike above the graybody levels. These areas must be considered crude estimates; however in the case of the "flame from stack" the inferred area agrees closely with the value obtained from the thermal imagery. The results are given in Table 9.

The separation of the emission into graybody and gaseous emission components appears to be valid except for the case of the stack flare. For that case, the continuum emission appears to have a slope much too high to be explained as heated metal emission. It is our hypothesis that this results either from particulates in the flame or perhaps H_2O emission from weak hot band lines. In

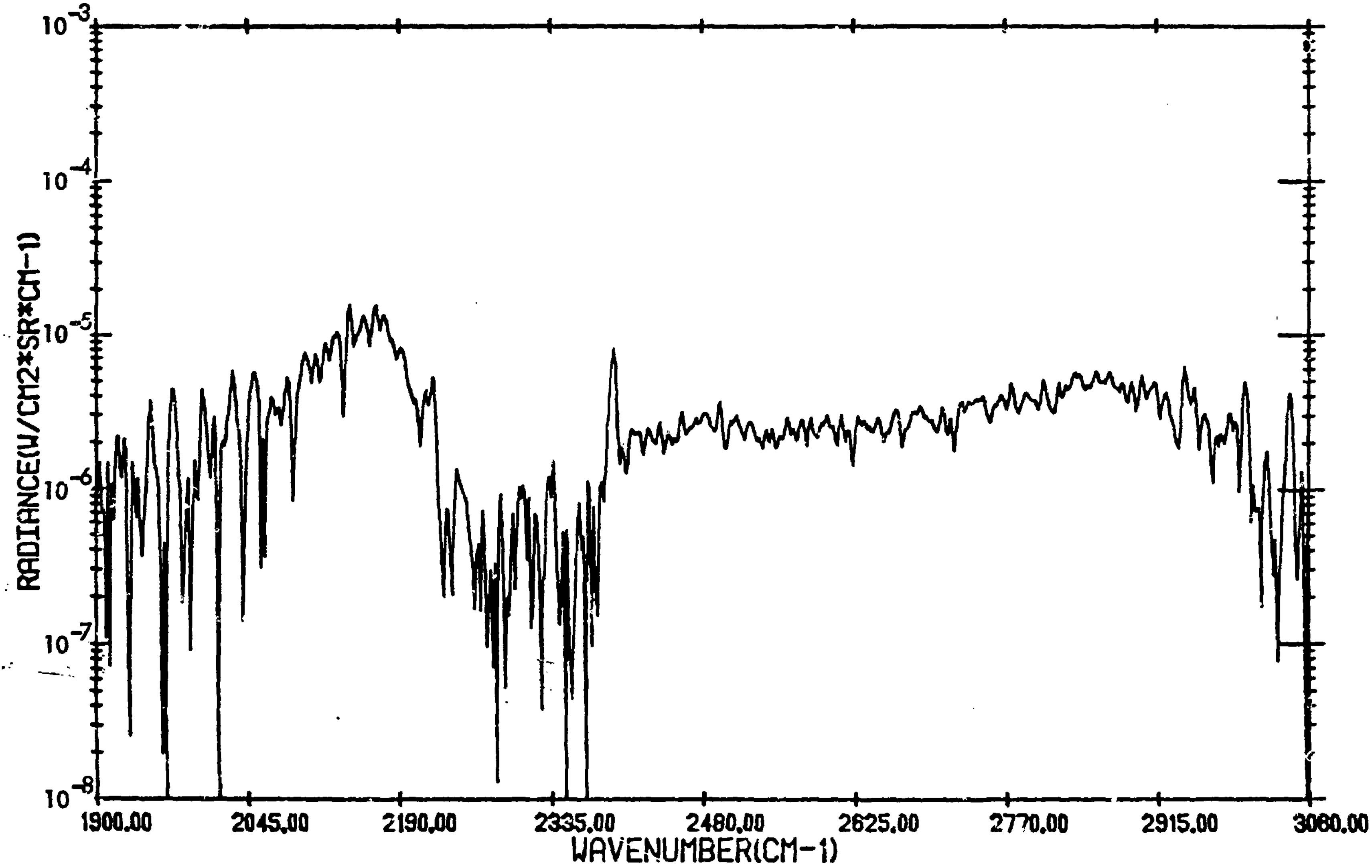

Figure 55. Measured Apparent Radiance of Stack Flare (Gas Burnoff) at Gary, IN

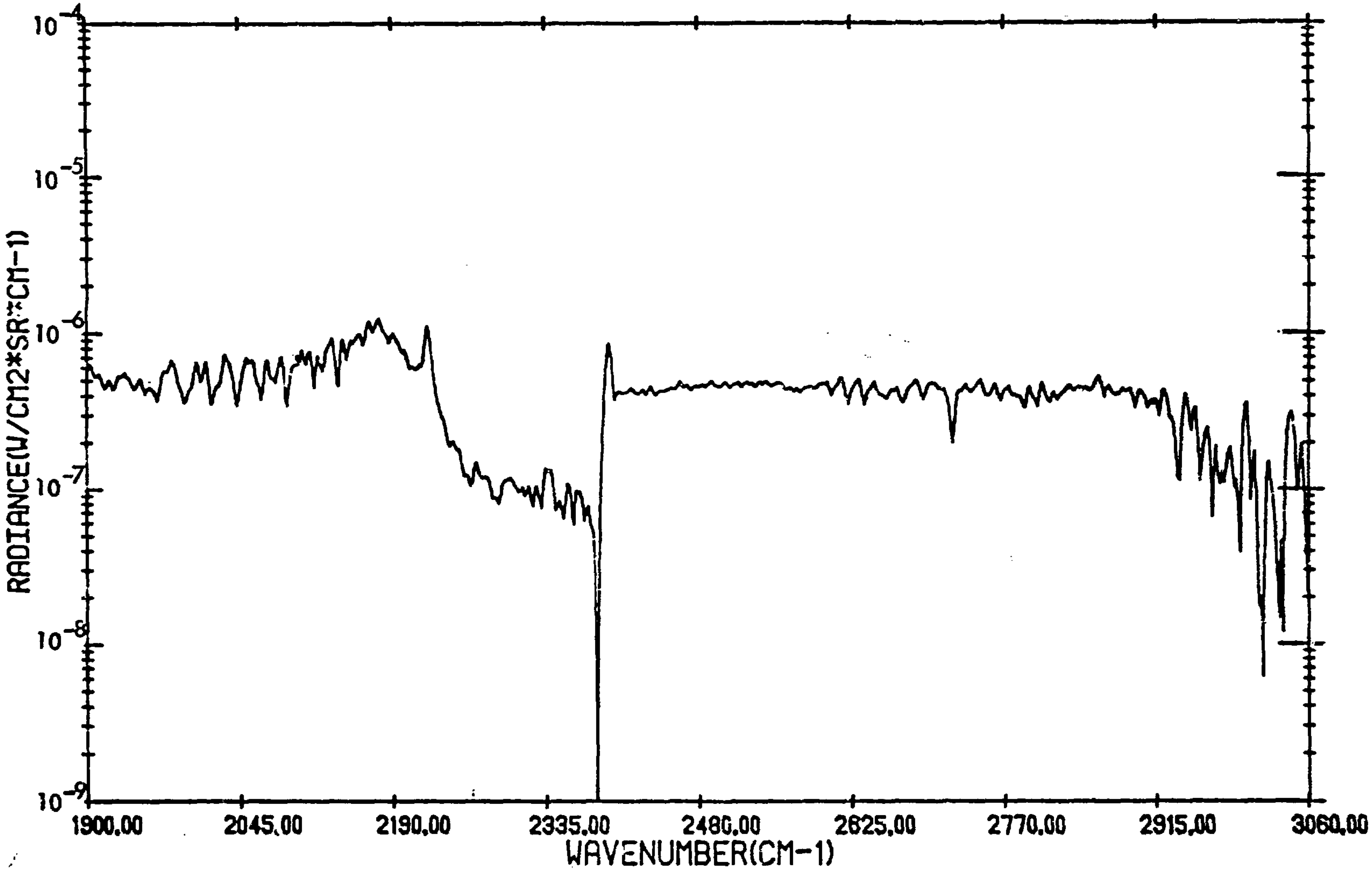

Figure 56. Measured Apparent Radiance of a Stack Flame at Ashland, KY

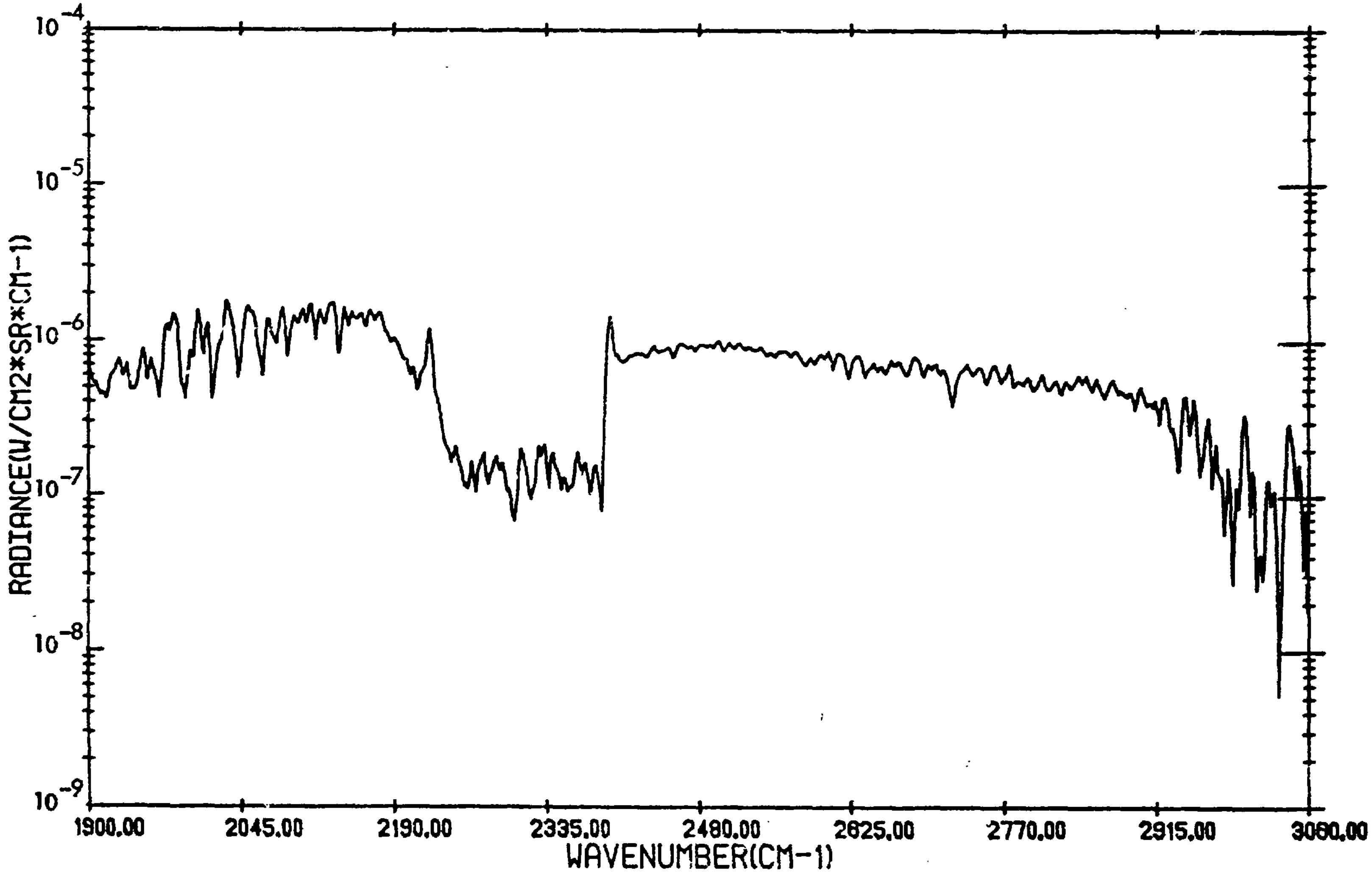

Figure 57. Measured Apparent Radiance of the Stack of a Large Rolling Mill at Gary, IN

general, the molecular emission from the flare or flame sources dominates the graybody emission; however, except for the blue spike, the molecular emission from the stack sources is dominated by the graybody emission from the hot stack or associated structures.

SECTION VII

REFUSE FIRE FALSE THREATS

Burning refuse material represents a serious and common false threat source over battlefield environments. The only direct spectral radiance measurement located for this type of threat is a spectrum of rice-stubble burnoff measured by AFGL during a flight over the San Joaquin Valley in California. This spectrum is shown in Figure 58. With the limited resolution of the data we have not been able to identify any molecular emission except a very weak blue spike CO_2 emission. Other molecular emission may be present; however, a careful computer analysis would probably be required to identify it.

The window region between 3.5 and 4.2 micrometers in the measured spectrum shows evidence of graybody emission similar to that seen in the hot industrial sources. We have analyzed the spectrum in a manner similar to that described in the previous section. The results indicate an effective graybody temperature of 575 ± 100 K and an effective emissivity-area of 7.5 percent of the instrument field-of-view. Given the AFGL estimate that the visible flame filled 1 to 2 percent of the field-of-view, this result for the effective emissivity-area of the source seems reasonable.

A set of measurements of the absorption of the products of refuse fires was located. This data is summarized in Table 10 and the measured spectra are shown in Figures 59 to 63. These measurements were made by burning the substance in question in the laboratory and collecting the gases and particulates produced in cells or on filters.

While it is doubtful that accurate source emission intensities could be obtained from this set of data, it does provide useful qualitative information. For most materials and spectral regions, the particulate absorptivities are much larger than the molecular absorptivities; but, there seems to be a window in the

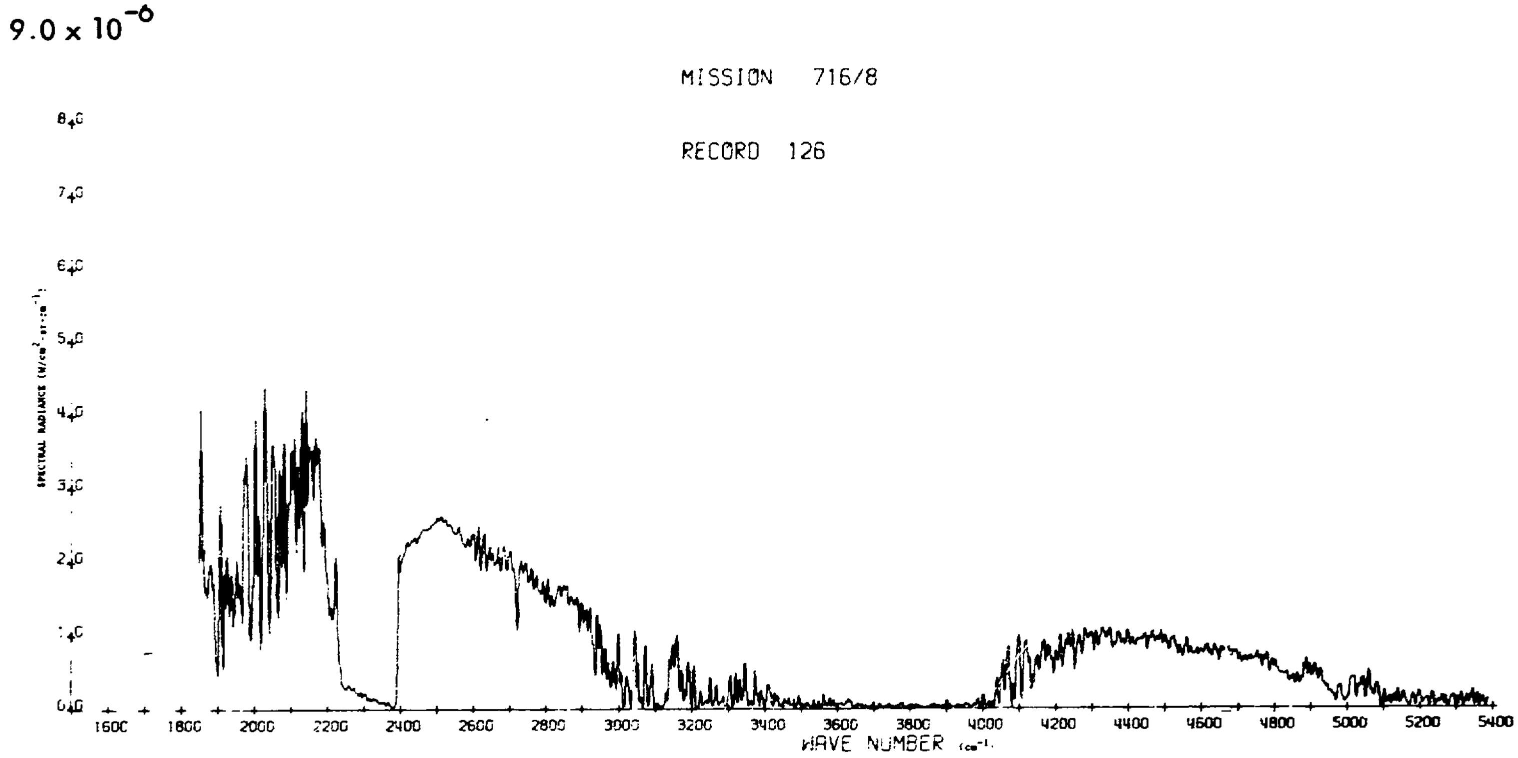

Figure 58. Measured Spectrum of Rice-Stubble Burnoff Measured by AFGL Over San Joaquin Valley. Mission 716, Run 8, Record 126.

TABLE 10

POTENTIAL REFUSE FIRE FALSE THREAT SOURCES

Refuse Type	H_2O	CO_2	CH_4	CO	HCl	N_2O	Other Gases	Particulates	$T(^{\circ}K)$	Typical Duration	References/Comments	Reference Figure
Grass	X	X	X	X			CH_3, OH, C_2H_2	.2-1/g-cm Structure from 2800-3400 cm^{-1}		Minutes	Barrett/Absorptivities of Gaseous and Particulate Products	59
Cotton Cloth	X	X	X	X			C_2H_2			Minutes	Barrett/As [illegible]	60
Wool Cloth		X		X			HCN, C_2H_2,	Structure from 2800-3400 cm^{-1}		Minutes	Barrett/As Above	61
Rubber		X	X	X			C_2H_4, Other Hydrocarbons			Minutes	Barrett/Absorptivities of Gaseous Products	62
Paper	X	X	X	X			C_2H_2			Minutes	Barrett/As Above	63
Gasoline Exhausts	X	X	X	X			HCN			Minutes	Barrett/As Above	

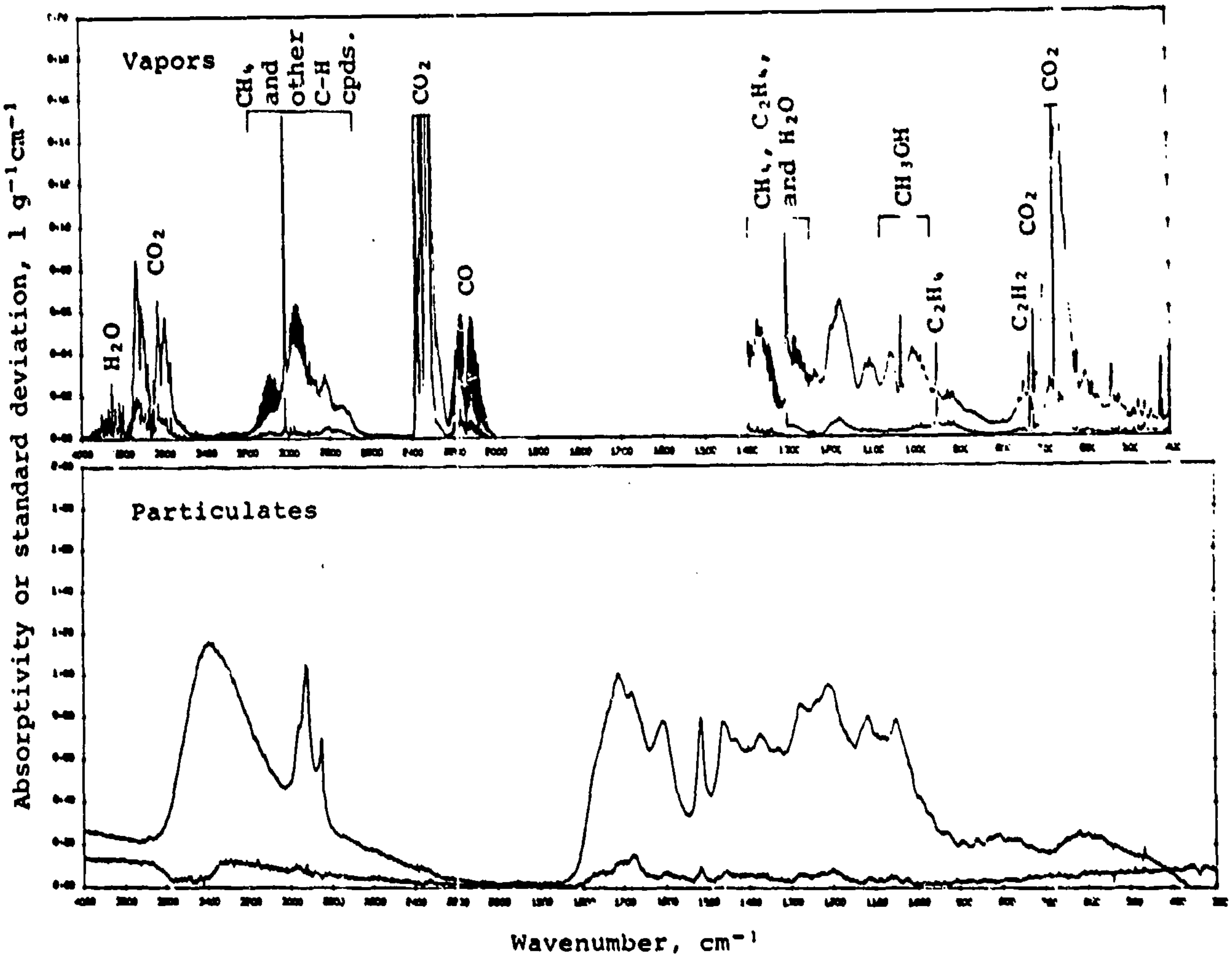

Figure 59 Absorptivities of the Products of Burning Gases[24]

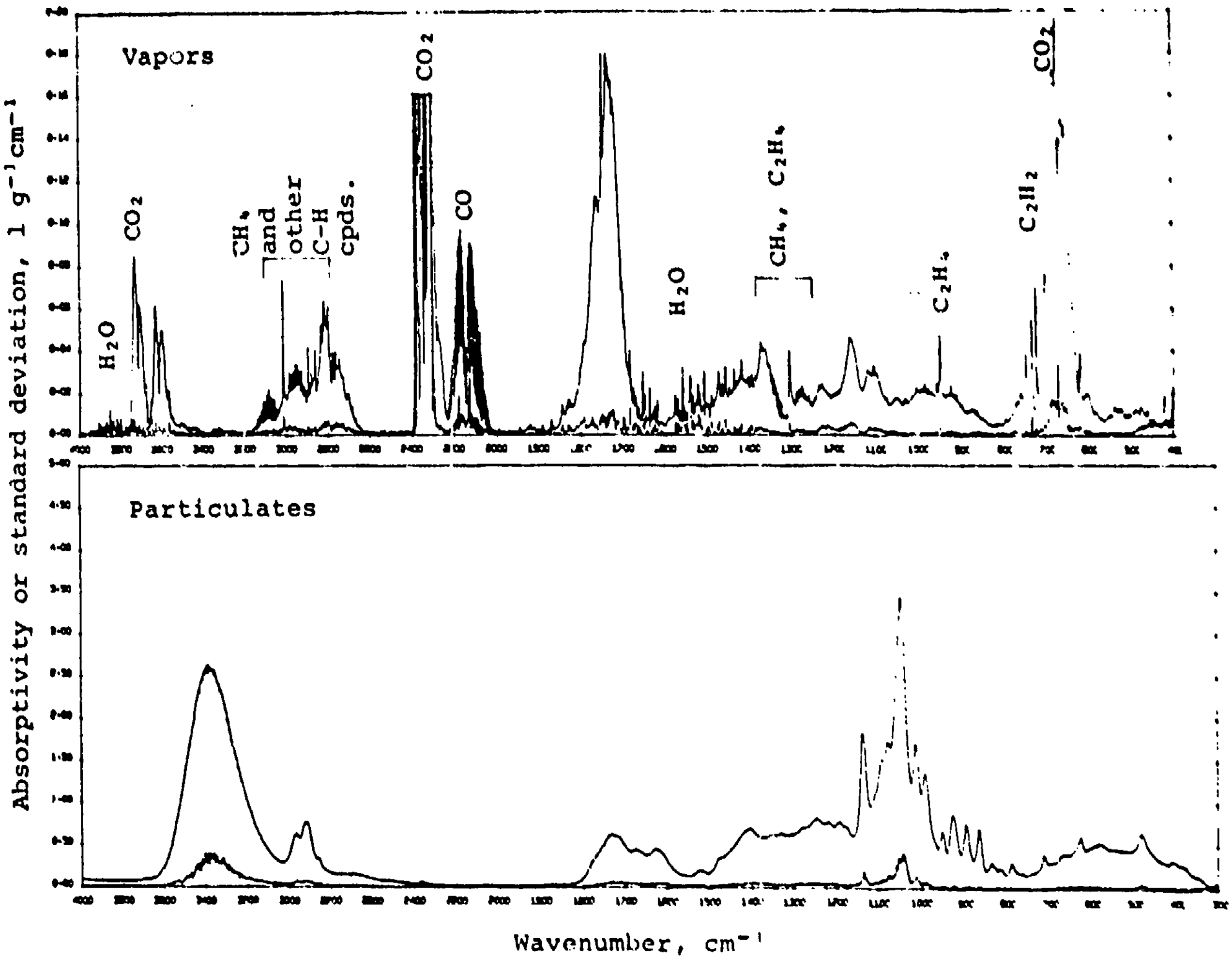

Figure 60. Absorptivity of the Products of Burning Cotton Cloth[24]

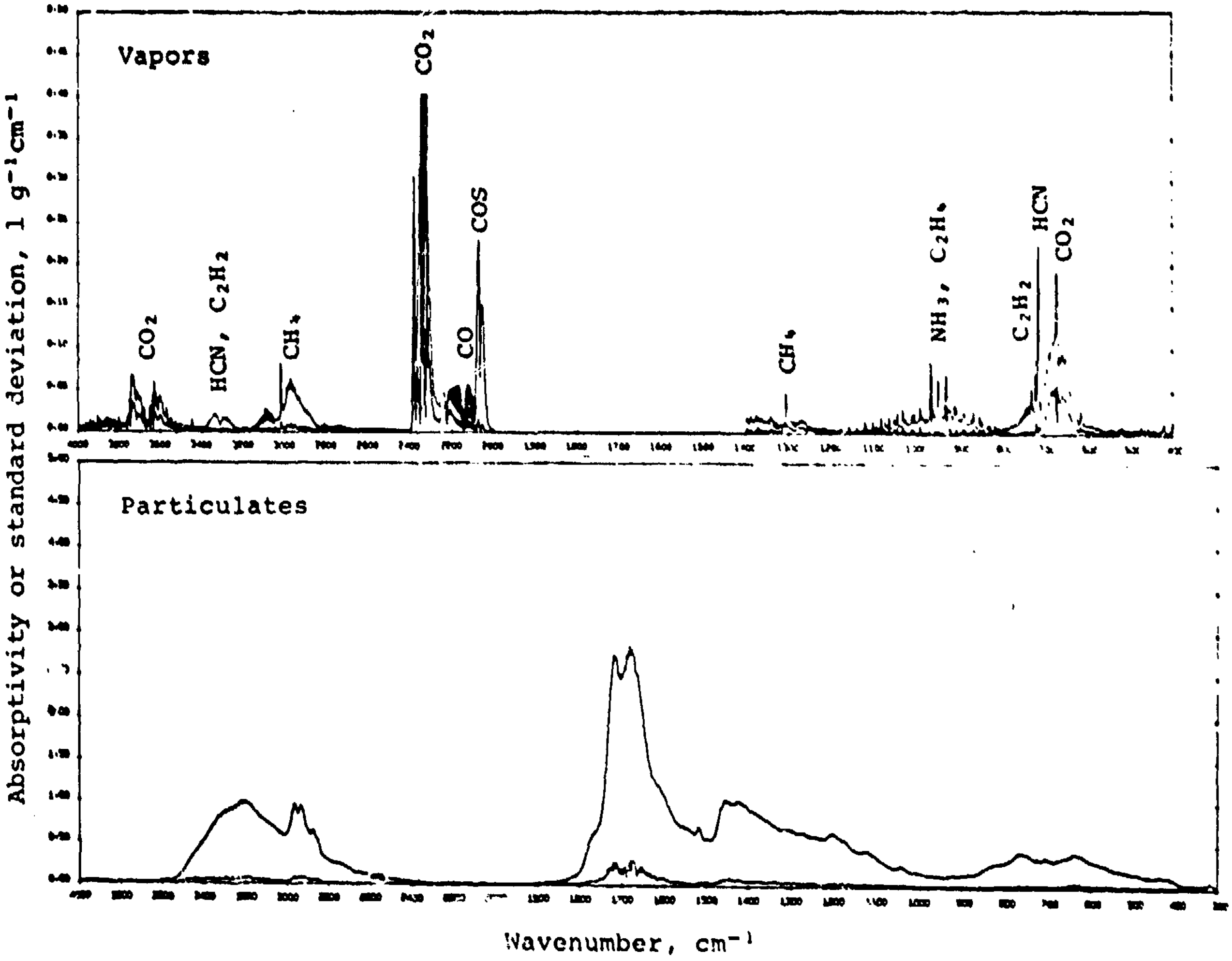

Figure 61. Absorptivity of the Products of Burning Wool Cloth

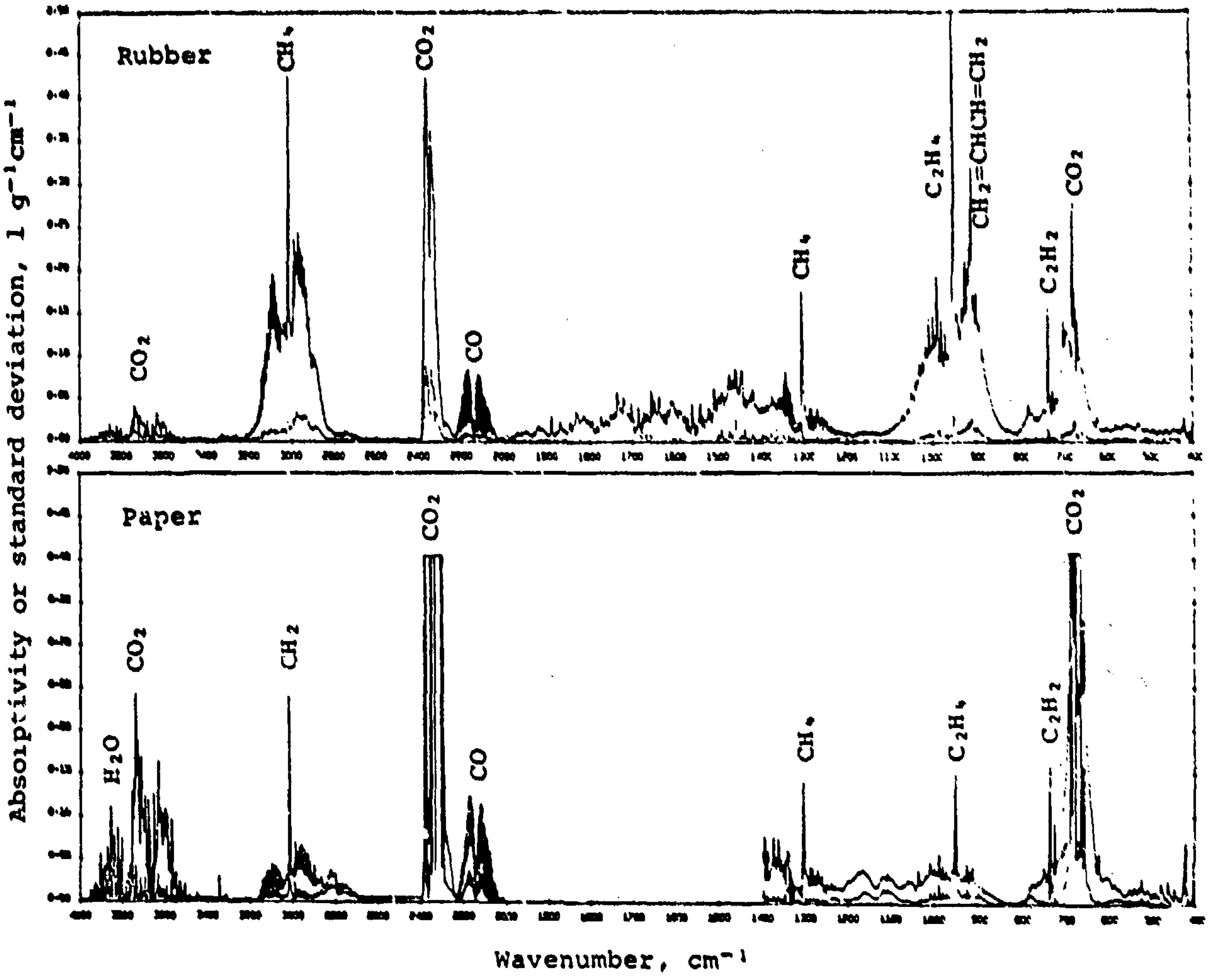

Figure 62. Absorptivity of the Gaseous Products of Burning Rubber and Paper[24]

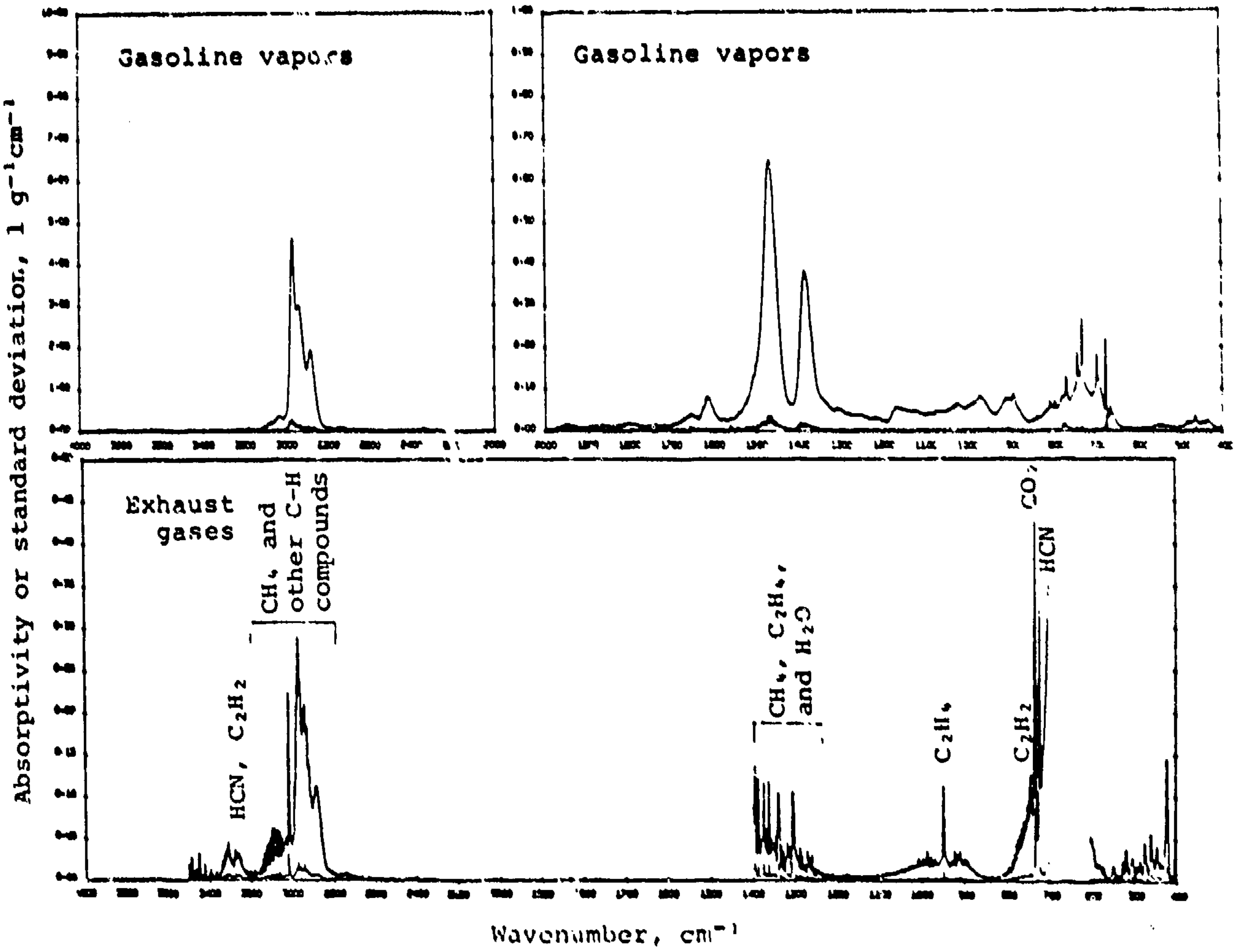

Figure 63. Absorptivities of Gasoline Vapors and Exhaust Gases[24]

particulate absorption between 1800 and 2800 cm^{-1} in the important molecular signature bands. All of the refuse material spectra show strong hydrocarbon and CO bands in contrast to the industrial site spectra. Thus, it seems that the presence of unburned hydrocarbons and particulates might be a good discriminant for refuse fires.

In order to calculate the spectral radiance of these sources it is necessary to obtain estimates of flame temperature and the size of the radiating volume, along with the size and spectral extinction coefficient of the smoke produced by the fire.

Several estimates of fire temperatures are available from USDA Forest Service Measurement Programs. Both Palmer[25] and Hirsch et al [26] report typical temperatures of 1000 K for large free-burning fires.

The size of the radiating flame volume can be determined semi-empirically from measurements by Thomas[27]. The basic relationship between the flame length (L) and the flame width (D) can be related to the material properties of the blaze by the expression:

$$L/D = 42 \left[m'' \left(\rho_o \sqrt{gD} \right)^{-1} \right]^{\eta}$$

where m" = mass fuel comsumption rate per unit area, ρ_o = combustion gas density, and g = acceleration of gravity. The magnitude of the exponent η is a function of burning material. A typical value for η is 0.61. Normally L/D will vary between 2 and 2.5 for kerosene pool fires that are several meters in diameter.

The size of large fire plumes has been studied extensively in the fluid mechanics literature. A useful relationship between the height (H) of the smoke and the rate of heat production (Q) by the fire was derived by Morton et al[28] for a stably stratified atmosphere with a known temperature gradient:

$$H = 31\ (1+m)^{-3/8}\ Q^{1/4},$$

where Q is the rate of heat production of the source in kilowatts and m is the ratio of the vertical gradient of the absolute temperature to the atmospheric lapse rate. Applying this expression to an ICAO standard atmosphere, Morton finds that H varies from 450 meters for a small bonfire to as much as 2200 meters for a burning forest.

The attenuation of the flame radiation by the smoke can be estimated from Mie scattering theory. The primary material in the smoke cloud is partially combusted hydrocarbon and carbon in a wide variety of particle sizes. Palmer[25] indicates that smoke particles from free-burning cellulose fires are generally less than 1 micrometer in radius. The maximum in the number density size distribution occurs around 0.3 micrometer near the bottom of the smoke column. The concentration of smoke particles varies, but a reasonable order of magnitude estimate is 10^5 particles/cm^3.

The exact Lorentz-Mie calculation of the smoke spectral extinction coefficient may often be replaced by approximate analytic solutions. A very useful result is due to Casperson[29] who generalized the anomalous diffraction method Van de Hulst to include absorbing particles. His expression for the exponential extinction coefficient is:

$$\Upsilon(\lambda) = (\pi a^2_{max}\ N_o/n^2)\ \left[2(n+2)(n+1) + \Upsilon_1 - \Upsilon_2 \sin \Upsilon_3 - \Upsilon_4 \cos \Upsilon_5\right]$$

where the $\Upsilon_i(\lambda)$ are given in Appendix F, N_o is the particle number density, a_{max} is the radius at which the particle distribution peaks, and n is the index for a power-law-exponential particle size distribution function. A plausible value for n that is typical of many smoke ensembles is n = 4.6. Casperson[29] gives several specific examples of $\Upsilon(\lambda)$ for absorbing water fogs and for non-absorbing smoke ensembles with an index of refraction equal to 1.5. The calculation of $\Upsilon(\lambda)$ for carbon smoke involves utilizing the optical constants of soot[30] which are quite different from fogs.

SECTION VIII

MUNITION AND SMOKE FALSE THREATS

The muzzle flash of artillery, explosive shell bursts and screening smoke dispersions may also cause false threat events in warning receivers. Table 11 summarizes the available information on these types of events.

A substantial amount of radiometric data and some moderate resolution (32 cm^{-1}) spectrometric data is available on muzzle flash signatures. Typical muzzle flash signatures have a blue and red spike CO_2 signature similar to a rocket exhaust but with an underlying continuum emission attributable to particulates in the plume. Typical duration of the flash is 5 to 100 milliseconds. Because of classification, none of the measurement results are included here; however, they are available in the Pardes and Robertson references.[31,32]

No shell burst data has been located for the spectral region considered in the present study. Radiometric measurements in the visible and near-IR indicate that shell bursts intensities are somewhat less than muzzle flashes of the related weapon and have pulse widths of from 1 to 5 milliseconds.

Screening smokes may be widely used in future ground engagements. Hexachloroethane (HC) and white phosphorous (WP) are generally disseminated by artillery fire and produce smoke through burning. Thus, the initial smoke temperatures are fairly high. As the smoke cloud diffuses in the wind, it is quickly cooled by mixing with the air and within 20 to 100 feet of the wind, it has cooled to within a few degrees of ambient. Sulphur trioxide (FS) and Fog Oil smoke are generally disseminated by a spray so they typically have lower temperatures than the pyrotechnic smokes. In the visible and near-IR, these smokes screen through aerosol scattering. In the mid-IR region of interest here, scattering and aerosol absorption are comparable effects (see Table 12). Thus, when observed in

TABLE 11
POTENTIAL MUNITION FALSE THREAT SOURCES

Munition Type	H_2O	CO_2	CH_4	CO	HCl	N_2O	Other Gases	Particulates	$T(^oK)$	Typical Duration	References/Comments	Reference Figure
Muzzle Flash	X	X						Carbon	2500	5-100 ms	Pardes,[31] Robertson,[32] LaRocca/[33] 2-15 µm Spectral @ 30 cm^{-1} Resolution, Various Broadband Radiometric Data from Visible to 5 µm Time Histories	-
Shell Bursts									2500	1-5 msec	Pardes/Very Little Information Available	-
Sulfur Trioxide (FS)								~.8 µm mmd Scattering Attenuation .3-1.0 m^2/g	350-293	Minutes	Smith,[34] Milhan,[35] Carlon/[36] Spectral Measurements .4-14 µm	64
Hexochloroethane (HC)		X		X	X		$COCl_2$, C_2Cl_4, C_2Cl_6	~1.0 µm mmd Scattering .4/cm-g Emission 3200-3600 cm^{-1} .4/cm-g	673-293	Minutes	Parrett[24]	65, 68
								~1.4 µm mmd Scattering 0.8-0.3 m^2/g			Milhan[35]	
White Phosphorous (WP) **Red Phosphorous (RP)**								~1.0 µm mmd Scattering .5-.15 m^2/g Absorption .1-.2 m^2/g	460-293	Minutes	Carlon[36]	66
Fog Oil							Various Hydrocarbons	~.4-2.0 µm mmd Scattering .6 m^2/g Absorption .2 m^2/g	400-293	Minutes	Smith,[34] Holst,[37] Carlon,[36] Morgan[38]	67

TABLE 11

POTENTIAL MUNITION FALSE THREAT SOURCES (continued)

Signaling Smokes	H_2O	CO_2	CH_4	CO	HCl	N_2O	Other Gases	Particulates	~T(°K)	Typical Duration	References/Comments	Reference Figure
Green	X	X	X	X			HCN, SO_2, C_2H_2 CS_2, COS	.5-3/g-cm		Minutes	Barrett/Absorptivities of Gases and Particles Sitton[39]/Size Distributions and Visible & 1.06 μm Laser	69
Red	X	X		X			CS_2, COS, SO_2	.5-3/g-cm		Minutes	Barrett/As Above Sitton/As Above	-
Yellow	X	X		X			COS, SO_2, CS_2	.5-3/g-cm		Minutes	Barrett/As Above Sitton/As Above	-
Violet	X	X		X			SO_2, COS, CS_2	.5-3/g-cm		Minutes	Barrett/As Above, Structure in the particulates near 3400 cm^{-1} Sitton/As Above	-

TABLE 12

CALCULATED FS SMOKE ATTENUATION FOR THE NOMINAL SIZE DISTRIBUTION AND 50% ACID DROPLET CONCENTRATION[34]

Laser Wavelength (μm)	Scattering Coefficient (m^2/g)	Absorption Coefficient (m^2/g)	Total Attenuation Coefficient (m^2/g)
0.55	3.526	0.000	3.526
1.06	2.104	0.000	2.104
3.39	0.237	0.216	0.453
3.80	0.187	0.162	0.349
10.60	0.058	0.146	0.204

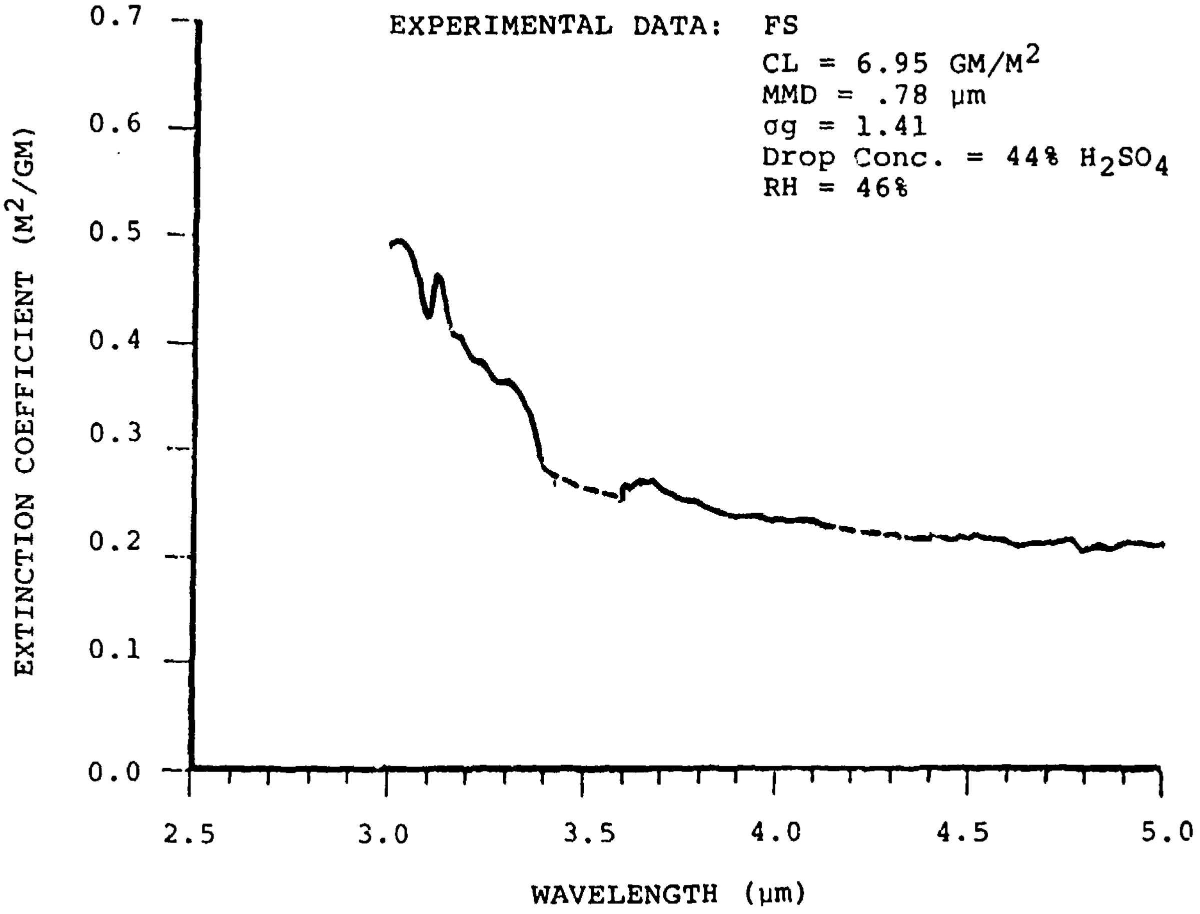

Figure 64. Measured Extinction for FS Smoke[35]

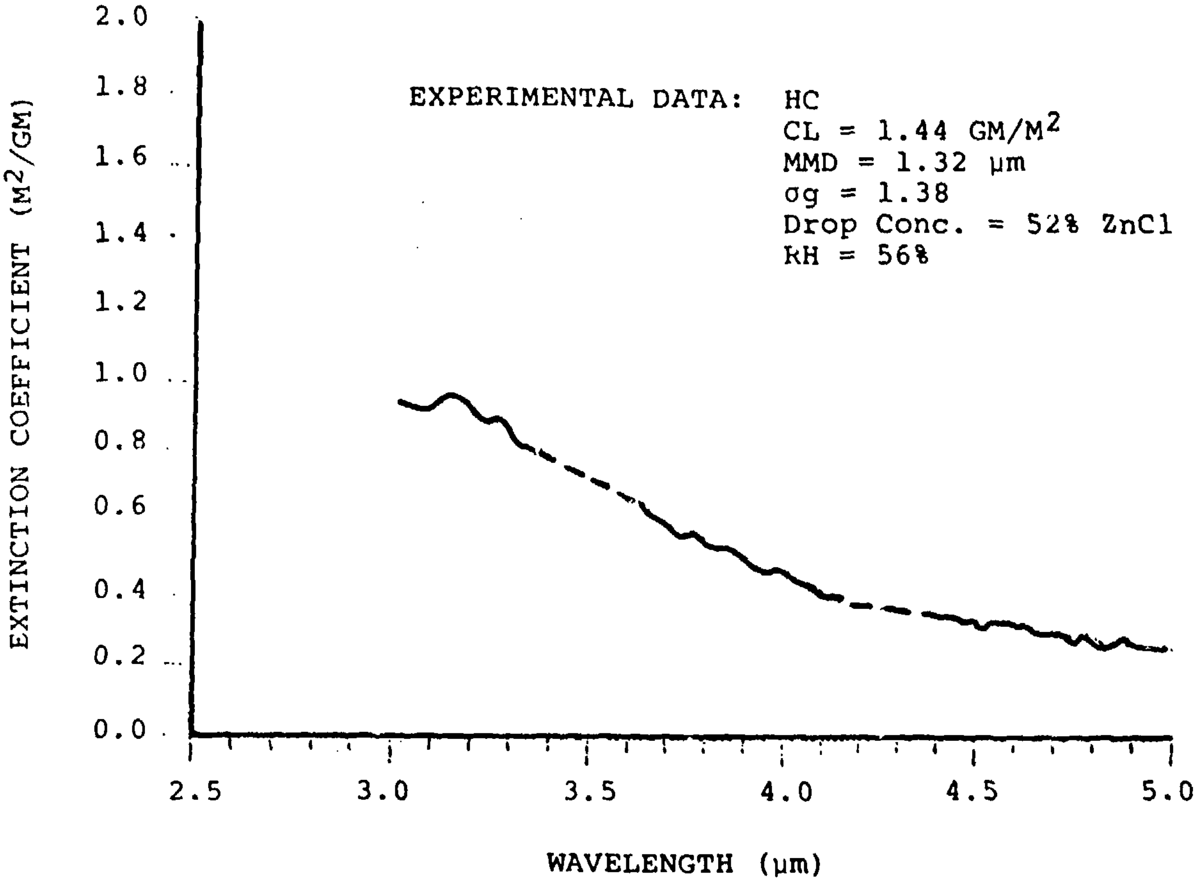

Figure 65. Measured Extinction of HC Smoke[35]

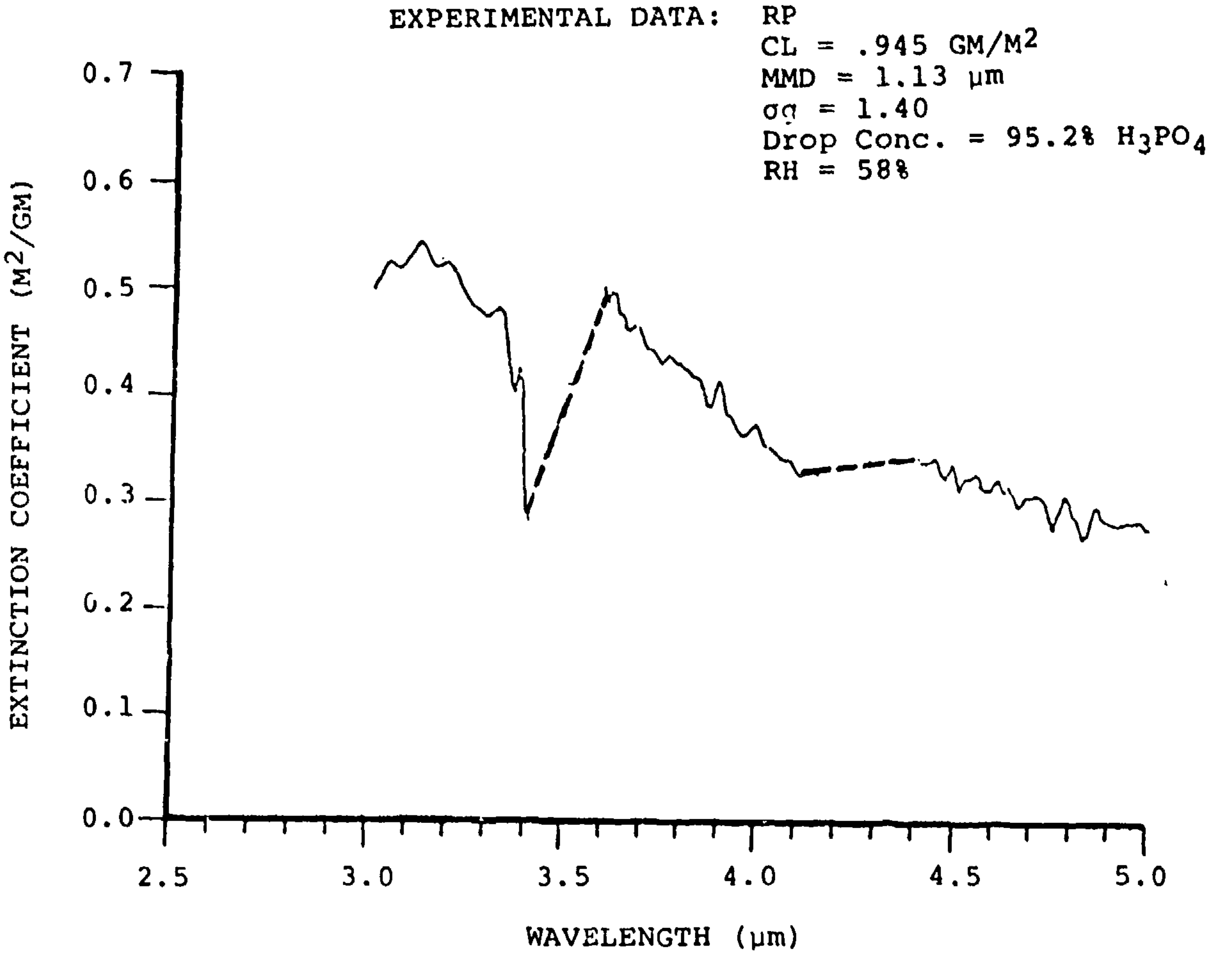

Figure 66. Measured Extinction of WP (RP) Smoke[35]

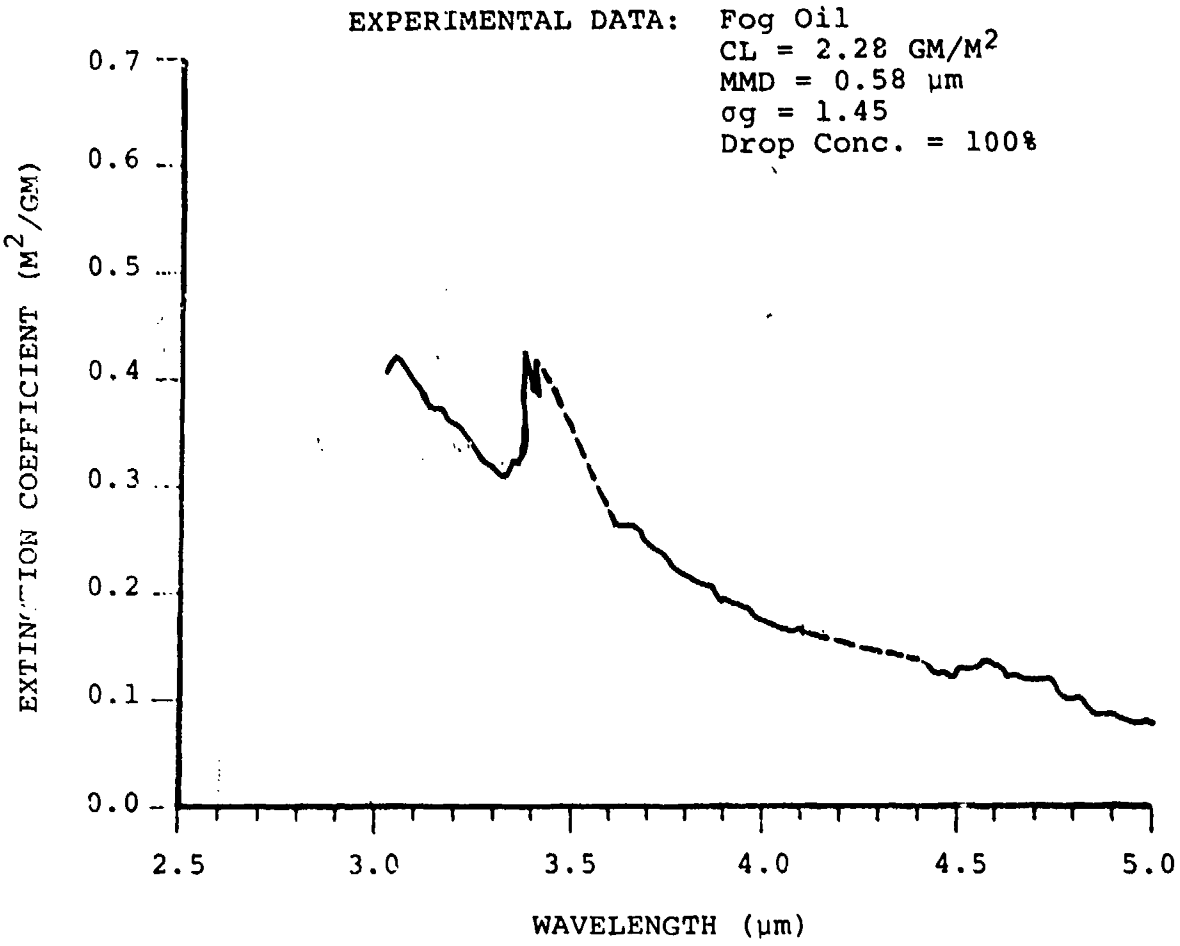

Figure 67. Measured Extinction of Fog Oil Smoke[35]

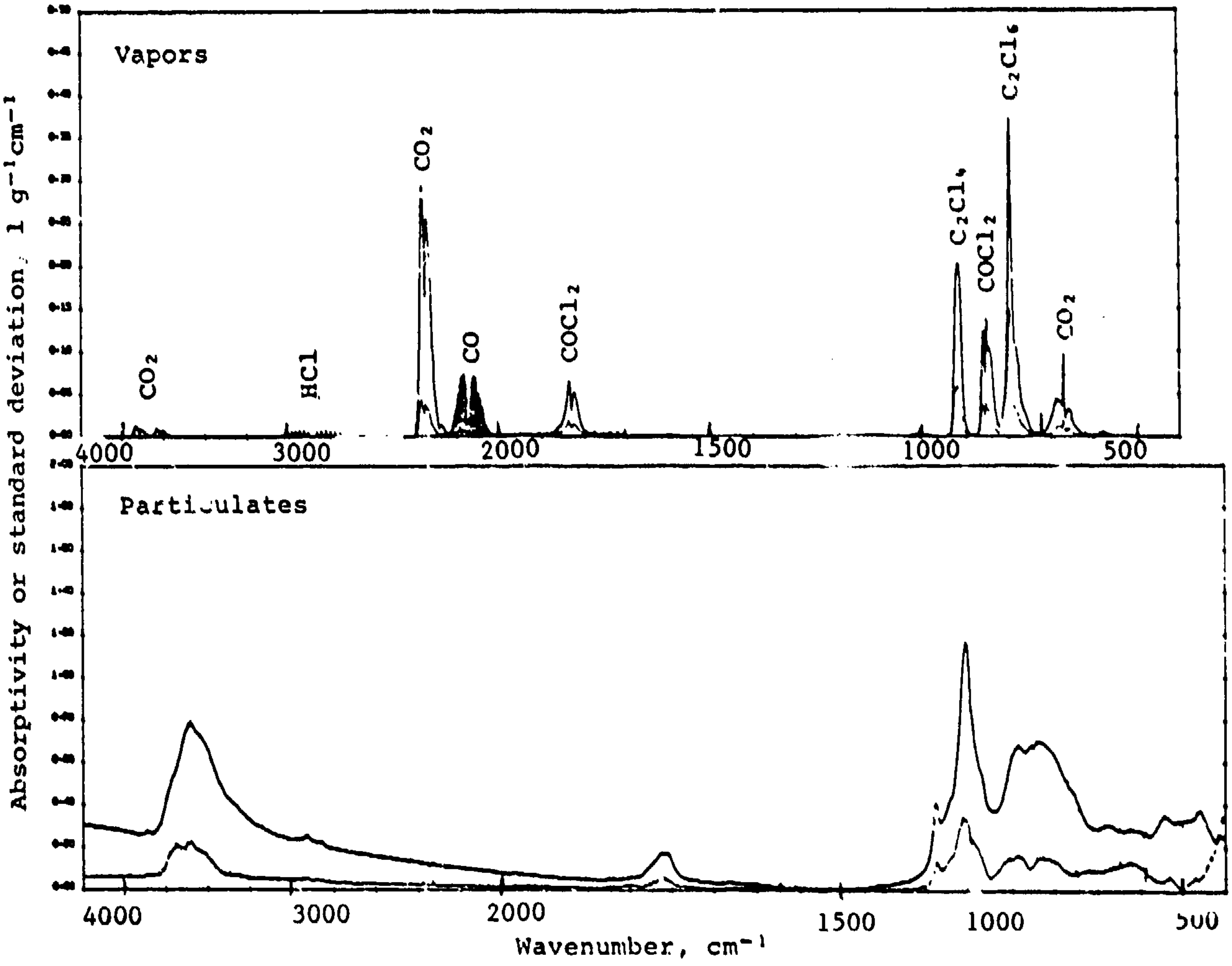

Figure 68. Absorptivities of the Components of HC Screening Smoke[24]

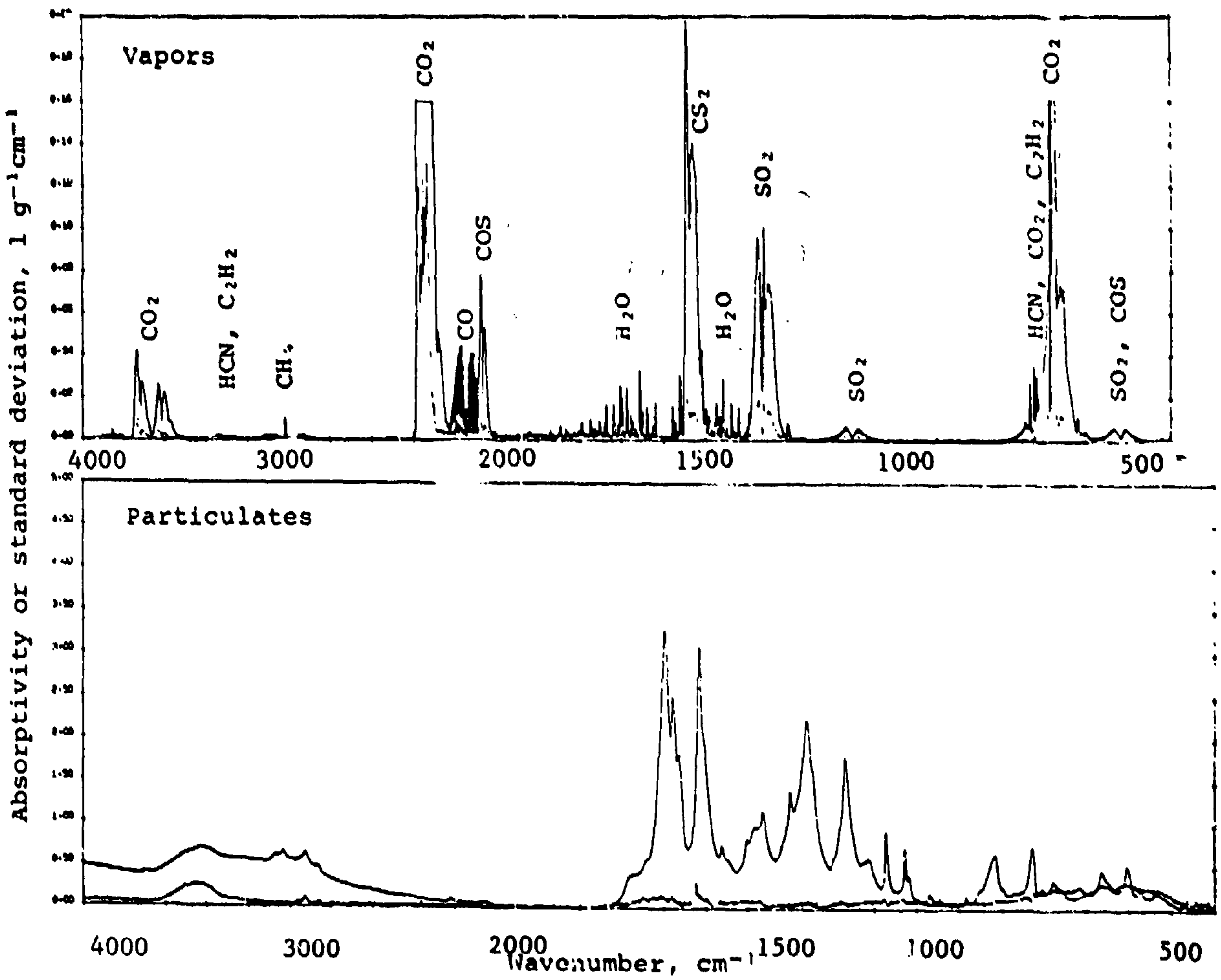

Figure 69. Absorptivities of the Components of Green Signaling Smoke[24]

this region, the screening smokes will appear primarily as continuous emitters at the temperature of the smoke. However, as shown by Figure 68, there is a significant molecular content to the smokes, and thus molecular absorption or emission may be superimposed on the graybody signatures.

Colored signaling smokes are also included in Table 11 and one spectral example is shown in Figure 69. While this type of smoke is not expected to be a large component in the battlefield, the spectra is interesting because it shows the large variety of molecular constituents which can be present in these sources.

APPENDIX A

SCATTERING PARAMETERS FOR CLOUD RADIANCE

These scattering parameters were computed by Eric Shettle of AFGL for log-normal distributions of water and ice spheres (see Section 3). Each of the 10 tables represents a particular type of particle (water or ice) and a particular mean radius for the log-normal distribution. The type and radius (in micrometers) is given by the first line.

The remainder of each table consists of 8 columns, which give the wavelength in micrometers; the real and imaginary indices of refraction; the extinction, scattering and absorption coefficients α_0, β_0, K_0 (each in units of cm^{-1} and representing a number density of 1 per cubic centimeter); the single HJscattering albedo ω_0; and the anisotropy parameter g. Only K_0, ω_0 and g are required by the cloud radiance model described in Section 3. The water and ice indices of refraction were taken from Hale and Querry.[3]

Table A-1

```
WATER      2.

  WAVLGH   REFR-INDICES EXTNC-COEF SCATT-COEF ABSRP-COEF  ALBDO    G
  2.6000   1.242 -.0032 8.3452E-07 7.7851E-07 5.6009E-08  .933   .8721
  2.6500   1.219 -.0067 8.2564E-07 7.2538E-07 1.0026E-07  .879   .8970
  2.7000   1.188 -.0190 7.8885E-07 5.9340E-07 1.9545E-07  .752   .9315
  2.7500   1.157 -.0590 7.0340E-07 3.9906E-07 3.0434E-07  .567   .9575
  2.8000   1.142 -.1150 6.6156E-07 3.1793E-07 3.4363E-07  .481   .9606
  2.8500   1.149 -.1850 6.7170E-07 3.1073E-07 3.6097E-07  .463   .9533
  2.9000   1.201 -.2680 7.0616E-07 3.3340E-07 3.7276E-07  .472   .9393
  2.9500   1.292 -.2980 7.3686E-07 3.5573E-07 3.8113E-07  .483   .9281
  3.0000   1.371 -.2720 7.5845E-07 3.7164E-07 3.8681E-07  .490   .9217
  3.0500   1.426 -.2400 7.7337E-07 3.8345E-07 3.8992E-07  .496   .9158
  3.1000   1.467 -.1920 7.8771E-07 3.9706E-07 3.9065E-07  .504   .9086
  3.1500   1.483 -.1350 8.0196E-07 4.1740E-07 3.8456E-07  .520   .8972
  3.2000   1.478 -.0924 8.1382E-07 4.4591E-07 3.6790E-07  .548   .8809
  3.2500   1.467 -.0610 8.2463E-07 4.8794E-07 3.3669E-07  .592   .8585
  3.3000   1.450 -.0368 8.3517E-07 5.5206E-07 2.8312E-07  .661   .8312
  3.3500   1.432 -.0261 8.4208E-07 6.0195E-07 2.4014E-07  .715   .8173
  3.4000   1.420 -.0195 8.4742E-07 6.4439E-07 2.0303E-07  .760   .8071
  3.4500   1.410 -.0132 8.5267E-07 6.9559E-07 1.5707E-07  .816   .7953
  3.5000   1.400 -.0094 8.5679E-07 7.3501E-07 1.2179E-07  .858   .7890
  3.6000   1.385 -.0052 8.6296E-07 7.8958E-07 7.3376E-08  .915   .7831
  3.7000   1.374 -.0036 3.6654E-07 8.1426E-07 5.2275E-08  .940   .7839
  3.8000   1.364 -.0034 8.6824E-07 8.2006E-07 4.8183E-08  .945   .7894
  3.9000   1.357 -.0038 8.6916E-07 8.1737E-07 5.1788E-08  .940   .7951
  4.0000   1.351 -.0046 8.6903E-07 8.0929E-07 5.9734E-08  .931   .8013
  4.1000   1.346 -.0056 8.6783E-07 7.9861E-07 6.9222E-08  .920   .8073
  4.2000   1.342 -.0069 8.6579E-07 7.8574E-07 8.0048E-08  .908   .8131
  4.3000   1.338 -.0085 8.6294E-07 7.7035E-07 9.2587E-08  .893   .8192
  4.4000   1.334 -.0103 8.5919E-07 7.5315E-07 1.0604E-07  .877   .8254
  4.5000   1.332 -.0134 8.5442E-07 7.2734E-07 1.2708E-07  .851   .8322
  4.6000   1.330 -.0147 8.5096E-07 7.1733E-07 1.3363E-07  .843   .8352
  4.7000   1.330 -.0157 8.4849E-07 7.1047E-07 1.3800E-07  .837   .8364
  4.8000   1.330 -.0150 8.4743E-07 7.1588E-07 1.3155E-07  .845   .8349
  4.9000   1.328 -.0137 8.4557E-07 7.2459E-07 1.2098E-07  .857   .8336
  5.0000   1.325 -.0124 8.4274E-07 7.3258E-07 1.1016E-07  .869   .8331
  5.1000   1.322 -.0111 8.3951E-07 7.4031E-07 9.9199E-08  .882   .8325
  5.2000   1.317 -.0101 8.3400E-07 7.4389E-07 9.0108E-08  .892   .8338
  5.3000   1.312 -.0098 8.2706E-07 7.4095E-07 8.6116E-08  .896   .8363
  5.4000   1.305 -.0103 8.1677E-07 7.2909E-07 8.7683E-08  .893   .8413
  5.5000   1.298 -.0116 8.0465E-07 7.1025E-07 9.4402E-08  .883   .8473
  5.6000   1.289 -.0142 7.8796E-07 6.7985E-07 1.0811E-07  .863   .8558
  5.7000   1.277 -.0203 7.6288E-07 6.2538E-07 1.3750E-07  .820   .8685
  5.8000   1.262 -.0330 7.2692E-07 5.4195E-07 1.8497E-07  .746   .8845
  5.9000   1.248 -.0622 6.8467E-07 4.3026E-07 2.5441E-07  .628   .9002
  6.0000   1.265 -.1070 6.8877E-07 3.7273E-07 3.1604E-07  .541   .9004
-1.0
```

Table A-2

```
WATER      4.

  WAVLGH   REFR-INDICES  EXTNC-COEF  SCATT-COEF  ABSRP-COEF    ALBDO    G
  2.6000   1.242 -.0032 3.0467E-06 2.6605E-06 3.8616E-07   .873   .8780
  2.6500   1.219 -.0067 3.0668E-06 2.4278E-06 6.3902E-07   .792   .9034
  2.7000   1.188 -.0190 3.0677E-06 2.0058E-06 1.0619E-06   .654   .9426
  2.7500   1.157 -.0590 2.9293E-06 1.5672E-06 1.3621E-06   .535   .9716
  2.8000   1.142 -.1150 2.7926E-06 1.3818E-06 1.4109E-06   .495   .9748
  2.8500   1.149 -.1850 2.7746E-06 1.3608E-06 1.4138E-06   .490   .9684
  2.9000   1.201 -.2680 2.8245E-06 1.4137E-06 1.4108E-06   .501   .9558
  2.9500   1.292 -.2980 2.8769E-06 1.4595E-06 1.4174E-06   .507   .9462
  3.0000   1.371 -.2720 2.9132E-06 1.4841E-06 1.4292E-06   .509   .9419
  3.0500   1.426 -.2400 2.9369E-06 1.4999E-06 1.4370E-06   .511   .9387
  3.1000   1.467 -.1920 2.9583E-06 1.5136E-06 1.4447E-06   .512   .9362
  3.1500   1.483 -.1350 2.9786E-06 1.5302E-06 1.4484E-06   .514   .9336
  3.2000   1.478 -.0924 2.9957E-06 1.5587E-06 1.4371E-06   .520   .9282
  3.2500   1.467 -.0610 3.0116E-06 1.6173E-06 1.3943E-06   .537   .9165
  3.3000   1.450 -.0368 3.0282E-06 1.7433E-06 1.2849E-06   .576   .8950
  3.3500   1.432 -.0261 3.0415E-06 1.8708E-06 1.1706E-06   .615   .8783
  3.4000   1.420 -.0155 3.0532E-06 2.0011E-06 1.0522E-06   .655   .8633
  3.4500   1.410 -.0132 3.0668E-06 2.1883E-06 8.7846E-07   .714   .8448
  3.5000   1.400 -.0094 3.0755E-06 2.3528E-06 7.2275E-07   .765   .8316
  3.6000   1.385 -.0052 3.0954E-06 2.6196E-06 4.7584E-07   .846   .8142
  3.7000   1.374 -.0036 3.1140E-06 2.7595E-06 3.5448E-07   .886   .8070
  3.8000   1.364 -.0034 3.1318E-06 2.8013E-06 3.3044E-07   .894   .8092
  3.9000   1.357 -.0038 3.1501E-06 2.7959E-06 3.5423E-07   .888   .8126
  4.0000   1.351 -.0046 3.1666E-06 2.7633E-06 4.0330E-07   .873   .8178
  4.1000   1.346 -.0056 3.1825E-06 2.7218E-06 4.6074E-07   .855   .8234
  4.2000   1.342 -.0069 3.1968E-06 2.6720E-06 5.2483E-07   .836   .8292
  4.3000   1.338 -.0085 3.2090E-06 2.6137E-06 5.9531E-07   .814   .8358
  4.4000   1.334 -.0103 3.2199E-06 2.5522E-06 6.6773E-07   .793   .8429
  4.5000   1.332 -.0134 3.2264E-06 2.4528E-06 7.7359E-07   .760   .8520
  4.6000   1.330 -.0147 3.2356E-06 2.4294E-06 8.0614E-07   .751   .8552
  4.7000   1.330 -.0157 3.2442E-06 2.4164E-06 8.2781E-07   .745   .8567
  4.8000   1.330 -.0150 3.2562E-06 2.4572E-06 7.9903E-07   .755   .8540
  4.9000   1.328 -.0137 3.2701E-06 2.5204E-06 7.4962E-07   .771   .8507
  5.0000   1.325 -.0124 3.2840E-06 2.5871E-06 6.9683E-07   .788   .8480
  5.1000   1.322 -.0111 3.2974E-06 2.6566E-06 6.4083E-07   .806   .8453
  5.2000   1.317 -.0101 3.3105E-06 2.7175E-06 5.9299E-07   .821   .8446
  5.3000   1.312 -.0098 3.3212E-06 2.7490E-06 5.7221E-07   .828   .8461
  5.4000   1.305 -.0103 3.3293E-06 2.7465E-06 5.8276E-07   .825   .8509
  5.5000   1.298 -.0116 3.3331E-06 2.7114E-06 6.2168E-07   .813   .8577
  5.6000   1.289 -.0142 3.3299E-06 2.6328E-06 6.9711E-07   .791   .8681
  5.7000   1.277 -.0203 3.3083E-06 2.4629E-06 8.4544E-07   .744   .8850
  5.8000   1.262 -.0330 3.2504E-06 2.1977E-06 1.0527E-06   .676   .9071
  5.9000   1.248 -.0622 3.1268E-06 1.8374E-06 1.2894E-06   .588   .9297
  6.0000   1.265 -.1070 3.0520E-06 1.6119E-06 1.4402E-06   .528   .9355
-1.0
```

Table A-3

```
WATER      8.

  WAVLGH   REFR-INDICES EXTNC-COEF SCATT-COEF ABSRP-COEF  ALBDO    G
  2.6000   1.242 -.0032 1.1357E-05 8.9470E-06 2.4100E-06  .788  .9072
  2.6500   1.219 -.0067 1.1373E-05 7.7950E-06 3.5785E-06  .685  .9304
  2.7000   1.188 -.0190 1.1408E-05 6.4456E-06 4.9622E-06  .565  .9626
  2.7500   1.157 -.0590 1.1281E-05 5.7621E-06 5.5188E-06  .511  .9814
  2.8000   1.142 -.1150 1.1056E-05 5.5550E-06 5.5011E-06  .502  .9817
  2.8500   1.149 -.1850 1.1001E-05 5.5835E-06 5.4170E-06  .508  .9750
  2.9000   1.201 -.2680 1.1079E-05 5.7481E-06 5.3314E-06  .519  .9627
  2.9500   1.292 -.2980 1.1172E-05 5.8649E-06 5.3071E-06  .525  .9535
  3.0000   1.371 -.2720 1.1235E-05 5.9135E-06 5.3219E-06  .526  .9497
  3=0500   1.426 -.2400 1.1277E-05 5.9446E-06 5.3325E-06  .527  .9471
  3.1000   1.467 -.1920 1.1314E-05 5.9632E-06 5.3503E-06  .527  .9460
  3.1500   1.483 -.1350 1.1346E-05 5.9692E-06 5.3773E-06  .526  .9465
  3.2000   1.478 -.0924 1.1373E-05 5.9778E-06 5.3957E-06  .526  .9472
  3.2500   1.467 -.0610 1.1398E-05 6.0205E-06 5.3775E-06  .528  .9459
  3.3000   1.450 -.0368 1.1422E-05 6.1725E-06 5.2496E-06  .540  .9394
  3.3500   1.432 -.0261 1.1443E-05 6.3861E-06 5.0570E-06  .558  .9314
  3.4000   1.420 -.0195 1.1455E-05 6.6565E-06 4.7990E-06  .581  .9215
  3.4500   1.410 -.0132 1.1483E-05 7.1560E-06 4.3266E-06  .623  .9054
  3.5000   1.400 -.0094 1.1493E-05 7.6867E-06 3.8067E-06  .669  .8911
  3.6000   1.385 -.0052 1.1538E-05 8.7459E-06 2.7921E-06  .758  .8675
  3.7000   1.374 -.0036 1.1576E-05 9.3745E-06 2.2019E-06  .810  .8563
  3.8000   1.364 -.0034 1.1613E-05 9.5271E-06 2.0859E-06  .820  .8550
  3.9000   1.357 -.0038 1.1626E-05 9.4190E-06 2.2070E-06  .810  .8586
  4.0000   1.351 -.0046 1.1631E-05 9.1797E-06 2.4518E-06  .789  .8643
  4.1000   1.346 -.0056 1.1651E-05 8.9166E-06 2.7344E-06  .765  .8698
  4.2000   1.342 -.0069 1.1680E-05 8.6415E-06 3.0383E-06  .740  .8754
  4.3000   1.338 -.0085 1.1710E-05 8.3557E-06 3.3545E-06  .714  .8818
  4.4000   1.334 -.0103 1.1740E-05 8.0831E-06 3.6573E-06  .688  .8885
  4.5000   1.332 -.0134 1.1769E-05 7.7055E-06 4.0630E-06  .655  .8979
  4.6000   1.330 -.0147 1.1797E-05 7.6129E-06 4.1840E-06  .645  .9005
  4.7000   1.330 -.0157 1.1820E-05 7.5600E-06 4.2603E-06  .640  .9018
  4.8000   1.330 -.0150 1.1845E-05 7.6825E-06 4.1622E-06  .649  .8983
  4.9000   1.328 -.0137 1.1874E-05 7.8852E-06 3.9890E-06  .664  .8933
  5.0000   1.325 -.0124 1.1905E-05 8.1102E-06 3.7951E-06  .681  .8884
  5.1000   1.322 -.0111 1.1939E-05 8.3609E-06 3.5784E-06  .700  .8833
  5.2000   1.317 -.0101 1.1976E-05 8.5902E-06 3.3854E-06  .717  .8796
  5.3000   1.312 -.0098 1.2014E-05 8.7109E-06 3.3035E-06  .725  .8786
  5.4000   1.305 -.0103 1.2053E-05 8.6950E-06 3.3577E-06  .721  .8812
  5.5000   1.298 -.0116 1.2092E-05 8.5583E-06 3.5333E-06  .708  .8865
  5.6000   1.289 -.0142 1.2130E-05 8.2781E-06 3.8516E-06  .682  .8958
  5.7000   1.277 -.0203 1.2158E-05 7.7474E-06 4.4104E-06  .637  .9122
  5.8000   1.262 -.0330 1.2145E-05 7.0881E-06 5.0574E-06  .584  .9335
  5.9000   1.248 -.0622 1.2003E-05 6.4062E-06 5.5971E-06  .534  .9538
  6.0000   1.265 -.1070 1.1815E-05 6.0201E-06 5.7953E-06  .510  .9585
-1.0
```

Table A-4

```
WATER      16.

  WAVLGH   REFR-INDICES EXTNC-COEF SCATT-COEF ABSRP-COEF  ALBDO    G
  2.6000   1.242 -.0032 4.3890E-05 3.0324E-05 1.3565E-05  .691   .9381
  2.6500   1.219 -.0067 4.3947E-05 2.6292E-05 1.7655E-05  .598   .9591
  2.7000   1.188 -.0190 4.3943E-05 2.3141E-05 2.0802E-05  .527   .9792
  2.7500   1.157 -.0590 4.3747E-05 2.2269E-05 2.1478E-05  .509   .9863
  2.8000   1.142 -.1150 4.3432E-05 2.2180E-05 2.1252E-05  .511   .9846
  2.8500   1.149 -.1850 4.3356E-05 2.2485E-05 2.0871E-05  .519   .9778
  2.9000   1.201 -.2680 4.3511E-05 2.3055E-05 2.0456E-05  .530   .9655
  2.9500   1.292 -.2980 4.3691E-05 2.3413E-05 2.0278E-05  .536   .9562
  3.0000   1.371 -.2720 4.3815E-05 2.3541E-05 2.0274E-05  .537   .9526
  3.0500   1.426 -.2400 4.3898E-05 2.3626E-05 2.0272E-05  .538   .9501
  3.1000   1.467 -.1920 4.3970E-05 2.3665E-05 2.0305E-05  .538   .9491
  3.1500   1.483 -.1350 4.4034E-05 2.3647E-05 2.0388E-05  .537   .9501
  3.2000   1.478 -.0924 4.4087E-05 2.3606E-05 2.0481E-05  .535   .9519
  3.2500   1.467 -.0610 4.4136E-05 2.3587E-05 2.0549E-05  .534   .9535
  3.3000   1.450 -.0368 4.4184E-05 2.3660E-05 2.0524E-05  .535   .9541
  3.3500   1.432 -.0261 4.4220E-05 2.3850E-05 2.0371E-05  .539   .9533
  3.4000   1.420 -.0195 4.4252E-05 2.4214E-05 2.0038E-05  .547   .9506
  3.4500   1.410 -.0132 4.4289E-05 2.5108E-05 1.9181E-05  .567   .9430
  3.5000   1.400 -.0094 4.4327E-05 2.6343E-05 1.7985E-05  .594   .9334
  3.6000   1.385 -.0052 4.4397E-05 2.9560E-05 1.4837E-05  .666   .9127
  3.7000   1.374 -.0036 4.4491E-05 3.1973E-05 1.2518E-05  .719   .8994
  3.8000   1.364 -.0034 4.4524E-05 3.2518E-05 1.2006E-05  .730   .8986
  3.9000   1.357 -.0038 4.4594E-05 3.2037E-05 1.2557E-05  .718   .9016
  4.0000   1.351 -.0046 4.4580E-05 3.0978E-05 1.3602E-05  .695   .9090
  4.1000   1.346 -.0056 4.4674E-05 2.9959E-05 1.4715E-05  .671   .9147
  4.2000   1.342 -.0069 4.4679E-05 2.8886E-05 1.5793E-05  .647   .9217
  4.3000   1.338 -.0085 4.4784E-05 2.7948E-05 1.6836E-05  .624   .9280
  4.4000   1.334 -.0103 4.4786E-05 2.7043E-05 1.7743E-05  .604   .9343
  4.5000   1.332 -.0134 4.4857E-05 2.6026E-05 1.8831E-05  .580   .9418
  4.6000   1.330 -.0147 4.4896E-05 2.5749E-05 1.9147E-05  .574   .9437
  4.7000   1.330 -.0157 4.4930E-05 2.5604E-05 1.9326E-05  .570   .9449
  4.8000   1.330 -.0150 4.5016E-05 2.5886E-05 1.9130E-05  .575   .9422
  4.9000   1.328 -.0137 4.5016E-05 2.6329E-05 1.8697E-05  .585   .9390
  5.0000   1.325 -.0124 4.5133E-05 2.6927E-05 1.8206E-05  .597   .9347
  5.1000   1.322 -.0111 4.5125E-05 2.7546E-05 1.7579E-05  .610   .9305
  5.2000   1.317 -.0101 4.5250E-05 2.8233E-05 1.7017E-05  .624   .9266
  5.3000   1.312 -.0098 4.5244E-05 2.8483E-05 1.6762E-05  .630   .9252
  5.4000   1.305 -.0103 4.5364E-05 2.8396E-05 1.6968E-05  .626   .9269
  5.5000   1.298 -.0116 4.5360E-05 2.7828E-05 1.7532E-05  .613   .9310
  5.6000   1.289 -.0142 4.5476E-05 2.6969E-05 1.8506E-05  .593   .9378
  5.7000   1.277 -.0203 4.5475E-05 2.5531E-05 1.9945E-05  .561   .9495
  5.8000   1.262 -.0330 4.5511E-05 2.4197E-05 2.1315E-05  .532   .9619
  5.9000   1.248 -.0622 4.5375E-05 2.3285E-05 2.2090E-05  .513   .9710
  6.0000   1.265 -.1070 4.5145E-05 2.3039E-05 2.2106E-05  .510   .9703
-1.0
```

Table A-5

```
WATER      32.

  WAVLGH    REFR-INDICES EXTNC-COEF  SCATT-COEF  ABSRP-COEF   ALBDO    G
  2.6000    1.242 -.0032 1.7059E-04 1.0342E-04 6.7173E-05   .606  .9606
  2.6500    1.219 -.0067 1.7067E-04 9.3449E-05 7.7218E-05   .548  .9757
  2.7000    1.188 -.0190 1.7065E-04 8.8546E-05 8.2104E-05   .519  .9851
  2.7500    1.157 -.0590 1.7026E-04 8.7516E-05 8.2748E-05   .514  .9878
  2.8000    1.142 -.1150 1.6975E-04 8.7754E-05 8.2000E-05   .517  .9857
  2.8500    1.149 -.1850 1.6967E-04 8.9062E-05 8.0607E-05   .525  .9789
  2.9000    1.201 -.2680 1.7000E-04 9.1066E-05 7.8929E-05   .536  .9665
  2.9500    1.292 -.2980 1.7036E-04 9.2269E-05 7.8092E-05   .542  .9573
  3.0000    1.371 -.2720 1.7061E-04 9.2661E-05 7.7953E-05   .543  .9536
  3.0500    1.426 -.2400 1.7079E-04 9.2924E-05 7.7865E-05   .544  .9511
  3.1000    1.467 -.1920 1.7094E-04 9.3023E-05 7.7917E-05   .544  .9501
  3.1500    1.483 -.1350 1.7107E-04 9.2907E-05 7.8166E-05   .543  .9512
  3.2000    1.478 -.0924 1.7118E-04 9.2699E-05 7.8485E-05   .542  .9532
  3.2500    1.467 -.0610 1.7129E-04 9.2506E-05 7.8781E-05   .540  .9552
  3.3000    1.450 -.0368 1.7139E-04 9.2326E-05 7.9062E-05   .539  .9573
  3.3500    1.432 -.0261 1.7147E-04 9.2253E-05 7.9218E-05   .538  .9590
  3.4000    1.420 -.0195 1.7155E-04 9.2446E-05 7.9105E-05   .539  .9595
  3.4500    1.410 -.0132 1.7163E-04 9.3374E-05 7.8257E-05   .544  .9581
  3.5000    1.400 -.0094 1.7171E-04 9.5149E-05 7.6557E-05   .554  .9549
  3.6000    1.385 -.0052 1.7183E-04 1.0189E-04 6.9940E-05   .593  .9429
  3.7000    1.374 -.0036 1.7201E-04 1.0872E-04 6.3288E-05   .632  .9325
  3.8000    1.364 -.0034 1.7208E-04 1.1041E-04 6.1669E-05   .642  .9313
  3.9000    1.357 -.0038 1.7225E-04 1.0873E-04 6.3515E-05   .631  .9347
  4.0000    1.351 -.0046 1.7236E-04 1.0559E-04 6.6772E-05   .613  .9406
  4.1000    1.346 -.0056 1.7248E-04 1.0259E-04 6.9890E-05   .595  .9461
  4.2000    1.342 -.0069 1.7259E-04 9.9978E-05 7.2608E-05   .579  .9512
  4.3000    1.338 -.0085 1.7272E-04 9.7706E-05 7.5017E-05   .566  .9556
  4.4000    1.334 -.0103 1.7281E-04 9.5923E-05 7.6891E-05   .555  .9594
  4.5000    1.332 -.0134 1.7294E-04 9.4075E-05 7.8861E-05   .544  .9632
  4.6000    1.330 -.0147 1.7303E-04 9.3640E-05 7.9393E-05   .541  .9643
  4.7000    1.330 -.0157 1.7315E-04 9.3431E-05 7.9718E-05   .540  .9647
  4.8000    1.330 -.0150 1.7328E-04 9.3844E-05 7.9434E-05   .542  .9638
  4.9000    1.328 -.0137 1.7338E-04 9.4575E-05 7.8807E-05   .545  .9624
  5.0000    1.325 -.0124 1.7352E-04 9.5540E-05 7.7980E-05   .551  .9607
  5.1000    1.322 -.0111 1.7365E-04 9.6769E-05 7.6881E-05   .557  .9585
  5.2000    1.317 -.0101 1.7375E-04 9.8013E-05 7.5734E-05   .564  .9567
  5.3000    1.312 -.0098 1.7390E-04 9.8631E-05 7.5266E-05   .567  .9560
  5.4000    1.305 -.0103 1.7400E-04 9.8208E-05 7.5788E-05   .564  .9574
  5.5000    1.298 -.0116 1.7411E-04 9.7045E-05 7.7069E-05   .557  .9602
  5.6000    1.289 -.0142 1.7422E-04 9.5177E-05 7.9042E-05   .546  .9643
  5.7000    1.277 -.0203 1.7428E-04 9.2715E-05 8.1563E-05   .532  .9701
  5.8000    1.262 -.0330 1.7428E-04 9.0846E-05 8.3435E-05   .521  .9750
  5.9000    1.248 -.0622 1.7405E-04 8.9905E-05 8.4145E-05   .517  .9774
  6.0000    1.265 -.1070 1.7376E-04 9.0206E-05 8.3554E-05   .519  .9743
-1.0
```

Table A-6

```
ICE        2.

  WAVLGH    REFR-INDICES EXTNC-COEF SCATT-COEF ABSRP-COEF  ALBDO    G
  2.5000    1.225 -.0040 8.2926E-07 7.5983E-07 6.9435E-08  .916   .8865
  2.5640    1.212 -.0040 8.2669E-07 7.5966E-07 6.7033E-08  .919   .8960
  2.6320    1.192 -.0050 8.1513E-07 7.3784E-07 7.7298E-08  .905   .9123
  2.7030    1.162 -.0080 7.7792E-07 6.7179E-07 1.0613E-07  .864   .9358
  2.7780    1.108 -.0200 6.2884E-07 4.4804E-07 1.8080E-07  .712   .9667
  2.8170    1.065 -.0380 4.6772E-07 2.3303E-07 2.3469E-07  .498   .9776
  2.8250    1.056 -.0440 4.4553E-07 1.9937E-07 2.4616E-07  .447   .9784
  2.8330    1.046 -.0520 4.3211E-07 1.7354E-07 2.5857E-07  .402   .9785
  2.8410    1.037 -.0690 4.2951E-07 1.6120E-07 2.6831E-07  .375   .9781
  2.8490    1.027 -.0680 4.3130E-07 1.5577E-07 2.7553E-07  .361   .9773
  2.8570    1.016 -.0790 4.4451E-07 1.6068E-07 2.8383E-07  .361   .9757
  2.8740     .995 -.1100 4.9389E-07 1.9336E-07 3.0053E-07  .391   .9698
  2.8900     .979 -.1460 5.4006E-07 2.2751E-07 3.1255E-07  .421   .9623
  2.9070     .960 -.1930 5.8215E-07 2.6106E-07 3.2109E-07  .448   .9522
  2.9240     .967 -.2570 6.2277E-07 2.8939E-07 3.3338E-07  .465   .9412
  2.9330     .978 -.2760 6.3334E-07 2.9565E-07 3.3769E-07  .467   .9386
  2.9410     .987 -.2950 6.4301E-07 3.0197E-07 3.4104E-07  .470   .9358
  2.9590    1.004 -.3310 6.5943E-07 3.1320E-07 3.4623E-07  .475   .9302
  2.9760    1.021 -.3670 6.7375E-07 3.2354E-07 3.5021E-07  .480   .9244
  2.9940    1.035 -.4110 6.8787E-07 3.3502E-07 3.5285E-07  .487   .9169
  3.0120    1.064 -.4660 7.0436E-07 3.4805E-07 3.5631E-07  .494   .9080
  3.0300    1.104 -.5220 7.1975E-07 3.6018E-07 3.5957E-07  .500   .8991
  3.0490    1.170 -.5840 7.3635E-07 3.7296E-07 3.6339E-07  .507   .8894
  3.0580    1.217 -.6120 7.4456E-07 3.7897E-07 3.6559E-07  .509   .8849
  3.0670    1.273 -.6270 7.5162E-07 3.8338E-07 3.6824E-07  .510   .8821
  3.0770    1.330 -.6250 7.5701E-07 3.8592E-07 3.7109E-07  .510   .8812
  3.0860    1.384 -.6140 7.6147E-07 3.8778E-07 3.7362E-07  .509   .8809
  3.0960    1.432 -.5930 7.6502E-07 3.8883E-07 3.7619E-07  .508   .8815
  3.1060    1.469 -.5640 7.6760E-07 3.8904E-07 3.7857E-07  .507   .8831
  3.1150    1.499 -.5390 7.6995E-07 3.8954E-07 3.8042E-07  .506   .8840
  3.1250    1.527 -.5150 7.7236E-07 3.9030E-07 3.8206E-07  .505   .8845
  3.1350    1.553 -.4910 7.7476E-07 3.9121E-07 3.8355E-07  .505   .8848
  3.1450    1.578 -.4650 7.7724E-07 3.9223E-07 3.8500E-07  .505   .8850
  3.1550    1.603 -.4380 7.7986E-07 3.9350E-07 3.8636E-07  .505   .8850
  3.1650    1.623 -.4060 7.8243E-07 3.9460E-07 3.8783E-07  .504   .8853
  3.1750    1.640 -.3720 7.8510E-07 3.9586E-07 3.8924E-07  .504   .8855
  3.1850    1.650 -.3360 7.8775E-07 3.9712E-07 3.9063E-07  .504   .8860
  3.2050    1.653 -.2670 7.9311E-07 4.0043E-07 3.9269E-07  .505   .8865
  3.2260    1.641 -.2100 7.9848E-07 4.0556E-07 3.9292E-07  .508   .8852
  3.2790    1.593 -.1210 8.1097E-07 4.2891E-07 3.8216E-07  .529   .8725
  3.3300    1.545 -.0740 8.2238E-07 4.6852E-07 3.5386E-07  .570   .8509
  3.3900    1.511 -.0410 8.3413E-07 5.3788E-07 2.9624E-07  .645   .8173
  3.4480    1.476 -.0240 8.4392E-07 6.1375E-07 2.3017E-07  .727   .7942
  3.5090    1.449 -.0150 8.5157E-07 6.7953E-07 1.7204E-07  .798   .7814
  3.5710    1.428 -.0090 8.5794E-07 7.3981E-07 1.1814E-07  .862   .7728
  3.6360    1.410 -.0080 8.6152E-07 7.5591E-07 1.0561E-07  .877   .7783
  3.7040    1.398 -.0070 8.6459E-07 7.7132E-07 9.3270E-08  .892   .7811
  3.8460    1.376 -.0070 8.6750E-07 7.7815E-07 8.9348E-08  .897   .7931
  4.0000    1.361 -.0100 8.6597E-07 7.5239E-07 1.1358E-07  .869   .8094
  4.1670    1.348 -.0120 8.6278E-07 7.3748E-07 1.2530E-07  .855   .8210
  4.2550    1.343 -.0150 8.5869E-07 7.1420E-07 1.4450E-07  .832   .8295
  4.3480    1.337 -.0200 8.5168E-07 6.7945E-07 1.7223E-07  .798   .8409
  4.3860    1.337 -.0230 8.4873E-07 6.6162E-07 1.8711E-07  .780   .8450
  4.4440    1.338 -.0260 8.4605E-07 6.4598E-07 2.0006E-07  .764   .8481
  4.5050    1.340 -.0290 8.4379E-07 6.3202E-07 2.1176E-07  .749   .8504
  4.5450    1.344 -.0300 8.4437E-07 6.2899E-07 2.1538E-07  .745   .8492
  4.6080    1.347 -.0250 8.4939E-07 6.5678E-07 1.9261E-07  .773   .8408
  4.6510    1.347 -.0210 8.5249E-07 6.8079E-07 1.7169E-07  .799   .8349
  4.7662    1.341 -.0150 8.5378E-07 7.2037E-07 1.3341E-07  .844   .8284
  5.0000    1.327 -.0120 8.4444E-07 7.3685E-07 1.0760E-07  .873   .8311
  5.2630    1.312 -.0140 8.2396E-07 7.0912E-07 1.1484E-07  .861   .8427
  5.5560    1.296 -.0240 7.8817E-07 6.2807E-07 1.6010E-07  .797   .8620
  5.7140    1.287 -.0350 7.6196E-07 5.6410E-07 1.9786E-07  .740   .8741
  5.7470    1.285 -.0380 7.5580E-07 5.4933E-07 2.0647E-07  .727   .8767
  5.7800    1.284 -.0420 7.5019E-07 5.3272E-07 2.1747E-07  .710   .8791
  5.8140    1.283 -.0460 7.4469E-07 5.1726E-07 2.2743E-07  .695   .8813
  5.8480    1.283 -.0520 7.3928E-07 4.9788E-07 2.4140E-07  .673   .8837
  5.8820    1.285 -.0570 7.3719E-07 4.8514E-07 2.5205E-07  .658   .8845
  6.0610    1.301 -.0690 7.4179E-07 4.6759E-07 2.7420E-07  .630   .8808
-1.0
```

Table A-7

```
ICE        4.

  WAVLGH   REFR-INDICES EXTNC-COEF SCATT-COEF ABSRP-COEF  ALBDO    G
  2.5000   1.225 -.0040 3.0433E-06 2.5754E-06 4.6789E-07  .846   .8914
  2.5640   1.212 -.0040 3.0640E-06 2.6086E-06 4.5533E-07  .851   .8980
  2.6320   1.192 -.0050 3.0961E-06 2.5768E-06 5.1928E-07  .832   .9124
  2.7030   1.162 -.0080 3.1206E-06 2.4418E-06 6.7873E-07  .782   .9376
  2.7780   1.108 -.0200 2.9771E-06 1.9667E-06 1.0105E-06  .661   .9742
  2.8170   1.065 -.0380 2.4870E-06 1.3124E-06 1.1746E-06  .528   .9868
  2.8250   1.056 -.0440 2.3707E-06 1.1693E-06 1.2015E-06  .493   .9878
  2.8330   1.046 -.0520 2.2741E-06 1.0466E-06 1.2274E-06  .460   .9882
  2.8410   1.037 -.0600 2.2259E-06 9.8082E-07 1.2451E-06  .441   .9881
  2.8490   1.027 -.0680 2.2024E-06 9.4743E-07 1.2550E-06  .430   .9877
  2.8570   1.016 -.0790 2.2230E-06 9.5760E-07 1.2654E-06  .431   .9865
  2.8740    .995 -.1100 2.3490E-06 1.0656E-06 1.2834E-06  .454   .9817
  2.8900    .979 -.1460 2.4631E-06 1.1703E-06 1.2927E-06  .475   .9754
  2.9070    .960 -.1930 2.5585E-06 1.2661E-06 1.2923E-06  .495   .9664
  2.9240    .967 -.2570 2.6459E-06 1.3403E-06 1.3057E-06  .507   .9566
  2.9330    .978 -.2760 2.6685E-06 1.3554E-06 1.3131E-06  .508   .9543
  2.9410    .987 -.2950 2.6988E-06 1.3710E-06 1.3178E-06  .510   .9517
  2.9590   1.004 -.3310 2.7228E-06 1.3990E-06 1.3238E-06  .514   .9466
  2.9760   1.021 -.3670 2.7518E-06 1.4251E-06 1.3268E-06  .518   .9413
  2.9940   1.035 -.4110 2.7799E-06 1.4552E-06 1.3246E-06  .523   .9342
  3.0120   1.064 -.4660 2.8125E-06 1.4887E-06 1.3237E-06  .529   .9256
  3.0300   1.104 -.5220 2.8427E-06 1.5196E-06 1.3231E-06  .535   .9170
  3.0490   1.170 -.5840 2.8752E-06 1.5512E-06 1.3240E-06  .539   .9076
  3.0580   1.217 -.6120 2.8911E-06 1.5651E-06 1.3260E-06  .541   .9032
  3.0670   1.273 -.6270 2.9046E-06 1.5736E-06 1.3310E-06  .542   .9006
  3.0770   1.330 -.6250 2.9147E-06 1.5763E-06 1.3384E-06  .541   .8999
  3.0860   1.384 -.6140 2.9227E-06 1.5770E-06 1.3456E-06  .540   .8999
  3.0960   1.432 -.5930 2.9287E-06 1.5754E-06 1.3533E-06  .538   .9008
  3.1060   1.469 -.5640 2.9328E-06 1.5714E-06 1.3614E-06  .536   .9026
  3.1150   1.499 -.5390 2.9364E-06 1.5690E-06 1.3674E-06  .534   .9038
  3.1250   1.527 -.5150 2.9401E-06 1.5675E-06 1.3726E-06  .533   .9046
  3.1350   1.553 -.4910 2.9437E-06 1.5665E-06 1.3772E-06  .532   .9053
  3.1450   1.578 -.4650 2.9474E-06 1.5657E-06 1.3817E-06  .531   .9059
  3.1550   1.603 -.4380 2.9511E-06 1.5654E-06 1.3857E-06  .530   .9064
  3.1650   1.623 -.4060 2.9546E-06 1.5640E-06 1.3906E-06  .529   .9074
  3.1750   1.640 -.3720 2.9581E-06 1.5625E-06 1.3956E-06  .528   .9084
  3.1850   1.650 -.3360 2.9614E-06 1.5602E-06 1.4012E-06  .527   .9099
  3.2050   1.653 -.2670 2.9680E-06 1.5552E-06 1.4128E-06  .524   .9134
  3.2260   1.641 -.2100 2.9748E-06 1.5517E-06 1.4231E-06  .522   .9166
  3.2790   1.593 -.1210 2.9914E-06 1.5581E-06 1.4332E-06  .521   .9192
  3.3330   1.545 -.0740 3.0079E-06 1.5980E-06 1.4099E-06  .531   .9128
  3.3900   1.511 -.0410 3.0255E-06 1.7192E-06 1.3064E-06  .568   .8903
  3.4480   1.476 -.0240 3.0431E-06 1.9102E-06 1.1328E-06  .628   .8637
  3.5090   1.449 -.0150 3.0584E-06 2.1269E-06 9.3148E-07  .695   .8413
  3.5710   1.428 -.0090 3.0721E-06 2.3720E-06 7.0018E-07  .772   .8211
  3.6360   1.410 -.0080 3.0894E-06 2.4458E-06 6.4358E-07  .792   .8193
  3.7040   1.398 -.0070 3.1062E-06 2.5232E-06 5.8303E-07  .812   .8163
  3.8460   1.376 -.0070 3.1300E-06 2.5642E-06 5.6582E-07  .819   .8218
  4.0000   1.361 -.0100 3.1573E-06 2.4609E-06 6.9638E-07  .779   .8360
  4.1670   1.348 -.0120 3.1812E-06 2.4236E-06 7.5761E-07  .762   .8454
  4.2550   1.343 -.0150 3.1898E-06 2.3411E-06 8.4871E-07  .734   .8548
  4.3480   1.337 -.0200 3.1963E-06 2.2259E-06 9.7038E-07  .696   .8680
  4.3860   1.337 -.0230 3.1959E-06 2.1657E-06 1.0302E-06  .678   .8737
  4.4440   1.338 -.0260 3.1971E-06 2.1171E-06 1.0800E-06  .662   .8782
  4.5050   1.340 -.0290 3.1978E-06 2.0750E-06 1.1228E-06  .649   .8819
  4.5450   1.344 -.0300 3.1991E-06 2.0637E-06 1.1354E-06  .645   .8816
  4.6080   1.347 -.0250 3.2123E-06 2.1593E-06 1.0530E-06  .672   .8711
  4.6510   1.347 -.0210 3.2228E-06 2.2521E-06 9.7077E-07  .699   .8625
  4.7662   1.341 -.0150 3.2475E-06 2.4425E-06 8.0510E-07  .752   .8495
  5.0000   1.327 -.0120 3.2840E-06 2.6008E-06 6.8328E-07  .792   .8459
  5.2630   1.312 -.0140 3.3066E-06 2.5815E-06 7.2503E-07  .781   .8569
  5.5560   1.296 -.0240 3.2981E-06 2.3545E-06 9.4366E-07  .714   .8819
  5.7140   1.287 -.0350 3.2669E-06 2.1675E-06 1.0994E-06  .663   .8988
  5.7470   1.285 -.0380 3.2571E-06 2.1254E-06 1.1317E-06  .653   .9024
  5.7800   1.284 -.0420 3.2448E-06 2.0737E-06 1.1712E-06  .639   .9062
  5.8140   1.283 -.0460 3.2326E-06 2.0272E-06 1.2054E-06  .627   .9095
  5.8480   1.283 -.0520 3.2156E-06 1.9649E-06 1.2507E-06  .611   .9134
  5.8820   1.285 -.0570 3.2045E-06 1.9211E-06 1.2834E-06  .600   .9155
  6.0610   1.301 -.0690 3.1961E-06 1.8485E-06 1.3476E-06  .578   .9155
-1.0
```

Table A-8

```
ICE        8.

 WAVLGH  REFR-INDICES EXTNC-COEF SCATT-COEF ABSRP-COEF  ALBDO    G
 2.5000  1.225 -.0040 1.1330E-05 8.5100E-06 2.8201E-06  .751  .9182
 2.5640  1.212 -.0040 1.1374E-05 6.5996E-06 2.7746E-06  .756  .9210
 2.6320  1.192 -.0050 1.1422E-05 8.3377E-06 3.0844E-06  .730  .9307
 2.7030  1.162 -.0080 1.1505E-05 7.7204E-06 3.7851E-06  .671  .9492
 2.7780  1.108 -.0200 1.1595E-05 6.7033E-06 4.8916E-06  .578  .9801
 2.8170  1.065 -.0380 1.0904E-05 5.6834E-06 5.2209E-06  .521  .9913
 2.8250  1.056 -.0440 1.0600E-05 5.3492E-06 5.2507E-06  .505  .9922
 2.8320  1.046 -.0520 1.0286E-05 5.0165E-06 5.2696E-06  .488  .9927
 2.8410  1.037 -.0600 1.0089E-05 4.8159E-06 5.2728E-06  .477  .9926
 2.8490  1.027 -.0680 9.9662E-06 4.7061E-06 5.2600E-06  .472  .9922
 2.8570  1.016 -.0790 9.9622E-06 4.7196E-06 5.2425E-06  .474  .9912
 2.8740   .995 -.1100 1.0191E-05 4.9912E-06 5.1997E-06  .490  .9869
 2.8900   .979 -.1460 1.0406E-05 5.2509E-06 5.1551E-06  .505  .9811
 2.9070   .960 -.1930 1.0581E-05 5.4936E-06 5.0877E-06  .519  .9726
 2.9240   .967 -.2570 1.0747E-05 5.6790E-06 5.0678E-06  .528  .9632
 2.9330   .978 -.2760 1.0791E-05 5.7143E-06 5.0762E-06  .530  .9610
 2.9410   .987 -.2950 1.0829E-05 5.7528E-06 5.0766E-06  .531  .9586
 2.9590  1.004 -.3310 1.0894E-05 5.8239E-06 5.0702E-06  .535  .9536
 2.9760  1.021 -.3670 1.0949E-05 5.8926E-06 5.0568E-06  .538  .9483
 2.9940  1.035 -.4110 1.1003E-05 5.9777E-06 5.0250E-06  .543  .9413
 3.0120  1.064 -.4660 1.1065E-05 6.0716E-06 4.9936E-06  .549  .9328
 3.0300  1.104 -.5220 1.1124E-05 6.1589E-06 4.9648E-06  .554  .9242
 3.0490  1.170 -.5840 1.1187E-05 6.2472E-06 4.9399E-06  .558  .9148
 3.0580  1.217 -.6120 1.1218E-05 6.2845E-06 4.9337E-06  .560  .9104
 3.0670  1.273 -.6270 1.1245E-05 6.3037E-06 4.9409E-06  .561  .9077
 3.0770  1.330 -.6250 1.1264E-05 6.3035E-06 4.9604E-06  .560  .9070
 3.0860  1.384 -.6140 1.1279E-05 6.2975E-06 4.9812E-06  .558  .9071
 3.0960  1.432 -.5930 1.1290E-05 6.2841E-06 5.0054E-06  .557  .9080
 3.1060  1.469 -.5640 1.1296E-05 6.2638E-06 5.0324E-06  .555  .9099
 3.1150  1.499 -.5390 1.1302E-05 6.2498E-06 5.0522E-06  .553  .9112
 3.1250  1.527 -.5150 1.1308E-05 6.2395E-06 5.0687E-06  .552  .9121
 3.1350  1.553 -.4910 1.1314E-05 6.2312E-06 5.0829E-06  .551  .9129
 3.1450  1.578 -.4650 1.1320E-05 6.2233E-06 5.0966E-06  .550  .9136
 3.1550  1.603 -.4380 1.1326E-05 6.2174E-06 5.1084E-06  .549  .9141
 3.1650  1.623 -.4060 1.1331E-05 6.2074E-06 5.1236E-06  .548  .9152
 3.1750  1.640 -.3720 1.1336E-05 6.1969E-06 5.1392E-06  .547  .9164
 3.1850  1.650 -.3360 1.1341E-05 6.1831E-06 5.1575E-06  .545  .9181
 3.2050  1.653 -.2670 1.1349E-05 6.1521E-06 5.1972E-06  .542  .9222
 3.2260  1.641 -.2100 1.1359E-05 6.1224E-06 5.2362E-06  .539  .9264
 3.2790  1.593 -.1210 1.1382E-05 6.0712E-06 5.3113E-06  .533  .9343
 3.3330  1.545 -.0740 1.1406E-05 6.0624E-06 5.3439E-06  .531  .9384
 3.3900  1.511 -.0410 1.1433E-05 6.1828E-06 5.2497E-06  .541  .9342
 3.4480  1.476 -.0240 1.1459E-05 6.5017E-06 4.9572E-06  .567  .9220
 3.5090  1.449 -.0150 1.1485E-05 7.0193E-06 4.4652E-06  .611  .9047
 3.5710  1.428 -.0090 1.1500E-05 7.7899E-06 3.7104E-06  .677  .8832
 3.6360  1.410 -.0080 1.1510E-05 8.0095E-06 3.5009E-06  .696  .8796
 3.7040  1.398 -.0070 1.1524E-05 8.2676E-0  3.2566E-06  .717  .8742
 3.8460  1.376 -.0070 1.1602E-05 8.3971E-06 3.2050E-06  .724  .8757
 4.0000  1.361 -.0100 1.1614E-05 7.9791E-06 3.7345E-06  .678  .8896
 4.1670  1.348 -.0120 1.1677E-05 7.6932E-06 3.9835E-06  .659  .8962
 4.2550  1.343 -.0150 1.1700E-05 7.3963E-06 4.3032E-06  .632  .9049
 4.3480  1.337 -.0200 1.1717E-05 7.0330E-06 4.6838E-06  .600  .9164
 4.3860  1.337 -.0230 1.1721E-05 6.8689E-06 4.8524E-06  .586  .9215
 4.4440  1.338 -.0260 1.1729E-05 6.7465E-06 4.9823E-06  .575  .9253
 4.5050  1.340 -.0290 1.1739E-05 6.6485E-06 5.0900E-06  .566  .9284
 4.5450  1.344 -.0300 1.1743E-05 6.6246E-06 5.1183E-06  .564  .9285
 4.6080  1.347 -.0250 1.1763E-05 6.8487E-06 4.9147E-06  .582  .9200
 4.6510  1.347 -.0210 1.1782E-05 7.0889E-06 4.6927E-06  .602  .9120
 4.7662  1.341 -.0150 1.1826E-05 7.6494E-06 4.1772E-06  .647  .8966
 5.0000  1.327 -.0120 1.1903E-05 8.1623E-06 3.7407E-06  .686  .8866
 5.2630  1.312 -.0140 1.1997E-05 8.0675E-06 3.9292E-06  .672  .8928
 5.5560  1.296 -.0240 1.2070E-05 7.3673E-06 4.7025E-06  .610  .9154
 5.7140  1.287 -.0350 1.2081E-05 6.9294E-06 5.1527E-06  .573  .9306
 5.7470  1.285 -.0380 1.2079E-05 6.8430E-06 5.2360E-06  .567  .9337
 5.7800  1.284 -.0420 1.2071E-05 6.7398E-06 5.3308E-06  .558  .9371
 5.8140  1.283 -.0460 1.2062E-05 6.6529E-06 5.4089E-06  .552  .9400
 5.8480  1.283 -.0520 1.2043E-05 6.5389E-06 5.5038E-06  .543  .9434
 5.8820  1.285 -.0570 1.2027E-05 6.4607E-06 5.5664E-06  .537  .9454
 6.0610  1.301 -.0690 1.2011E-05 6.3340E-06 5.6771E-06  .527  .9464
-1.0
```

Table A-9

```
ICE        16.

 WAVLGH    REFR-INDICES EXTNC-COEF SCATT-COEF ABSRP-COEF   ALBDO     G
 2.5000    1.225 -.0040 4.3834E-05 2.8673E-05 1.5161E-05   .654   .9484
 2.5640    1.212 -.0040 4.3913E-05 2.8882E-05 1.5031E-05   .658   .9494
 2.6320    1.192 -.0050 4.3942E-05 2.7792E-05 1.6150E-05   .632   .9571
 2.7030    1.162 -.0080 4.4033E-05 2.5656E-05 1.8376E-05   .583   .9698
 2.7780    1.108 -.0200 4.4153E-05 2.3152E-05 2.1001E-05   .524   .9876
 2.8170    1.065 -.0380 4.3533E-05 2.2093E-05 2.1440E-05   .507   .9940
 2.8250    1.056 -.0440 4.3063E-05 2.1650E-05 2.1414E-05   .503   .9946
 2.8330    1.046 -.0520 4.2470E-05 2.1126E-05 2.1344E-05   .497   .9948
 2.8410    1.037 -.0600 4.2028E-05 2.0775E-05 2.1253E-05   .494   .9947
 2.8490    1.027 -.0680 4.1716E-05 2.0582E-05 2.1134E-05   .493   .9943
 2.8570    1.016 -.0790 4.1625E-05 2.0641E-05 2.0984E-05   .496   .9933
 2.8740     .995 -.1100 4.1941E-05 2.1292E-05 2.0649E-05   .508   .9892
 2.8900     .979 -.1460 4.2292E-05 2.1941E-05 2.0351E-05   .519   .9836
 2.9070     .960 -.1930 4.2593E-05 2.2606E-05 1.9987E-05   .531   .9753
 2.9240     .967 -.2570 4.2900E-05 2.3124E-05 1.9775E-05   .539   .9661
 2.9330     .978 -.2760 4.2984E-05 2.3218E-05 1.9766E-05   .540   .9639
 2.9410     .987 -.2950 4.3058E-05 2.3325E-05 1.9732E-05   .542   .9614
 2.9590    1.004 -.3310 4.3182E-05 2.3532E-05 1.9650E-05   .545   .9565
 2.9760    1.021 -.3670 4.3288E-05 2.3739E-05 1.9549E-05   .548   .9512
 2.9940    1.035 -.4110 4.3392E-05 2.4010E-05 1.9382E-05   .553   .9442
 3.0170    1.064 -.4660 4.3514E-05 2.4309E-05 1.9205E-05   .559   .9356
 3.0390    1.104 -.5220 4.3630E-05 2.4590E-05 1.9040E-05   .564   .9269
 3.0490    1.170 -.5840 4.3757E-05 2.4873E-05 1.8883E-05   .568   .9173
 3.0580    1.217 -.6120 4.3819E-05 2.4991E-05 1.8829E-05   .570   .9129
 3.0670    1.273 -.6270 4.3873E-05 2.5044E-05 1.8829E-05   .571   .9102
 3.0770    1.330 -.6250 4.3911E-05 2.5029E-05 1.8883E-05   .570   .9095
 3.0860    1.384 -.6140 4.3941E-05 2.4995E-05 1.8946E-05   .569   .9096
 3.0960    1.432 -.5930 4.3963E-05 2.4936E-05 1.9027E-05   .567   .9105
 3.1060    1.469 -.5640 4.3975E-05 2.4853E-05 1.9122E-05   .565   .9125
 3.1150    1.499 -.5390 4.3986E-05 2.4795E-05 1.9191E-05   .564   .9138
 3.1250    1.527 -.5150 4.3998E-05 2.4751E-05 1.9247E-05   .563   .9147
 3.1350    1.553 -.4910 4.4009E-05 2.4714E-05 1.9295E-05   .562   .9155
 3.1450    1.578 -.4650 4.4020E-05 2.4679E-05 1.9341E-05   .561   .9163
 3.1550    1.603 -.4380 4.4031E-05 2.4651E-05 1.9379E-05   .560   .9168
 3.1650    1.623 -.4060 4.4040E-05 2.4608E-05 1.9432E-05   .559   .9180
 3.1750    1.640 -.3720 4.4048E-05 2.4563E-05 1.9485E-05   .558   .9192
 3.1850    1.650 -.3360 4.4055E-05 2.4506E-05 1.9549E-05   .556   .9209
 3.2050    1.653 -.2670 4.4069E-05 2.4379E-05 1.9690E-05   .553   .9251
 3.2260    1.641 -.2100 4.4084E-05 2.4255E-05 1.9829E-05   .550   .9294
 3.2790    1.593 -.1210 4.4126E-05 2.4015E-05 2.0111E-05   .544   .9381
 3.3330    1.545 -.0740 4.4171E-05 2.3851E-05 2.0319E-05   .540   .9445
 3.3900    1.511 -.0410 4.4221E-05 2.3841E-05 2.0380E-05   .539   .9474
 3.4480    1.476 -.0240 4.4264E-05 2.4115E-05 2.0149E-05   .545   .9469
 3.5090    1.449 -.0150 4.4315E-05 2.4912E-05 1.9403E-05   .562   .9410
 3.5710    1.428 -.0090 4.4357E-05 2.5657E-05 1.7700E-05   .601   .9272
 3.6360    1.410 -.0080 4.4368E-05 2.7243E-05 1.7125E-05   .614   .9250
 3.7040    1.398 -.0070 4.4464E-05 2.8045E-05 1.6419E-05   .631   .9203
 3.8460    1.376 -.0070 4.4520E-05 2.8244E-05 1.6277E-05   .634   .9219
 4.0000    1.361 -.0100 4.4571E-05 2.6676E-05 1.7894E-05   .599   .9347
 4.1670    1.348 -.0120 4.4672E-05 2.6100E-05 1.8571E-05   .584   .9400
 4.2550    1.343 -.0150 4.4710E-05 2.5361E-05 1.9349E-05   .567   .9464
 4.3480    1.337 -.0200 4.4763E-05 2.4585E-05 2.0178E-05   .549   .9531
 4.3860    1.337 -.0230 4.4762E-05 2.4280E-05 2.0482E-05   .542   .9558
 4.4440    1.338 -.0260 4.4775E-05 2.4075E-05 2.0700E-05   .538   .9576
 4.5050    1.340 -.0290 4.4807E-05 2.3933E-05 2.0873E-05   .534   .9588
 4.5450    1.344 -.0300 4.4828E-05 2.3913E-05 2.0915E-05   .533   .9586
 4.6080    1.347 -.0250 4.4873E-05 2.4269E-05 2.0603E-05   .541   .9548
 4.6510    1.347 -.0210 4.4892E-05 2.4687E-05 2.0205E-05   .550   .9508
 4.7662    1.341 -.0150 4.4978E-05 2.5863E-05 1.9114E-05   .575   .9414
 5.0000    1.327 -.0120 4.5132E-05 2.7084E-05 1.8047E-05   .600   .9333
 5.2630    1.312 -.0140 4.5253E-05 2.6634E-05 1.8619E-05   .589   .9375
 5.5560    1.296 -.0240 4.5364E-05 2.4872E-05 2.0492E-05   .548   .9528
 5.7140    1.287 -.0350 4.5410E-05 2.4051E-05 2.1359E-05   .530   .9607
 5.7470    1.285 -.0380 4.5416E-05 2.3917E-05 2.1499E-05   .527   .9622
 5.7800    1.284 -.0420 4.5417E-05 2.3771E-05 2.1645E-05   .523   .9636
 5.8140    1.283 -.0460 4.5416E-05 2.3656E-05 2.1759E-05   .521   .9648
 5.8480    1.283 -.0520 4.5400E-05 2.3522E-05 2.1878E-05   .518   .9660
 5.8820    1.285 -.0570 4.5388E-05 2.3445E-05 2.1943E-05   .517   .9666
 6.0610    1.301 -.0690 4.5405E-05 2.3382E-05 2.2025E-05   .515   .9657
-1.0
```

Table A-10

```
ICE       32.

  WAVLGH   REFR-INDICES EXTNC-COEF  SCATT-COEF  ABSRP-COEF   ALBDO    G
  2.5000   1.225 -.0040 1.7046E-04  9.8810E-05  7.1653E-05   .580   .9684
  2.5640   1.212 -.0040 1.7059E-04  9.9205E-05  7.1388E-05   .582   .9695
  2.6320   1.192 -.0050 1.7066E-04  9.6356E-05  7.4302E-05   .565   .9750
  2.7030   1.162 -.0080 1.7078E-04  9.1642E-05  7.9134E-05   .537   .9832
  2.7790   1.108 -.0200 1.7073E-04  8.7162E-05  8.3571E-05   .511   .9921
  2.8170   1.065 -.0380 1.6979E-04  8.5576E-05  8.4214E-05   .504   .9954
  2.8250   1.056 -.0440 1.6916E-04  8.5100E-05  8.4060E-05   .503   .9957
  2.8330   1.046 -.0520 1.6828E-04  8.4530E-05  8.3755E-05   .502   .9958
  2.8410   1.037 -.0600 1.6756E-04  8.4172E-05  8.3385E-05   .502   .9956
  2.8490   1.027 -.0680 1.6699E-04  8.4050E-05  8.2941E-05   .503   .9952
  2.8570   1.016 -.0790 1.6675E-04  8.4404E-05  8.2346E-05   .506   .9942
  2.8740    .995 -.1100 1.6715E-04  8.6219E-05  8.0930E-05   .516   .9903
  2.8900    .979 -.1460 1.6772E-04  8.8093E-05  7.9630E-05   .525   .9847
  2.9070    .960 -.1930 1.6826E-04  9.0173E-05  7.8088E-05   .536   .9765
  2.9240    .967 -.2570 1.6884E-04  9.1814E-05  7.7030E-05   .544   .9672
  2.9330    .978 -.2760 1.6901E-04  9.2098E-05  7.6910E-05   .545   .9650
  2.9410    .987 -.2950 1.6915E-04  9.2441E-05  7.6711E-05   .546   .9626
  2.9590   1.004 -.3310 1.6940E-04  9.3116E-05  7.6280E-05   .550   .9576
  2.9760   1.021 -.3670 1.6961E-04  9.3809E-05  7.5798E-05   .553   .9523
  2.9940   1.035 -.4110 1.6981E-04  9.4745E-05  7.5068E-05   .558   .9452
  3.0120   1.064 -.4660 1.7006E-04  9.5783E-05  7.4274E-05   .563   .9366
  3.0300   1.104 -.5220 1.7029E-04  9.6764E-05  7.3525E-05   .568   .9278
  3.0490   1.170 -.5840 1.7055E-04  9.7761E-05  7.2786E-05   .573   .9181
  3.0580   1.217 -.6120 1.7068E-04  9.8171E-05  7.2504E-05   .575   .9136
  3.0670   1.273 -.6270 1.7078E-04  9.8343E-05  7.2441E-05   .576   .9109
  3.0770   1.330 -.6250 1.7087E-04  9.8268E-05  7.2597E-05   .575   .9102
  3.0860   1.384 -.6140 1.7093E-04  9.8125E-05  7.2802E-05   .574   .9102
  3.0960   1.432 -.5930 1.7097E-04  9.7891E-05  7.3081E-05   .573   .9112
  3.1060   1.469 -.5640 1.7100E-04  9.7571E-05  7.3428E-05   .571   .9132
  3.1150   1.499 -.5390 1.7102E-04  9.7345E-05  7.3677E-05   .569   .9145
  3.1250   1.527 -.5150 1.7105E-04  9.7171E-05  7.3876E-05   .568   .9155
  3.1350   1.553 -.4910 1.7107E-04  9.7025E-05  7.4045E-05   .567   .9163
  3.1450   1.578 -.4650 1.7109E-04  9.6886E-05  7.4207E-05   .566   .9171
  3.1550   1.603 -.4380 1.7112E-04  9.6773E-05  7.4342E-05   .566   .9176
  3.1650   1.623 -.4060 1.7113E-04  9.6602E-05  7.4531E-05   .564   .9188
  3.1750   1.640 -.3720 1.7115E-04  9.6425E-05  7.4725E-05   .563   .9200
  3.1850   1.650 -.3360 1.7116E-04  9.6200E-05  7.4962E-05   .562   .9218
  3.2050   1.653 -.2670 1.7119E-04  9.5702E-05  7.5485E-05   .559   .9261
  3.2260   1.641 -.2100 1.7121E-04  9.5218E-05  7.5996E-05   .556   .9304
  3.2790   1.593 -.1210 1.7130E-04  9.4269E-05  7.7029E-05   .550   .9393
  3.3330   1.545 -.0740 1.7139E-04  9.3567E-05  7.7822E-05   .546   .9459
  3.3900   1.511 -.0410 1.7149E-04  9.3146E-05  7.8348E-05   .543   .9502
  3.4480   1.476 -.0240 1.7159E-04  9.2955E-05  7.8638E-05   .542   .9537
  3.5090   1.449 -.0150 1.7169E-04  9.3496E-05  7.8192E-05   .545   .9545
  3.5710   1.428 -.0090 1.7178E-04  9.5931E-05  7.5851E-05   .558   .9505
  3.6360   1.410 -.0080 1.7189E-04  9.6925E-05  7.4963E-05   .564   .9501
  3.7040   1.398 -.0070 1.7196E-04  9.8386E-05  7.3574E-05   .572   .9482
  3.8460   1.376 -.0070 1.7217E-04  9.8739E-05  7.3429E-05   .574   .9499
  4.0000   1.361 -.0100 1.7232E-04  9.5467E-05  7.6856E-05   .554   .9578
  4.1670   1.348 -.0120 1.7254E-04  9.4362E-05  7.8178E-05   .547   .9613
  4.2550   1.343 -.0150 1.7263E-04  9.3175E-05  7.9453E-05   .540   .9642
  4.3480   1.337 -.0200 1.7271E-04  9.2115E-05  8.0598E-05   .533   .9670
  4.3860   1.337 -.0230 1.7275E-04  9.1791E-05  8.0954E-05   .531   .9678
  4.4440   1.338 -.0260 1.7280E-04  9.1607E-05  8.1193E-05   .530   .9681
  4.5050   1.340 -.0290 1.7286E-04  9.1503E-05  8.1354E-05   .529   .9682
  4.5450   1.344 -.0300 1.7290E-04  9.1536E-05  8.1362E-05   .529   .9678
  4.6080   1.347 -.0250 1.7299E-04  9.1915E-05  8.1075E-05   .531   .9667
  4.6510   1.347 -.0210 1.7305E-04  9.2384E-05  8.0671E-05   .534   .9656
  4.7662   1.341 -.0150 1.7323E-04  9.3919E-05  7.9313E-05   .542   .9627
  5.0000   1.327 -.0120 1.7352E-04  9.5847E-05  7.7670E-05   .552   .9590
  5.2630   1.312 -.0140 1.7382E-04  9.4917E-05  7.8910E-05   .546   .9630
  5.5560   1.296 -.0240 1.7409E-04  9.2078E-05  8.2011E-05   .529   .9700
  5.7140   1.287 -.0350 1.7416E-04  9.1059E-05  8.3101E-05   .523   .9728
  5.7470   1.285 -.0380 1.7417E-04  9.0911E-05  8.3262E-05   .522   .9733
  5.7800   1.284 -.0420 1.7418E-04  9.0774E-05  8.3401E-05   .521   .9736
  5.8140   1.283 -.0460 1.7418E-04  9.0672E-05  8.3504E-05   .521   .9738
  5.8480   1.283 -.0520 1.7416E-04  9.0580E-05  8.3578E-05   .520   .9739
  5.8820   1.285 -.0570 1.7415E-04  9.0565E-05  8.3585E-05   .520   .9737
  6.0610   1.301 -.0690 1.7426E-04  9.0796E-05  8.3459E-05   .521   .9719
-1.0
```

APPENDIX B

RADIOSONDE DATA/LOWTRAN INPUTS

This appendix gives meteorological profiles used in computing LOWTRAN transmittances and radiances for the model validations. Tables B-1 through B-3 correspond to AFGL missions that provided cloud radiance data (see Section 3). Tables B-4 and B-5 correspond to missions that observed specular sunglints from lakes and ponds (see Section 4). The remaining tables correspond to missions that observed industrial sites (see Section 6).

Tables B-1 through B-5 are listings of the input cards to the modified LOWTRAN 4 code (the listings include additional cards that identify columns and fields, as well as a header card). The pressure, temperature and dew point profiles are based on radiosonde data provided by AFGL.

Tables B-6 through B-9 give the raw radiosonde data provided by AFGL for mission 815 and 816.

Table B-1   INPUTS TO MODIFIED LOWTRAN 4 FOR MISSION 726

```
MISSION 726
123456789012345678901234567890123456789012345678901234567890123456789
 7  2  2          1         2 21  1
0.          12.6        8.88
 ALT        PRES        TEMP        DEW PT
(KM)        (MB)        (C)          (C)
0.          1004.       18.4        13.4
0.13        1000.       17.2        12.5
.40         972.        14.2        12.3
.76         929.        12.4        11.
.9          914.        12.6        6.9
1.3         873.        15.6        -14.4
1.5         850.        15.         -15.
2.52        753.        10.2        -19.8
3.125       700.        9.6         -20.4
4.7         576.        -0.3        -30.3
5.83        500.        -9.5        -39.5
6.46        460.        -14.1       -34.1
6.58        453.        -13.7       -43.7
7.51        400.        -21.        -51.
9.57        300.        -38.        -68.
10.8        250.        -48.        -68.
12.25       200.        -55.        -74.
14.07       150.        -61.        -77.
16.5        100.        -64.        -77.
20.         54.         -64.        -76.
30.         11.         -64.        -72.
123456789012345678901234567890123456789012345678901234567890123456789
1.829       0.9144      95.                                     20.
1800.       3600.       5.
```

Table B-2 INPUTS TO MODIFIED LOWTRAN 4 FOR MISSION 727

```
MISSION 727
123456789012345678901234567890123456789012345678901234567890123456789
  7  2   2         1          2 17   1
0.         -32.        14.25
 ALT       PRES        TEMP      DEW PT
(KM)       (MB)        (C)         (C)
0.         1010.       23.2        0.2
0.6        940.        23.2        0.2
1.34       864.        23.2        0.2
1.45       850.        22.         1.0
3.09       700.        6.0         -6.0
5.75       500.        -11.5       -22.5
6.95       430.        -19.3       -49.3
7.42       400.        -24.0       -40.0
9.01       319.        -37.5       -47.5
9.45       300.        -41.0       -55.
10.66      250.        -51.        -61.
10.95      238.        -54.1       -66.
12.1       200.        -54.3       -70.
13.93      150.        -58.5       -74.
16.47      100.        -61.5       -77.
20.        54.         -62.        -77.
30.        11.         -62.        -72.
123456789012345678901234567890123456789012345678901234567890123456789
6.000      8.40        75.75                               20.
1800.      3600.       5.
```

Table B-3   INPUTS TO MODIFIED LOWTRAN 4 FOR MISSION 817

```
MISSION 817
12345678901234567890123456789012345678901234567890123456789
  7  2  2        1        2 26  1
0.        -49.3     2.6
 ALT      PRES      TEMP     DEW PT
(KM)      (MB)      (C)       (C)
0.        1020.     14.4      10.7
.104      1000.     14.4      10.7
.70       931.      14.4      10.7
1.05      895.      10.4      8.7
1.477     850.      7.8       6.6
2.62      737.      2.6       -0.8
3.059     700.      -0.5      -1.8
3.55      656.      -4.3      -5.6
3.98      622.      -5.7      -17.7
4.48      584.      -8.5      -17.5
4.91      552.      -12.1     -14.7
5.3       526.      -13.9     -18.9
5.67      500.      -16.7     -20.8
6.13      469.      -20.5     -26.5
7.06      430.      -25.5     -32.5
7.31      400.      -29.5     -39.5
7.52      388.      -31.1     -40.
8.54      334.      -39.7     -46.
9.29      300.      -45.5     -56.
10.25     259.      -53.3     -62.
10.48     250.      -50.9     -63.
10.71     241.      -48.9     -64.
11.95     200.      -47.3     -69.
13.19     167.      -46.3     -72.
13.85     150.      -48.1     -73.
16.5      100.      -52.5     -77.
12345678901234567890123456789012345678901234567890123456789
10.058    9.754     92.5                          20.
1800.     3600.     5.
```

Table B-4   INPUTS TO MODIFIED LOWTRAN 4 FOR MISSION 729

```
MISSION 729
12345678901234567890123456789012345678901234567890123456789
  7  2  2        1        2 19
0.        3.5        7.34
 ALT      PRES      TEMP     DEW PT
(KM)      (MB)      (C)       (C)
0.        1011.     23.3      6.4
0.099     1000.     21.8      11.8
0.5       949.      20.2      1.2
1.4       857.      13.6      -5.4
1.54      842.      15.0      -15.0
2.2       780.      11.2      -18.8
2.47      755.      11.8      -18.2
3.11      700.      7.8       -22.2
5.78      500.      -12.      -52.2
6.28      470.      -15.7     -45.7
6.9       421.      -22.1     -50.
7.45      400.      -25.2     -55.
9.47      300.      -42.7     -65.
10.69     250.      -48.7     -68.
12.13     200.      -52.7     -72.
13.96     150.      -58.9     -75.
16.47     100.      -63.7     -77.
20.00     54.       -64.      -76.
30.00     11.       -64.      -72.
12345678901234567890123456789012345678901234567890123456789
4.572     0.        97.34                         37.
```

Table B-5 INPUTS TO MODIFIED LOWTRAN 4 FOR MISSION 803

```
MISSION 803
12345678901234567890123456789012345678901234567890123456789
  7  2 2         1        3 18
0.        3.5        5.85
 ALT      PRES      TEMP     DEW PT
(KM)      (MB)      (C)       (C)
1.25      876.      18.3      -4.7
1.509     850.      17.5      -5.5
2.024     800.      15.5      -14.5
3.137     700.      6.4       -10.8
3.592     662.      3.0       -13.4
4.603     583.      -6.5      -16.6
4.903     561.      -8.6      -15.4
5.42      525.      -7.6      -19.3
5.80      500.      -9.2      -23.2
6.44      460.      -12.5     -42.5
7.48      400.      -22.7     -52.7
9.52      300.      -40.4     -65.0
10.74     250.      -49.9     -68.
12.2      200.      -50.2     -72.
14.04     150.      -58.2     -75.
16.52     100.      -71.6     -77.
20.       56.       -61.2     -76.
30.       12.       -55.      -72.
12345678901234567890123456789012345678901234567890123456789
5.79      1.95      113.63                        130.
1800.     5400.     20.
```

Table B-6 RADIOSONDE DATA APPLICABLE TO MISSION 816, RUNS 1-4

MIDWAY 23 1846Z JUNE 78 (Used for GARY data)

Height* H(km)	Pressure P(mb)	Temperature T(C)	Dew Point (C)
0.173	1000	--	--
(surface)	998	17.8	6.8
	988	17.8	4.8
	980	21.0	1.0
	968	21.0	2.0
	875	13.0	-1.0
1.558	850	11.4	5.4
	813	8.4	5.3
	769	7.2	-0.8
	743	0.6	-5.5
3.156	700	2.0	-1.8

*Mean height above sea-level. Heights given at TTAA (mandatory) levels. Heights at TTBB (significant) levels may be obtained by interpolating H vs. ln P.

Table B-7 RADIOSONDE DATA APPLICABLE TO MISSION 816, RUNS 6-10

FLINT 23 1849Z JUNE 78 (Used for WYANDOTTE data)

H (km)	P (mb)	T (C)	Dew Point (C)
0.178	1000	--	--
(Surface)*	993	10.6	8.3
	980	12.2	5.2
	922	12.2	2.2
1.536	850	9.0	2.0
	797	4.6	-2.4
	781	4.0	-12.0
3.119	700	2.2	-27.8
	680	2.2	-27.8
	542	-9.7	-39.7 ?
5.760	500	-14.9	-44.9 ?
	451	-21.7	-38.7
	420	-24.3	-54.3 ?
7.410	400	-27.1	-57.1 ?
9.41	300	-42.1	--
10.63	250	-52.5	--
12.04	200	-57.5	--
13.88	150	-55.3	--
16.45	100	-57.3	--

*Surface data:

DETROIT 23 1408Z T = 69F, Dew Point = 44F
DETROIT 23 1611Z T = 72F, Dew Point = 50F

Table B-8 RADIOSONDE DATA APPLICABLE TO MISSION 815/2

ASHLAND 22 1453Z JUNE 78

H (km)	P (mb)	T (C)	Dew Point (C)
0.160	1000	--	--
(Surface)	990	17.2	13.9
	969	16.0	10.0
	950	17.2	8.2
	905	15.8	6.8
1.544	850	12.4	11.4
	792	8.6	7.5
	775	8.6	-0.4
	723	3.0	-1.2
	713	2.0	-8.0
	710	4.4	-25.6
3.146	700	5.4	-24.6
5.81	500	-13.1	-33.1 ?
7.47	400	-25.3	-55.3 ?
9.48	300	-43.3	--
10.69	250	-49.9	--
12.13	200	-52.3	--
13.98	150	-55.1	--
16.55	100	-59.3	--

Table B-9 RADIOSONDE DATA APPLICABLE TO MISSION 815/4

BIRMINGHAM 22 1454Z JUNE 78 (Used for FAIRFIELD data)

H (km)	P (mb)	T (C)	Dew Point (C)
0.144	1000	--	--
(Surface)*	995	22.0	20.5
	984	22.2	19.8
	973	23.2	19.3
	962	24.0	19.3
	947	22.2	17.5
	915	20.2	16.8
	882	18.8	11.8
	877	18.6	11.8
	866	17.8	11.8
1.552	850	17.0	9.0
	832	15.8	6.8
	826	15.8	6.8
	812	14.0	9.4
	783	13.0	3.0
	763	11.2	5.2
	734	9.4	2.4
	728	9.0	0.0
3.182	700	6.8	-0.2

*Near surface use:

HUNTINGTON 13Z T = 66F, Dew Point = 55F

APPENDIX C

DEVELOPMENT OF SUNGLITTER MODEL

A successful model for predicting the IR spectral radiance of sunlight reflected by a rough ocean surface or other body of water has been developed using the Cox-Munk (Reference C1) geometric optics approximation. Although the model has been verified by comparison with ocean sunglitter data obtained by the AFGL Background Measurement Program, one may also apply the results to computations involving the specular reflectance of the sun from smooth or convex surfaces. This appendix outlines a step-by-step computation procedure that serves to define the model as well as describe the details of its implementation.

Reflection Geometry

A cartesian coordinate system is used to define the reflection geometry with the u and v axes defining the horizontal plane of the undisturbed ocean surface (Figure C-1). The Z axis points vertically upward and the u axis is directed upwind. The locations of the sun and the observer are given by the solar zenith angle ϕ, the solar azimuthal angle ν with respect to the upwind direction and the corresponding zenith angle β and azimuthal angle α of the observer. The orientation of the reflecting facet of the surface is given by the tilt angle μ and the local angle of incidence ω at the facet. The tilt angle points in the direction of the local surface normal and is related to the scattering geometry angles $(\phi, \nu; \alpha, \beta)$ by the expression (Reference C2).

$$\cos \mu = [\cos \phi + \cos \beta]/2 \cos \omega \qquad \text{(C1)}$$

Likewise, the local angle of incidence can be expressed in terms of the scattering geometry.

$$\cos (2\omega) = \cos \phi \cos \beta - \sin \beta \sin \phi \cos (\nu - \alpha) \qquad \text{(C2)}$$

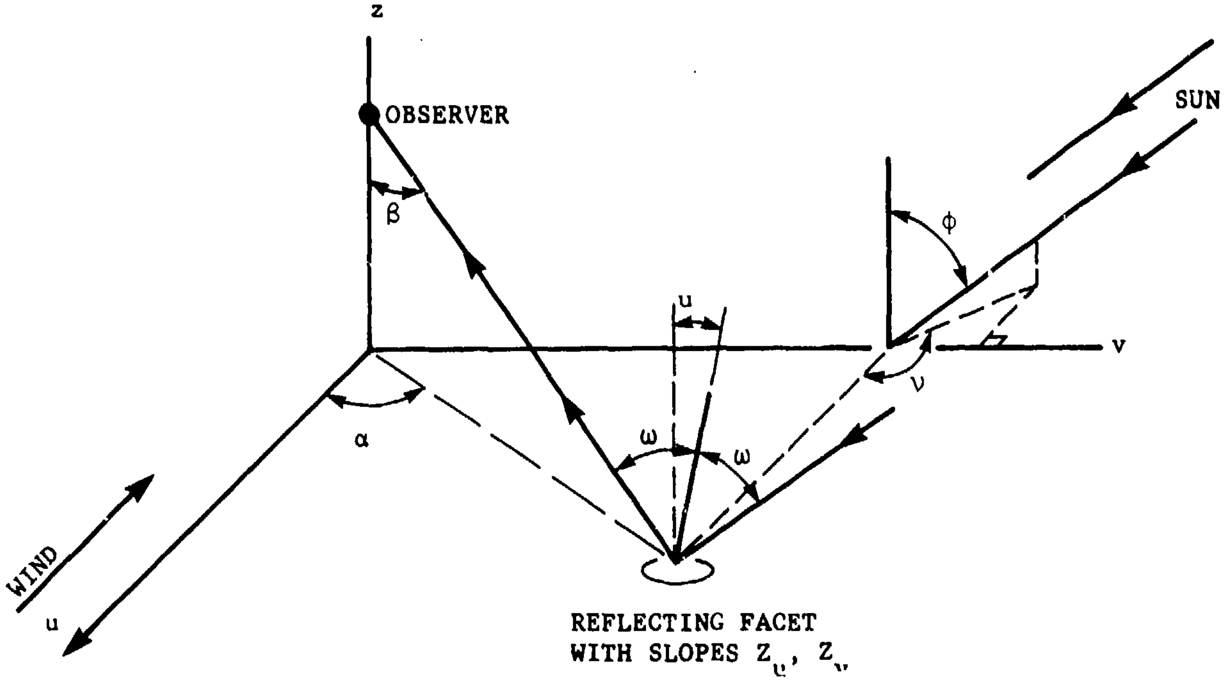

Figure C-1 SEA SURFACE REFLECTION COORDINATE SYSTEM. The observer is located at azimuthal angle α and zenith angle β. The sun orientation is given by azimuthal angle ν and zenith angle φ.

It will also be necessary to relate the wave slope components for specular reflection to the scattering geometry. These results will be useful when determining the probability of occurrence of slope components Z_u and Z_v.

$$Z_u = \partial Z/\partial u = (\sin\beta\cos\alpha - \sin\phi\cos\nu)(\cos\phi + \cos\beta)^{-1} \qquad (C3)$$

$$Z_v = \partial Z/\partial v = (\sin\beta\sin\alpha - \sin\phi\sin\nu)(\cos\phi + \cos\beta)^{-1} \qquad (C4)$$

Basic Equations for Reflected Components

The geometric optics expression for the spectral reflected sea radiance is given by:

$$N_a(\lambda) = \rho_a(\omega,\lambda)\,\frac{H_o}{\pi}(\lambda)\;T(\lambda)\;S(\omega)\;(\alpha,\beta;\gamma,\phi)\;P(Z_u, Z_v, W) \qquad (C5)$$

The parameters in this expression are:

N_a - spectral sea radiance for polarization a and wavelength λ

a - polarization state of the reflected radiation which is defined to be either vertical (a = v, parallel to plane of incidence) or horizontal (a = h, perpendicular to plane of incidence)

H_o - spectral solar irradiance outside the earth's atmosphere

T - atmospheric transmission along with path defined by a line extending from the sun to the surface and then to the receiver

S - a slope shadowing factor which prevents N from becoming infinite at the horizon due to the sec β term in the geometric factor g (S = 0 when sec β = 0) [Reference]C3 .

g - a geometric scattering factor which is defined later

P - probability of the occurrence of a particular wave slope having components Z_u and Z_v for a wind velocity W

$_a$ - reflectance of the surface for incident polarization state a and local angle of incidence ω.

If one makes the assumption that the receiver response is insensitive to the polarization of the source, then the total spectral reflected solar radiation at the receiver is just the sum of the two possible polarization states (v = vertical and h = horizontal).

$$N_{sun}(\lambda) = N_v(\lambda) + N_h(\lambda) \tag{C6}$$

A complete definition of $N_a(\lambda)$ requires further expressions which completely define the parameters which appear in the Equation (C5).

A geometric scattering factor is used to account for the angular distribution of the scattered sunlight (Reference C2).

$$g(\alpha,\beta;\nu,\phi) = \sec\beta\left[1 + \cos\beta\,\cos\phi - \sin\beta\,\sin\phi\,\cos(\nu - \alpha)\right]^2 (\cos\beta + \cos\phi)^{-4} \tag{C7}$$

Saunders (Reference C3) derives a simplified expression for the surface shadowing factor:

$$S = 2\left[1 + \mathrm{erf}(\nu) + (\nu\sqrt{\pi})^{-1}\,\mathrm{erf}(-\nu^2)\right]^{-1} \tag{C8}$$

where $\nu = \sigma^{-1}\tan\phi$, σ is the rms surface slope,, and erf (ν) denotes the error function.

The entire expression for $N_a(\lambda)$ requires a knowledge of the probability of occurrence of wave slopes with the correct orientations. Cox and Munk (Reference C1) have measured this function for surface wind velocities up to 14 m/s (at 12 m above sea level).

$$P\ (Z_u, Z_v, W) = (2\pi\, \sigma_u \sigma_v)^{-1}\ \exp\left[-1/2(\xi^2 + \eta^2)\right]\left[1 - C(W)\right] \qquad \text{(C9)}$$

The rms values of surface slopes in the u and the v directions are given by σ_u and σ_v; ξ and η are normalized slopes that describe the deviation of the slopes of the waves from a Gaussian distribution.

$$\begin{aligned} C(W) = {} & \frac{1}{2}\ C_{21}\ (\xi^2 - 1)\eta + \frac{1}{6}\ C_{03}\ (\eta^3 - 3\eta) \\ & - \frac{1}{24}\ C_{40}\ (\xi^4 - 6\xi^2 + 3) - \frac{1}{4}\ C_{22}\ (\xi^2 - 1)(\eta^2 - 1) \qquad \text{(C10)} \\ & - \frac{1}{24}\ C_{04}\ (\eta^4 - 6\eta^2 + 3) \end{aligned}$$

It is important to note that Equation C9 is only valid for values of ξ and η that are less than 2.5 in magnitude and for $\phi \leq 55^{\circ}$ because of experimental limitations on the surface measurements. Furthermore Cox and Munk measured values of rms slope components for a clean surface of

$$\begin{aligned} \sigma_v^{\ 2} &= 0.003 + 0.00192\ W \\ \sigma_u^{\ 2} &= 0.000 + 0.00316\ W \qquad \text{(C11)} \\ \sigma^2 &= 0.003 + 0.00512\ W \end{aligned}$$

along with coefficients determining the skewness and peakedness of the surface slope distribution.

C21 = 0.01 - 0.0086 W
C03 = 0.04 - 0.033 W
C40 = 0.40
C22 = 0.12
C04 = 0.23

The most important parameter for this study is the sea surface spectral reflection coefficient ρ_a for polarization a. Theoretical expressions for ρ_a for an absorbing medium such as sea water are given by Friedman (Reference C4) along with a tabulation of the index of refraction n and the extinction coefficient k of water for wavelengths from 1.5 to 15μ.

$$\rho_v = \frac{b + c\cos^2\omega - 2\left[d(n^2-k^2) + 2\,ekn\right]\cos\omega}{b + c\cos^2\omega + 2\left[d(n^2-k^2) + 2\,ekn\right]\cos\omega} \tag{C13}$$

$$\rho_h = \frac{b + \cos^2\omega - 2d\cos\omega}{b + \cos^2\omega + 2d\cos\omega} \tag{C14}$$

where

$$\begin{aligned} a &= n^2 + k^2 - \sin^2\omega \\ b^2 &= a^2 + 4k^2 n^2 \\ c &= (n^2 - k^2)^2 + 4\,k^2 n^2 \\ d^2 &= 1/2\ (b + a) \\ e^2 &= 1/2\ (b - a) \end{aligned} \tag{C15}$$

The spectral reflectances depend upon measurements of n and k. A recent tabulation of n (λ) and k (λ) from 0.200 to 200 μm has been performed by Hale and Querry (Reference C5) for pure water. Research by Hobson and Williams (Reference C6) indicates that one can also use the pure water data for ocean water in the spectral range 2-8 μm. One should also note that this tabulation is only for "clean" water that has no foreign surface films on it. The presence of surface contaminants will greatly alter the reflectances.

Several interesting features of the k (λ) and n (λ) data are plotted in Figure C-2. The influence of the two major absorption bands at 2.94 μm (3400 cm^{-1}) and 6.09 μm (1640 cm^{-1}) are clearly evident.

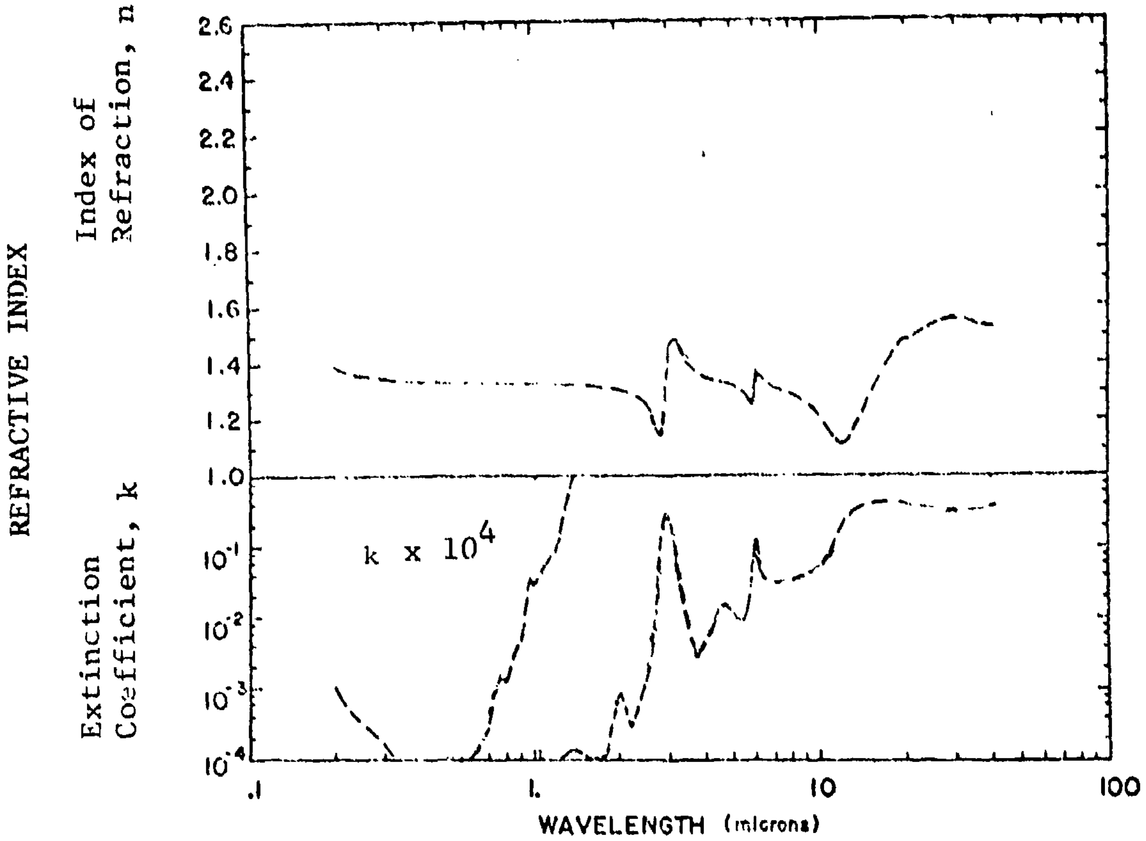

Figure C-2 INDEX OF REFRACTION AND EXTINCTION COEFFICIENT OF WATER FROM 0.1 TO 50 μm (REF. C5)

References

C1. C. Cox and W. Munk, "Measurement of the Roughness of the Sea Surface from Photographs of the Sun's Glitter," J. Opt. Society Am. 44, 838 (1954).

C2. K.S. Krishnan and N.A. Peppers, Optical Techniques for the Measurement of Ocean-Surface Parameters (U), Standard Research Institute Report SRI 76-0760, November 1975 (Confidential).

C3. P.M. Saunders, "Radiance of Sea and Sky in the Infrared Window 800-1200 cm^{-1}," J. Opt. Society Am. 58, 645 (1968).

C4. D. Friedman, "Infrared Characteristics of Ocean Water (1.5 - 15μ)," Applied Optics 8, 2073 (1969).

C5. G.M. Hale and M.R. Querry, "Optical Constants of Water In the 200-nm to 200-μm Wavelength Region," Applied Optics 12, 555 (1973).

C6. D.G. Hobson, Jr. and D. Williams, "Infrared Spectral Reflectance of Sea Water," Applied Optics 10, 2372 (1971).

APPENDIX D

AFGL INDUSTRIAL SITE SPECTRA

This appendix contains plots of 27 AFGL spectra provided to SAI by Honeywell. The spectra are plotted over three regions, from 1900–3060 cm^{-1}, 3060–4220 cm^{-1}, and 4220–5380 cm^{-1}. Also an atmospheric correction has been made to the spectra over the 1900–3060 cm^{-1} region, and plots of these adjusted values are included with each data set. Thus each data set consists of 4 plates. The missing data in the adjusted spectra between 2290 and 2380 cm^{-1} results from the fact that LOWTRAN shows zero transmission in this region. The ranges used to make the atmospheric corrections are shown in the preface of the appendix; meteorological data were taken from radiosondes given in Appendix B.

Table D-1 IDENTIFICATION OF SPECTRA FOR AFGL MISSIONS 816 and 815

LOCATION	MISSION/RUN	DERIVED RANGE (ft)	TIME		SCENE	PAGE
Gary, IN 23 June 78	816/1	11,500	1344	12.6	Bright orange flame or hot ore near blast furnace	166-169
	816/1	11,500	1345	00.0	Background-narrow bridge and river	170-173
	816/2	11,500	1348	45.1	Hot slag	174-177
	816/2	11,500	1355	17.3	Water background	178-181
	816/3	12,700	1401	55.5	Hot coke oven	182-185
	816/3	15,300	1405	49.6	Background-parking lot	186-189
	816/3	15,300	1406	33.8	Stack flare (gas burnoff)	190-193
	816/4	14,300	1415	07.9	Stacks of large capacity rolling mill	194-197
	816/4	14,300	1415	42.2	Background	198-201
Wyandotte, MI 23 June 78	816/6	15,477	1502	25.0	Blast furnace	202-205
	816/6	8,182	1503	28.3	Background	206-209
	816/7	9,155	1507	42.7	Coke oven	210-213
	816/7	8,913	1510	34.5	Background-dark barren area	214-217
	816/8	11,318	1527	34.3	Stacks with railroad cars behind	218-221
	816/8	10,411	1529	14.8	Background	222-225
	816/8	10,421	1528	05.4	Railroad cars with hot metal	226-229
	816/10	10,424	1540	00.0	BASF stack, nearly invisible flame	230-233
	816/10	7,972	1543	14.8	Water background	234-237
Ashland, KY 22 June 78	815/2	10,725	1133	26.5	Flame from stack	238-241
	815/2	12,406	1136	31.6	Background	232-245
	815/2	9,550	1143	13.2	Refinery complex	246-249
Fairfield, AL 22 June 78	815/4	9,408	1257	26.2	Tip of stack (no visible flame)	250-253
	815/4	10,513	1258	51.6	Background	254-257
	815/4	10,056	1303	28.9	Grey building (hot?)	258-261
	815/4	8,510	1307	05.9	Orange hot metal (or flame?) (moving?) (in railroad car?)	262-265
Ashland, KY 22 June 78	815/2*	11,729	1136	11.8	Background (barge on river)	266-269
	815/2*	8,823	1143	49.2	Refinery complex	270-273

*From wide-field interferometer (104); all other spectra are from narrow-field interferometer (103).

GARY, INDIANA (816/1) - 13:44:12.6 - HOT ORE

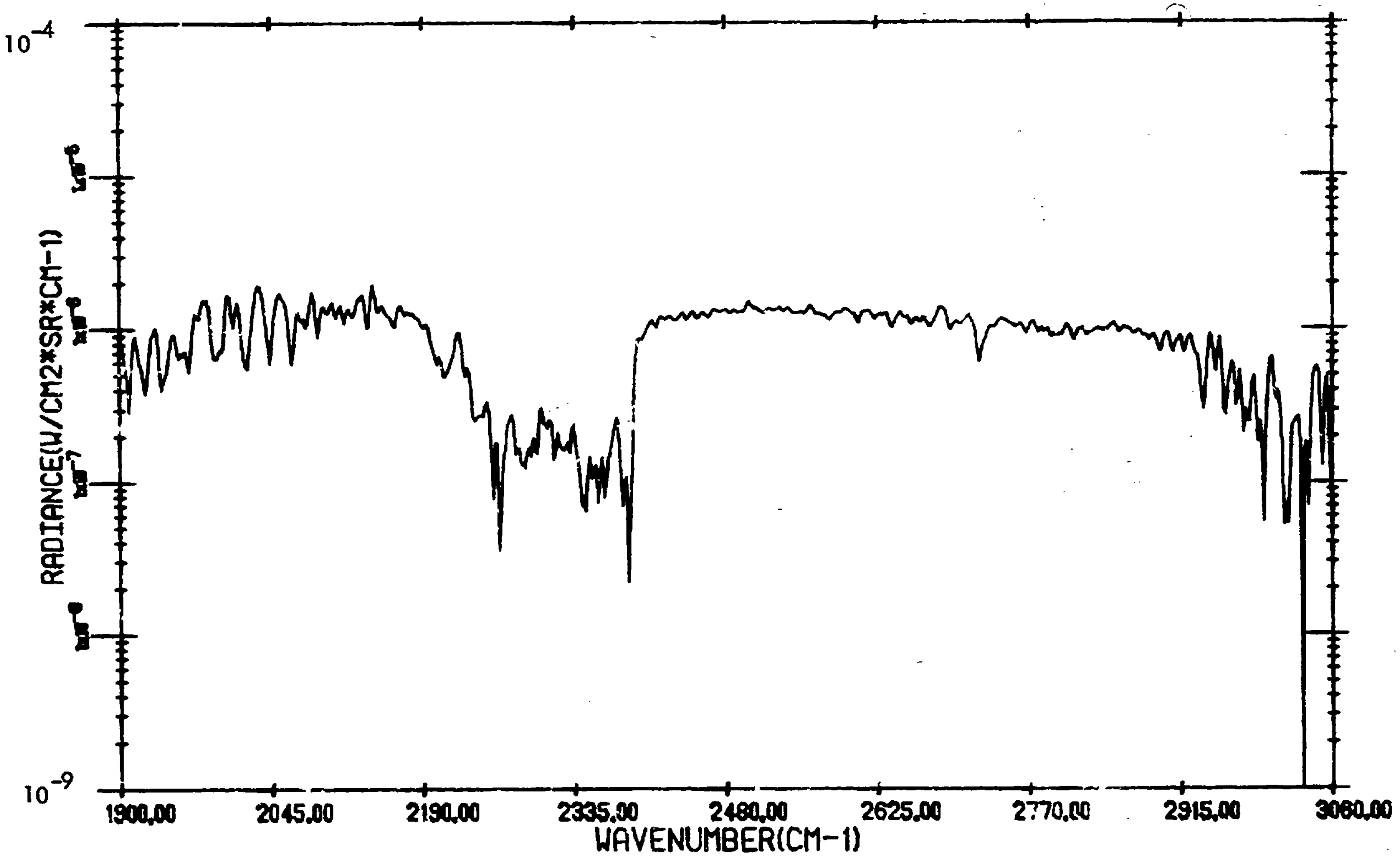

TARGET RADIANCE

GARY, INDIANA (816/1) - 13:44:12.6 - HOT ORE

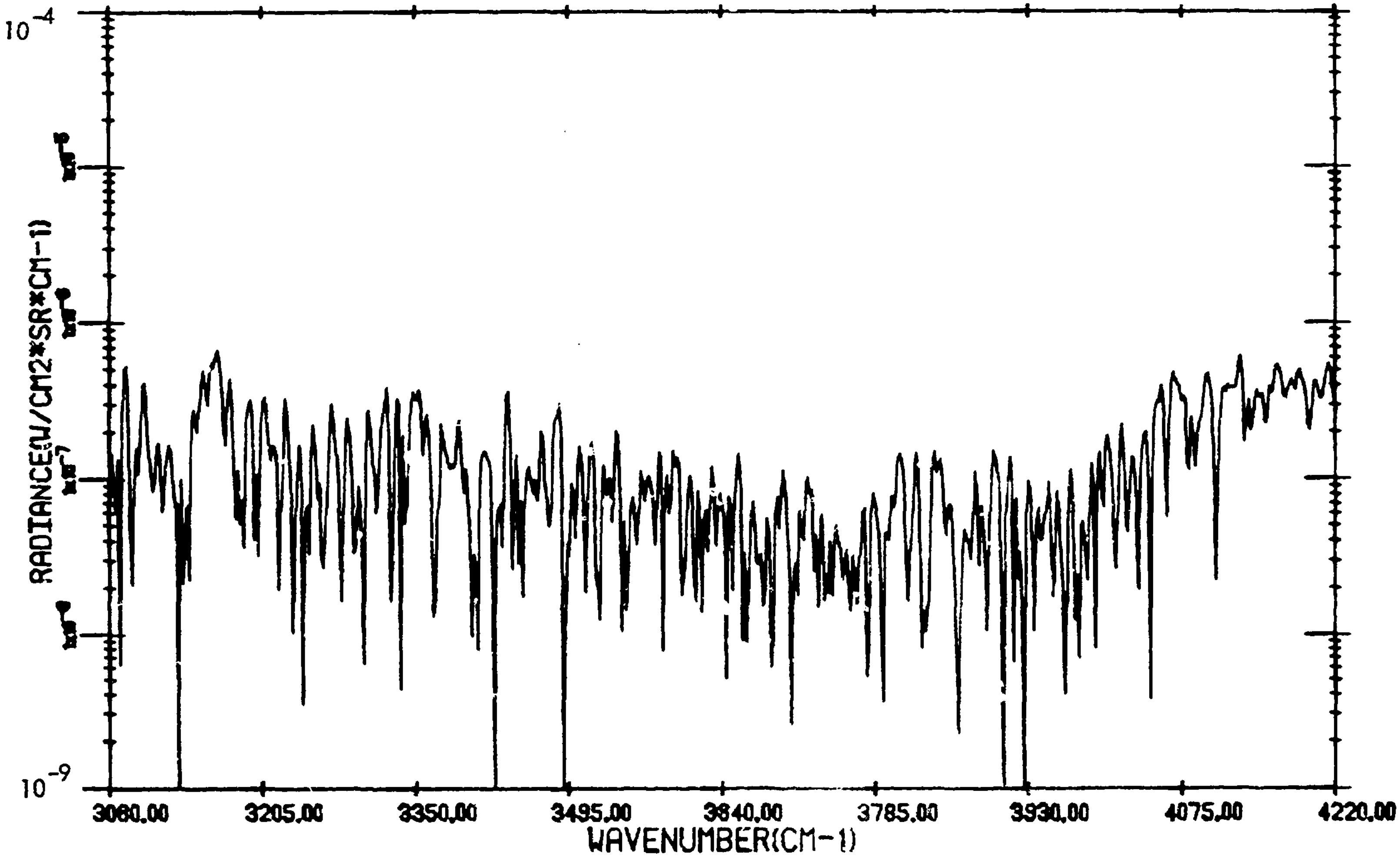

TARGET RADIANCE

GARY, INDIANA (816/1) - 13:44:12.6 - HOT ORE

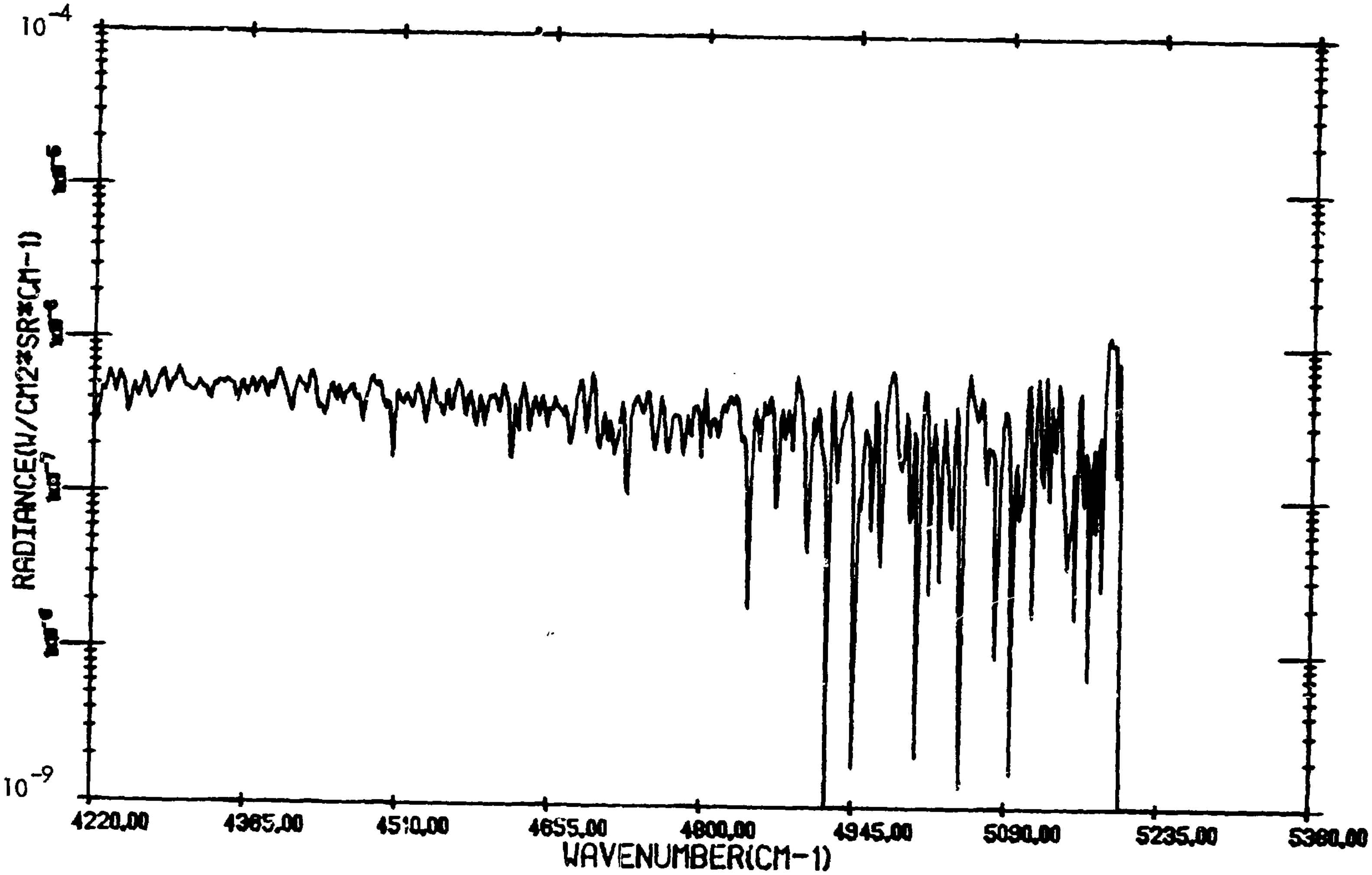

TARGET RADIANCE

(816/1)

GARY, INDIANA - 13:44:12.6 - HOT ORE (WITH ATMOSPHERIC TRANSMITTANCE CORRECTION)

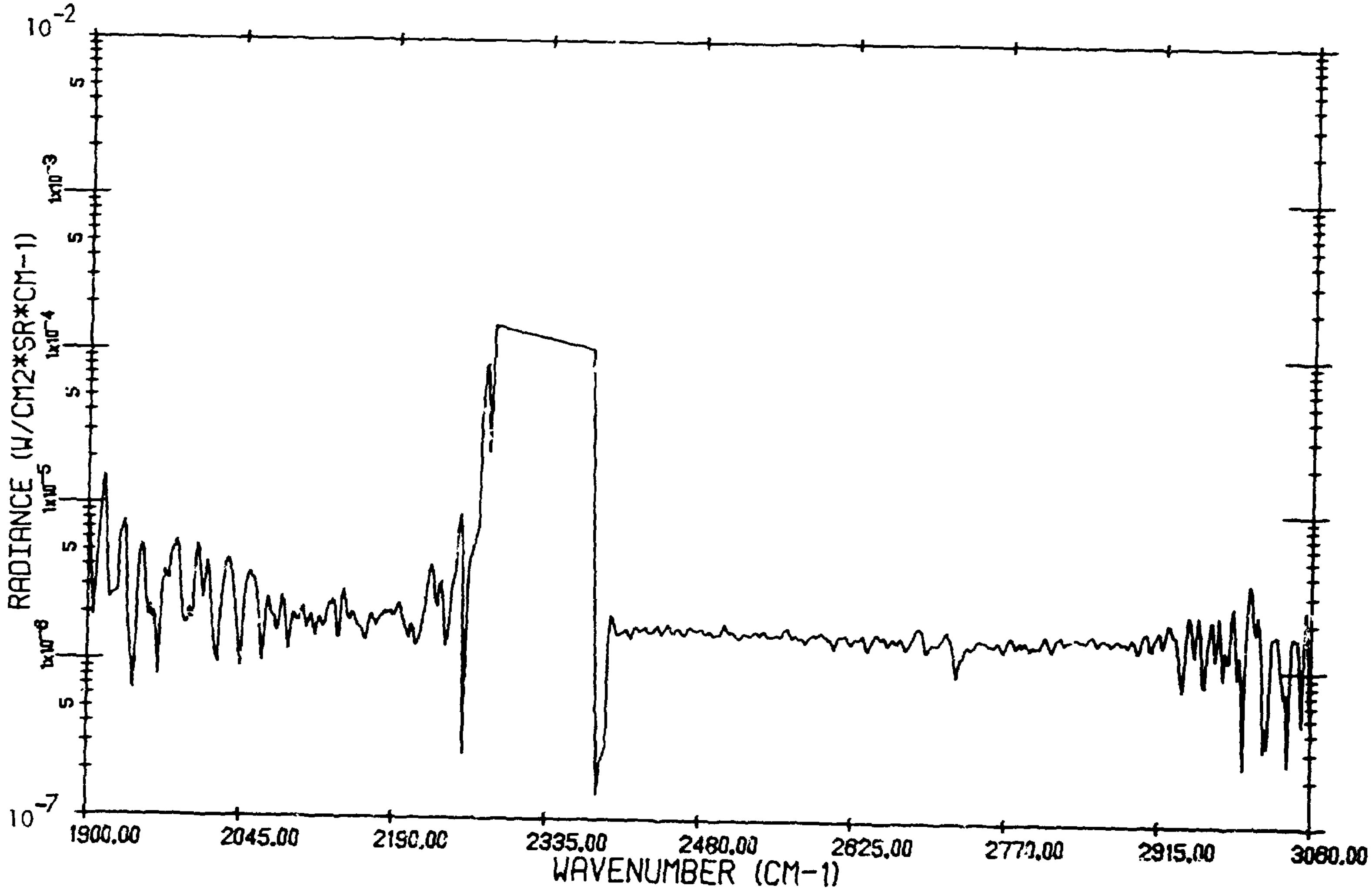

GARY, INDIANA (816/1) - 13:45:0.0 - BACKGROUND

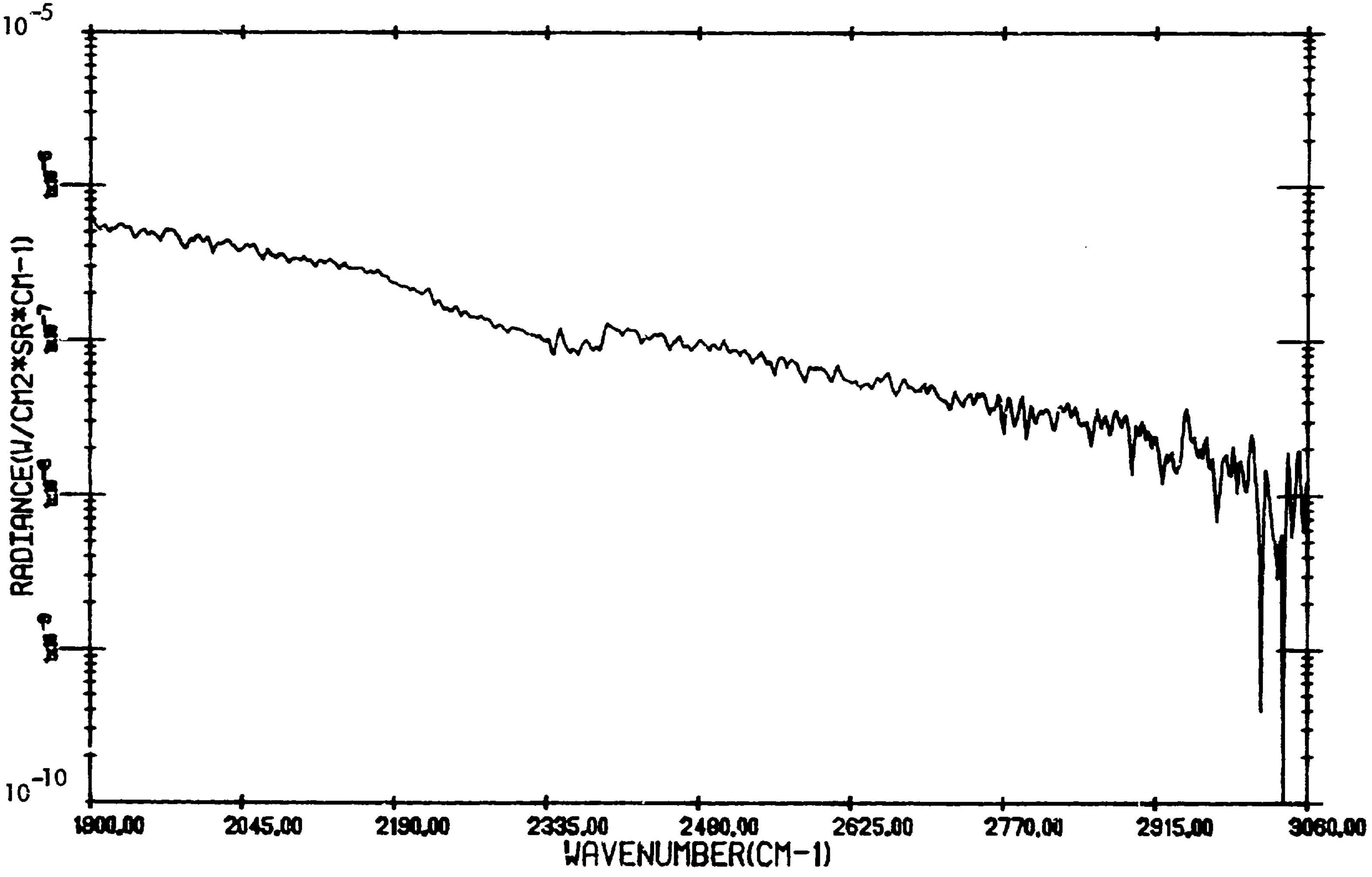

BACKGROUND RADIANCE

GARY, INDIANA (816/1) - 13:45:0.0 - BACKGROUND

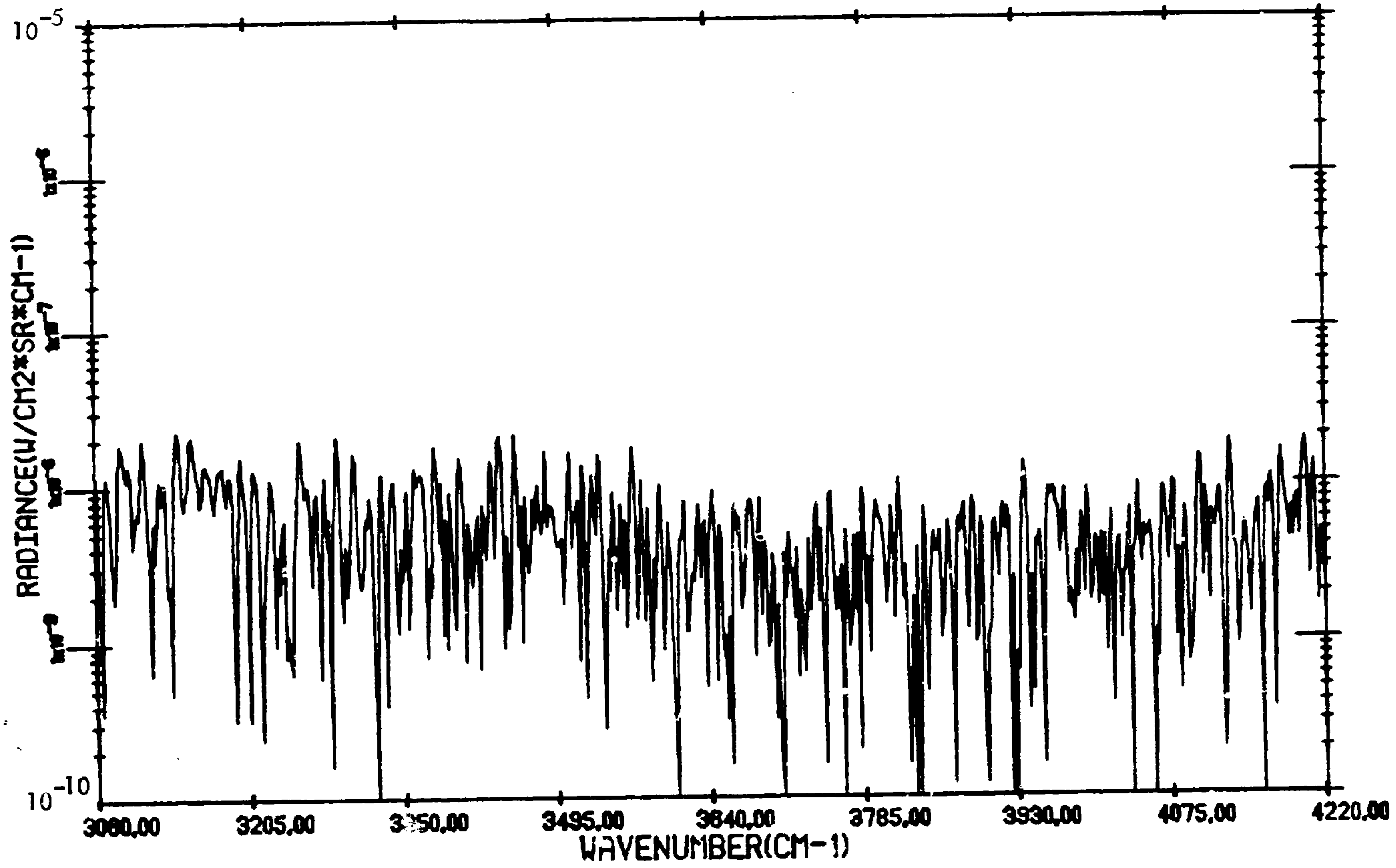

BACKGROUND RADIANCE

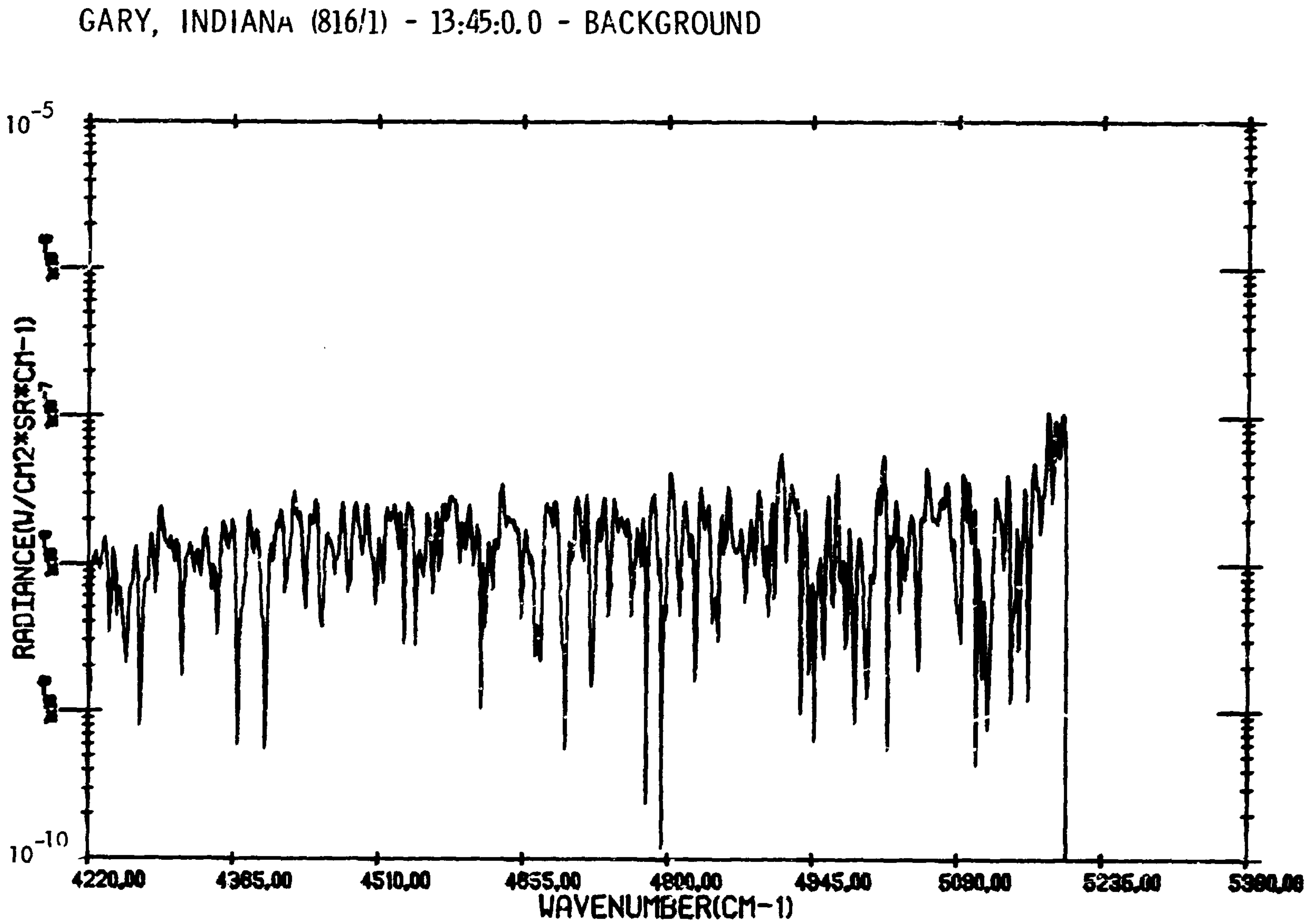

BACKGROUND RADIANCE

(816/1)

GARY, INDIANA - 13:45:0.0 - BACKGROUND (WITH ATMOSPHERIC TRANSMITTANCE CORRECTION)

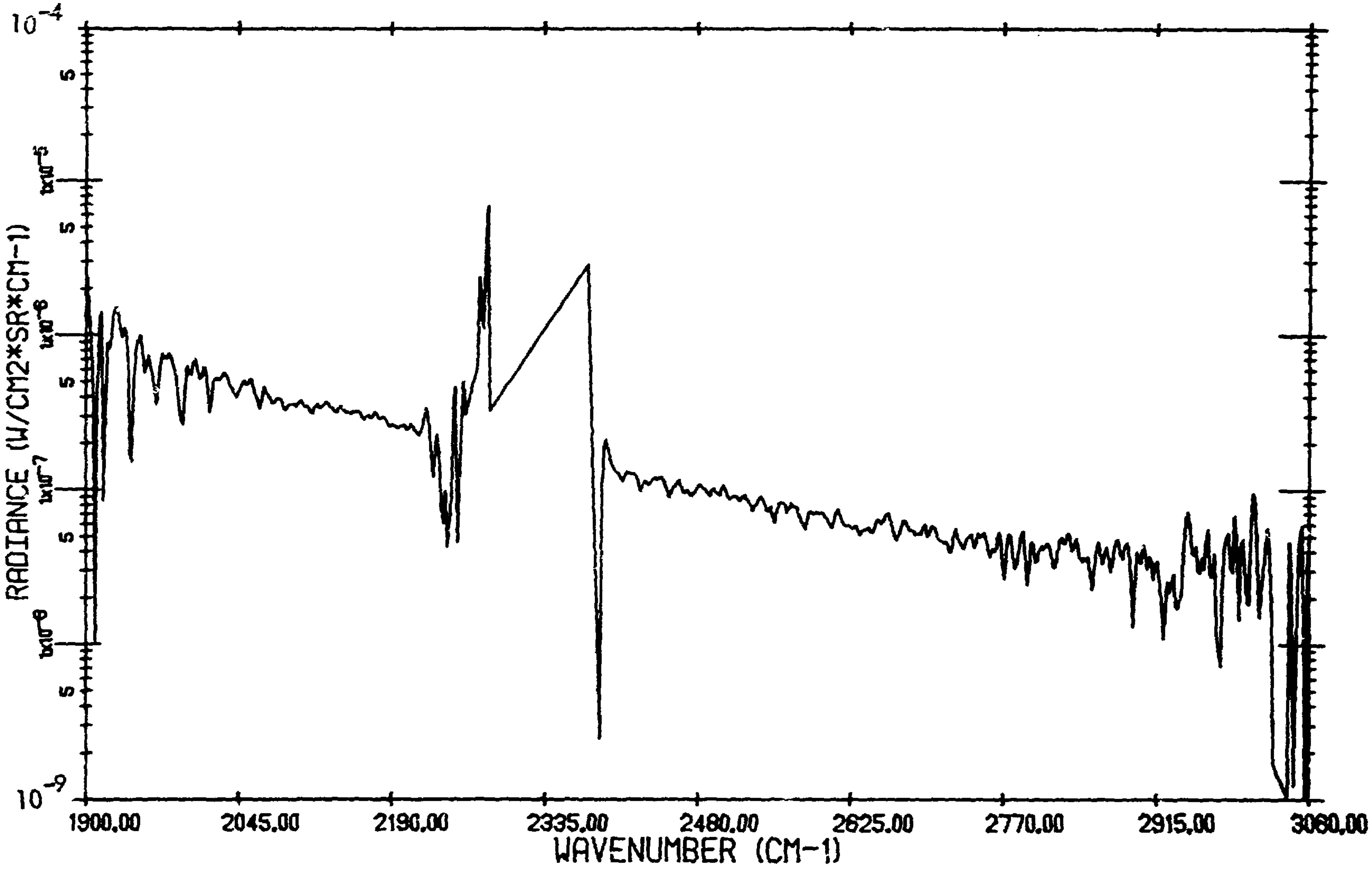

GARY, INDIANA (816/2) - 13:48:45.1 - HOT SLAG

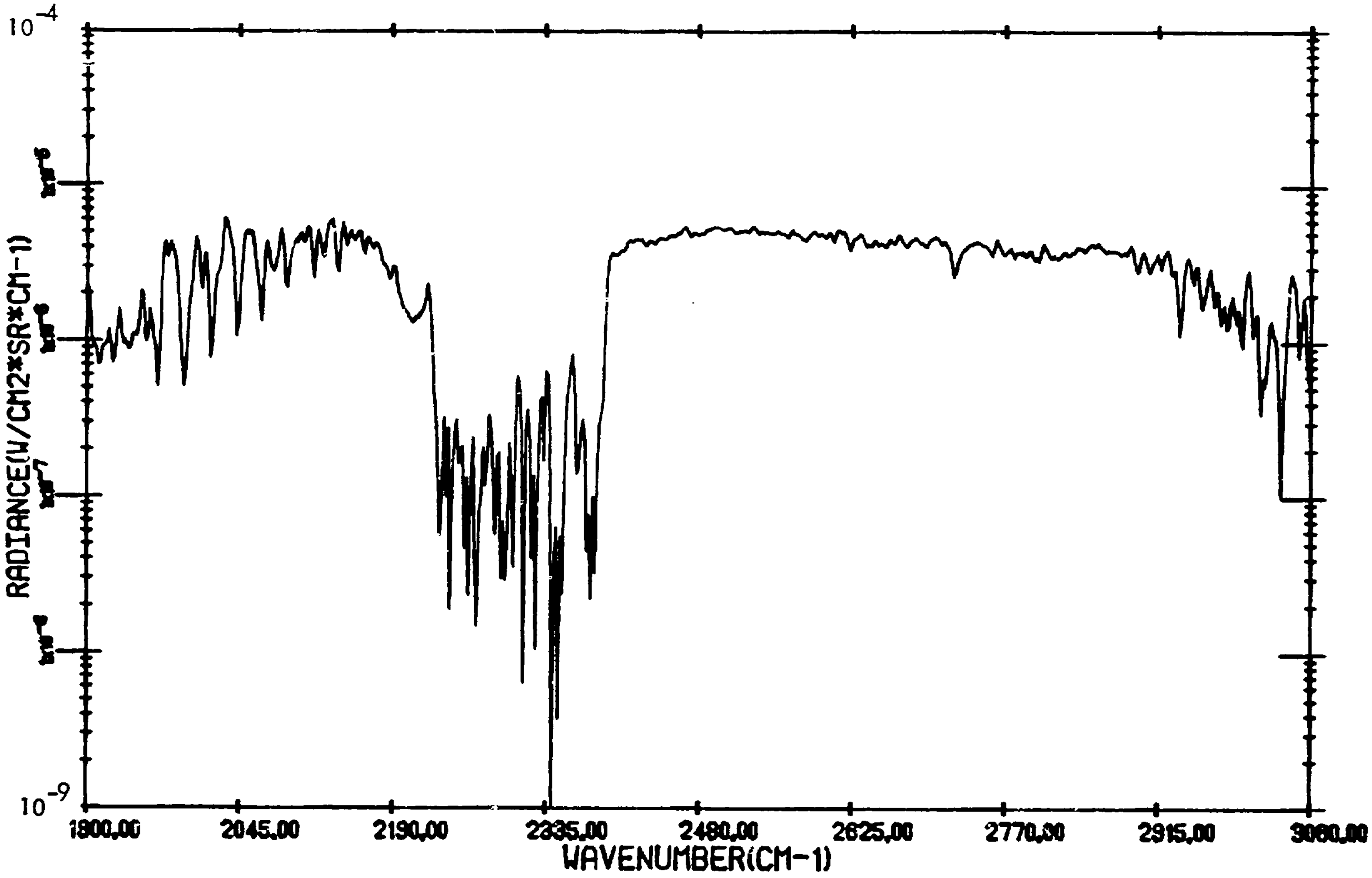

TARGET RADIANCE

GARY, INDIANA (816/2) - 13:48:45.1 - HOT SLAG

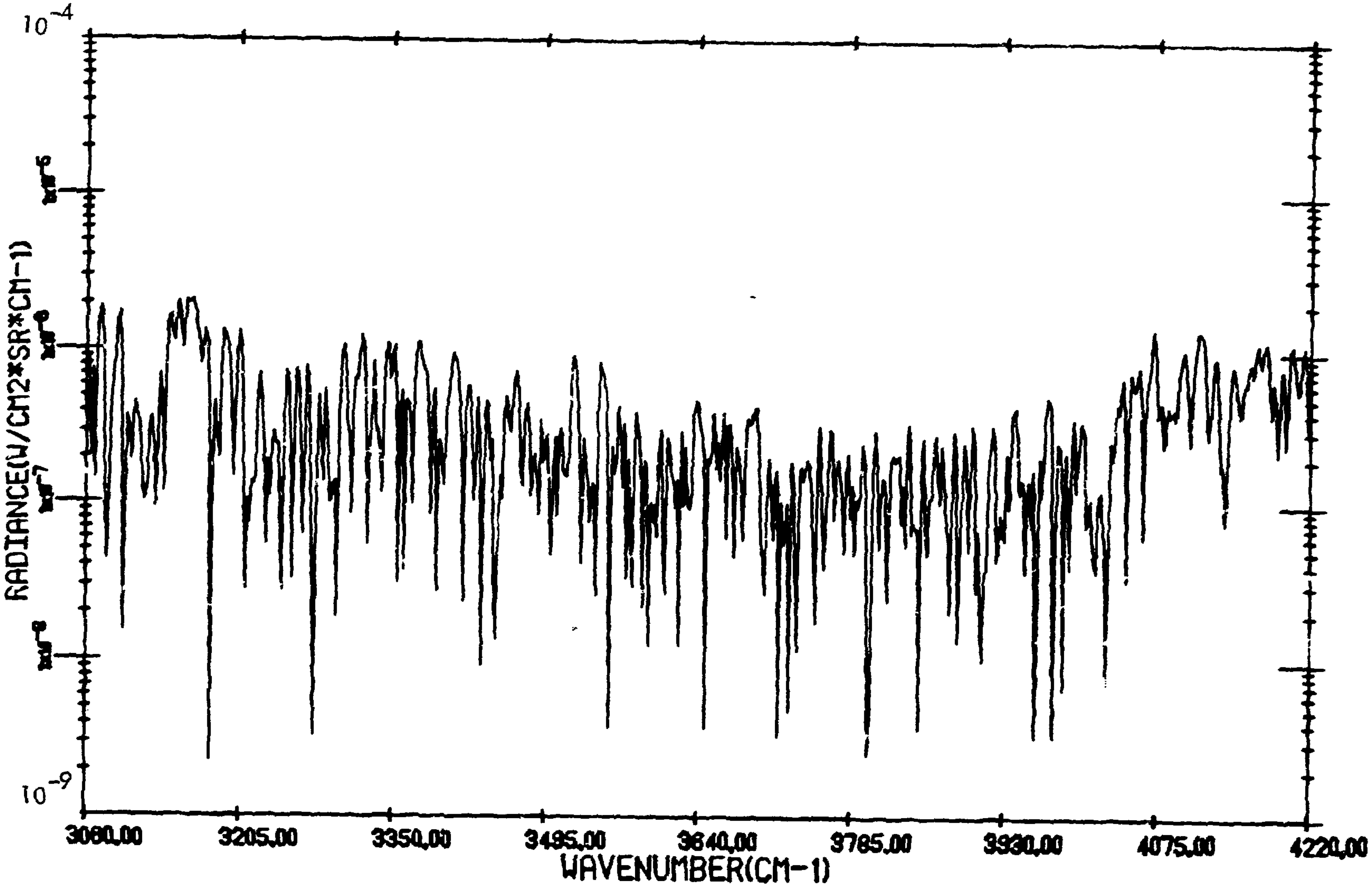

TARGET RADIANCE

GARY, INDIANA (816/2) - 13:48:45.1 - HOT SLAG

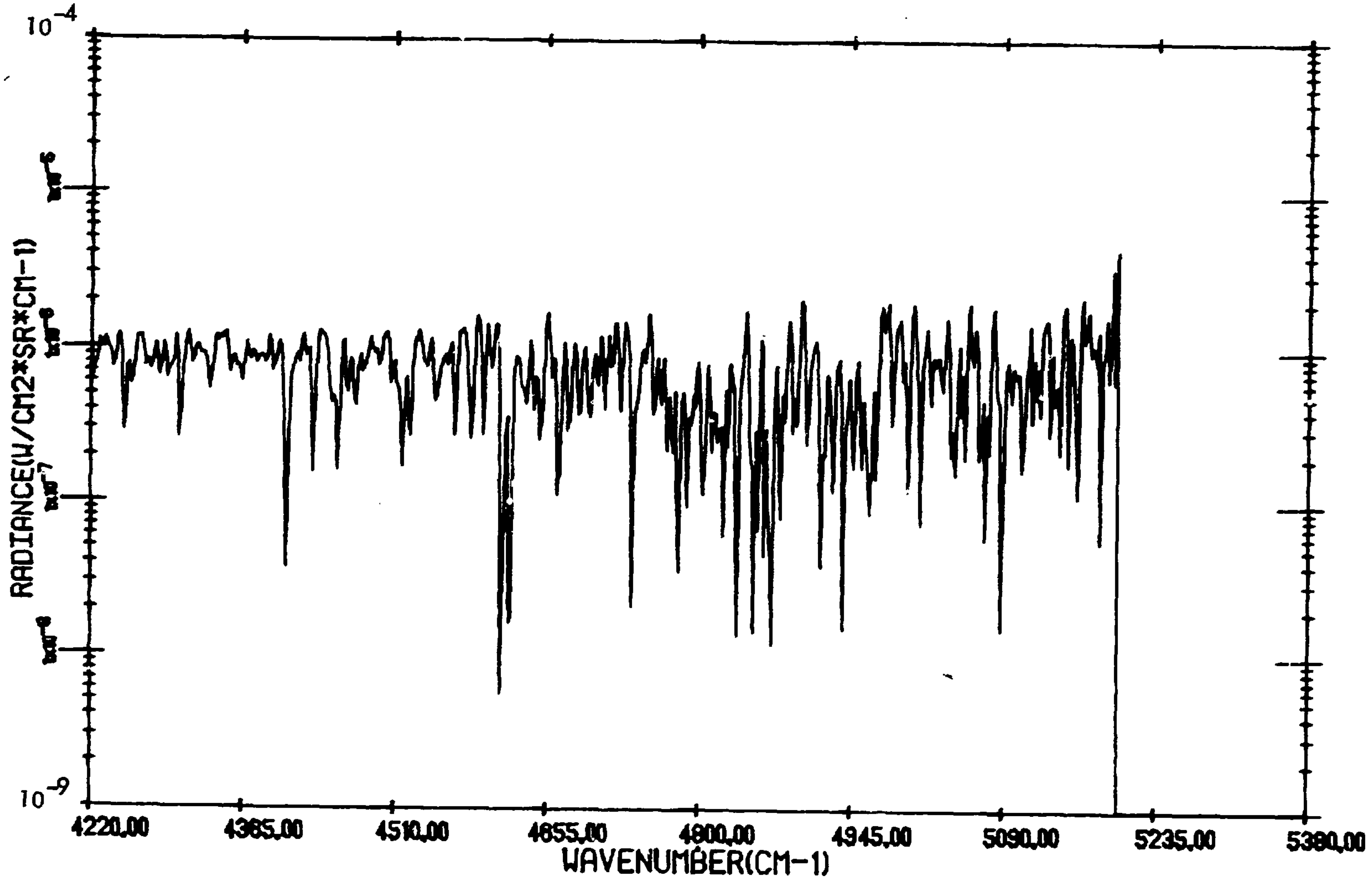

TARGET RADIANCE

(816/2)

GARY, INDIANA - 13:48:45.1 - HOT SLAG (WITH ATMOSPHERIC TRANSMITTANCE CORRECTION)

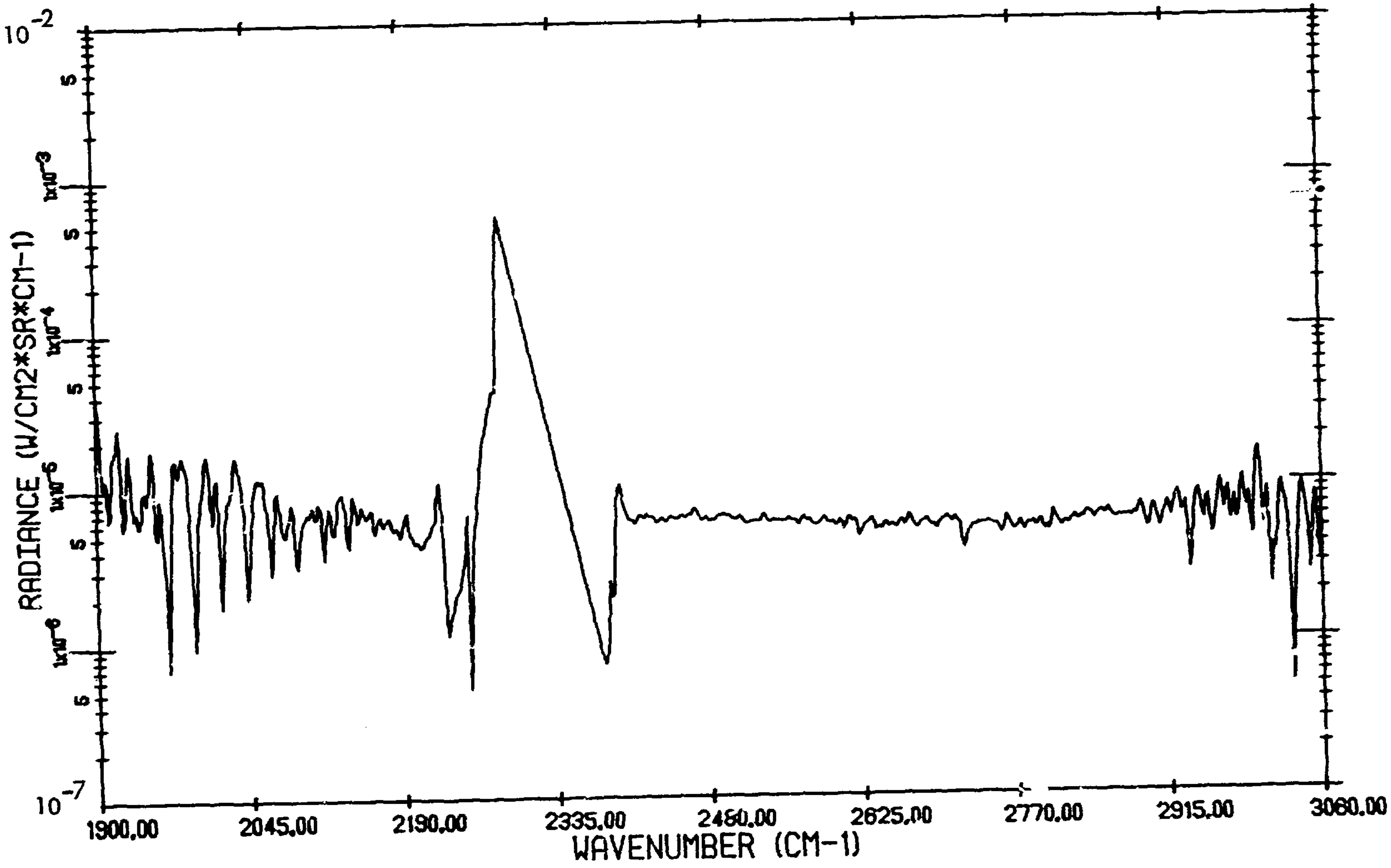

CORRECTED TARGET RADIANCE

GARY, INDIANA (316/2) - 13:55:17.3 - BACKGROUND

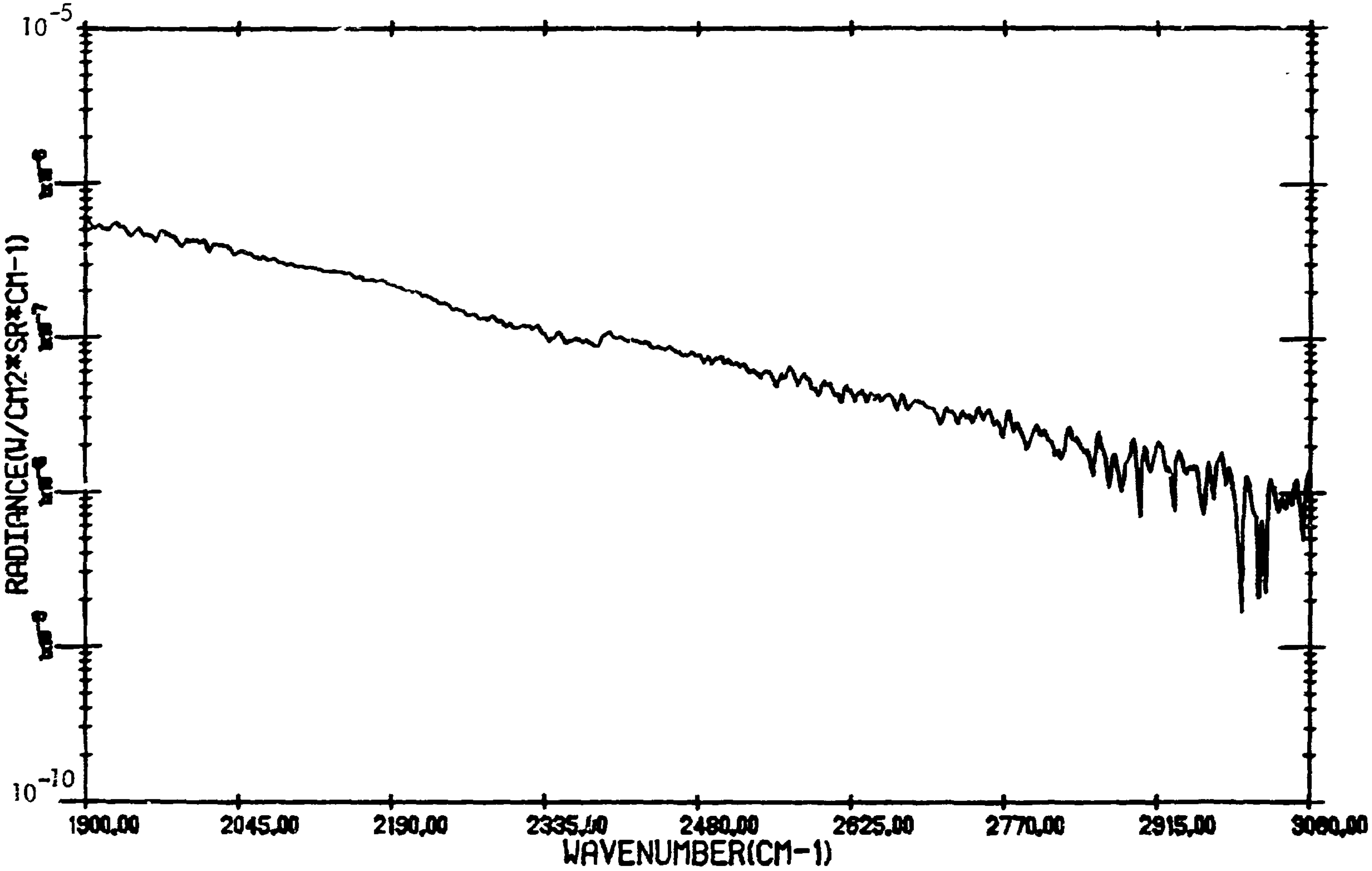

BACKGROUND RADIANCE

GARY, INDIANA (816/2) - 13:55:17.3 - BACKGROUND

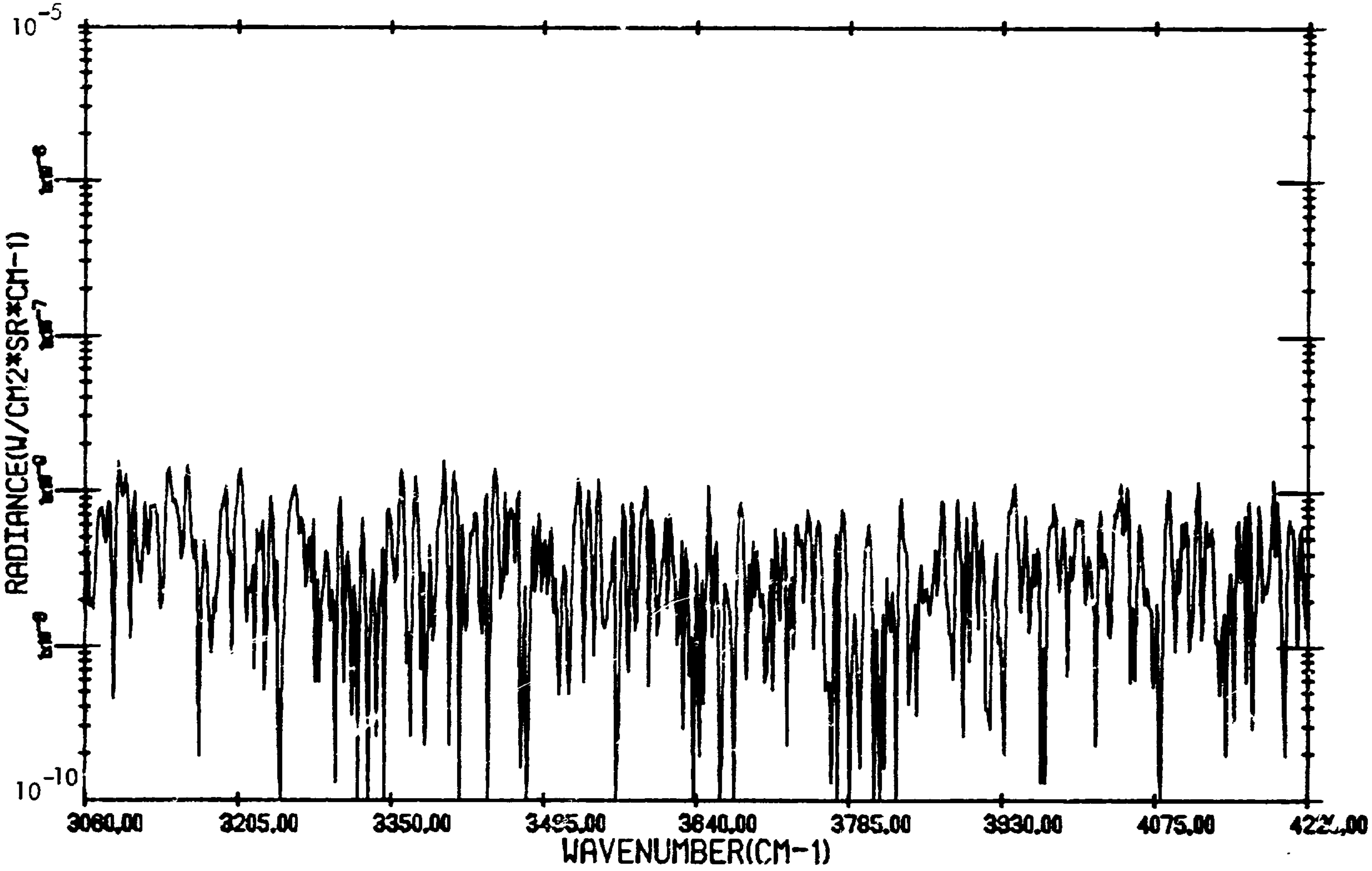

BACKGROUND RADIANCE

GARY, INDIANA (816/2) - 13:55:17.3 - BACKGROUND

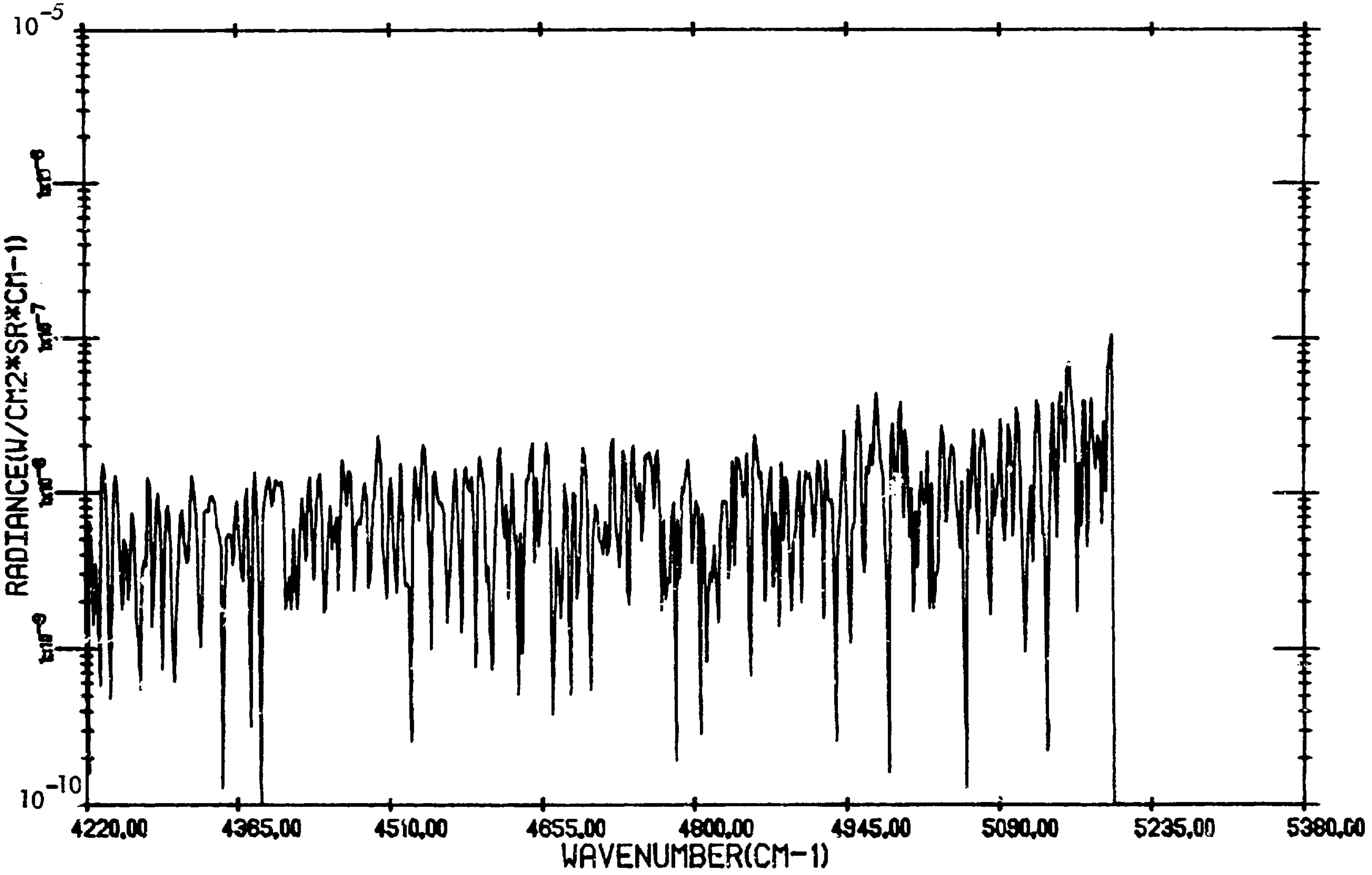

BACKGROUND RADIANCE

(816/2)

GARY, INDIANA - 13:55:17.3 - BACKGROUND (WITH ATMOSPHERIC TRANSMITTANCE CORRECTION)

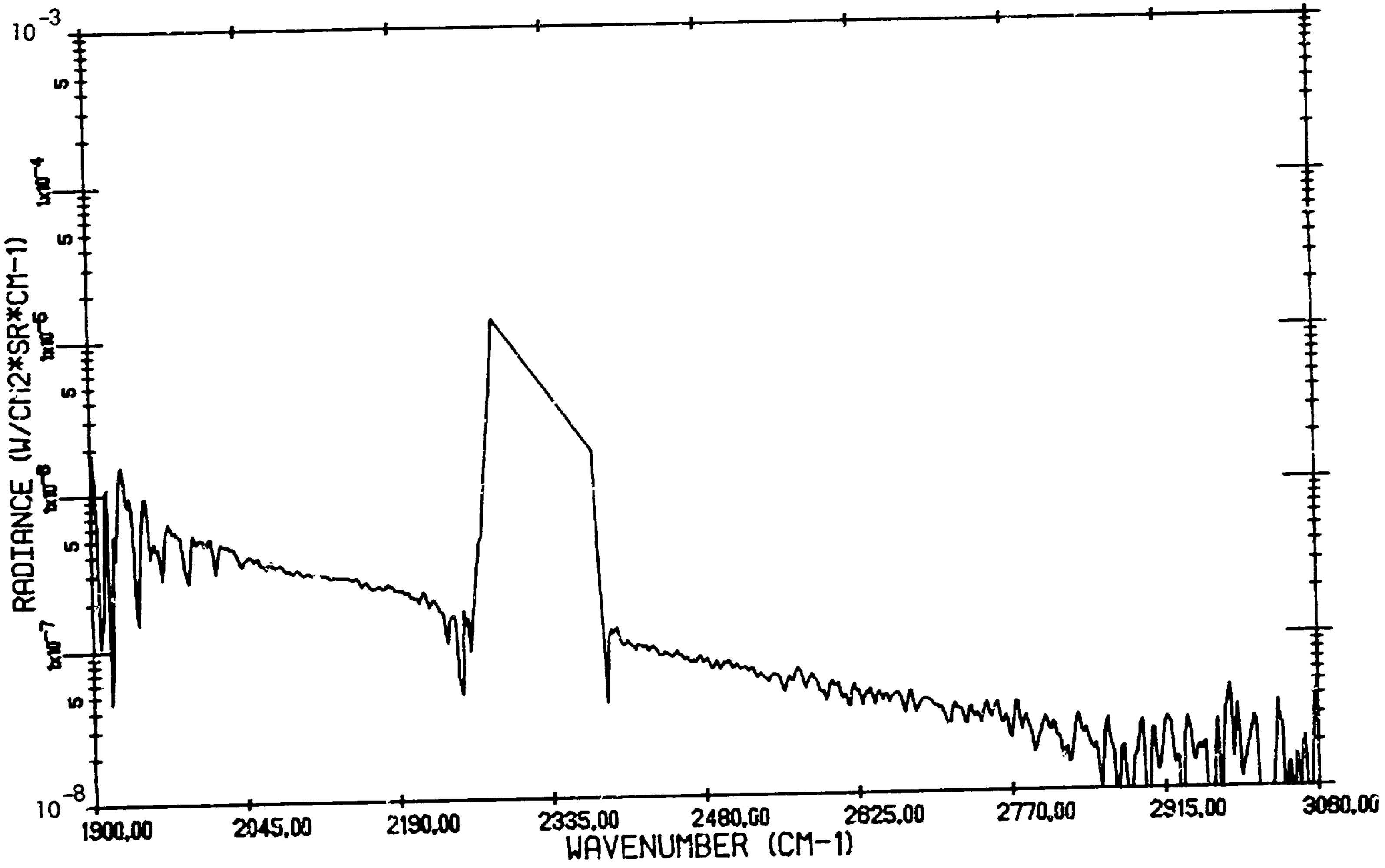

CORRECTED BACKGROUND RADIANCE

GARY, INDIANA (816/3) - 14:01:15.5 - HOT COKE OVEN

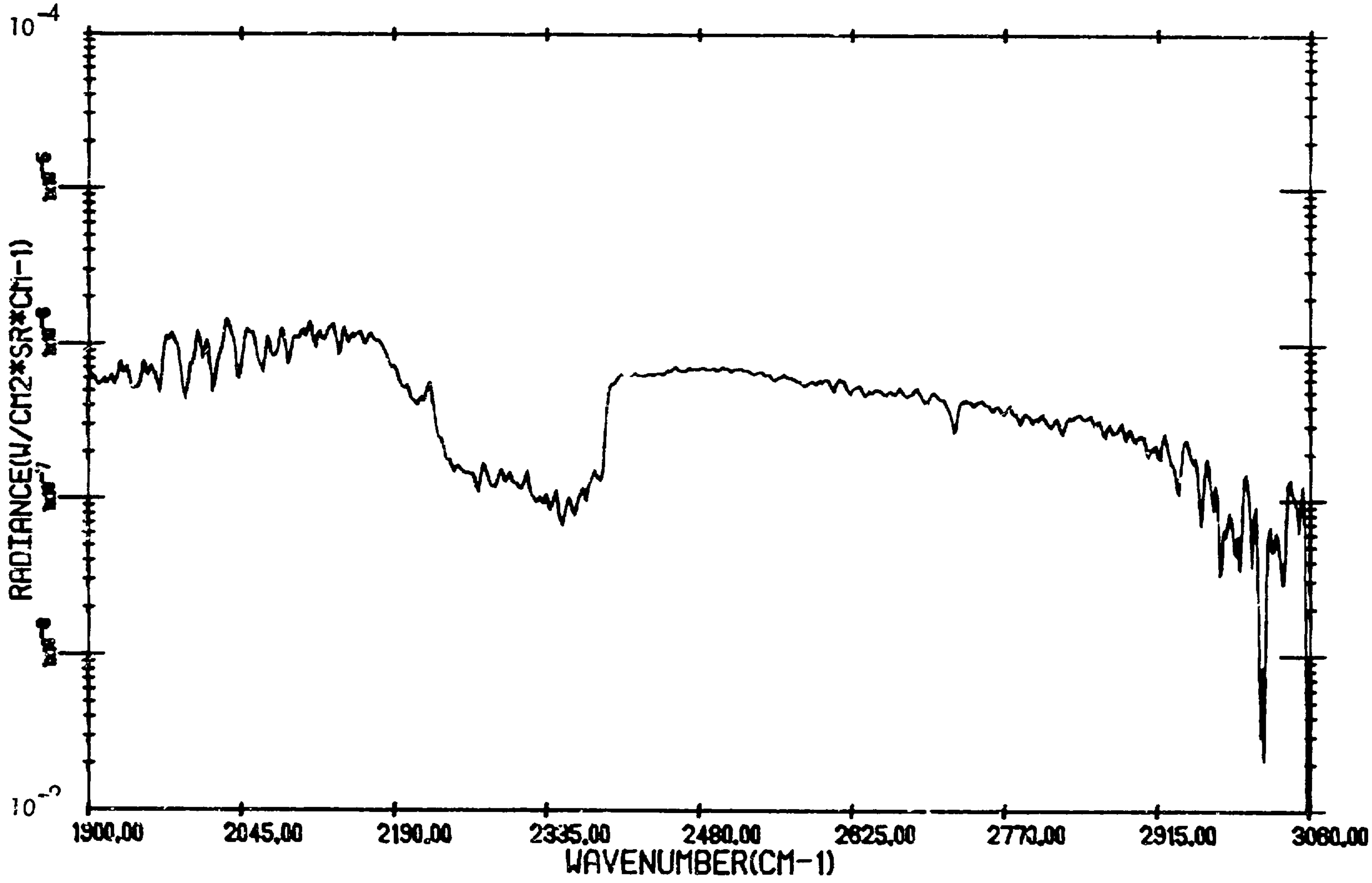

TARGET RADIANCE

GARY, INDIANA (816/3) - 14:01:55.5 - HOT COKE OVEN

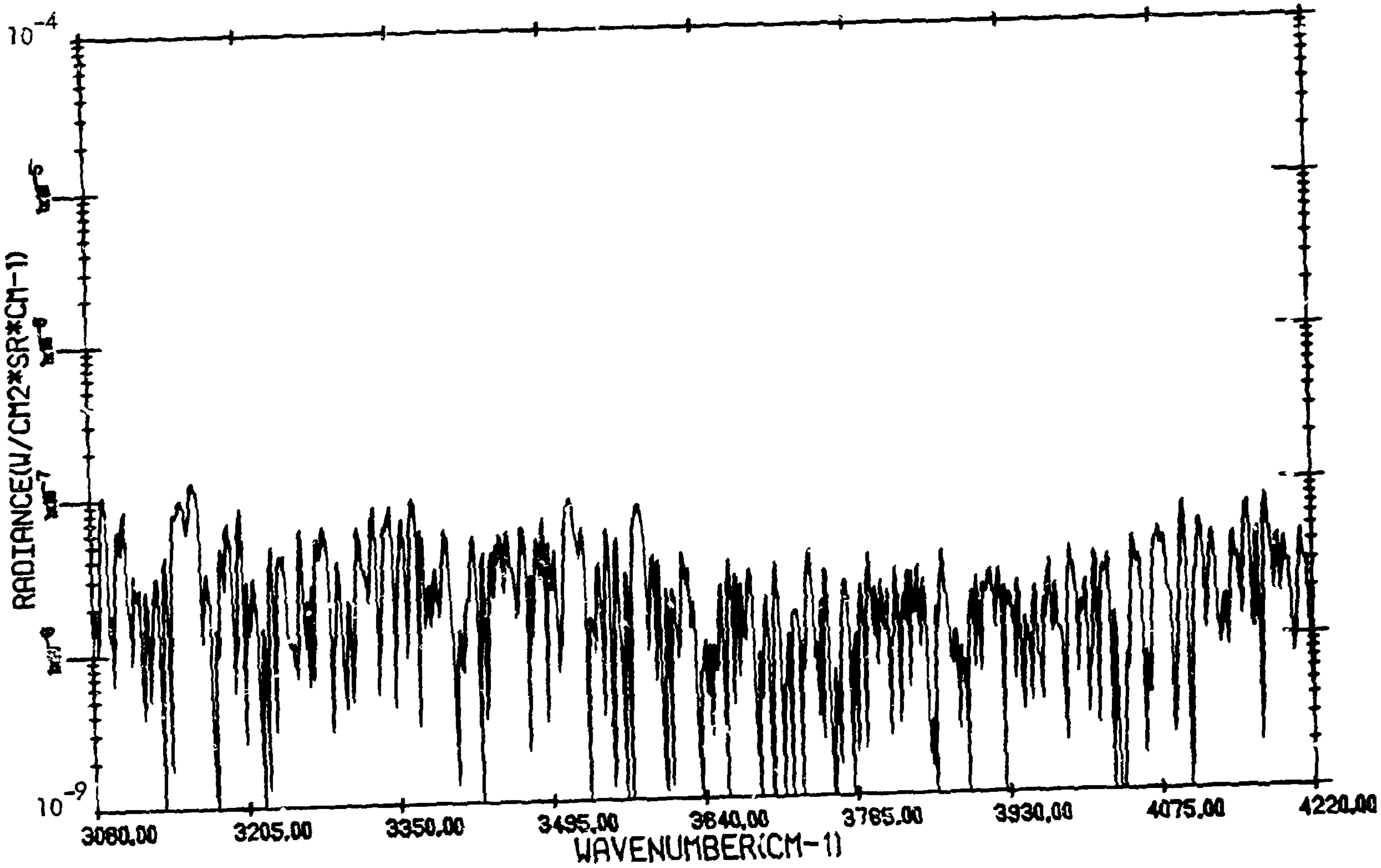

TARGET RADIANCE

GARY, INDIANA (816/3) - 14:01:55.5 - HOT COKE OVEN

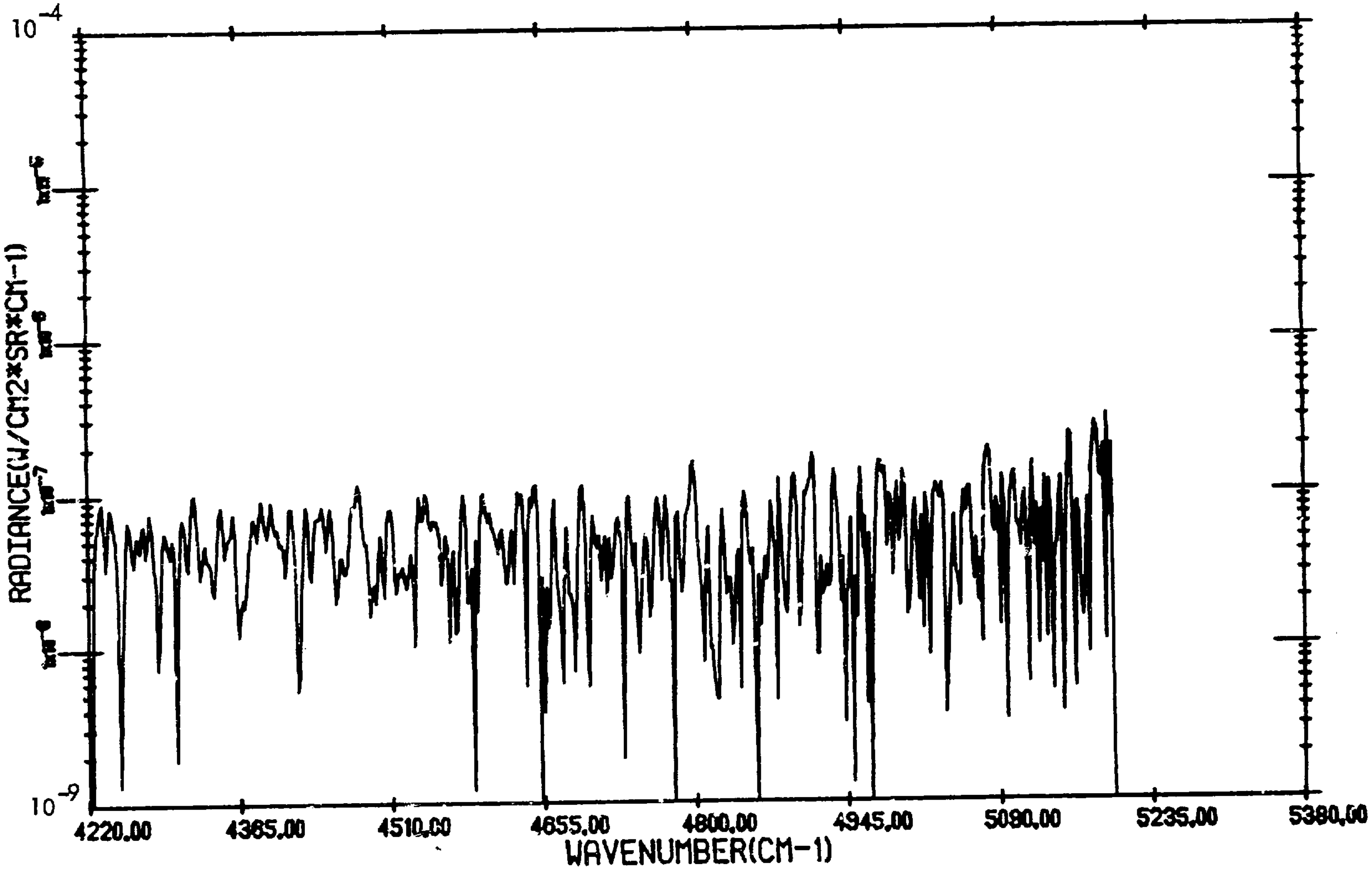

TARGET RADIANCE

(816/3)

GARY, INDIANA - 14:01:55.5 - HOT COKE OVEN (WITH ATMOSPHERIC TRANSMITTANCE CORRECTION)

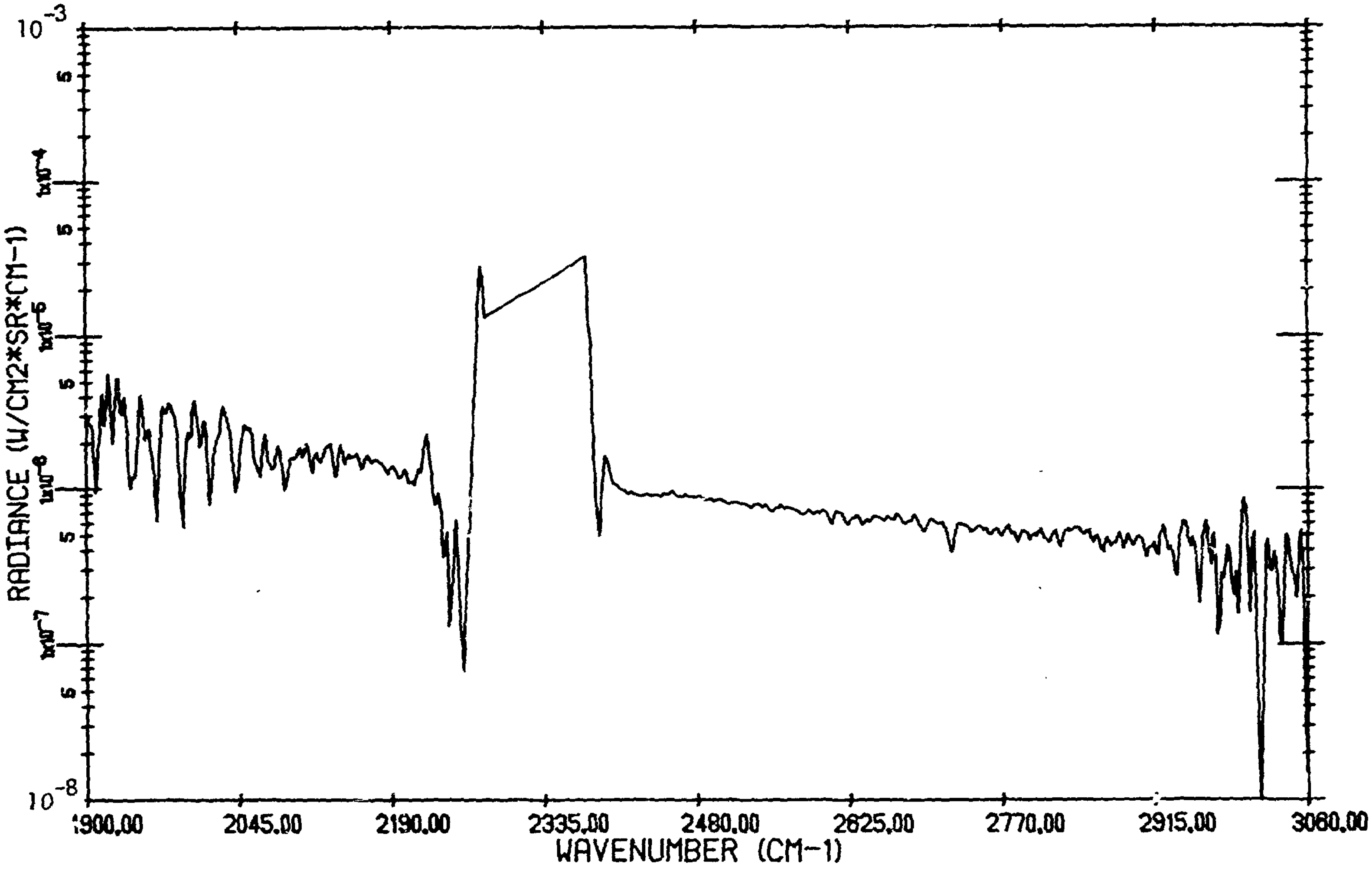

GARY, INDIANA (816/3) - 14:05:49.6 - BACKGROUND

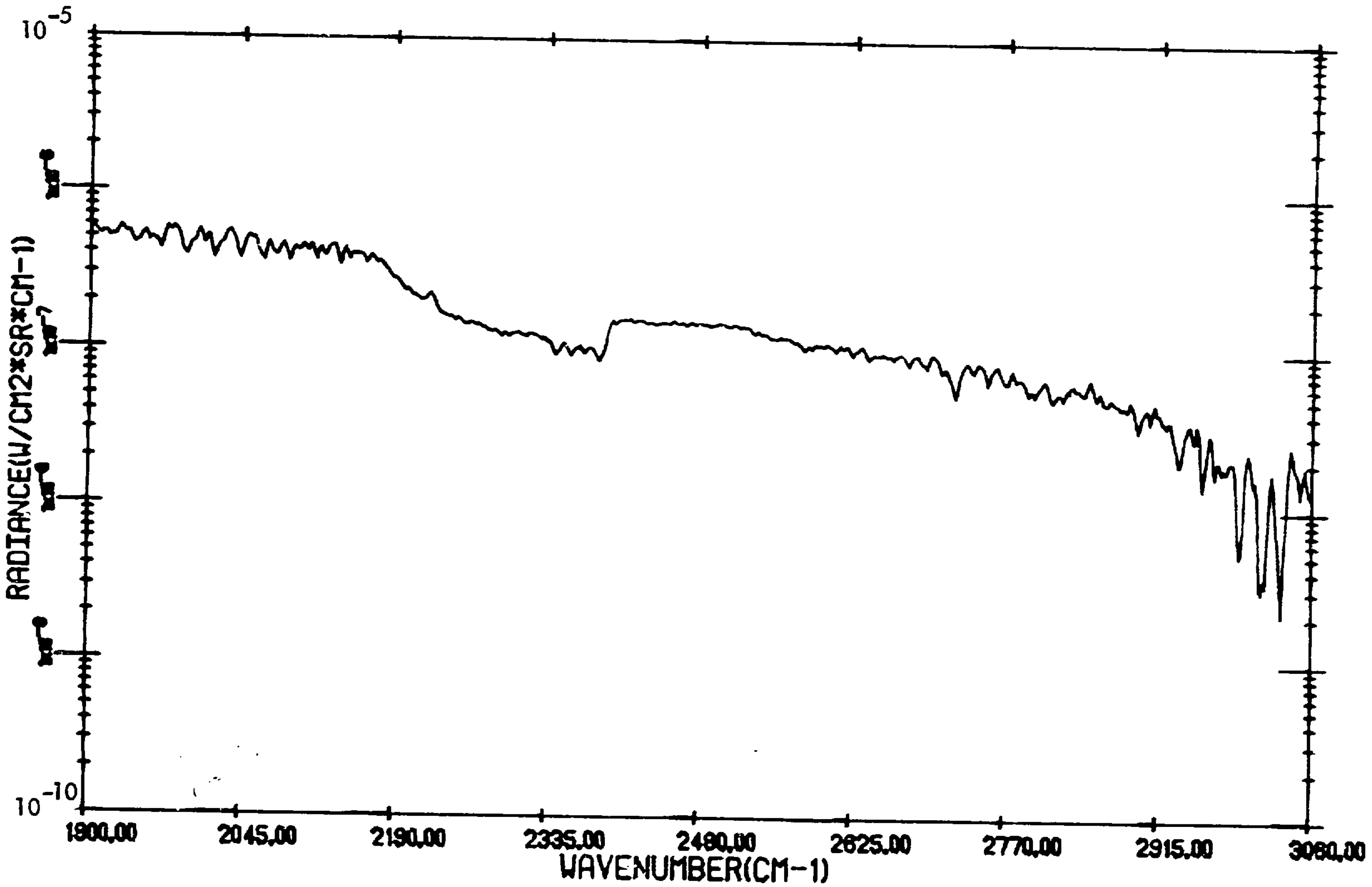

BACKGROUND RADIANCE

GARY, INDIANA *816/31 - 14:05:49.6 - BACKGROUND

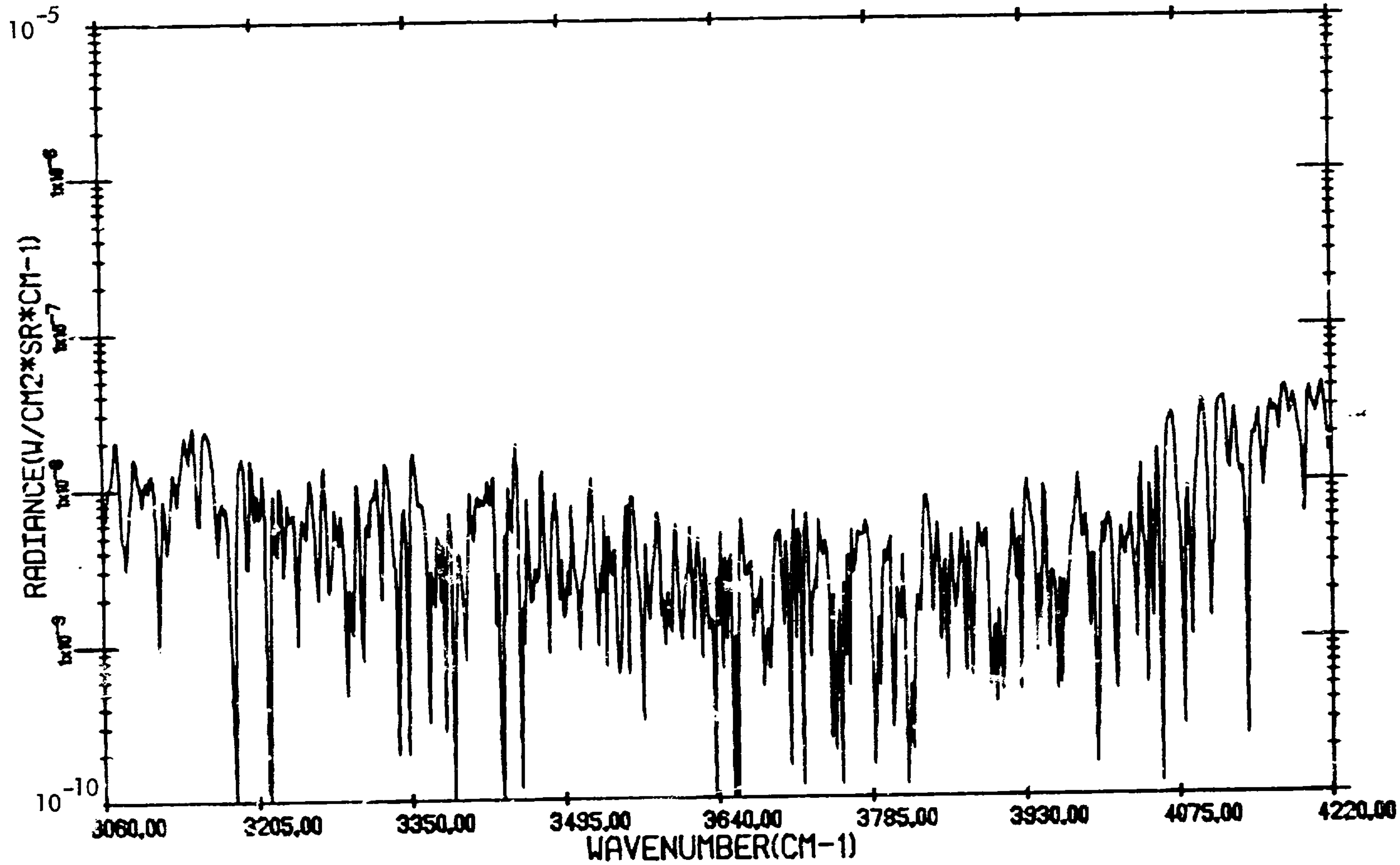

BACKGROUND RADIANCE

GARY, INDIANA (816/3) - 14:05:49.6 - BACKGROUND

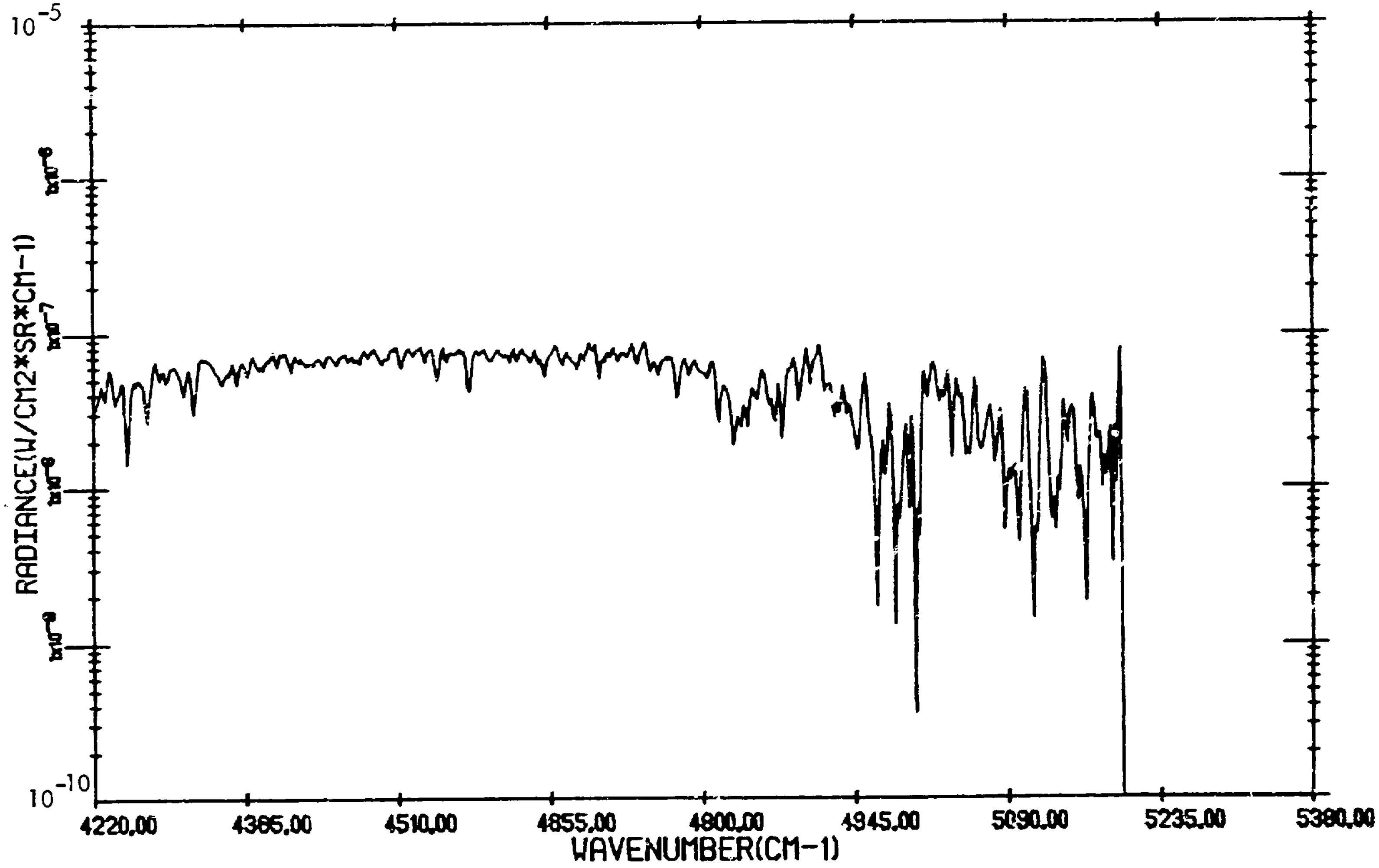

BACKGROUND RADIANCE

(816/3)

GARY, INDIANA - 14:05:49.6 - BACKGROUND (WITH ATMOSPHERIC TRANSMITTANCE CORRECTION)

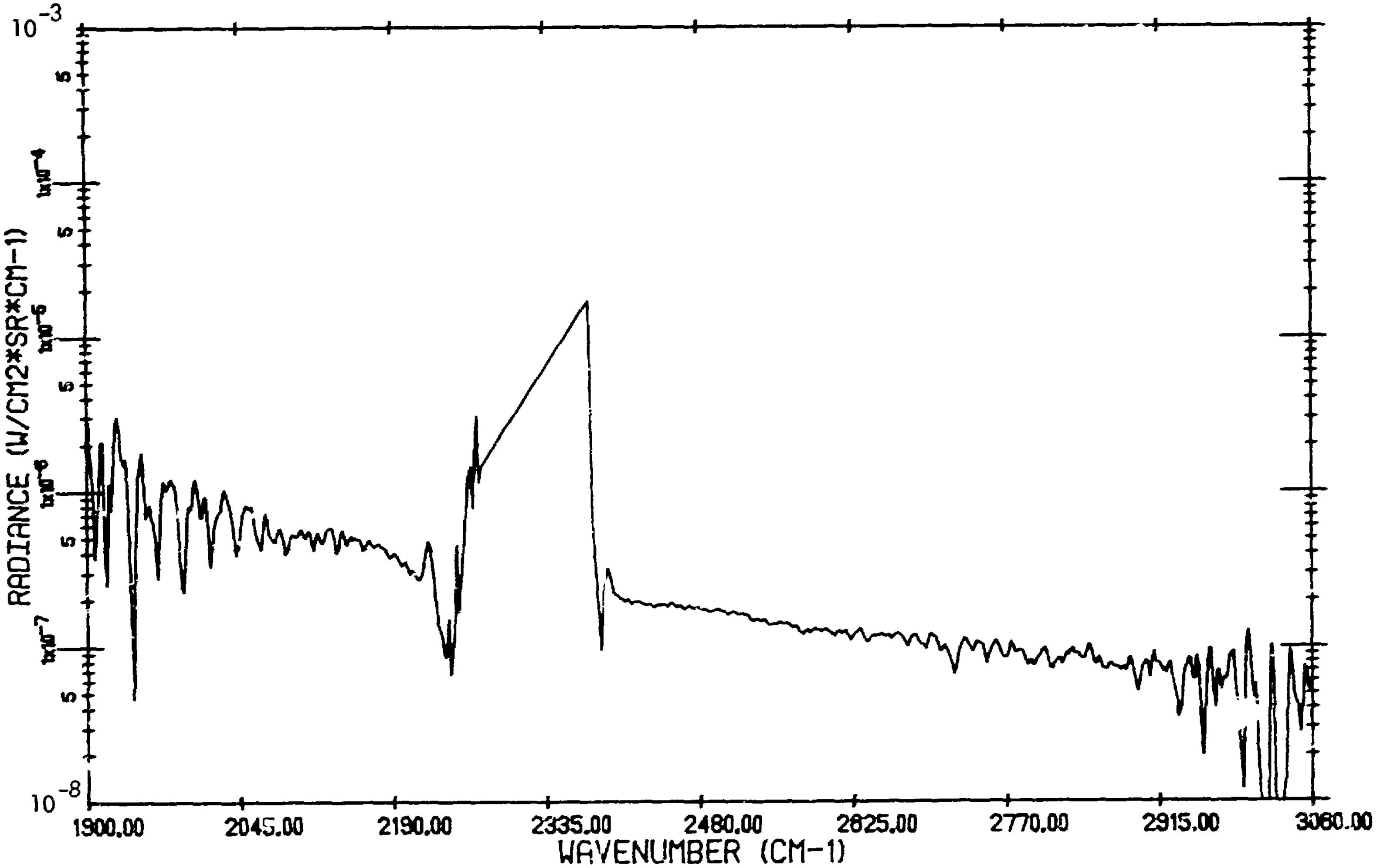

CORRECTED BACKGROUND RADIANCE

GARY, INDIANA (816/3) - 14:06:33.8 - STACK FLARE (GAS BURN-OFF)

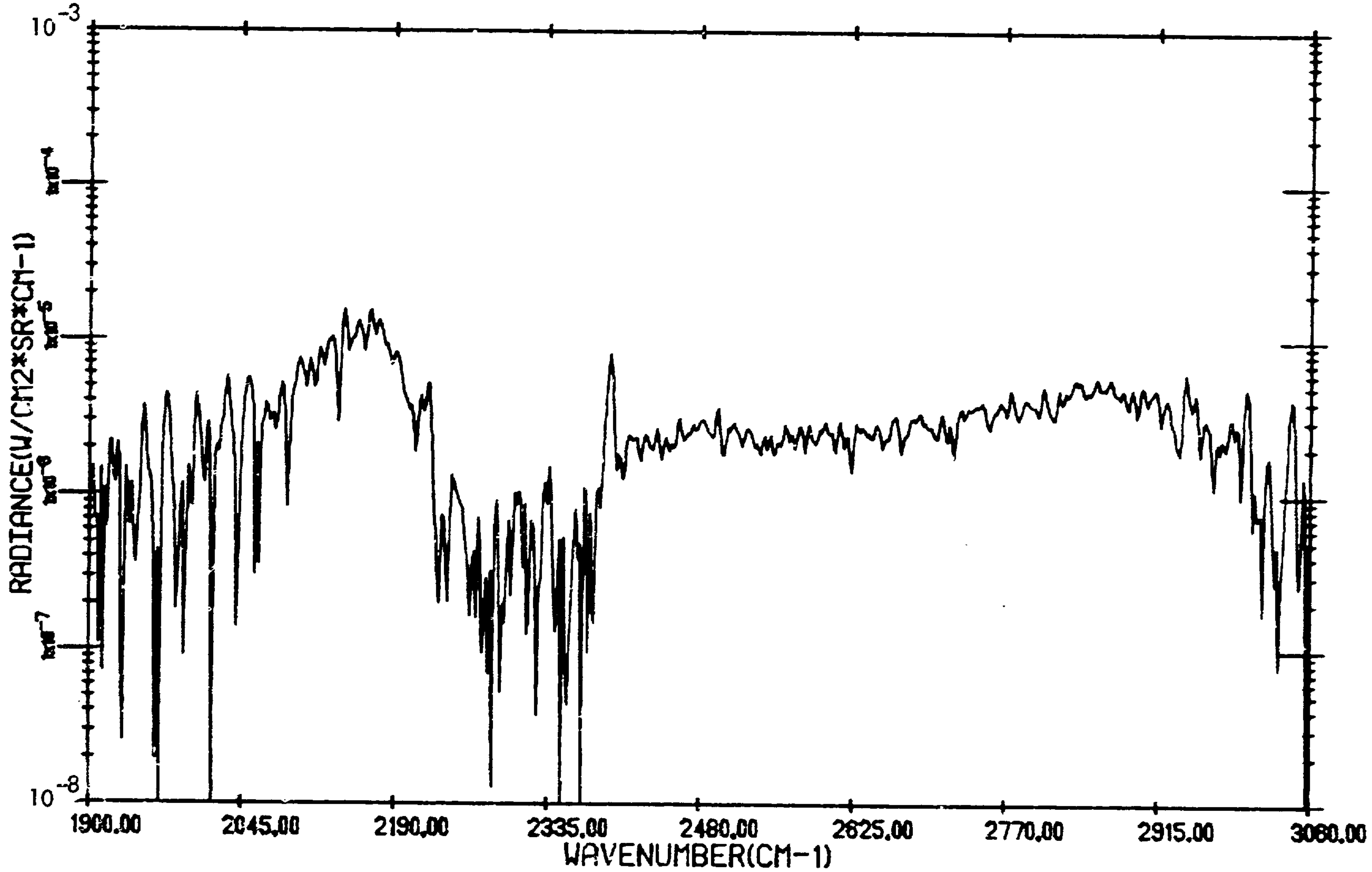

TARGET RADIANCE

GARY, INDIANA (8̇16/3) - 14:06:33.8 - STACK FLARE (GAS BURN-OFF)

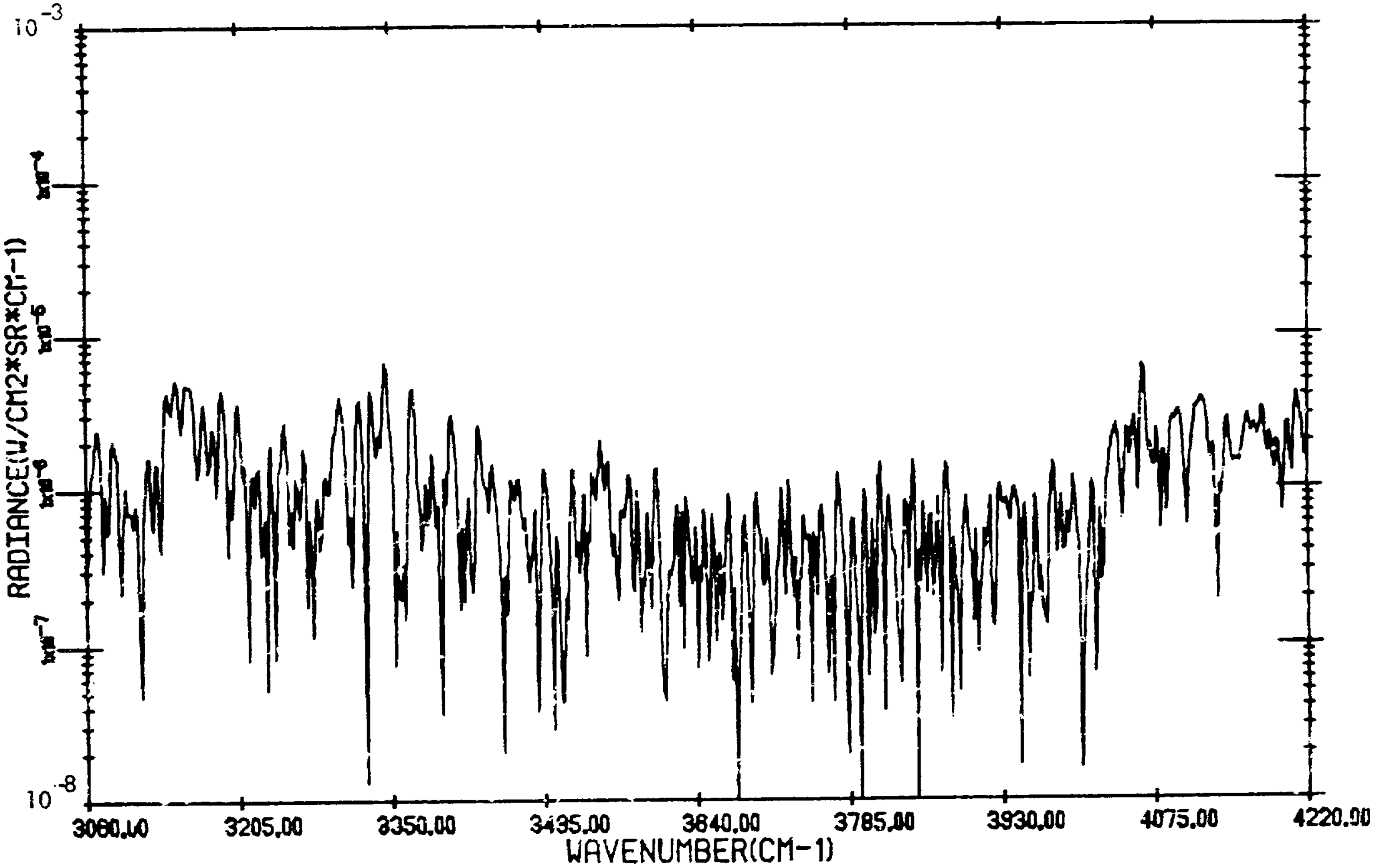

TARGET RADIANCE

GARY, INDIANA (816/3) - 14:06:33.8 - STACK FLARE (GAS BURN-OFF)

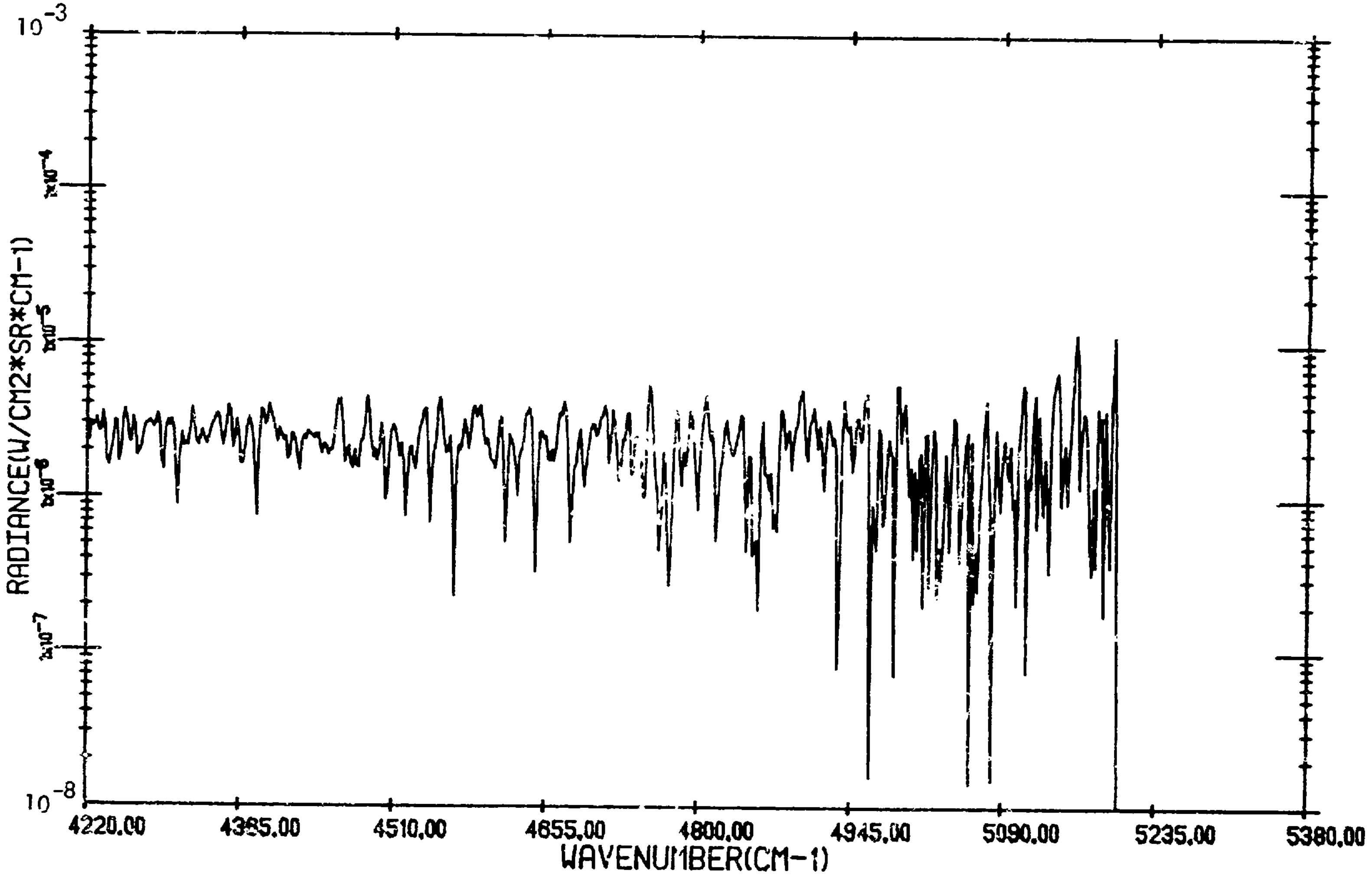

TARGET RADIANCE

(816/3)

GARY, INDIANA - 14:06:33.8 - STACK FLARE (GAS BURN-OFF) (WITH ATMOSPHERIC TRANSMITTANCE CORRECTION)

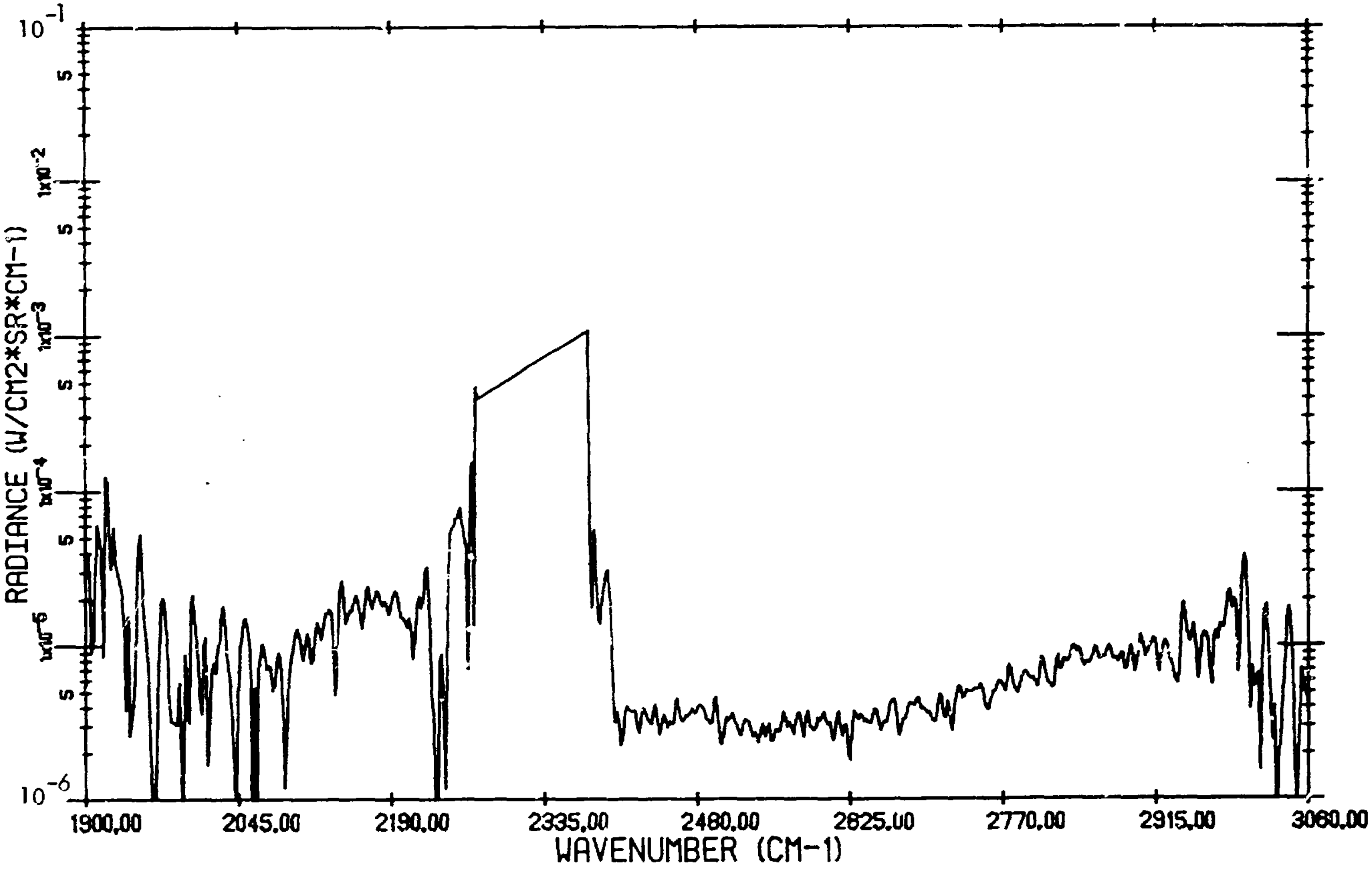

CORRECTED TARGET RADIANCE

GARY, INDIANA (816/4) - 14:15:7.9 - STACKS OF ROLLING MILL

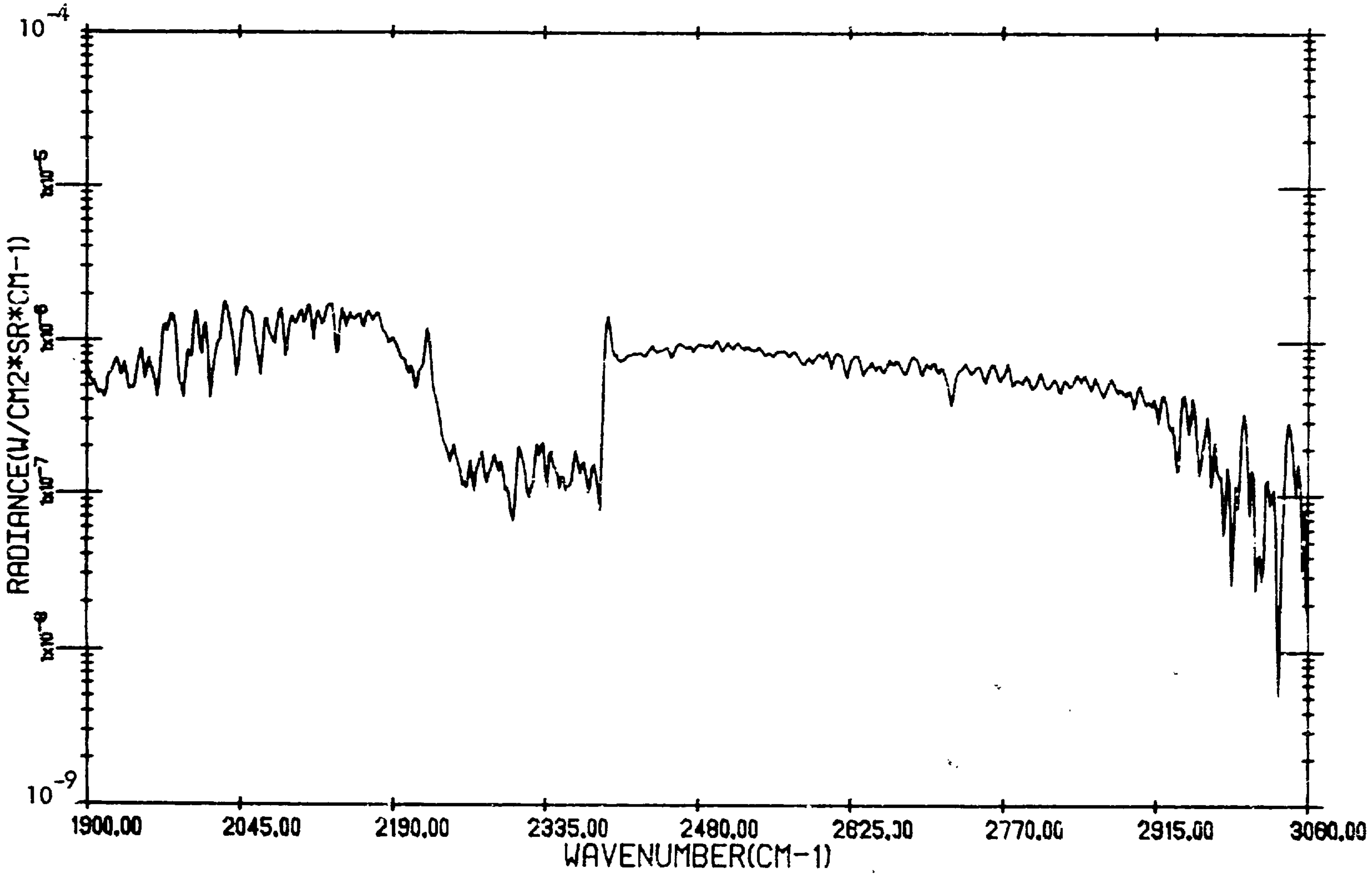

TARGET RADIANCE

GARY, INDIANA (816/4) - 14:15:7.9 - STACKS OF ROLLING MILL

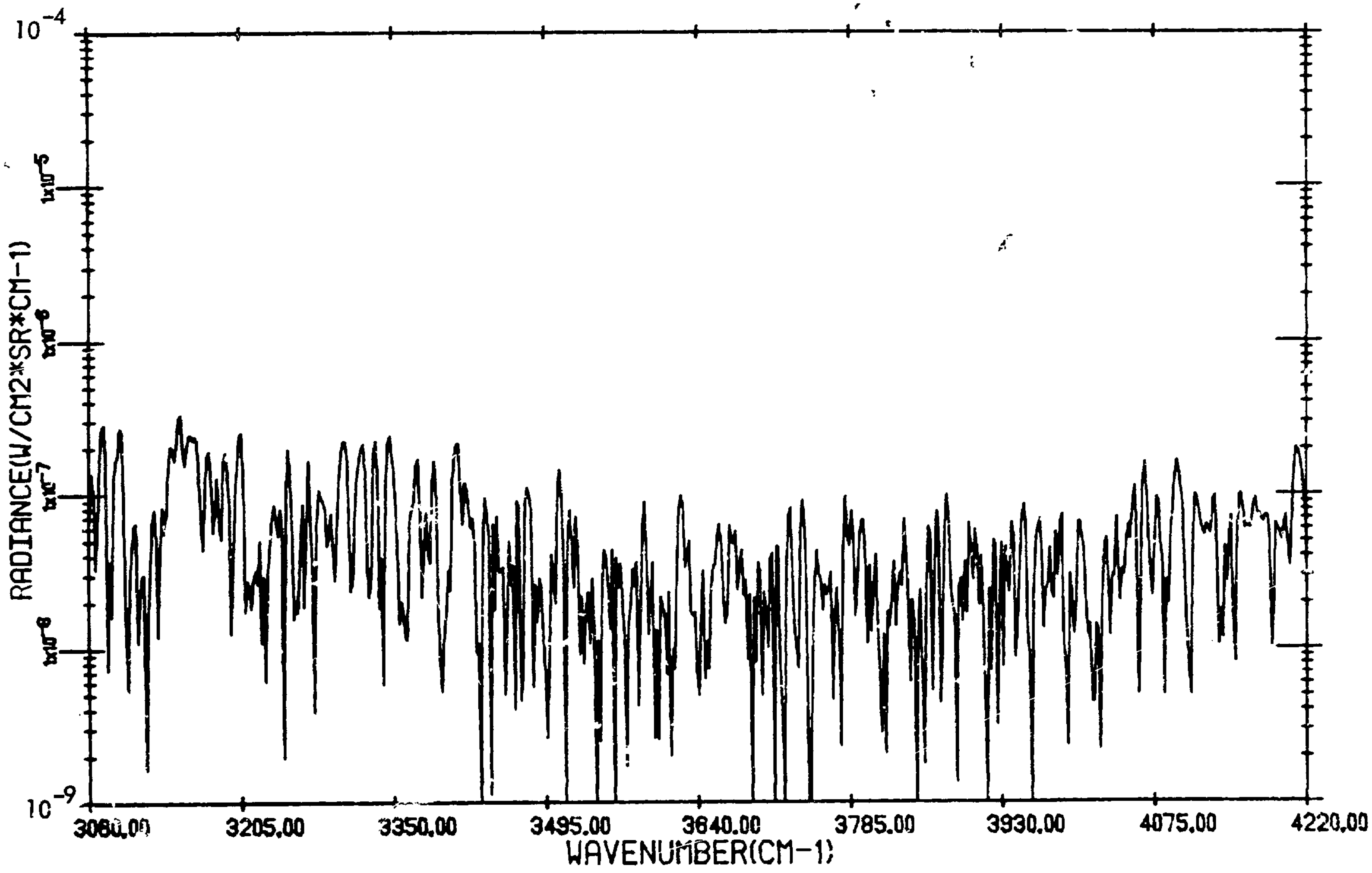

TARGET RADIANCE

GARY, INDIANA (816/4) - 14:15:7.9 - STACKS OF ROLLING MILL

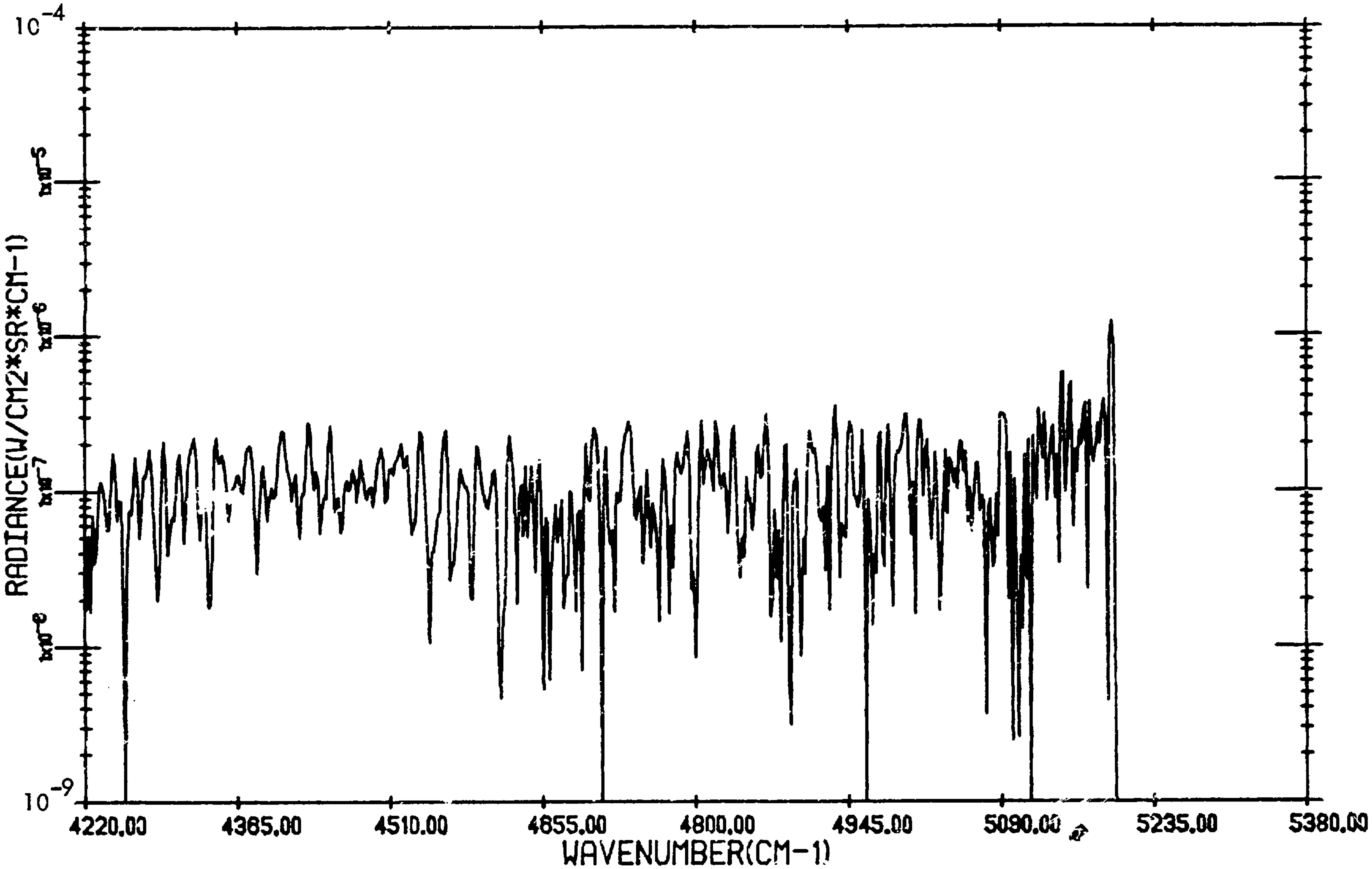

TARGET RADIANCE

(816/4)

GARY, INDIANA - 14:15:7.9 - STACKS OF ROLLING MILL (WITH ATMOSPHERIC TRANSMITTANCE CORRECTION)

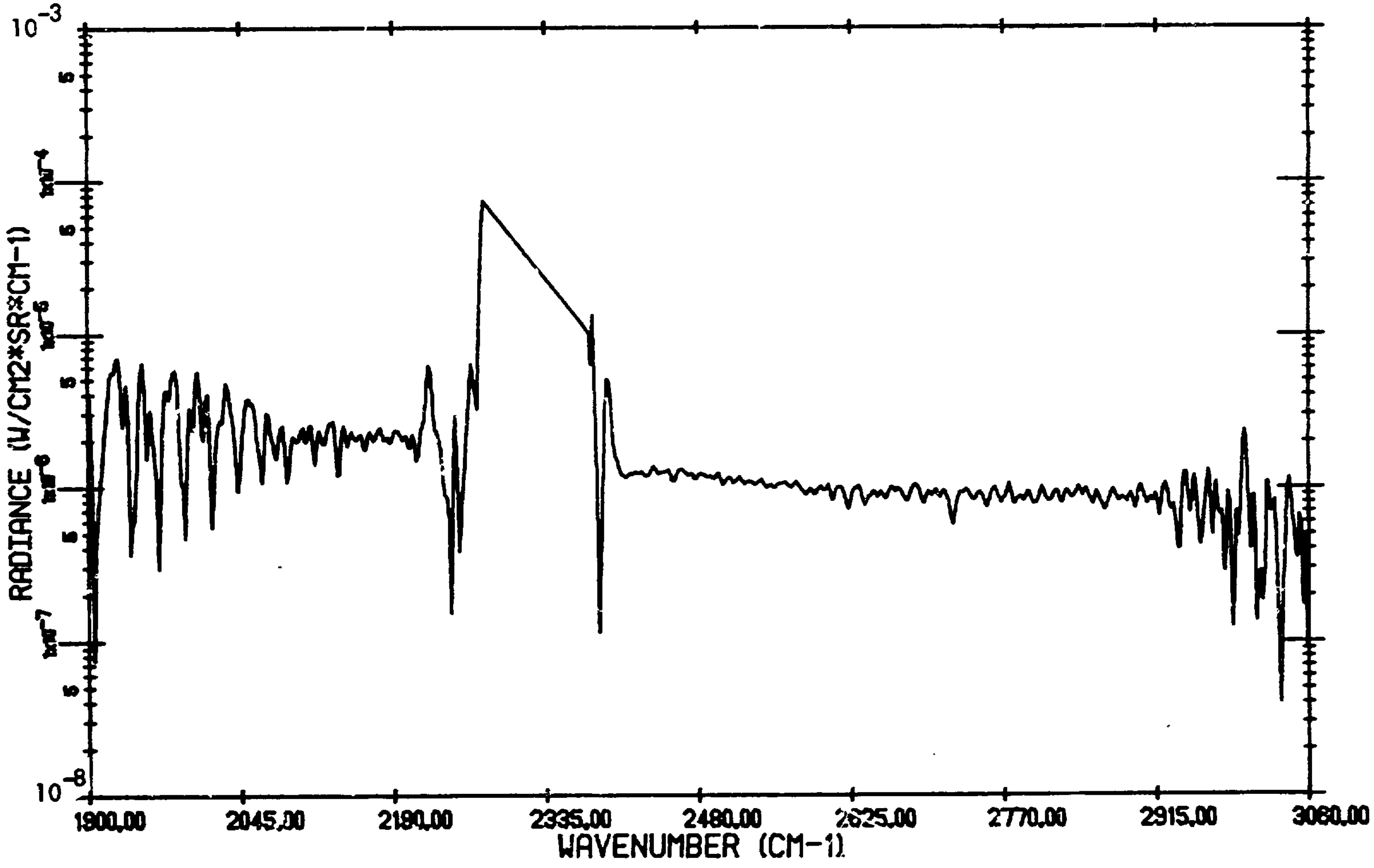

CORRECTED TARGET RADIANCE

GARY, INDIANA (816/4) - 14:15:42.2 - BACKGROUND

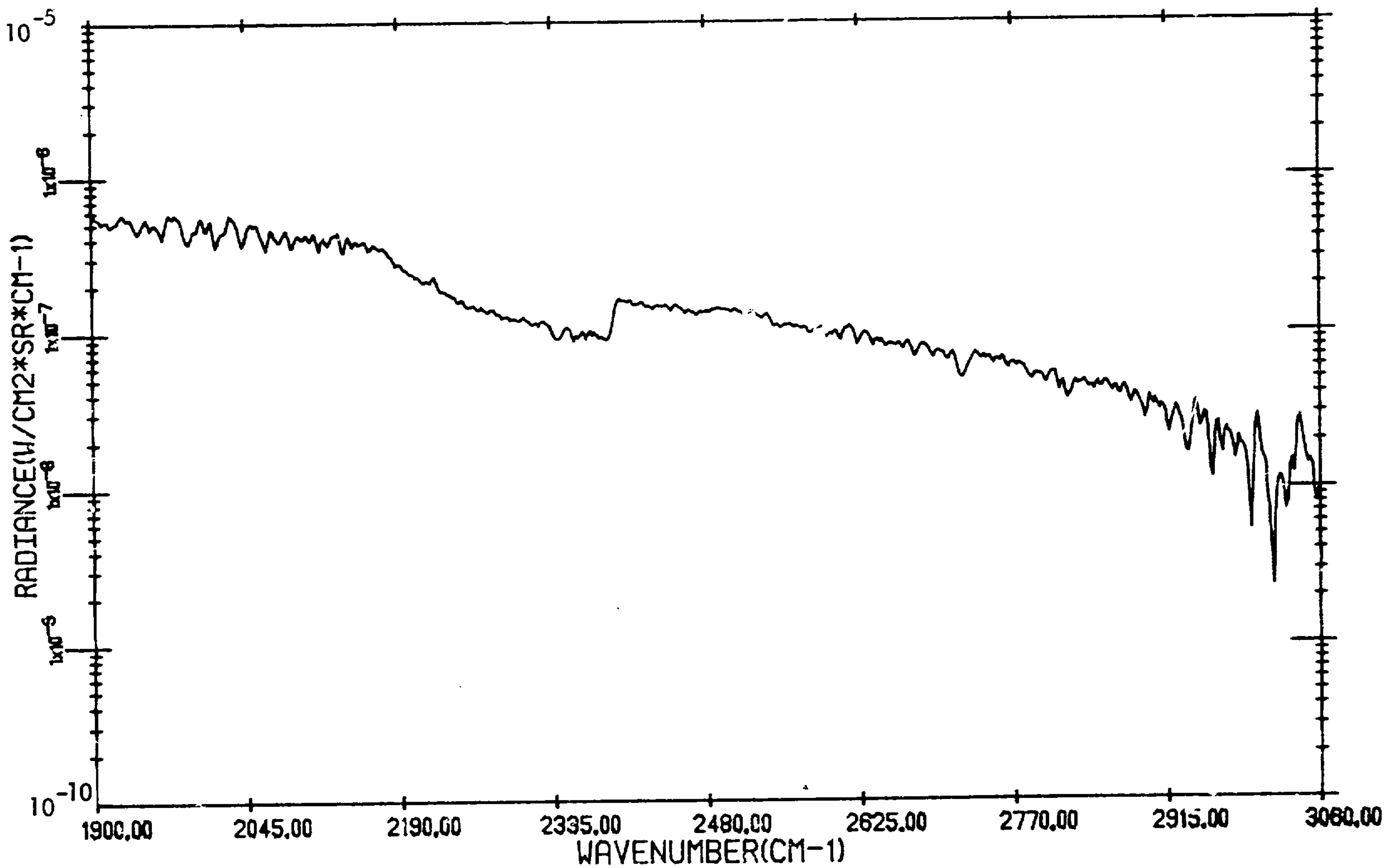

BACKGROUND RADIANCE

GARY, INDIANA (816/4) - 14:15:42.2 - BACKGROUND

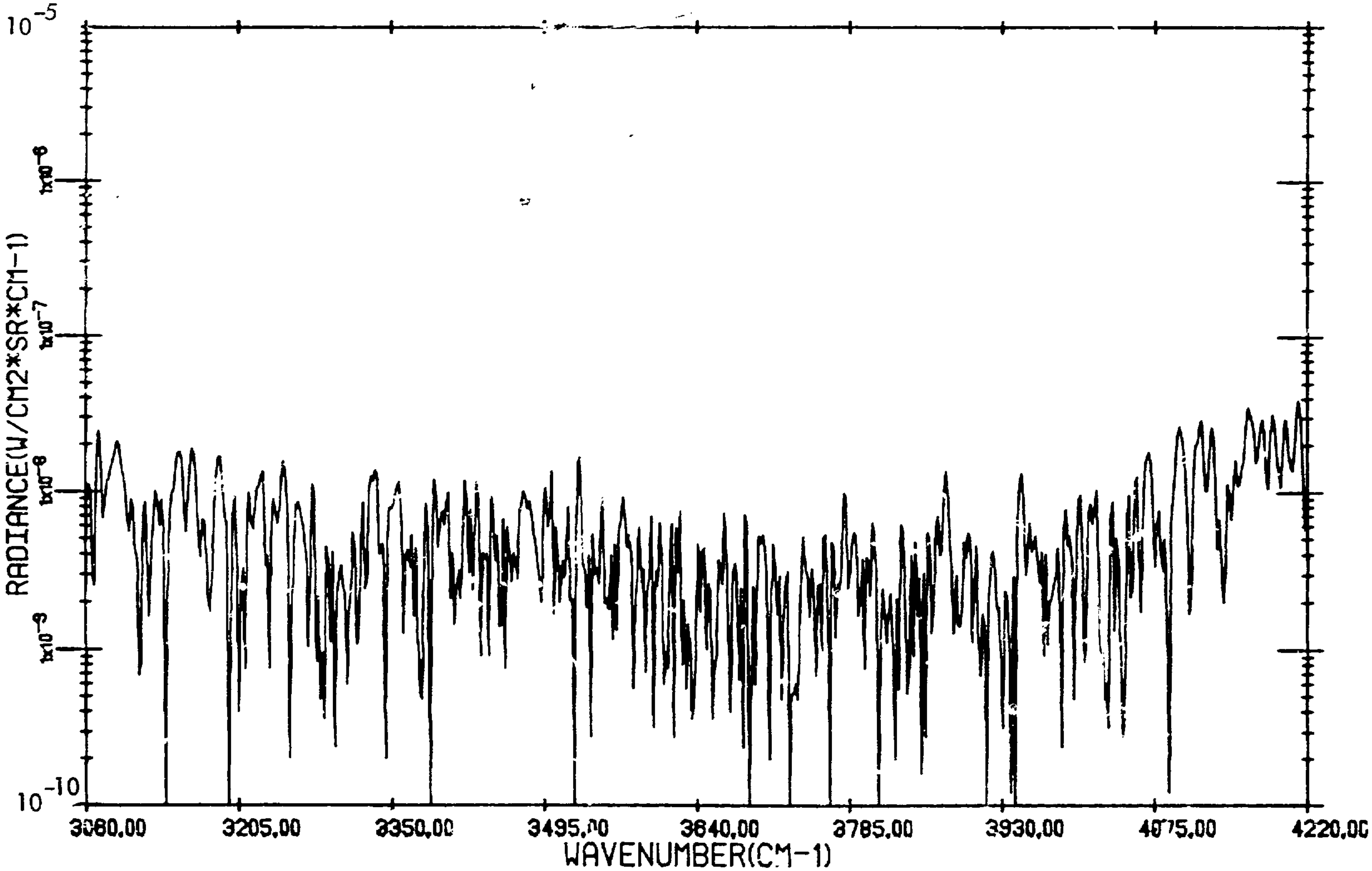

BACKGROUND RADIANCE

GARY, INDIANA (816/4) - 14:15:42.2 - BACKGROUND

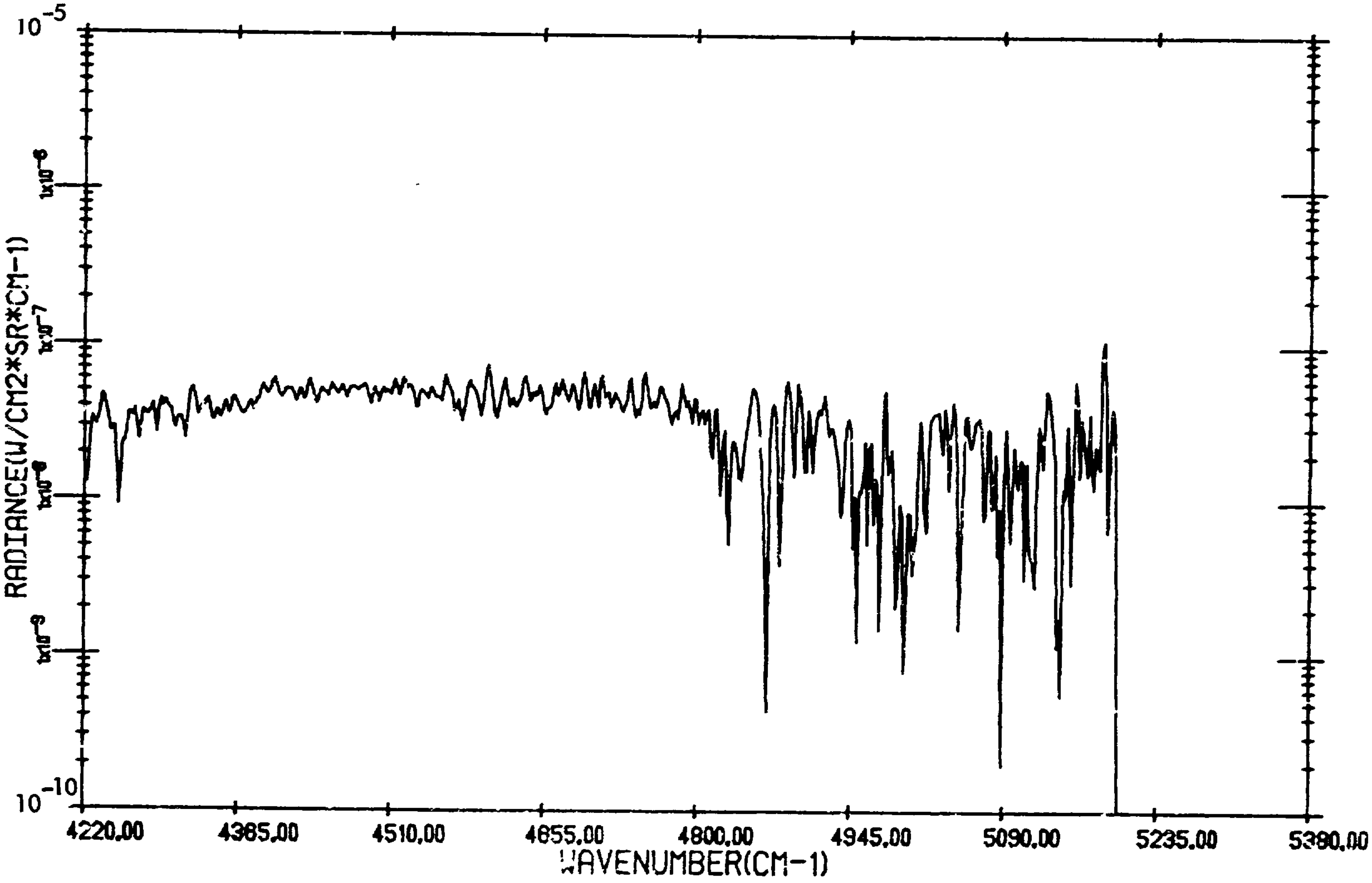

BACKGROUND RADIANCE

(816/4)

GARY, INDIANA - 14:15:42.2 - BACKGROUND (WITH ATMOSPHERIC TRANSMITTANCE CALCULATION)

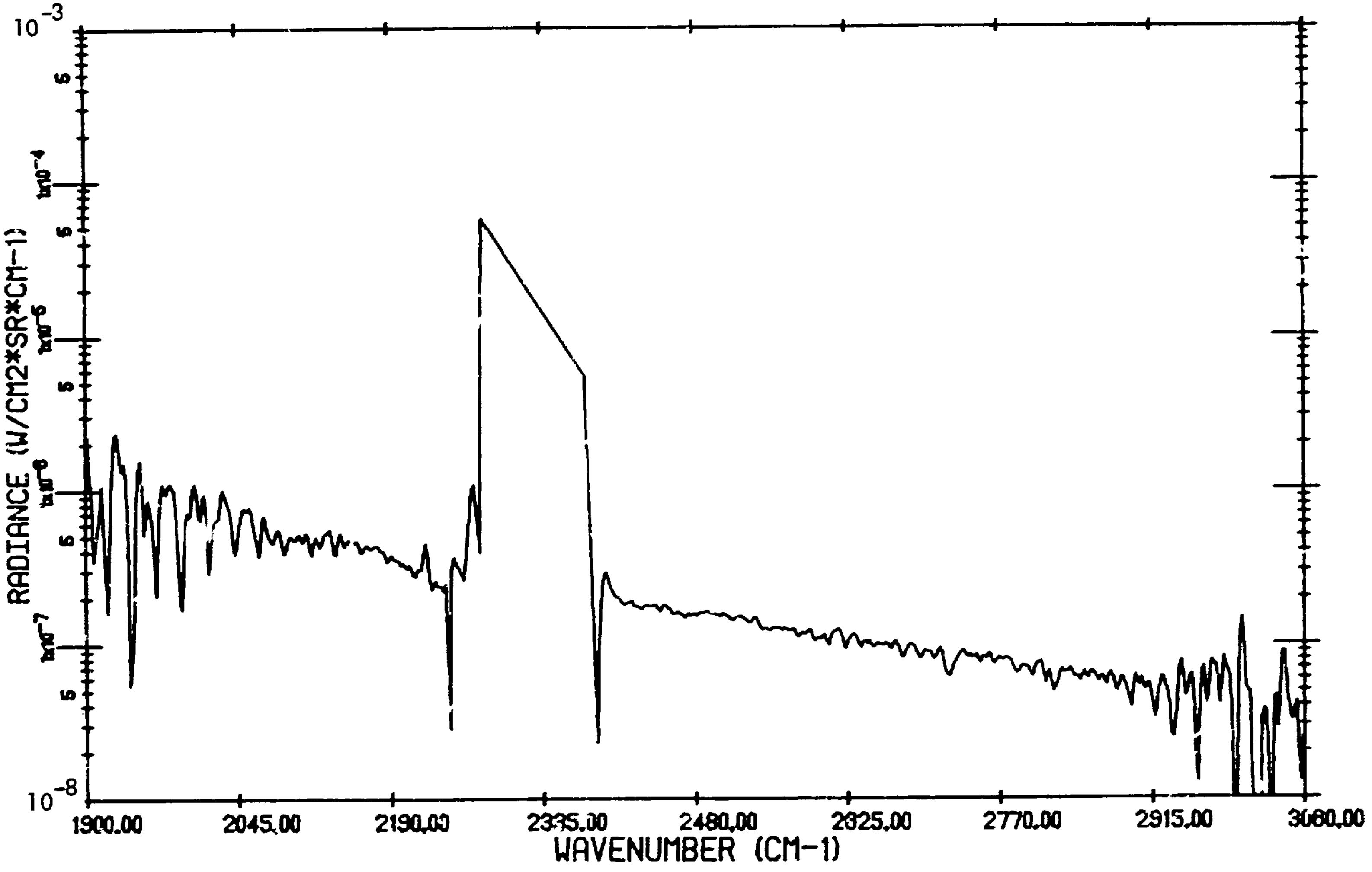

CORRECTED BACKGROUND RADIANCE

WYANDOTTE, MICHIGAN - (816/6) - 15:02:25.0 - BLAST FURNACE

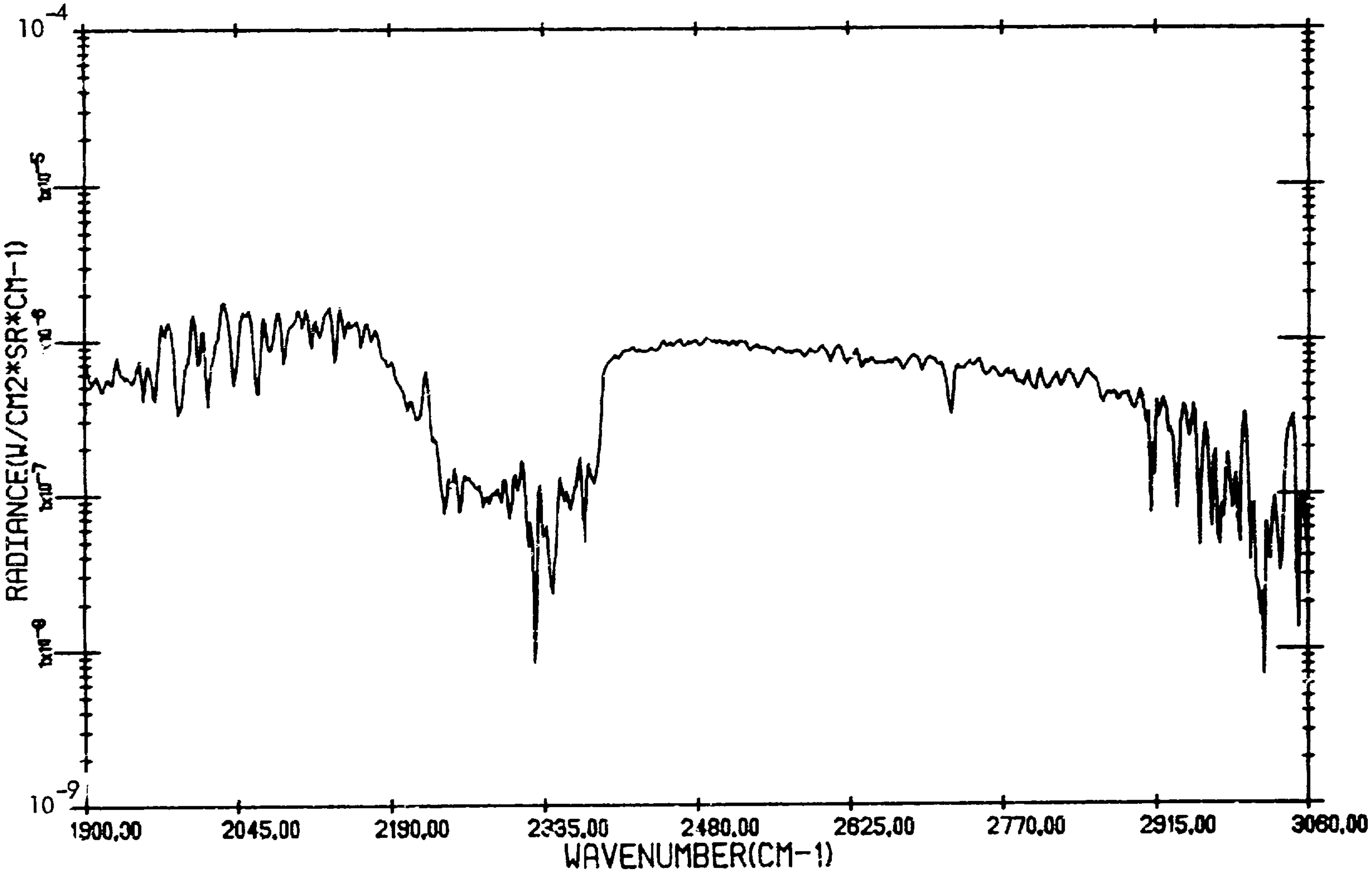

TARGET RADIANCE

WYANDOTTE, MICHIGAN (816/6) - 15:02:25.0 - BLAST FURNACE

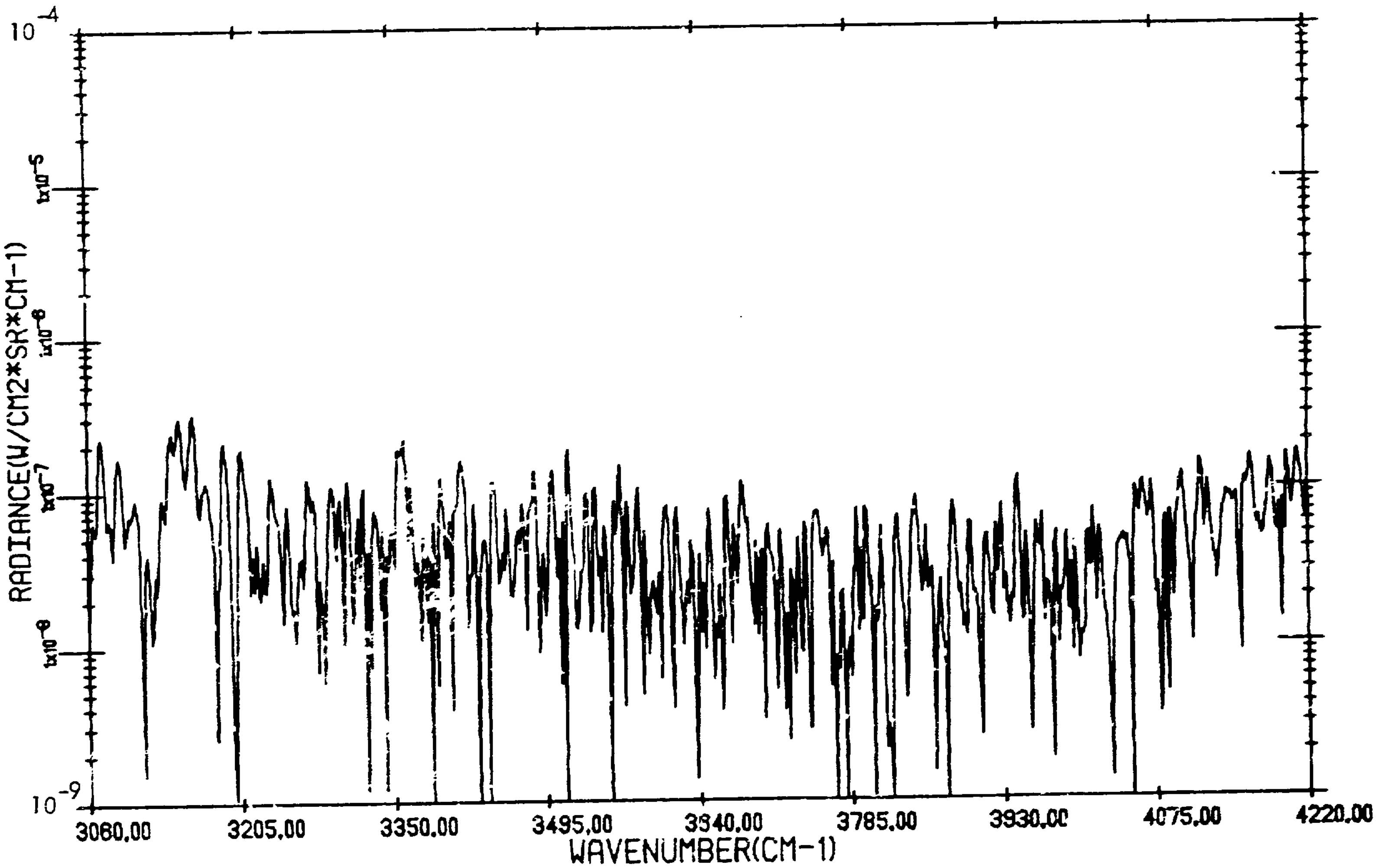

TARGET RADIANCE

WYANDOTTE, MICHIGAN - (816/6) - 15:02:25.0 - BLAST FURNACE

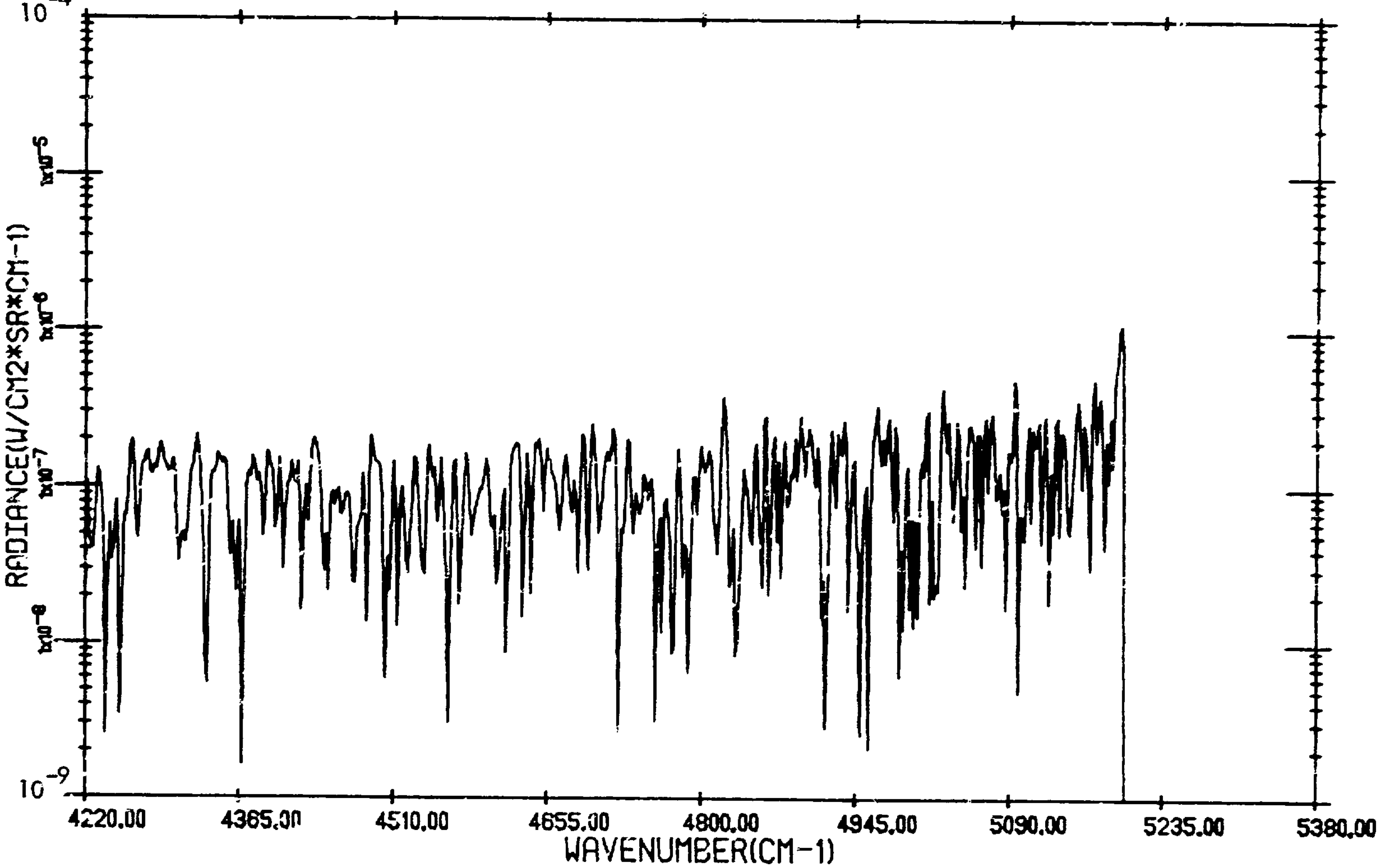

TARGET RADIANCE

(816/6)

WYANDOTTE, MICHIGAN - 15:02:25.0 - BLAST FURNACE (WITH ATMOSPHERIC TRANSMITTANCE CORRECTION)

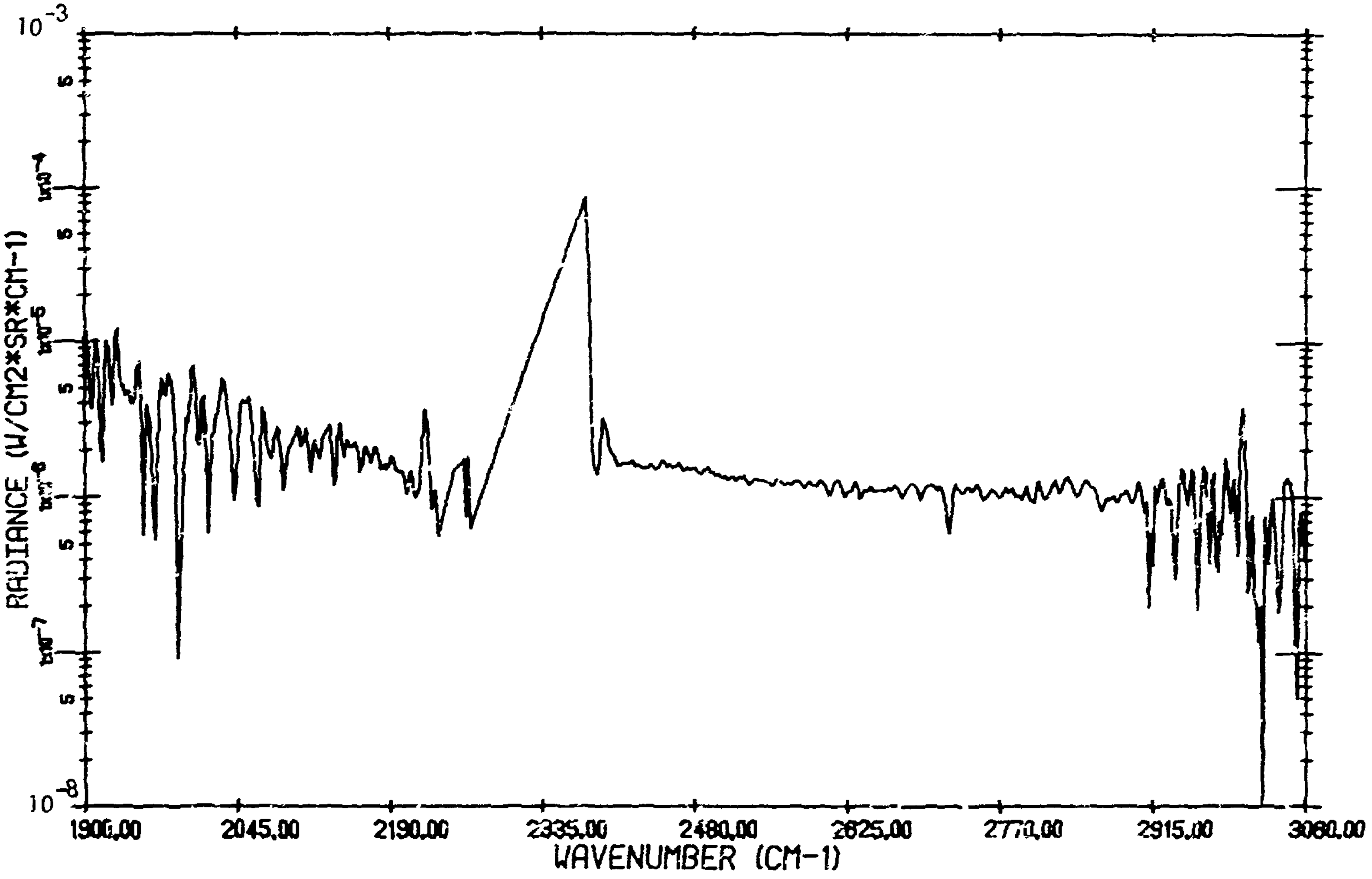

CORRECTED TARGET RADIANCE

WYANDOTTE, MICHIGAN - (816/6) - 15:03:28.3 - BACKGROUND

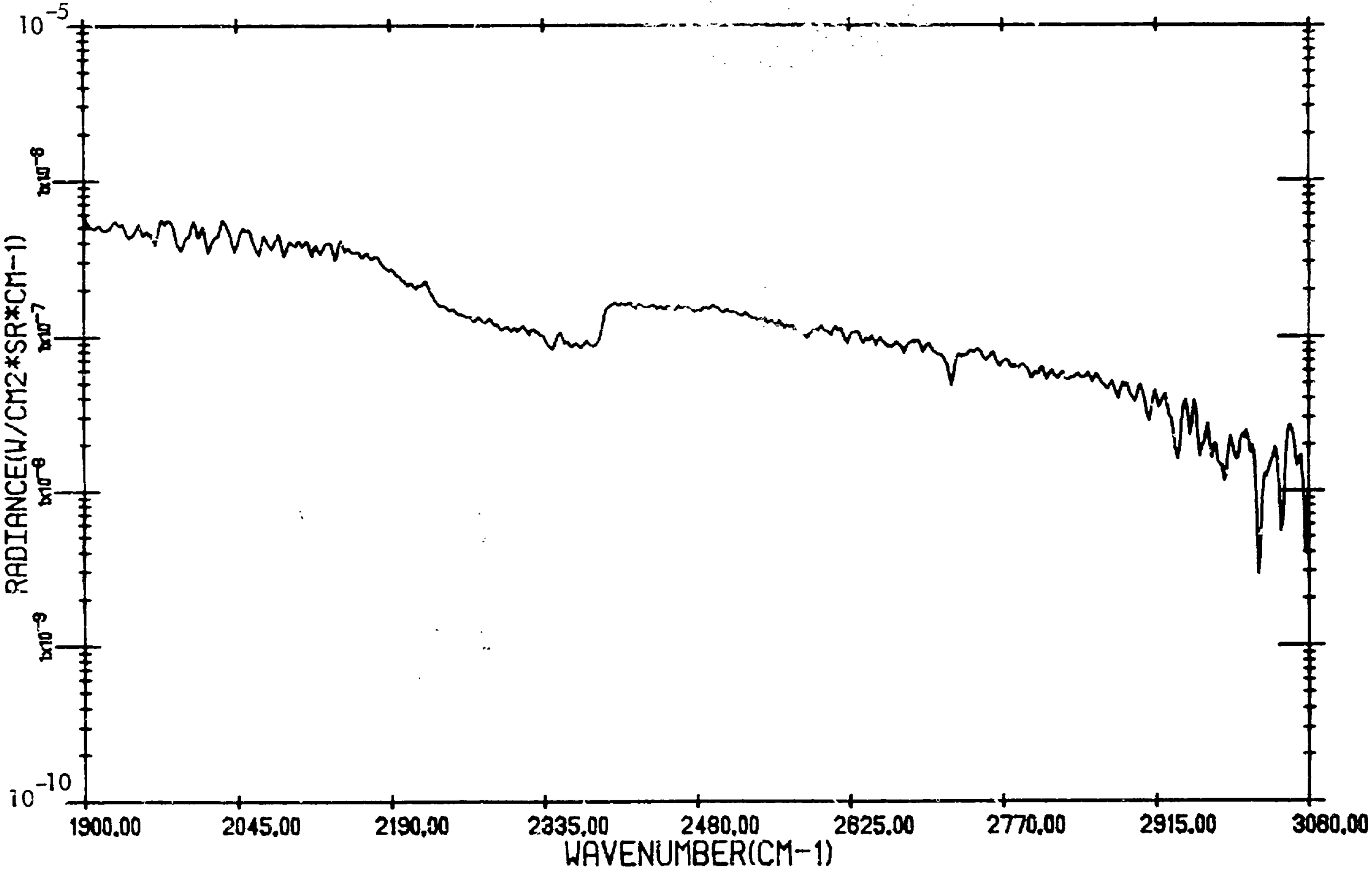

BACKGROUND RADIANCE

WYANDOTTE, MICHIGAN - (816/6) - 15:03:28.3 - BACKGROUND

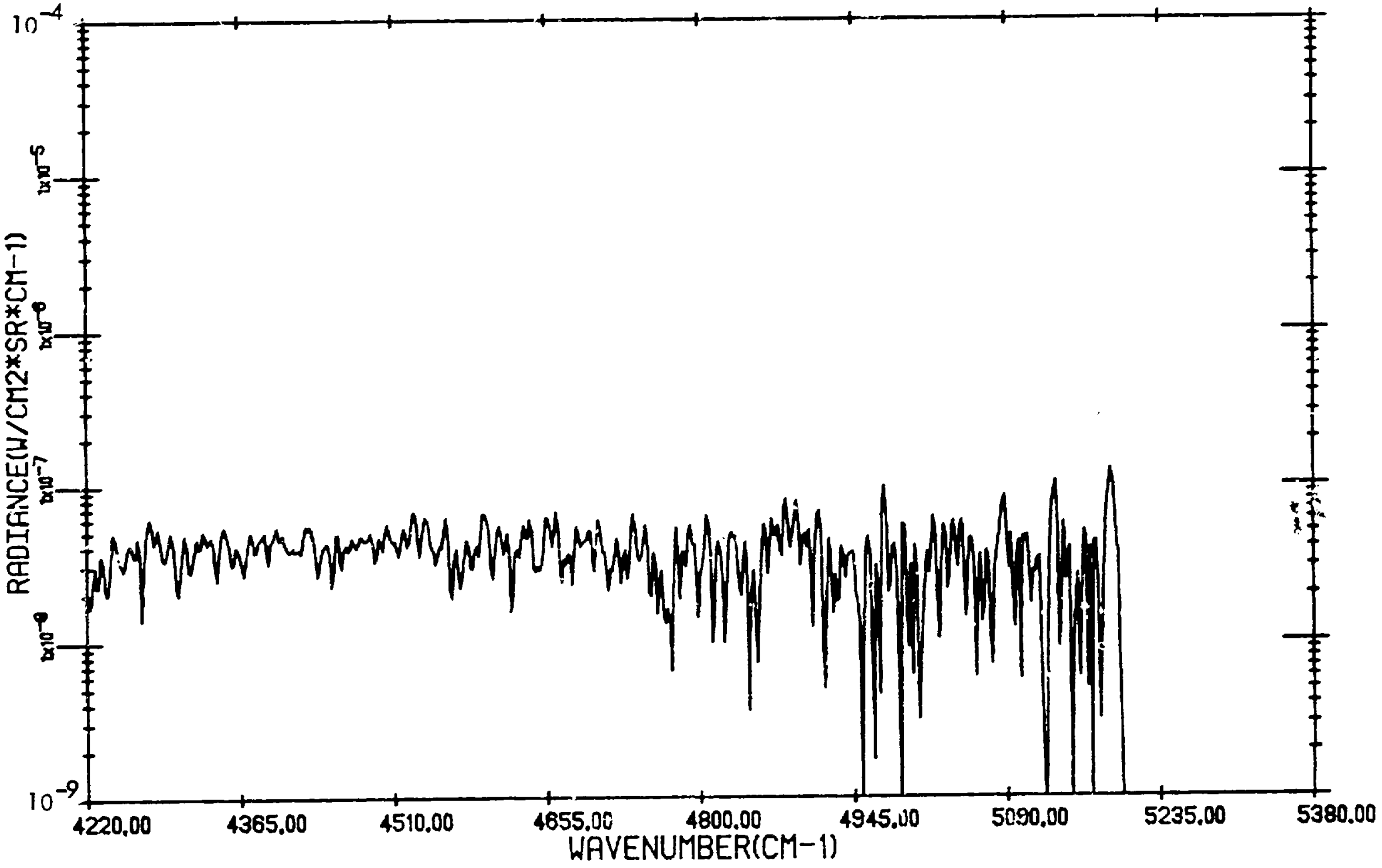

TARGET RADIANCE

WYANDOTTE, MICHIGAN - (816/6) - 15:03:28.3 - BACKGROUND

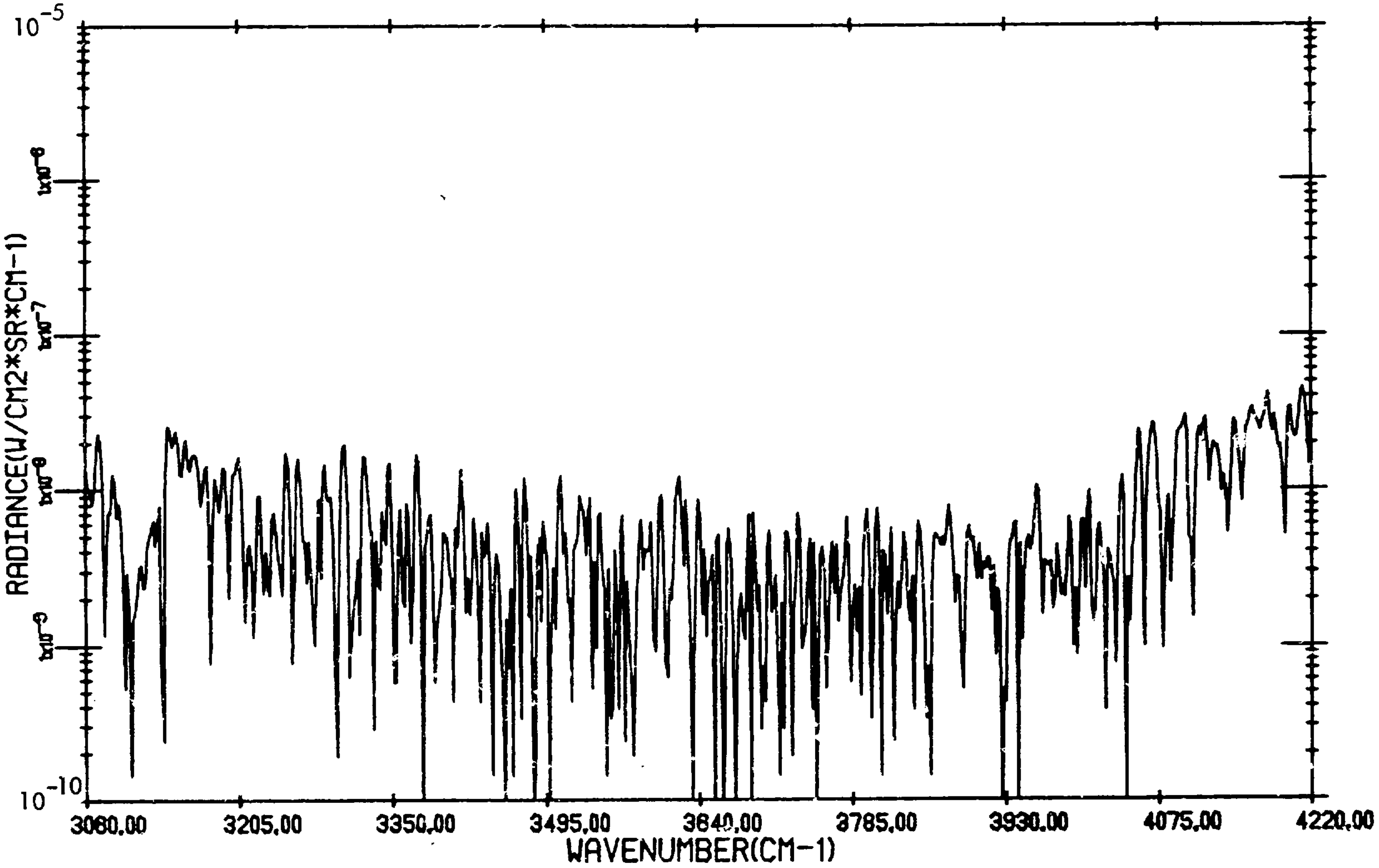

BACKGROUND RADIANCE

WYANDOTTE, MICHIGAN - (816/6) - 15:03:28.3 - BACKGROUND (WITH ATMOSPHERIC
TRANSMITTANCE CORRECTION)

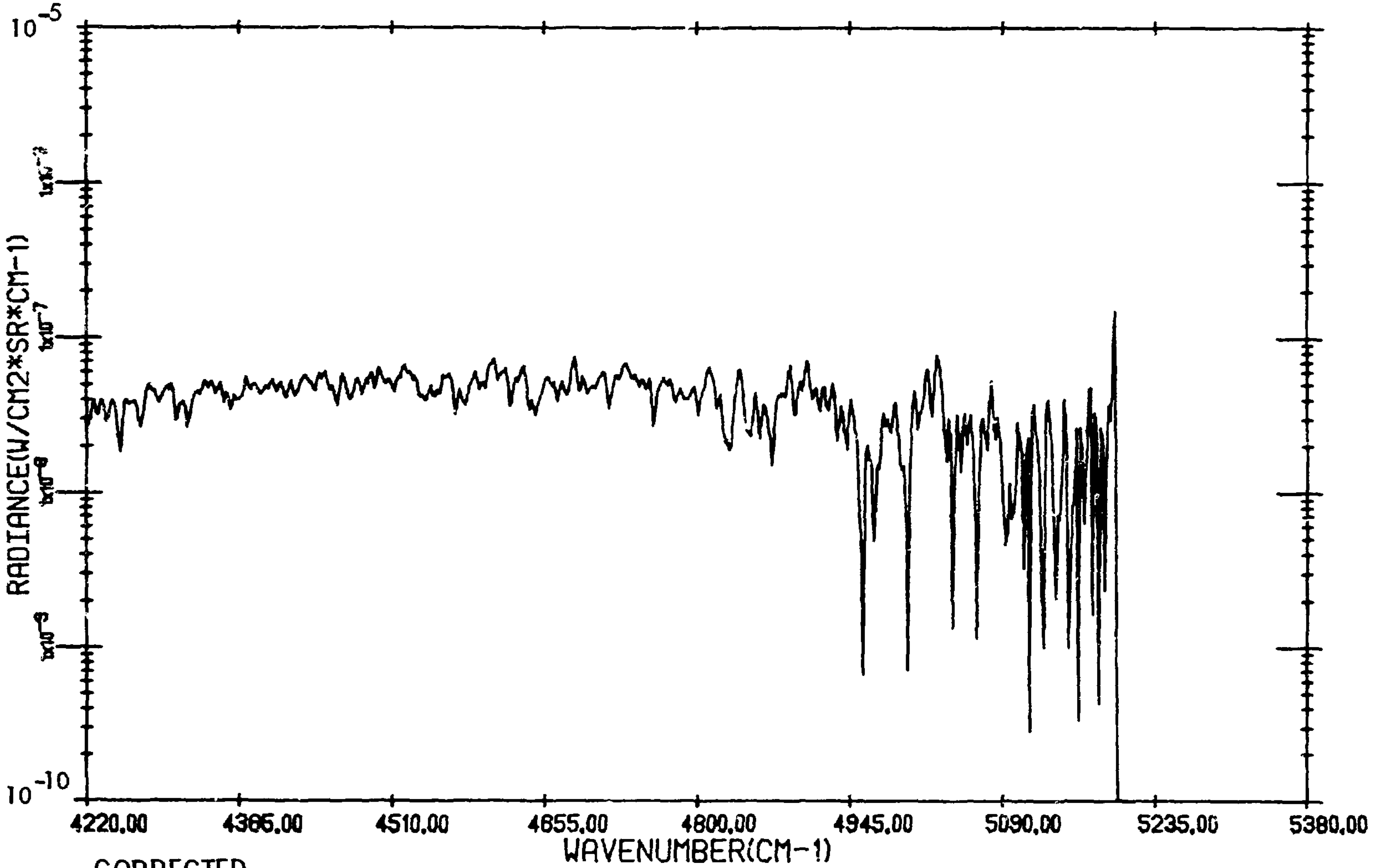

CORRECTED

BACKGROUND RADIANCE

(816/6)

WYANDOTTE, MICHIGAN - 15:03:28.3 - BACKGROUND (WITH ATMOSPHERIC TRANSMITTANCE CORRECTION)

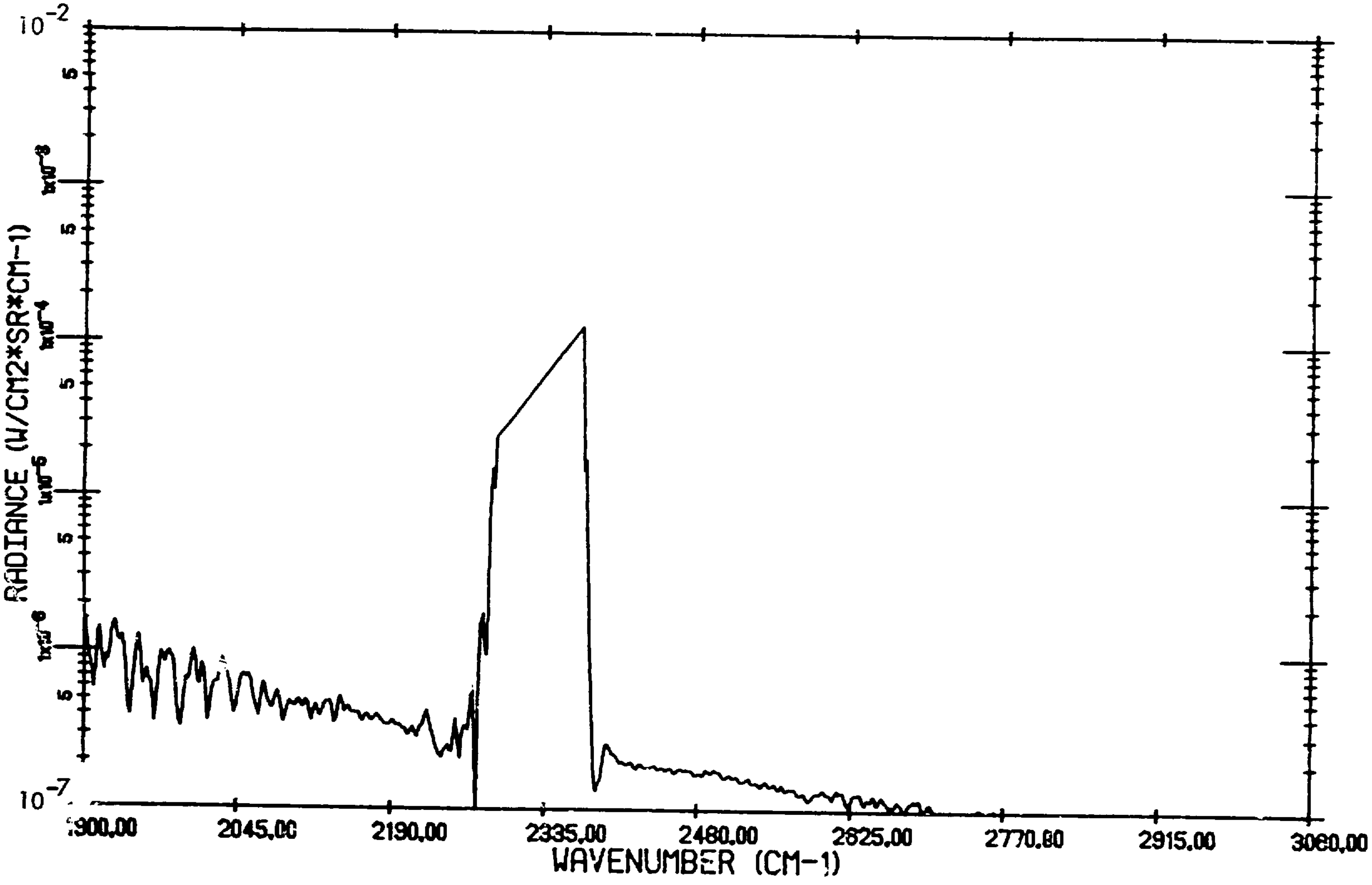

CORRECTED BACKGROUND RADIANCE

WYANDOTTE, MICHIGAN - (816/7) - 15:07:42.7 - COKE OVEN

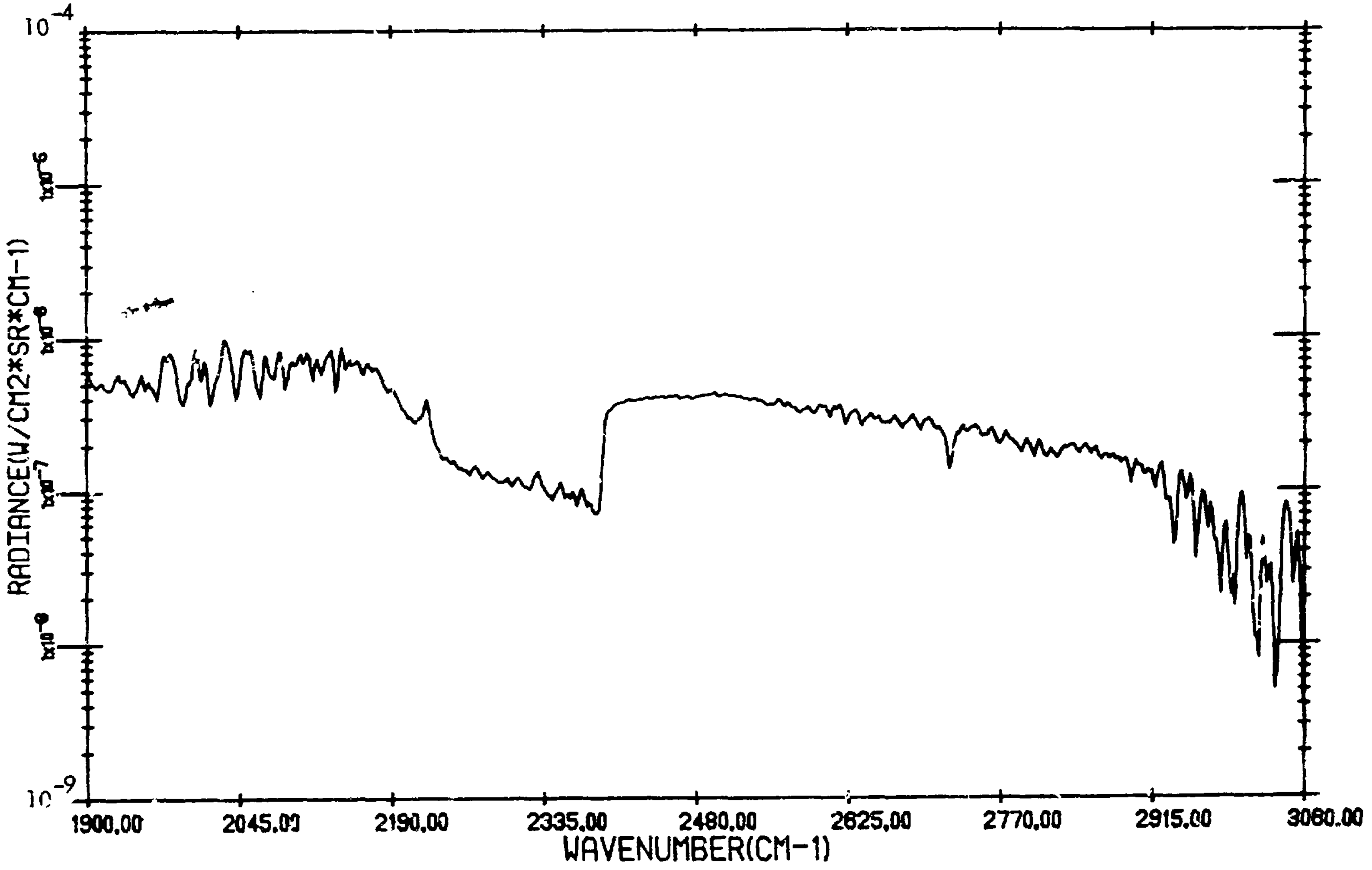

TARGET RADIANCE

WYANDOTTE, MICHIGAN - (816/7) - 15:07:42.7 - COKE OVEN

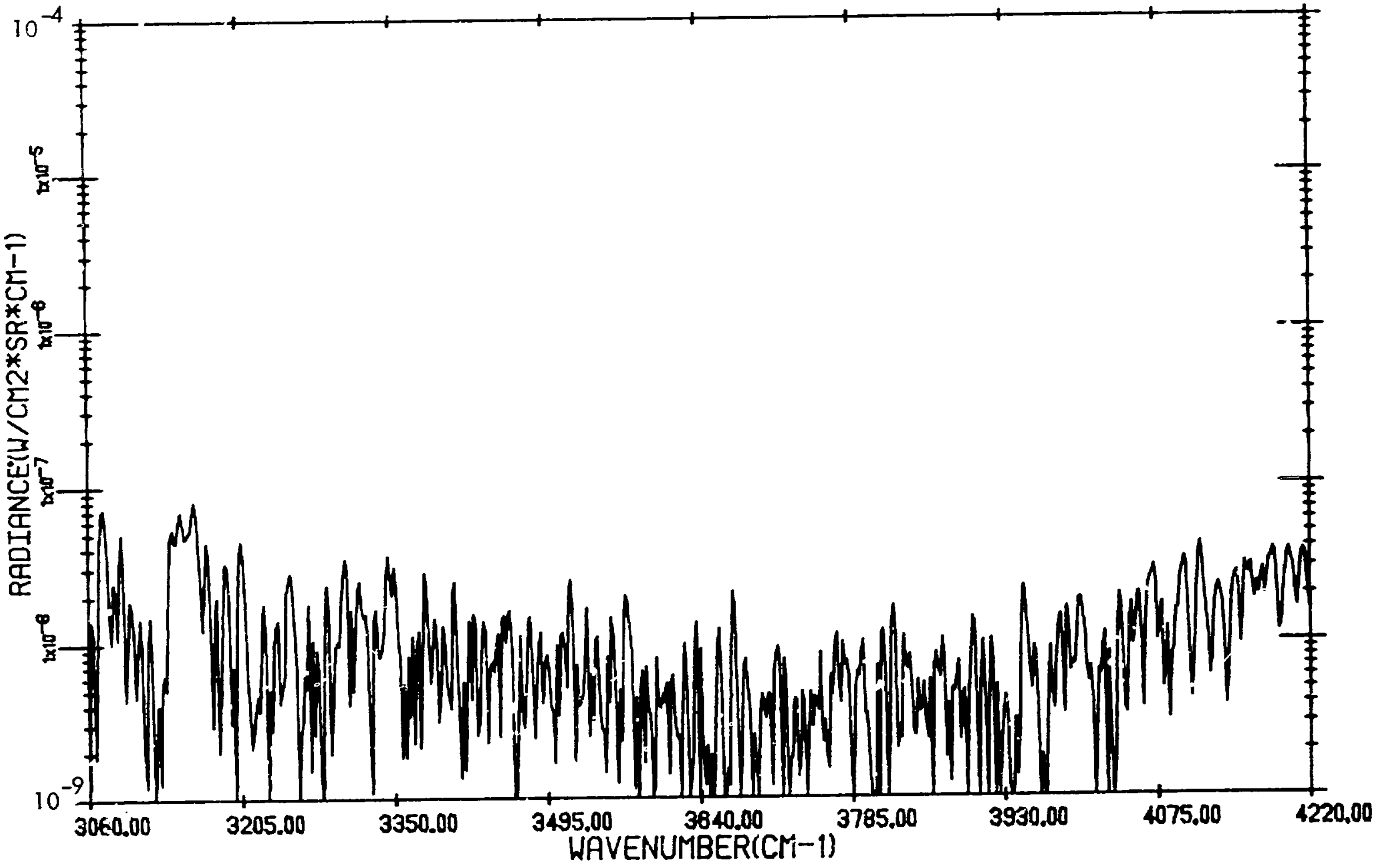

TARGET RADIANCE

(816/7)

WYANDOTTE, MICHIGAN - 15:07:42.7 - COKE OVEN (WITH ATMOSPHERIC TRANSMITTANCE CORRECTION)

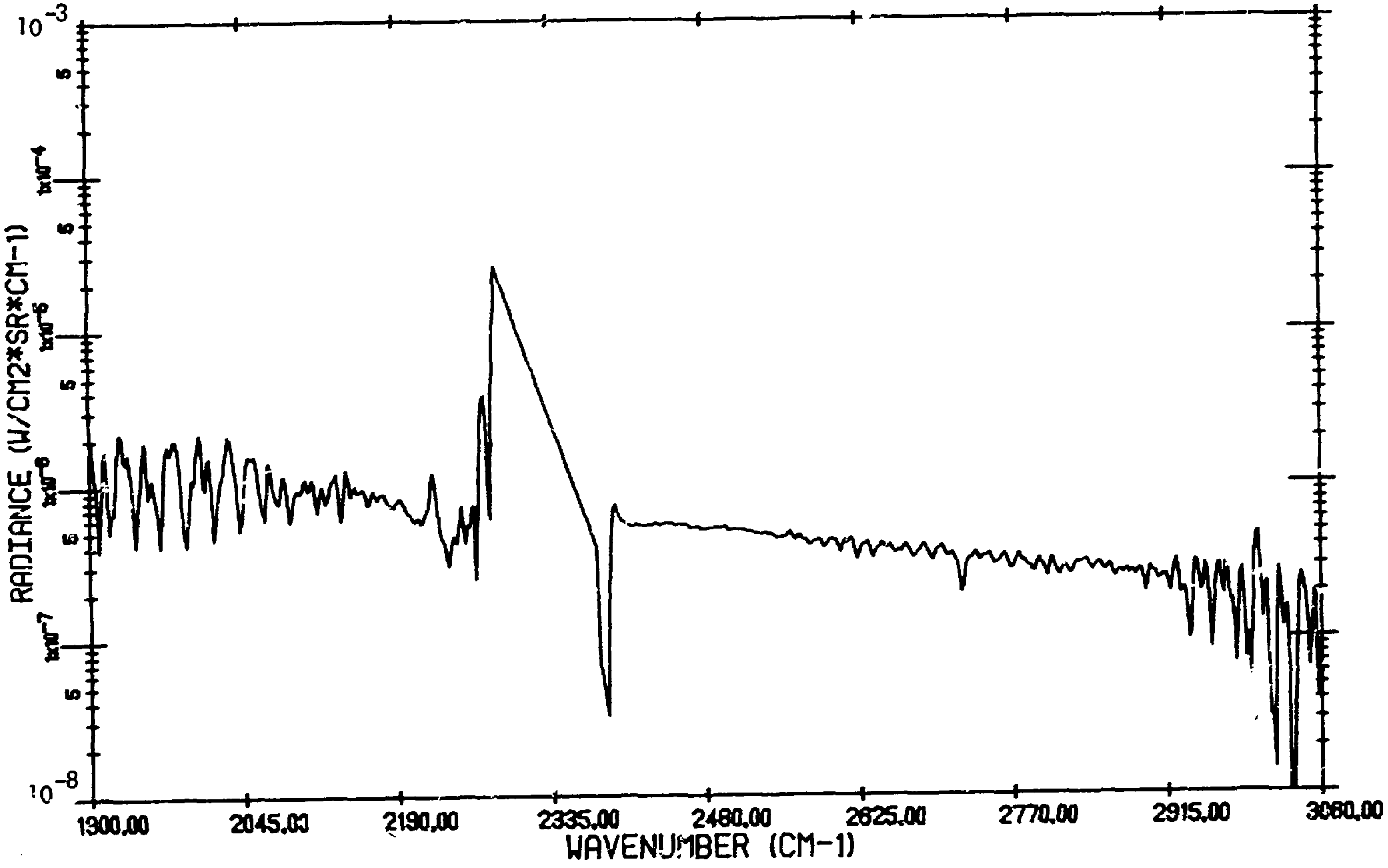

CORRECTED TARGET RADIANCE

WYANDOTTE, MICHIGAN (816/7) - 15:10:34.5 - BACKGROUND

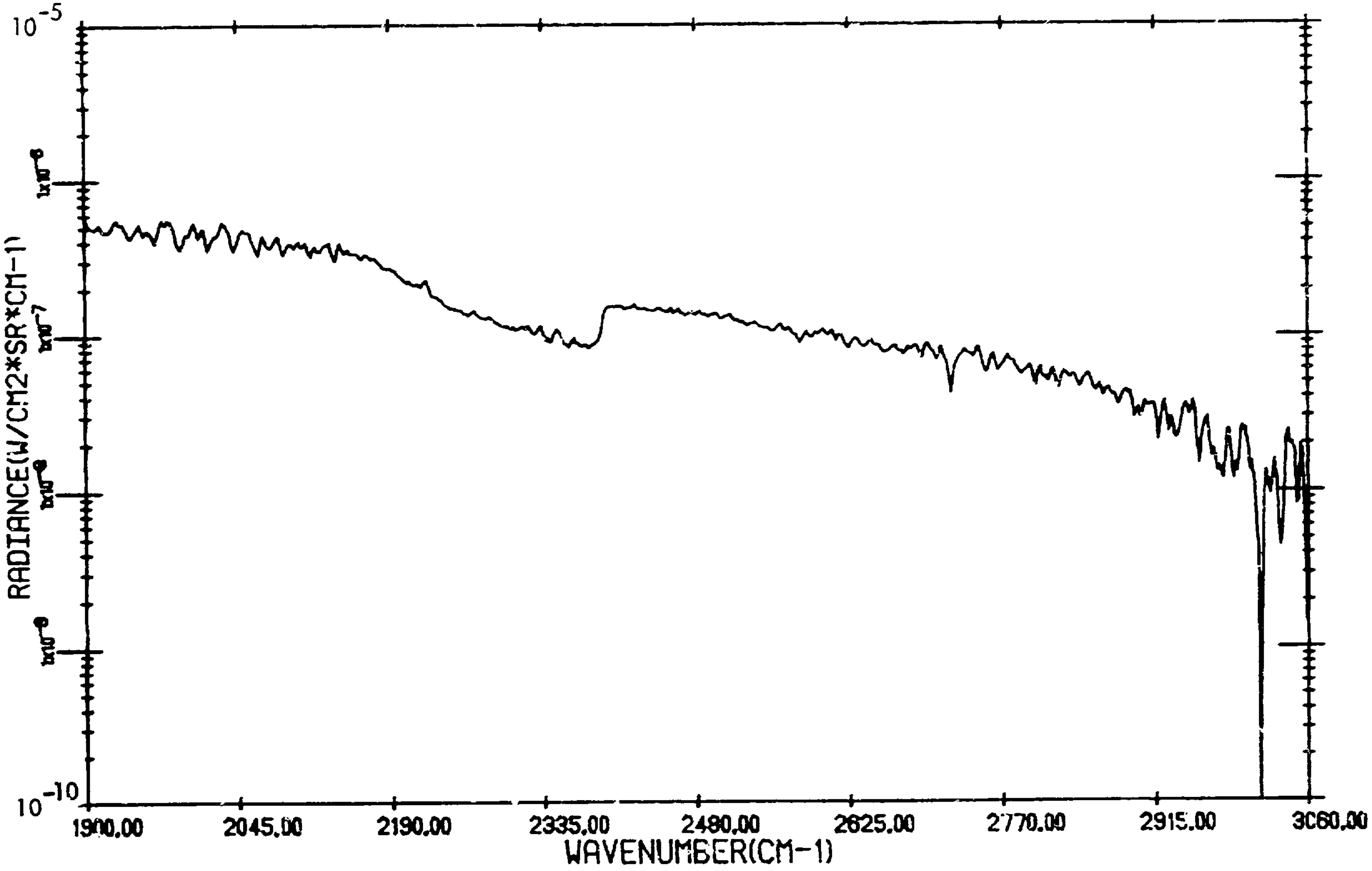

BACKGROUND RADIANCE

WYANDOTTE, MICHIGAN - (816/7) - 15:10:34.5 - BACKGROUND

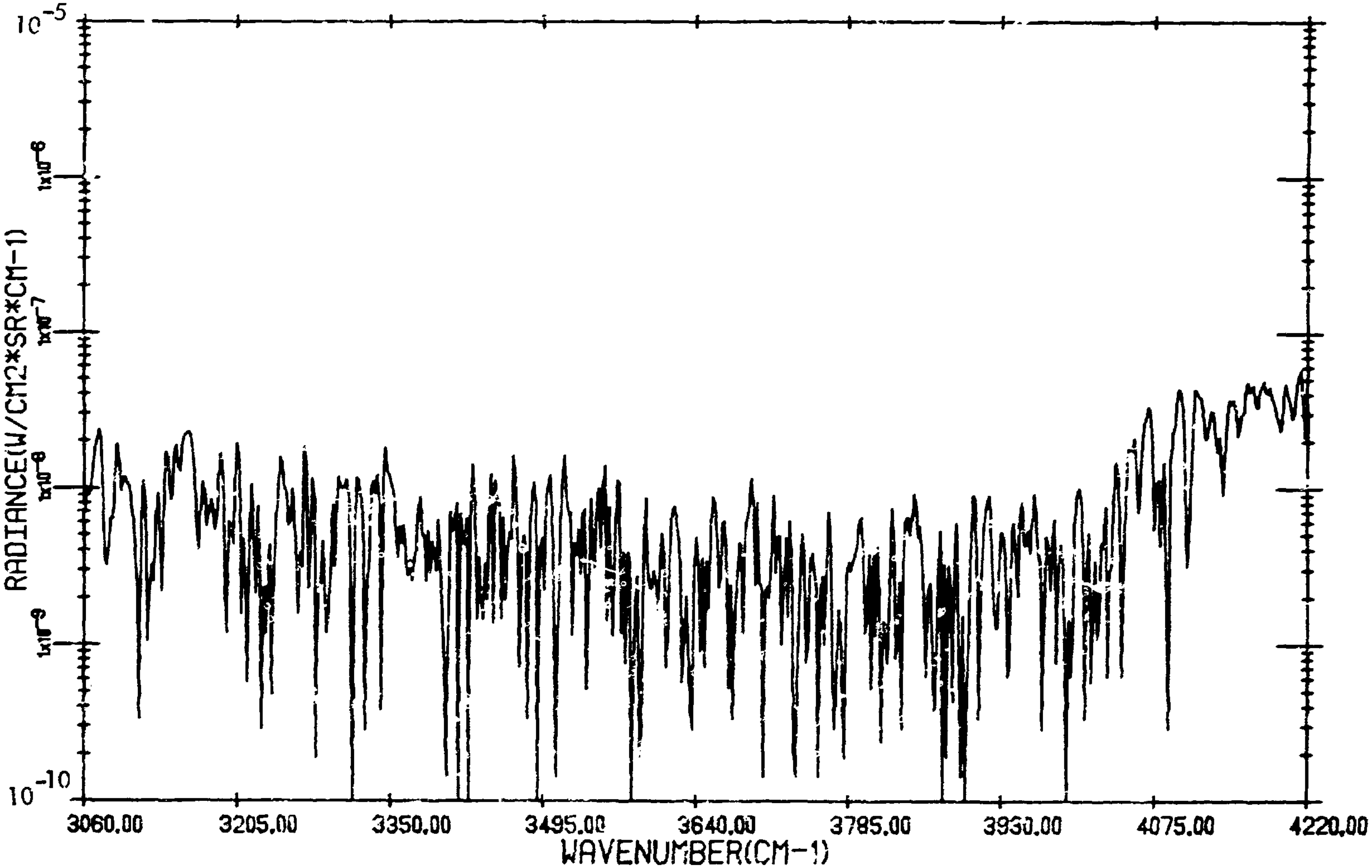

BACKGROUND RADIANCE

WYANDOTTE, MICHIGAN - (816/7) - 15:10:34.5 - BACKGROUND

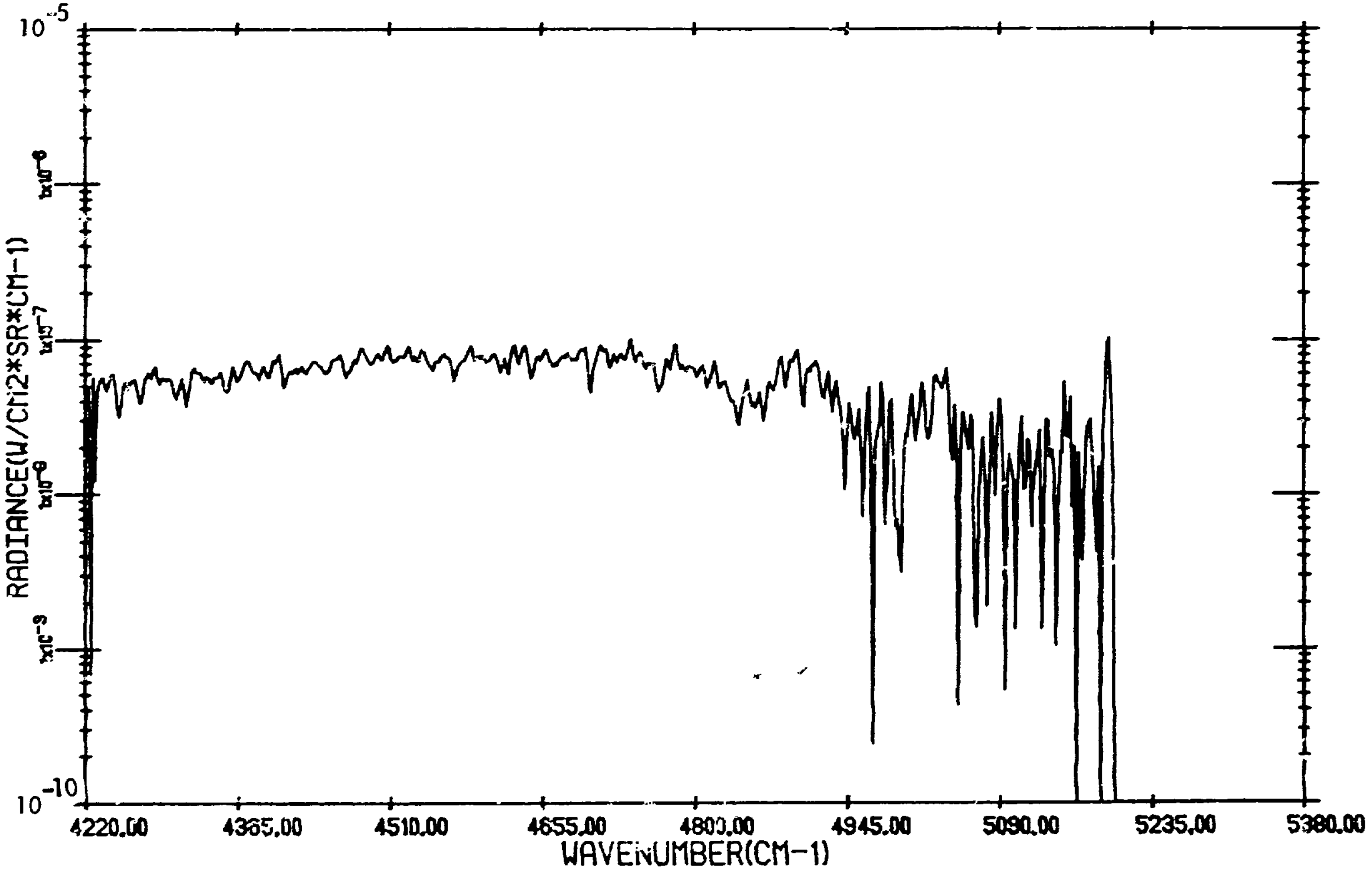

BACKGROUND RADIANCE

(816/7)

WYANDOTTE, MICHIGAN - 15:10:34.5 - BACKGROUND (WITH ATMOSPHERIC TRANSMITTANCE CORRECTION)

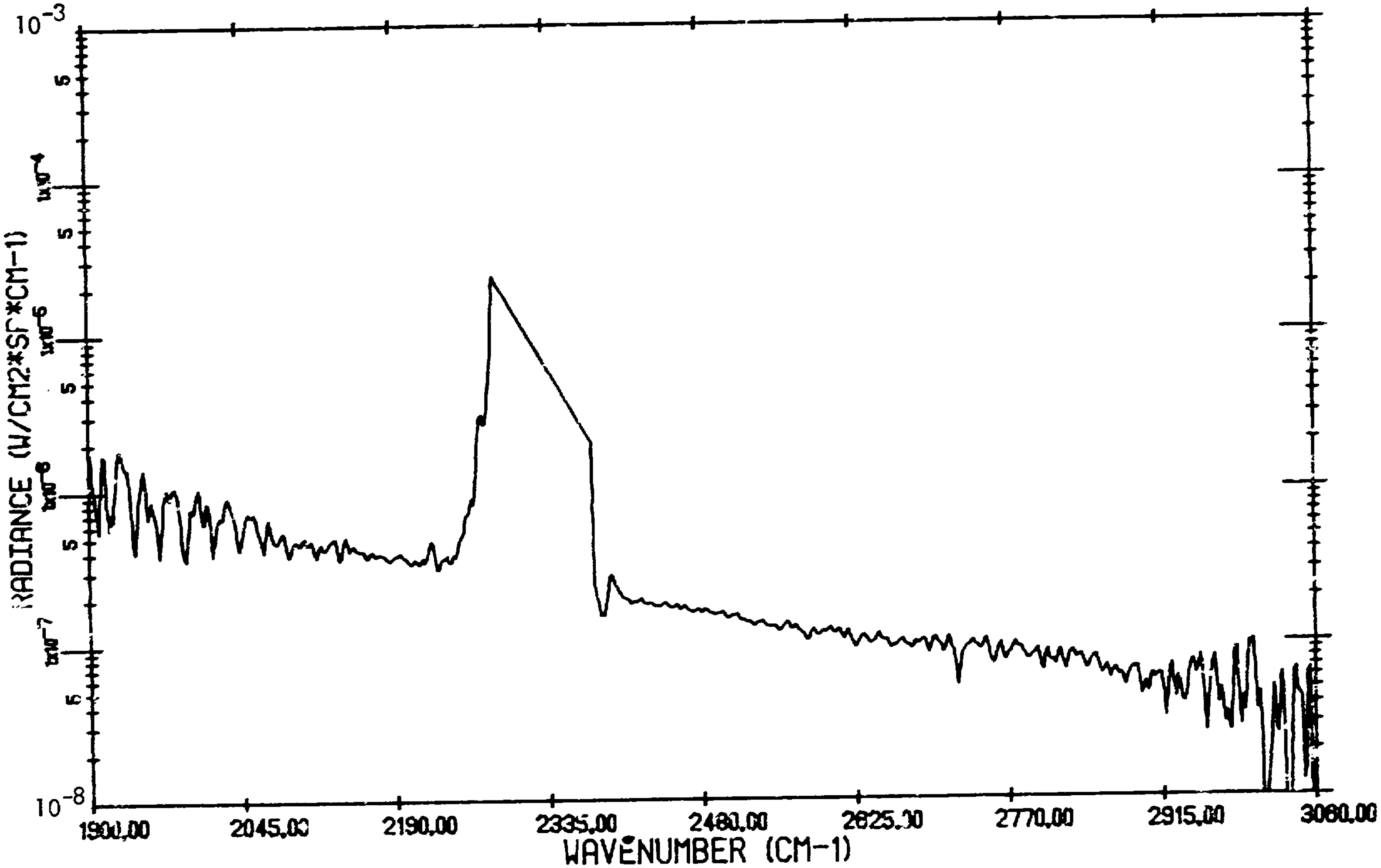

CORRECTED BACKGROUND RADIANCE

WYANDOTTE, MICHIGAN - (816/8) - 15:27:34.3 - STACKS WITH RR CARS

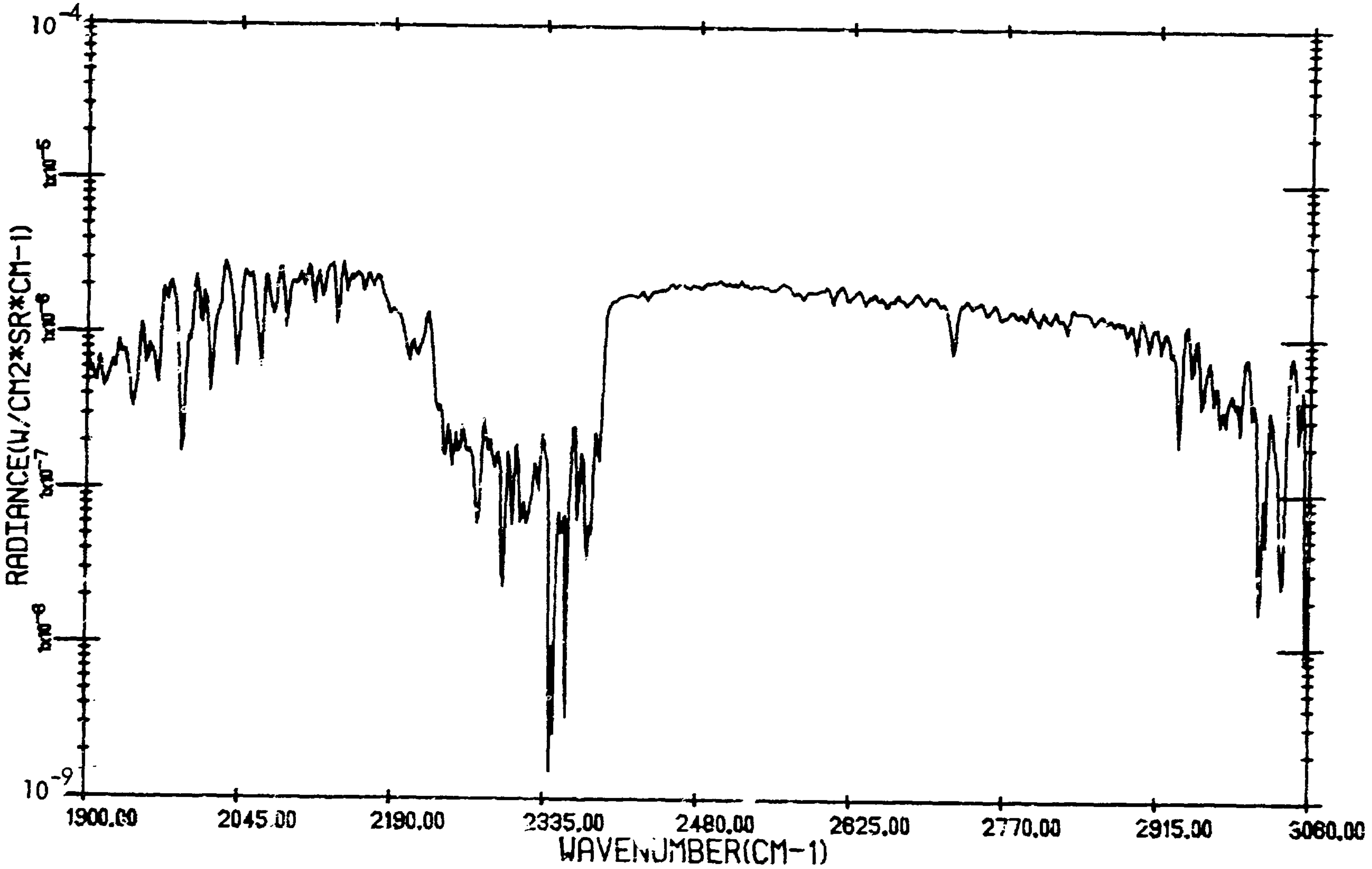

TARGET RADIANCE

WYANDOTTE, MICHIGAN - (816/8) - 15:27:34.3 - STACKS WITH RR CARS

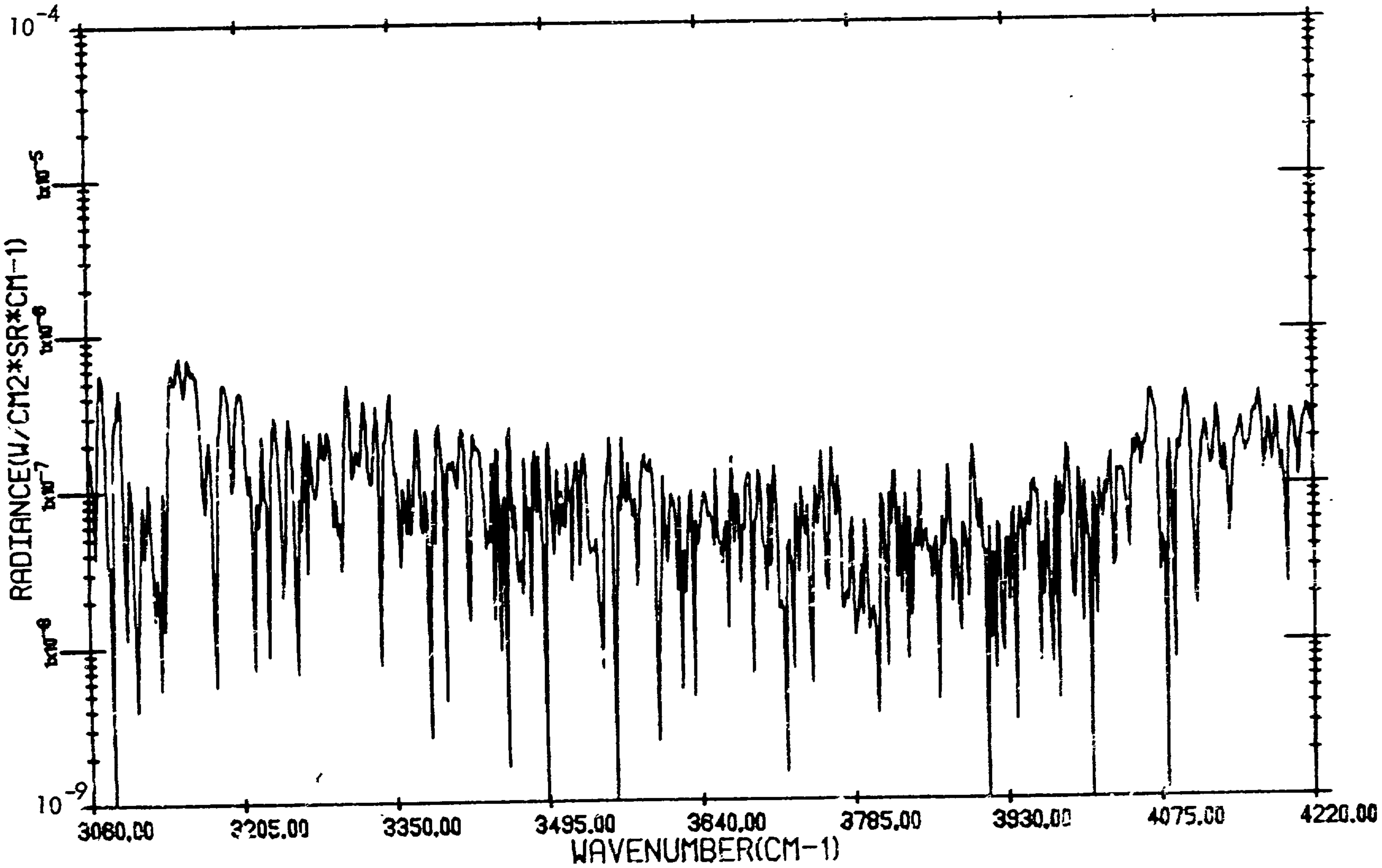

TARGET RADIANCE

WYANDOTTE, MICHIGAN - (816/8) - 15:27:34.3 - STACKS WITH RR CARS

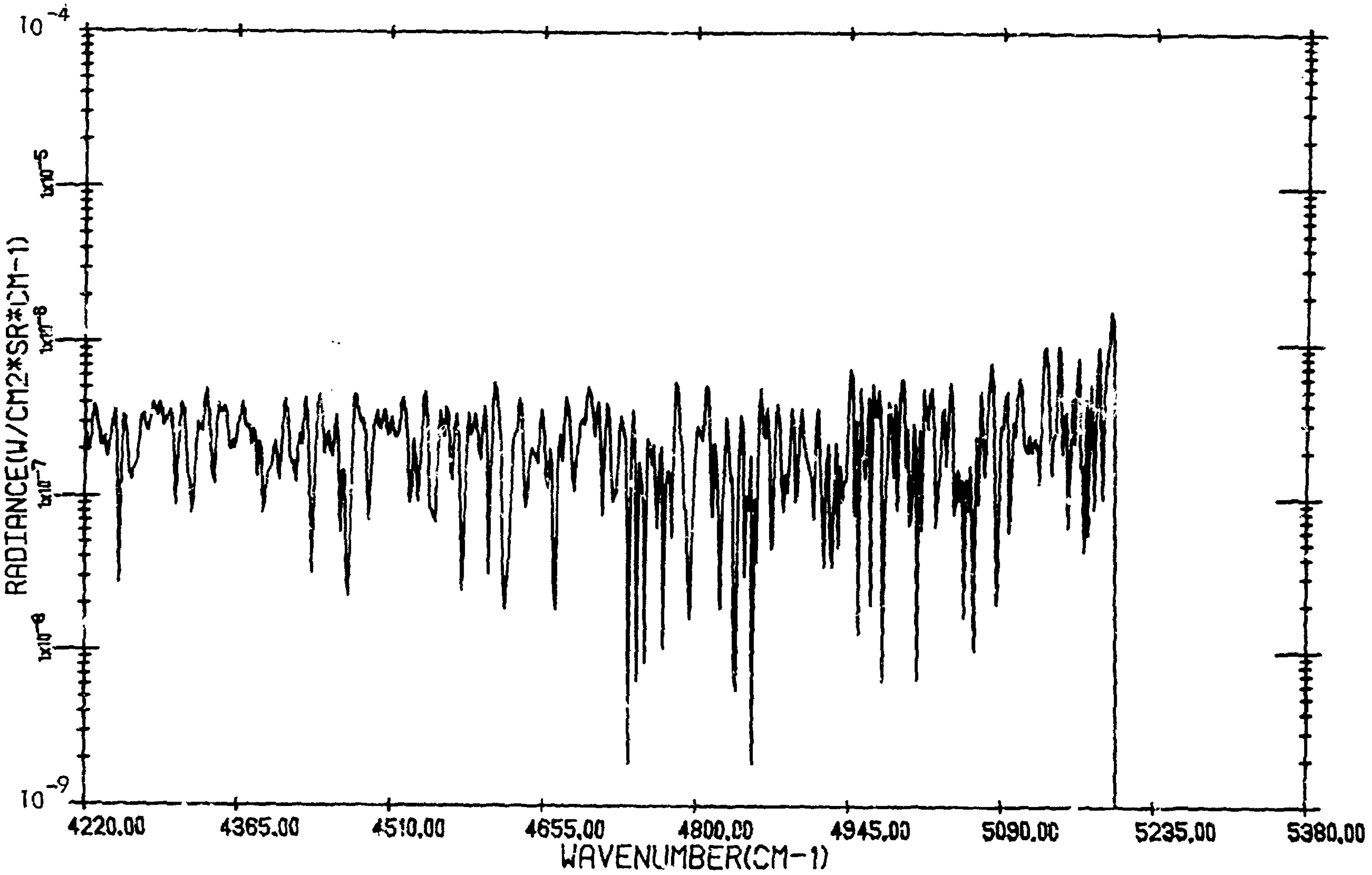

TARGET RADIANCE

(816/8)
WYANDOTTE, MICHIGAN - 15:27:34.3 - STACKS WITH RR CARS (WITH ATMOSPHERIC
TRANSMITTANCE CORRECTION)

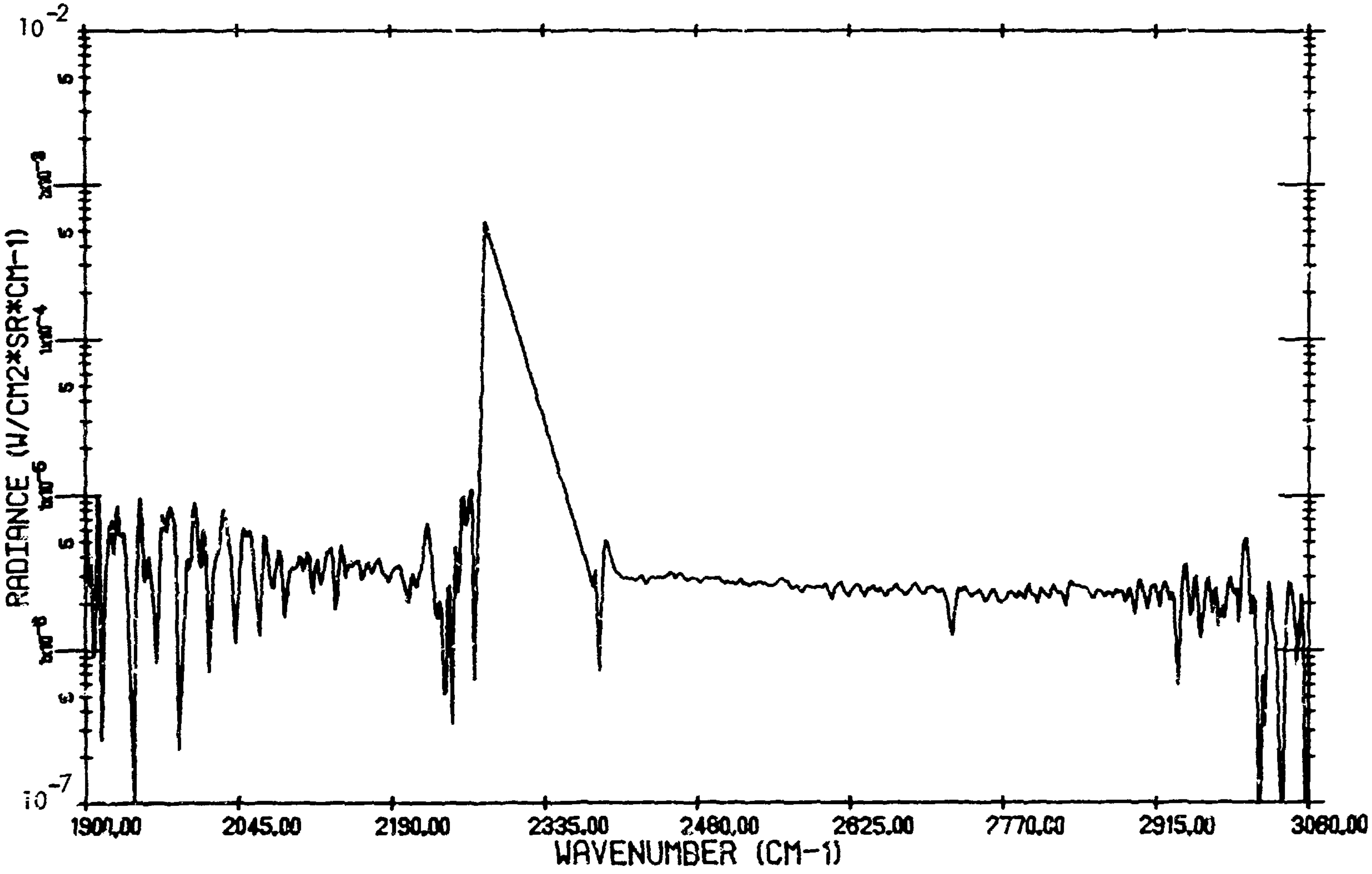

CORRECTED TARGET RADIANCE

WYANDOTTE, MICHIGAN - (816/8) - 15:29:14.8 - BACKGROUND

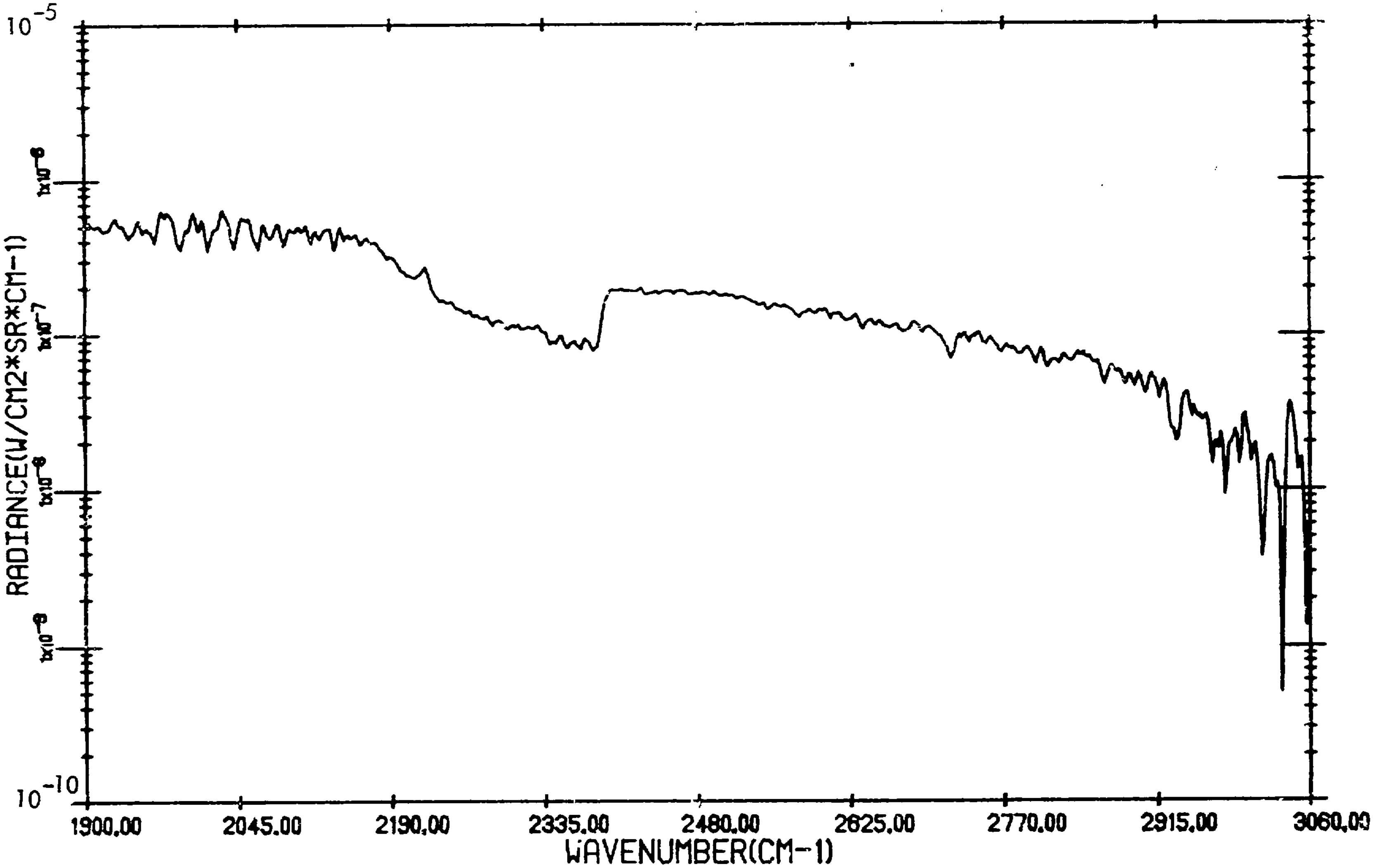

BACKGROUND RADIANCE

WYANDOTTE, MICHIGAN - (816/8) - 15:29:14.8 - BACKGROUND

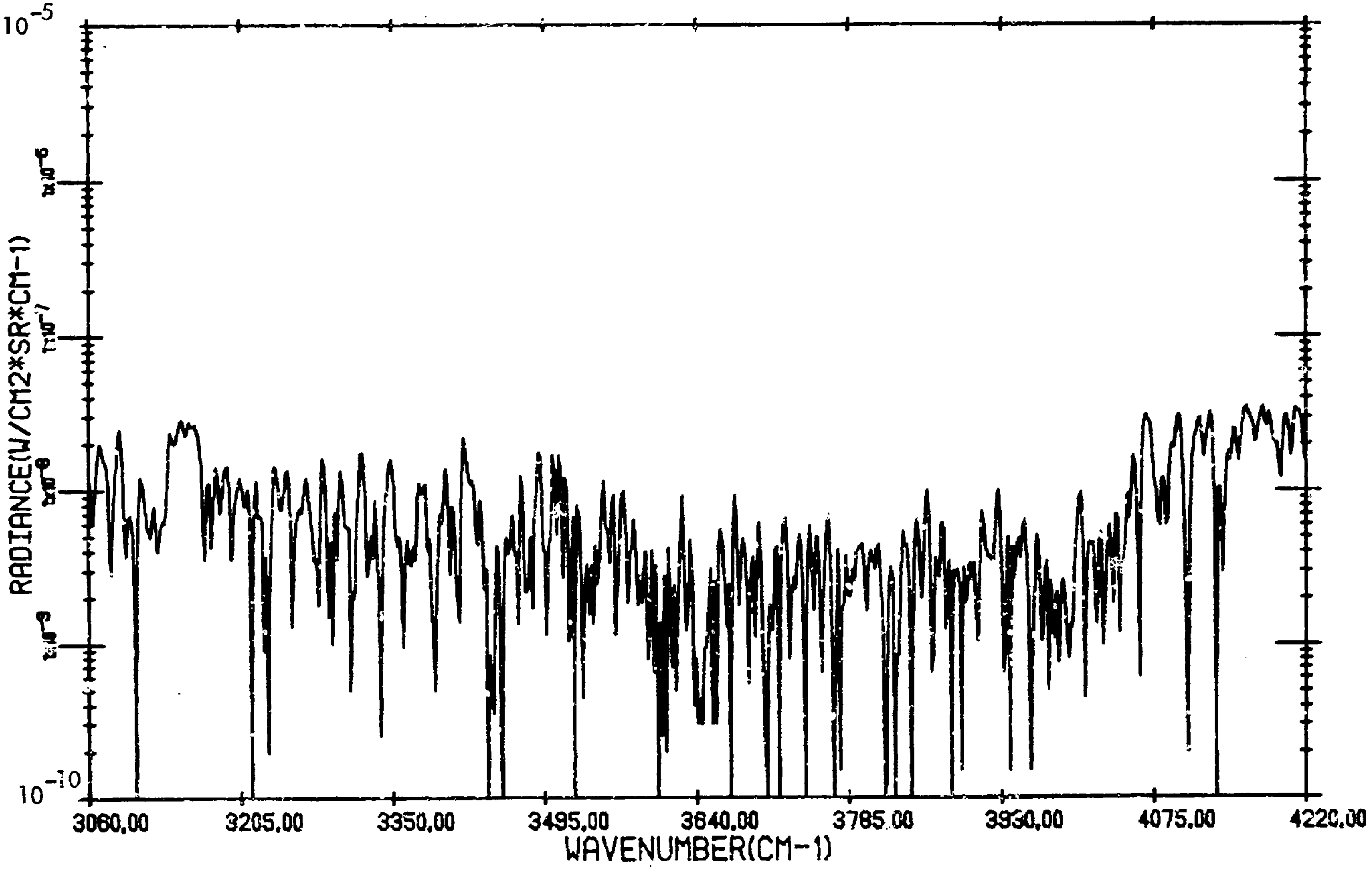

BACKGROUND RADIANCE

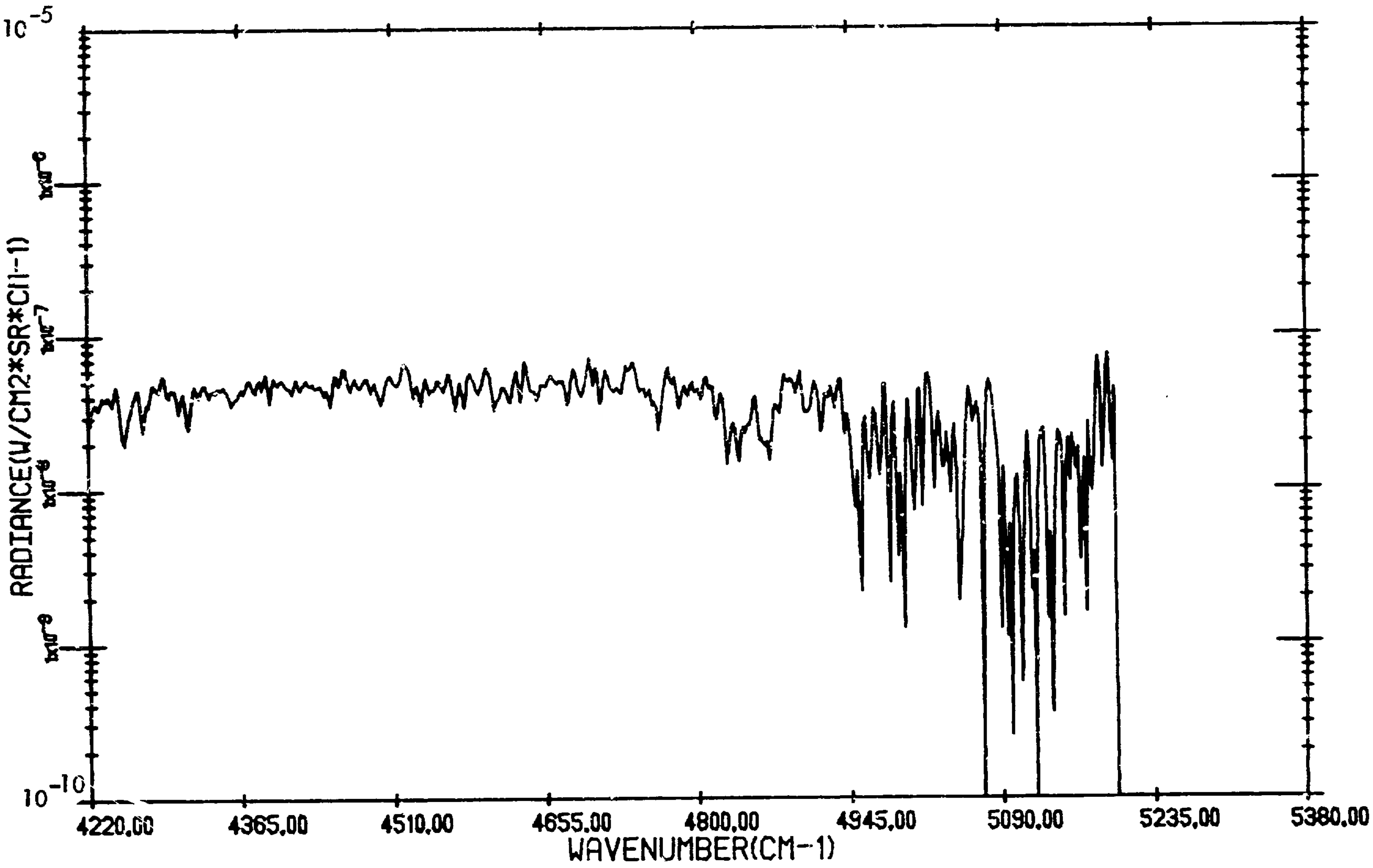
WYANDOTTE, MICHIGAN - (816/8) - 15:29:14.8 - BACKGROUND

BACKGROUND RADIANCE

(816/8)

WYANDOTTE, MICHIGAN - 15:29:14.8 - BACKGROUND (WITH ATMOSPHERIC TRANSMITTANCE CORRECTION)

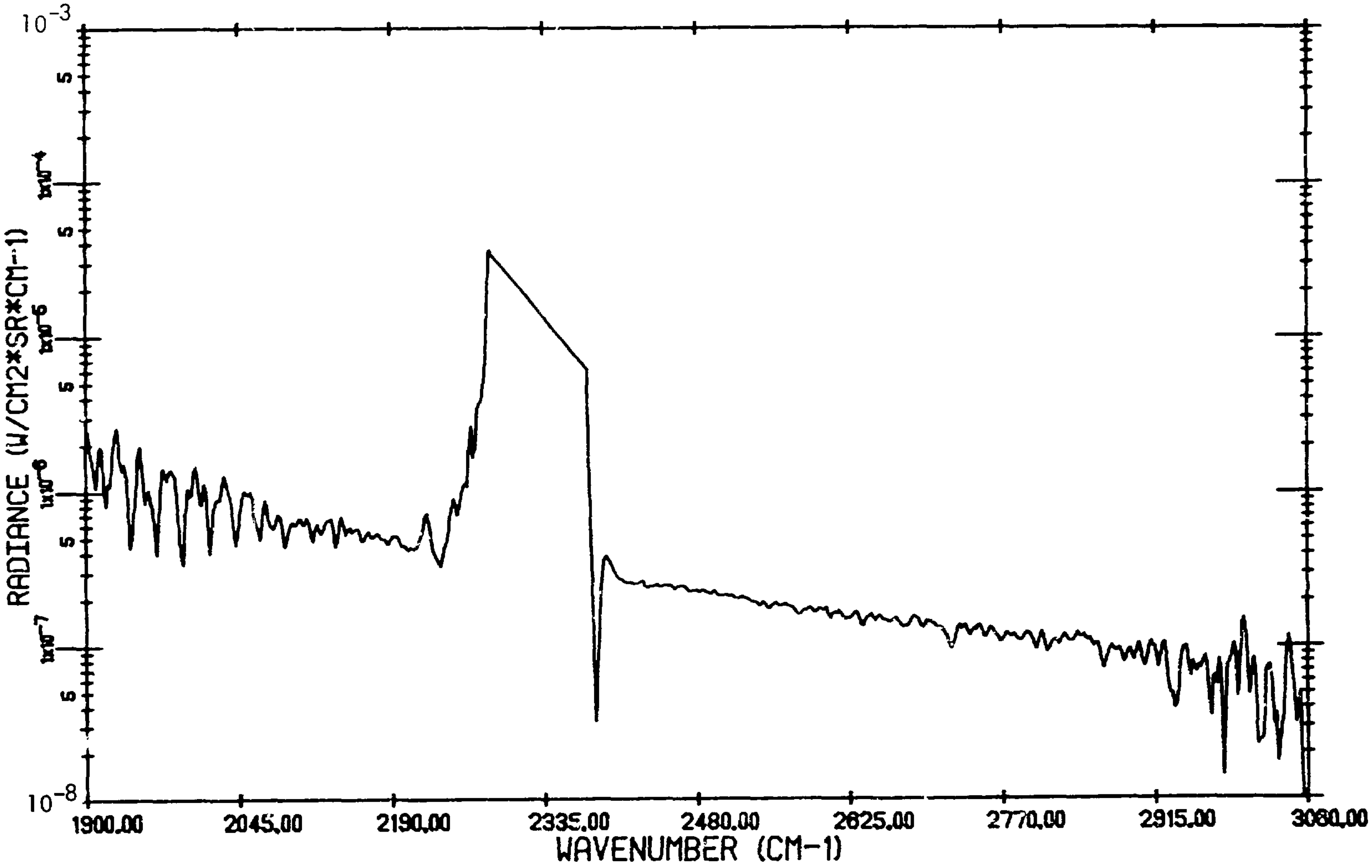

CORRECTED BACKGROUND RADIANCE

WYANDOTTE, MICHIGAN - (816/8) - 15:28:5.4 - RR CARS WITH HOT METAL

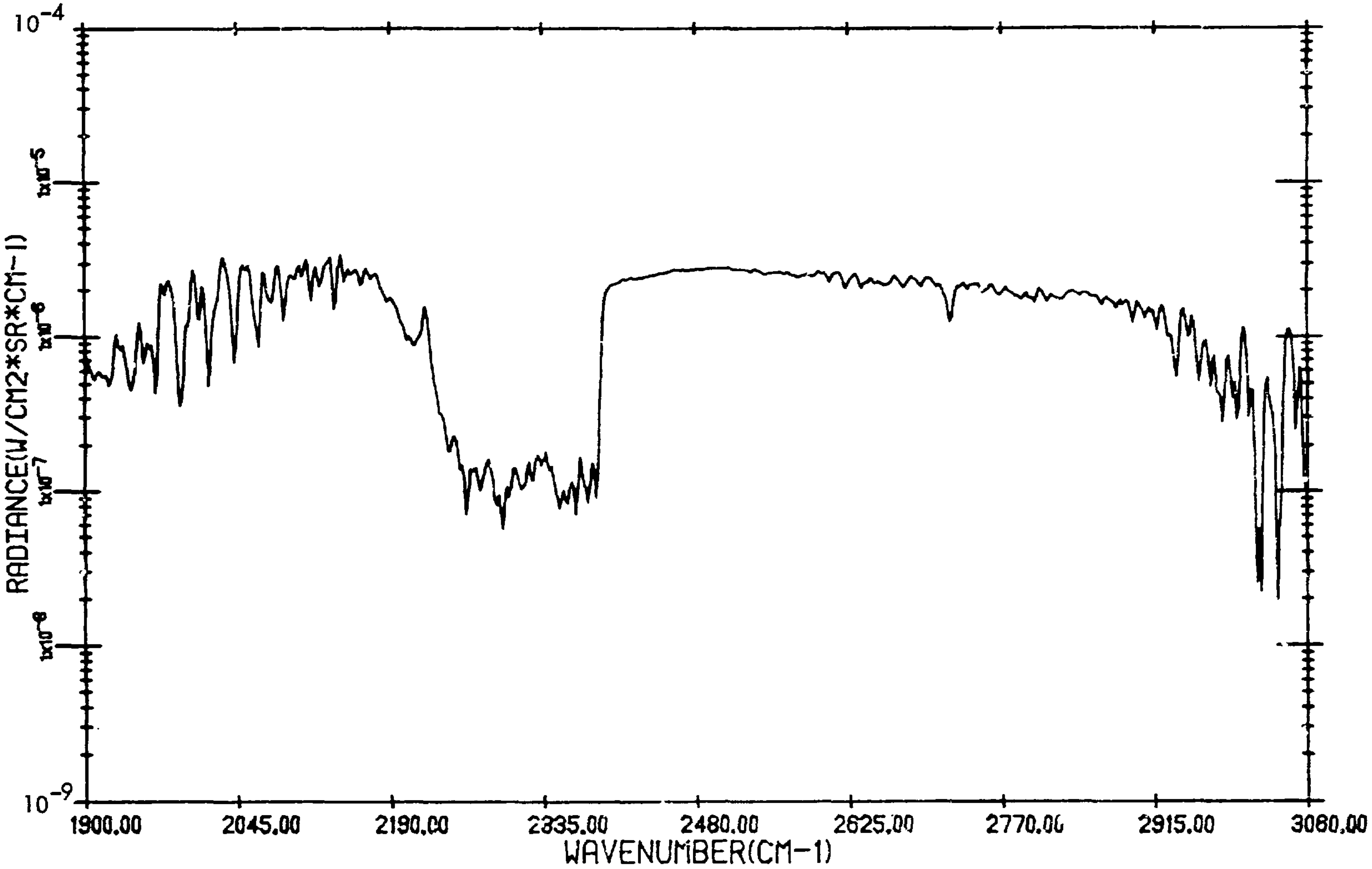

TARGET RADIANCE

WYANDOTTE, MICHIGAN - (816/8) - 15:28:5.4 - RR CARS WITH HOT METAL

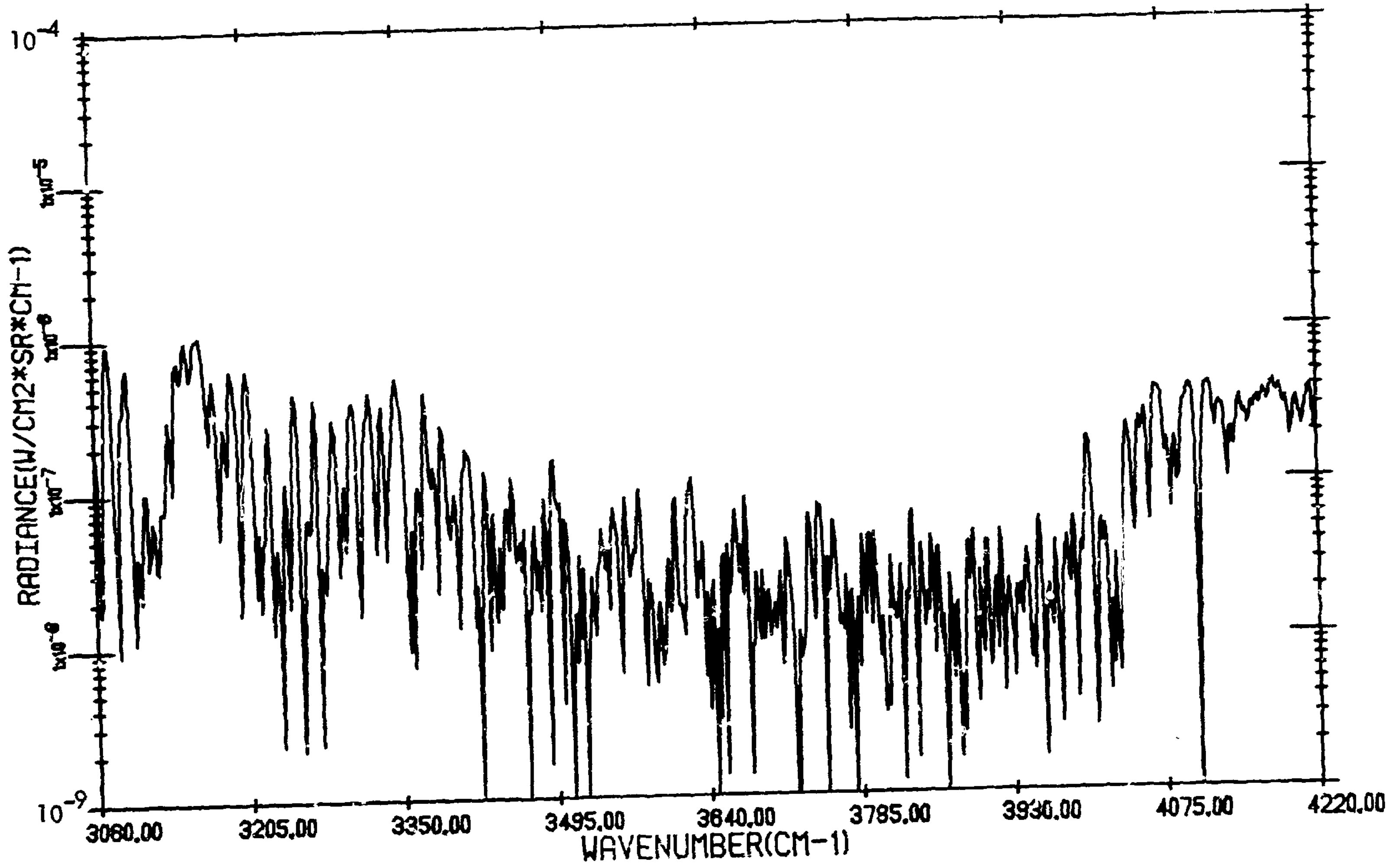

TARGET RADIANCE

WYANDOTTE, MICHIGAN - (816/8) - 15:28:5.4 - RR CARS WITH HOT METAL

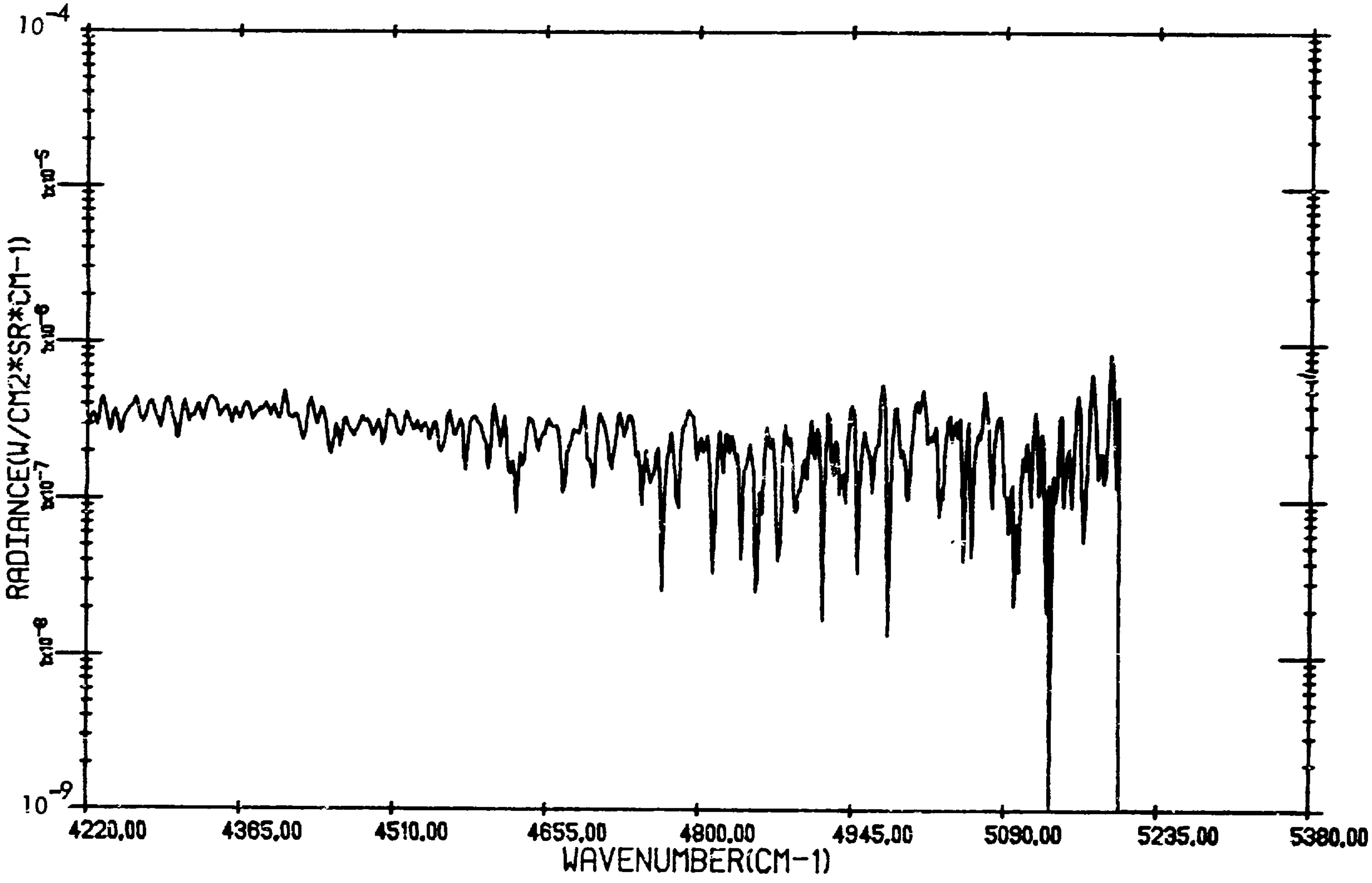

TARGET RADIANCE

(816/8)

WYANDOTTE, MICHIGAN - 15:28:5.4 - RR CARS WITH HOT METAL (WITH ATMOSPHERIC TRANSMITTANCE CORRECTION)

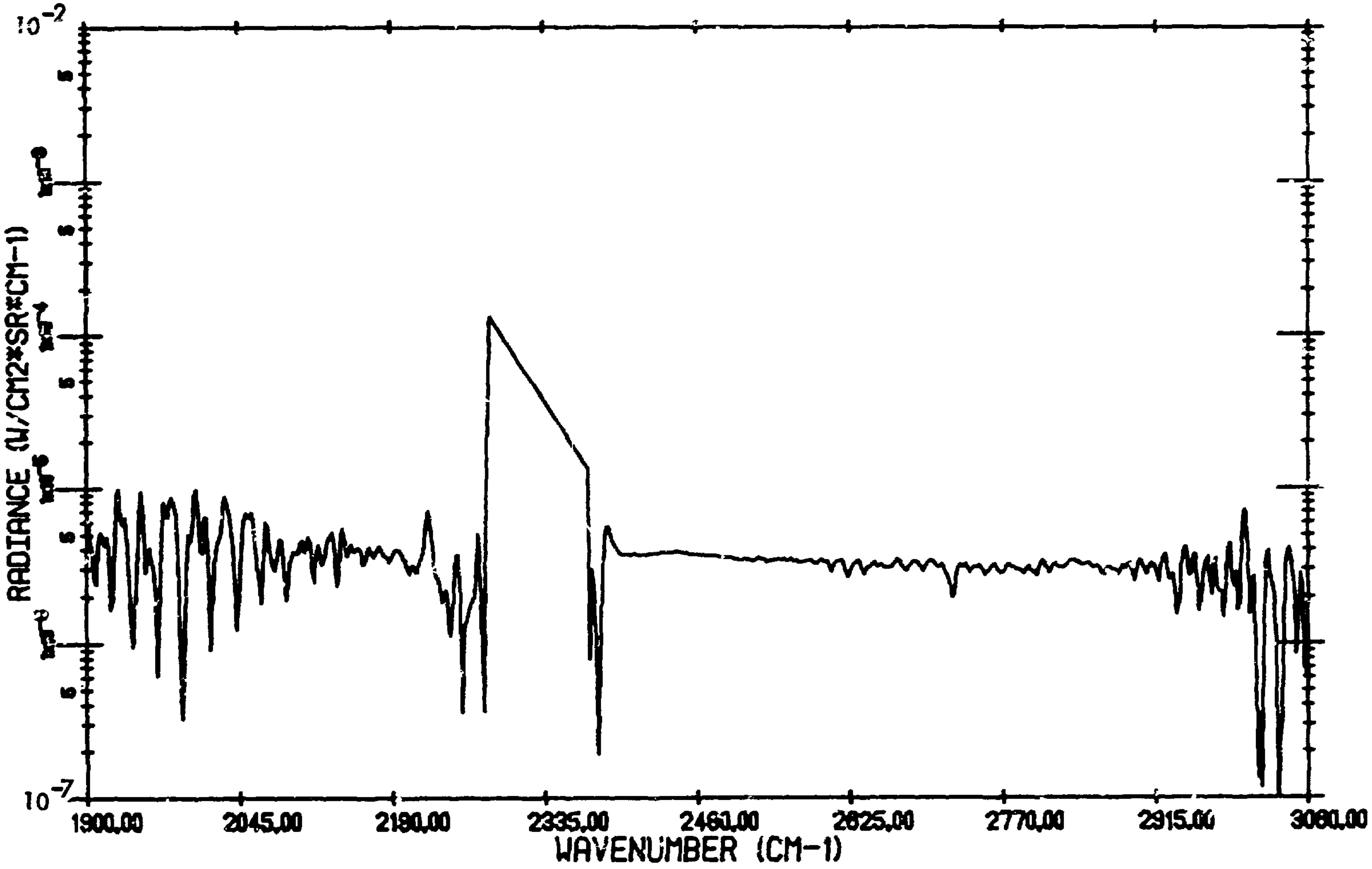

CORRECTED TARGET RADIANCE

WYANDOTTE, MICHIGAN - (816/10) - 15:40:0.0 - BASF STACK

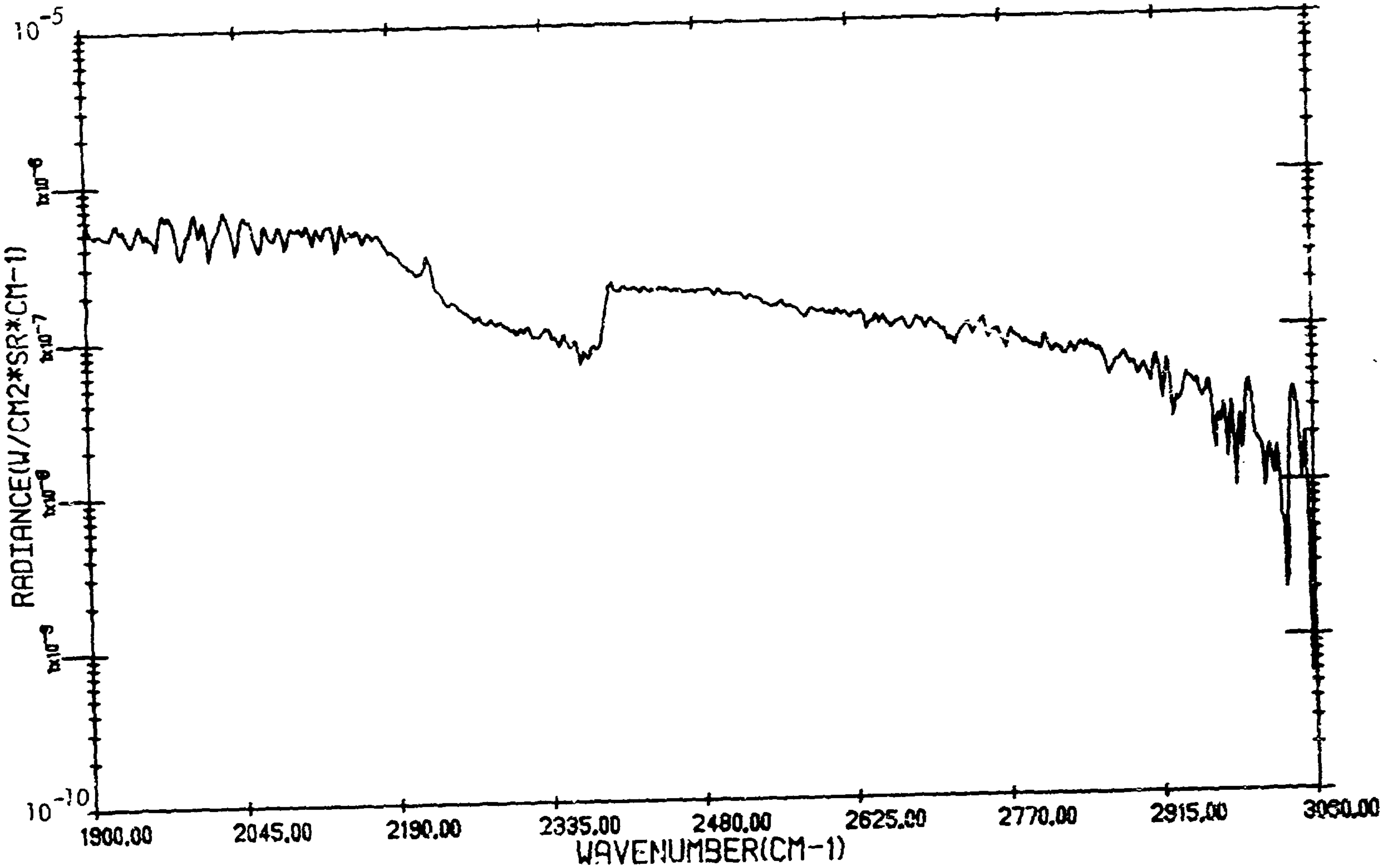

TARGET RADIANCE

WYANDOTTE, MICHIGAN - (816/10) - 15:40:0.0 - BASF STACK

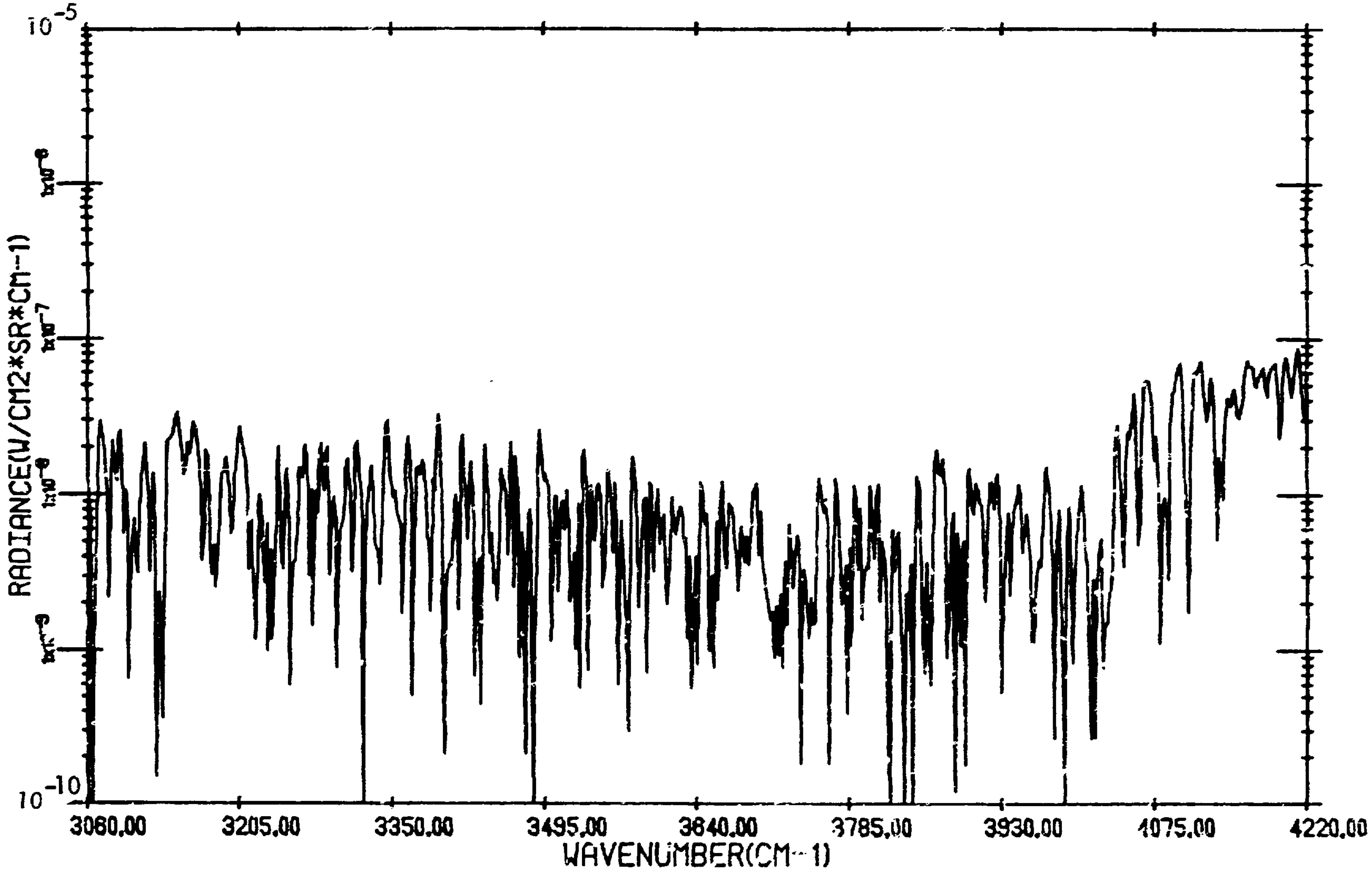

TARGET RADIANCE

WYANDOTTE, MICHIGAN - (816/10) - 15:40:0.0 - BASF STACK

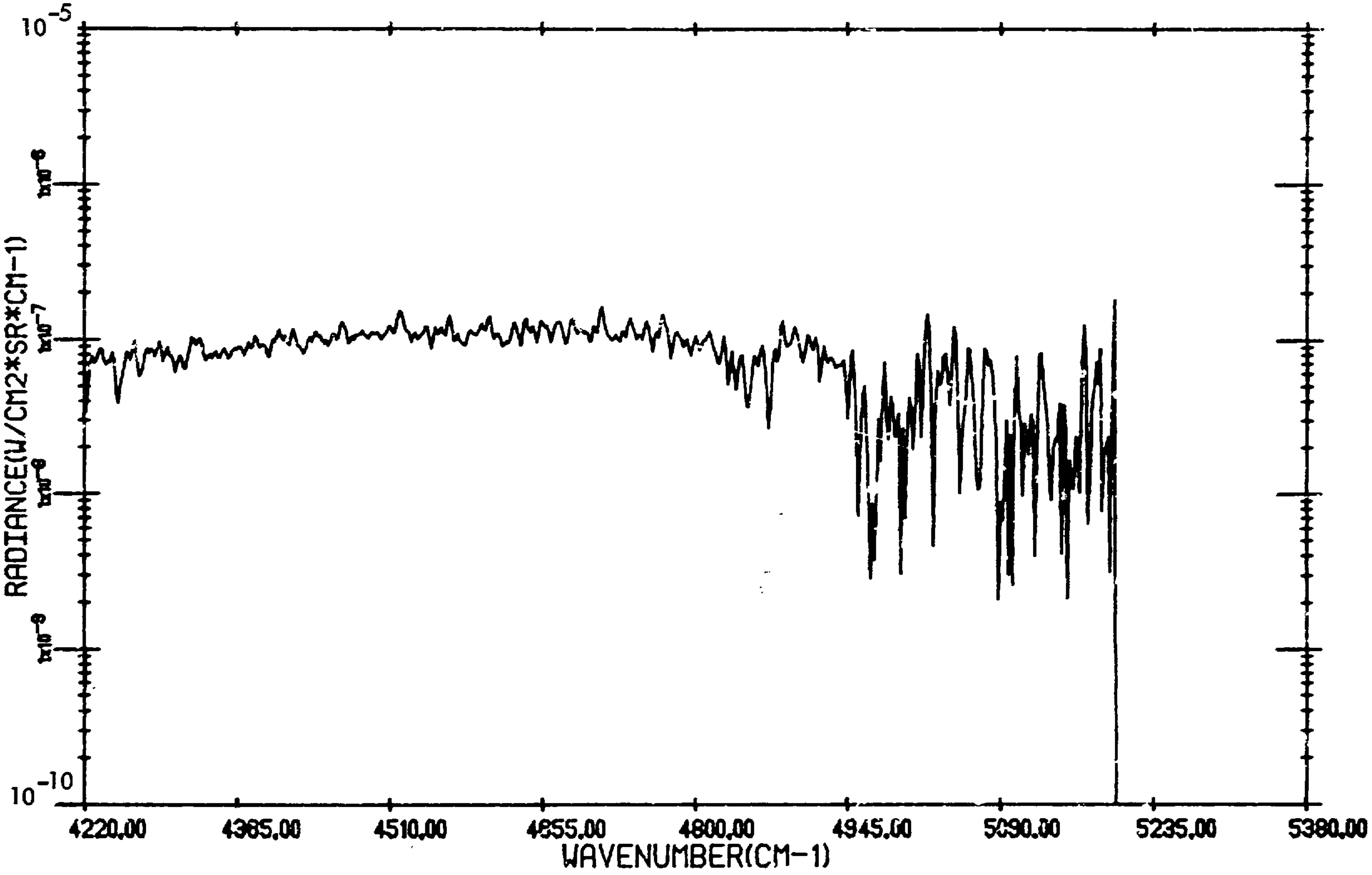

TARGET RADIANCE

(816/10)
WYANDOTTE, MICHIGAN - 15:40:0.0 - BASF STACK (WITH ATMOSPHERIC TRANSMITTANCE CORRECTION)

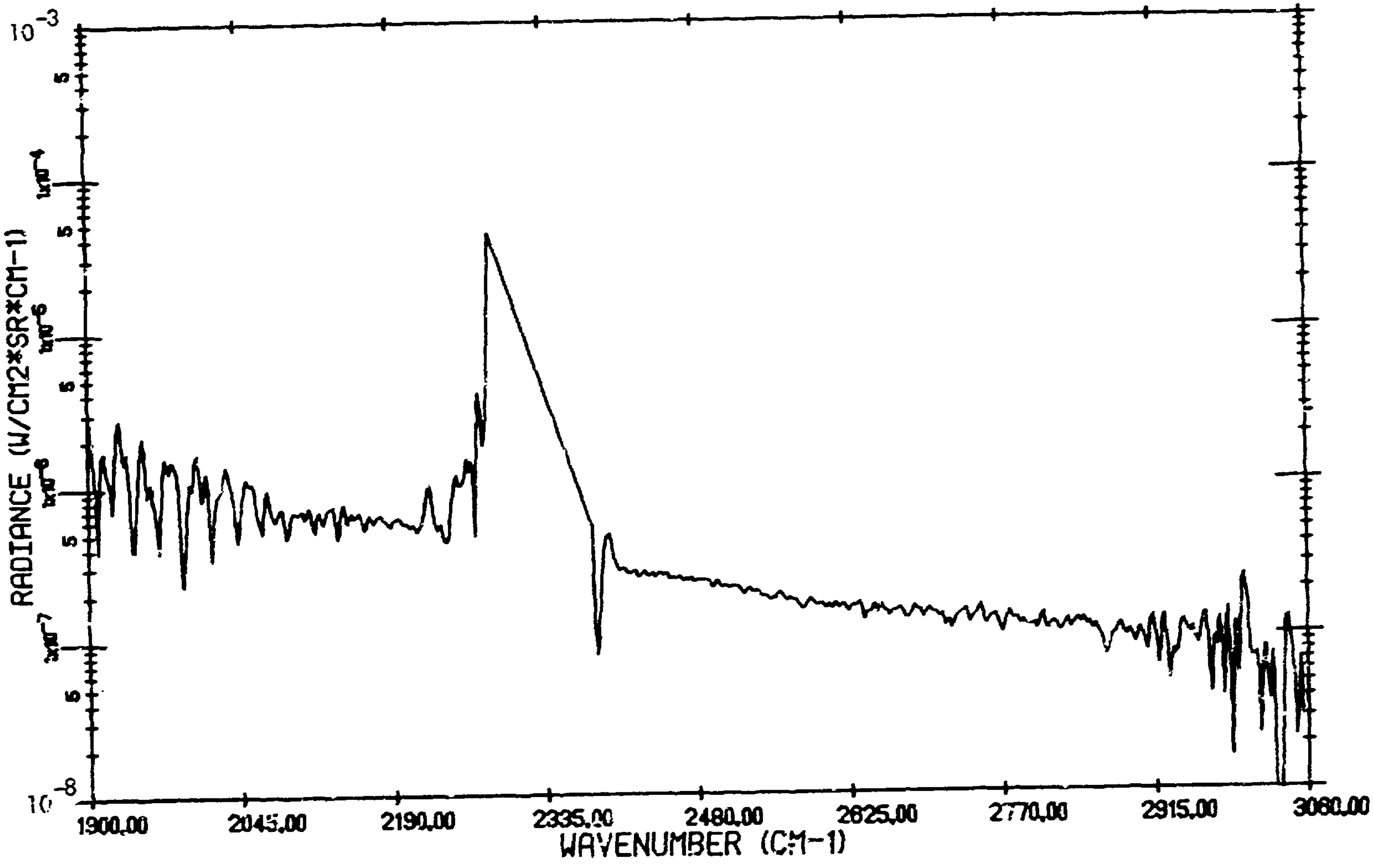

CORRECTED TARGET RADIANCE

WYANDOTTE, MICHIGAN - (816/10) - 15:43:14.8 - BACKGROUND

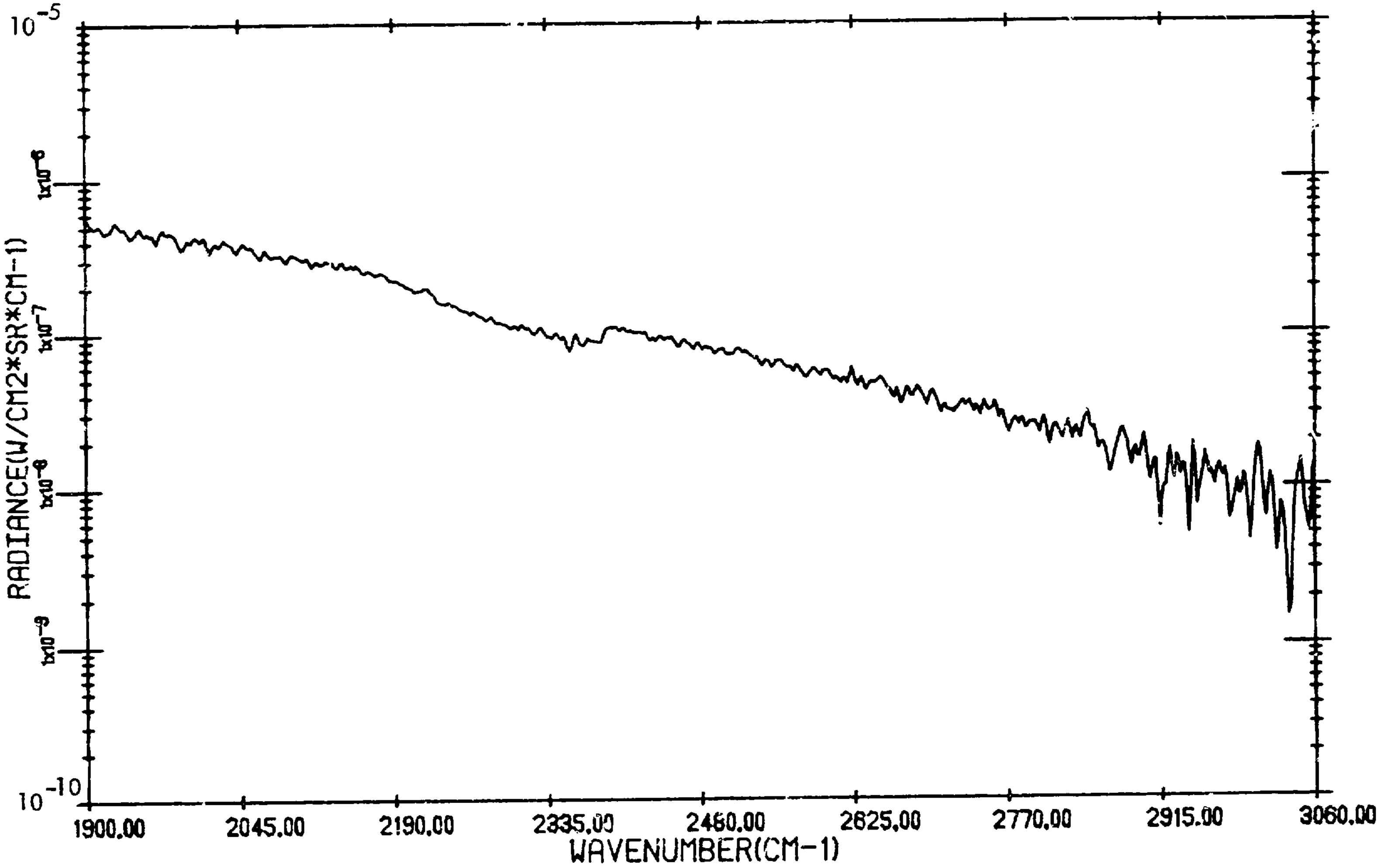

BACKGROUND RADIANCE

WYANDOTTE, MICHIGAN - (816/10) - 15:43:14.8 - BACKGROUND

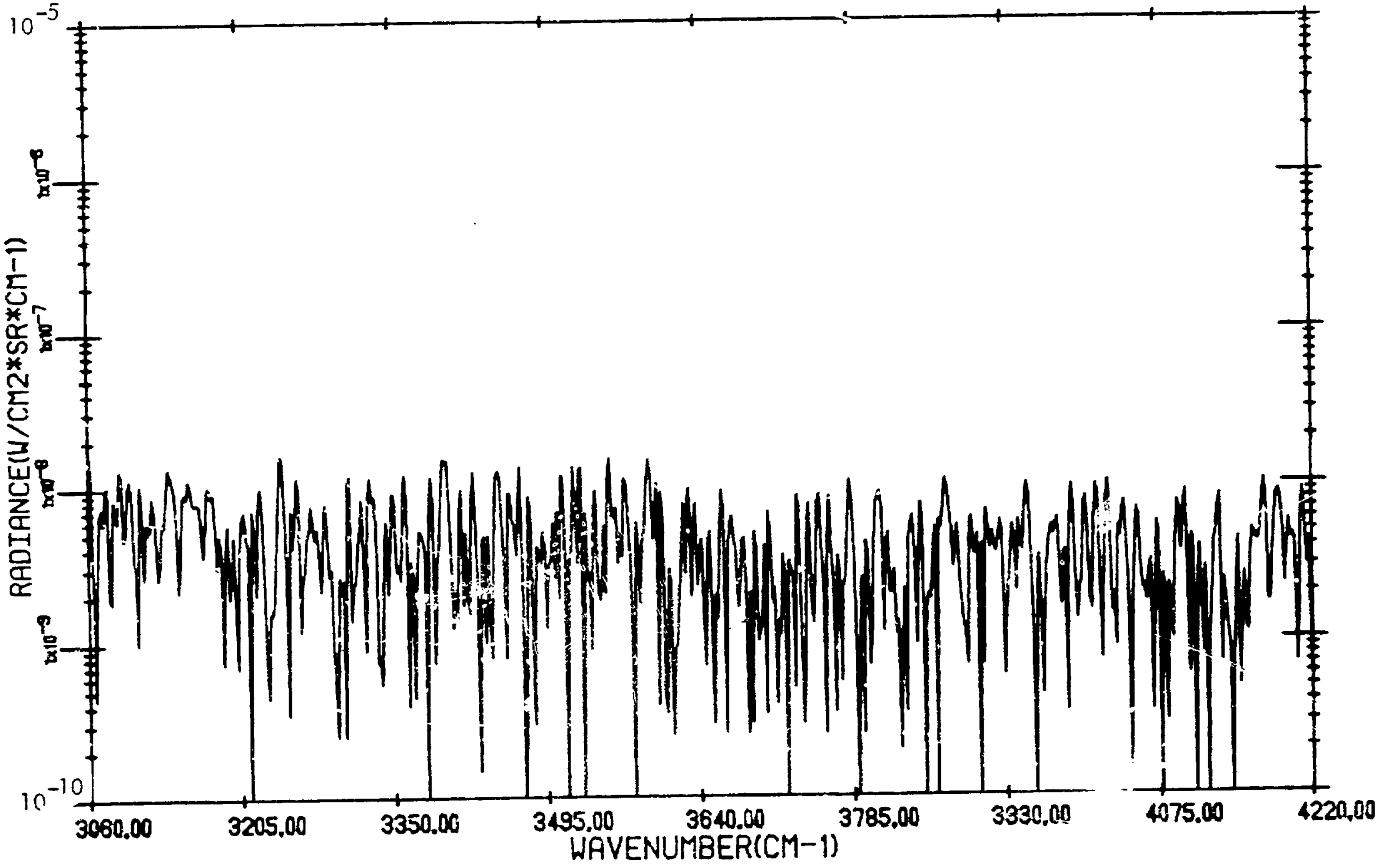

BACKGROUND RADIANCE

WYANDOTTE, MICHIGAN - (816/10) - 15:43:14.8 - BACKGROUND

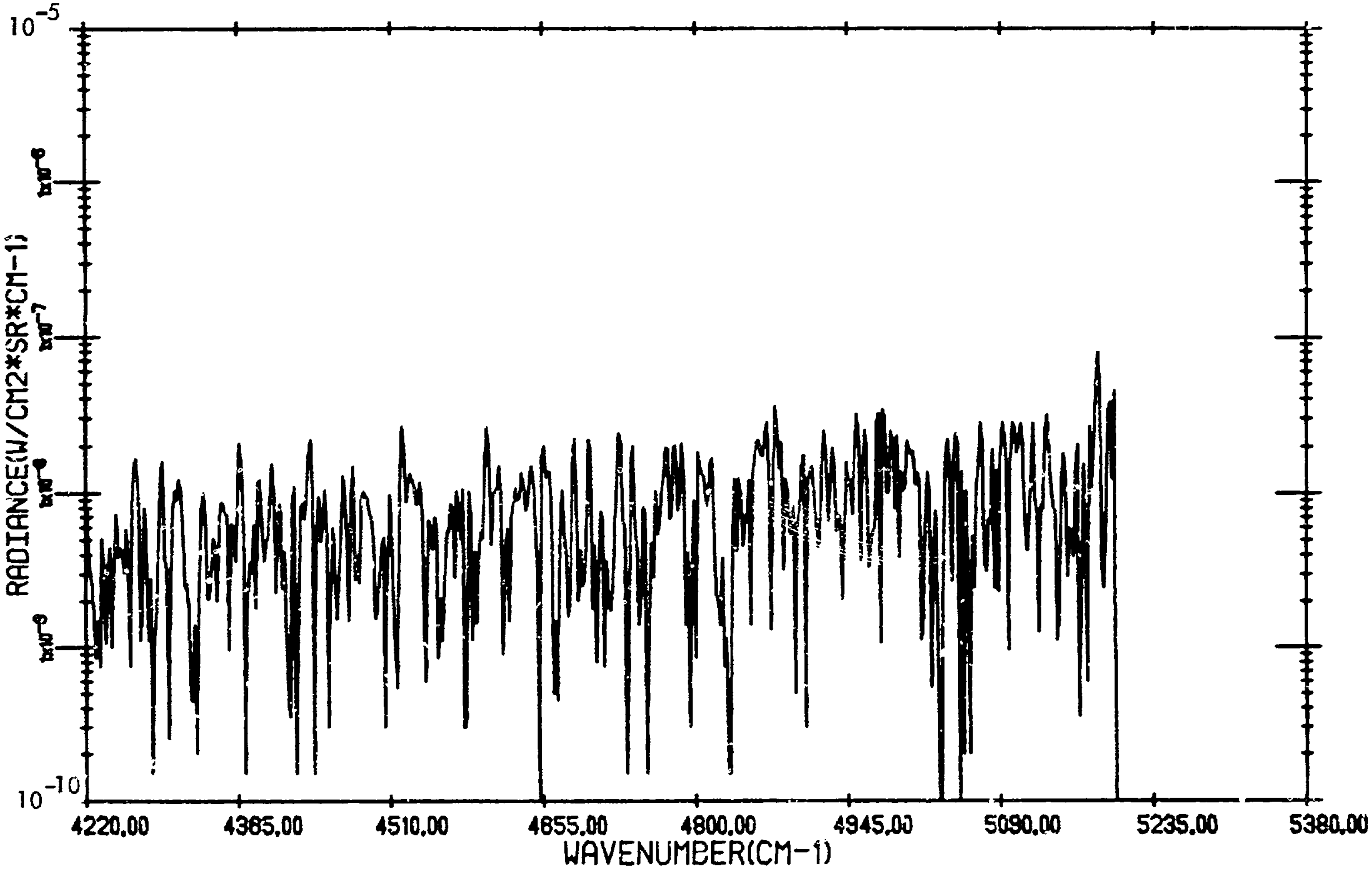

BACKGROUND RADIANCE

(816/10)
WYANDOTTE, MICHIGAN - 15:43:14.8 - BACKGROUND (WITH ATMOSPHERIC TRANSMITTANCE CORRECTION)

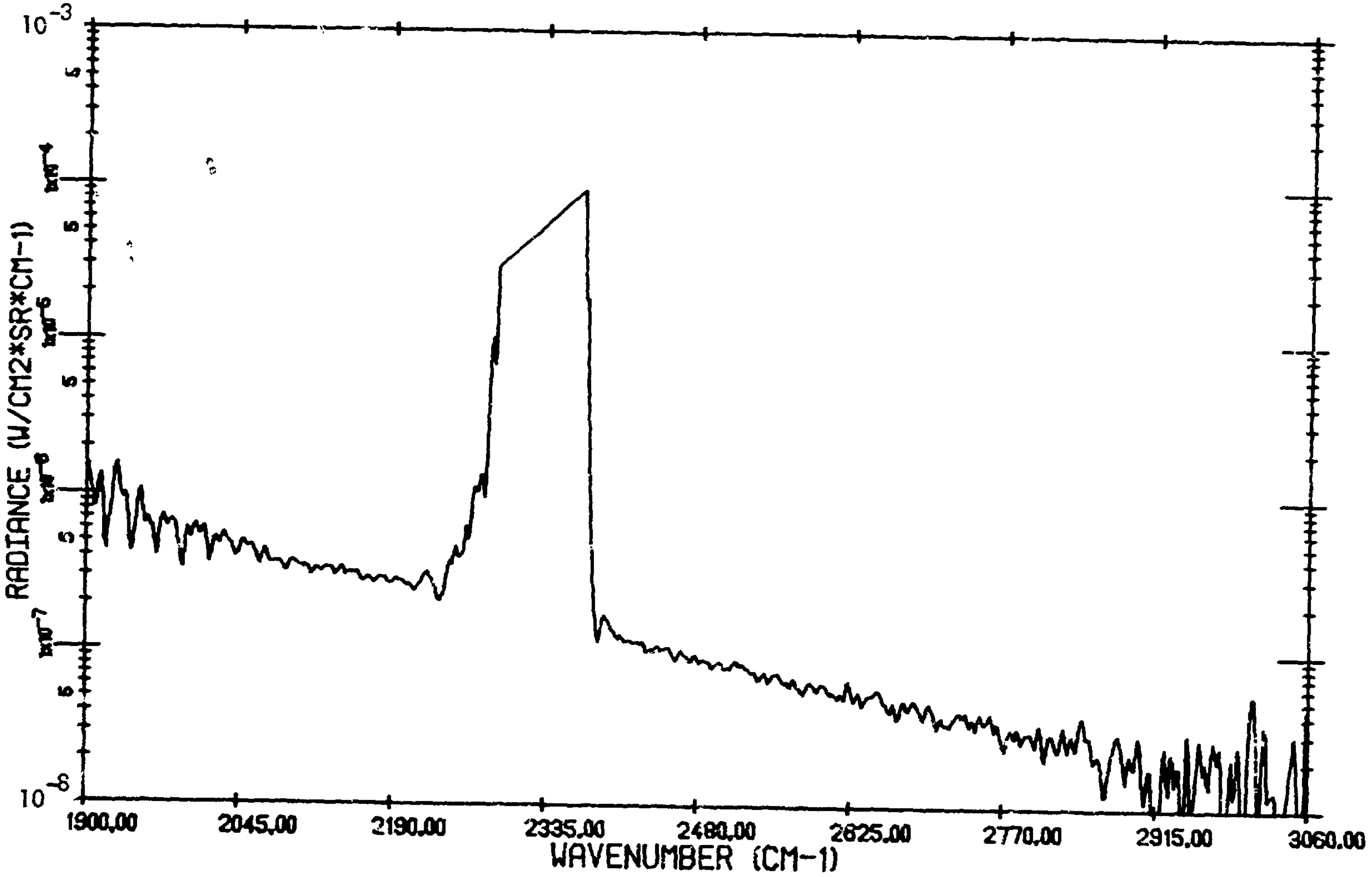

CORRECTED BACKGROUND RADIANCE

ASHLAND, KENTUCKY - (815/2) - 11:33:26.5 - FLAME FROM STACK

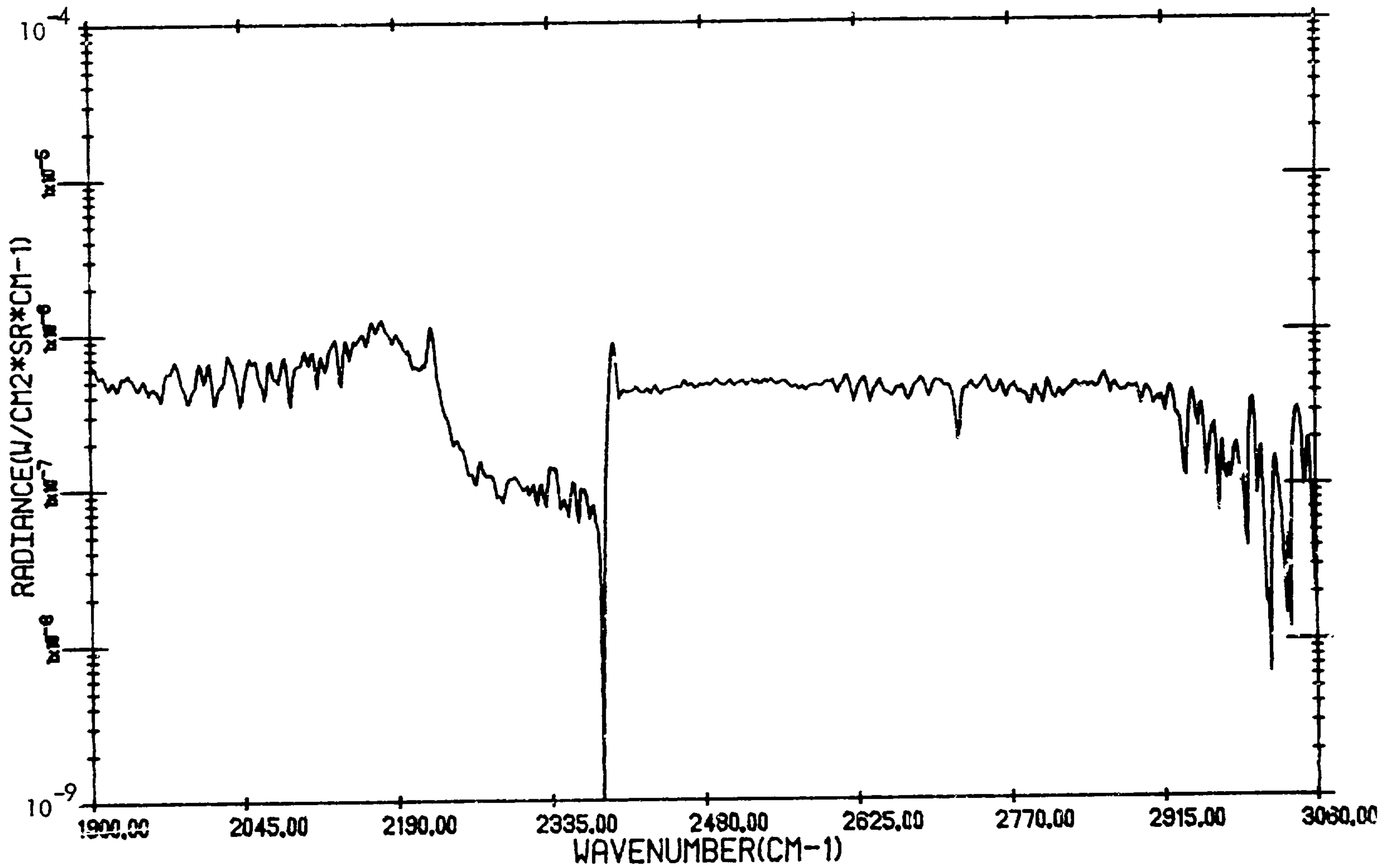

TARGET RADIANCE

ASHLAND, KENTUCKY - (815/2) - 11:33:26.5 - FLAME FROM STACK

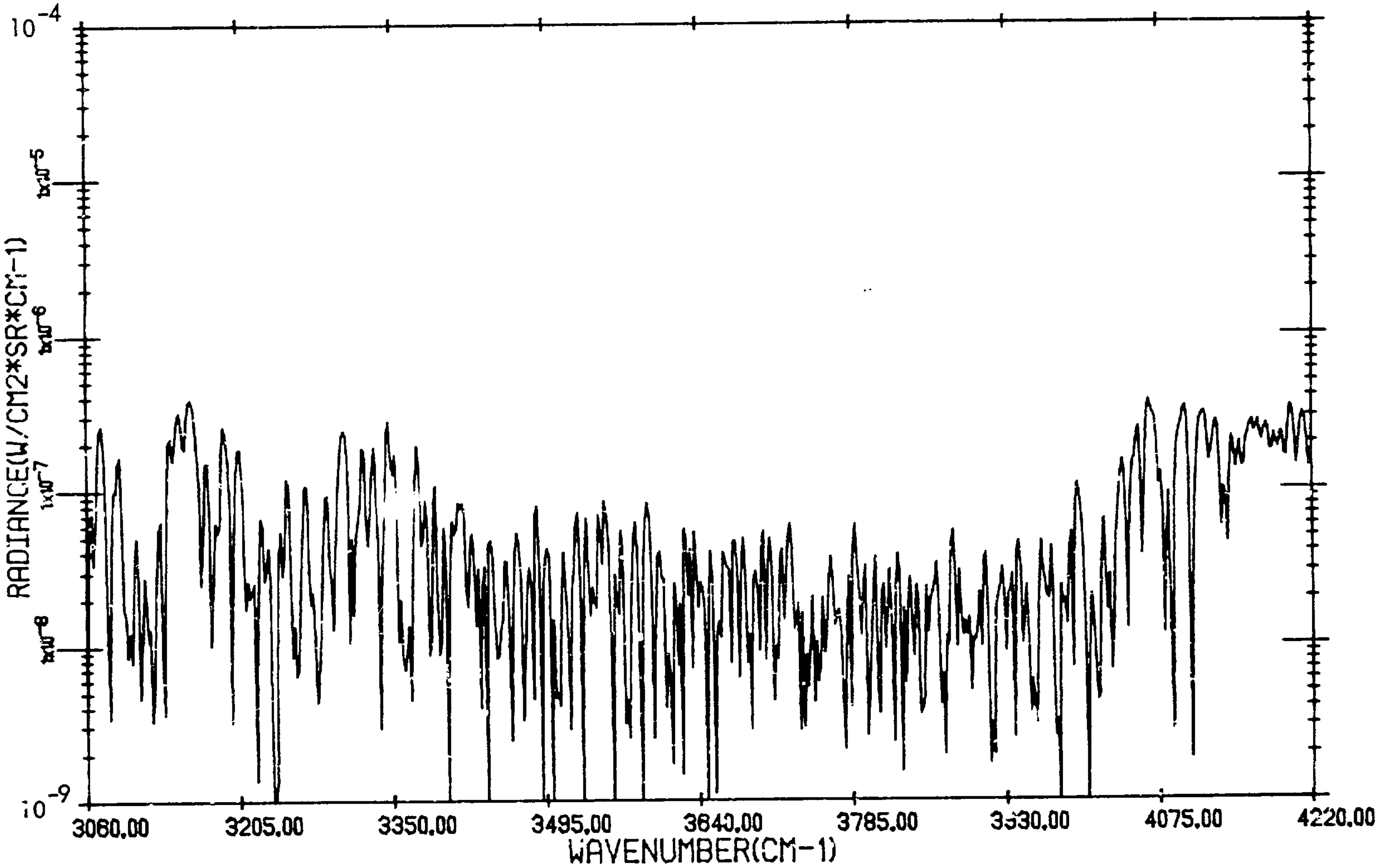

TARGET RADIANCE

ASHLAND KENTUCKY - (815/2) - 11:33:26.5 - FLAME FROM STACK

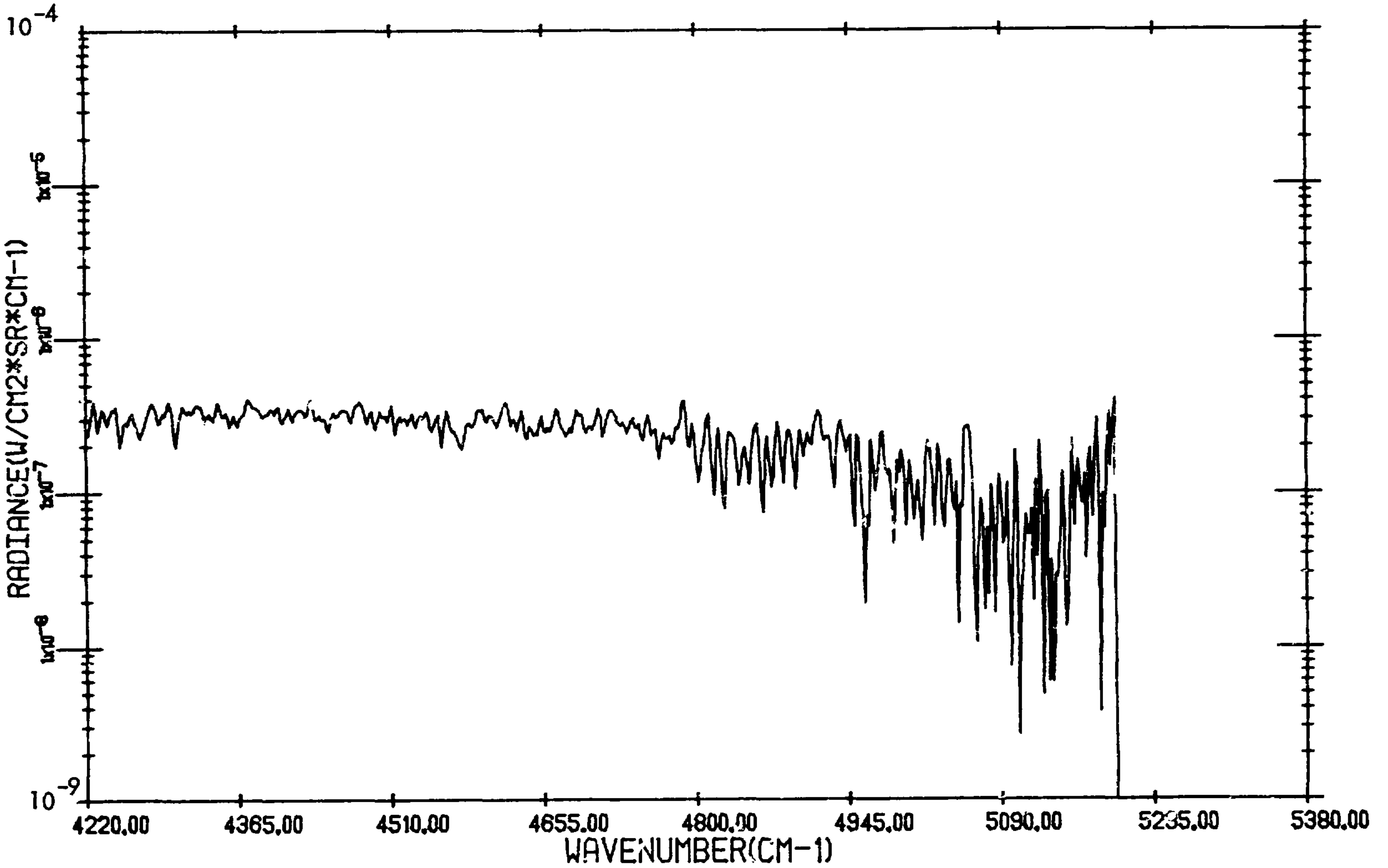

TARGET RADIANCE

(815/2)

ASHLAND, KENTUCKY - 11:33:26.5 - FLAME FROM STACK (WITH ATMOSPHERIC TRANSMITTANCE CORRECTION)

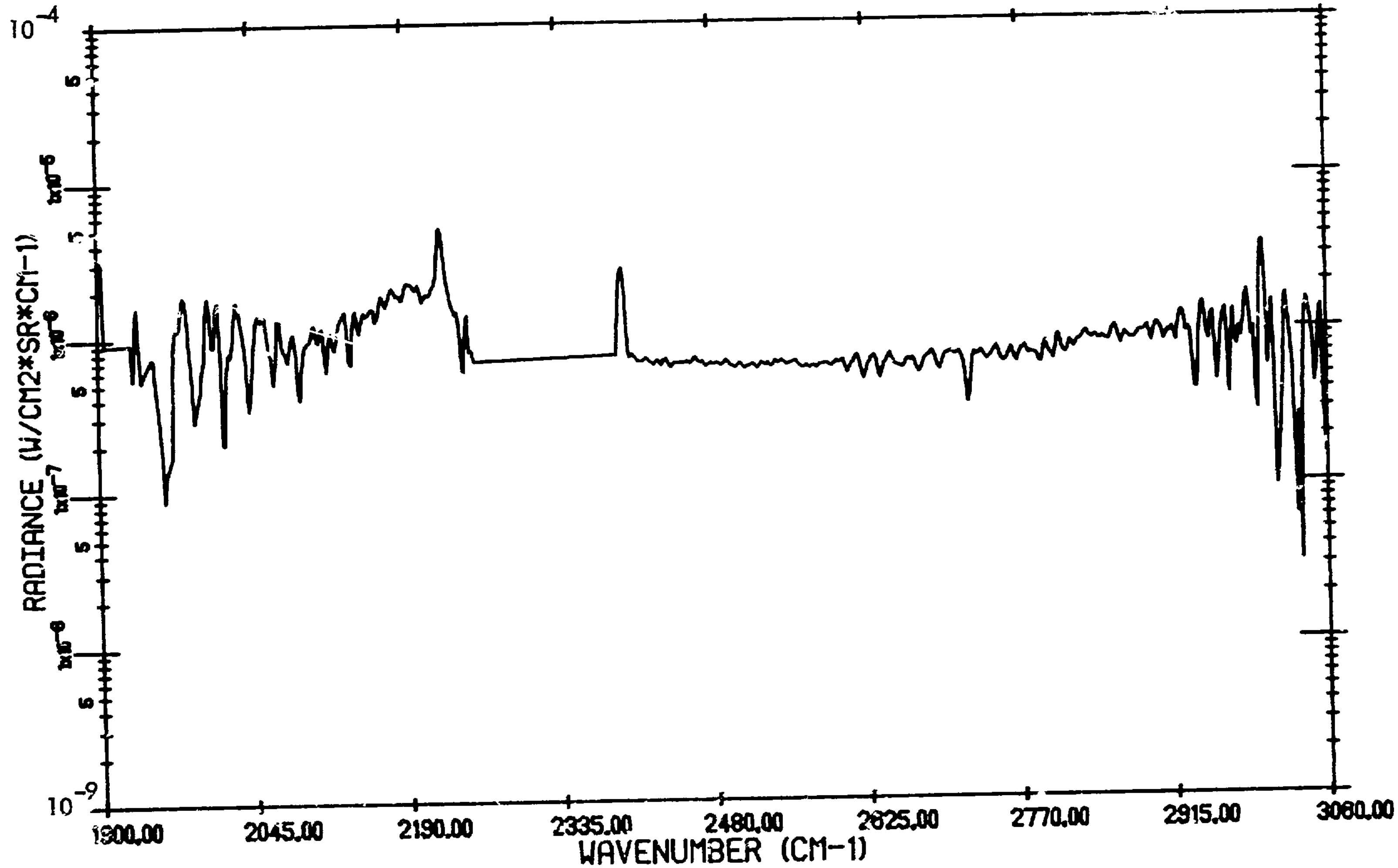

CORRECTED TARGET RADIANCE

ASHLAND, KENTUCKY - (815/2) - 11:36:31.6 - BACKGROUND

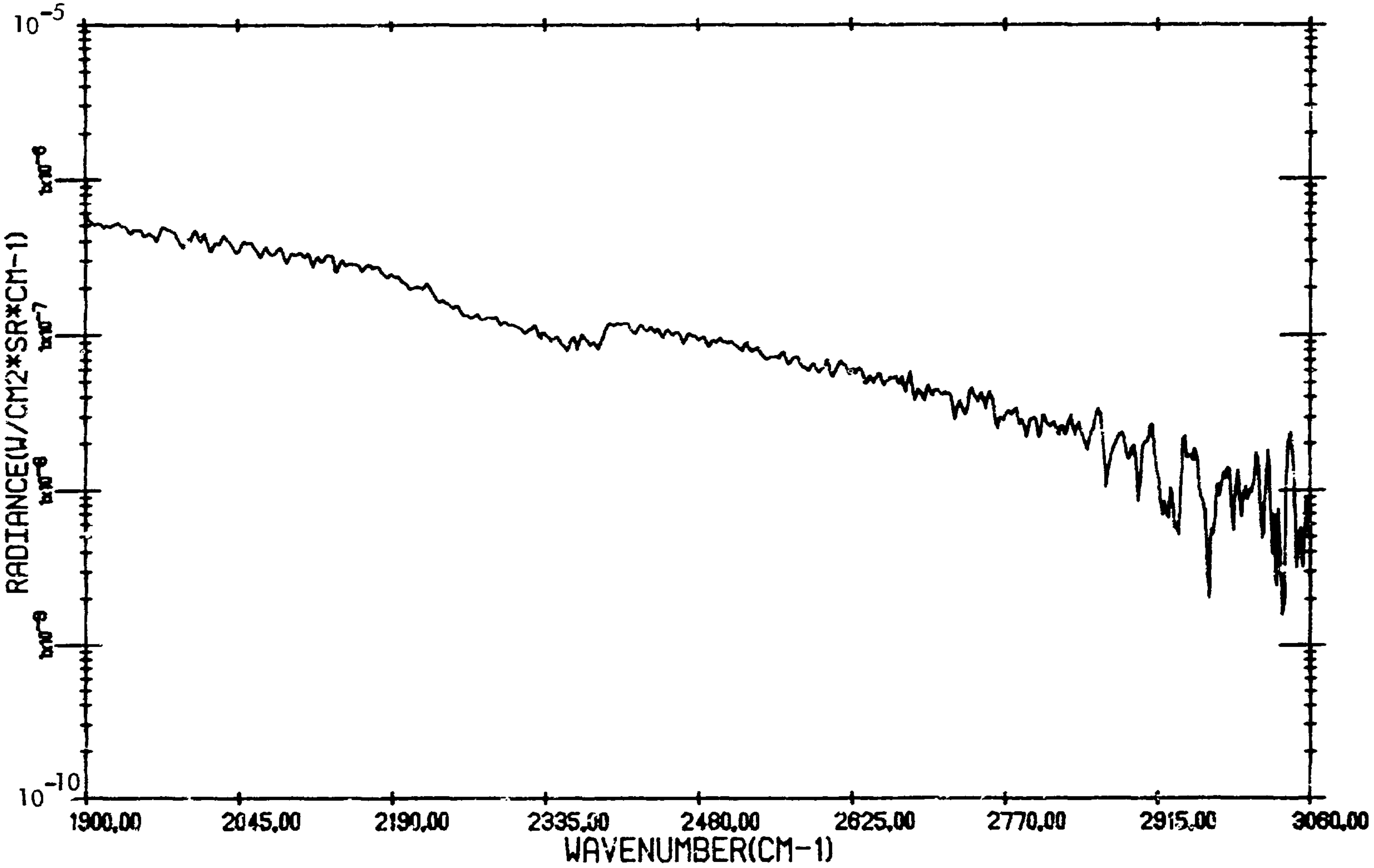

BACKGROUND RADIANCE

ASHLAND, KENTUCKY - (815/2) - 11:36:31.6 - BACKGROUND

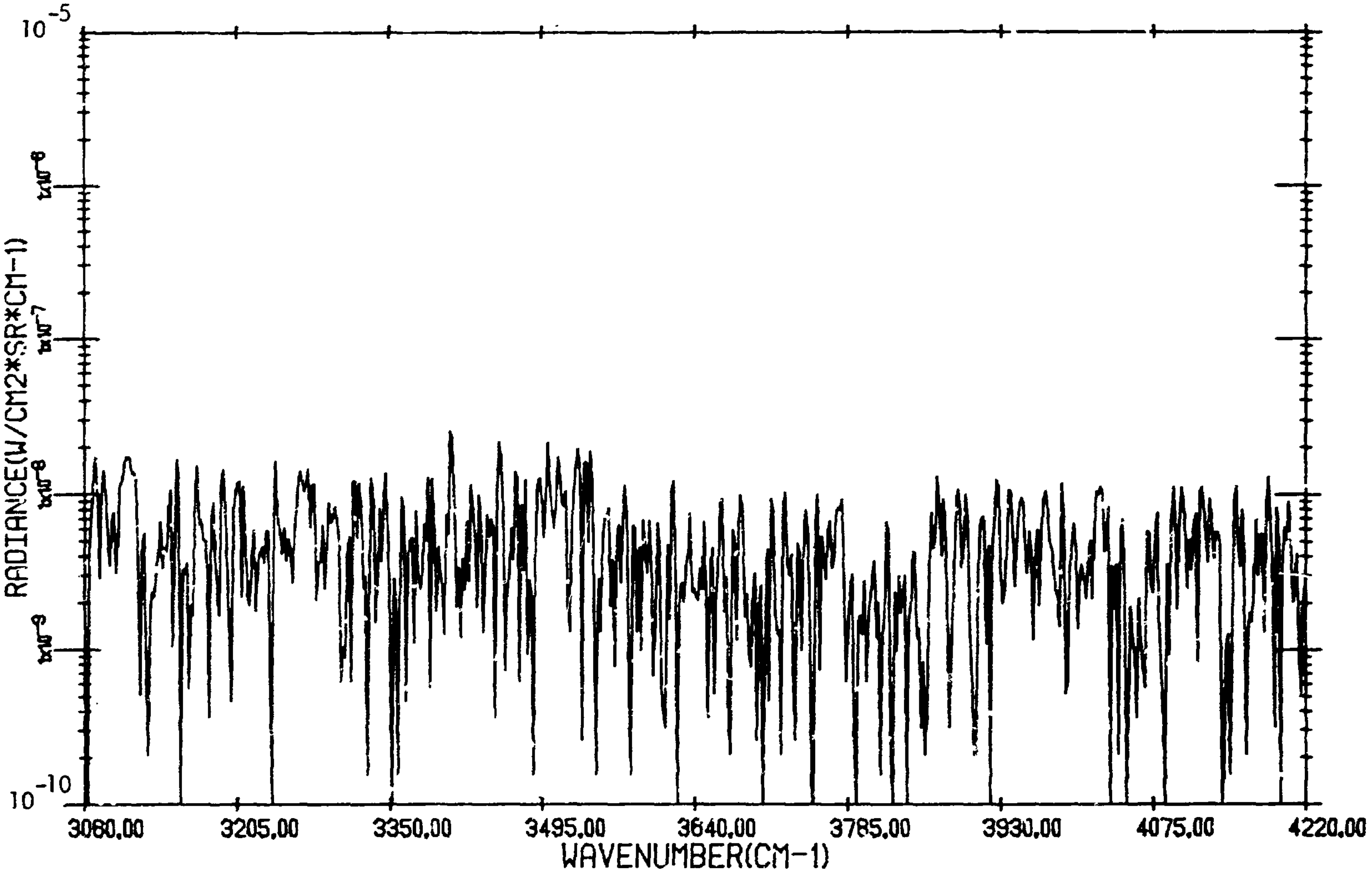

BACKGROUND RADIANCE

ASHLAND, KENTUCKY - (815/2) - 11:36:31.6 - BACKGROUND

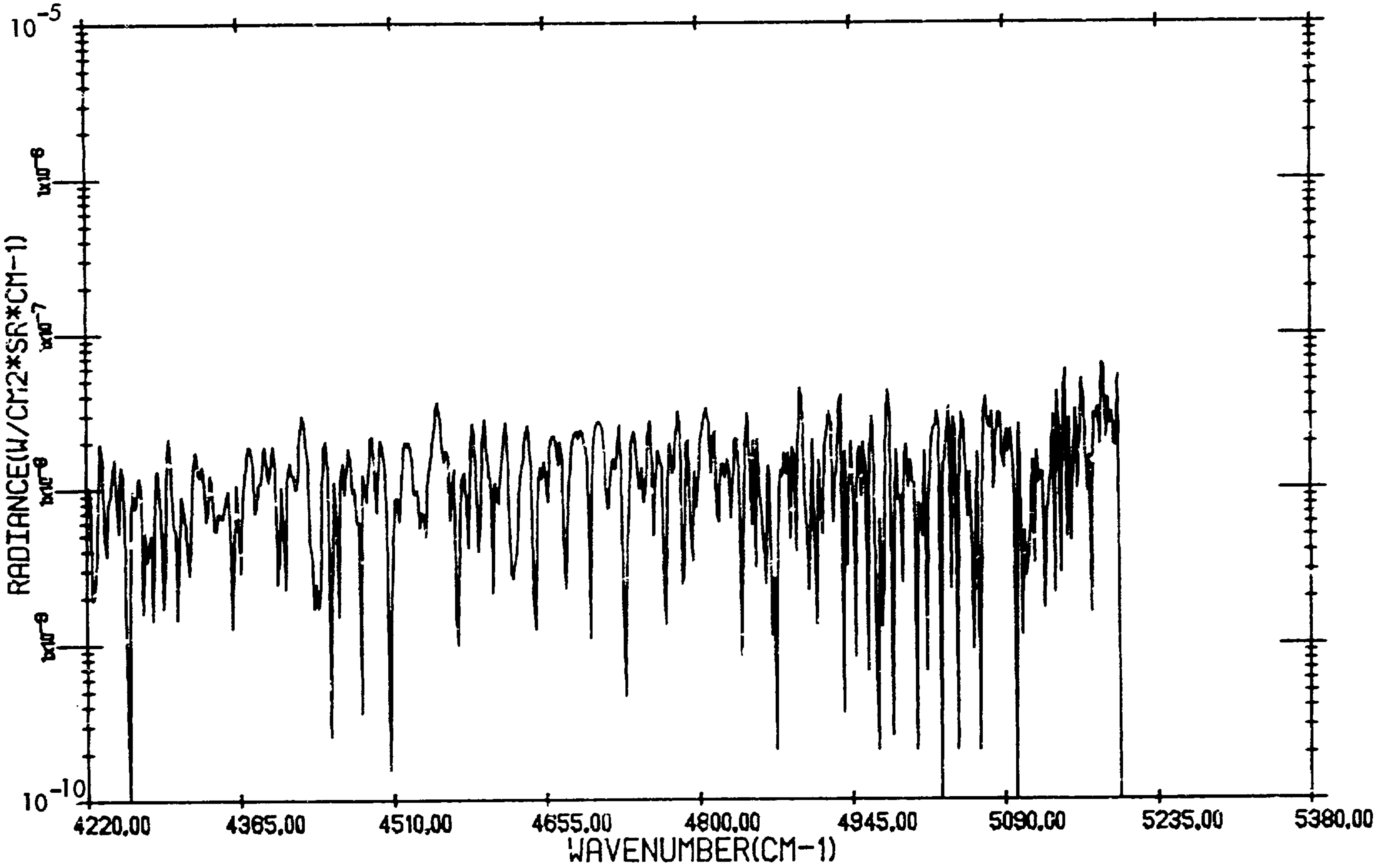

BACKGROUND RADIANCE

(815/2)
ASHLAND, KENTUCKY - 11:36:31.6 - BACKGROUND (WITH ATMOSPHERIC TRANSMITTANCE CORRECTION)

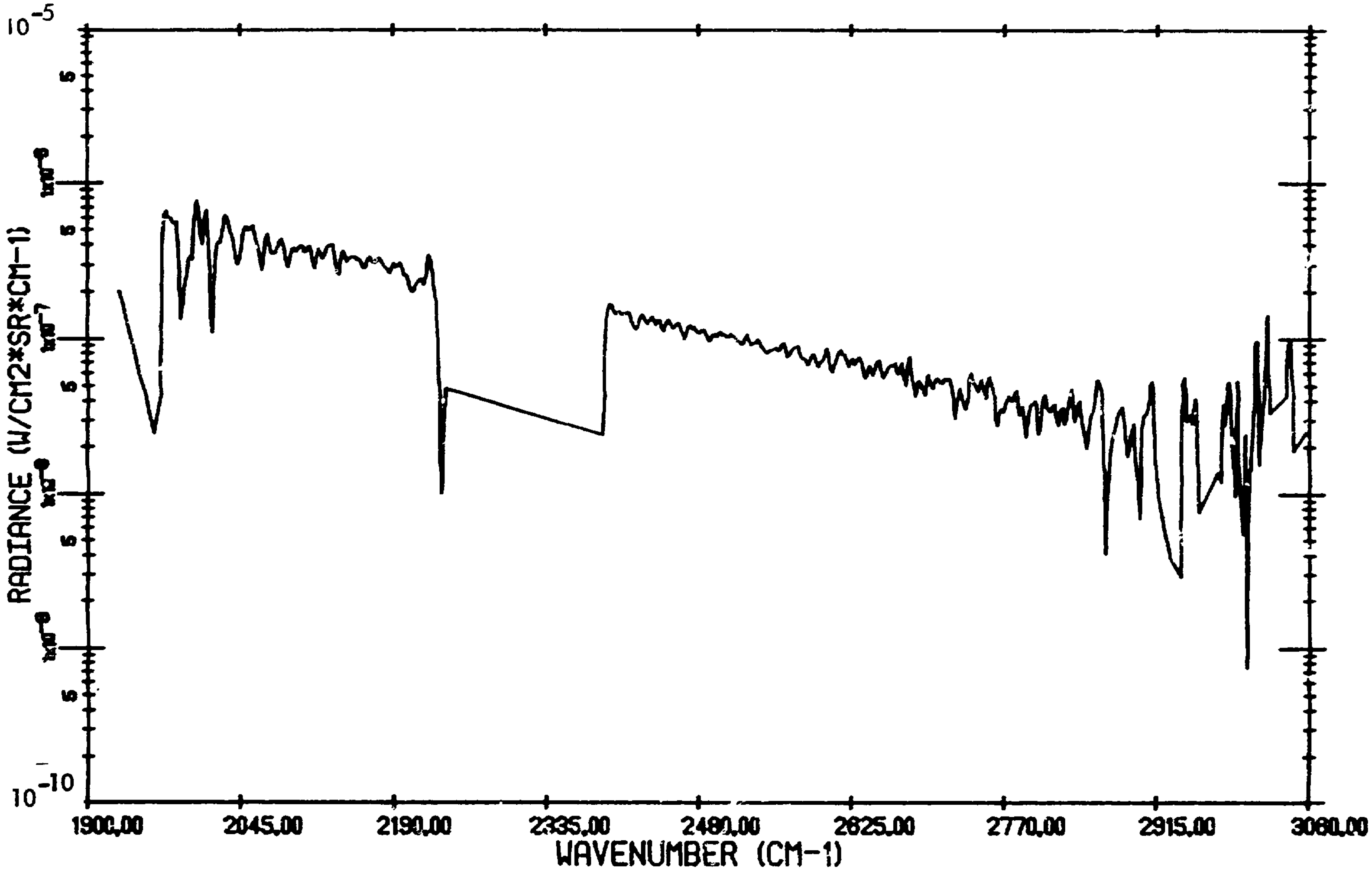

CORRECTED BACKGROUND RADIANCE

ASHLAND, KENTUCKY - (815/2) - 11:43:13.2 - REFINERY COMPLEX

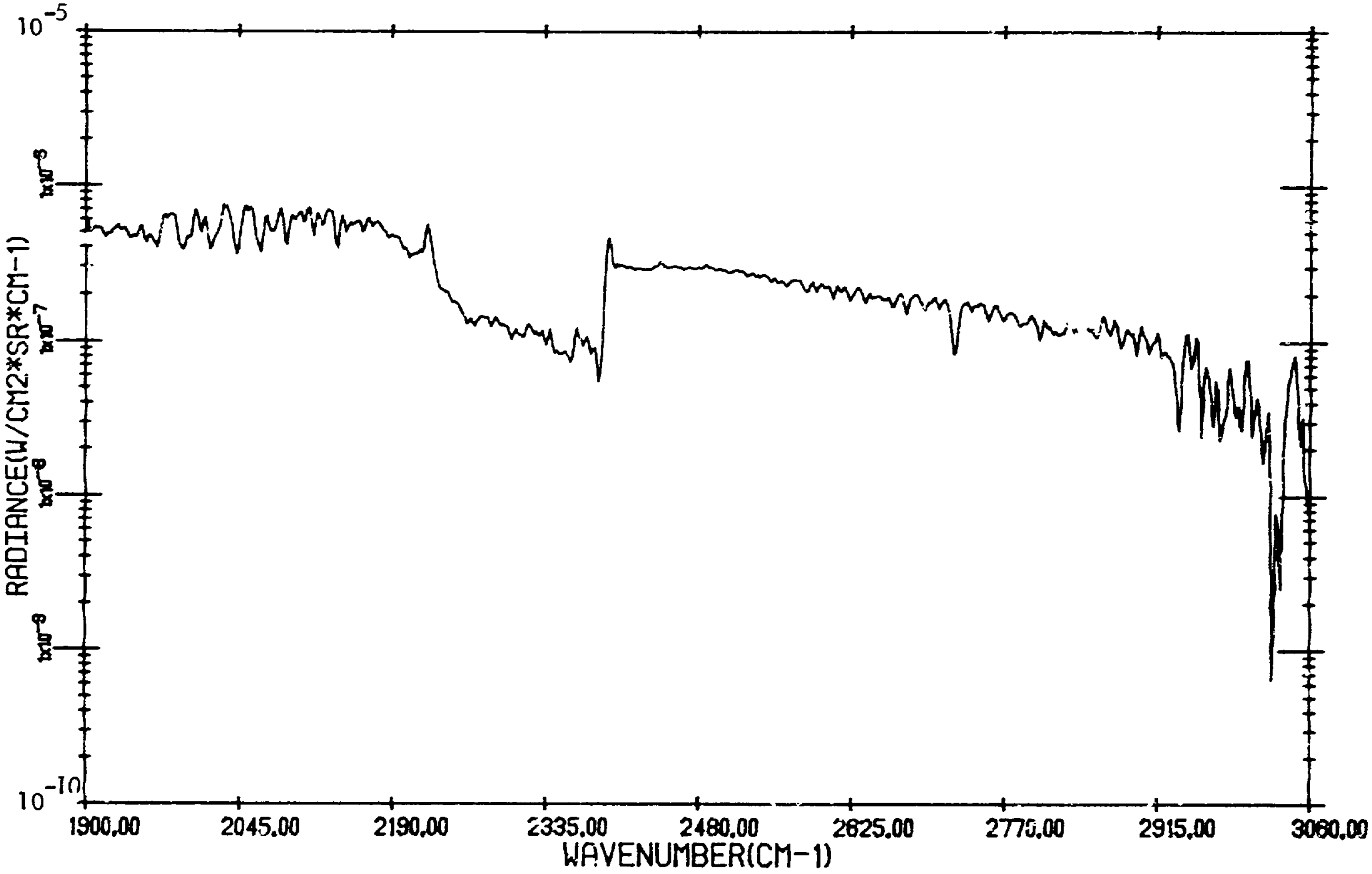

TARGET RADIANCE

ASHLAND, KENTUCKY - (815/2) - 11:43:13.2 - REFINERY COMPLEX

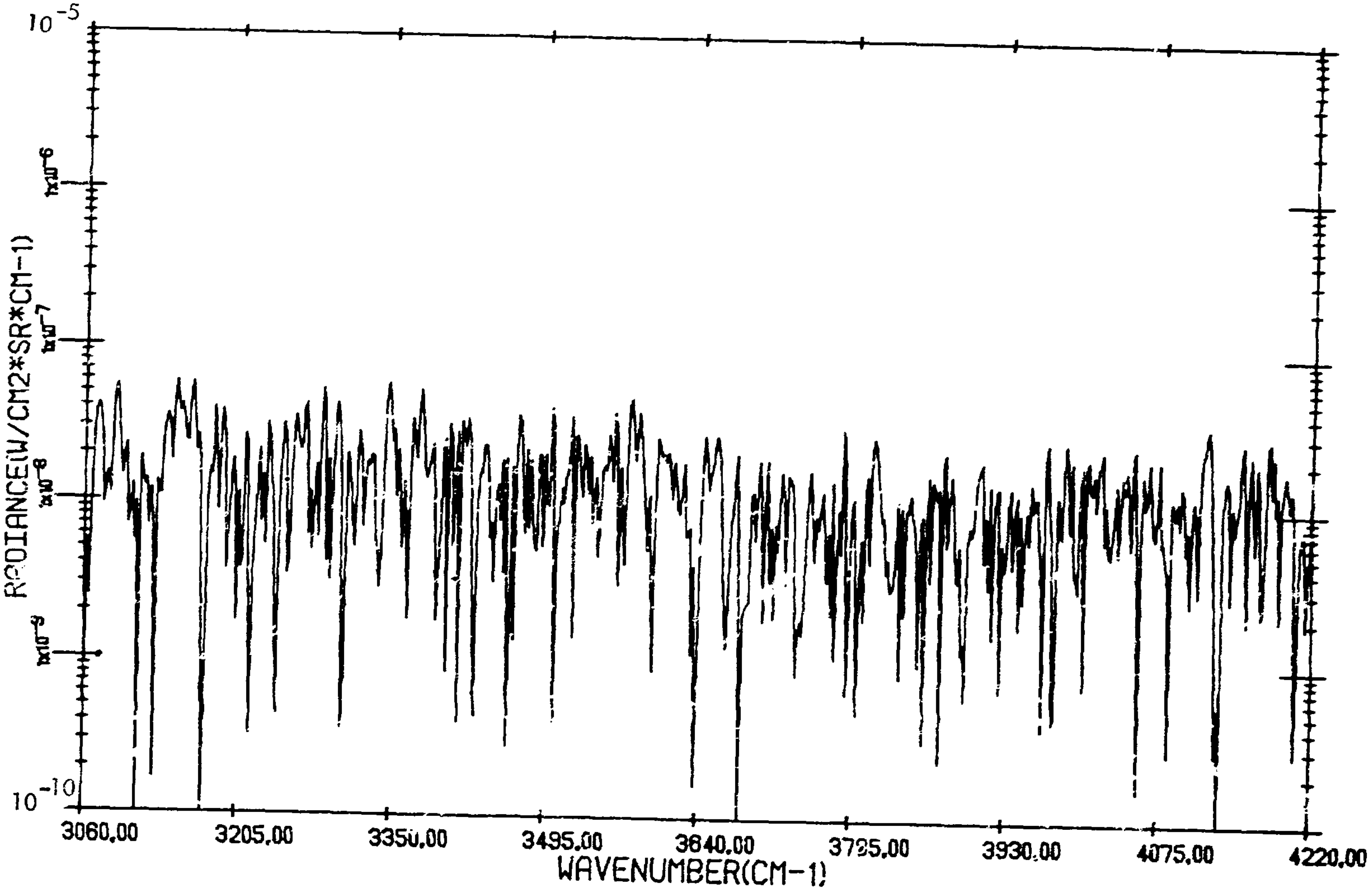

TARGET RADIANCE

ASHLAND, KENTUCKY - (815/2) - 11:43:13.2 - REFINERY COMPLEX

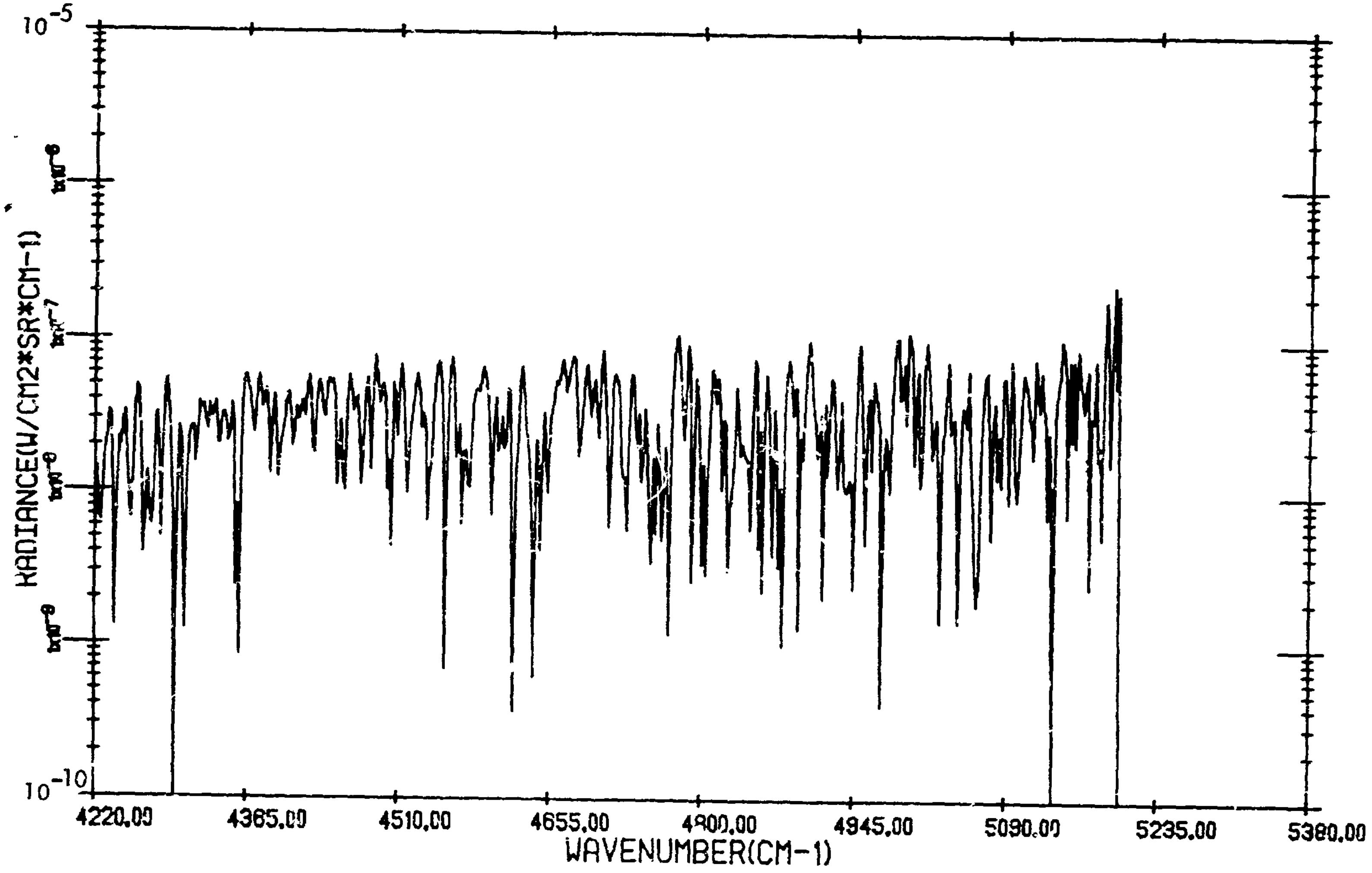

TARGET RADIANCE

(815/2)

ASHLAND, KENTUCKY - 11:43:13.2 - REFINERY COMPLEX (WITH ATMOSPHERIC TRANSMITTANCE CORRECTION)

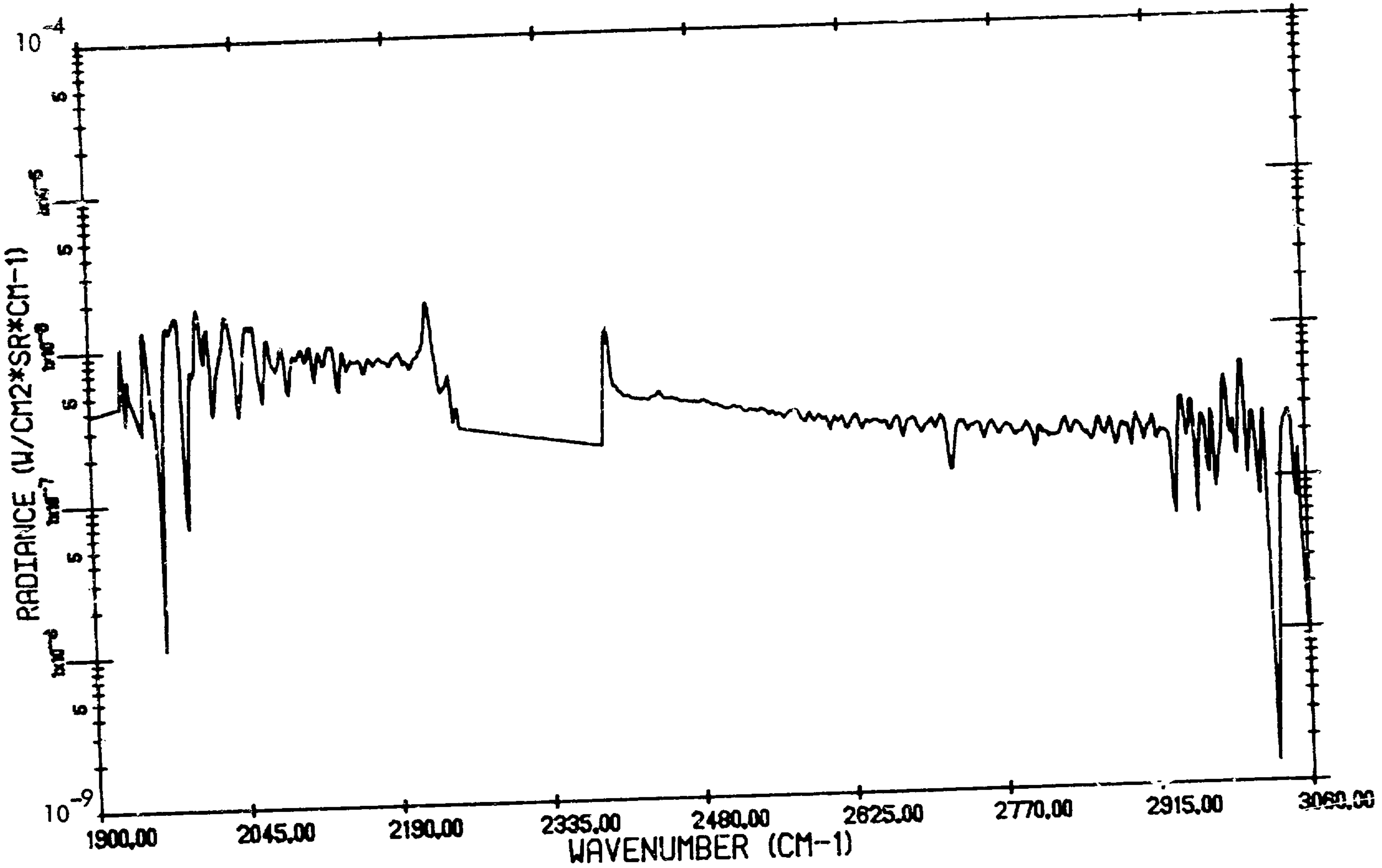

CORRECTED TARGET RADIANCE

FAIRFIELD, ALABAMA - (815/4) - 12:57:26.2 - TIP OF STACK

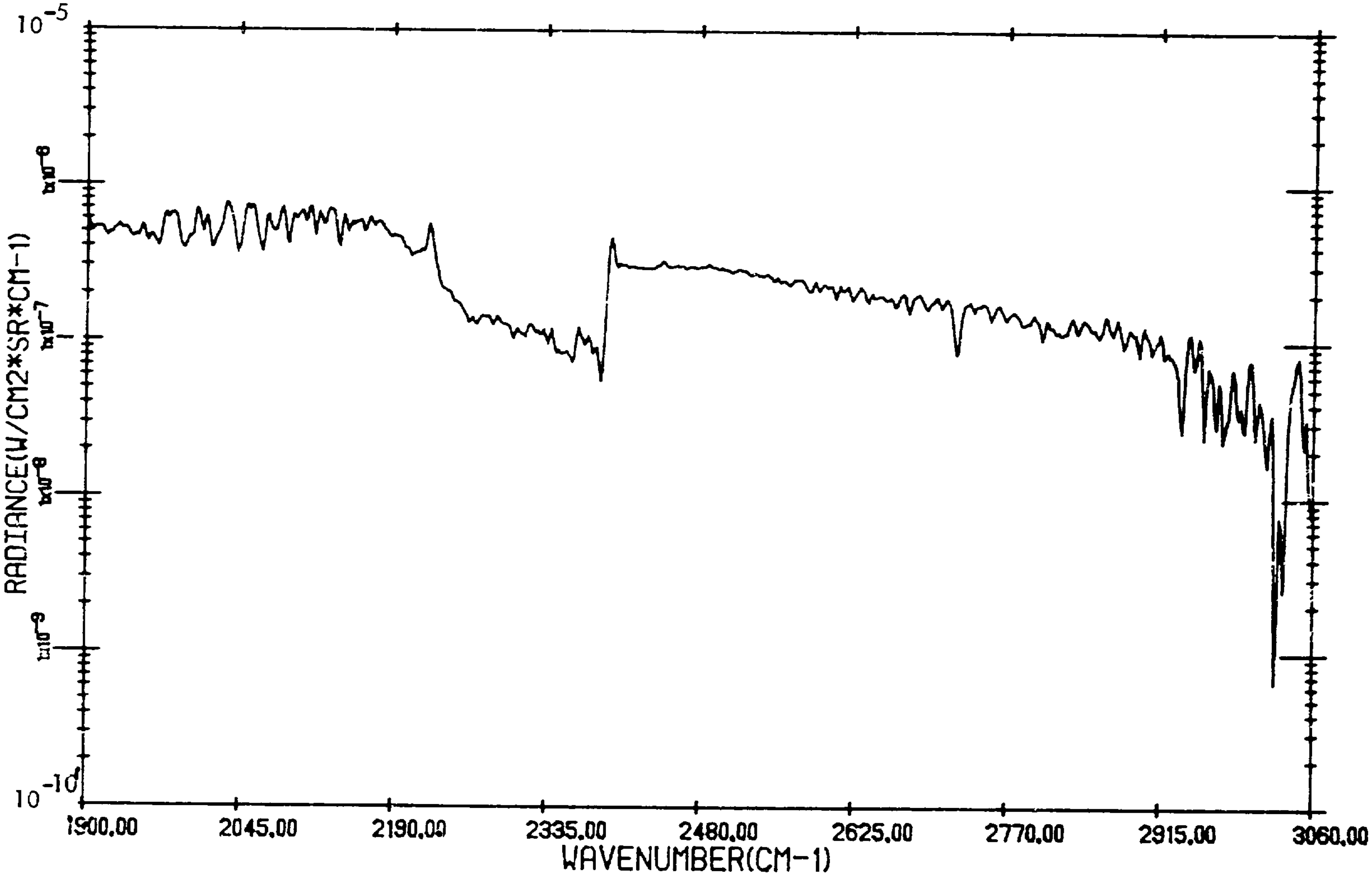

TARGET RADIANCE

FAIRFIELD, ALABAMA - (815/4) - 12:57:26.2 - TIP OF STACK

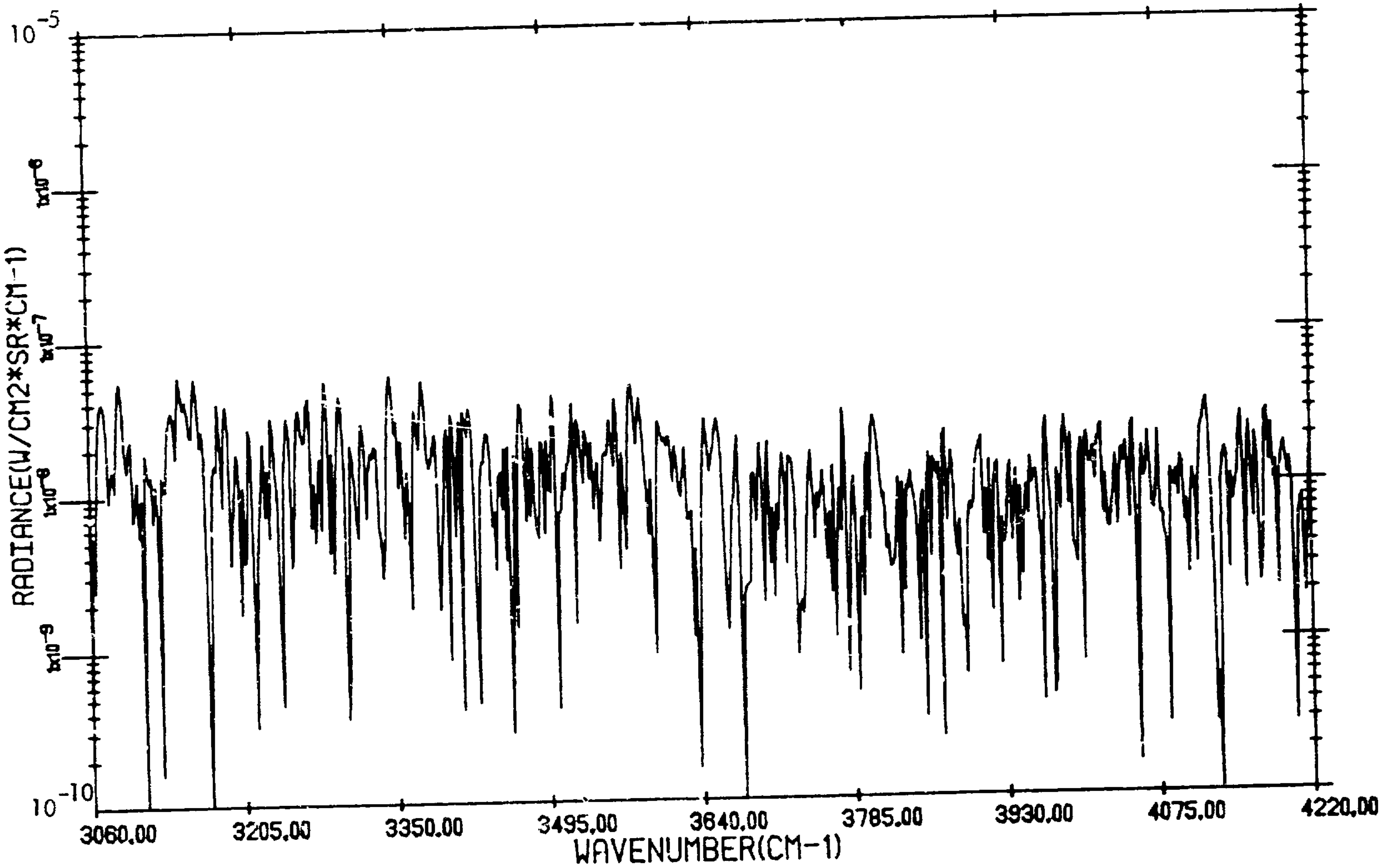

TARGET RADIANCE

FAIRFIELD, ALABAMA - (815/4) - 12:57:26.2 - TIP OF STACK

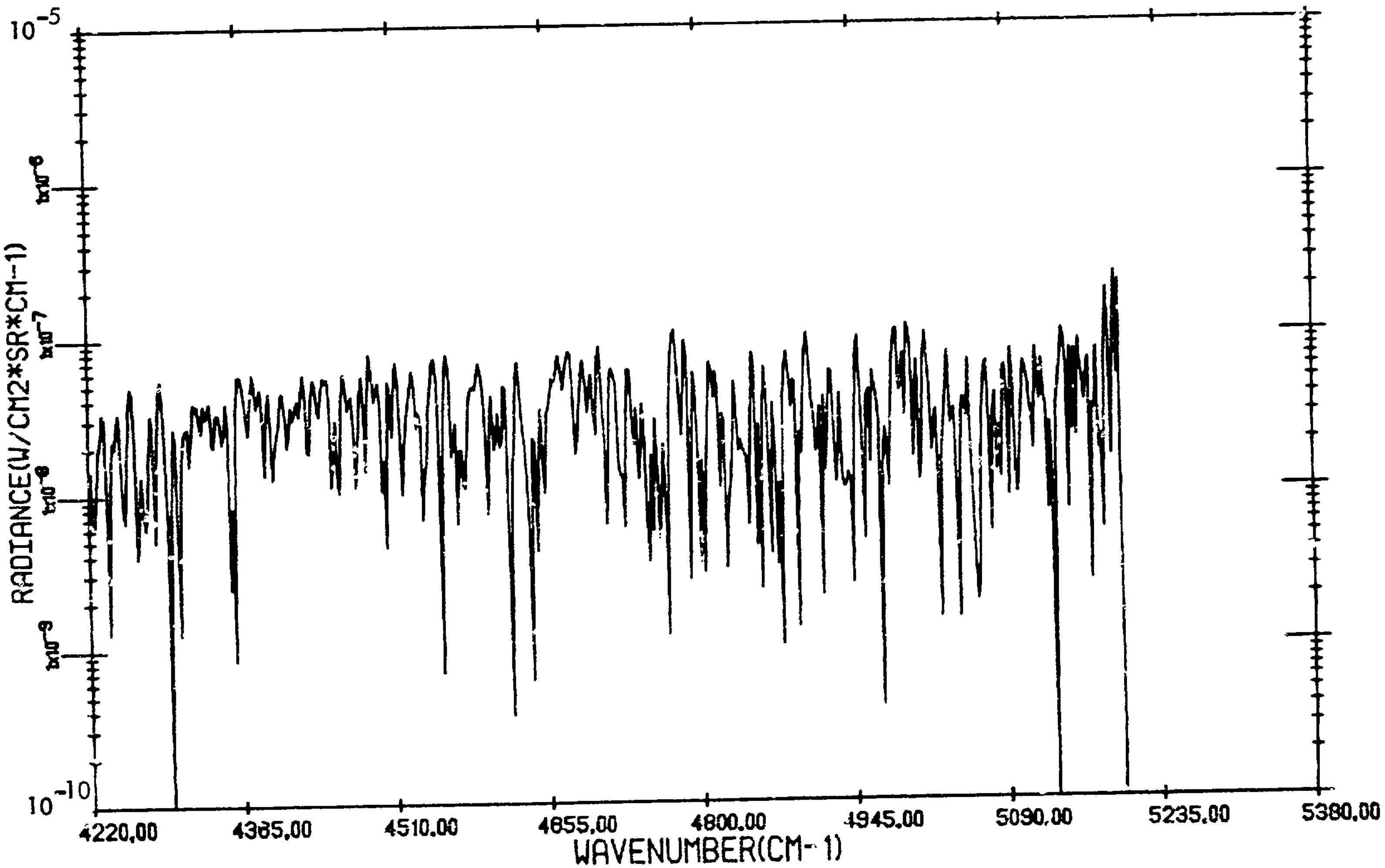

TARGET RADIANCE

(815/4)

FAIRFIELD, ALABAMA - 12:57:26.2 - TIP OF STACK (WITH ATMOSPHERIC TRANSMITTANCE CORRECTION)

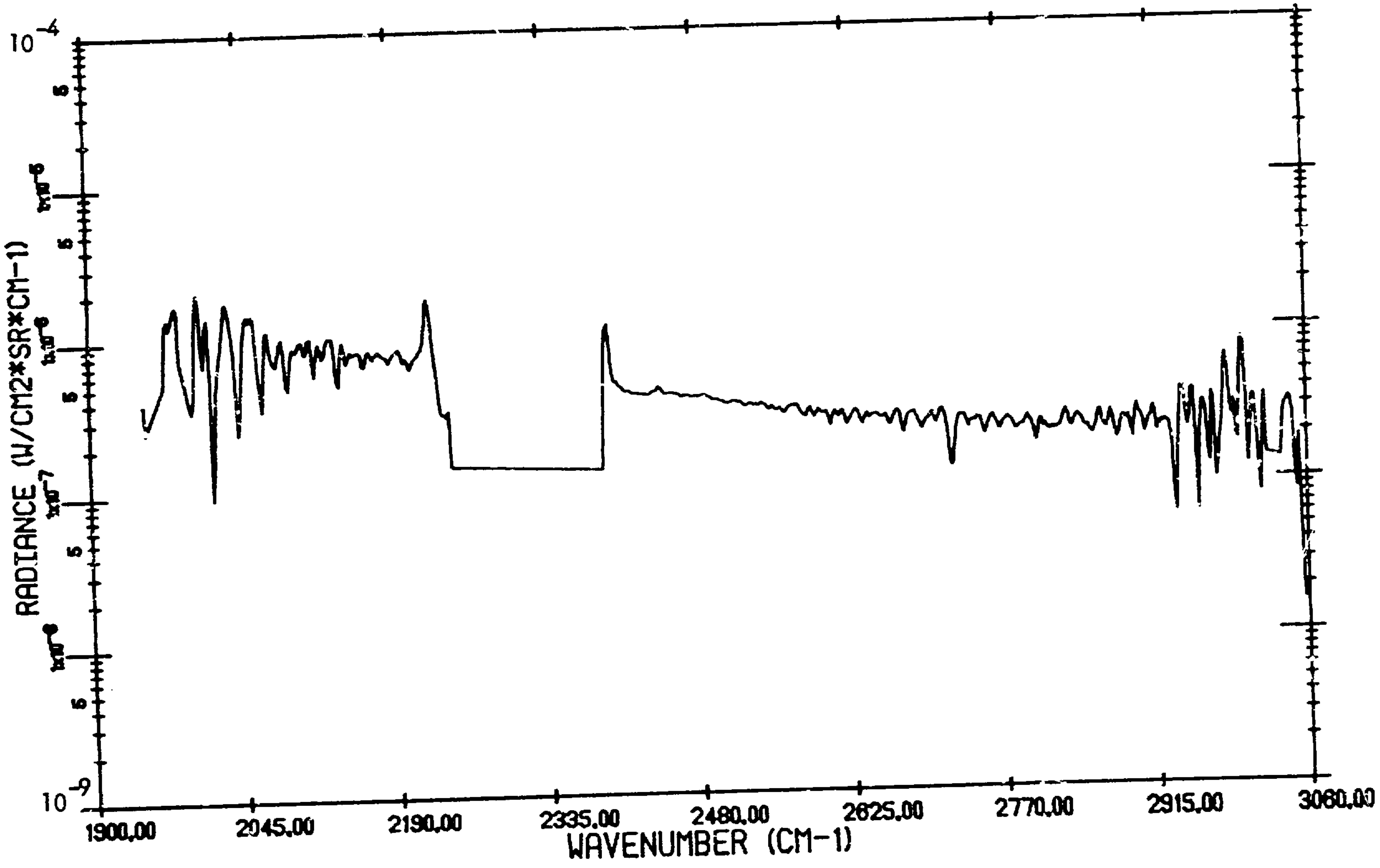

CORRECTED TARGET RADIANCE

FAIRFiELD, ALABAMA - (815/4) - 12:58:51.6 - BACKGROUND

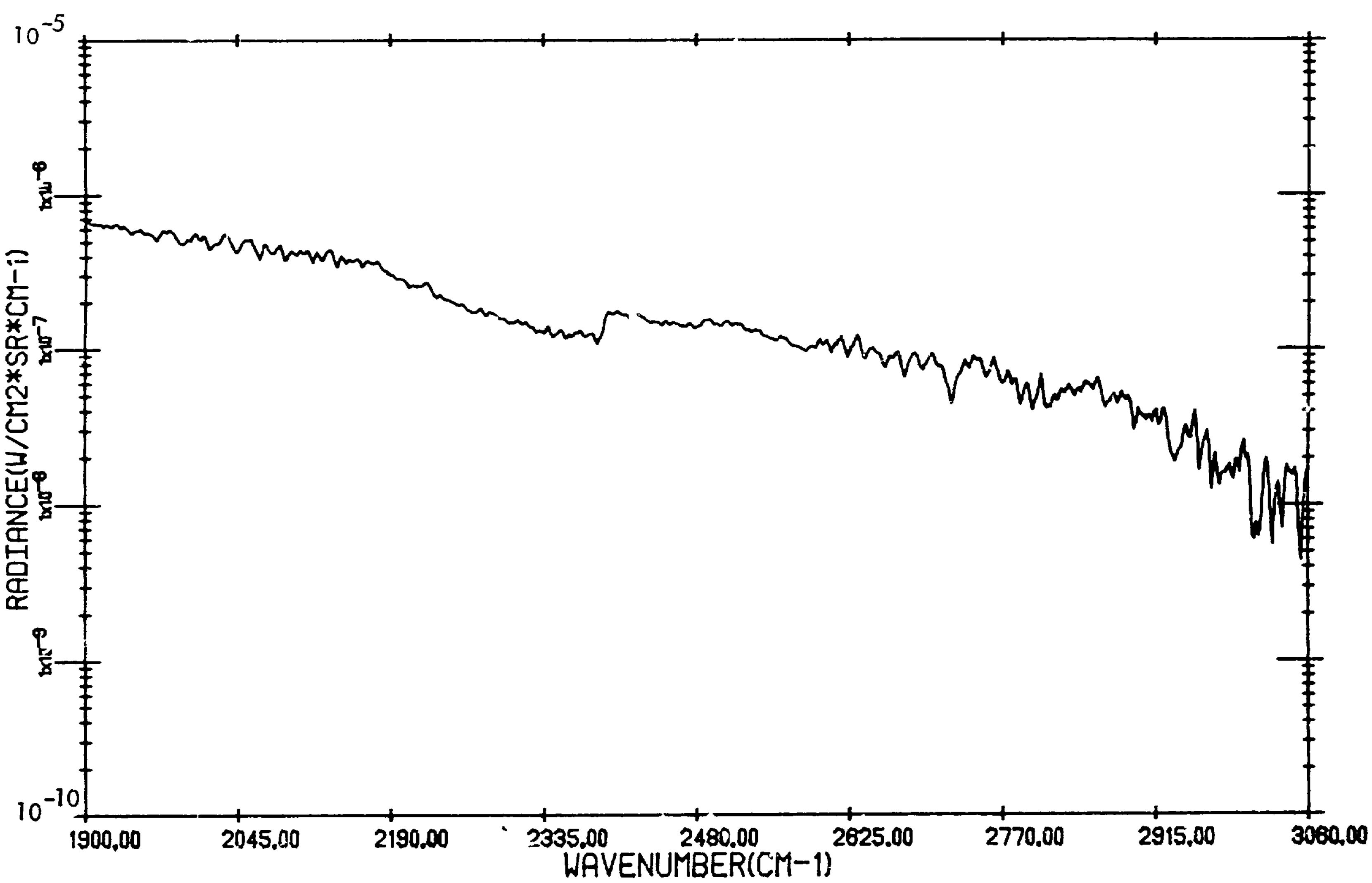

BACKGROUND RADIANCE

FAIRFIELD, ALABAMA - (815/4) - 12:58:51.6 - BACKGROUND

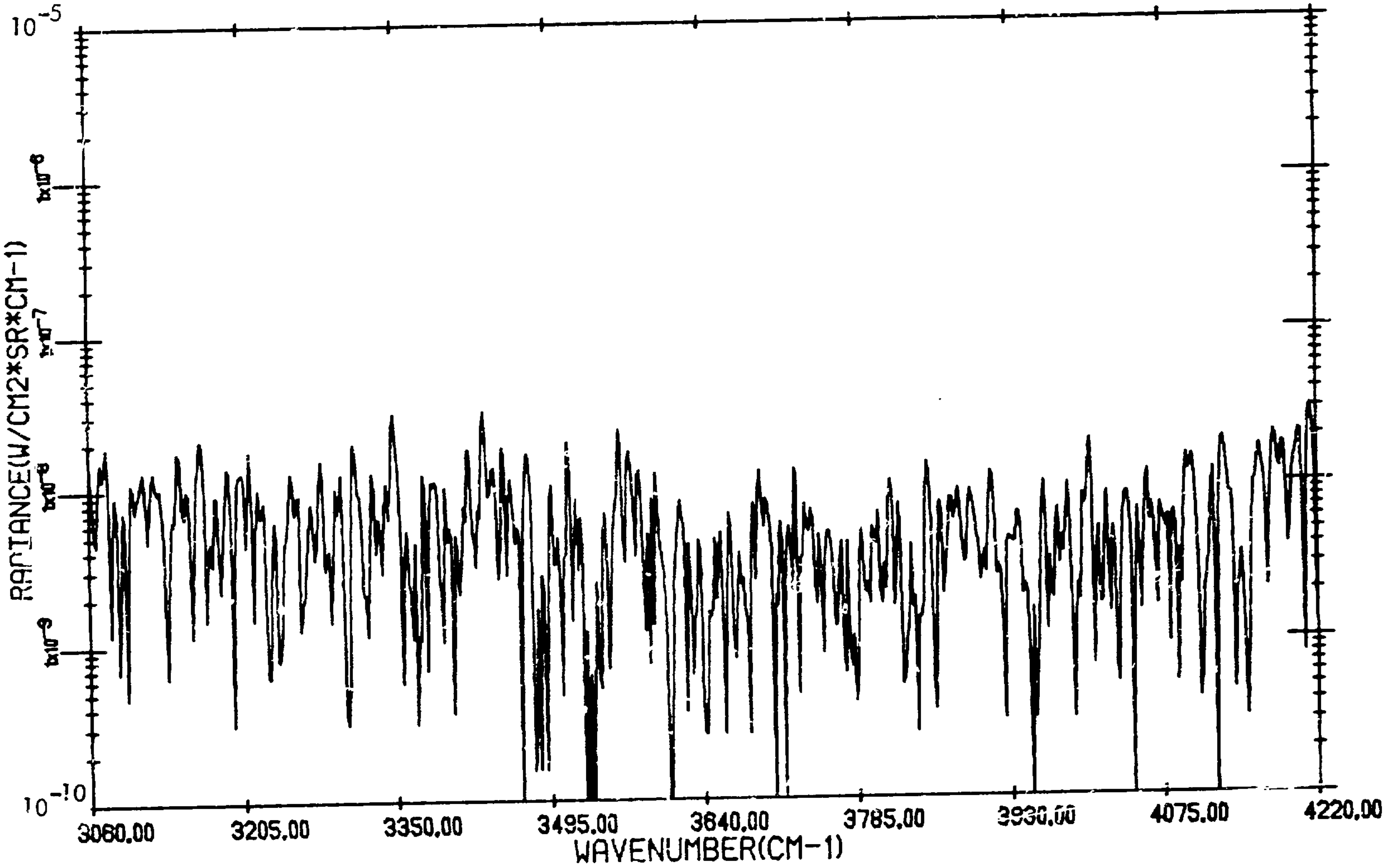

BACKGROUND RADIANCE

FAIRFIELD, ALABAMA - (815/4) - 12:58:51.6 - BACKGROUND

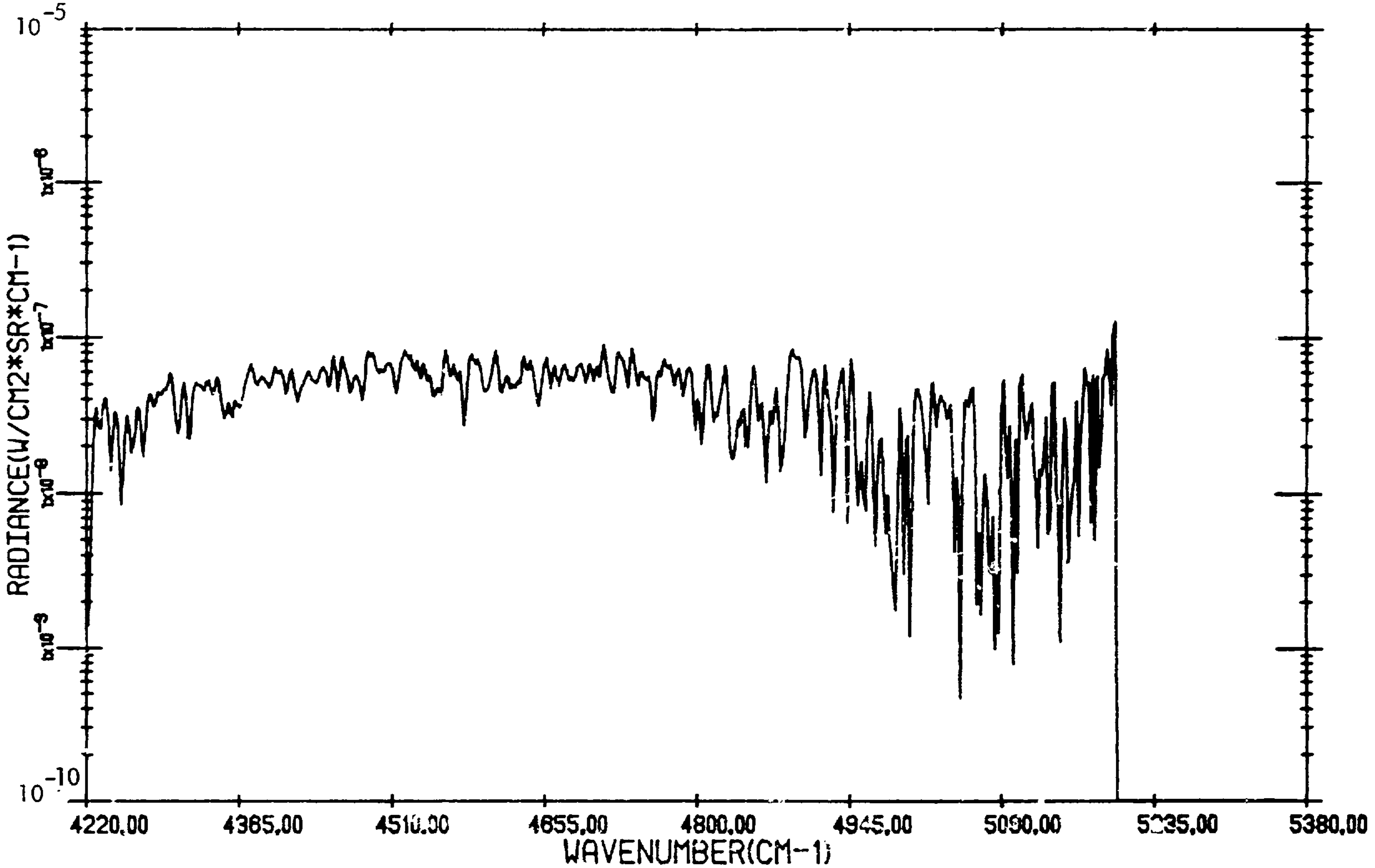

BACKGROUND RADIANCE

(815/4)

FAIRFIELD, ALABAMA - 12:58:51.6 - BACKGROUND (WITH ATMOSPHERIC TRANSMITTANCE CORRECTION)

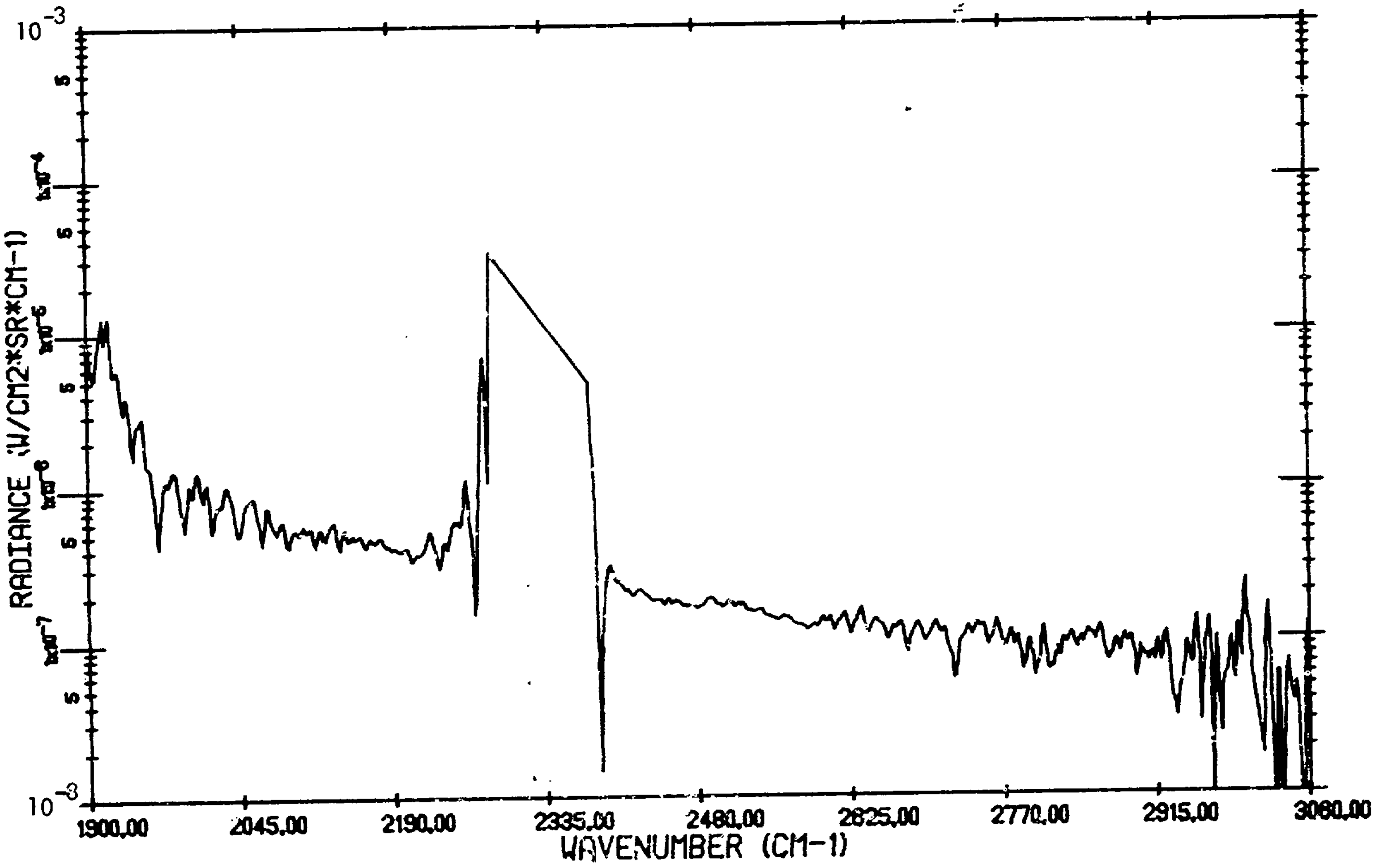

CORRECTED BACKGROUND RADIANCE

FAIRFIELD, ALABAMA - (815/4) - 13:03:28.9 - GREY BUILDING

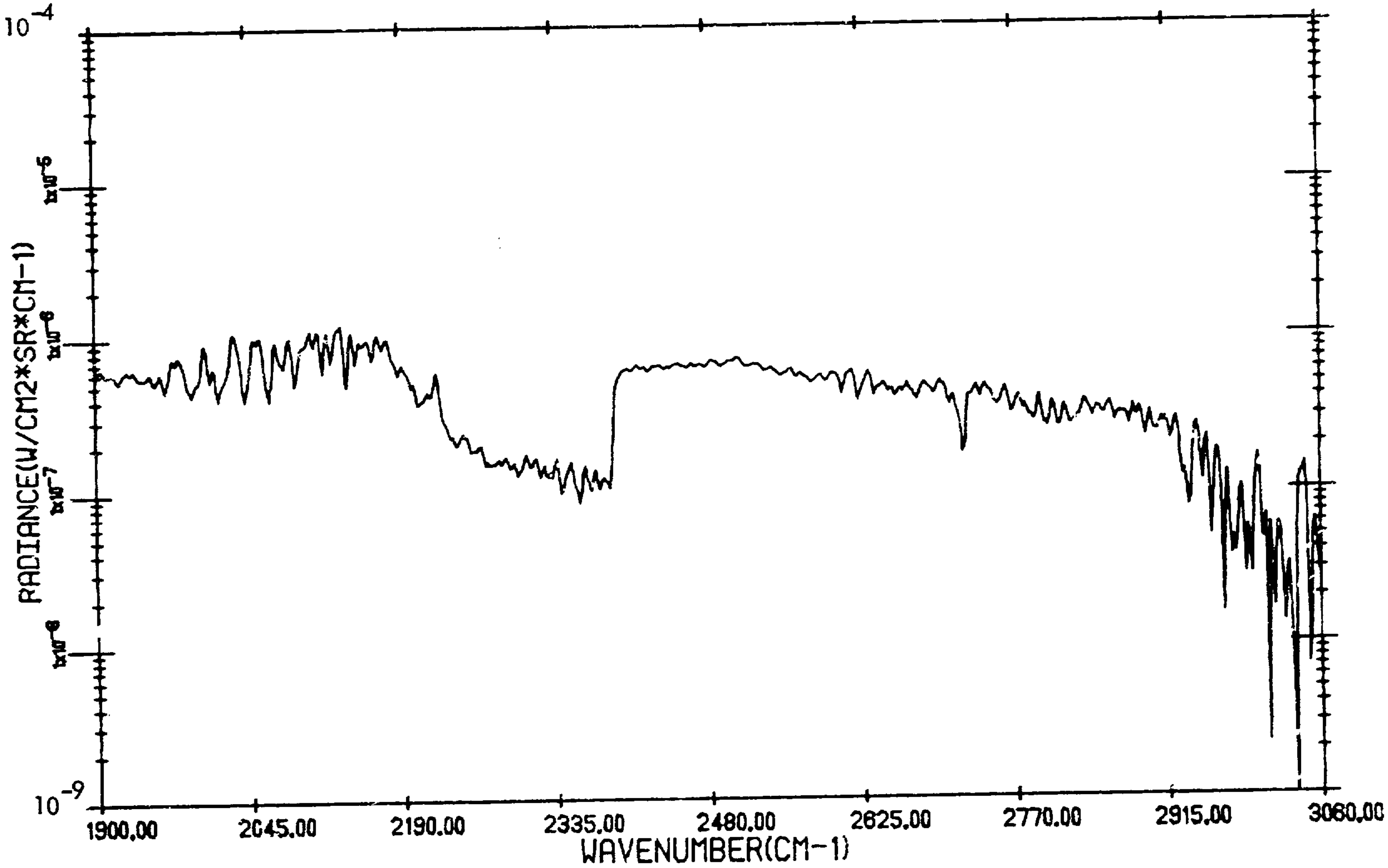

TARGET RADIANCE

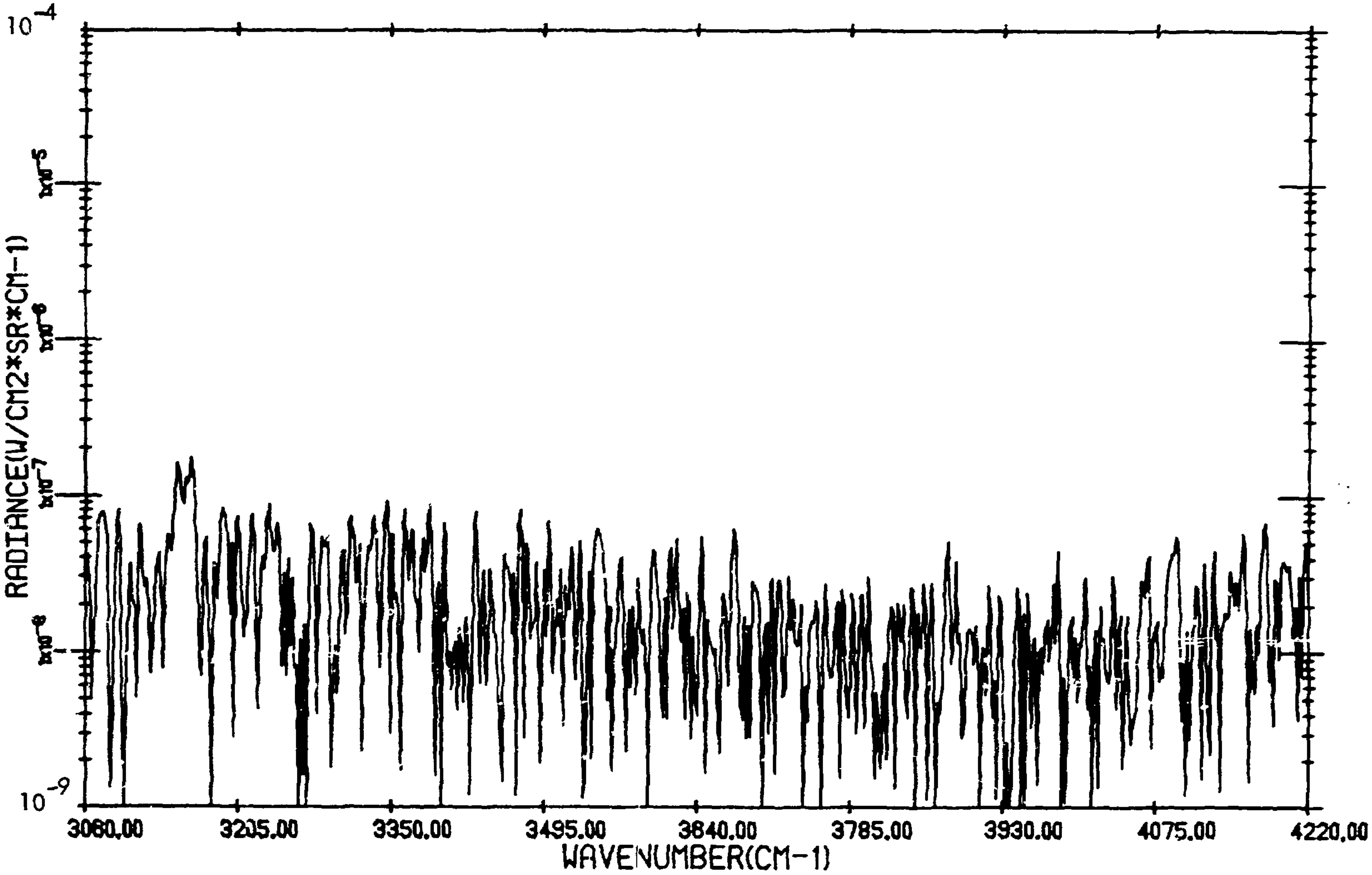

FAIRFIELD, ALABAMA - (815/4) - 13:03:28.9 - GREY BUILDING

TARGET RADIANCE

FAIRFIELD, ALABAMA - (815/4) - 13:03:28.9 - GREY BUILDING

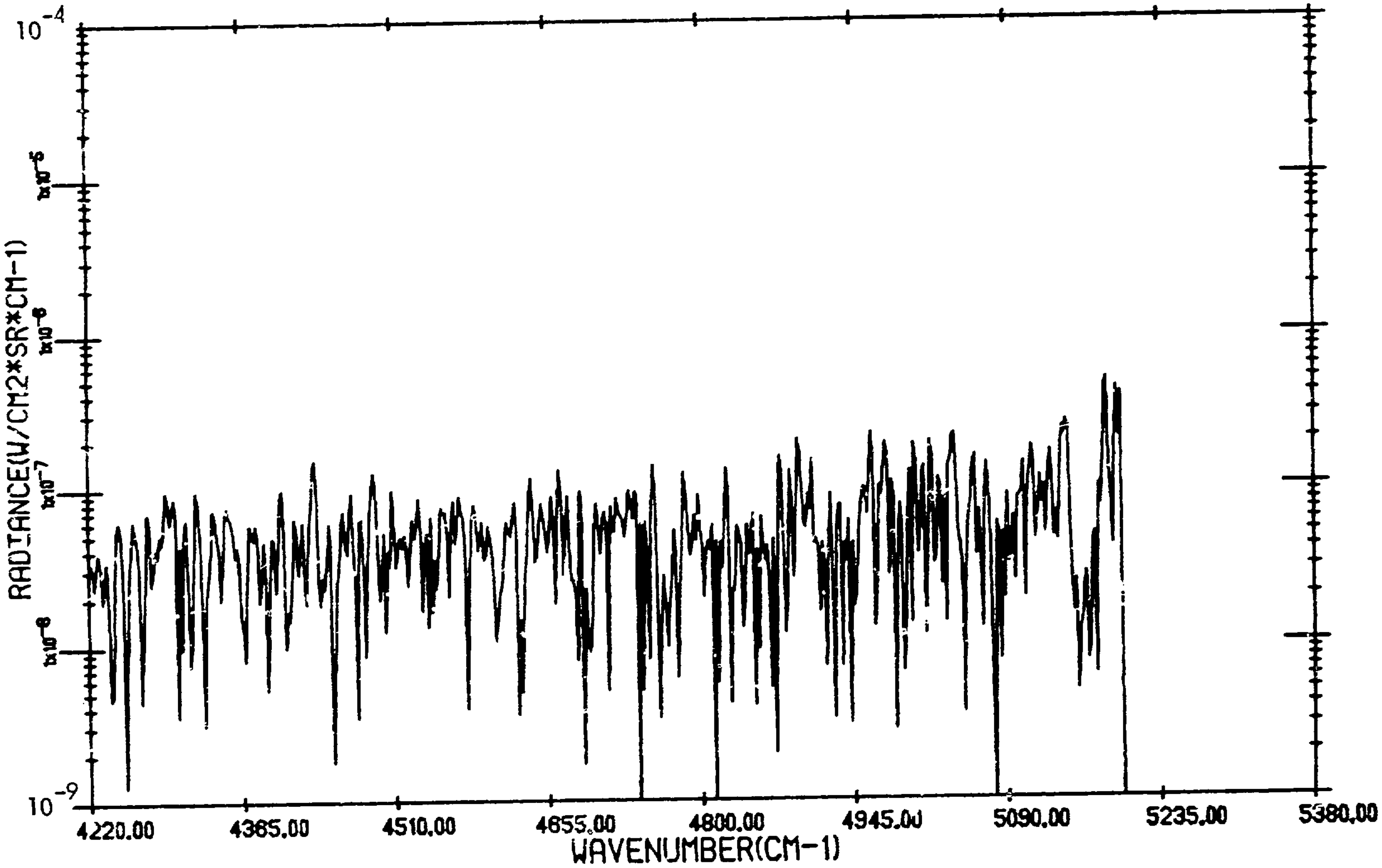

TARGET RADIANCE

(815/4)

FAIRFIELD, ALABAMA - 13:03:28.9 - GREY BUILDING (WITH ATMOSPHERIC TRANSMITTANCE CORRECTION)

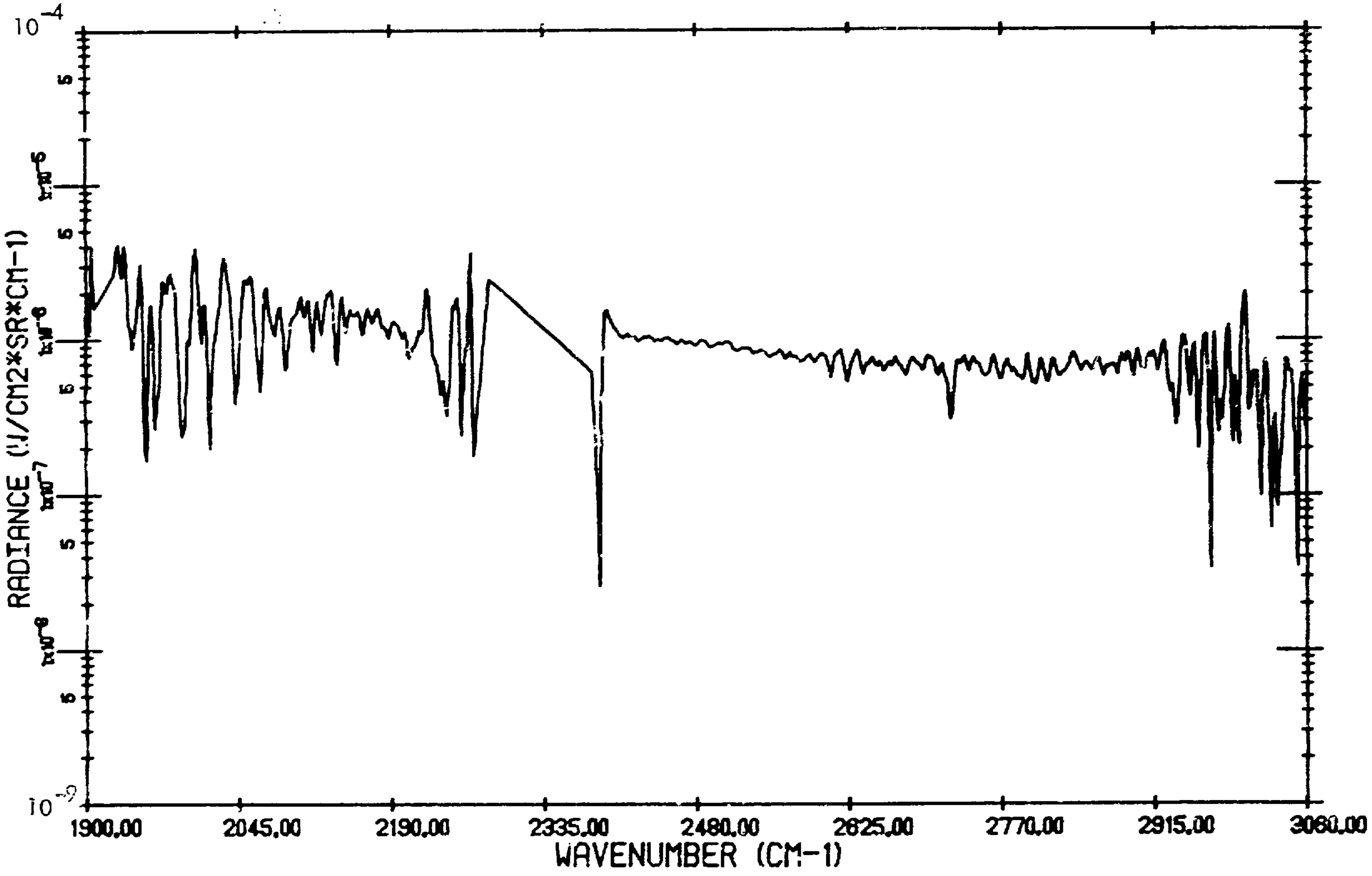

CORRECTED TARGET RADIANCE

FAIRFIELD, ALABAMA (815/4) - 13:07:5.9 - ORANGE HOT METAL

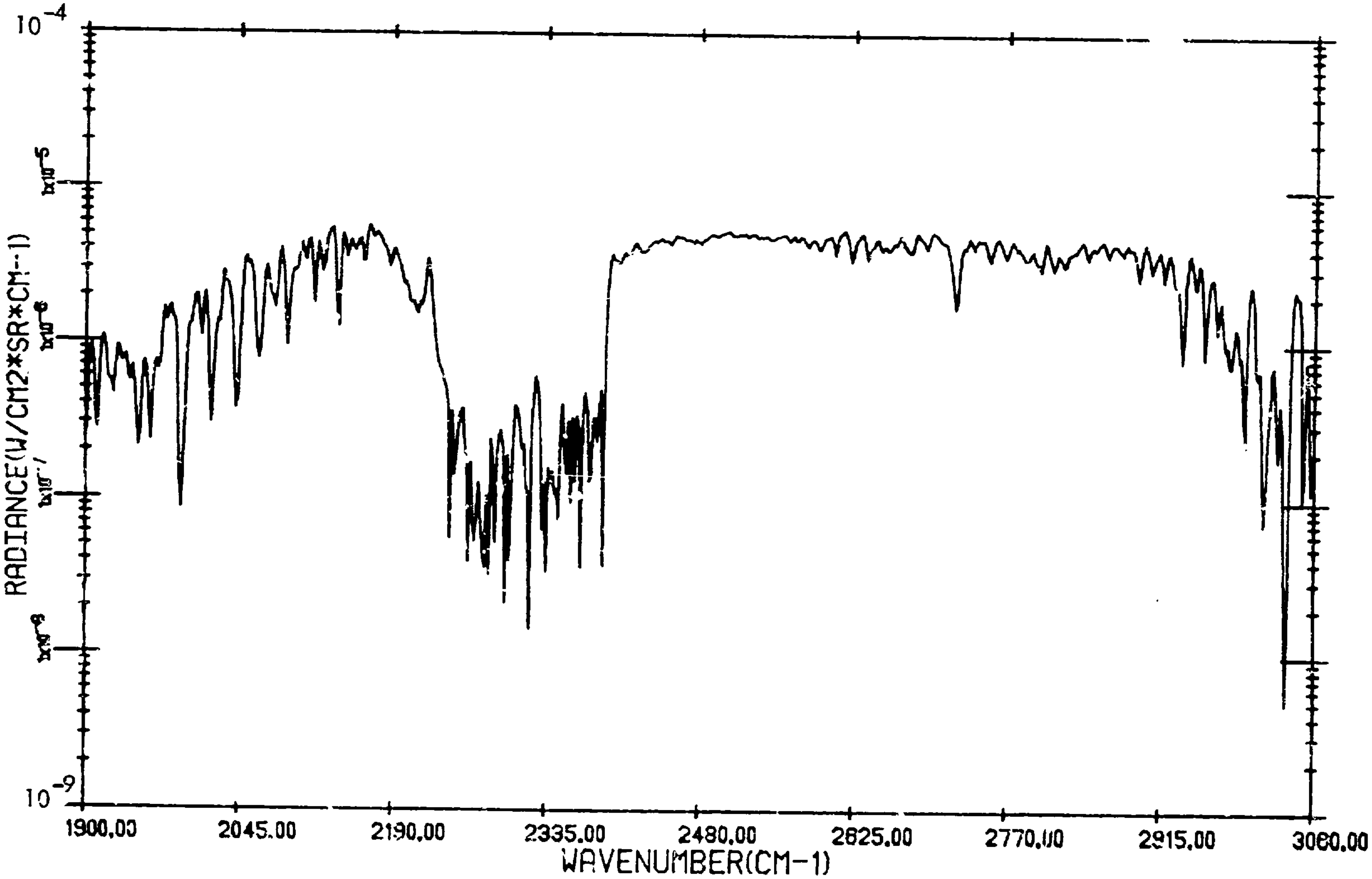

TARGET RADIANCE

FAIRFIELD, ALABAMA - (815/4) - 13:07:5.9 - ORANGE HOT METAL

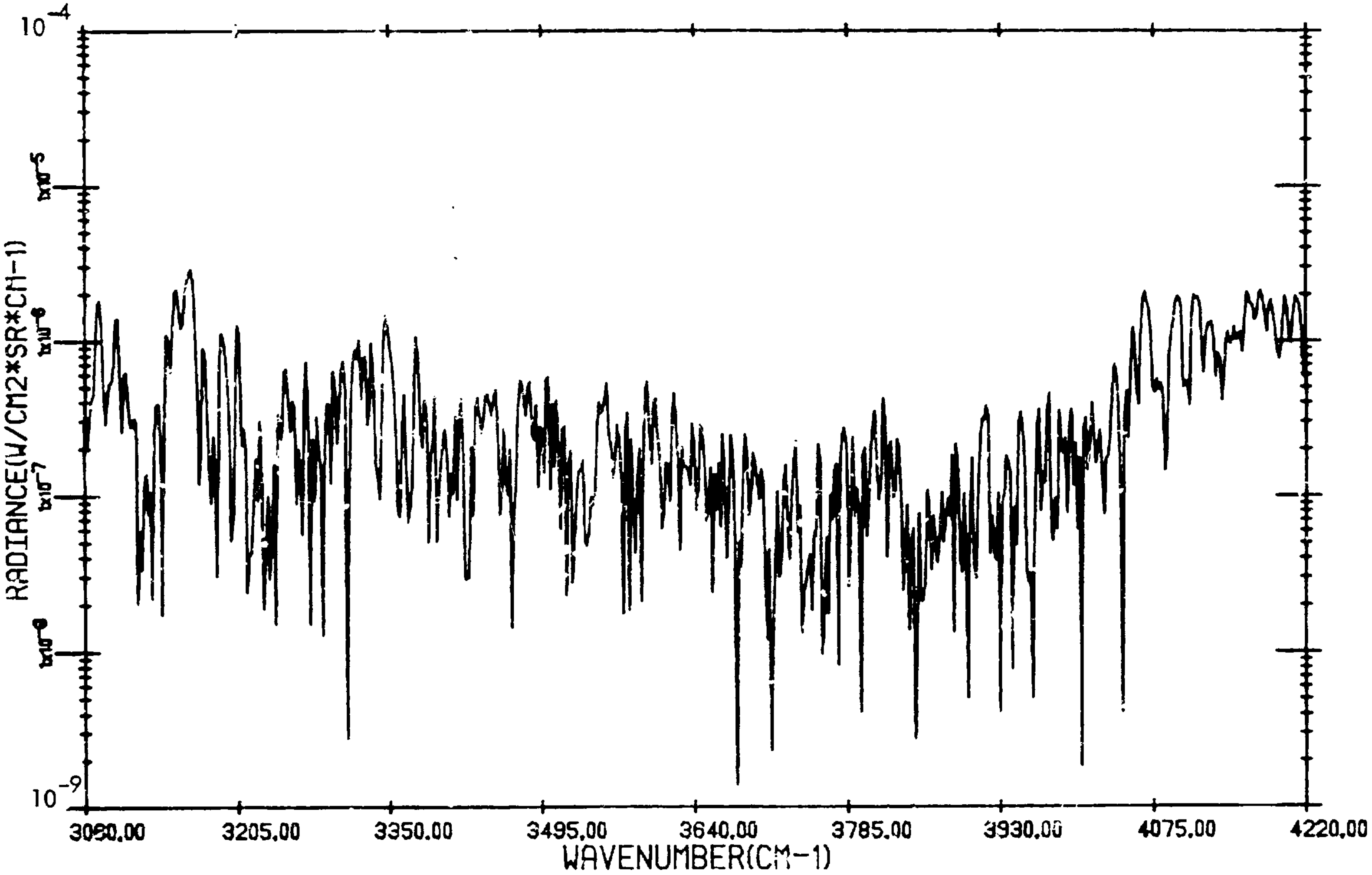

TARGET RADIANCE

FAIRFIELD, ALABAMA - (815/4) - 13:07:5.9 - ORANGE HOT METAL

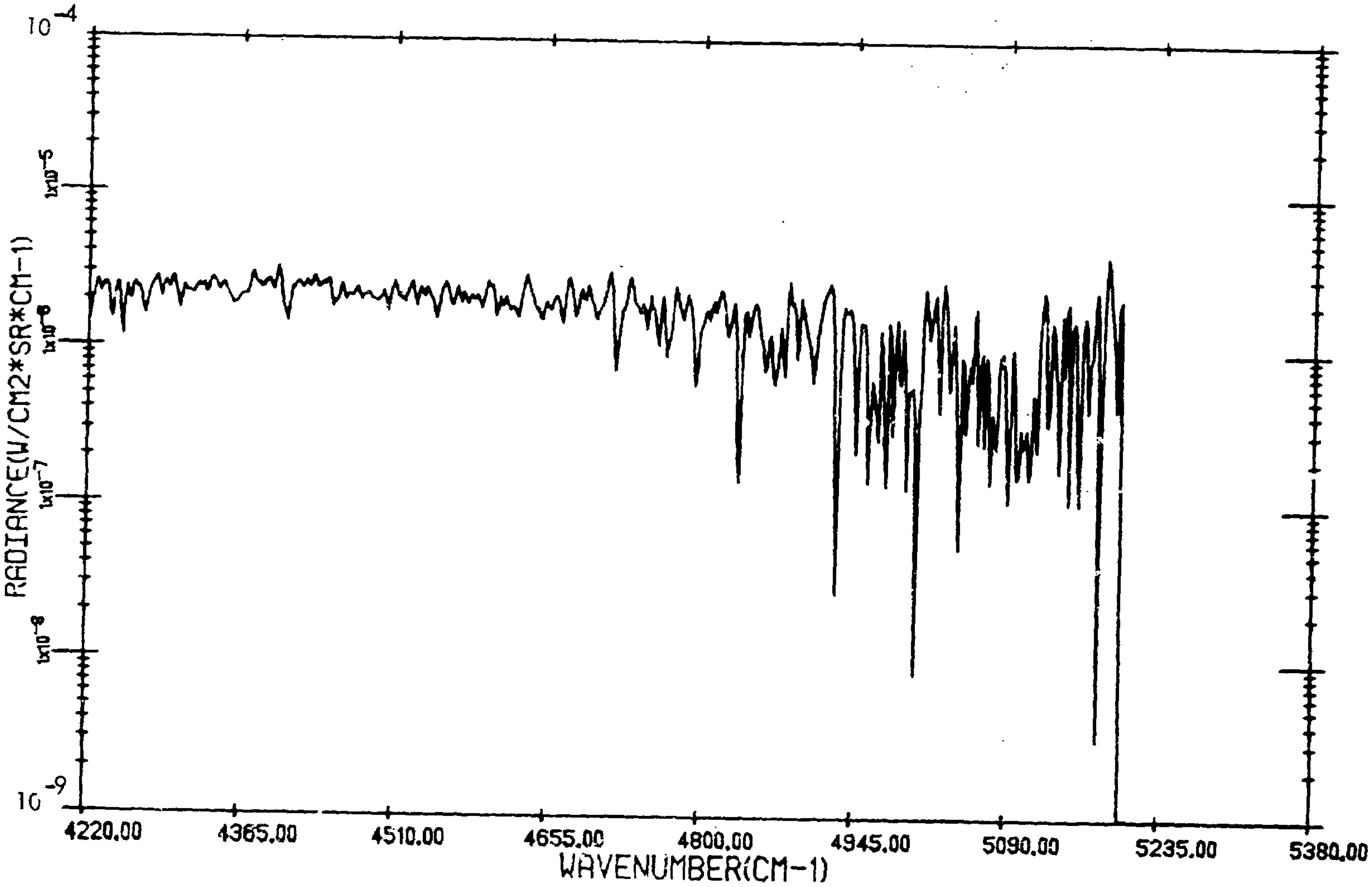

TARGET RADIANCE

(815/4)

FAIRFIELD,ALABAMA - 13:07:5.9 - ORANGE HOT METAL (WITH ATMOSPHERIC TRANSMITTANCE CORRECTION)

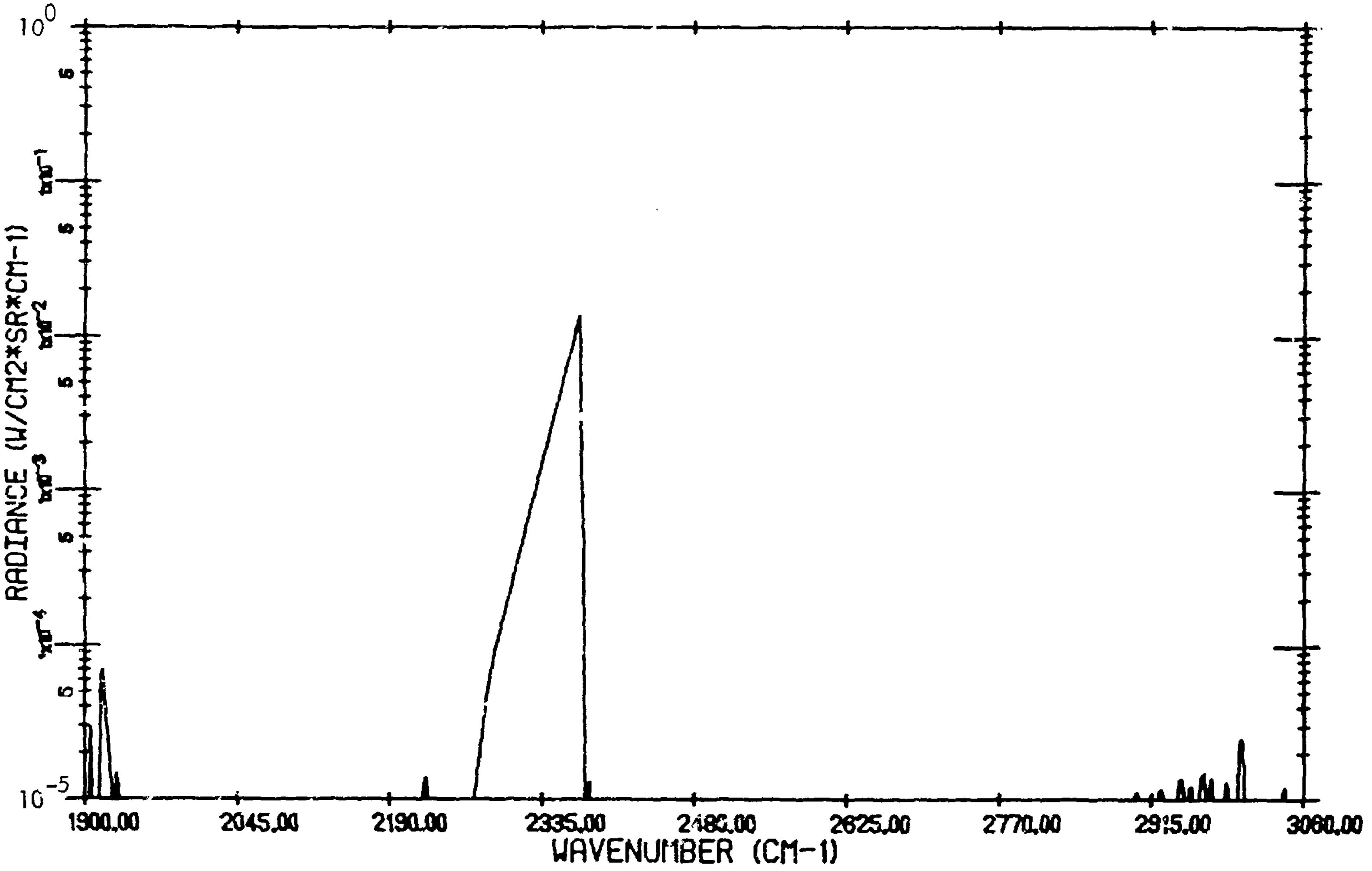

CORRECTED TARGET RADIANCE

ASHLAND, KENTUCKY - (815/2 *) - 11:36:11.8 - BACKGROUND

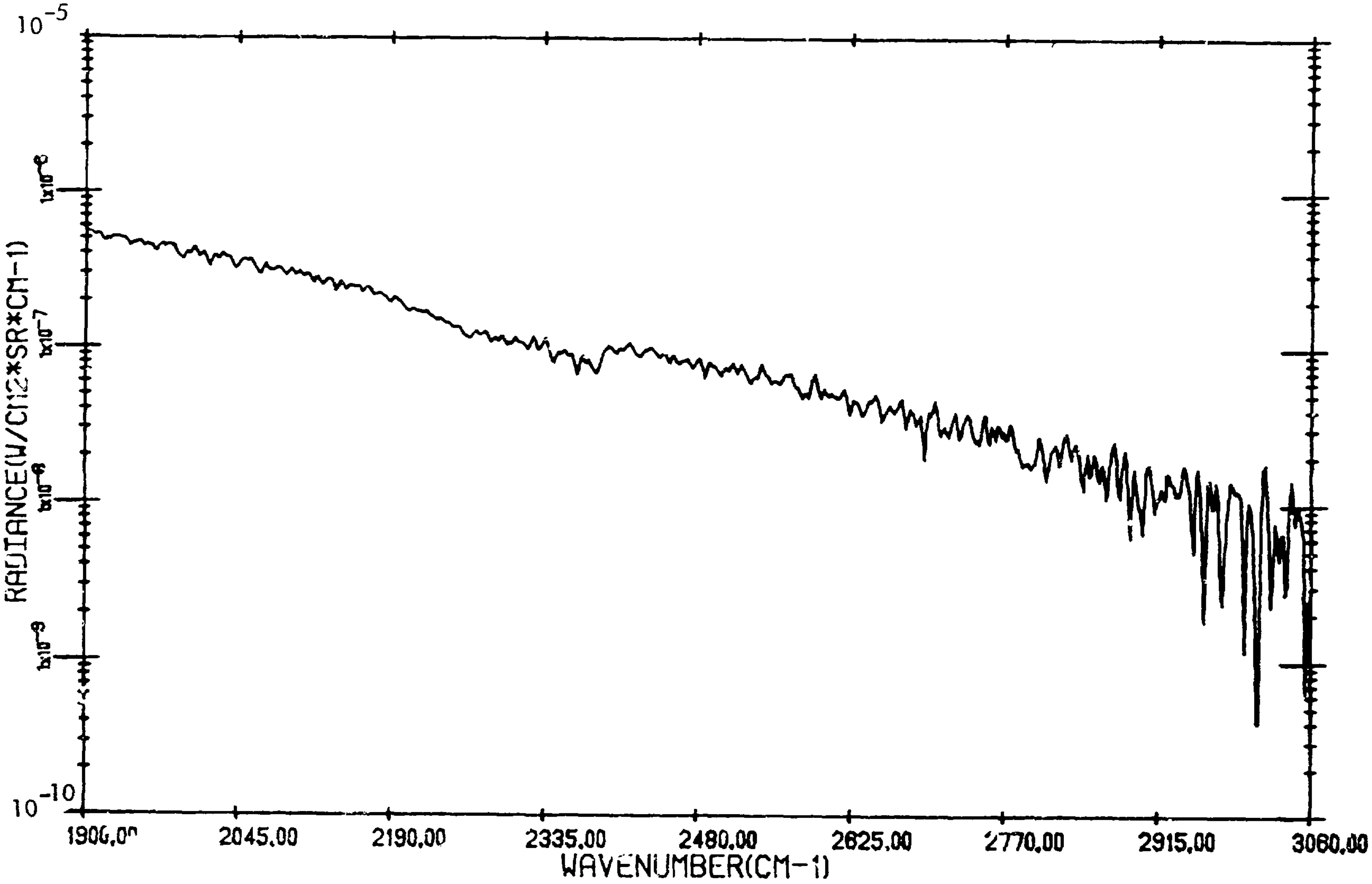

BACKGROUND RADIANCE

ASHLAND, KENTUCKY - (815/2 *) - 11:36:11.8 - BACKGROUND

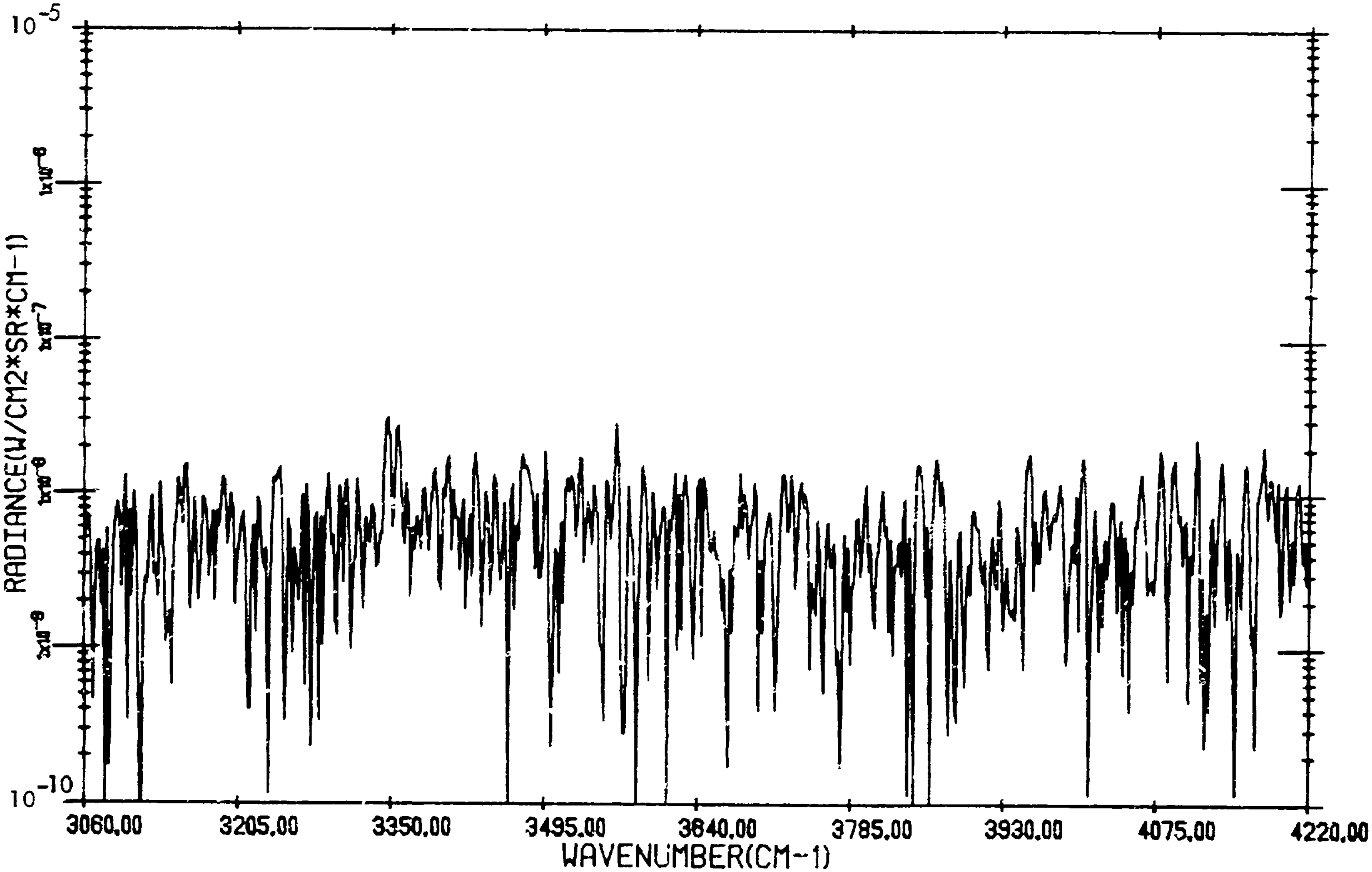

BACKGROUND RADIANCE

AƷHLAND, KENTUCKY - (815/2 *) - 11:36:11.8 - BACKGROUND

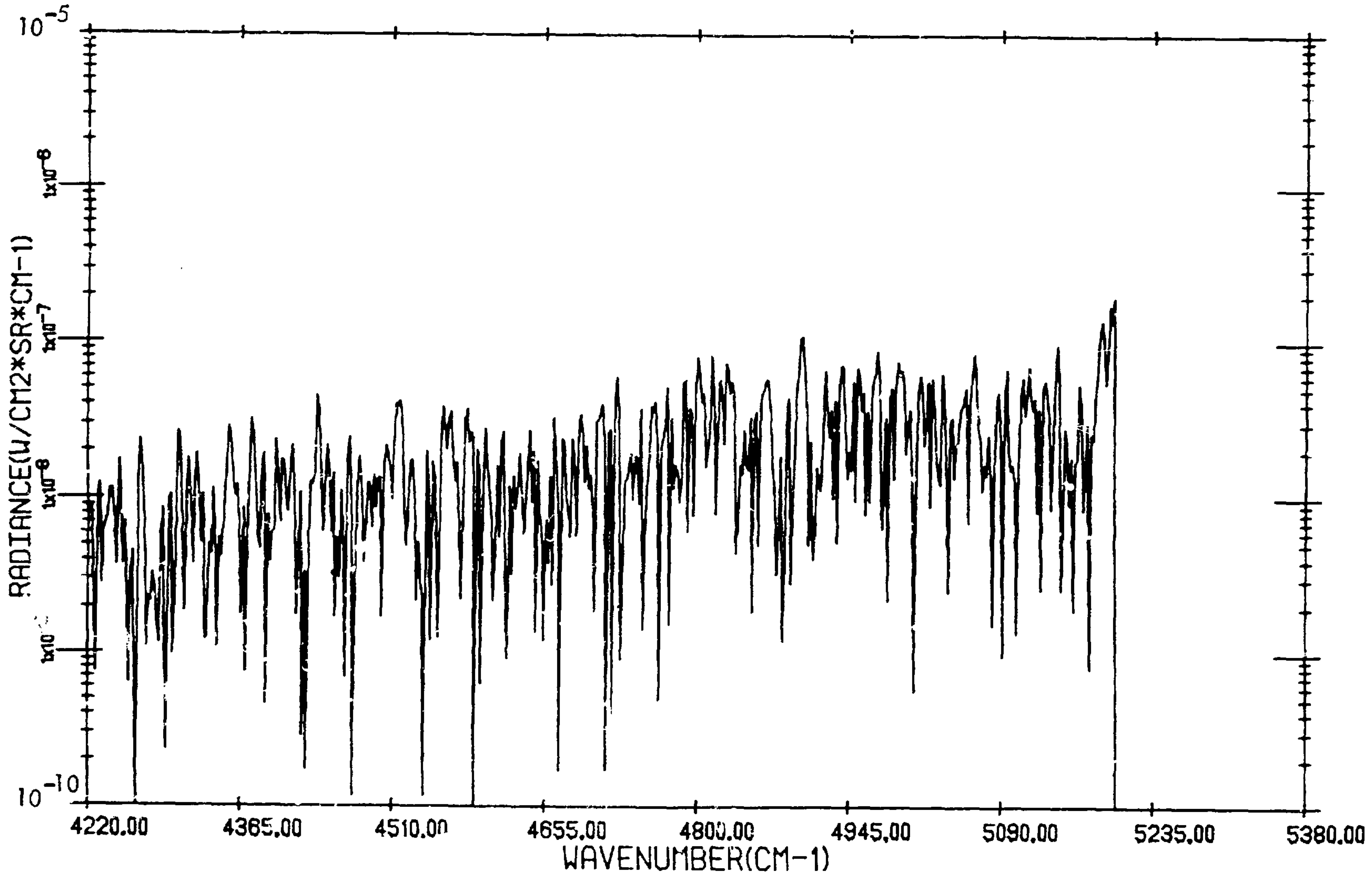

BACKGROUND RADIANCE

(815/2 *)

ASHLAND, KENTUCKY - 11:36:11.8 - BACKGROUND (WITH ATMOSPHERIC TRANSMITTANCE CORRECTION)

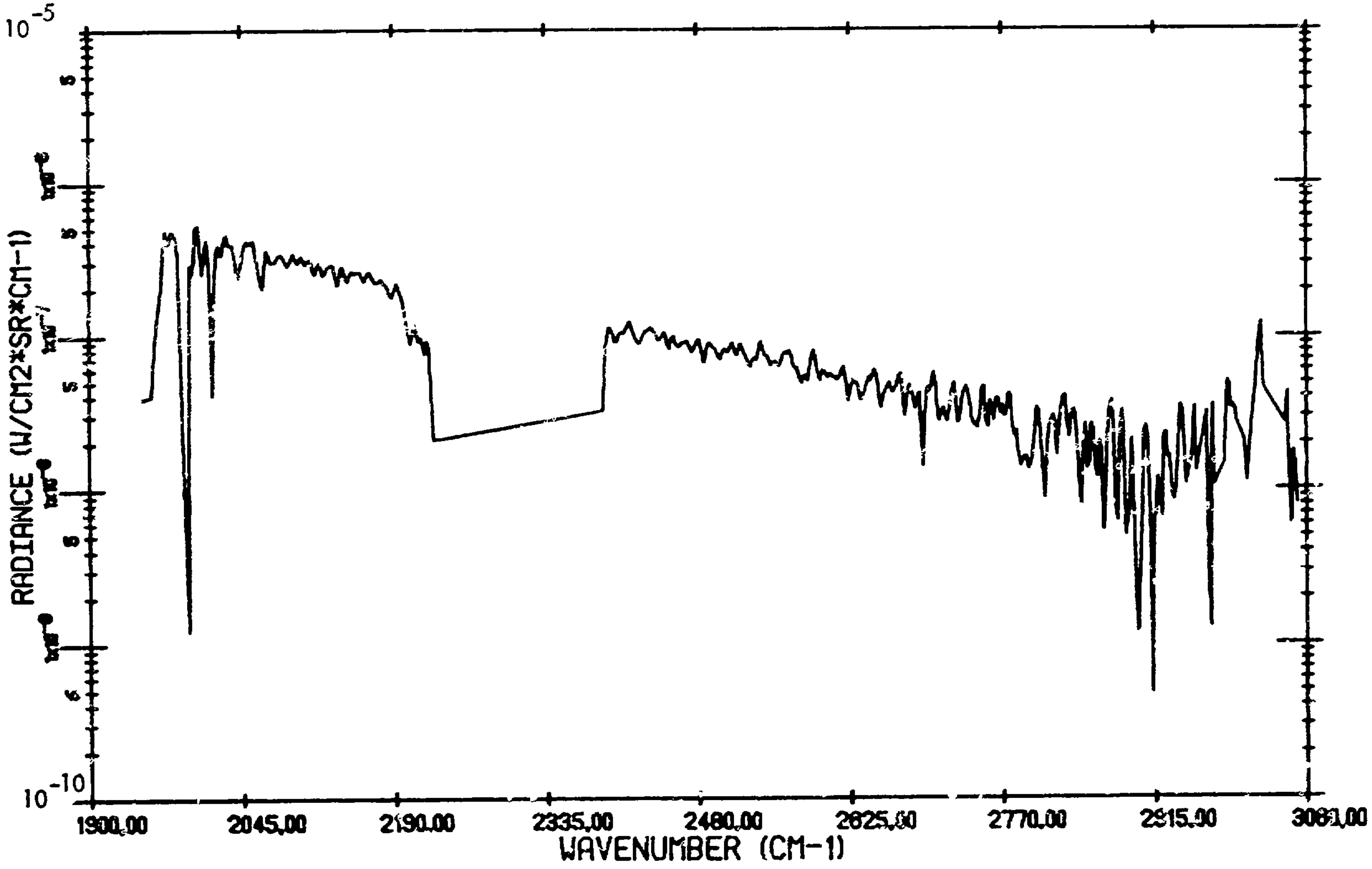

CORRECTED BACKGROUND RADIANCE

ASHLAND, KENTUCKY - (815/2 *) - 11:43:49.2 - REFINERY COMPLEX

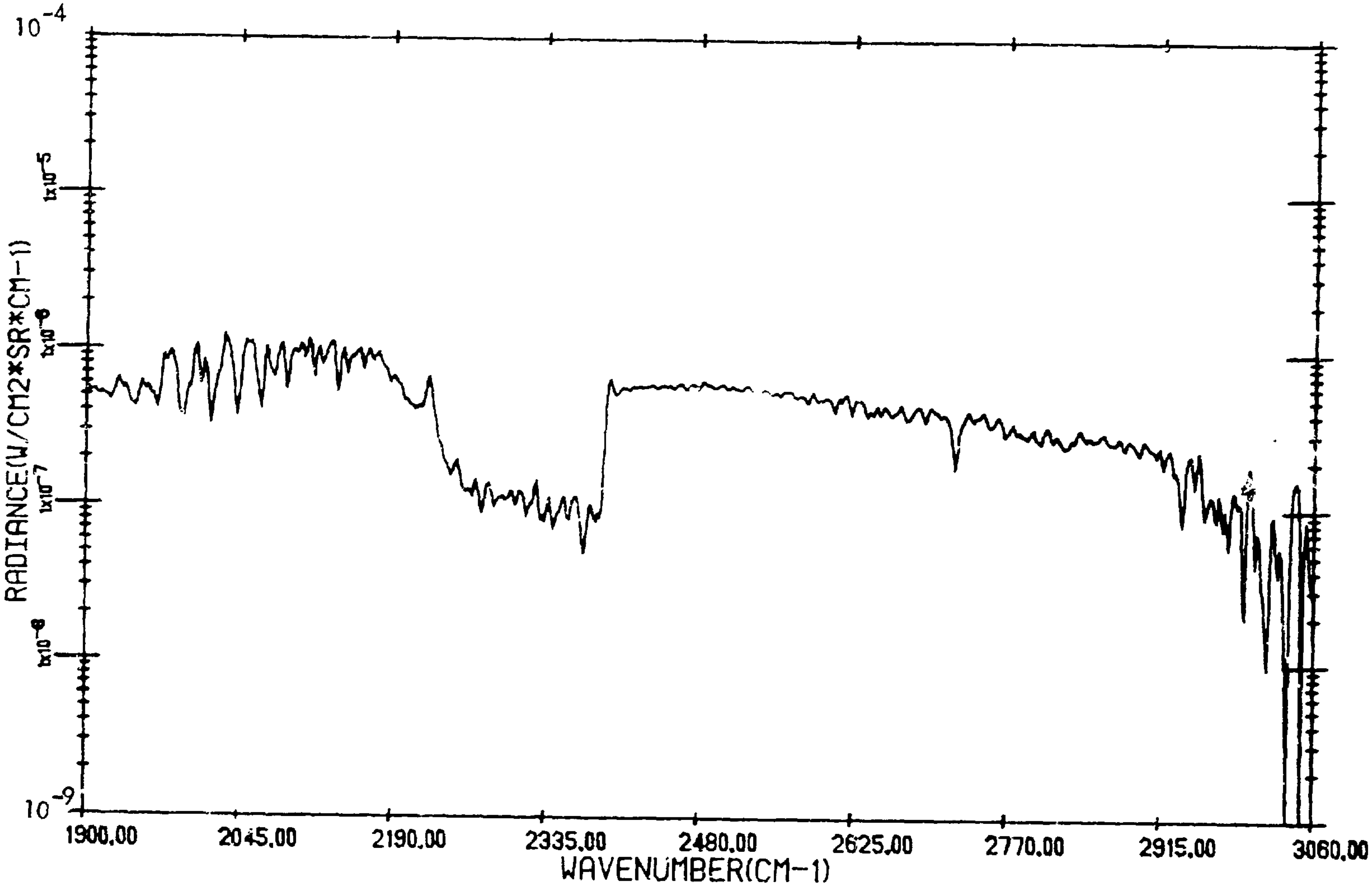

TARGET RADIANCE

ASHLAND, KENTUCKY - (815/2 *) - 11:43:49.2 - REFINERY COMPLEX

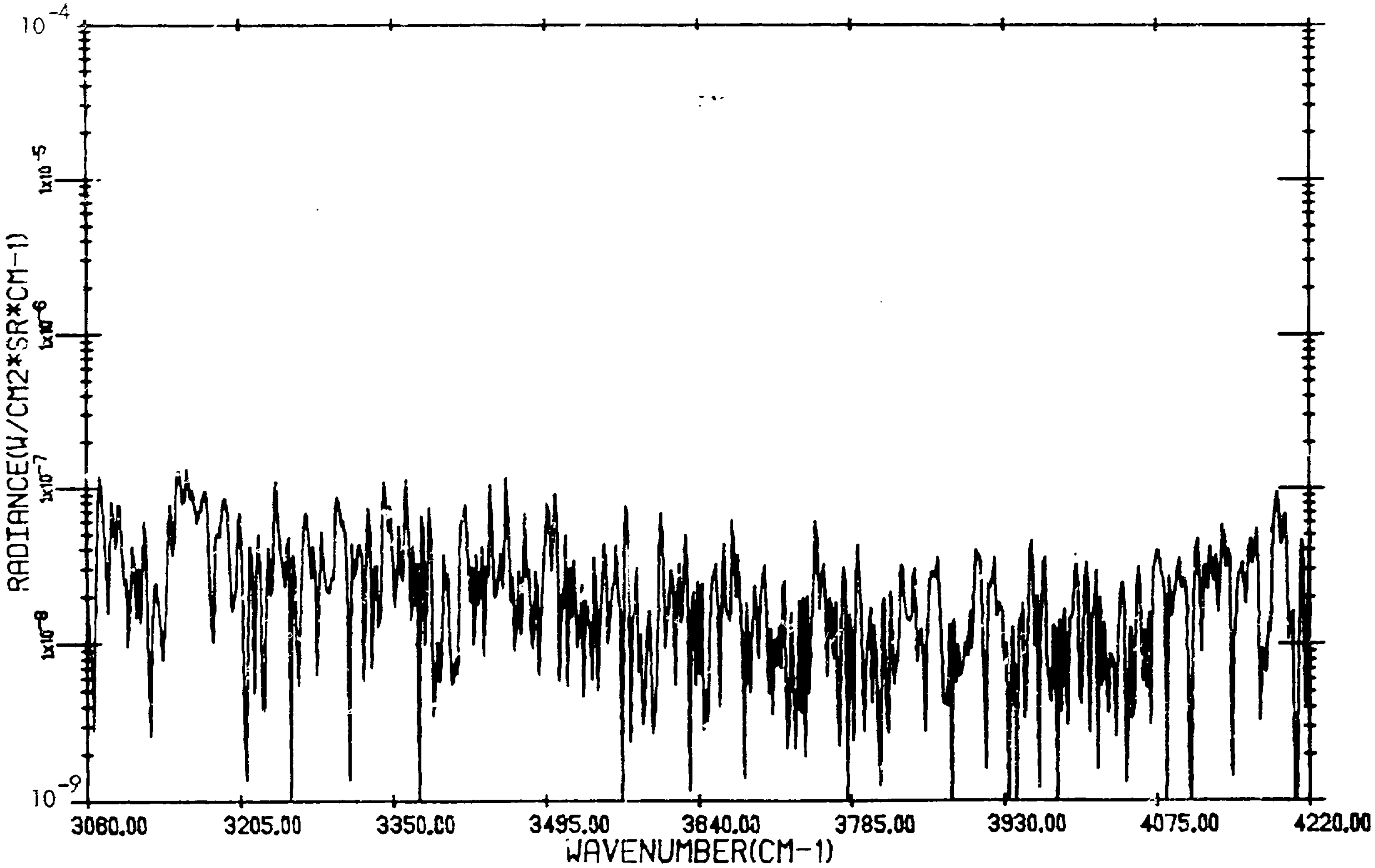

TARGET RADIANCE

ASHLAND, KENTUCKY - (815/2 *) - 11:43:49.2 - REFINERY COMPLEX

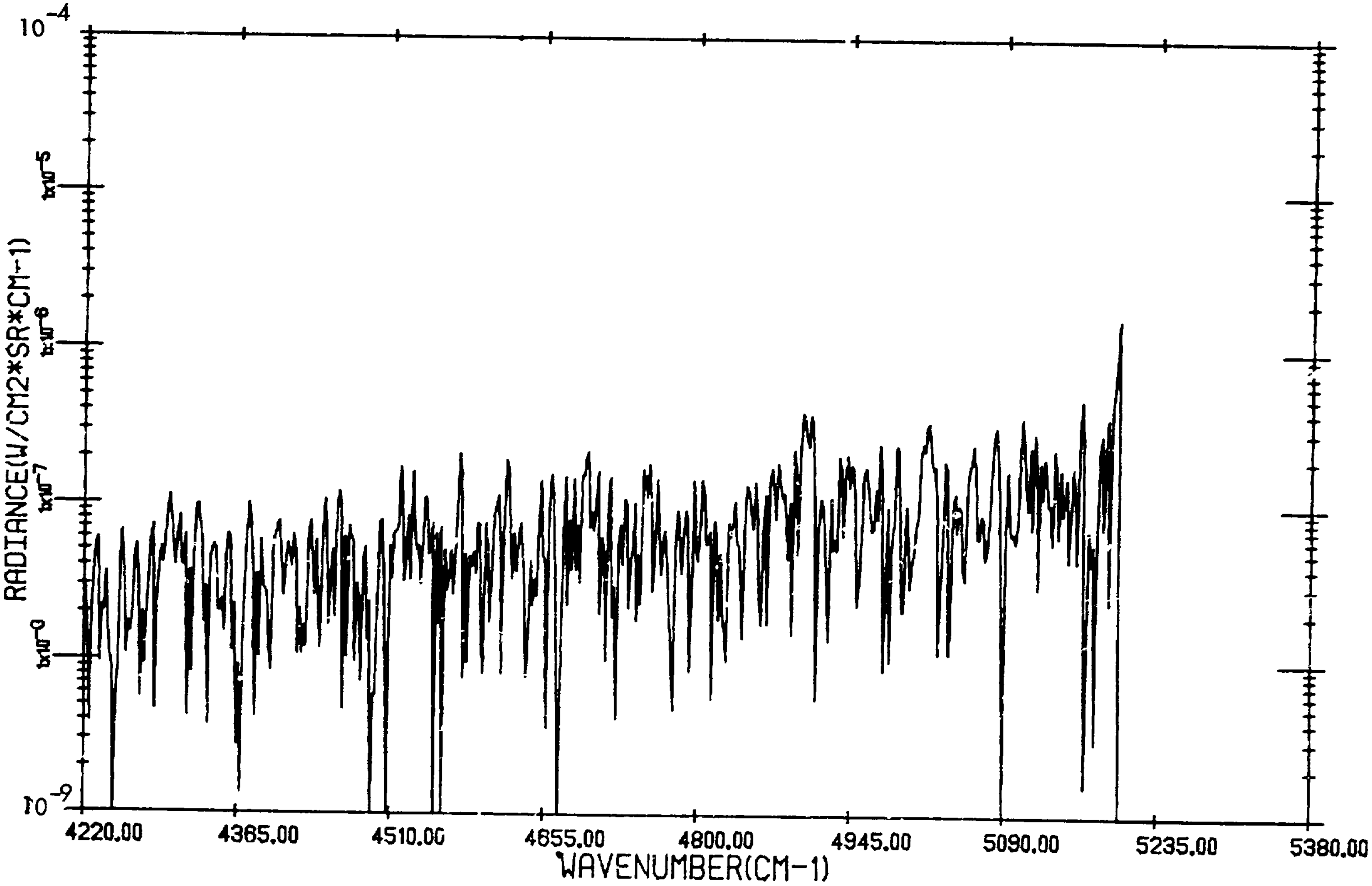

TARGET RADIANCE

(815/2 *)

ASHLAND, KENTUCKY - 11:43:49.2 - REFINERY COMPLEX (WITH ATMOSPHERIC TRANSMITTANCE CORRECTION)

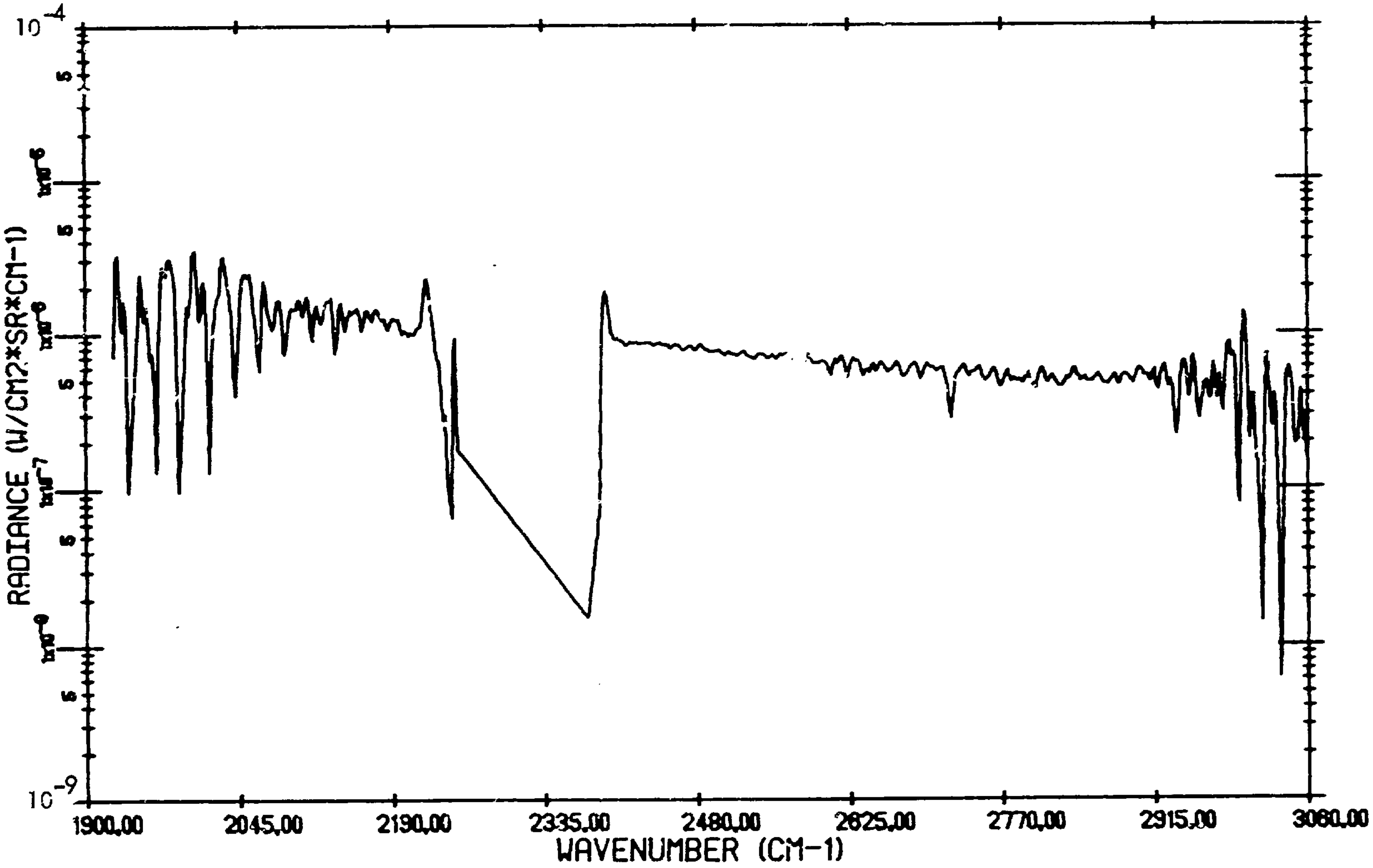

CORRECTED TARGET RADIANCE

APPENDIX E

GRAYBODY TARGET TEMPERATURE DETERMINATION

For a radiating, absorbing (nonscattering) atmosphere, the spectral radiance $L_\nu(\tau)$ at wavenumber ν and optical depth τ is given by

$$L_\nu(\tau) = L_\nu(0)\, e^{-\tau} + e^{-\tau} \int_0^{\tau} B_\nu(\tau')\, e^{\tau'}\, d\tau' \qquad \text{(E-1)}$$

where $B_\nu(\tau)$ is the Planck radiation function at optical depth τ and $L_\nu(0)$ is the radiance at $\tau = 0$. The Planck function is given by

$$B_\nu = \frac{a\nu^3}{e^{b\nu} - 1} \qquad \text{(E-2)}$$

where

$$a = 1.191062 \times 10^{-12}\,\text{Watts/cm}^2\text{-sr-cm}^{-4}$$

and

$$b = \frac{1.438786}{u(K)}$$

where u is the temperature.

If the radiation function $B_\nu(\tau)$ is independent of optical thickness then Equation (E-1) becomes

$$L_\nu(\tau) = L_\nu(0)e^{-\tau} + B_\nu(1 - e^{-\tau}) \qquad \text{(E-3)}$$

or

$$L_\nu(T_\nu) = L_\nu(0)T_\nu + B_\nu(1 - T_\nu) \qquad \text{(E-4)}$$

where T_ν is the spectral transmittance.

If the surface also emits radiation thermally then integrating Equation (E-4) over a narrow spectral band gives

$$\bar{L}_\nu = \varepsilon_\nu B_{\nu s}\bar{T}_\nu + B_{\nu a}(1 - \bar{T}_\nu) \qquad \text{(E-5)}$$

where ε_ν is the emissivity of the surface and $B_{\nu s}$ and $B_{\nu a}$ are the Planck functions for the surface and atmosphere respectively.

Knowing the value of $\bar{L}_\nu$ experimentally one must subtract the path radiance and divide by the transmittance in Equation (E-5) in order to find the surface radiance $\varepsilon_\nu B_{\nu s}$.

Algorithm for Temperature Determination: The spectral radiance for the surface is given by

$$L_\nu = \varepsilon_\nu B_\nu \qquad \text{(E-6)}$$

where we do not know either the emissivity ε_ν or the temperature u. Nevertheless, if we know the radiance L_ν and assume a grey surface, i.e., $\varepsilon_\nu = \varepsilon$ we can find the temperature. The derivative of Equation (E-6) is

$$L'_\nu = c\left[\frac{3a\left(e^{b\nu} - 1\right)\nu^2 - a\nu^3\, be^{b\nu}}{\left(e^{b\nu} - 1\right)^2}\right] \qquad \text{(E-7)}$$

Dividing Equation (E-7) by (E-6) gives

$$\frac{\nu L'}{L\nu} = 3 - \frac{xe^x}{e^x - 1} \qquad \text{(E-8)}$$

where $x = b\nu$. Since the left hand side of Equation (E-8) is known, the right hand side can be solved for x. The temperature is then given by

$$u(K) = \frac{1.438786\nu(\text{cm}^{-1})}{x_o} \qquad \text{(E-9)}$$

where x_o is the solution of Equation (E-8).

Once the effective temperature has been determined using the above algorithm, the emissivity can then be determined by inverting Equation (E-6), i.e.,

$$\epsilon = \frac{L\nu}{B\nu} \qquad \text{(E-10)}$$

APPENDIX F

SMOKE CLOUD EXTINCTION MODEL

Casperson[32] has developed an analytical approximation to the exact Lorentz-Mie treatment of attenuation of light beams propagating through ensembles of spherical particles with complex index of refraction. The general form for his exponential extinction coefficient is

$$\gamma = (\pi a_{max}^2 N_o/n^2) \left[2 (n + 2)(n + 1) + \gamma_1 - \gamma_2 \sin \gamma_3 - \gamma_4 \sin \gamma_5\right]$$

where N_o is the particle number density, a_{max} is the radius at which the particle distribution function peaks, and n is the index for the power-law-exponential particle size distribution function. A typical value of n is 4.6.

The γ_i can be expressed in terms of a normalized wavelength $\lambda' = (nk)^{-1}$ and an absorption coefficient ϕ yielding

$$\gamma_1 (\lambda) = \frac{4n2 \lambda'^2}{(1 + \lambda'^2 \phi^2)} \left[\frac{2}{(1 + \lambda'^2 \phi^2)}^{-1}\right]$$

$$\gamma_2 (\lambda) = \frac{4n(n + 1)\lambda'}{(1 + \lambda'^2 \phi^2)^{1/2}} \left[\frac{n^2 \lambda'^2}{n^2 \lambda'^2 (1 + \phi/n)^2 + 1}\right]^{(n + 2)/2}$$

$$\gamma_3 (\lambda) = (n + 2) \tan^{-1} \left[\frac{1}{n\lambda' (1 + \phi/n)}\right] - \tan^{-1}(\lambda' \phi)$$

$$\gamma_4 (\lambda) = \frac{4n^2 \lambda'}{(1 + \lambda'^2 \phi^2)} \left[\frac{n^2 \lambda'^2}{n^2 \lambda'^2 (1 + \phi/n)^2 + 1}\right]^{(n + 1)/2}$$

$$\gamma_5 (\lambda) = (n + 1) \tan^{-1} \left[\frac{1}{n \lambda' (1 + \phi/n)}\right] - 2 \tan^{-1} (\lambda' /\phi)$$

The absorption coefficient ϕ is related to the exponential amplitude absorption coefficients α_1, outside the sphere and α_2 inside the sphere by

$$\phi = 2a_{max} (\alpha_2 - \alpha_1)$$

The coefficient K is related to the index of refraction of the particle n_2, the index of refraction of the surrounding medium n_1, and the vacuum wavelength λ by

$$nK = 4\pi (n_2 - n_1) a_{max}/\lambda$$

Dalzell & Sarofim have developed explicit expressions for n and k that are appropriate for carbon smokes. Their dispersion model is based upon fitting classical electron theory to room temperature measurement of n and α.

$$n^2 - \alpha^2 = 1 - \left[\frac{F_c e^2/m \varepsilon_o}{g_c^2 + \omega^2}\right] + \sum_j \frac{F_j (\omega_j^2 - \omega^2) e^2/m \varepsilon_o}{(\omega_j^2 - \omega^2) + \omega^2 g_j^2}$$

$$2n\alpha = \left[\frac{F_c g_c e^2/m \varepsilon_o}{(g_c^2 + \omega^2)}\right] + \sum_j \frac{F_j \omega g_j e^2/m \varepsilon_o}{(\omega_j - \omega)^2 + \omega^2 g_j{}^2}$$

In these equations F is the number of effective electrons per unit volume, q is the electron damping constant, ω is the frequency of the radiation, $_j$ is the natural frequency of the j^{th} electron, and $e^2/m \varepsilon_o$ is the square of the electronic charge divided by the mass of the electron and the electric permittivity. Three electrons, two bound (subscript j) and one free (subscript c) were employed to fit the experimental data. The constants used in the final dispersion model for propane soot are presented in Table F.1.

Table F.1

CONSTANTS IN THE DISPERSION MODEL

Electron	F_1 electrons $/m^3$	q, sec^{-1}	ω, sec^{-1}
C	4.06×10^{27}	6.00×10^{15}	...
1	2.60×10^{27}	6.00×10^{15}	1.25×10^{15}
2	2.86×10^{28}	7.25×10^{15}	7.25×10^{15}

REFERENCES

1. B.P. Sandford, et al, Aircraft Signatures in the Infrared 1.2 to 5.5 Micron Region, Volume II: Background Measurements, AFGL-TR-76-0133 (II), 28 June 1976.
2. R.E. Turner, Remote Sensing of Earth Resources, Vol. II, F. Shahrokhi, ed., Selected Papers From the Conference on Earth Resources Observation and Information Analysis Systems, Tullahoma, Tennessee, March, 1973.
3. G.M. Hale and M.R. Querry, Appl. Opt. 12, 555 (1973).
4. J.E.A. Selby, et al, Atmospheric Transmittance/Radiance: Computer Code LOWTRAN 4, AFGL-TR-78-0053, 28 February 1978.
5. S.L. Valley, ed., Handbook of Space of Geophysics and Space Environments, (McGraw-Hill, New York, 1965).
6. B. Sandford, Air Force Geophysics Laboratory, Bedford, Massachusetts, Personal Communication.
7. C. Cox and W. Munk, J. Opt. Soc. Am. 44, 838 (1954).
8. K.S. Krishnan and N.A. Peppers, Optical Techniques for the Measurement of Ocean-Surface Parameters (U), Stanford Research Institute Report SRI 76-0760, November, 1975 (Confidential).
9. M.P. Thekaekara, Solar Electromagnetic Radiation, NASA SP-8005, revised May 1973 (see Section 3.2).
10. W.M. Elsasser, Phys. Rev. 54, 126 (1938).
11. B.H. Winters, S. Silverman and W.S. Benedict, J. Quant. Spectrosc. Radiat. Transfer 4, 527 (1964).
12. D.E. Burch, et al., J. Opt. Soc. Am. 59, 267 (1969).
13. G. Yamamoto, J. Quant. Spectrosc., Radiat. Transfer 9, 371 (1969).
14. R. O'B. Carpenter, Emission and Absorption in the 4.3-μm CO_2 Band, Baird Atomic Final Report, Contract AF19(604)-2405.
15. R.A. McClatchey, et al., AFCRL Atmospheric Absorption Line Parameters Compilation, Air Force Cambridge Research Laboratories Report AFCRL-TR-73-0096 (1973).
16. L.D. Gray, J. Quant. Spectrosc. Radiat. Transfer 5, 569 (1965).
17. I. Gradshteyn and M. Ryzhik, Tables of Integrals, Series and Products, Fourth Edition, (Academic Press, New York, 1965).

18. M. Abramowitz and I. Stegun, Handbook of Mathematical Functions, U.S. Department of Commerce, Applied Mathematics Series 55, June 1964.

19. H. Ory, R&D Associates, Marina Del Rey, California, Personal Communication.

20. G. Yamamoto, M. Tanaka and T. Aoki, J. Quant. Spectrosc. Radiat. Transfer 9, 371 (1969).

21. D.E. Burch and D.A. Gryvnak, Laboratory Measurements of the IR Absorption by H_2O and CO_2 in Regions of Weak Absorption, Proceedings of the Society of Photo-Optical Instrumentation Engineers, Vol. 142, Optical Properties of the Atmosphere, March 1978, Washington D.C.

22. William Herget, Environmental Science Research Lab, EPA, Personal Communications.

23. S.J. Young, Description and Use of the Plume Radiation Code ATLES, SAMSO—TR—77-100, 13 May 1977.

24. W.J. Barrett, et al., Infrared Spectral Studies of Agent, and Field Contaminants, Southern Research Institute, Report 24, 1969.

25. T.Y. Palmer, Absorption by Smoke Particles of Thermal Radiation in Large Fires, J. Fire & Flammability 7 460 (1976).

26. S.N. Hirsch, R.F. Kruckeberg, and F.H. Madden, The Bispectral Forest Fire Detection System, Proceedings of the Seventh Internation Symposium on Remote Sensing of the Environment, Willow Run Laboratory Report 10259-1-X, pages 2253—2272, 17-21 May, 1971.

27. P.H. Thomas, The Size of Flames from Natural Fires, Ninth Symposium on Combustion, Ithaca, 1962 (Academic Press, New York, 1963).

28. B.R. Morton, G. Taylor and J.S. Turner, Turbulent Gravitational Convention from Maintained & Instantaneous Sources, Proceedings of the Royal Society, 234A: 1 (1956).

29. L.W. Casperson, Light Extinction in Polydisperse Particulate Systems, Appl. Opt. 16: 3183 (1977).

30. W.H. Dalzell and A.F. Sarofim, Optical Constants of Soot and Their Application to Heat Flux Calculation, Trans. ASME Journal of Heat Transfer, 100 (1969).

31. H. Pardes, Compendium of Muzzle Flash and Shellburst Data, USAECOM, Fort Monmouth, N.J.

32. D. Robertson, et. al., Munitions Signatures: Review and Recommendations, Aerodyne Research, ARI—RN—100, 1977.

33. A.J. LaRocca, et al., *Radiometric Measurements of Muzzle Flash*, Univ. of Mich., WRL, TR-1852-9-F, July 1969.

34. F.G. Smith, et al., *DF and CO_2 Laser Performance Through Battlefield Aerosols and DF Laser Device Molecular Absorption Coefficients*, Science Applications, Inc., SAI-76-012-A, 1976.

35. M. Milham, *A. Catalog of Optical Extinction Data for Various Aerosol/Smokes*, Edgewood Arsenal, APG, MD.

36. H.R. Carlon and D.H. Anderson, *Aerosol Spectroscopy in the Infrared*, Paper presented at U.S. Army Science Conference, June 1976.

37. G.C. Holst, E.W. Stubing and R.W. Doherty, *Image and Laser Screening by Tactical Smoke*, Paper presented at the DoD Low Power Laser Conference, April 1976.

38. W.L. Morgan and R.L. Spellicy, *Measurements Program for Oil Slick Characteristics*, Interim and Final Reports, 2766-5-P and 2766-7-F, Willow Run Laboratories, the University of Michigan, October 1969.

39. R.L. Sitton, et al., *Effects of Tactical Aerosols on Laser Beam Propagation*, USAMICOM, RE-TR-72-6, 1972.

☆U.S. Government Printing Office: 1979 — 657-002/722